

EXPLORING VOLCANIC PAROXYSMAL EXPLOSIVE ACTIVITY FROM MAGMA SOURCE TO GROUND AND ATMOSPHERE

EDITED BY: Sonia Calvari, Alessandro Bonaccorso, Clive Oppenheimer and
Letizia Spampinato

PUBLISHED IN: *Frontiers in Earth Science*



frontiers

Frontiers Copyright Statement

© Copyright 2007-2019 Frontiers Media SA. All rights reserved.

All content included on this site, such as text, graphics, logos, button icons, images, video/audio clips, downloads, data compilations and software, is the property of or is licensed to Frontiers Media SA ("Frontiers") or its licensees and/or subcontractors. The copyright in the text of individual articles is the property of their respective authors, subject to a license granted to Frontiers.

The compilation of articles constituting this e-book, wherever published, as well as the compilation of all other content on this site, is the exclusive property of Frontiers. For the conditions for downloading and copying of e-books from Frontiers' website, please see the Terms for Website Use. If purchasing Frontiers e-books from other websites or sources, the conditions of the website concerned apply.

Images and graphics not forming part of user-contributed materials may not be downloaded or copied without permission.

Individual articles may be downloaded and reproduced in accordance with the principles of the CC-BY licence subject to any copyright or other notices. They may not be re-sold as an e-book.

As author or other contributor you grant a CC-BY licence to others to reproduce your articles, including any graphics and third-party materials supplied by you, in accordance with the Conditions for Website Use and subject to any copyright notices which you include in connection with your articles and materials.

All copyright, and all rights therein, are protected by national and international copyright laws.

The above represents a summary only. For the full conditions see the Conditions for Authors and the Conditions for Website Use.

ISSN 1664-8714

ISBN 978-2-88963-133-9

DOI 10.3389/978-2-88963-133-9

About Frontiers

Frontiers is more than just an open-access publisher of scholarly articles: it is a pioneering approach to the world of academia, radically improving the way scholarly research is managed. The grand vision of Frontiers is a world where all people have an equal opportunity to seek, share and generate knowledge. Frontiers provides immediate and permanent online open access to all its publications, but this alone is not enough to realize our grand goals.

Frontiers Journal Series

The Frontiers Journal Series is a multi-tier and interdisciplinary set of open-access, online journals, promising a paradigm shift from the current review, selection and dissemination processes in academic publishing. All Frontiers journals are driven by researchers for researchers; therefore, they constitute a service to the scholarly community. At the same time, the Frontiers Journal Series operates on a revolutionary invention, the tiered publishing system, initially addressing specific communities of scholars, and gradually climbing up to broader public understanding, thus serving the interests of the lay society, too.

Dedication to Quality

Each Frontiers article is a landmark of the highest quality, thanks to genuinely collaborative interactions between authors and review editors, who include some of the world's best academicians. Research must be certified by peers before entering a stream of knowledge that may eventually reach the public - and shape society; therefore, Frontiers only applies the most rigorous and unbiased reviews.

Frontiers revolutionizes research publishing by freely delivering the most outstanding research, evaluated with no bias from both the academic and social point of view. By applying the most advanced information technologies, Frontiers is catapulting scholarly publishing into a new generation.

What are Frontiers Research Topics?

Frontiers Research Topics are very popular trademarks of the Frontiers Journals Series: they are collections of at least ten articles, all centered on a particular subject. With their unique mix of varied contributions from Original Research to Review Articles, Frontiers Research Topics unify the most influential researchers, the latest key findings and historical advances in a hot research area! Find out more on how to host your own Frontiers Research Topic or contribute to one as an author by contacting the Frontiers Editorial Office: researchtopics@frontiersin.org

EXPLORING VOLCANIC PAROXYSMAL EXPLOSIVE ACTIVITY FROM MAGMA SOURCE TO GROUND AND ATMOSPHERE

Topic Editors:

Sonia Calvari, Istituto Nazionale di Geofisica e Vulcanologia, Italy

Alessandro Bonaccorso, Istituto Nazionale di Geofisica e Vulcanologia, Italy

Clive Oppenheimer, University of Cambridge, United Kingdom

Letizia Spampinato, Istituto Nazionale di Geofisica e Vulcanologia, Italy



Image: Il Nido dell'Etna.

Photo of the 5 January 2012 paroxysm occurred at Etna volcano, kindly donated by "Il nido dell'Etna" hotel in Linguaglossa, showing the lava fountain at the base of the image (in red) and the eruptive column and plume rising from the New SE Crater and reaching an estimated height of more than 9 km above sea level. The view is from Linguaglossa, North-East base of the volcano.

Paroxysmal explosive activity is one of the most spectacular natural phenomena, which is recognized as having strong impact not only at a local scale but whose effects can also reach far areas and, indeed, can significantly affect the atmosphere, and the environment in the overall. The most devastating and recent example occurred in 2010, when the Icelandic Eyjafjallajökull volcano erupted disrupting air traffic all over Europe and the North Atlantic for weeks. Between 2008 and 2013, the long-lasting eruption of Chaitén volcano in Chile produced plumes 14–20 km high reaching the coast of Argentina and causing ash fallout as far as 800 km from the vent, and the continuously erupting volcanoes of the Kamchatka Peninsula and of the Aleutian arc have caused often treats to air traffic. The eruption of Pinatubo (Philippines) in 1991 had a strong impact all over the globe, causing significant and measurable atmospheric perturbation and impacting the world temperature. More recently, Mount Etna in Italy displayed tens of paroxysmal explosive episodes affecting the air traffic, viability, settlements, environment, and economics.

Over time, several studies have been devoted to understanding what drives paroxysmal explosive activity. Owing to the treating characteristics, so far great efforts have been made trying to detect precursory signals, parameterize the phenomena, apply conceptual and experimental models, and assess the associated hazards. Published papers have used (i) geophysical data aimed at constraining the source region (depth, size, and position), (ii) gas chemistry and mineral geochemistry and petrology to identify the driving force of explosions and characterize the nature of the involved magmas, (iii) volcanology data and observations as well as ground-based and satellite remote sensing to quantify the volumes of erupted products and track the eruptive process, and (iv) laboratory experiments and plume models to characterize the rheology of the erupted products and forecast the impact of the eruptive clouds on the environment, climate, and the whole planet. In this book, we present a collection of ten papers written by 67 authors spanning from seismicity and ground deformation to geochemistry, volcanology and other geophysical techniques applied to the characterization of paroxysms at several active volcanoes.

Citation: Calvari, S., Bonaccorso, A., Oppenheimer, C., Spampinato, L., eds. (2019). Exploring Volcanic Paroxysmal Explosive Activity From Magma Source to Ground and Atmosphere. Lausanne: Frontiers Media. doi: 10.3389/978-2-88963-133-9

Table of Contents

- 06 Editorial: Exploring Volcanic Paroxysmal Explosive Activity From Magma Source to Ground and Atmosphere**
Sonia Calvari, Alessandro Bonaccorso, Clive Oppenheimer and Letizia Spampinato
- 09 An Overview of the Dynamics of the Volcanic Paroxysmal Explosive Activity, and Related Seismicity, at Andesitic and Dacitic Volcanoes (1960–2010)**
Vyacheslav M. Zobin
- 25 Coupled Short- and Medium-Term Geophysical Signals at Etna Volcano: Using Deformation and Strain to Infer Magmatic Processes From 2009 to 2017**
Marco Aloisi, Alessandro Bonaccorso, Flavio Cannavò and Gilda M. Currenti
- 38 Mapping Volcanic Deposits of the 2011–2015 Etna Eruptive Events Using Satellite Remote Sensing**
Gaetana Ganci, Annalisa Cappello, Giuseppe Bilotta, Alexis Herault, Vito Zago and Ciro Del Negro
- 50 Understanding the SO₂ Degassing Budget of Mt Etna's Paroxysms: First Clues From the December 2015 Sequence**
Roberto D'Aleo, Marcello Bitetto, Dario Delle Donne, Mauro Coltelli, Diego Coppola, Brendan McCormick Kilbride, Emilio Pecora, Maurizio Ripepe, Lois Claire Salem, Giancarlo Tamburello and Alessandro Aiuppa
- 73 Mass Eruption Rates of Tephra Plumes During the 2011–2015 Lava Fountain Paroxysms at Mt. Etna From Doppler Radar Retrievals**
Valentin Freret-Logeril, Franck Donnadieu, Simona Scollo, Ariel Provost, Patrick Fréville, Yannick Guéhenneux, Claude Hervier, Michele Prestifilippo and Mauro Coltelli
- 89 First Volcanic Plume Measurements by an Elastic/Raman Lidar Close to the Etna Summit Craters**
Antonella Boselli, Simona Scollo, Giuseppe Leto, Ricardo Zanmar Sanchez, Alessia Sannino, Xuan Wang, Mauro Coltelli and Nicola Spinelli
- 101 Tephra From the 3 March 2015 Sustained Column Related to Explosive Lava Fountain Activity at Volcán Villarrica (Chile)**
Jorge E. Romero, Franco Vera, Margherita Polacci, Daniele Morgavi, Fabio Arzilli, Mohammad Ayaz Alam, Jorge E. Bustillos, Alicia Guevara, Jeffrey B. Johnson, José L. Palma, Mike Burton, Evelyn Cuenca and Werner Keller
- 115 Magma Budget From Lava and Tephra Volumes Erupted During the 25–26 October 2013 Lava Fountain at Mt Etna**
Daniele Andronico, Boris Behncke, Emanuela De Beni, Antonino Cristaldi, Simona Scollo, Manuela Lopez and Maria D. Lo Castro

- 131** *Assessing Impact to Infrastructures Due to Tephra Fallout From Öraefajökull Volcano (Iceland) by Using a Scenario-Based Approach and a Numerical Model*
Sara Barsotti, Dario Ingi Di Rienzo, Thorvaldur Thordarson, Bogi Brynjar Björnsson and Sigrún Karlsdóttir
- 148** *Paroxysmal Explosions, Lava Fountains and Ash Plumes at Etna Volcano: Eruptive Processes and Hazard Implications*
Sonia Calvari, Flavio Cannavò, Alessandro Bonaccorso, Letizia Spampinato and Alessandra G. Pellegrino



Editorial: Exploring Volcanic Paroxysmal Explosive Activity From Magma Source to Ground and Atmosphere

Sonia Calvari^{1*}, Alessandro Bonaccorso¹, Clive Oppenheimer² and Letizia Spampinato¹

¹ Istituto Nazionale di Geofisica e Vulcanologia, Osservatorio Etneo - Sezione di Catania, Catania, Italy, ² Department of Geography, University of Cambridge, Cambridge, United Kingdom

Keywords: explosive activity, paroxysm, ash plume, volcanoes, Etna volcano, geophysical data, gas geochemistry, satellite remote sensing

Editorial on the Research Topic

Exploring Volcanic Paroxysmal Explosive Activity From Magma Source to Ground and Atmosphere

Volcanic paroxysmal explosive activity has enormous potential destructive power and usually causes widespread damages to the Society (NAS–National Academies of Sciences Engineering Medicine, 2017). Serious problems can occur even during explosive activity related to modest eruptions, such as the case of the 2010 Eyjafjallajökull eruption in Iceland that paralyzed the air traffic in the European continent and in the North Atlantic. In general, a crucial issue, and also an intriguing challenge, is to evaluate the state of the preparatory phase leading to an eruption. It is important to understand the characteristics of the volcano state both for the long-term preparatory phases, usually anticipating the strongest eruptions, and also for the medium- to short-term phases preceding the more frequent and usually less powerful eruptions, but with more immediate consequences.

The first paper of the collection gives an overview of the long-term dynamics of the volcanic paroxysmal activity at andesitic and dacitic volcanoes during 1960–2010 (Zobin). In this study two groups of eruptions with VEI 5–6 and VEI 3–4 were considered. The main tool used was the seismic monitoring of the volcanoes. The eruptions of the first group are characterized by long periods of quiescence (longer than 120 years) and precursory volcano tectonic seismic swarms. The second group develops in more individual styles, each typical of a certain volcano. The study suggests that the eruptions with higher VEI are related to a plugged magmatic conduit, whereas eruptions with lower VEI are usually associated to open conduits.

As a specific case of volcano producing frequent explosive eruptions with low VEI, the second paper of this Research Topic considers the Etna eruptive activity during 2009–2017 by using ground deformation and strain data (Aloisi et al.). Etna volcano was characterized over this period by an incredible lively eruptive activity. This comprised 44 lava fountain episodes from the New South East Crater, two sequences of lava fountains from the Voragine crater, as well as some periods of summit effusive activity with a more prolonged supply of lava flows. The authors produced a complete representation of the different sources that characterized the different periods both in the medium-term (i.e., the preparatory phases showing inflation and the eruptive phases showing deflation) and in the short-term (i.e., the fast discharge associated with eruptive events).

Ganci et al. investigated the middle-term behavior of Mt. Etna. Detection of the thermal anomalies allowed retrieval of radiative power time-series and associated volumes, and thus characterization of each of the paroxysms in terms of intensity and magnitude. Topographic data

OPEN ACCESS

Edited and reviewed by:

Valerio Acocella,
Roma Tre University, Italy

*Correspondence:

Sonia Calvari
sonia.calvari@ingv.it

Specialty section:

This article was submitted to
Volcanology,
a section of the journal
Frontiers in Earth Science

Received: 09 August 2019

Accepted: 19 August 2019

Published: 03 September 2019

Citation:

Calvari S, Bonaccorso A,
Oppenheimer C and Spampinato L
(2019) Editorial: Exploring Volcanic
Paroxysmal Explosive Activity From
Magma Source to Ground and
Atmosphere. *Front. Earth Sci.* 7:227.
doi: 10.3389/feart.2019.00227

derived from satellite imagery gave the total volume of products erupted from 2005 to 2015. Overall, the integration of thermal and topographic data highlighted that the 2011–2012 lava fountains had higher intensity than those of 2013–2015 and that the total volumes erupted from 2005 to 2015 resulted being below those typically erupted by Mt. Etna in a decadal time scale.

Recent eruptive activity from Etna offered a great opportunity to measure the SO₂ gas flux from ground-based and satellite instruments prior to, during and after the paroxysmal sequences (D'Aleo et al.), allowing to detect the switch from an active crater to another on the basis of increased and decreased SO₂ flux. Based on these measurements, the degassed magma volume was estimated, leading to inferring on the fraction of erupted magma compared to the amount emplaced into the shallow feeding system. Another important parameter essential for hazard assessment is Mass Eruption Rate (MER), which has been estimated for 47 paroxysmal episodes using a Doppler Radar installed on Etna (Freret-Lorgeril et al.). The Lidar detection of the volcanic plume, volcanic ash concentration in atmosphere, and characterization of optical properties of volcanic particles, represent the distal characterization of the paroxysmal activity, essential for modeling volcanic ash clouds and their impact (Boselli et al.).

Mapping of the erupted products and measurement and retrieval of the main eruptive parameters are crucial to understand the eruptive dynamics and investigate into the volcano shallow feeder system. Nowadays, volcanology can take advantage from different measurement techniques and methodologies spanning from direct field observations to ground- and satellite-based remote sensing. Indeed, the opportunity to inspect volcanic phenomena by multidisciplinary approaches allows getting overall view of the volcanic scenarios. The study of the tephra fallout produced by the 3 March 2015 lava fountain at Villarrica basaltic-andesitic volcano by field surveys, laboratory analysis, and satellite imagery provided characterization and parameterization of the paroxysm (Romero et al.). The integration of the key constraints shed light in the mechanism that triggered the paroxysmal explosion in a volcano that commonly shows persistent activity associated to lava lake-like dynamics. At Mt. Etna, the multidisciplinary approach permitted the study of the recent paroxysmal activity at the volcano summit at both short- and long-time scale. Andronico et al. focused on the 25–26 October 2013 lava fountain. Using field observations and ground- and satellite-based imagery and photogrammetry, they mapped the lava flow field and estimated the volume of the pyroclastic cone. Mapping of the fallout deposit in field and laboratory analysis gave grain size distribution, composition, and total erupted mass.

The hazards posed by explosive activity is a function of the size of the eruption and of the elevation reached by the eruptive column and ash plume, that may impact the atmosphere

or even the stratosphere and affect aviation, infrastructures, viability, climate, and health. The Volcanic Explosivity Index (VEI; Newhall and Self, 1982) is a way to estimate the size of an explosive eruption, with a VEI 6 posing severe hazard all over the country and a VEI 2–4 having only local effects. The last two papers of this collection evaluate the hazard posed by two end-member eruptions, such as the VEI 6 potential for Öraefajökull volcano in Iceland (Barsotti et al.) and the VEI 2–4 of Etna volcano in Sicily (Calvari et al.). Barsotti et al. use a numerical model to assess the impact on infrastructures in Iceland caused by a rare but potentially highly destructive activity occurring at the Öraefajökull volcano, which experienced this event only once during the last 1100 years. Etna instead has experienced hundreds of mild VEI 2–4 eruptions during the last decades, and Calvari et al. statistically analyze several of these events to propose an empirical law that allows them to evaluate the maximum elevation of an ash plume as soon as the lava fountain height has reached the peak steady value, measured using the images recorded by the monitoring thermal camera network.

Most of the papers comprised in this collection pertain to Mt. Etna, which has been identified as Decade Volcano by the International Association of Volcanology and Chemistry of the Earth's Interior (IAVCEI), thus confirming itself as an ideal volcano laboratory (Bonaccorso et al., 2004). The empirical laws thus far proposed for predicting the extension and impact of the eruptive clouds (Calvari et al.) are thus applicable just to this volcano, and in the future a greater effort has to be dedicated to multidisciplinary studies involving more volcanoes and cross-analyses of their data (e.g., Zobin) in order to obtain general statements, laws and/or formulas that could be applicable to those volcanoes which are less monitored. More peculiar and still unknown processes could arise from in depth studies of other basaltic volcanoes from the Earth and other planets, increasing our ability to understand and predict their behavior. A growing attention is dedicated to the use of UAV (unmanned aerial vehicles; e.g., Neri et al., 2017; Favalli et al., 2018), remote-sensing (Boselli et al.; Calvari et al.; D'Aleo et al.; Freret-Lorgeril et al.) and satellite measurements (Ganci et al.) for their safety issues, low cost and broad perspective, that result in an important integration of field studies (Andronico et al.; Romero et al.), numerical simulations (Barsotti et al.), and laboratory experiments (e.g., Dellino et al., 2010). It is a general feeling that the innovative methods will grow even more in the future, possibly coupled with virtual reality, allowing results and simulations of volcanic processes impossible to imagine nowadays.

AUTHOR CONTRIBUTIONS

All authors listed have made a substantial, direct and intellectual contribution to the work, and approved it for publication.

REFERENCES

- Bonaccorso, A., Calvari, S., Coltelli, M., Del Negro, C., and Falsaperla, S. (eds.). (2004). "Mt. Etna: volcano laboratory," in *American Geophysical Union, Geophysical Monograph Series*, v. 143:350.
- Dellino, P., Dioguardi, F., Zimanowski, B., Büttner, R., Mele, D., LaVolpe, L., et al. (2010). Conduit flow experiments help constraining the regime of explosive eruptions. *J. Geophys. Res.* 115:B04204. doi: 10.1029/2009JB006781
- Favalli, M., Fornaciai, A., Nannipieri, L., Harris, A., Calvari, S., and Lormand, C. (2018). UAV-based remote sensing surveys of lava flow fields: a case study from Etna's 1974 channel-fed lava flows. *Bull. Volcanol.* 80:29. doi: 10.1007/s00445-018-1192-6
- NAS–National Academies of Sciences Engineering and Medicine (2017). *Volcanic Eruptions and Their Repose, Unrest, Precursors, and Timing*. Washington, DC: The National Academies Press.
- Neri, M., De Maio, M., Crepaldi, S., Suozzi, E., Lavy, M., Marchionatti, F., et al. (2017). Topographic maps of mount Etna summit crater's area, 14 december 2015. *J. Maps* 13, 674–683. doi: 10.1080/17445647.2017.1352041
- Newhall, C. G., and Self, S. (1982). The volcanic explosivity index (VEI): an estimate of explosive magnitude for historical volcanism. *J. Geophys. Res.* 87, 1231–1238. doi: 10.1029/JC087iC02p01231

Conflict of Interest Statement: The authors declare that the research was conducted in the absence of any commercial or financial relationships that could be construed as a potential conflict of interest.

Copyright © 2019 Calvari, Bonaccorso, Oppenheimer and Spampinato. This is an open-access article distributed under the terms of the Creative Commons Attribution License (CC BY). The use, distribution or reproduction in other forums is permitted, provided the original author(s) and the copyright owner(s) are credited and that the original publication in this journal is cited, in accordance with accepted academic practice. No use, distribution or reproduction is permitted which does not comply with these terms.



An Overview of the Dynamics of the Volcanic Paroxysmal Explosive Activity, and Related Seismicity, at Andesitic and Dacitic Volcanoes (1960–2010)

Vyacheslav M. Zobin*

Centro Universitario de Estudios Volcanológicos, Universidad de Colima, Colima, Mexico

OPEN ACCESS

Edited by:

Alessandro Bonaccorso,
Istituto Nazionale di Geofisica e
Vulcanologia (INGV), Italy

Reviewed by:

Sonia Calvari,
Istituto Nazionale di Geofisica e
Vulcanologia (INGV), Italy
Luca D'Auria,
Instituto Volcanológico de Canarias,
INVOLCAN, Spain
Paul Davis,
UCLA Department of Earth, Planetary,
and Space Sciences, United States

*Correspondence:

Vyacheslav M. Zobin
vzobin@ucol.mx

Specialty section:

This article was submitted to
Volcanology,
a section of the journal
Frontiers in Earth Science

Received: 07 September 2017

Accepted: 13 April 2018

Published: 03 May 2018

Citation:

Zobin VM (2018) An Overview of the
Dynamics of the Volcanic Paroxysmal
Explosive Activity, and Related
Seismicity, at Andesitic and Dacitic
Volcanoes (1960–2010).
Front. Earth Sci. 6:46.
doi: 10.3389/feart.2018.00046

Understanding volcanic paroxysmal explosive activity requires the knowledge of many associated processes. An overview of the dynamics of paroxysmal explosive eruptions (PEEs) at andesitic and dacitic volcanoes occurring between 1960 and 2010 is presented here. This overview is based mainly on a description of the pre-eruptive and eruptive events, as well as on the related seismic measurements. The selected eruptions are grouped according to their Volcanic Explosivity Index (VEI). A first group includes three eruptions of VEI 5–6 (Mount St. Helens, 1980; El Chichón, 1982; Pinatubo, 1991) and a second group includes three eruptions of VEI 3 (Usu volcano, 1977; Soufriere Hills Volcano (SHV), 1996, and Volcán de Colima, 2005). The PEEs of the first group have similarity in their developments that allows to propose a 5-stage scheme of their dynamics process. Between these stages are: long (more than 120 years) period of quiescence (stage 1), preliminary volcano-tectonic (VT) earthquake swarm (stage 2), period of phreatic explosions (stage 3) and then, PEE appearance (stage 4). It was shown also that the PEEs of this group during their Plinian stage “triggered” the earthquake sequences beneath the volcanic structures with the maximum magnitude of earthquakes proportional to the volume of ejecta of PEEs (stage 5). Three discussed PEEs of the second group with lower VEI developed in more individual styles, not keeping within any general scheme. Among these, one PEE (SHV) may be considered as partly following in development to the PEEs of the first group, having stages 1, 3, and 4. The PEEs of Usu volcano and of Volcán de Colima had no preliminary long-term stages of quiescence. The PEE at Usu volcano came just at the end of the preceding short swarm of VT earthquakes. At Volcán de Colima, no preceding swarm of VT occurred. This absence of any regularity in development of lower VEI eruptions may refer, among other reasons, to different conditions of opening of the magmatic conduit during these eruptions.

Keywords: volcano seismology, eruption dynamics, magma ascent dynamics, seismicity and tectonics, volcanoes andesitic and dacitic

INTRODUCTION

Understanding volcanic paroxysmal explosive activity requires the knowledge of many associated processes. Paroxysmal volcanic eruption is defined in “Geological dictionary” (Paffengoltz, 1978) as “particularly violent eruption of the volcano, which is the most dangerous and tense stage of this eruptive cycle, at which the whole cavity of the crater is opened”. An overview on the dynamics of six paroxysmal explosive eruptions (PEEs) at andesitic and dacitic volcanoes, occurring between 1960 and 2010, is presented here. The selected eruptions are grouped according to their Volcanic Explosivity Index (VEI, Newhall and Self, 1982).

The paroxysmal explosive eruption (PEE) of the first group with VEI 5–6 (height of plume more than 25 km; volume of ejecta 10^9 – 10^{11} m³) can significantly destroy the volcano and affect the atmosphere, and the environment in the overall. For example, as a result of the paroxysmal 27 August 1883 explosion of Krakatau volcano, the northern two-thirds of the Krakatau Island, which is situated between Java and Sumatra Islands (**Figure 1**), collapsed beneath the sea, generating series of devastating pyroclastic flows, which traveled for the runout distances up to 40 km across the Sunda Strait, and immense tsunamis that ravaged adjacent coastlines. The explosions and tsunamis killed 36,417 persons, devastating 165 villages. The ash cloud rose 60 km above the volcano. Millions of tons of dust were hurled into the atmosphere and stratosphere around the world, for many years producing exotic colors in the sky, halos around the sun and moon, and a spectacular array of anomalous sunsets and sunrises. Acoustic waves from this explosion had traveled around the Earth seven times (Winchester, 2003; <http://volcano.si.edu/volcano.cfm?vn=262000>).

The paroxysmal explosive eruption of the second group with VEI 3–4 (height of plume from 3 to 25 km; volume of ejecta 10^7 – 10^9 m³) may destroy the summit of volcano, or lava dome in the crater, or crater sectors by Vulcanian explosions, emplacing pyroclastic current densities (PCDs) that may affect the nearest settlements and threaten aviation. The 4–5 November 2010 PEEs at Merapi volcano, Java Island (**Figure 1**), represent an example of this type. The explosion sequence destroyed the large lava dome, and the summit crater had enlarged to a diameter of 300–400 m. Ash column that ascended to 17 km altitude was produced emplacing a pyroclastic flow that traveled for runout distance of about 16 km. The PCDs and related surges of 4–5 November destroyed numerous villages over broad area of the upper slopes of the volcano. More than 300,000 habitants were evacuated; 386 deaths were recorded. Residents in the towns up to 240 km away reported that “heavy gray ash” blanketed trees, cars, and roads (Surono et al., 2012).

In this review article, we present the case studies of PEEs of andesitic and dacitic volcanoes that occurred during 50 years, from 1960 to 2010, to show the development and effects of PEEs and to highlight any regularity in their dynamics during the eruptive cycles.

Here we selected six PEEs of andesitic and dacitic volcanoes with VEI 3–6 (<http://volcano.si.edu/>) that occurred during this period. The first group of PEEs includes three VEI 5–6

paroxysmal explosive events of andesitic and dacitic type recorded during the period of study (Mount St. Helens, 1980; El Chichón, 1982; and Pinatubo, 1991). The forth event that occurred during this period, the VEI 5 1963 Agung eruption, had no detailed observations for discussion. Three events of the second group (VEI 3) are selected from the long list of eruptions as the only having the detailed observations and seismic monitoring comparable with the information obtained for the three events of the first group (Usu, 1977; Soufriere Hills volcano, 1996; and Volcán de Colima, 2005).

The case descriptions are represented by two groups of information. The Research Topic of this Special Issue is concerned with the Exploring Volcanic Paroxysmal Explosive Activity from Magma Source to Ground and Atmosphere. According to this definition of the topic, “from magma source to ground and atmosphere,” the first group of information includes the geological, visual, and satellite observations.

For a long time, including the period of our reviewed eruptions, the only tool that allowed reconstructing in details the dynamics of eruptions was seismic monitoring of the volcanoes. So we discuss the seismic information within the second group of information. We use the catalogs of seismic events recorded during the eruptive cycles of selected volcanoes together with the descriptions of these events to reconstruct the main stages in the development of their paroxysmal eruptive activity. Earthquake location catalogs are not an exact representation of the true earthquake locations. The most important source of systematic errors in earthquake locations is the inherent dependence of earthquake locations on the assumed seismic velocity structure of the Earth’s crust, the number of seismic stations and configuration of the seismic network. Within this article, we consider the accuracy of earthquake locations by the local seismic networks around volcanoes as ± 1 –3 km for epicenters and ± 2 –4 km for hypocenters.

The magnitudes of earthquakes used in the article were taken from the original catalogs.

DYNAMICS OF PAROXYSMAL EXPLOSIVE ERUPTIONS OF THE FIRST GROUP (VEI 5–6)

In this section, three paroxysmal explosive eruptions of the first group (VEI 5–6) at volcanoes Mount St. Helens, El Chichon, and Pinatubo, seismically monitored during eruptive activity, are discussed. The main data about these eruptions are collected in **Table 1**.

Mount St. Helens, Cascades, USA, 1980

Mount St. Helens (MSH) is a stratovolcano of 2,950 m of height. It is situated within the Cascade Range in the state of Washington, U.S.A. The eruptive history of MSH began about 40,000 years ago with dacitic volcanism. The products of eruptive activity during the past 2,500 years were represented mainly by dacite-andesite-dacites. The volcano had been apparently dormant since 1857 (Mullineaux and Crandell, 1981).

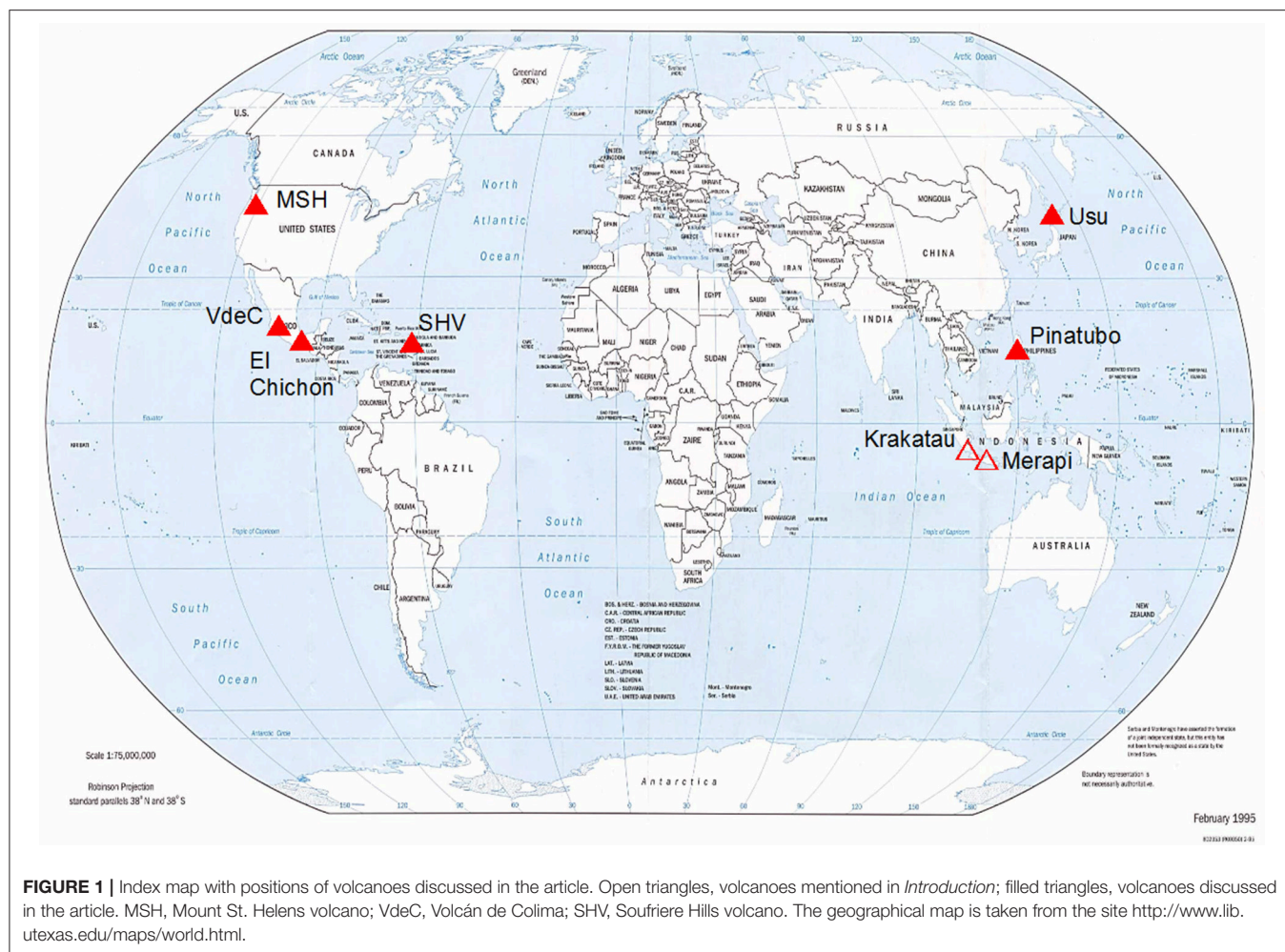


FIGURE 1 | Index map with positions of volcanoes discussed in the article. Open triangles, volcanoes mentioned in *Introduction*; filled triangles, volcanoes discussed in the article. MSH, Mount St. Helens volcano; VdeC, Volcán de Colima; SHV, Soufriere Hills volcano. The geographical map is taken from the site <http://www.lib.utexas.edu/maps/world.html>.

TABLE 1 | List of paroxysmal explosive eruptions (PEEs) of the first group (VEI 5–6).

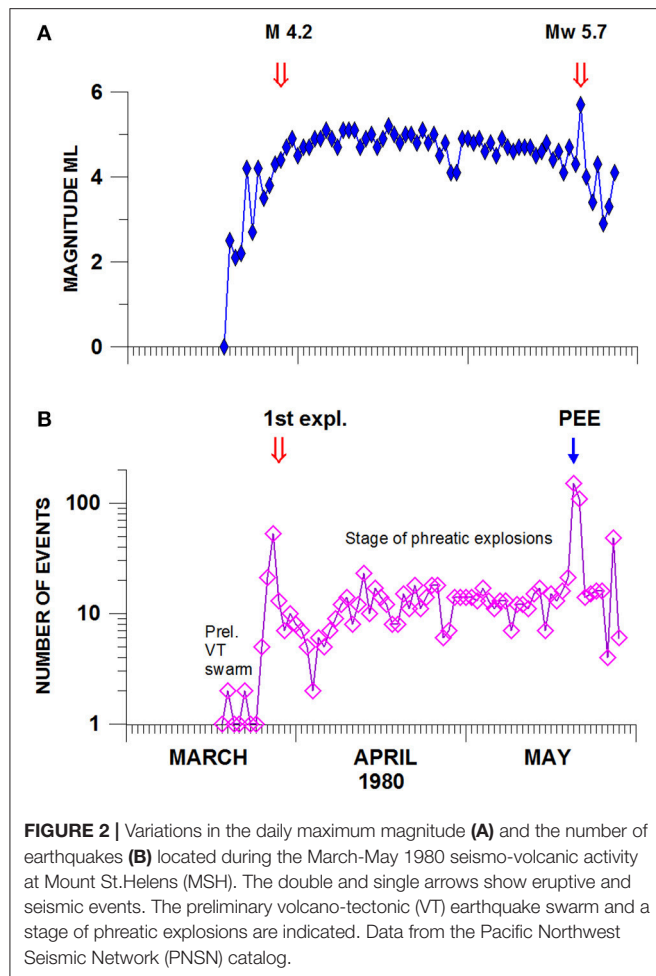
Volcano	Period of quiescence prior to PEE, years	Eruptive cycle including PEE	Date of PEE, local time	VEI	Height of plume of PEE, km	Volume of ejecta of PEE, m ³	References
Mount St. Helens, USA	120	16 March–18 May 1980 ²	18 May 08:32, 1980 ²	5 ¹	> 20 ²	2.3×10^{92}	1, 2
El Chichón, México	550 ⁴	1 March–3 April 1982 ⁴	3 April 19:35 1982 ⁴	5 ¹	24 ³	0.8×10^{93}	1, 3, 4
Pinatubo, Philippines	500 ⁶	15 March–2 September 1991 ⁶	15 June 13:42, 1991 ⁵	6 ¹	34 ⁵	$8.4\text{--}10.4 \times 10^{95}$	1, 5, 6

1, Simkin and Siebert, 1994; 2, Christiansen and Peterson, 1981; 3, Carey and Sigurdsson, 1986; 4, Macías et al., 2003; 5, Scott et al., 1996; 6, Newhall et al., 1996.

Paroxysmal Eruption of 18 May 1980, Its Prelude and Its Effects

The eruption cycle of re-awakening of Mt. St. Helens volcano, that included the paroxysmal explosive eruption of 18 May 1980, began on 16 March 1980 with a preliminary swarm of volcano-tectonic earthquakes (Figure 2). The first phreatic eruption from its summit crater was observed on March 27, and was followed then by a sequence of small phreatic explosive eruptions up to the climactic eruption on the morning of 18 May (Mullineaux and Crandell, 1981).

According to a series of photos taken during the first minutes of the eruption (Voight, 1981), the eruption began with a large-scale collapse of the volcanic edifice which was followed by a directed blast eruption. The northward-directed lateral blast of the bulging north flank of the volcano erupted about 2 km³ of cold and juvenile material and devastated an area of nearly 600 km². These events triggered a 9-hr magmatic eruption that drove a vertical Plinian column more than 20 km high. A new crater, with an area of 1.5 × 3.0 km² and of depth of about 500 m, formed in the northern flank and summit of the volcano. The



height of the volcano was reduced by about 400 m (Christiansen and Peterson, 1981).

The local effects of the 18 May eruption were observed within the 600-km² devastated area. Fifty-seven people were killed and missing. Autopsies showed that most of the people killed in the eruption likely died from asphyxiation after inhaling hot ash (Bernstein et al., 1986). Civil infrastructures such as highways, railways, airports bridges, buildings, etc., immediately north of the volcano were almost completely destroyed by the lateral blast and debris avalanche (Schuster, 1981).

The 18 May eruption sent large amounts of dust and volcanic ash into the atmosphere. The plume spread quickly to the east, bringing darkness, and reduced visibility for the northern states of the USA (Robock, 1982). The dust cloud produced cooling of surface air temperatures during the daytime and warming at night. However, the amount of sulfur injected into the stratosphere was low, and thus had no impact on climate (Robock, 1981).

Seismic History of the Mt. St. Helens's PEE

Figure 2 shows temporal variations in daily number of volcano-tectonic seismic events, recorded by the regional

Pacific Northwest Seismic Network (PNSN, <https://pnsn.org/pnsn-data-products/earthquake-catalogs>), and their maximum magnitudes during two stages of activity: pre-eruptive and before the great 18 May PEE. The 1980 swarm of volcano-tectonic shallow earthquakes began on 16 March with small events; the first significant M_L 4.2 event was recorded beneath Mount St. Helens on 20 March. The number and magnitude of earthquakes sharply increased starting 25 March with peak number on 27 March, when the first phreatic explosion occurred. After the beginning of the eruption, the number of earthquakes gradually decreased during one month; then their number was more or less stable up to 18 May. The magnitudes of volcano-tectonic earthquakes of this period were rather high; seven April earthquakes were in the range of M_L between 5.0 and 5.2. During period from 1 to 16 May, the maximum magnitudes of earthquakes decreased, six of them were in the range of M_L between 4.3 and 4.7.

The pre-eruptive 93 earthquakes, occurring before the 27 March explosions, were located within the area of about 10 × 20 km² along the NW-SE structure, including MSH in its NW part (Figure 3A). These seismic events formed two clusters: a shallow one, at the depth range of 0 to 5 km, and a deep one, at the depth range from 18 to 25 km (Figure 3B). During the active period, from 27 March and until the PEE of 18 May, totally 627 located earthquakes occurred around the volcanic edifice, mainly within the depth range from 0 to 10 km; the deeper pre-eruption cluster disappeared.

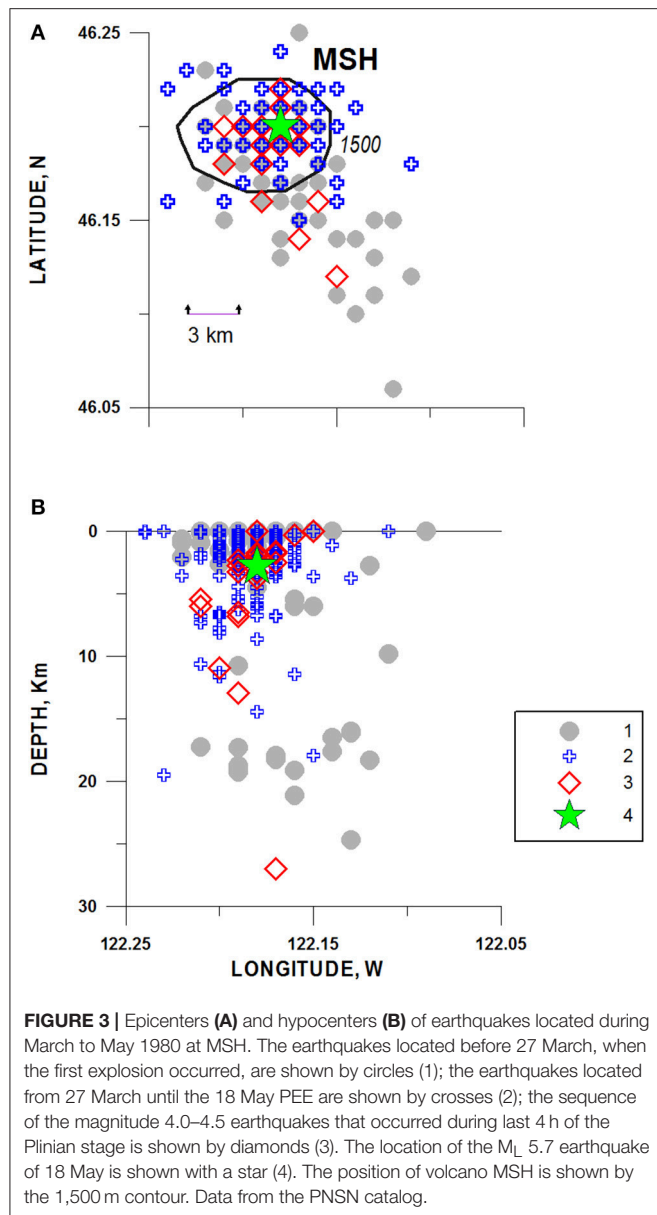
The largest earthquake with M_L 5.7 occurred on 18 May at 08:32:11.4¹ on the background of lower-level seismic activity, just before the great directed blast of the volcano that initiated at 08:32:21, about 10 s after the earthquake-trigger (Voight, 1981). This seismic event was located at the depth of 2.8 km beneath the NW flank of MSH (Figure 3). Study of its *P*-wave focal mechanism (Zobin, 1992) and its comparison with the CMT solution (Dziewonski et al., 1988) showed that this event represented initial left-lateral strike-slip along the NE-SW oriented fault that in a few seconds was transformed in a normal fault triggering a sector failure of volcanic edifice.

As mentioned by Christiansen and Peterson (1981), the Plinian phase of paroxysmal eruption continued for about 9 h. On the background of decreasing intensity of the Plinian phase, a 4-h sequence of 21 magnitude 4.0 and 4.5 events was recorded (Figure 3). The earthquake foci repeated mainly the distribution of the foci recorded during the stage before the 18 May PEE.

El Chichon Volcano, México, 1982

El Chichón Volcano (1,100 m a.s.l.) is located in the state of Chiapas, southern Mexico. All the magmas, produced during the past 370,000 years, are K-alkaline andesites. Before the 1982 eruption, the volcanic structure consisted of two nested andesitic lava domes inside the crater that have been repeatedly reactivated during the Holocene (Layer et al., 2009). The last dated Plinian eruption occurred in 1320–1433 A.D. (Macías et al., 2003), then the volcano was inactive.

¹Here and later in the article, local time for all volcanic events was used.



Paroxysmal Eruptions of 3–4 April 1982, Their Prelude and Their Effects

The eruption cycle of re-awakening of El Chichón volcano, that included the PEEs of 3–4 April 1982, began on 1 March 1982 with a swarm of volcano-tectonic earthquakes (Havskov et al., 1983). Near mid-night (at 23:32) of 28 March El Chichón exploded abruptly and vigorously; the eruption then continued until ~ 06:00 the next morning. This powerful explosive eruption fed a 20-km high eruption column and produced heavy ashfalls. During next 6 days (29 March–3 April), the eruptive activity continued intermittently at much-reduced level, consisting of occasional small phreatic explosions. Then, in the evening of 3 April at 19:35 and early morning of 4 April at 05:22, the El Chichón's two paroxysmal eruptions (VEI 5) occurred. The Plinian eruption columns of the explosions that occurred during

3 April and 4 April were 24 km high, with volume of $0.8 \times 10^9 \text{ m}^3$, and 22 km high, with volume of $0.8 \times 10^9 \text{ m}^3$, respectively. While of shorter duration (each lasting <2 h), both these eruptions were more powerful than the 28 March eruption. In addition to producing voluminous ashfalls, each eruption also generated pyroclastic flows and surges that swept all flanks of the volcano. As a result of this sequence of great explosions, a nearly complete excavation of El Chichón summit dome was performed, and the 1-km-wide crater formed in its place (Carey and Sigurdsson, 1986; Tilling, 2009).

Local effects of this eruption were tragic. Pyroclastic flows and surges obliterated some villages within a roughly 7 km radius of the volcano, killing about 2,000 people, and ashfalls downwind posed socio-economic hardships for many thousands of inhabitants of the states of Chiapas and Tabasco. The unexpected and vigorous eruption of 28 March caused hasty, confused evacuation of most villagers in the area. Eruptive activity greatly diminished during the next 5 days, and then the most powerful and lethal eruptions occurred 3–4 April—tragically, after many evacuees were allowed by authorities to return home (Tilling, 2009).

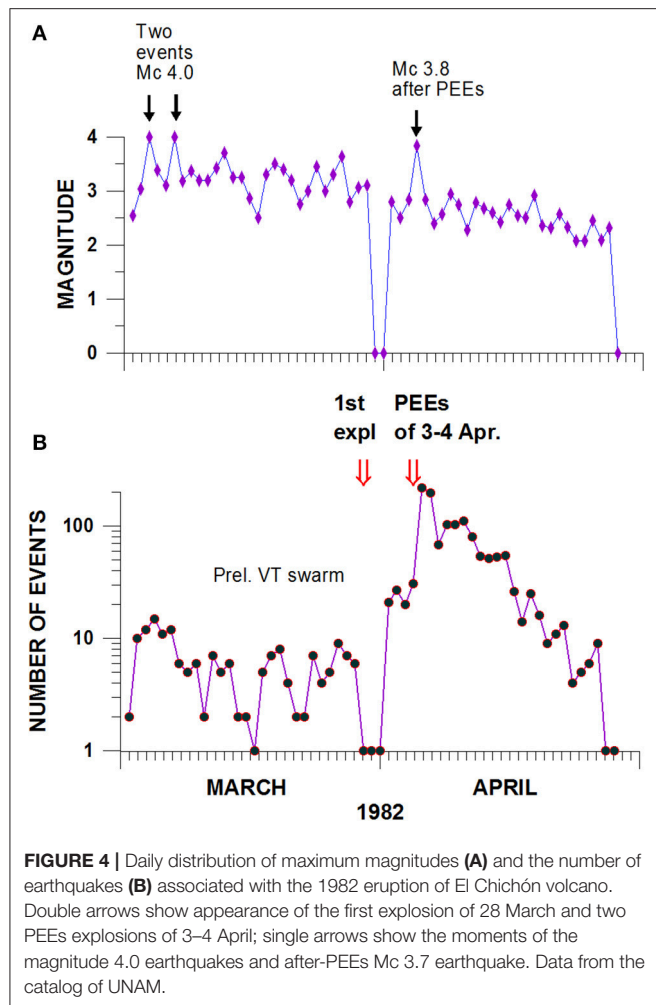
The stratospheric cloud, created by the eruption of El Chichón, was about 2.5 km wide and reached an altitude of 25 km; over 20 million tons of sulfur gases were emitted during this event. The stratospheric cloud quickly spread out, encircling the globe in about three week's time. A maximum drop of 0.2°C in the global temperature was measured within two months of the eruption (Vignola, 1999). A significant 10% ozone decrease was recorded in the north temperate regions of North America, Europe, and Asia within the atmospheric layers of 8–16 and 16–24 km during four seasons after the eruption (Angell, 1998).

Seismic History of the El Chichon's PEEs

The eruption was preceded by a 28-day seismic swarm of volcano-tectonic earthquakes (Figures 4, 5), which began on 1 March 1982. Seismic activity was fortuitously recorded by the 14-station seismic network of Comisión Federal de Electricidad, installed by UNAM during 1979–1980 around the Chichuasén hydroelectric plant (~ 50 km south of the volcano's summit; Havskov et al., 1983; Jiménez et al., 1999). Totally 270 events with magnitude $M_c \geq 2$ of the 1 March - 4 April swarm were located (Figure 5).

The swarm began with a sharp increase in the number of earthquakes during the first 6 days of activity. Two maximum magnitude events (M_c 4) of the swarm were recorded on 3 and 6 March. Then a gradual decrease in the seismic activity in number and magnitudes of events was observed during the next 2 weeks. The activity increased again beginning from 19 March. The majority (~80%) of earthquakes, preceding the first explosion of 28 March, occurred within an area of $10 \times 20 \text{ km}^2$ having the volcano in the center of this area, ranging within depths from 0 to 25 km (Figure 5B).

Just after the explosion of 28 March seismic activity disappeared but 2 days prior to the PEEs of 3–4 April, the number of earthquakes with $M_c \geq 2$ began to increase. After the first explosion of 28 March and before and during the two PEE events of 3 and 4 April, the earthquake foci had filled a vertical N-S

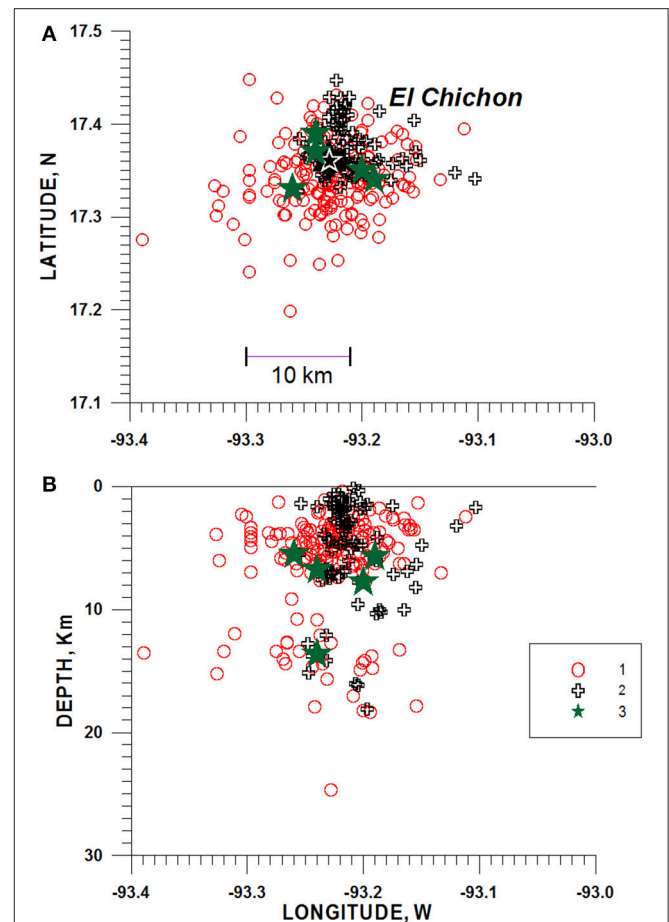


oriented volume beneath the volcano at the depth interval from 0 to 8 km (Figure 5B).

The PEE of 4 April (05:35) was followed by a sequence of five intermediate-size (M_c 3.7–3.8) earthquakes that occurred beginning from 07:53 during 5 h on the background of decreasing intensity of the Plinian activity of the volcano (Figure 5). The earthquake foci were distributed around and beneath the focal volume filled during the stage before the 3–4 April PEEs.

Pinatubo Volcano, Luzon Island, Philippines, 1991

Mount Pinatubo is a composite volcano of 1,745 m elevation and is situated in the Luzon volcanic arc (Figure 1). Pre-1991 eruption, Mount Pinatubo represented a dacite-andesite dome complex and stratovolcano that was surrounded by an extensive apron of pyroclastic-flow and lahar deposits from large explosive dacitic eruptions. Large, late-stage dome, filling the crater before the 1991 eruption, was left by the penultimate Plinian eruption that occurred about 500 year before the recent eruption (Newhall et al., 1996).



Paroxysmal Eruption of 15 June 1991, Its Prelude and Effects

The eruption cycle of re-awakening of Pinatubo volcano, which included the paroxysmal explosive eruption of 15 June 1991, began in March 1991 (Figure 6A). Citizens of small communities on the lower northwest flank of Mount Pinatubo felt earthquakes beginning from 15 March, 1991. On 2 April, 1991, during or just after phreatic explosions, vigorous steam vents opened on the upper north slope of the volcano.

From 2 April to late May, steam jetted to heights of 300 to 800 meters. Sometimes these jets were accompanied by ash emissions that reached heights of 1,500 to 3,000 meters. By 9 June, continuous ash emission and occasional small explosions produced ash clouds dense enough to flow slowly down the volcano's western slopes. A new lava dome began to grow in the crater from 9 June. Then a series of strong explosive eruptions began on 12 June, 1991. These culminated in the violent climactic Plinian eruption (VEI 6) of 15 June at 13:42 (L.T.) which caused

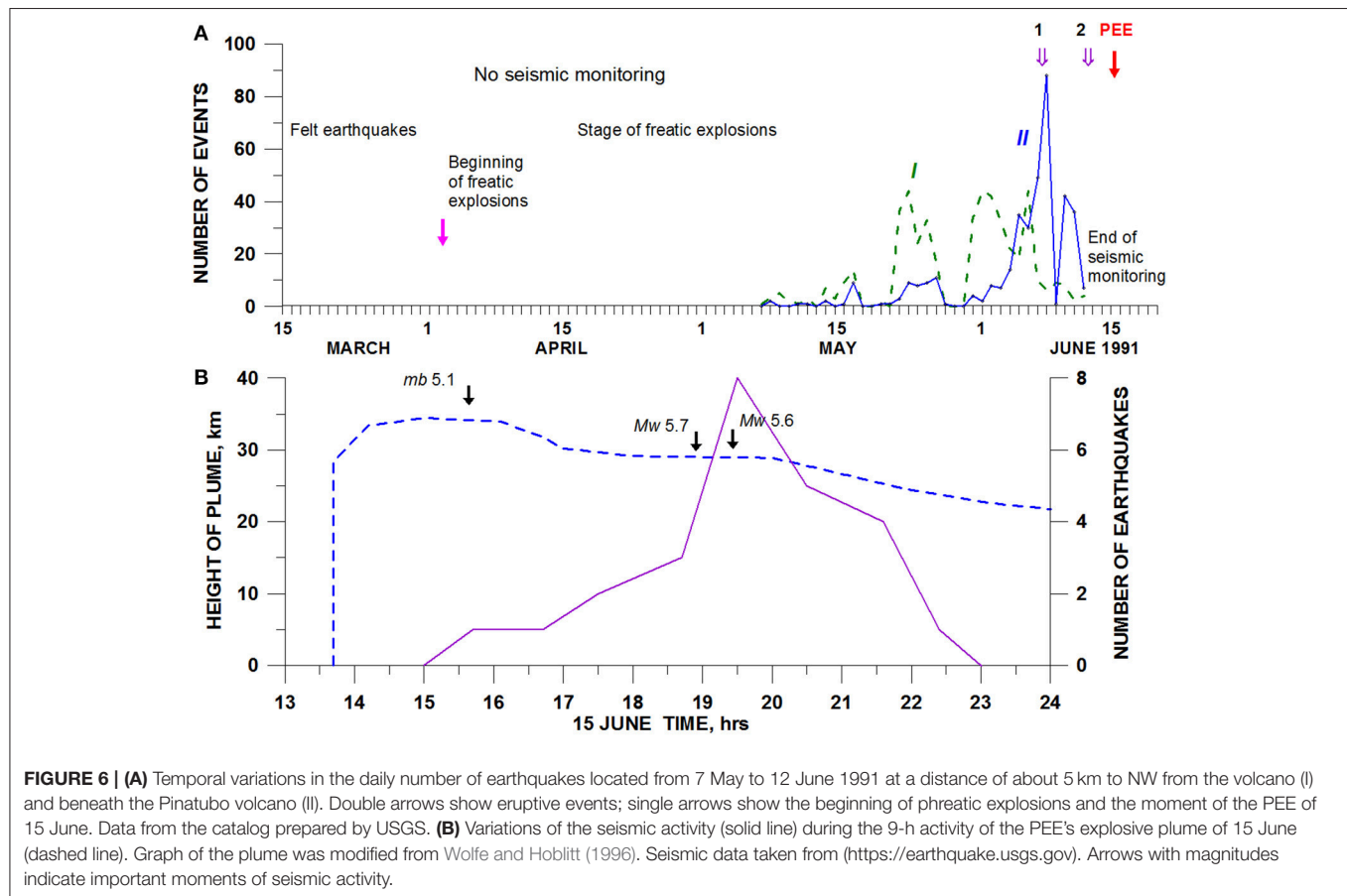


FIGURE 6 | (A) Temporal variations in the daily number of earthquakes located from 7 May to 12 June 1991 at a distance of about 5 km to NW from the volcano (I) and beneath the Pinatubo volcano (II). Double arrows show eruptive events; single arrows show the beginning of phreatic explosions and the moment of the PEE of 15 June. Data from the catalog prepared by USGS. **(B)** Variations of the seismic activity (solid line) during the 9-h activity of the PEE's explosive plume of 15 June (dashed line). Graph of the plume was modified from Wolfe and Hoblitt (1996). Seismic data taken from (<https://earthquake.usgs.gov>). Arrows with magnitudes indicate important moments of seismic activity.

the collapse of the volcano summit and lasted ~ 9 h. This eruption produced about 10 km^3 of porous, pumiceous deposits, and formed a caldera of 2.5 km in diameter (Sabit et al., 1996; Wolfe and Hoblitt, 1996).

Local effects of this paroxysmal eruption were significant. Pyroclastic flows that were emplaced from the Plinian column during the 15 June paroxysmal eruption traveled as much as 12 to 16 km from the vent in all sectors, impacted directly an area of almost 400 km^2 , and profoundly altered the landscape (Scott et al., 1996). The successive forecasting of the eruptive events and their effects enabled Philippine civil leaders to organize massive evacuations, including the evacuation of Clark Air Base (U.S. Air Force), which was located just east of the volcano. Those evacuations saved thousands of lives. Nonetheless, the climactic eruption coincided with a typhoon on June 15 that caused 200 to 300 deaths and extensive property damage, owing to an extraordinarily broad distribution of heavy, wet tephra-fall deposits (Wolfe and Hoblitt, 1996).

From about 13:40 to about 22:30 on 15 June, Mount Pinatubo produced the largest stratospheric SO_2 cloud ever observed by modern instruments, and the major stratospheric aerosol event since Krakatau exploded in 1883. The giant umbrella cloud covered an area of $300,000 \text{ km}^2$ at 19:40 and was sustained and growing during the whole 9 h climax, eventually reaching $>1,100 \text{ km}$ in diameter. The altitude of umbrella cloud was

estimated as 25 km at the eastern edge and 34 km at its center for the 15:40 image. The stratospheric cloud was observed by the TOMS satellites to encircle the Earth in about 22 days (Self et al., 1996). After the 1991 Pinatubo eruption, the globally averaged stratospheric temperature rose by about 2°C for about 2 years (Robock, 2000). It was noted also that the sulfuric aerosols, released before and during the eruption, circled the Earth within 3 weeks and remained in the atmosphere for 3 years, reflecting enough sunlight to cool the entire planet by half a degree Celsius during that time (Wendel and Kumar, 2016).

Seismic History of the Pinatubo PEE

As it was noted, the citizens of small communities on the lower northwest flank of Mount Pinatubo felt earthquakes beginning on 15 March, 1991 but the local seismic observations began by the USGS seismologists only on 7 May (Figure 6A). Therefore, the earthquake swarm prior to the 2 April initial re-awakening of the volcano was not instrumentally recorded. At the same time, no events with magnitude ≥ 4.5 were located by the worldwide seismic survey of USGS (<https://earthquake.usgs.gov>) in the region of the volcano during March-May.

Figures 6A, 7 show the development of the seismic activity beginning from 7 May, when the local network was installed, and until 12 June, 1991, when the seismic network was destroyed by large explosions. Volcano-tectonic seismic events were recorded

within two clusters (**Figure 7A**): at a distance of about 5 km NW of the summit (I) and just beneath the summit (II). The first cluster of seismic events developed mainly within the depth range from 7 to 3 km while the second group of events was shallower, forming a vertical column within the depth range from 4 km b.s.l. to 1 km a.s.l. This shift of earthquake foci from cluster I to cluster II supposedly indicated the migration of seismicity to the surface beneath the volcano along the fault shown with a dashed line in **Figure 7A**.

The events from the distant zone I dominated from 21 May to 5 June. Then seismicity of zone II beneath the volcano began to increase its activity, and the intensive swarm of low magnitude (from 0 to 1; largest magnitude 1.5) events was recorded there during 6 to 7 June (**Figure 6A**). This swarm culminated in the 7 June lava dome extrusion. Just after the beginning of the lava dome growth, the number of earthquakes sharply decreased, and the strong 12 June explosion occurred on the background of low-level seismicity for both seismic zones.

During the culminated stage of great explosions, which occurred from June 12 to 15, the local seismic network was out of service, and the only information about seismic activity was obtained from the worldwide seismic survey of USGS (<https://earthquake.usgs.gov>) at the level of magnitudes ≥ 4.5 . This suggests that the 9-h climactic sequence of explosions of 15 June that began at 13:42 was accompanied by a swarm of earthquakes “triggered” by the explosion (**Figure 6B**).

During the 9-h climactic sequence of explosions, totally 25 earthquakes of magnitude range from 4.5 to 5.7 were recorded. They were located within Luzon island to the north and north-east of the volcano (note that during March–14 June no seismic events of this magnitude range were recorded there). Epicenters of five of these earthquakes, located within the area of the seismic swarms occurring 7 May–12 June, are shown in **Figure 7A**. The precision of the depths estimations of these events is very low, and for all of them the USGS survey took the depths simply as 10 km that means “shallower than 33 km” (<https://earthquake.usgs.gov/earthquakes/eventpage/terms.php>). Therefore, they are not shown in the distribution of hypocenters of **Figure 7B**.

The comparative 9-h development of the eruption plume and of the seismic activity is shown in **Figure 6B**. The first earthquakes of this sequence, with magnitude *mb* 5.1, occurred at 15:39, about 2 h after the beginning of the explosion sequence (**Figure 6B**). The number of events and magnitudes of the swarm reached a maximum on the background of decrease in the plume height 5–6 h after the beginning of the explosion. Earthquake with magnitude *Mw* 5.7 was recorded at 18:41; earthquake with magnitude *Mw* 5.6 was recorded at 19:15.

DYNAMICS OF PAROXYSMAL EXPLOSIVE ERUPTIONS OF THE SECOND GROUP (VEI 3–4)

In this section, three PEEs of the second group (VEI 3–4) of volcanoes Usu, Soufriere Hills and Volcán de Colima are discussed. They were selected from the database of the Global Volcanism Program (<http://volcano.si.edu/>) as the most detailed

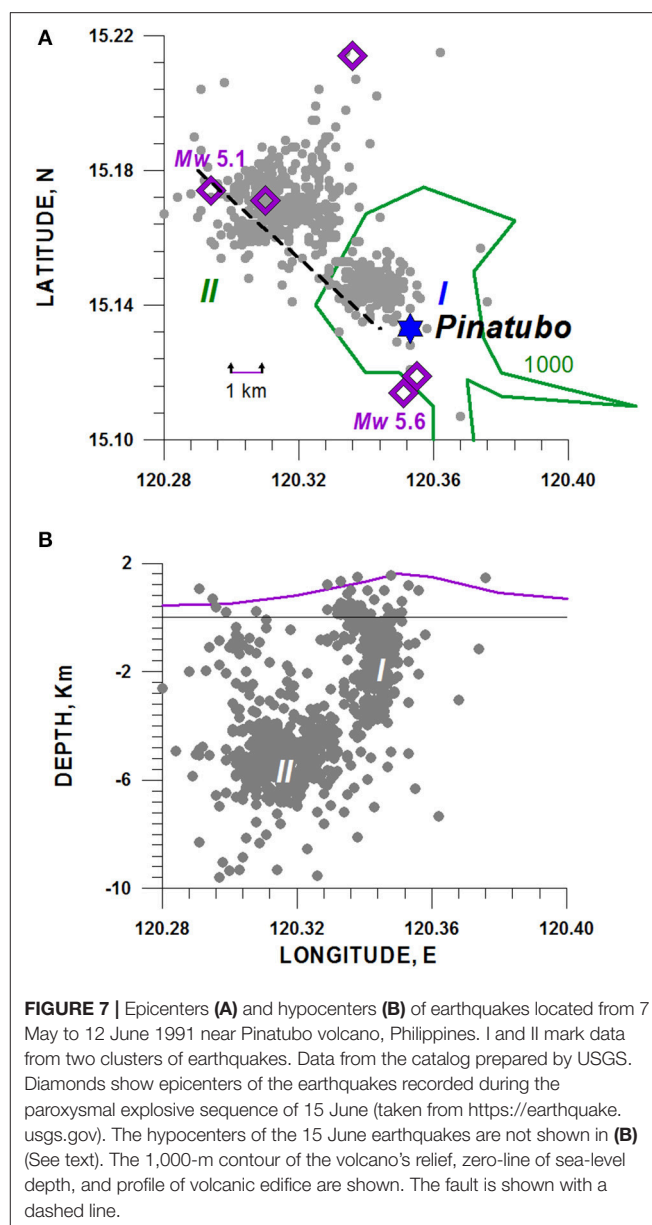


FIGURE 7 | Epicenters (**A**) and hypocenters (**B**) of earthquakes located from 7 May to 12 June 1991 near Pinatubo volcano, Philippines. I and II mark data from two clusters of earthquakes. Data from the catalog prepared by USGS. Diamonds show epicenters of the earthquakes recorded during the paroxysmal explosive sequence of 15 June (taken from <https://earthquake.usgs.gov>). The hypocenters of the 15 June earthquakes are not shown in (**B**) (See text). The 1,000-m contour of the volcano's relief, zero-line of sea-level depth, and profile of volcanic edifice are shown. The fault is shown with a dashed line.

described with the field observations and having continuous seismic monitoring. The main data about these eruptions are collected in **Table 2**.

Usu Volcano, Hokkaido, Japan, 1977

Usu Volcano is located on the southern rim of the Toya Caldera, Hokkaido (**Figure 1**). It is a truncated stratovolcano with the highest peak of about 700 m above sea level (a.s.l.) crowned with a small caldera, 1.8 km across and about 500 m deep (**Figure 8B**). Within the summit caldera there are two lava domes, Ko-Usu and Oo-Usu. The historic activities commenced in 1663 with a Plinian eruption of rhyolitic pumice. Characteristic eruptions of dacitic magma including *nuee ardente* and lava dome or cryptodome building have been repeated every 30 to 50 years. The eruptions

TABLE 2 | List of paroxysmal explosive eruptions (PEEs) of the second group (VEI 3–4).

Volcano	Period of quiescence prior to PEE, years	Eruptive cycle including PEE	Date of PEE, local time	VEI	Height of plume of PEE, km	Volume of ejecta of PEE, m ³	References
Usu, Hokkaido	32 ¹	6 August 1977–February 1982 ³	7 August 1977, 09:12 ¹	3 ²	12 ¹	<0.08 × 10 ⁹ ¹	1, 2, 3
Soufriere Hills Volcano, Montserrat	450 ⁴	18 July 1995–8 October 2003 ⁴	17 September 1996, 23:42 ⁵	3 ⁴	11–15 ⁵	0.003 × 10 ⁹ ⁵	4, 5
Volcán de Colima, México	3 ⁶	22 November 1997–21 June 2011 ⁶	5 June 2005, 14:20 ⁶	3 ⁶	9 ⁷	Not estimated	6, 7

1, Katsui et al., 1978; 2, Simkin and Siebert, 1994; 3, Katsui et al., 1985; 4, GVP, <http://volcano.si.edu/volcano.cfm?vn=360050>; 5, Robertson et al., 1998; 6, GVP, <http://volcano.si.edu/volcano.cfm?vn=341040>; 7, Savov et al., 2008.

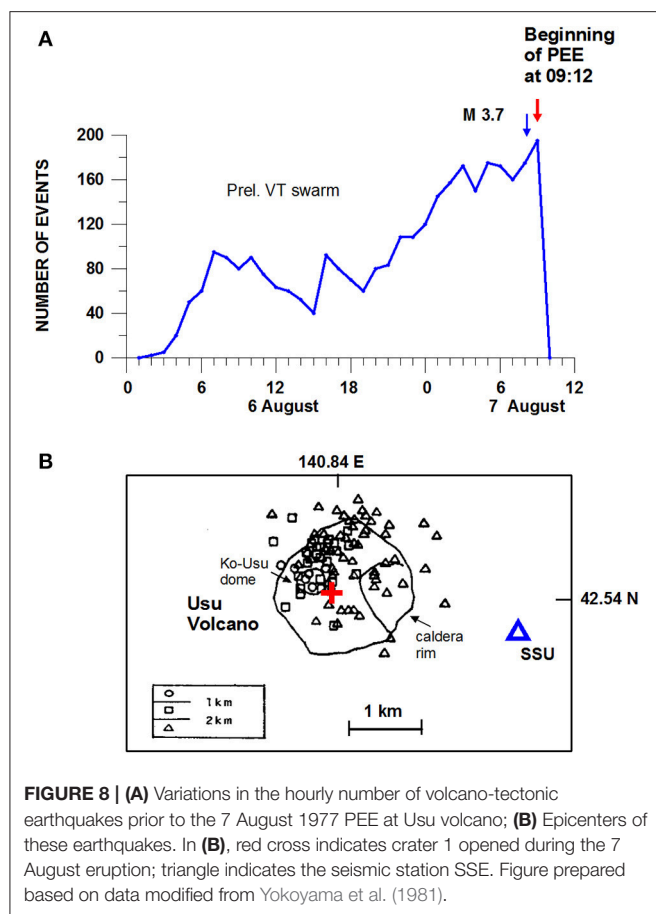


FIGURE 8 | (A) Variations in the hourly number of volcano-tectonic earthquakes prior to the 7 August 1977 PEE at Usu volcano; (B) Epicenters of these earthquakes. In (B), red cross indicates crater 1 opened during the 7 August eruption; triangle indicates the seismic station SSE. Figure prepared based on data modified from Yokoyama et al. (1981).

occurred both from the summit and the northeastern base of Usu Volcano (Niida et al., 1980; Yokoyama et al., 1981; Katsui et al., 1985).

Paroxysmal Eruption of 7 August 1977, Its Prelude and Effects

The eruption cycle of Usu volcano, which included the paroxysmal explosive eruption of 7 August 1977, began on 6 August 1977 after 32 years of quiescence (Table 2). A major

pumice eruption of hypersthene dacite occurred from the summit after 32-h preceding earthquake swarm. Large eruptions lasted for a week from August 7 to 14, opening craters 1–4, each about 100 m across.

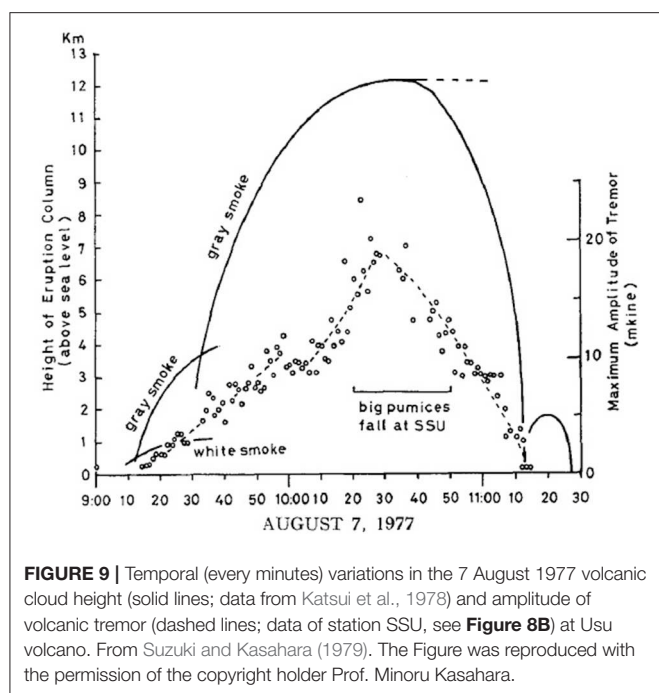
The first explosion in this sequence was paroxysmal. An ash-laden gray cloud rose from the southeastern base of Ko-Usu beginning from 09:12 of 7 August without notable explosion sounds. The eruption column grew rapidly, and at 10:30 rose up to a maximum height of 12 km in elevation. The eruption lasted about 2.5 h and ceased at 11:40. A new crater (Crater I), about 100 m across, opened at the southeastern base of the Ko-Usu lava dome (Figure 8B; Katsui et al., 1978, 1985).

Large volume of pumice and ash was ejected and transported to the southeast of the volcano by the westerly wind. The pumice and ash showers caused destruction of cultivated fields and forests around the volcano. The alarm was issued by the Japan Meteorological Agency before the beginning of eruption (Yokoyama et al., 1981), and no one was killed or injured seriously by the eruption activity, though some damage was caused not only to cultivated lands and forests by the ejecta, but also to some buildings, underground constructions and others by the subsequent crustal movements (Katsui et al., 1978).

Seismic History of the Usu PEE

The first earthquake of the premonitory swarm of volcano-tectonic earthquakes occurred at 01:09 on 6 August (Figure 8A). Beginning from 03:30, the earthquakes were strong enough to be felt in the whole area around the Usu Volcano, up to about 8 km from the volcano, but no damage was caused. Rapid increase in frequency of earthquakes occurred about 01:00 on 7 August and continued to the time of beginning of PEE eruption (Figure 8A; Suzuki and Kasahara, 1979; Katsui et al., 1985).

The earthquake swarm consisted of about 3,000 small (magnitude 1–2) volcano-tectonic earthquakes that were located beneath the summit crater at a depth from 0 to 2 km (Figure 8B). The new eruptive Crater 1 (shown as a cross in Figure 8B) was situated within the epicentral zone of earthquakes. The maximum magnitude *M* 3.7 earthquake was observed half an hour before the beginning of eruption (Yokohama and Seino, 2000).



During the PEE, volcano-tectonic earthquakes disappeared but volcanic tremor accompanied the total process of the volcanic column growth. **Figure 9** shows the temporal variations in the height of the eruption column together with the variation in the amplitudes of tremor observed at the seismic station SSU (2.5 km from Crater 1). There is a good correlation between these parameters. The amplitude of tremors reached maximum values when the eruption cloud reached its maximum height (Suzuki and Kasahara, 1979).

Soufrière Hills Volcano, Montserrat, 1996

Andesitic stratovolcano Soufrière Hills (SHV) with the height of 915 m is situated in the southern part of Montserrat Island, West Indies (**Figure 1**) and represents a Peleean lava dome complex constructed largely of hornblende andesite. The SHV edifice consists of four andesite lava domes and a fan of associated pyroclastic flow deposits. Its summit crater was likely formed c. 4,000 years ago. Castle Peak Dome, a small andesitic lava dome, partially filled the crater about 450 years ago (Young et al., 1998; <http://volcano.si.edu/volcano.cfm?vn=360050>).

Paroxysmal Eruption of 17 September 1996, Its Prelude and Effects

The eruption cycle of Soufrière Hills volcano (SHV), which included the paroxysmal explosive eruption of 17 September 1996, began with phreatic explosion on 18 July 1995 after 450 years of dormancy without any preliminary seismic activity beneath the volcano (<http://volcano.si.edu/volcano.cfm?vn=360050>). Several steam vents formed a NNW line across the Castle Peak Dome. Phreatic explosions with associated steam and ash columns rose to 3 km in height. The largest explosion occurred on 21 August. These explosions continued for four

months and gave a way to continuous eruption of juvenile andesitic magma in the form of lava dome and lava flows that began around 15 November 1995 and continued until the PEE of 17 September 1996 (Young et al., 1998).

On 17 September 1996, the SHV started a 9-h period of dome collapse. This collapse began at 11:30 and was followed by pyroclastic flows generation involving totally $11.7 \times 10^6 \text{ m}^3$ (Dense Rock Equivalent, DRE) in which 40% of the dome collapsed. After 2.5 h of quiescence, a paroxysmal explosive eruption occurred at 23:42. Explosive activity continued for about 50 min. A large crater-like depression 210 m deep formed in the dome open to the east. The height of plume reached 11–15 km, the volume of ejecta was estimated as $3.2 \times 10^6 \text{ m}^3$ (DRE). Pumice and lithic lapilli fell widely across southern Montserrat and houses were destroyed in the nearest village (Robertson et al., 1998).

The image of 4-band Advanced Very High Resolution Radiometer (AVHRR) multispectral data, provided from the NOAA polar-orbiting satellite series, shows that the cloud, elongating from Montserrat about 1 h after the 17 September PEE, was 175 km long E-W and 75 km wide N-S. The image, taken later in about 5 h, shows that with a distance from the island the cloud quickly became very diffuse (<http://www.geo.mtu.edu/volcanoes/west.indies/soufriere/govt/images>).

Seismic History of the Soufrière Hills Volcano PEE

We use the catalog of volcano-tectonic earthquakes prepared by (Aspinall et al., 1998; Miller et al., 1998). This catalog included about 600 volcano-tectonic earthquakes with magnitudes from -0.5 to 2.4 that were located from 28 July 1995 (10 days after beginning of the eruption on 18 July) to the end of February 1997. Gardner and White (2002) wrote that the 18 July vent opened without notable accompanying seismicity.

The pre-PEE July 1995–September 1996 volcano-tectonic earthquakes occurred within three epicentral zones (**Figure 10A**): beneath St. George Hill (SGH), that is situated about 5 km to the NW from the volcano (I), along the structure extending to the NE of the volcano (II), and beneath Soufrière Hills volcano (III).

As noted before, the eruption developed into two main stages: phreatic and magmatic, separated by a long (about 1 year) stage of the construction of lava dome and emplacement of associated lava flows. We describe here the variations in seismic activity associated with the stage of phreatic explosions that reached its peak on 21 August 1995 and the stage of occurrence of magmatic PEE that occurred on 17 September 1996.

Increase in seismic activity before the phreatic explosion of 21 August began with a 2-day swarm of earthquakes along the NE extent of the SHV (Zone II) from 5 to 6 August, then a new two-day swarm was recorded beneath SGH (Zone I) that continued from 12 to 13 August (**Figures 10A, 11A,C**). These seismic events occurred at the depth range from 6 to 3 km b.s.l. Beginning from 20 August the seismic foci migrated upward to the surface filling the volume III beneath the volcano. During 2 days, 20 and 21 August, about 140 earthquakes with magnitudes between -0.5 and 0.4 were recorded. The seismic events recorded

beneath the volcano clustered within a vertical column shape volume extending from 3 km b.s.l. to the summit of the volcano.

The explosion occurred at 08:03 of 21 August (B. Voight, personal communication, 2002) during the maximum level of seismic activity within zone III beneath the volcano. Just after the explosion, the number of seismic events sharply decreased.

The magmatic PEE of this SHV's eruptive cycle occurred 1 year later, on 17 September 1996. The seismic activity that preceded this paroxysmal explosion from 10 August is shown in **Figures 10B, 11B,D**. The zones I and II, that were active before the 21 August 1995 phreatic explosion, now were calm. The earthquake foci were clustered mainly beneath the SHV (zone III) forming a vertical column rising from the depth of 3 km b.s.l. to the summit of the volcano.

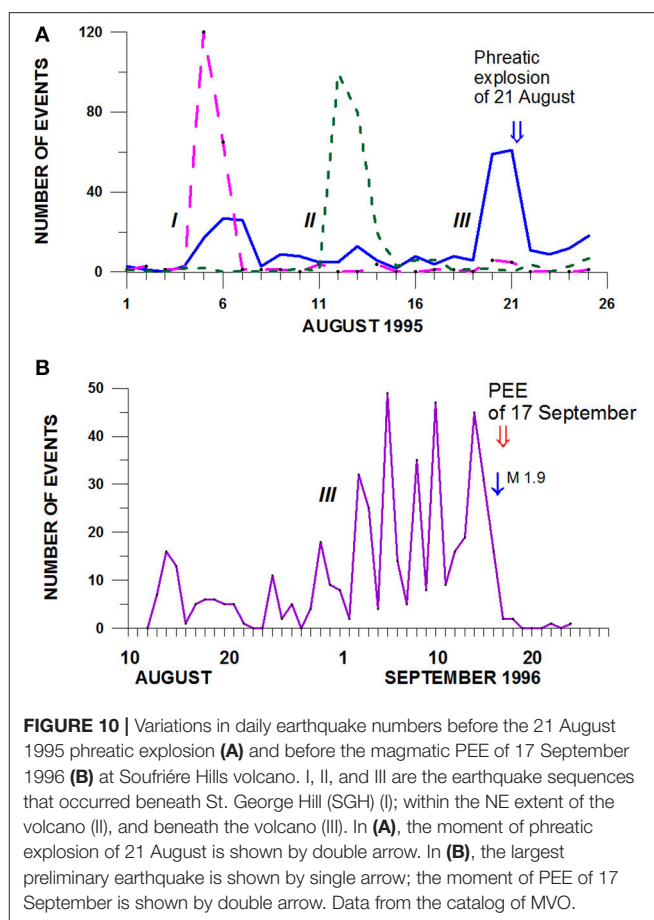
The swarm of earthquakes had no clear beginning (**Figure 10B**); it occurred on the background of continuous seismic activity due to the process of partial collapsing of the dome that began in July 1996. Nevertheless, we can mark the gradual increase in earthquake numbers beginning from 29 August; therefore, the swarm continued for about 23–24 days. The earthquakes were of low magnitudes between 0 and 1.9; the largest event with magnitude 1.9 occurred on 17 September at 10:01, just before the 9-h crater collapse preceding the PEE. The explosion occurred during the apparent decrease in number of seismic events. After the PEE event, the number of earthquakes sharply decreased.

Volcán de Colima, México, 2005

Andesitic stratovolcano Volcán de Colima (height of 3,860 m) is the most active in Mexico (**Figure 1**). Eruptions of Volcán de Colima during the last 480 years involved a wide spectrum of eruption styles, including small phreatic explosions, major block-lava emissions, and large explosive events including Plinian, sub-Plinian and Vulcanian eruptions (Bretón González et al., 2002). The 1997–2011 cycle, discussed below, was preceded 3 years earlier by a short episode on 13–21 July 1994 culminated in the phreatic explosion of 21 July. The explosion destroyed the 1991 crater dome and produced avalanches and ash fall. It formed a shallow crater approximately 140 m in diameter and 50 m in depth (Jiménez et al., 1995).

Paroxysmal Eruption of 5 June 2005, Its Prelude and Effects

The eruption cycle of Volcán de Colima, which included the 2004–2005 episode with paroxysmal explosive eruption of 5 June 2005, began on 22 November 1997 with 1-year sequence of volcano-tectonic earthquake swarms. Beginning from 20 November 1998, sequence of four endogenous episodes of lava dome construction and three episodes of lava domes destroyed by Vulcanian explosions, was recorded. The most intense Vulcanian explosions (VEI 3) were recorded during the 2004–2005 episode of lava dome construction-destruction. The extrusions of andesitic magma, which occurred during September–November 2004, had formed a new lava dome filling the active crater. The March 2005 explosions destroyed the 2004 lava dome. The repetitive building of new small-size domes was then observed during the April to July, 2005 explosive activity; each of them was destroyed by the following explosions. Finally,



a crater ~ 260 m across and ~ 30 m deep was left (Zobin et al., 2010). A photo, taken on 16 June from the southern side of the volcano (Zobin et al., 2010), shows the erosion channel at the summit, which was formed by pyroclastic flows related to the recent explosions. Many small impact craters formed on the floor of the crater.

The explosion, which occurred on 5 June 2005 at 14:20, was the largest in this sequence and may be considered as the paroxysmal event of the 2004–2005 episode as well as the total 1997–2011 cycle. This PEE blasted an ash plume which reached 9 km a.s.l. and had a length of 222 km. The time duration of the PEE, considering the time of explosion column growth and development, was not estimated but it continued during less than half of hour. The eruption column collapse was followed by emplacement of pyroclastic density currents with runout of 5.1 km and volume of $2.3 \times 10^5 \text{ m}^3$. Fall of ash was observed in the nearest villages. The local airport canceled all flights for a day. After the explosion of 5 June, evacuation was carried out of the village of Juan Barragan located nearest to the volcano (Zobin et al., 2016; <http://volcano.si.edu/volcano.cfm?vn=341040>).

Seismic History of the Volcán de Colima PEE

The 1998–2013 sequence of the lava dome constructions-destructions was preceded by a swarm of volcano-tectonic earthquakes only before the first 1998–1999 episode. The third episode of the cycle that developed during September 2004 to

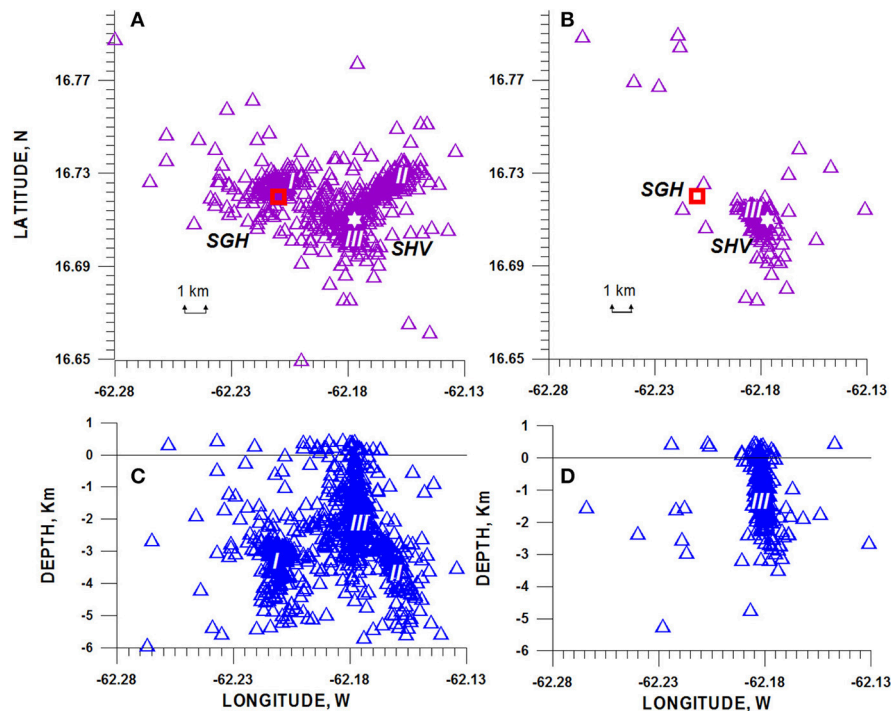


FIGURE 11 | Distribution of epicenters and hypocenters of earthquakes (triangles) located at Soufrière Hills volcano before the 21 August 1995 phreatic explosion (A,C) and before the magmatic PEE of 17 September 1996 (B,D). I, II, and III are the earthquake sequences that occurred beneath St. George Hill (SGH) (I); within the NE extent of the volcano (II), and beneath the volcano (III). The square marks SGH, the star marks Soufrière Hills volcano (SHV). Zero-line of sea-level depth is shown. Data from the catalog of MVO.

December 2005 (<http://volcano.si.edu/volcano.cfm?vn=341040>) was not preceded by any volcano-tectonic seismicity. As it can be seen in **Figures 12, 13**, the seismic activity before and during the episode was produced by numerous rockfalls, pyroclastic flows, and small explosions. Their daily number sharply increased during the lava dome extrusion occurring from the end of September 2004 to the beginning of November 2004 and stayed at a level of 200–300 rockfall events and 50–60 small explosions. Before the beginning of and during the sequence of the March–April 2005 large explosions, the number of the seismic signals of rockfalls and small explosions was at low level, between 1 to 5 daily events. The number of the seismic events of both types began to increase until 10–20 daily earthquakes in the middle of May. The beginning of June, before the 5 June PEE, was characterized by a sharp decrease of small explosions but also increase in the number of rockfalls (**Figure 12**). Another type of the seismic activity before the PEE was represented by microearthquakes that sharply increased in their number about 12 h before the PEE (**Figure 13B**). These microearthquakes, clearly seen on the seismogram recorded at a distance of 1.6 km from the crater (**Figure 13A**), were identified as micro-explosions and micro-rockfalls (Zobin et al., 2010).

DISCUSSION

Now let us discuss the dynamics of paroxysmal explosive activity of andesitic and dacitic volcanoes presented in this article. At first, we consider the dynamics of PEEs of the first group (VEI

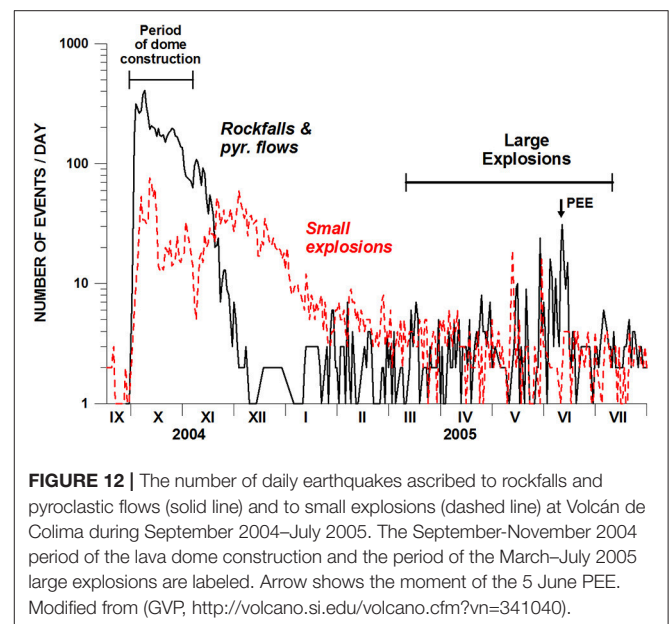


FIGURE 12 | The number of daily earthquakes ascribed to rockfalls and pyroclastic flows (solid line) and to small explosions (dashed line) at Volcán de Colima during September 2004–July 2005. The September–November 2004 period of the lava dome construction and the period of the March–July 2005 large explosions are labeled. Arrow shows the moment of the 5 June PEE. Modified from (GVP, <http://volcano.si.edu/volcano.cfm?vn=341040>).

5–6) that occurred at the volcanoes of Mount St. Helens, El Chichon, and Pinatubo. The following main stages of their dynamics may be formulated:

1. Stage of quiescence. It may continue from 120 years (MSH) till 500–550 years (Pinatubo, El Chichón).

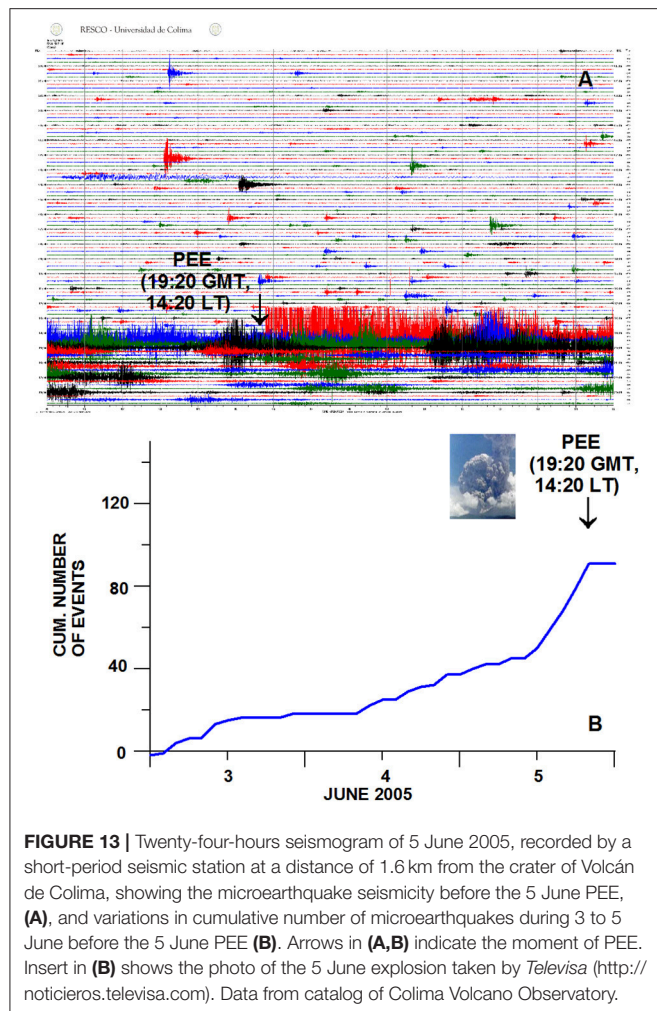


FIGURE 13 | Twenty-four-hours seismogram of 5 June 2005, recorded by a short-period seismic station at a distance of 1.6 km from the crater of Volcán de Colima, showing the microearthquake seismicity before the 5 June PEE, (A), and variations in cumulative number of microearthquakes during 3 to 5 June before the 5 June PEE (B). Arrows in (A,B) indicate the moment of PEE. Insert in (B) shows the photo of the 5 June explosion taken by Televisa (<http://noticieros.televisa.com>). Data from catalog of Colima Volcano Observatory.

2. Stage of re-awakening. This stage is characterized by appearance of swarms of volcano-tectonic earthquakes in the surroundings of the volcano and beneath the volcano indicating the arrival of a new portion of magma. It may continue from 11 days (MSH) till 28 days (El Chichón).
3. Stage of phreatic explosions. This stage reflects the rise of magma. The foci of volcano-tectonic earthquakes form a vertical column beneath the volcano suggesting the progressive rise of magma. Decoupling between this magma and the faster rising pressurized gases may be the cause for the observed phreatic eruptions. This stage was observed before the PEE at MSH during 54 days; at Pinatubo, during 51 days. At El Chichón volcano, the stage of phreatic activity began after the 28 March large explosion, and the foci of volcano-tectonic earthquakes formed a vertical column beneath the volcano during the period of 4 days, just until the PEE of 3 April. The stage may culminate with the largest earthquakes of the swarm preceding the PEE, as it was recorded just before the directed blast at MSH (M_W 5.7).
4. Stage of PEE. The PEEs may occur as a directed blast (MSH), if associated with a sector collapse, or as a vertical eruptive

column with collapse of the edifice summit (El Chichón and Pinatubo).

5. Stage of co-PEE seismo-reaction. Swarms of earthquakes appeared during decreasing intensity of the Plinian activity of PEEs. At MSH, a sequence of 21 magnitude 4.0–4.5 events was recorded during 4 h; at El Chichón, a 5-h sequence of five intermediate-size (M_c 3.7–3.8) earthquakes was recorded; at Pinatubo, a sequence of 25 earthquakes of magnitude range from 4.5 to 5.7 was recorded during 7 h.

Let us discuss the nature and significance of these stages in development of eruption process. The stage of re-awakening, represented by the swarms of volcano-tectonic (VT) earthquakes, may indicate the input of new magma in the system of magma reservoirs beneath the volcano. This process covers areas significantly exceeding the area of volcanic structures and occurs within the depths between 10 and 25 km and the surface.

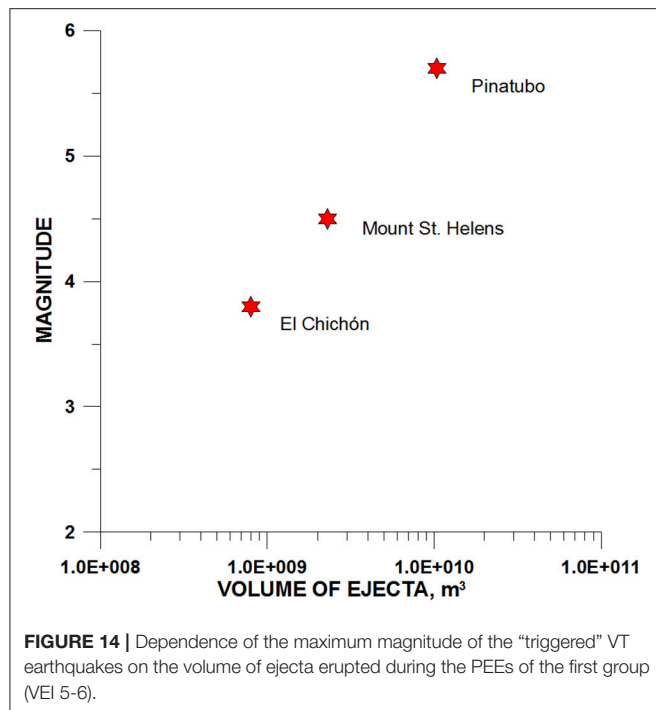
When magma reaches the volcanic edifice, the volcanic conduit filling begins. The foci of VT earthquakes cluster within a vertical volume just beneath the crater indicating magma ascent. The process of volatile exsolution from the melt as well as gas expansion during the stage of phreatic explosions promotes stress accumulation within the volcanic structure for initiation of the PEE.

During the PEEs, a great volume of volcanic rocks ejects, liberating space in the interiors beneath the volcano. It causes collapse of the upper magmatic system and, as a consequence, the swarms of “triggered” earthquakes whose magnitude may reach up to 5.7. The observations, obtained at our three PEEs of the first group (See **Table 1** and text), show that the maximum magnitude of “triggered” earthquakes, M_{max} , has a tendency of log-linear dependence on the volume of ejecta, V , during PEEs (**Figure 14**).

The appearance of these “triggered” seismic events during the PEEs indicates the partial emptying of the magma reservoirs, possibly also associated with the reactivation of regional tectonic structures. The areas of activation of post-eruption seismicity allow locating these magma reservoirs (Zobin, 2017).

In the case of MSH, the 50 km long regional structure within Cascade Range was activated to the north and to the south of the volcano, in addition to outward dipping fault zones merging below the volcano (Scandone and Malone, 1985). The depths of earthquakes reached 20 km (Weaver et al., 1981). In the case of El Chichón, the earthquake foci filled the depth interval from 0 to 25 km beneath the volcano (Jiménez et al., 1999). In the case of Pinatubo, the zone beneath the volcano spread to the west within volcanic edifice and occupied all beneath-volcano space filling it up to the depths of 25 km, about 20 km deeper than before the 15 June explosion. The seismicity also showed a clustering along outward dipping fault zones merging just below the volcanic edifice (Mori et al., 1996).

The dynamics of three selected PEEs of the second group (VEI 3), Usu volcano, SHV and Volcán de Colima, was out of the above-mentioned scheme. The dynamics of the PEE development at SHV was the only that partly kept within the main phases of the PEEs of the first group. At first, it was re-awakening volcano having stage 1 of quiescence during 450 years



before the 1995-1996 cycle of eruption. The stage 2 was absent; no preliminary volcano-tectonic activity was recorded. At the same time, as was noted by Aspinall et al. (1998), the spatial separation of some of the hypocenters into two clusters, one under SGH and another under the SHV, recorded during a phreatic stage (stage 3 for SHV) was reminiscent of pre-eruption activity (Stage 2) recorded in 1991 at Pinatubo volcano (compare **Figures 7, 11**). Stage 5 was absent; probably due to low ejecta volume (two-three orders of volume less than ejected during the PEEs of the first group; see **Tables 1, 2**), no “triggered” earthquakes were recorded during the 50-min plume development.

The appearance of PEEs at Usu volcano and Volcán de Colima was out of the proposed stage schemes. The preliminary VT swarm at Usu volcano was short, and lasted only for 32 h. No phreatic explosion stage was observed before the PEE. Probably due to low ejecta volume, no “triggered” earthquakes were recorded during the 2-h plume development, only volcanic tremor accompanied the PEE (See **Figure 9**).

The PEE appearance at Volcán de Colima was developed as standard lava dome construction-destruction. No preliminary VT swarm was recorded, only seismic signals associated with rockfalls and small explosions suggested such a process. The PEE simply “cleaned” the crater, removing the lava dome, without any destruction of the crater.

This absence of any regularity in the development of lower VEI eruptions of the second group may refer, among other reasons, to different conditions of opening of the magmatic conduit during these eruptions. All three PEEs of the first group

were preceded by a stage of quiescence that continued from 120 years (MSH) until 500–550 years (Pinatubo, El Chichón). This indicates the similar plugged conditions of their conduits and, as a result, the similar 5-stage development of eruptions. Among the PEEs of the second group, only SHV, having a stage of quiescence that continued for about 370 years, may be considered as a plugged conduit volcano. As we see, the build-up of its eruption was characterized by at least three of five stages noted for the PEEs of the first group. The two other PEEs, at Usu and Volcán de Colima, were supposedly developed in the conditions of open or semiplugged conduit, as suggested by their recent pre-PEE activity.

Therefore, this study confirms that eruptions with higher VEI are more likely to be related to a plugged magmatic conduit, whereas eruptions with lower VEI are usually more associated to open conduit conditions.

CONCLUSIONS

Review of the dynamics of PEEs development at andesitic and dacitic volcanoes during 1960–2010 was made for two groups of PEEs, of VEI 5-6 and VEI 3-4. The first group included three eruptions of VEI 5-6 and the second group included three eruptions of VEI 3. The PEEs of the first group have similarity in their development: long (more than 120 years) period of quiescence, preliminary VT swarm, period of phreatic explosions and then, PEE appearance. It was shown that the PEEs during their Plinian stage “triggered” the earthquake activity beneath the volcanic structures with the maximum magnitude of earthquakes proportional to the volume of ejecta of PEEs. For these PEEs of the first group, a 5-stage scheme of development process is proposed. The three discussed PEEs of the second group developed in more individual styles, probably resulting from the different conditions of opening or plugging of the magmatic systems. Therefore, this study confirms that eruptions with higher VEI are more likely to be related to a plugged magmatic conduit, whereas eruptions with lower VEI are usually more associated to open conduit conditions.

AUTHOR CONTRIBUTIONS

The author confirms being the sole contributor of this work and approved it for publication.

ACKNOWLEDGMENTS

The comments of V. Acocella, A. Bonaccorso, S. Calvari, and two reviewers helped to improve the manuscript. N. Stalbout helped to improve our English grammar. The catalogs of volcano-tectonic earthquakes were provided by Z. Jiménez (El Chichon volcano), J. Mori (Pinatubo volcano), and W. Aspinall (Soufriere Hills Volcano) and taken from the WEBSITE <https://pnsn.org/pnsn-data-products/earthquake-catalogs> (Mount St. Helens) and <https://earthquake.usgs.gov> (Pinatubo volcano).

REFERENCES

- Angell, J. K. (1998). Impact of El Chichon and Pinatubo on ozonesonde profiles in north extratropics. *Geophys. Res. Lett.* 25, 4485–4488. doi: 10.1029/1998GL900224
- Aspinall, W. P., Miller, A. D., Lynch, L. L., Latchman, J. L., Stewart, R. C., White, R. A., et al. (1998). Soufriere Hills eruption, Montserrat, 1995–1997: volcanic earthquake locations and fault plane solutions. *Geophys. Res. Lett.* 25, 3397–3400. doi: 10.1029/98GL00858
- Bernstein, R. S., Baxter, P. J., Falk, H., Foster, L., and Frost, F. (1986). Immediate public health concerns and actions in volcanic eruptions: lessons from the Mount St. Helens eruptions, May 18–October 18, 1980. *Am. J. Public Health* 76(Suppl.) 25–38.
- Bretón González, M., Ramírez, J. J., and Navarro, C. (2002). Summary of the historical eruptive activity of Volcán de Colima, México 1519–2000. *J. Volcanol. Geotherm. Res.* 117, 21–46. doi: 10.1016/S0377-0273(02)00233-0
- Carey, S. N., and Sigurdsson, H. (1986). The 1982 eruptions of El Chichón volcano, Mexico (2): Observations and numerical modeling of tephra fall distribution. *Bull. Volcanol.* 48, 127–141. doi: 10.1007/BF01046547
- Christiansen, R. L., and Peterson, D. W. (1981). “Chronology of the 1980 eruptive activity,” in *The 1980 Eruptions of Mount St. Helens. Geol. Surv. Prof. Paper*, eds P. W. Lipman and D. R. Mullineaux (Washington).
- Dziewonski, A. M., Ekstrom, G., and Franzen, J. E. (1988). Global seismicity of 1980: centroid-moment tensor solutions for 515 earthquakes. *Phys. Earth Planet. Int.* 50, 125–154. doi: 10.1016/0031-9201(88)90003-9
- Gardner, C. A., and White, R. A. (2002). “Seismicity, gas emission and deformation from 18 July to 25 September 1995 during the initial phreatic phase of the eruption of Soufriere Hills Volcano, Montserrat,” in *The eruption of Soufriere Hills Volcano, Montserrat from 1995 to 1999*, eds T. H. Druitt, and B. P. Kokelaar (London; Memoirs: Geological Society), 567–581.
- Havskov, J., De la Cruz-Reyna, S., Singh, S. K., Medina, F., and Gutiérrez, C. (1983). Seismic activity related to the March–April, 1982 eruption of El Chichón volcano, Chiapas, México. *Geophys. Res. Lett.* 10, 293–296. doi: 10.1029/GL010i004p00293
- Jiménez, Z., Espíndola, V. H., and Espíndola, J. M. (1999). Evolution of the seismic activity from the 1982 eruption of El Chichon Volcano, Chiapas, Mexico. *Bull. Volcanol.* 61, 411–422. doi: 10.1007/s004450050282
- Jiménez, Z., Reyes, G., and Espíndola, J. M. (1995). The July 1994 episode of seismic activity at Colima volcano, México. *J. Volcanol. Geotherm. Res.* 64, 321–326. doi: 10.1016/0377-0273(94)00118-Z
- Katsui, Y., Komuro, H., and Uda, T. (1985). Development of faults and growth of Usu-Shinzan cryptodome in 1977–1982 at Usu volcano, North Japan. *J. Fac. Sci. Hokkaido Univ.* 21, 339–362.
- Katsui, Y., Oba, Y., Suzuki, T., Kondo, Y., Watanabe, T., Niida, K., et al. (1978). Preliminary report of the 1977 eruption of Usu Volcano. *J. Fac. Sci. Hokkaido Univ.* 18, 385–408.
- Layer, P. W., García-Palomo, A., Jones, D., Macías, J. L., Arce, J. L., and Mora, J. C. (2009). El Chichón Volcanic complex, Chiapas, México: stages of evolution based on field mapping and 40Ar/39Ar geochronology. *Geofis. Int.* 48, 33–54.
- Macías, J. L., Arce, J. L., Mora, J. C., Espíndola, J. M., Saucedo, R., and Manetti, P. (2003). A 550-year-old Plinian eruption at El Chichón Volcano, Chiapas, México: explosive volcanism linked to reheating of the magma reservoir. *J. Geophys. Res.* 108:2569. doi: 10.1029/2003JB002551
- Miller, A. D., Steward, R. C., White, R. A., Luckett, R., Baptie, B. J., Aspinall, W. P., et al. (1998). Seismicity associated with dome growth and collapse at Soufrière Hills volcano, Montserrat. *Geophys. Res. Lett.* 25, 3401–3404.
- Mori, J., White, R. A., Harlow, D. H., Okubo, P., Power, J. A., Hoblitt, R. P., et al. (1996). “Volcanic earthquakes following the 1991 climactic eruption of Mount Pinatubo: strong seismicity during a waning period,” in *Fire and Mud. Eruptions and lahars of Mount Pinatubo, Philippines* eds C. G. Newhall and R. S. Punongbayan (Seattle, WA: University of Washington Press), 339–350.
- Mullineaux, D. R., and Crandell, D. R. (1981). “The eruptive history of Mount St. Helens,” in *The 1980 Eruptions of Mount St. Helens*, eds P. W. Lipman, and D. R. Mullineaux (Washington, DC: Geological Survey Professional Paper 1250), 3–15.
- Newhall, C. G., Daag, A. S., Delfin, F. G. Jr., Hoblitt, R. P., McGeethin, J., Pallister, J. S., et al. (1996). “Eruptive history of Mount Pinatubo,” in *Fire and Mud. Eruptions and Lahars of Mount Pinatubo, Philippines*, eds C. G. Newhall and R. S. Punongbayan (Seattle, WA: University of Washington Press), 165–196.
- Newhall, C. G., and Self, S. (1982). The volcanic explosivity index (VEI): an estimate of explosive magnitude for historical volcanism. *J. Geophys. Res.* 87, 1231–1238. doi: 10.1029/JC087iC02p01231
- Niida, K., Katsui, Y., Suzuki, T., and Kondō, Y. (1980). The 1977–1978 eruption of Usu volcano. *J. Fac. Sci. Hokkaido Univ.* 19, 357–394.
- Paffengoltz, K. N. (ed.). (1978). *Geological Dictionary*. Moscow: Nedra.
- Robertson, R., Cole, P., Sparks, R. S. J., Harford, C., Lejeune, A. M., McGuire, W. J. et al., (1998). The explosive eruption of Soufriere Hills Volcano, Montserrat, West Indies, 17 September 1996. *Geophys. Res. Lett.* 25, 3429–3432. doi: 10.1029/98GL01442
- Robock, A. (1981). The Mount St. Helens volcanic eruption of 18 May 1980: minimal climatic effect. *Science* 212, 1383–1384.
- Robock, A. (2000). Volcanic eruptions and climate. *Rev. Geophys.* 38, 191–219. doi: 10.1029/1998RG000054
- Robock, A., and Mass, C. (1982). Mount St. Helens volcanic eruption of 18 May 1980: large short-term surface temperature effects. *Science* 216, 628–630. doi: 10.1126/science.216.4546.628
- Sabit, J. P., Pigtail, R. C., and de la Cruz, E. G. (1996). “The west-side story: observations of the 1991 Mount Pinatubo eruptions from the west,” in *Fire and Mud. Eruptions and lahars of Mount Pinatubo, Philippines*, eds C. G. Newhall and R. S. Punongbayan, (Seattle, WA: University of Washington Press), 445–456.
- Savoy, I. P., Luhr, J. F., and Navarro-Ochoa, C. (2008). Petrology and geochemistry of lava and ash erupted from Volcán Colima, Mexico, during 1998–2005. *J. Volcanol. Geotherm. Res.* 174, 241–256. doi: 10.1016/j.jvolgeores.2008.02.007
- Scandone, R., and Malone, S. (1985). Magma supply, magma discharge and readjustment of the feeding system of Mount St Helens during 1980. *J. Volcanol. Geotherm. Res.* 23, 239–262. doi: 10.1016/0377-0273(85)90036-8
- Schuster, R. L. (1981). “Effects of the eruptions on civil works and operations in the Pacific Northwest,” in *The 1980 Eruptions of Mount St. Helens. Geol. Surv. Prof. Paper*, eds P. W. Lipman and D. R. Mullineaux (Washington).
- Scott, W. E., Hoblitt, R. P., Torres, R. C., Self, S., Martinez, M. L., and Nillos, T. Jr. (1996). “Pyroclastic flows of the June 15, 1991, climactic eruption of Mount Pinatubo,” in *Fire and Mud. Eruptions and lahars of Mount Pinatubo, Philippines*, eds C. G. Newhall and R. S. Punongbayan (Seattle, WA: University of Washington Press), 545–570.
- Self, S., Zhao, J., Holasek, R. E., Torres, R. C., and King, A. J. (1996). “The atmospheric impact of the 1991 Mount Pinatubo eruption,” in *Fire and Mud. Eruptions and lahars of Mount Pinatubo Philippines* eds C. G. Newhall and R. S. Punongbayan, (Seattle, WA: University of Washington Press), 1089–1115.
- Simkin, T., and Siebert, L. (1994). *Volcanoes of the World, 2nd Edn*. Tucson: Geoscience Press. 349.
- Surono, Jousset, P., Pallister, J., Boichu, M., Buongiorno, M. F., Budisantoso, A., et al. (2012). The 2010 explosive eruption of Java’s Merapi volcano—A ‘100-year’ event. *J. Volcanol. Geotherm. Res.* 241–242, 121–135. doi: 10.1016/j.jvolgeores.2012.06.018
- Suzuki, S., and Kasahara, M. (1979). Seismic activity immediately before and in the early stage of the 1977 eruption of Usu volcano, Hokkaido, Japan. *J. Fac. Sci. Hokk. Univ. Ser. VII* 6, 239–254.
- Tilling, R. (2009). El Chichón’s “surprise” eruption in 1982: lessons for reducing volcano risk. *Geofis. Int.* 48, 3–19.
- Vignola, F. (1999). “Impact of aerosols from the eruption of El Chichón on beam radiation in the Pacific Northwest,” in *Pacific Northwest Solar Radiation Data* (Eugene: UO Solar Monitoring Lab), 27–32.
- Voight, B. (1981). “Time scale for the first moments of the May 18 eruption,” in *The 1980 Eruptions of Mount St. Helens, Geol. Surv. Prof. Paper*, eds P. W. Lipman and D. R. Mullineaux (Washington).
- Weaver, C. S., Grant, W. C., Malone, S. D., and Endo, E. T. (1981). “Post-May 18 seismicity: volcanic and tectonic implications,” in *The 1980 Eruptions of Mount St. Helens, Geol. Surv. Prof. Paper*, eds P. W. Lipman and D. R. Mullineaux (Washington).
- Wendel, J., and Kumar, M. (2016). Pinatubo 25 years later: eight ways the eruption broke ground. *EOS* 97.
- Winchester, S. (2003). *“Krakatau”*. New York, NY: Harper Collins Publishers

- Wolfe, E. W., and Hoblitt, R. P. (1996). "Overview of the eruptions," in *Fire and Mud. Eruptions and lahars of Mount Pinatubo, Philippines*, eds C. G. Newhall and R. S. Punongbayan (Seattle, WA: University of Washington Press), 3–20.
- Yokohama, Y., and Seino, M. (2000). Geophysical comparison of the three eruptions in the 20th century of Usu volcano, Japan. *Earth Planets Space* 52, 73–89.
- Yokoyama, I., Yamashita, H., Watanabe, H., and Okada, H. M. (1981). Geophysical characteristics of dacite volcanism – The 1977–1978 eruption of Usu volcano. *J. Volcanol. Geotherm. Res.* 9, 335–358. doi: 10.1016/0377-0273(81)90043-3
- Young, S. R., Sparks, R. S., Aspinall, W. P., Lynch, L., Miller, A. D., Robertson, R. E. A., et al. (1998). Overview of the eruption of Soufriere Hills volcano, Montserrat, 18 July 1995 to December 1997. *Geophys. Res. Lett.* 25, 3389–3392. doi: 10.1029/98GL01405
- Zobin, V. M. (1992). Volcanotectonic significance of the large earthquake of May 18, 1980 on . *Volcanol. Seismol.* 3, 63–72.
- Zobin, V. M. (2017). *Introduction to Volcanic Seismology*, 3rd Edn. Amsterdam; New York, NY; Tokyo: Elsevier.
- Zobin, V. M., Carrasco-Núñez, G., and Vargas-Gutiérrez, V. (2016). Field and seismic evaluation of the block-and-ash flows emplaced from eruption columns of the 2005 Vulcanian explosions at Volcán de Colima, México. *Bull. Volcanol.* 78:27. doi: 10.1007/s00445-016-1019-2
- Zobin, V. M., Melnik, O. E., Gonzalez, M., Macedo, O., and Bretón, M. (2010). Swarms of micro-earthquakes associated with the 2005 Vulcanian explosion sequence at Volcán de Colima, México. *Geophys. J. Int.* 182, 808–828. doi: 10.1111/j.1365-246X.2010.04647.x
- Conflict of Interest Statement:** The author declares that the research was conducted in the absence of any commercial or financial relationships that could be construed as a potential conflict of interest.
- The reviewer, SC, and handling editor declared their shared affiliation.
- Copyright © 2018 Zobin. This is an open-access article distributed under the terms of the Creative Commons Attribution License (CC BY). The use, distribution or reproduction in other forums is permitted, provided the original author(s) and the copyright owner are credited and that the original publication in this journal is cited, in accordance with accepted academic practice. No use, distribution or reproduction is permitted which does not comply with these terms.



Coupled Short- and Medium-Term Geophysical Signals at Etna Volcano: Using Deformation and Strain to Infer Magmatic Processes From 2009 to 2017

Marco Aloisi, Alessandro Bonaccorso*, Flavio Cannavò and Gilda M. Currenti

Istituto Nazionale di Geofisica e Vulcanologia, Sezione di Catania-Osservatorio Etneo, Catania, Italy

OPEN ACCESS

Edited by:

Roberto Sulpizio,
Università degli studi di Bari Aldo
Moro, Italy

Reviewed by:

Marco Viccaro,
Università degli Studi di Catania, Italy
Geoff Kilgour,
GNS Science, New Zealand

*Correspondence:

Alessandro Bonaccorso
alessandro.bonaccorso@ingv.it

Specialty section:

This article was submitted to
Volcanology,
a section of the journal
Frontiers in Earth Science

Received: 27 March 2018

Accepted: 20 July 2018

Published: 10 August 2018

Citation:

Aloisi M, Bonaccorso A, Cannavò F
and Currenti GM (2018) Coupled
Short- and Medium-Term Geophysical
Signals at Etna Volcano: Using
Deformation and Strain to Infer
Magmatic Processes From 2009 to
2017. *Front. Earth Sci.* 6:109.
doi: 10.3389/feart.2018.00109

In active volcanoes a main challenge is to identify and characterize the dynamics of magmatic sources from deformation and strain data. This task is of primary importance in frequently eruptive volcanoes, such as Etna. After the main flank eruption of 2008–2009 and until 2017, Etna volcano was characterized by a lively eruptive activity of different phases. These comprised 44 lava fountain episodes from the New South East Crater (NSEC), two sequences of close episodes of lava fountains from the Voragine crater (VOR), as well as some periods of summit effusive activity with a more prolonged supply of lava flows. Several studies have described and modeled single lava fountains episodes of the NSEC and VOR, in particular through high precision data from borehole strain-meters. In this study, we broaden the analysis also considering the medium-term volcano recharging/discharging periods preceding/accompanying the different eruptive phases during 2009–2017 by constraining the source positions through deformation recorded by the permanent GPS network. Together with the modeling deduced from the strain-meter data we produce a more complete representation of the different sources that characterized the different periods both in the medium-term (i.e., the preparatory phases showing inflation and the eruptive phases showing deflation) and in the short-term (i.e., the fast discharge associated with eruptive events). Our modeling explains the pathway of magma from the intermediate-shallow plumbing system to the surface and highlights a clear separation between the inflation and the deflation source depths, coherently with petrological constraints on the spatio-temporal evolution of magma transfer and storage.

Keywords: deformation and strain, volcano sources, inflation/deflation phases, eruptions, Etna volcano

INTRODUCTION

The monitoring and study of ground deformation pursue the goal to provide a clear contribution to understanding of magma ascent processes both during the preparatory and final phases leading to the eruptions in the various volcanoes that are monitored throughout the world. Magma during ascent can usually be stored in reservoirs that form, through the gradual accumulation of magma, sources of internal overpressure. In turn, these gradually deform the volcanic edifice, which responds with an inflation. Then, during the eruptive phases the volcano releases the accumulated

pressures and its edifice returns to equilibrium showing a deflation. Through the recording of the deformation patterns, the geodetic techniques allow us to constrain the position and the shape of the magmatic sources (for a review Dzurisin, 2003, 2007 and citations herein).

Two general problems characterize the modeling of the deformation signals recorded in the last decades: (i) eruptions are usually not frequent phenomena in the same volcano, and in most of the active volcanoes it is necessary to wait long intervals (from several years to tens-hundreds of years) between subsequent eruptions; (ii) the smaller the eruptions, i.e., if they involve reduced erupted volumes, the more difficult it is to detect appreciable deformation variations because of the resolution of the current instrumentation. As a result, in the various volcanoes worldwide, the few strongest eruptions are usually better studied.

Etna has been frequently erupting in the last 40 years, showing a great variety of eruptive styles. Since 1971, there have been eighteen major flank eruptions, numerous summit eruptions, periods of permanent Strombolian activity and hundreds of explosive events generating lava fountains (for a review of the Etna activity see Branca and Del Carlo, 2004; Allard et al., 2006). In the 30-year period (1980–2010), the ground deformation monitoring systems on Etna enabled investigating and modeling the storage sources of numerous effusive flank eruptions. All these major eruptions shared the same deformation dynamics: a medium-term recharging period (lasting months to years) that precedes the eruption producing the inflation of the volcano. The recharge phase ends with the propagation of the final intrusions (i.e., the feeder dikes) that produce marked and rapid deformation. The eruptive phase then begins, characterizing the discharge phase causing the volcano deflation. During 1980–2010 the deformation sources associated with these cycles of charging/discharging medium-term phases were inferred at depths ranging between 0 and 9 km b.s.l. (e.g., Bonforte et al., 2008; Aloisi et al., 2011), a zone that is defined as the shallow-intermediate plumbing system. Results of the modeling of the sources for the main eruptions, as obtained from ground deformation studies, are reported in Bonaccorso and Davis (2004), Bonforte et al. (2008), Aloisi et al. (2011), Bruno et al. (2012), and Patanè et al. (2013). The studies mainly investigated the pressurization phases recorded during the inflation preceding the eruption onset. For the period from 2002 to 2006 Palano et al. (2017) reviewed the inflation /deflation preceding /accompanying the three main flank eruptions 2002–2003, 2004 and 2006 by using GPS data in a common modeling approach. However, the heterogeneity of the models and approaches used by the various Authors in the previous studies poses serious problems when a comparison of the inferred source is needed to investigate the long-period/multi-eruption dynamics. Indeed, the identification of different sources and mechanical parameters of the medium does not guarantee a comparable class of solutions, which should be required to avoid bias and to compare the positions, dimensions and volumes changes of the sources with consistency.

The co-eruptive deformation associated with lava fountains has usually been very small and difficult to detect by classic

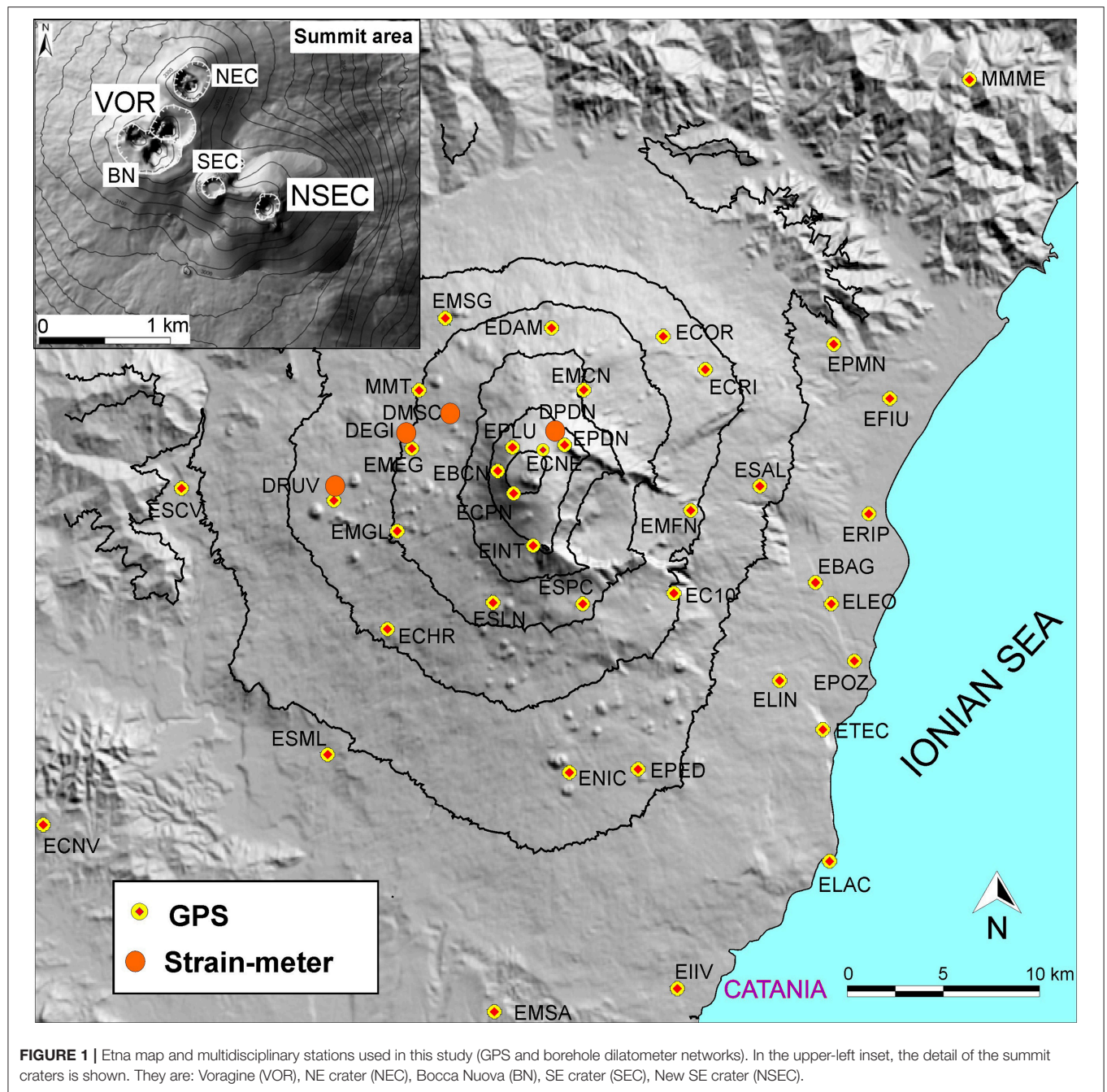
geodetic measurements such as GPS. However, by the end of 2014, four high precision borehole strain-meters have been installed. These instruments were capable of detecting clear strain changes associated with the lava fountaining activity, providing a tool to infer the source feeding the associated explosive activity (i.e., Bonaccorso et al., 2013, 2016).

In this paper, we provide a homogenous and consistent overview of the different active sources in the period 2009–2017. We did this by re-analyzing the medium-term recharging phases that preceded the different eruptions and the medium-term discharge periods characterized by cycles of several lava fountains or prolonged effusive phases. Finally, for some significant periods, we constrained the positions of the pressure sources and their volume changes that produced the deformation patterns recorded by the permanent GPS network. We used a uniform modeling approach to obtain comparable solutions of the inferred sources. This allowed a more complete and robust representation of the different sources that acted during the different recharging (i.e., medium-term preparatory phases) and discharging (i.e., the eruptive phases) phases. We highlight and discuss how the inferred sources are in agreement with a recent conceptual model of the Etnean plumbing system, made up of different magma storage zones, which were constrained by petrological and geochemistry studies (i.e., Kahl et al., 2015; Cannata et al., 2018). To the best of our knowledge, this is the first study where results from GPS and borehole strain-meter networks are used together to investigate medium- and short-term deformation sources at Etna volcano.

Etna 2009–2017 Activity

In the last decade, the activity of Mt. Etna did not produce major flank eruptions but instead has been characterized by tens of lava fountain events. A lava fountain is a powerful gas emission ejecting lava fragments to heights ranging from tens to hundreds of meters (Wilson and Head, 1981; Wolff and Sumner, 2000). In the Hawaiian cases the lava fountains typically range from ~ 10 to 100 m in height, and occasionally reach more than 500 m. Most of the material returns to the surface to form pyroclastic cones, rootless flows or lava ponds (Head and Wilson, 1987). Lava fountains at Etna are often different from the Hawaiian style for their more explosive power and for the formation of a several kilometers high, sustained eruptive column causing widespread ash fallout (e.g., Calvari et al., 2011; Bonaccorso et al., 2014). It is for this reason that they have often been referred as “paroxysmal” (e.g., Bonaccorso et al., 2011a,b, 2013; Gambino et al., 2016) to highlight their greater power when compared to the Hawaiian lava fountains.

After the last flank eruption of 2008–2009, there were 52 lava fountains from January 2011 to May 2016, erupted from Etna’s main craters (**Figure 1**). 45 episodes (44 from January 2011 to December 2013, and one episode in December 2014) led to the formation of the New South East crater (NSEC), next to the existing South East crater (SEC) SEC crater (inset in **Figure 1**). Moreover, two sequences of 4 and 3 events took place at the Voragine crater (VOR) on 3–5 December 2016 and



18–21 May 2016, respectively. Generally, all of the 2011–2013 lava fountain episodes from the NSEC showed generally similar main characteristics, with the height of the lava fountain reaching 300–1,000 m, ash columns reaching 5–9 km, and associated 4–6 km long lava flows descending the eastern flank of the volcano (i.e., Calvari et al., 2011; Behncke et al., 2014; De Beni et al., 2015). The average total DRE (density rock equivalent) volume of magma emitted during each of the 2011–2013 NSEC lava fountains, including both pyroclastic products and lava flows, was $\sim 2.5 \times 10^6 \text{ m}^3$ per event (De Beni et al., 2015). After the 2011–2013 NSEC lava fountains, the eruptive activity

switched to moderate lava effusion from the NSEC toward NE during January–April and July–August 2014. On 28 December 2014, a further lava fountain episode occurred at the NSEC (Gambino et al., 2016).

VOR is part of the main central crater and, in the last decades, has been much less active than the NSEC. Before 2015, the two main eruptive episodes were a sub-plinian explosion on 22 July, 1998 (Bonaccorso, 2006) and a powerful lava fountain on 4 September, 1999 (Calvari et al., 2002; Harris and Neri, 2002). After these two episodes, activity through the VOR was relatively quiet for several years until the sudden and powerful

sequence on 3–5 December, 2015, with a further eruption in May, 2016. The lava fountains of 3–5 December 2015 rank among the most violent to have occurred at Etna in the last two decades (Aloisi et al., 2017; Bonaccorso and Calvari, 2017). A summary of 2009–2017 eruptive activity is shown in **Table 1**.

The 2011–2016 lava fountains were characterized by a marked explosivity feeding a gas thrust region of several hundreds of meters. This sustained a several kilometer-high eruptive column expanding well beyond the lava fountain portion and causing widespread ash fallout (e.g., Calvari et al., 2011; Bonaccorso et al., 2014; Bonaccorso and Calvari, 2017). The short lived activity of lava fountains, although spectacular, emitted limited volumes of magma ($\sim 2.5 \times 10^6 \text{ m}^3$ per event) compared to the prolonged effusive flank eruptions, which usually emit from 1.0×10^7 to $2.0 \times 10^8 \text{ m}^3$. However, during 2011–2014, the high frequency of the NSEC lava fountain episodes erupted a total volume (pyroclastics products plus effusive flows) of $\sim 150 \times 10^6 \text{ m}^3$ (De Beni et al., 2015). Over this 2011–2014 time interval, this total erupted volume gives an average magma eruption rate similar (even higher) to the long-term output rate in the last decades through the usual effusive eruptions that is $25 \times 10^6 \text{ m}^3$ per year (Harris et al., 2011; Bonaccorso Calvari and Calvari, 2013). In other words, the 2011–2014 NSEC activity was characterized by an unusually high frequency of explosive episodes compared to Etna's activity in past decades, although the average magma erupted rate in this interval is close to the long-term output rate of the volcano mainly emitted through major effusive eruptions.

Strain and Deformation Monitoring Networks

The first permanent GPS stations were installed on Mt. Etna during November 2000 and, since then, the network has been further developed (Palano et al., 2010). At present, the volcanic edifice is monitored by 39 permanent stations (**Figure 1**). In this paper, we consider the data recorded by the GPS network from June 2009, immediately after the end of the 2008 flank eruption, to November 2017. Daily raw observations were processed using the GAMIT/GLOBK software (Herring et al., 2010) adopting the methodology described in Gonzalez and Palano (2014). Using the GLRED module of GLOBK, precise baselines of the whole network have been computed on a daily based solution. To further investigate the dynamics of fast ground displacements during the strongest eruptions, we considered also GPS data solutions at high rate (1 Hz). In particular, the high-rate GPS data were collected from the network dual-frequency GPS receivers and processed through Geodetics[®] RTD software package by epoch-by-epoch algorithm (Bock et al., 2001; Nikolaidis et al., 2001) to obtain a solution of position every second for all the measured points. Then, the solutions were post-processed to improve their reliability, eliminating the outliers by using an inter-quartile range (IQR) filter and filtered for the multipath noise (due to multi-path ground reflections of GPS signal) following the technique by Nikolaidis et al. (2001) and implemented in Cannavò et al. (2015). The remaining solutions were used

TABLE 1 | Eruptive periods from June 2009 to April 2017 with the type of eruptive activity and the detected inflation or deflation phases modeled in this study.

Eruptive periods (dd/mm/yyyy)	Activity type	Detected inflation/deflation phases	Modeled phases (see Table 2)
14/06/2009–31/12/2010	Recharging	INFLATION	I
20/05/2011–16/07/2011	Recharging	INFLATION	II
11/01/2011–12/05/2011	4 lava fountain at NSEC		
09/07/2011–15/11/2011	14 lava fountain at NSEC	DEFLATION	III
05/01/2012–24/04/2012	7 lava fountain at NSEC		
26/04/2012–15/02/2013	Recharging	INFLATION	IV
19/02/2013–12/04/2013	13 lava fountain at NSEC	DEFLATION	V
03/05/2013–23/10/2013	Recharging	INFLATION	VI
26/10/2013–2/12/2013	6 lava fountain at NSEC		
14–16/12/2013	Strombolian activity with overflows		
29–31/12/2013	Strombolian activity with overflows		
21/01/2014–01/04/2014	Effusive eruption from summit craters	DEFLATION	VII
05/07/2014–15/08/2014	Effusive eruption from summit craters	DEFLATION	VIII
28/12/2014	1 lava fountain at NSEC		
31/01/2015–02/02/2015	explosive activity and overflows		
16/05/2015	Explosive activity and overflows		IX
18/05/2015–01/12/2015	Recharging	INFLATION—IXa	
03–05/12/2015	Sequence of 4 lava fountains at VOR	DEFLATION	
06–08/12/2015	Effusive eruption from summit craters	DEFLATION	
07/12/2015–16/05/2016	Recharging	INFLATION—IXb	
18–21/05/2016	Sequence of 3 lava fountains at VOR	DEFLATION	
27/02/2017–27/04/2017	Several episodes of explosive activity with overflows from NSEC		

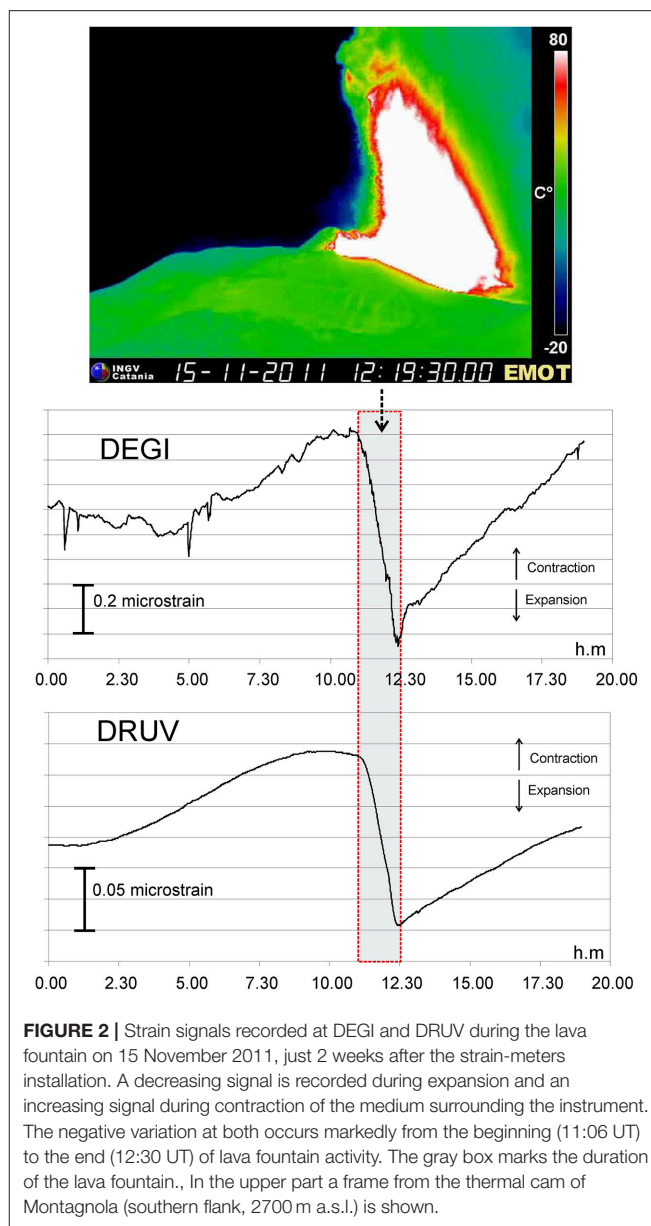
to estimate the baseline variation between pair stations in a time window of 3 min, as this is the minimum interval to obtain a satisfactory signal-to-noise ratio in the baseline time series.

In November 2011, two high precision borehole strain-meters, installed at a depth of 180 m in the western flank (DRUV and DEGI, **Figure 1**), began operating. Another two sensors were installed in November 2014 at a depth of 120 m in the upper heights of the volcano (DMSC and DPDN, in **Figure 1**). During 2015–2016, DPDN had several interruptions due to technical problems at the station. A description of the installations and implementation of the network is reported in Bonaccorso et al. (2016). The strain-meters are all Sacks-Evertson instruments, also called dilatometers, which measure the volumetric strain (change in volume/original volume) of the surrounding rock with a nominal precision up to 10^{-11} in a wide frequency range (10^{-7} – 10^2 Hz). This type of strain-meter is considered the most sensitive instrument used for monitoring deformation in geophysics. A detailed description of the design and capabilities of these instruments is given in Roeloffs and Linde (2007). The high sensitivity of the instrument is also affected by strain changes induced by environmental effects; however, installation at depths greater than 100 m reduces the noise generated in near surface rocks (e.g., by thermo-elastic effects). GPS and borehole strain-meters measurements are complementary techniques. The GPS network has a lower precision of $\sim 10^{-6}$ (resolution of millimeters over kilometer distances) but on Etna it has a denser coverage and is able to detect the cumulated medium-term inflation/deflation phases. The borehole strain-meters have a better precision and can detect the effect of small and brief transient phenomena such as the lava fountains, whose associated strain are in the range of 10^{-7} – 10^{-8} , difficult to be detected with GPS.

RESULTS-STRAIN AND DEFORMATION MODELING

Co-eruptive Short-Term Deformation and Inferred Sources

Despite the long-term drift characterizing the instruments during the first years of setup, clear strain changes were revealed during the short duration of the lava fountain episodes at NSEC (Bonaccorso et al., 2013, 2014). Soon after their installation, the borehole dilatometers detected the short-term variations produced by the lava fountains with high accuracy (**Figure 2**). All the recorded lava fountains showed the common aspect that the duration of the strain change coincides with the duration (usually a few hours) of the lava fountain. The strain change starts when the lava fountain begins and stops when the lava fountain finishes (**Figure 2**). It is interesting to note that strain suddenly changes only during the lava fountain, which suddenly empties the feeding reservoir, implying that the strain is sensitive to the magma output and the source emptying (e.g., Bonaccorso et al., 2013, 2016). Similar conclusions were also obtained from strain changes recorded during the frequent Vulcanian



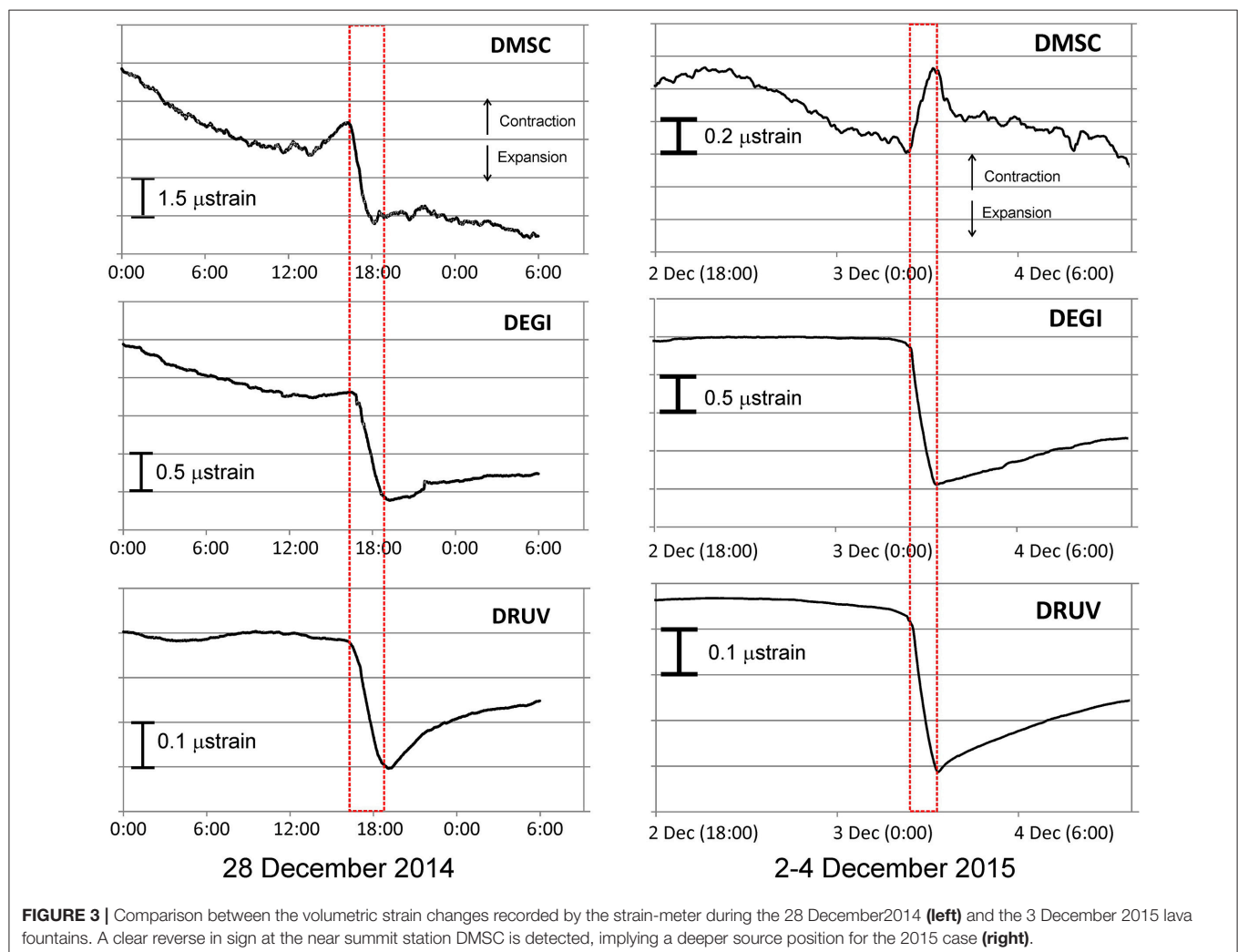
eruptions at Sakurajima volcano, Japan (Iguchi et al., 2008). The strain changes recorded during the 2011–2013 lava fountains erupted from the NSEC allowed constraining the decompression source at a shallow level (shallow plumbing system). Bonaccorso et al. (2013) applied a numerical model by using the finite element method (FEM) to evaluate the elastic response of the volcano edifice to a deflating source. The Authors inverted the average strain changes at the two working strain-meters (DEGI and DRUV), together with the average tilts recorded at radial distances of 2.2, 4, and 6–8 km. The best model reproducing the recorded strain and tilt changes was an ellipsoidal source constrained at sea level, with an aspect ratio of 0.5 (i.e., more elongated vertically), that underwent a change in volume of $\sim 2 \times 10^6$ m³. Bonaccorso et al. (2013) also estimated $\sim 0.5 \times 10^6$ m³ as the additional volume of erupted magma due to the

compressibility of residing magma within the source, therefore inferring a mean volume for each lava fountain episode coherent with the one deduced by surveys and aerophotogrammetry (De Beni et al., 2015).

Short-term strain changes were also recorded during the two powerful December 2015 and May 2016 sequences at VOR. Preliminary data analysis and modeling show that the strain changes at the three stations (DRUV, DEGI, and DMSC) are caused by the activation of a deeper portion of the magmatic plumbing system (Bonaccorso and Calvari, 2017). **Figure 3** shows a comparison between the strain signals recorded during the lava fountains of 28 December 2014 at NSEC and 3 December 2015 at VOR, respectively. As mentioned, the source of the NSEC was inferred at 0 km (b.s.l.) in agreement with all the episodes from the NSEC (Bonaccorso et al., 2016). All the strainmeters recorded negative changes temporally coincident with the duration of the lava fountain event. On the contrary, a clear positive change during the VOR episode was recorded at DMSC. In the case of a deflating pressure source, the volumetric strain reverses its sign moving radially from the source, as it goes from

compressional (positive) to extensional (negative) regime. This transition from positive to negative depends on the source depth. Therefore, the negative/positive pattern of the strain variations at the stations may enable to constrain the source depth. Generally, the deeper the source, the higher the radial distance at which the strain changes from positive to negative (Roeloffs and Linde, 2007). During the NSEC events, no positive strain changes were recorded at any of the stations, indicating a shallow source producing a narrow compressional pattern close to the summit area. Conversely, during the VOR episode the positive change recorded at DMSC is a clear indication of the activation of a deeper deflating source, whose associated strain pattern produces a compressional regime at higher radial distance from the source (Bonaccorso and Calvari, 2017).

Very weak deformation was recorded in the GPS time series during the NSEC events; instead, concurrent changes in the baseline variations, computed from high frequency GPS data analysis, were observed during the VOR activity (**Figure 4**). Coherently with the high frequency solutions, for the first episode, the GPS daily-based solutions showed displacements, up



to 5 mm, recorded at the entire network and showed a coherent radial pattern of deflation (Aloisi et al., 2017). The time series of high frequency solutions at the summit stations allowed us to follow the entire dynamic of the fountain in detail (Figure 4). In particular, the comparison between the mean baseline variation recorded by the GPS for the summit baselines crossing the crater area and the strain time series recorded by strain-meters shows a synchronous beginning of variation with the onset of the fountain event (Figure 4).

Medium-Term Recharging /Discharging Phases Inferred by GPS Data

We investigated the deflation-inflation cycles observed between June 2009 and November 2017, presenting an analytical solution to model the recorded GPS data. The variation of the area (Figure 5), recorded at an intermediate altitude triangle (EMEG-EMCN-ESLN), represents the average deformation of the volcano edifice well, clearly showing deflation-inflation cycles (e.g., Aloisi et al., 2011; Bruno et al., 2012; Patanè et al., 2013). The area of the triangle increases during periods of magma ascent, causing inflation. It decreases during and after eruptive periods, when magma outpours from the magmatic accumulation zones. As mentioned, the analyzed time interval has been studied in previous works. In particular, Aloisi et al. (2011) analyzed the 2009–2010 time period; Patanè et al. (2013) investigated the year 2011; Spampinato et al. (2015) and Bruno et al. (2016) analyzed some ground deformation phases observed during 2012–2013; Cannata et al. (2015) and Greco et al. (2016) analyzed some

phases recorded during the 2013; Viccaro et al. (2016) and Gambino et al. (2016) investigated the 2014 event; finally, Aloisi et al. (2017); Bonaccorso and Calvari (2017) and Cannata et al. (2018) studied the 2015–2017 activity. Different approaches were used by the Authors to model the observed deformation patterns. With the aim of obtaining comparable solutions among the sources in terms of the involved volumes and their locations, we decided to re-analyze some significant phases in the considered time window, using a uniform approach, i.e., to apply the same methodology to the different phases. Different inflation and deflation phases were selected from the areal dilation time series (Figure 5). In particular, assuming that any change in the area dilatation at the surface means that the deformation source is changing in position, pressurization or volume, we selected time spans characterized by coherent crustal deformation patterns, during which a homogeneous volcanic source is reasonably acting inside the volcano. We chose to investigate the following intervals, representing a selection of some of the more significant observed variations (Tables 1, 2): (I) a first phase of lasting inflation from 14 June 2009 to 31 December 2010; (II) a second phase of short inflation observed from 20 May 2011 to 16 July 2011; (III) the following third phase showing a deflation from 16 July 2011 to 17 October 2011; (IV) a fourth phase showing a new inflation of the volcano edifice from 26 April 2012 to 15 February 2013; (V) the following fifth phase of deflation from 15 February 2013 to 30 April 2013; (VI) a sixth phase of inflation from 3 May 2013 to 23 October 2013; (VII) and (VIII) two following phases of deflation from 20 January 2014 to 1

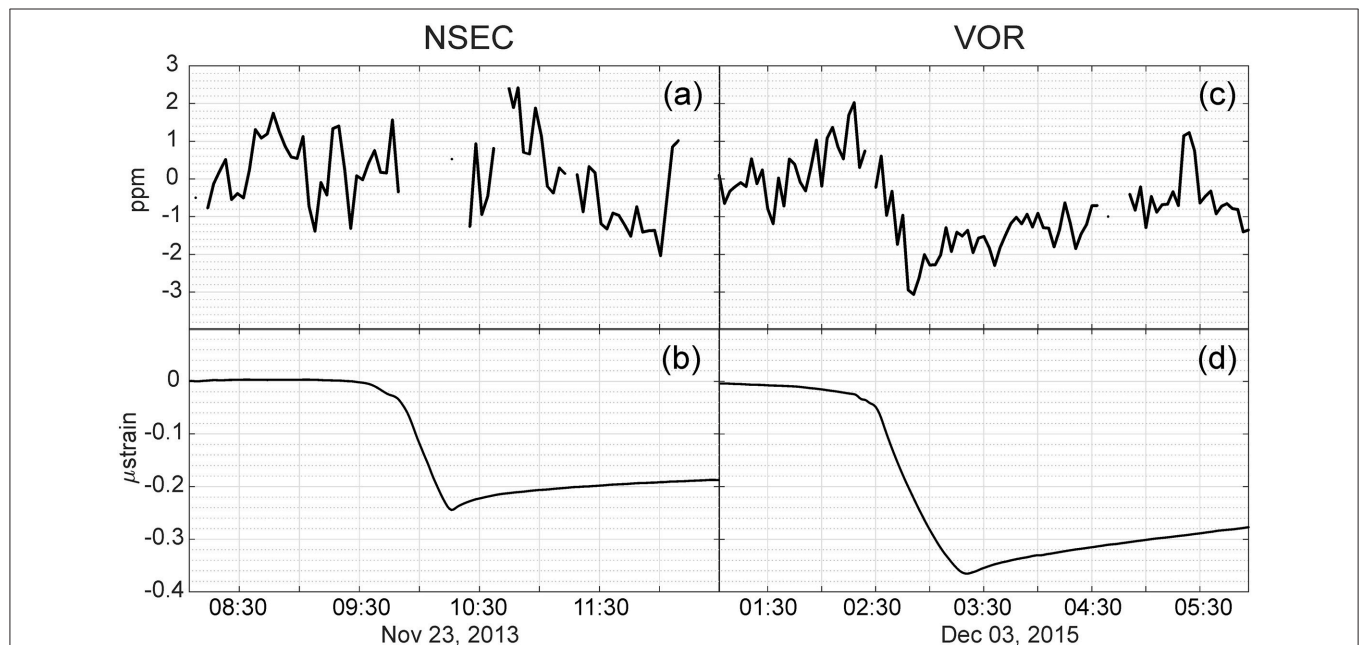
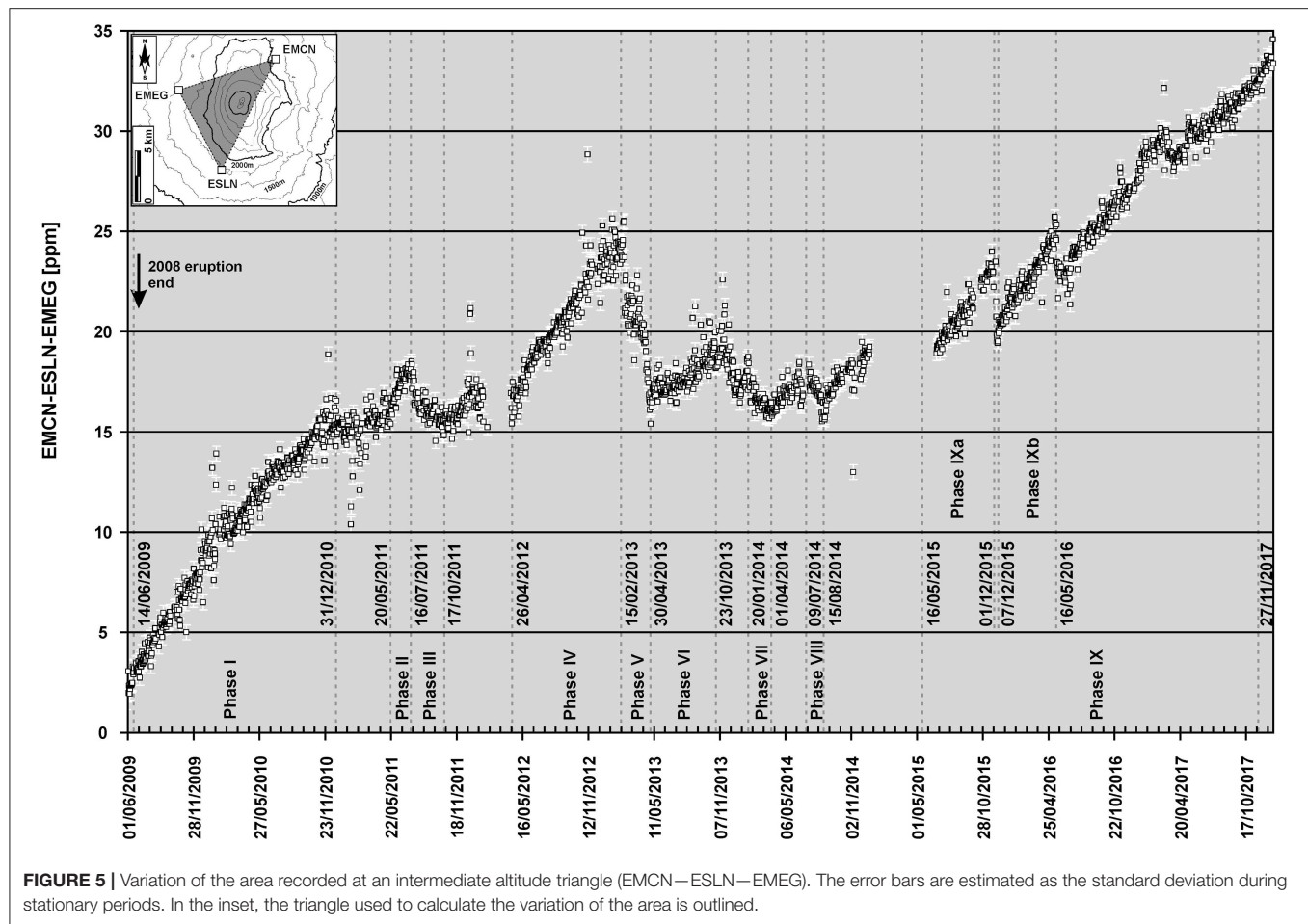


FIGURE 4 | Recorded strain and GPS signals during the lava fountains at NSEC and VOR craters. The 23 November 2013 lava fountain was one of the most powerful events of the 44 recorded from NSEC in 2011–2013. **(A)** Mean baseline variation calculated in percentile for the summit baselines crossing the crater area and **(B)** strain detected at DRUV station during the lava fountain of 23 November 2013 at NSEC. **(C)** Mean baseline variation calculated in percentile for the summit baselines crossing the crater area and **(D)** strain detected at DRUV station during the lava fountain of 3 December 2015 at VOR crater. The GPS did not detect changes during the lava fountains at NSEC, while a clear negative change (i.e., line contraction) was detected during the VOR more powerful event. Instead the strain-meter recorded small negative changes, i.e., expansion of the medium surrounding the station, during the NSEC lava fountains but recorded a bigger change during the VOR event.



April 2014 and from 09 July 2014 to 15 August 2014; (IX) a ninth phase representing the inflation recorded from 16 May 2015 to 27 November 2017. The last chosen phase is interrupted by short sub-periods of deflation related to the VOR explosive activity. As mentioned in the previous paragraph, we also detailed each lava fountain occurring at the VOR crater on Mount Etna, during the first days of December 2015. Moreover, to better understand this eruptive phase, it was useful to study the short cycles of inflation that preceded the December 2015 (from 18 May to 1 December 2015, phase IXa) and the May 2016 (from 7 December 2015 to 16 May 2016, phase IXb) VOR explosive sequences.

For each different deformation phase, we computed the baseline variations recorded at the GPS network in the corresponding time interval. Baseline estimations are not affected by possible biases in the choice of a local reference frame, and moreover they show lower levels of noise than the single GPS components. Therefore, with large GPS networks and for weak deformation, directly inverting baseline variations can represent a robust method to constrain a model for the recorded data, avoiding added uncertainties into the source modeling. We used the entire GPS network except the stations located on the lower eastern flank of the volcano (ERIP, EBAG, ELEG, EPOZ, ELIN,

TABLE 2 | Final optimal solutions for each modeled period.

Modeled period (dd/mm/yyyy)	Phase number	xc [m]	yc [m]	zc [m]	ΔV [m ³]
14/06/2009–31/12/2010	I	498,100	4178808	–6910	1.5E+07
20/05/2011–16/07/2011	II	499,288	4178699	–5429	2.9E+06
16/07/2011–17/10/2011	III	499,308	4177873	–3945	–1.6E+06
26/04/2012–15/02/2013	IV	499,184	4178794	–7469	1.6E+07
15/02/2013–30/04/2013	V	499,621	4178360	–4929	–8.2E+06
03/05/2013–23/10/2013	VI	499,405	4178125	–6077	3.3E+06
20/01/2014–01/04/2014	VII	500,132	4178908	–3968	–1.7E+06
09/07/2014–15/08/2014	VIII	499,931	4178620	–4485	–2.3E+06
16/05/2015–27/11/2017	IX	498,912	4179261	–7443	2.E+07
18/05/2015–01/12/2015	IXa	499,279	4178456	–5408	6.4E+06
07/12/2015–16/05/2016	IXb	499,400	4178394	–6246	7.3E+06

Estimated center coordinates (X_c , Y_c , Z_c) and volume change of the source are reported. We estimated uncertainties of ~ 300 [m] for the horizontal components, of ~ 700 [m] for the vertical component and, finally, of $\sim 1.9 \times 10^7$ [m³] for the volume change.

ETEC, EBDA, ELAC; see Figure 1) because it is well known that the eastern flank of Mt. Etna is affected by an almost constant ESE-ward sliding motion (for a review see, e.g., Aloisi et al.,

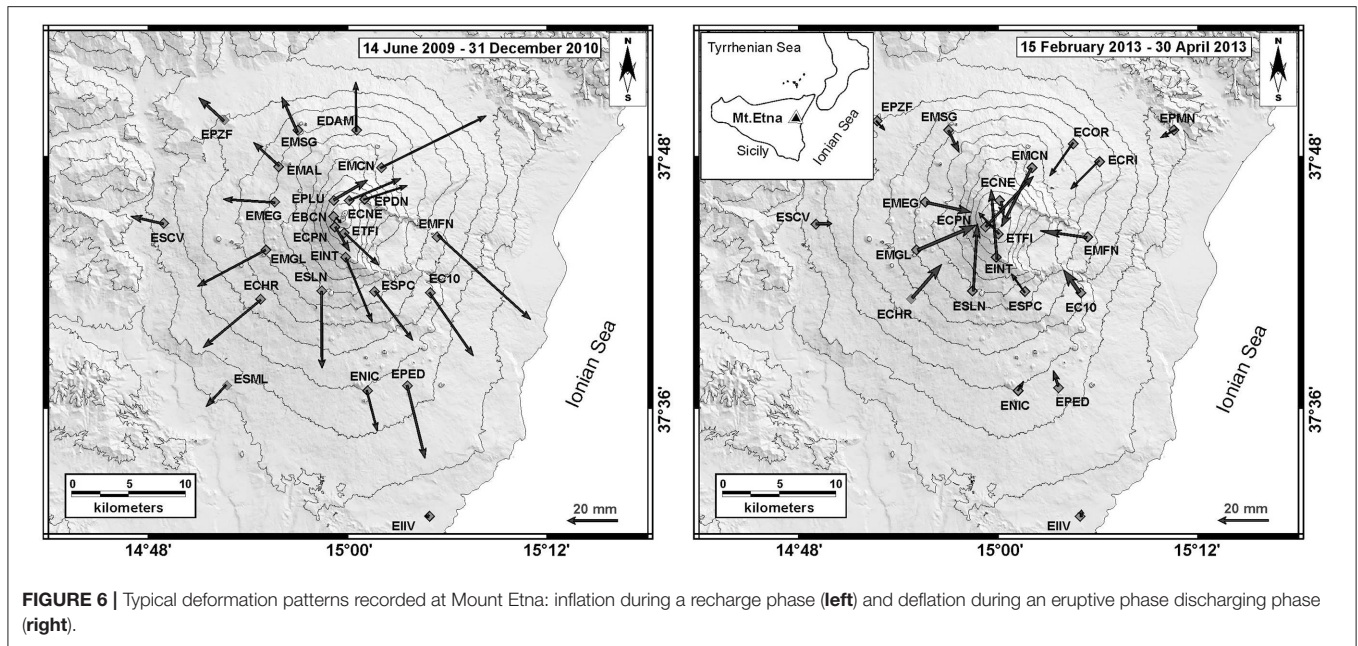


FIGURE 6 | Typical deformation patterns recorded at Mount Etna: inflation during a recharge phase (left) and deflation during an eruptive phase discharging phase (right).

2011; Murray et al., 2018). This large displacement is most likely not directly linked to the magma recharging/discharging processes; therefore, it is appropriate to exclude this area of the GPS network when the volcano plumbing system is investigated. For all the phases, we performed an analytical inversion of GPS baselines, describing the pressure source with a finite spherical magma body using the analytical solution of McTigue (1987). We chose this source model among other analytical models available in the literature since it showed a good trade-off between the number of degrees of freedom and the obtained data fit. This deformation source is described by five parameters: the coordinates “x,” “y,” and “z” of the sphere center, the radius “r” and the overpressure “P” on the source wall. It can be used to infer the centroid of the pressurizing/depressurizing sources. Model parameters were estimated for each phase, performing an inversion by means of the Pattern Search technique (Lewis and Torczon, 1999) together with a local Genetic Algorithm Search (Goldberg, 1989), finally followed by a non-linear least squares to better refine the solution. The uncertainty of each model parameter was estimated adopting a Jackknife re-sampling method (Efron, 1982). We included the effects of the topography using the method of Williams and Wadge (2000). The medium was assumed to be homogeneous and isotropic with a Young modulus of 75 GPa and a Poisson ratio of 0.25 (e.g., Aloisi et al., 2011). The volume change ΔV was estimated by means of the formulation described in Tiampo et al. (2000), using a shear modulus of 30 GPa. It is noteworthy that this value is an overestimation for a hot volcanic region and that a more correct evaluation of the shear modulus needs more attention, for example using a non-elastic rheology that is beyond the scope of this work. The modeled and recorded deformation pattern for two typical phases of inflation and deflation are shown in **Figure 6**. Final optimal solutions for each phase are shown in **Figure 7**, **Table 2**.

By using a uniform approach for all the selected periods (i.e., same kind of representative source, inversion method, and rheology parameters) we provided highly comparable solutions avoiding the bias that may often affect the solutions of different approaches. Under these conditions, the result highlights a clear separation between the inflation and deflation source depths. This is a new insight into the reconstruction of the magma movement and storage within the plumbing system of Mt. Etna volcano, as discussed in depth below.

DISCUSSION AND CONCLUSION

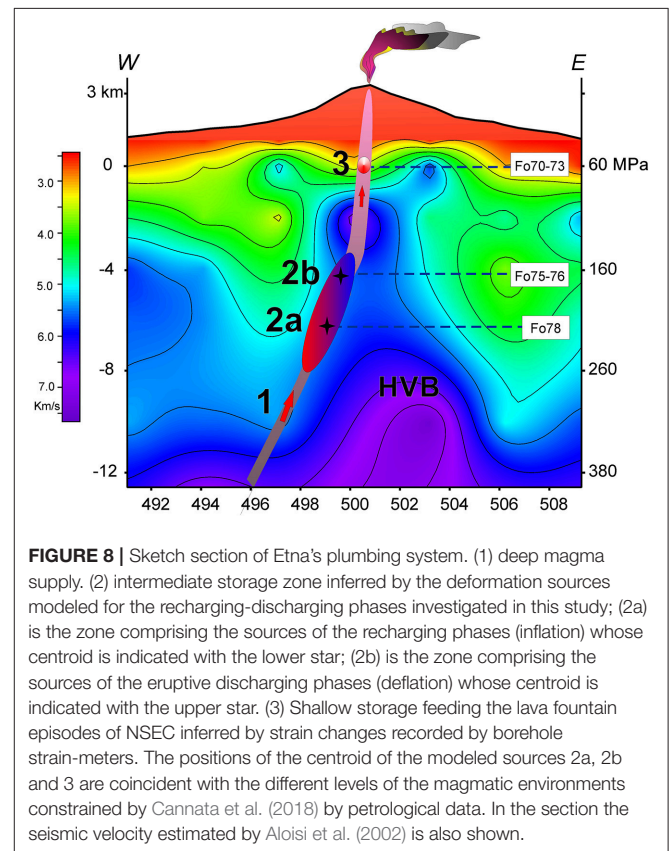
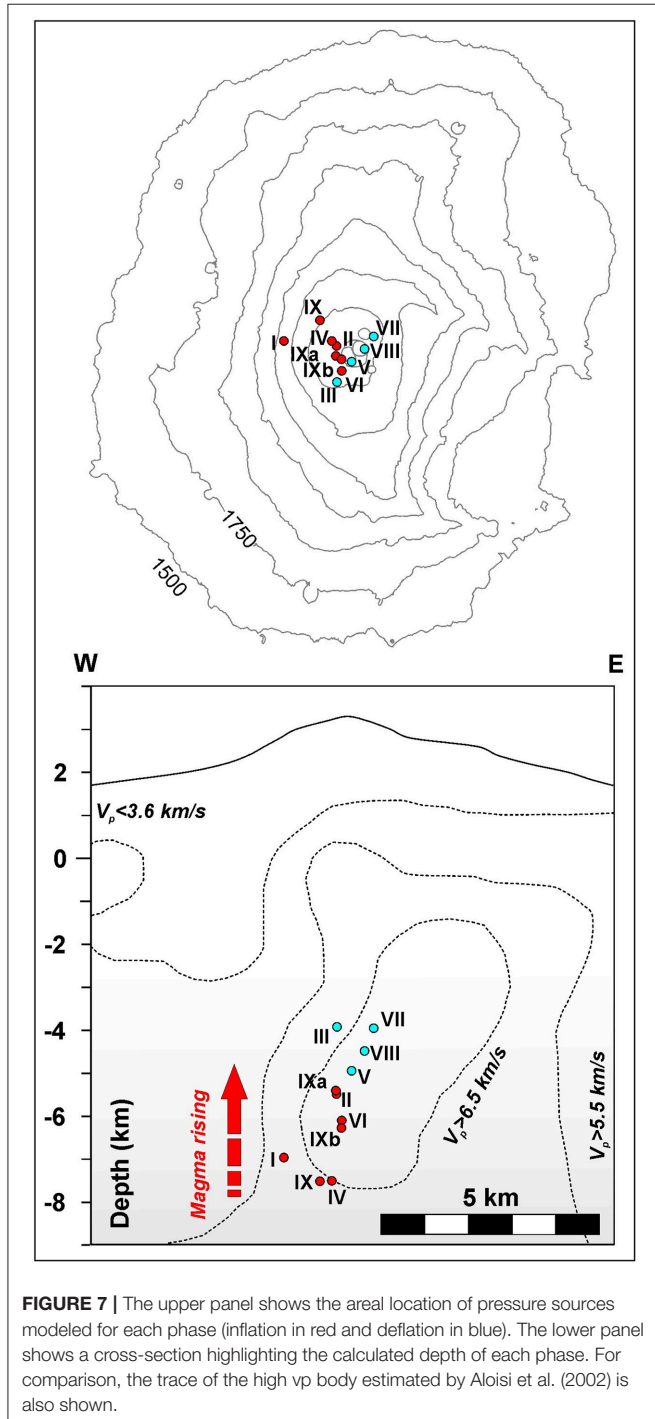
Medium- and short- term deformation sources at Etna volcano have been investigated with the aid of GPS and strain-meter data. These two kinds of deformation measurements have proven complementary to each other. The high-resolution and accuracy of the strain data have enabled us to follow rapid transient deformation related to the short-term discharge of magma through each fountaining event. GPS daily time series have been used to detect medium-term deformation processes related to the recharging of the magmatic plumbing system. Medium-term processes are difficult to recognize in the strain data because of the instrumental drift, while short-term processes are hidden in the GPS data due to the lower signal-to-noise ratio. For the most powerful eruptive events however, the processing of high rate GPS data has shown a general agreement in the temporal variations with respect to strain changes. The comparison of both datasets enabled us to assess their intrinsic advantages and drawbacks.

At Etna basaltic magmas and bubbles/liquid mixture rise for their positive buoyancy in the 22–2 km b.s.l. and, mainly related to their amount of H_2O , they can stall and form magmatic storage at different depths (Corsaro and Pompilio, 2004) that can cause the volcano deformation.

As previously found by many Authors (see Aloisi et al., 2011 for an overview), the pressure sources modeled here are located along the western border of the high velocity body (HVB), delineated using seismic tomographies (e.g., Patanè et al., 2006) (Figure 8). Furthermore, there is a general agreement that this border zone is coincident with the pathway that the magma takes toward the surface (e.g., Bonforte et al., 2008). Along this pathway, the magma can store and differentiate at various

depths, forming a multilevel plumbing system characterized by several magmatic environments, where different types of olivines can form (e.g., Kahl et al., 2015; Cannata et al., 2018). Thanks to the uniform approach of modeling applied here, for the inflation/deflation phases modeled by GPS data in the investigated period, our results highlight a very clear separation in depth between the inflation and the deflation sources (Figure 7). The centroid of the inflation sources is located at ~ 6.5 km (b.s.l.), the centroid of the deflation sources is located at ~ 4.5 km (b.s.l.).

With regards to the frequent short-term explosive lava fountains, for the NSEC events the strain changes constrained a shallower source located at a depth of 0 km b.s.l. (Bonaccorso et al., 2013). Regarding the four events that involved the VOR crater during the first days of December 2015, both Aloisi et al. (2017) and Cannata et al. (2018) found that the recorded deformation pattern is compatible with a deflation source located under the crater, at a depth of ~ 5 km b.s.l. Comparing with data recorded for the NSEC lava fountains, this result suggests that eruptions through VOR are sourced from a deeper portion of the magmatic plumbing system. This evidence agrees with petrological data that show the activation of magmatic environments deeper than those generally observed for other recent Etnean eruptions, involving deep basic magmas brought to shallow crustal levels in very short time scales (Cannata et al., 2018). Particularly, the olivine populations and



the associated magmatic storage zones, although comparable with those recognized in the products emitted from the NSEC crater, show a different distribution. The most abundant olivine samples Fo70–73 (expressed in Fo%), attributable to the shallow portion of the plumbing system, decrease from 63% in the case of NSEC events (Giuffrida and Viccaro, 2017) to 37% in the case of the VOR events. Concurrently, the olivine populations associated with deeper zoning patterns increase significantly. Therefore, the NSEC events were predominantly supplied by the shallow magma storage with main cycles of near regular recharging/discharging of this source that fed the lava fountains. As anticipated, this accords with the previous source modeling obtained by the analysis of the strain changes (Bonaccorso et al., 2013). For the lava fountains of NSEC, several geochemical and geophysical studies (Aiuppa et al., 2010; Bonaccorso et al., 2011a,b; Calvari et al., 2011; Ganci et al., 2012; Corsaro et al., 2017) supported the interpretation that these events were violent releases of bubble-rich magma layers previously decoupled from the melt and trapped at shallow depths close to sea level. The observed behavior for the NSEC lava fountains is a cyclic process of charge/discharge. This interpretation supports the “foam collapse” model proposed by Jaupart and Vergnolle (1989), as derived from a combination of theoretical approaches and laboratory experiments. The strain data confirm the validity of this eruptive model indicating a depressurizing source located at about sea level that is incapable of accumulating larger magma volumes and triggers frequent events with a nearly similar amount of magma stored (Bonaccorso et al., 2013).

Instead, the VOR events were sustained by different storage zones of the magmatic plumbing system with a higher contribution from deeper zones, which implicate a more complex dynamics that is more difficult to be modeled with simple shaped sources. Therefore, we believe that VOR eruption needs further in-depth studies.

In a general framework, these zones of the plumbing system identified by different deformation sources perfectly agree with three of the magmatic environments found in Cannata et al. (2018), as inferred by petrological data (**Figure 8**). In particular, the Authors found a magmatic environment at 290–230 MPa (~ 7 –10 km b.s.l.), where the composition of the olivine Fo78 (expressed in Fo%) forms. This environment corresponds to the depth level that we found for the medium-term inflation phases. Another level at 160–120 MPa (about 3–5 km b.s.l.) referred to crystals with Fo75–76 cores is related to the depth found for the medium-term deflation phases and the periods of lava fountains. And, finally, a shallower level close to the sea level with Fo70–73 is related to the NSEC activity. In **Figure 8** it is reported the scheme with the comparison of the position of the three magmatic environments inferred by petrological data and the geodetic sources inferred for the inflation and deflation phases (by GPS data) and for the NSEC lava fountain events (by high precision strain-meters).

It is noteworthy that the depth levels found for the intermediate storage, where the inflation/deflation processes are observed, and the shallow one are approximately coincident with the levels of two main geological discontinuities separating different main units in the Etnean crust (**Figure 8**). These levels

are (i) the separation between the Hyblean carbonate platform and the upper flyschoid units of the Apennine-Maghrebide chain, found at about 6 km b.s.l. (Lentini, 1982); (ii) the discontinuity between the Apennine-Maghrebide chain and the volcanic cover, located at about sea level (Monaco et al., 2011). Moreover, a persistent level of magma ponding at the depth of the deeper discontinuity (~ 6 km depth b.s.l.) is also supported by melt inclusion studied for previous eruptions (Métrich et al., 2004). Therefore, we believe that the depth of about 6 km (b.s.l.) represents a critical level for the magma ascending toward the surface. Along the western border of the HVB, where magma is believed to ascend, at this depth level, tomographic studies (e.g., Aloisi et al., 2002) estimated density values in the range 2,300–2,600 kg/m³. At about 10 km (b.s.l.), the estimated values are about 2,700–2,900 kg/m³. Therefore, in the depth range 5.5–7.5 km (b.s.l.), where inflation processes occur, basaltic magma (with a density of $\sim 2,800$ kg/m³) should pond for negative buoyancy. Likely, the structural discontinuity between the Hyblean platform and Apennine — Maghrebide chain, facilitates magma ponding. In this intermediate storage, due to the almost continuous magma input from depth (Bonaccorso Calvari and Calvari, 2013), the magma can accumulate, producing the observed inflation phases. During ponding, differentiation processes are also observed (Cannata et al., 2018). When the value of the magma overpressure is enough to break the medium and to reach the surface, the apical portion of this intermediate storage (~ 4.5 km depth b.s.l., **Figure 8**) ascends, producing the observed deflation phases.

This interpretation on the vertical shift of the inflation and deflation sources would mainly characterize the phases preceding (inflation) and accompanying (deflation) the eruptions with a more explosive behavior. This aspect is also confirmed by the results of previous studies. During the 2009–2010 inflation period, Aloisi et al. (2011) observed a progressive deepening of the deformation source over time, ascribed by the Authors to the role of the volatiles in preparing a more explosive eruption. Confirmation of this hypothesis can be found in Palano et al. (2017) where the Authors found that the 2002–03 flank eruption, characterized by a strong explosive activity, show a shift between the inflation and deflation sources. In particular, the Authors found that for the 2002–2003 eruption the deflation source was about 2 km shallower than the inflation source. Instead, for the less explosive 2004–2005 and 2006 flank eruptions, they observed the separation between inflation/deflation sources was not so marked. This separation between the centroids of the inflation/deflations sources is particularly clear in our results because shown for more cases of eruptive phases modeled by using a uniform approach.

AUTHOR CONTRIBUTIONS

AB conceived the study objectives. AB, GC, and MA coordinated and shared the writing of the paper and the research it is based on, static GPS data modeling was performed by MA. High frequency GPS data treatment was taken care of by FC. All authors contributed to the discussion of the results.

ACKNOWLEDGMENTS

We would like to thank the two Reviewers and the Editor in Chief V. Acocella for their constructive comments, which helped us to substantially improve the manuscript. We are particularly

indebted to the technical staff of Ground Deformation Group of INGV-OE who ensure the regular working of the permanent GPS and borehole strain-meter monitoring networks. We thank S. Conway for correcting and improving the English of the paper.

REFERENCES

- Aiuppa, A., Cannata, A., Cannovo, F., and Puglisi, G. (2010). Patterns in the recent 2007–2008 activity of Mount Etna volcano investigated by integrated geophysical and geochemical observations. *Geochem. Geophys. Geosyst.* 11:Q09008. doi: 10.1029/2010GC003168
- Allard, P., Behncke, B., D'Amico, S., Neri, M., and Gambino, S. (2006). Mount Etna 1993–2005: anatomy of an evolving eruptive cycle. *Earth Sci. Rev.* 78, 85–114. doi: 10.1016/j.earscirev.2006.04.002
- Aloisi, M., Cocina, O., Neri, G., Orecchio, B., and Privitera, E. (2002). Seismic tomography of the crust underneath the Etna volcano, Sicily, Phys. *Earth Planet. Inter.* 134, 139–155. doi: 10.1016/S0031-9201(02)00153-X
- Aloisi, M., Jin, S., Pulvirenti, F., and Scaltrito, A. (2017). The december 2015 Mount Etna eruption: an analysis of inflation/deflation phases and faulting processes. *J. Geodynamics* 107, 34–45. doi: 10.1016/j.jog.2017.03.003
- Aloisi, M., Mattia, M., Ferlito, C., Palano, M., Bruno, V., and Cannavò, F. (2011). Imaging the multi-level magma reservoir at Mt. Etna volcano (Italy). *Geophys. Res. Lett.* 38:L16306. doi: 10.1029/2011GL048488
- Behncke, B., Branca, S., Corsaro, R. A., De Beni, E., Miraglia, L., and Proietti, C. (2014). The 2011–2012 summit activity of Mount Etna: birth, growth and products of the new SE crater. *J. Volcanol. Geoth. Res.* 270, 10–21. doi: 10.1016/j.jvolgeores.2013.11.012
- Bock, Y., de Jonge, P. J., Honcik, D., and Wilson, S. (2001). “Epoch-By-Epoch™ Positioning applied to dam deformation monitoring At Diamond Valley Lake, Southern California,” in *Proceedings of 10th FIG International Symposium on Deformation Measurements* (Orange, CA), 78–87.
- Bonaccorso, A. (2006). Explosive activity at Mt. Etna summit craters and source modelling by using high precision continuous tilt. *J. Volc. Geoth. Res.* 158, 221–234. doi: 10.1016/j.jvolgeores.2006.05.007
- Bonaccorso, A., Caltabiano, T., Currenti, G., Del Negro, C., Gambino, S., Ganci, G., et al. (2011a). Dynamics of a lava fountain revealed by geophysical, geochemical and thermal satellite measurements: the case of the 10 April 2011 Mt Etna eruption. *Geophys. Res. Lett.* 38:L24307. doi: 10.1029/2011GL049637
- Bonaccorso, A., and Calvari, S. (2013). Major effusive eruptions and recent lava fountains: balance between expected and erupted magma volumes at Etna volcano. *Geophys. Res. Lett.* 40, 6069–6073. doi: 10.1002/2013GL058291
- Bonaccorso, A., and Calvari, S. (2017). A new approach to investigate an eruptive paroxysmal sequence using camera and strainmeter networks: lessons from the 3–5 December 2015 activity at Etna volcano. *Earth Planet. Sci. Lett.* 475, 231–241. doi: 10.1016/j.epsl.2017.07.020
- Bonaccorso, A., Calvari, S., Linde, A., and Sacks, S. (2014). Eruptive processes leading to the most explosive lava fountain at Etna volcano: the 23 November 2013 episode. *Geophys. Res. Lett.* 41, 4912–4919. doi: 10.1002/2014GL060623
- Bonaccorso, A., Cannata, R. A., Corsaro, G., Di Grazia, S., Gambino, F., Pistorio, A., et al. (2011b). Multidisciplinary investigation on a lava fountain preceding a flank eruption: the 10 April 2008 Etna case. *Geochem. Geophys. Geosyst.* 12:Q07009. doi: 10.1029/2010GC003480
- Bonaccorso, A., Currenti, G., Linde, A., and Sacks, S. (2013). New data from borehole strainmeters to infer lava fountain sources (Etna 2011–2012). *Geophys. Res. Lett.* 40, 3579–3584. doi: 10.1002/grl.50692, 2013
- Bonaccorso, A., and Davis, P. M. (2004). Modeling of ground deformation associated with recent lateral eruptions: mechanics of magma ascent and intermediate storage at Mt. Etna. *Geophys. Monograph. Ser.* 143, 293–306. doi: 10.1029/143GM18
- Bonaccorso, A., Linde, A., Currenti, G., Sacks, S., and Sicali, A. (2016). The borehole dilatometers network of Mt. Etna: a powerful tool to detect and infer volcano dynamics. *J. Geophys. Res. Solid Earth* 121. doi: 10.1002/2016JB012914
- Bonforte, A., Bonaccorso, A., Guglielmino, F., Palano, M., and Puglisi, G. (2008). Feeding system and magma storage beneath Mt. Etna as revealed by recent inflation/deflation cycles. *J. Geophys. Res.* 113:B05406. doi: 10.1029/2007JB005334
- Branca, S., and Del Carlo, P. (2004). “Eruptions of Mt. Etna during the past 3,200 years: a revised compilation integrating the historical and stratigraphic records,” in *Geophysical Monograph Series*, eds A. Bonaccorso, S. Calvari, M. Coltelli, C. Del Negro, and S. Falsaperla (Washington, DC: Etna volcano laboratory; AGU) 143, 1–27.
- Bruno, V., Ferlito, C., Mattia, M., Monaco, C., Rossi, M., and Scandura, D. (2016). Evidence of a shallow magma intrusion beneath the NE Rift system of Mt. Etna during 2013. *Terra Nova* 28, 356–363. doi: 10.1111/ter.12228
- Bruno, V., Mattia, M., Aloisi, M., Palano, M., Cannavò, F., and Holt, W. E. (2012). Ground deformations and volcanic processes as imaged by CGPS data at Mt. Etna (Italy) between 2003 and 2008. *J. Geophys. Res. Solid Earth* 117:B07208. doi: 10.1029/2011JB009114
- Calvari, S., Neri, M., and Pinkerton, H., (2002). Effusion rate estimations during the 1999 summit eruption on Mount Etna, and growth of two distinct lava flow fields. *J. Volcanol. Geotherm. Res.* 119, 107–123. doi: 10.1016/S0377-0273(02)00308-6
- Calvari, S., Salerno, G. G., Spampinato, L., Gouhier, M., La Spina, A., Pecora, E., et al. (2011). An unloading foam model to constrain Etna's 11–13 January 2011 lava fountaining episode. *J. Geophys. Res.* 116:B11207. doi: 10.1029/2011JB008407
- Cannata, A., Di Grazia, G., Giuffrida, M., Gresta, S., Palano, M., Sciutto, M., et al. (2018). Space-time evolution of magma storage and transfer at Mt. Etna volcano (Italy): The 2015–2016 reawakening of Voragine crater. *Geochem. Geophys. Geosys.* 19, 471–495. doi: 10.1002/2017GC007296
- Cannata, A., Spedalieri, G., Behncke, B., Cannavò, F., Di Grazia, G., Gambino, S., et al. (2015). Pressurization and depressurization phases inside the plumbing system of Mount Etna volcano: evidence from a multiparametric approach. *J. Geophys. Res. Solid Earth* 120, 5965–5982. doi: 10.1002/2015JB01222
- Cannavò, F., Camacho, A. G., González, P. J., Mattia, M., Puglisi, G., and Fernández, J. (2015). Real time tracking of magmatic intrusions by means of ground deformation modeling during volcanic crises. *Sci. Rep.* 5:10970. doi: 10.1038/s210970
- Corsaro, R. A., Andronico, D., Behncke, B., Branca, S., Caltabiano, T., Ciancitto, F., et al. (2017). Monitoring the December 2015 summit eruptions of Mt. Etna (Italy): implications on eruptive dynamics. *J. Volcanol. Geotherm. Res.* 341, 53–69. doi: 10.1016/j.jvolgeores.2017.04.018
- Corsaro, R. A., and Pompilio, M. (2004). Buoyancy-controlled eruption of magmas at Mt Etna. *Terra Nova* 16, 16–22. doi: 10.1046/j.1365-3121.2003.00520.x
- De Beni, E., Behncke, B., Branca, S., Nicolosi, I., Carluccio, R., D'Ajello Caracciolo, F., et al. (2015). The continuing story of Etna's New Southeast Crater (2012–2014): evolution and volume calculations based on field surveys and aerophotogrammetry. *J. Volcanol. Geotherm. Res.* 303, 175–186. doi: 10.1016/j.jvolgeores.2015.07.021
- Dzurisin, D. (2003). A comprehensive approach to monitoring volcano deformation as a window on the eruption cycle. *Rev. Geophys.* 41:29. doi: 10.1029/2001RG000107
- Dzurisin, D. (2007). *Volcano Deformation. Geodetic Monitoring Techniques*, New York, NY: Springer-Verlag.
- Efron, B. (1982). *The Jackknife, Bootstrap and Other Resampling Plans*. Philadelphia, PA: Society for Industrial and Applied Mathematics.
- Gambino, S., Cannata, A., Cannavò, F., La Spina, A., Palano, M., Sciutto, M., et al. (2016). The unusual 28 December 2014 dike-fed paroxysm at Mount Etna: timing and mechanism from a multidisciplinary perspective. *J. Geophys. Res. Solid Earth* 121, 2037–2053. doi: 10.1002/2015JB012379
- Ganci, G., Harris, A. J. L., Del Negro, C., Guéhenneux, Y., Cappello, A., Labazuy, P., et al. (2012). A year of lava fountaining at Etna: volumes from SEVIRI. *Geophys. Res. Lett.* 39:L06305. doi: 10.1029/2012GL051026

- Giuffrida, M., and Viccaro, M. (2017). Three years (2011–2013) of eruptive activity at Mt. Etna: working modes and timescales of the modern volcano plumbing system from micro-analytical studies of crystals. *Earth Sci. Rev.* 171, 289–322. doi: 10.1016/j.earscirev.2017.06.003
- Goldberg, D. E. (1989). *Genetic Algorithms in Search, Optimization and Machine Learning*. Boston, MA: Kluwer Academic Publishers.
- Gonzalez, P. J., and Palano, M. (2014). Mt. Etna 2001 eruption: new insights into the magmatic feeding system and the mechanical response of the western flank from a detailed geodetic dataset. *J. Volcanol. Geotherm. Res.* 274, 108–121. doi: 10.1016/j.jvolgeores.2014.02.001
- Greco, F., Currenti, G., Palano, M., Pepe, A., and Pepe, S. (2016). Evidence of a shallow persistent magmatic reservoir from joint inversion of gravity and ground deformation data: the 25–26 October 2013 Etna lava fountaining event. *Geophys. Res. Lett.* 43, 3246–3253. doi: 10.1002/2016GL068426
- Harris, A. J. L., and Neri, M. (2002). Volumetric observations during paroxysmal eruption at Mount Etna: pressurized drainage of a shallow chamber or pulsed supply? *J. Volcanol. Geotherm. Res.* 116, 79–95. doi: 10.1016/S0377-0273(02)00212-3
- Harris, A. J. L., Steffke, A., Calvari, S., and Spampinato, L. (2011). Thirty years of satellite-derived lava discharge rates at Etna: implications for steady volumetric output. *J. Geophys. Res.* 116:B08204. doi: 10.1029/2011JB008237
- Head, J. W. I., and Wilson, L. (1987). Lava fountain heights at Pu'u 'O'o, Kilauea, Hawaii: indicators of amount and variations of evolved magma volatiles. *J. Geophys. Res.* 92, 13715–13719. doi: 10.1029/JB092iB13p13715
- Herring, T. A., King, R. W., and McClusky, S. C. (2010). *Introduction to GAMIT/GLOBK, Release 10.4*. Cambridge, MA: Massachusetts Institute of Technology.
- Iguchi, M., Yakiwara, H., Tameguri, T., Hendrasto, M., and Hirabayashi, J. (2008). Mechanism of explosive eruption revealed by geophysical observations at the Saku-rajima, Suwanosejima and Semeru volcanoes. *J. Volcanol. Geotherm. Res.* 178, 1–9. doi: 10.1016/j.jvolgeores.2007.10.010
- Jaupart, C., and Vergnolle, S. (1989). The generation and collapse of foam layer at the roof of a basaltic magma chamber. *J. Fluid Mech.* 203, 347–380.
- Kahl, M., Chakraborty, S., Pompilio, M., and Costa, F. (2015). Constraints on the nature and evolution of the magma plumbing system of Mt. Etna Volcano (1991–2008) from a combined thermodynamic and kinetic modelling of the compositional record of minerals. *J. Petrol.* 56, 1–43. doi: 10.1093/ptrology/egv063
- Lentini, F. (1982). The geology of Mt Etna basement, *Mem. Soc. Geol. Ital.* 23, 7–25.
- Lewis, R. M., and Torczon, V. (1999). Pattern search algorithms for bound constrained minimization. *SIAM J. Optim.* 9, 1082–1099. doi: 10.1137/S1052623496300507
- McTigue, D. F. (1987). Elastic stress and deformation near a finite spherical magmabody: resolution of the point source paradox. *J. Geophys. Res.* 92, 12931–12940. doi: 10.1029/JB092iB12p12931
- Métrich, N., Allard, P., Spilliaert, N., Andronico, D., and Burton, M. (2004). 2001 flank eruption of the alkali- and volatile-rich primitive basalt responsible for Mount Etna's evolution in the last three decades. *Earth Planet. Sci. Lett.* 228, 1–17. doi: 10.1016/j.epsl.2004.09.036
- Monaco, C., De Guidi, G., and Ferlito, C. (2011). The morphotectonic map of Mt. Etna, It. *J. Geosci.* 129, 409–428. doi: 10.3301/IJG.2010.11
- Murray, J. B., van Wyk de Vries, B., Pitty, A., Sargent, P., and Wooller, L. (2018). Gravitational sliding of the Mt. Etna massif along a sloping basement. *Bull. Volcanol.* 80:40. doi: 10.1007/s00445-018-1209-1
- Nikolaidis, R. M., de Jonge, P. J., Shearer, P., Agnew, D. C., and Van Domselaar, M. (2001). Seismic wave observations with the global positioning system. *J. Geophys. Res.* 106, 21897–21916. doi: 10.1029/2001JB000329
- Palano, M., Rossi, M., Cannavò, F., Bruno, V., Aloisi, M., Pellegrino, D., et al. (2010). Etn@ref: a geodetic reference frame for Mt. Etna GPS networks. *Ann. Geophys.* 53, 49–57. doi: 10.4401/ag-4879
- Palano, M., Viccaro, M., Zuccarello, F., and Gresta, S. (2017). Magma transport and storage at Mt. Etna (Italy): a review of geodetic and petrological data for the 2002–03, 2004 and 2006 eruption. *J. Volc. Geoth. Res.* 347, 149–164. doi: 10.1016/j.jvolgeores.2017.09.009
- Patanè, D., Aiuppa, A., Aloisi, M., Behncke, B., Cannata, A., Coltelli, M., et al. (2013). Insights into magma and fluid transfer at Mount Etna by a multiparametric approach: a model of the events leading to the 2011 eruptive cycle. *J. Geophys. Res. Solid Earth* 118, 3519–3539. doi: 10.1002/jgrb.50248
- Patanè, D., Barberi, G., Cocina, O., De Gori, P., and Chiarabba, C. (2006). Time-resolved seismic tomography detects magma intrusions at Mount Etna. *Science* 313, 821–823. doi: 10.1126/science.1127724
- Roeloffs, E. A., and Linde, A. T. (2007). “Borehole observations and continuous strain and fluid pressure,” in *Volcano Deformation Geodetic Measurements Techniques*, ed D. Dzurisin (New York, NY: Springer-Verlag), 305–322.
- Spampinato, L., Sciutto, M., Cannata, A., Cannavò, F., La Spina, A., Palano, M., et al. (2015). Multiparametric study of the February–April 2013 paroxysmal phase of Mt. Etna New South-East crater. *Geochem. Geophys. Geosyst.* 16, 1932–1949. doi: 10.1002/2015GC005795
- Tiampo, K. F., Rundle, J. B., Fernandez, J., and Langbein, J. O. (2000). Spherical and ellipsoidal volcanic sources at Long Valley caldera, California, using a genetic algorithm inversion technique. *J. Volcanol. Geotherm. Res.* 102, 189–206. doi: 10.1016/S0377-0273(00)00185-2
- Viccaro, M., Zuccarello, F., Cannata, A., Palano, M., and Gresta, S. (2016). How a complex basaltic volcanic system works: constraints from integrating seismic, geodetic, and petrological data at Mount Etna volcano during the July–August 2014 eruption. *J. Geophys. Res. Solid Earth* 121, 5659–5678. doi: 10.1002/2016JB013164
- Williams, C. A., and Wadge, G. (2000). An accurate and efficient method for including the effects of topography in three-dimensional elastic models of ground deformation with applications to radar interferometry. *J. Geophys. Res.* 105, 8103–8120. doi: 10.1029/1999JB900307
- Wilson, L., and Head, J. W. III. (1981). Ascent and eruption of basaltic magma on the earth and moon. *J. Geophys. Res.* 86, 2971–3001. doi: 10.1029/JB086iB04p02971
- Wolff, J. A., and Sumner, J. M. (2000). “Lava fountains and their products,” in *Encyclopedia of Volcanoes*, ed H. Sigurdsson (San Diego, CA: Academic), 321–329.

Conflict of Interest Statement: The authors declare that the research was conducted in the absence of any commercial or financial relationships that could be construed as a potential conflict of interest.

Copyright © 2018 Aloisi, Bonaccorso, Cannavò and Currenti. This is an open-access article distributed under the terms of the Creative Commons Attribution License (CC BY). The use, distribution or reproduction in other forums is permitted, provided the original author(s) and the copyright owner(s) are credited and that the original publication in this journal is cited, in accordance with accepted academic practice. No use, distribution or reproduction is permitted which does not comply with these terms.



Mapping Volcanic Deposits of the 2011–2015 Etna Eruptive Events Using Satellite Remote Sensing

Gaetana Ganci^{1*}, Annalisa Cappello¹, Giuseppe Bilotta¹, Alexis Herault^{1,2}, Vito Zago^{1,3} and Ciro Del Negro¹

¹ Istituto Nazionale di Geofisica e Vulcanologia, Osservatorio Etneo, Catania, Italy, ² Conservatoire National des Arts et Métiers, Paris, France, ³ Dipartimento di Ingegneria Elettrica Elettronica e Informatica, Università di Catania, Catania, Italy

OPEN ACCESS

Edited by:

Clive Oppenheimer,
University of Cambridge,
United Kingdom

Reviewed by:

Diego Coppola,
Università degli Studi di Torino, Italy
Klemen Zaksek,
Universität Hamburg, Germany
Laura Becerril Carretero,
Instituto de Ciencias de la Tierra
Jaume Almera (ICTJA), Spain

*Correspondence:

Gaetana Ganci
gaetana.ganci@ingv.it

Specialty section:

This article was submitted to
Volcanology,
a section of the journal
Frontiers in Earth Science

Received: 14 March 2018

Accepted: 04 June 2018

Published: 21 June 2018

Citation:

Ganci G, Cappello A, Bilotta G, Herault A, Zago V and Del Negro C (2018) Mapping Volcanic Deposits of the 2011–2015 Etna Eruptive Events Using Satellite Remote Sensing. *Front. Earth Sci.* 6:83. doi: 10.3389/feart.2018.00083

Estimates of lava volumes provide important data on the lava flooding history and evolution of a volcano. For mapping volcanic deposits, including lava flows, the advancement of satellite remote sensing techniques offers a great potential. Here we characterize the eruptive events occurred at Mt Etna between January 2011 and December 2015 leading to the emplacement of numerous lava flows and to the formation of a new pyroclastic cone (NSEC) on the eastern flank of the South East Crater. The HOTSAT system is used to analyze remote sensing data acquired by the SEVIRI sensor in order to detect the thermal anomalies from active lava flows and calculate the associated radiative power. The time-series analysis of SEVIRI data provides an estimation of event magnitude and intensity of the effusive material erupted during each event. The cumulative volume estimated from SEVIRI images from 2011 to 2015 adds up to ~106 millions of cubic meters of lava, with a time-averaged rate of ~0.68 m³ s⁻¹. This estimate is independently supported and bounded using a topographic approach, i.e., by subtracting the last topography of Etna updated to 2005 from a 2015 digital elevation model (DEM), produced using tri-stereo Pléiades satellite images acquired on December 18, 2015. The total volume of products erupted from 2005 to 2015, calculated from topography difference by integration of the thickness distribution over the area covered, is about 287 × 10⁶ m³, of which ~55 × 10⁶ m³ is the volume of the NSEC cone. This 10-year volume is below the typical erupted volumes on decadal scale at Mt Etna, interrupting its stable and resilient output trend.

Keywords: Etna volcano, satellite remote sensing, SEVIRI, Pléiades imagery, digital elevation model

INTRODUCTION

Mapping the volcanic deposits constitute a critical component for constraining magma supply, understanding magma plumbing system, and controlling lava flow morphological parameters, and represents an important indication of the amount of magma the volcanic system is capable of transporting during an eruptive event (Wadge et al., 1975; Stevens et al., 1999). In particular quantifying the emitted lava volumes gives insights into emplacement processes and may aid computer simulations of lava flow paths for hazard assessment studies, providing both input data for predictive lava flow modeling, and tools for iterative validation and/or refining of parameters

(Del Negro et al., 2013; Cappello et al., 2016). However, the calculation of the amounts of lava erupted is still source of uncertainty, and problems occur when comparing volume values that are measured using different approaches (Harris et al., 2007).

Generally, volcanic products can be mapped following two different approaches. The simplest method is based on field measurements by multiplying the covered area, which can be determined with a good precision, by an estimated average thickness that remains the major source of uncertainty (Behncke et al., 2014). The second approach requires accurate mapping of the pre and post-eruption Digital Elevation Models (DEMs). This topographic approach is advantageous because deposit thickness is mapped throughout the flow field, resulting in detailed three-dimensional measurements of the morphology and yielding a highly accurate volume estimate. The method is limited by the availability of topographic data of the surface underneath the volcanic deposit of interest, and such measurements are difficult, if not impossible, to be made retrospectively (Del Negro et al., 2016).

The recent availability of satellite images gives new opportunities for mapping volcanic products. Indeed high spatial resolution data acquired in stereo or tri-stereo configuration (e.g., Pléiades) can be used to frequently update the topography in volcanic areas and thus provides a new tool for measuring volcanic deposits by differencing successive topographies. In addition, high temporal resolution data provided by geostationary infrared remote sensing (e.g., SEVIRI) allow to estimate mean eruptive rates associated to the lava flow and to compute the related volumes.

Here we employed both Pléiades data to map the eruptive products and SEVIRI data to characterize the eruptive episodes occurred at Mt Etna between January 11th, 2011 and December 8th, 2015.

Mt Etna is one of the most active volcanoes in the world, showing a persistent activity at the summit craters and frequent effusive eruptions from eruptive vents located on the volcano flanks (Cappello et al., 2013). Today five craters are active on the summit of Mt Etna (Neri et al., 2017): the North-East Crater (NEC), the Voragine (VOR), the Bocca Nuova (BN), the South-East Crater (SEC), and the New South-East Crater (NSEC). NEC, VOR, and BN formed inside the old Central Crater in 1911, 1945 and 1968, respectively. SEC, which has been the most active summit crater over recent decades, was built up during the 1971 eruption. Finally, the NSEC has formed in 2007 as a pit crater at the South-east base of the SEC (Acocella et al., 2016), but rapidly grew during the lava fountains occurred since January 2011 (Vicari et al., 2011). After the last flank eruption in 2008–2009 (Ganci et al., 2012b), the volcanic activity of Etna has shown a more explosive behavior, with an increasing number of paroxysmal events at the summit craters (Bonaccorso and Calvari, 2013; Cappello et al., 2013). Indeed, from 2011 to 2015, the SEC area has been the source of 53 eruptive episodes, most of them characterized by the emission of lava fountains, pyroclastic material, and short-lasting lava flows that mostly spread within the Valle del Bove (VdB).

In the following we estimated the effusion rate and hence the lava flow volume from SEVIRI data and computed some

morphometric parameters (area, maximum length, thickness, and volume) from the three-dimensional distribution of the volcanic deposits obtained by DEM difference using a new 2015 digital topography of Mt Etna derived from Pléiades data. The volcanic deposits obtained from DEM difference provide an independent maximum bound to the SEVIRI-derived lava flow volume and possibly an estimate of loose materials.

MATERIALS AND METHODS

Thermal-Infrared Satellite Data Sources and Analyses

Volcanic hotspots (i.e., high temperature areas or pixels) were detected and processed from SEVIRI images (sample time: 15 min, pixel resolution: 3 km at nadir) using the HOTSAT system for thermal monitoring of volcanoes (Ganci et al., 2011a,b). HOTSAT takes as input mid-infrared (MIR) and thermal infrared (TIR) channels acquired by the Spinning Enhanced Visible and Infrared Imager (SEVIRI), and provides cloud mask and thermal anomalies maps (if applicable). Since clouds can obscure thermal anomalies, we used an algorithm based on textons (Ganci et al., 2011a) to avoid underestimations in satellite-derived results. The detection of thermal anomalies associated to active lava flows is based on a contextual algorithm (Harris et al., 1995), which compares the “volcanic” area (where the thermal anomaly is expected) with a “non-volcanic” area (close to the volcano, where the thermal anomaly is not foreseen). The lava thermal flux is computed considering all those pixels classified as “hot” by using the mid-infrared radiance approach introduced by Wooster et al. (2003), which allows estimating the radiant heat flux radiated by a sub-portion of the thermally anomalous pixels approximating the Planck’s radiation law to a fourth order power law. This approach is particularly efficient with low spatial resolution sensors, such as SEVIRI, or moderate spatial resolution sensors such as Moderate Resolution Imaging Spectroradiometer (MODIS), given that the extent of lava flow fields is often subpixel in size (Ganci et al., 2013). During an eruption, the system computes an estimation of the thermal flux radiated by lava for each image, giving as result a heat flux curve describing the event. This heat flux curve can be converted in time-averaged discharge rate (TADR in m³/s—the effusion rate averaged over a specified period) adopting a straightforward relationship between the radiant heat loss from an active lava flow and the effusion rate (e.g., Harris et al., 1997; Wright et al., 2001):

$$TADR = \frac{Q}{\rho(C_p \Delta T + C_L \Delta \varphi)} \quad (1)$$

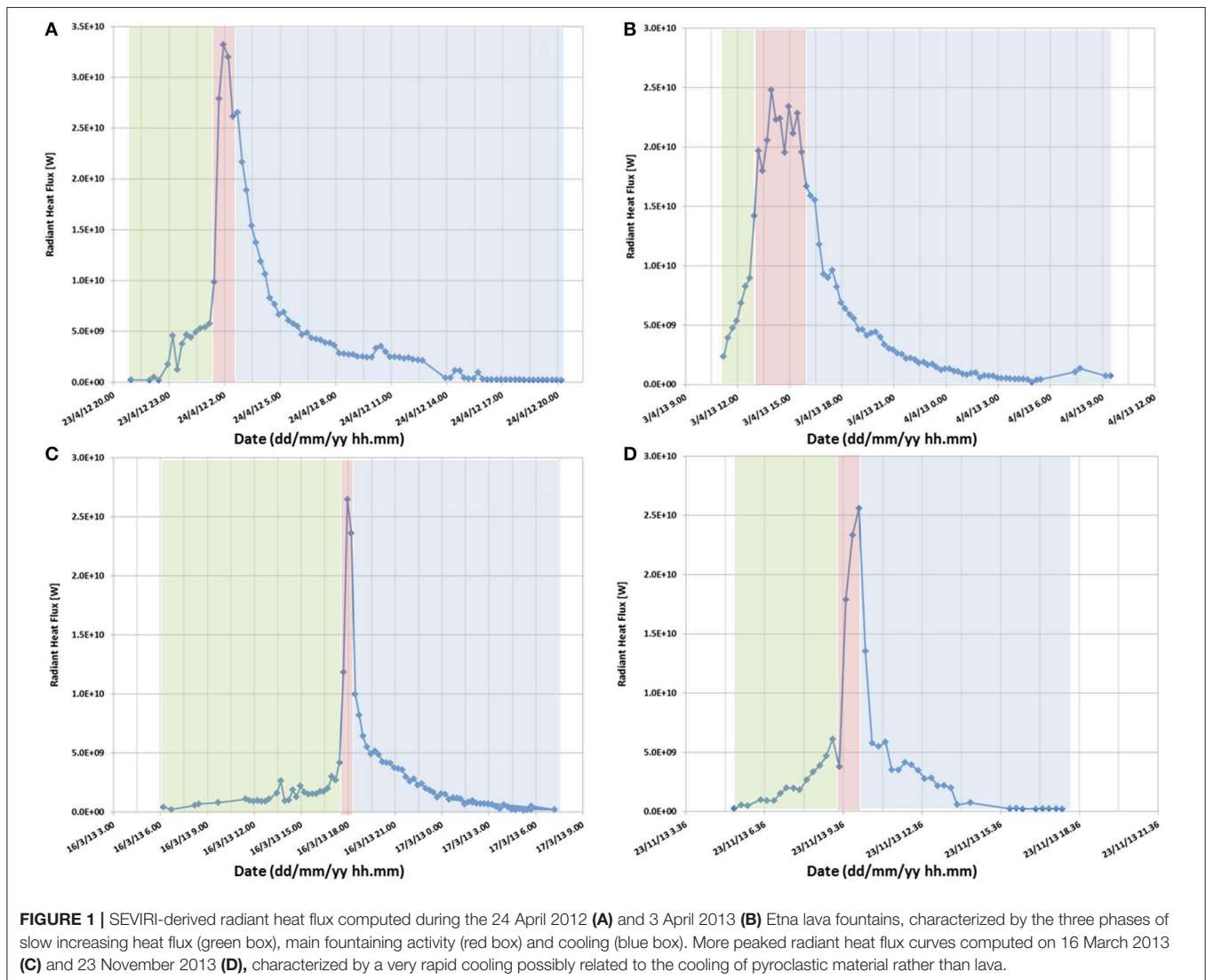
where Q is the total radiant heat loss obtained summing up the radiant heat flux computed for each hot spot pixel, ρ is the lava density, C_p is the specific heat capacity, ΔT is the eruption temperature minus temperature at which flow stops, C_L is the latent heat of crystallization, and $\Delta \varphi$ is the volume percent of crystals that form while cooling through ΔT . HOTSAT computes a minimum and maximum estimates for TADR by considering the respectively largest and smallest values that each

lava parameter can take, resulting in a volume variation of $\pm 25\%$ (Ganci et al., 2016).

During short-lived paroxysmal events the volcanic hotspot is often affected by the tephra/ash column accompanying the climax, which can attenuate or obscure the thermal anomaly; vice-versa, when not obscured, due to the huge radiated power released, it can easily saturate the sensor. As a consequence, the TADR cannot always be calculated during the peak fountaining phase. Moreover conversion between radiant heat flux and TADR is possible only if a thermal steady state is reached (Garel et al., 2012) and this is not true for very short and transient events, like lava fountains at Mt Etna. A way to provide an estimation of the event magnitude, i.e., mass in kg or volume in m^3 , and intensity, i.e., mean output rate (MOR) in kg/s or m^3/s , has been introduced by Ganci et al. (2012a) by modeling the plume- and saturation-free cooling curve apparent in the heat flux time series. In fact during short-lived eruptive events, the SEVIRI-derived heat flux curve is

characterized by three phases: a slight increase in the heat fluxes (first phase), a rapid increase to higher heat fluxes during the main fountaining activity, often marked by a trough and/or scattered behavior, due to plume obscuration (second phase); a waning flux during the cooling of the emplaced lava (third phase). In this case, volumes are inferred by minimizing the difference between the modeled and the SEVIRI-derived cooling curve. By considering the R-squared index, we computed the uncertainties on the estimated volumes ranging within $\pm 20\%$ (Ganci et al., 2012a).

Here we applied the technique of Ganci et al. (2012a) to catalogue the short lived events occurred during the 2011–2013 period, for which the duration of the three phases is < 2 days (Figure 1). For the longest effusive events occurred during 2014–2015 (Figure 2), we used the standard HOTSAT approach (Ganci et al., 2011b), and computed the total lava volumes by integrating the TADR curves. In this way we obtained the cumulated volume of lava emitted from 2011 to 2015.



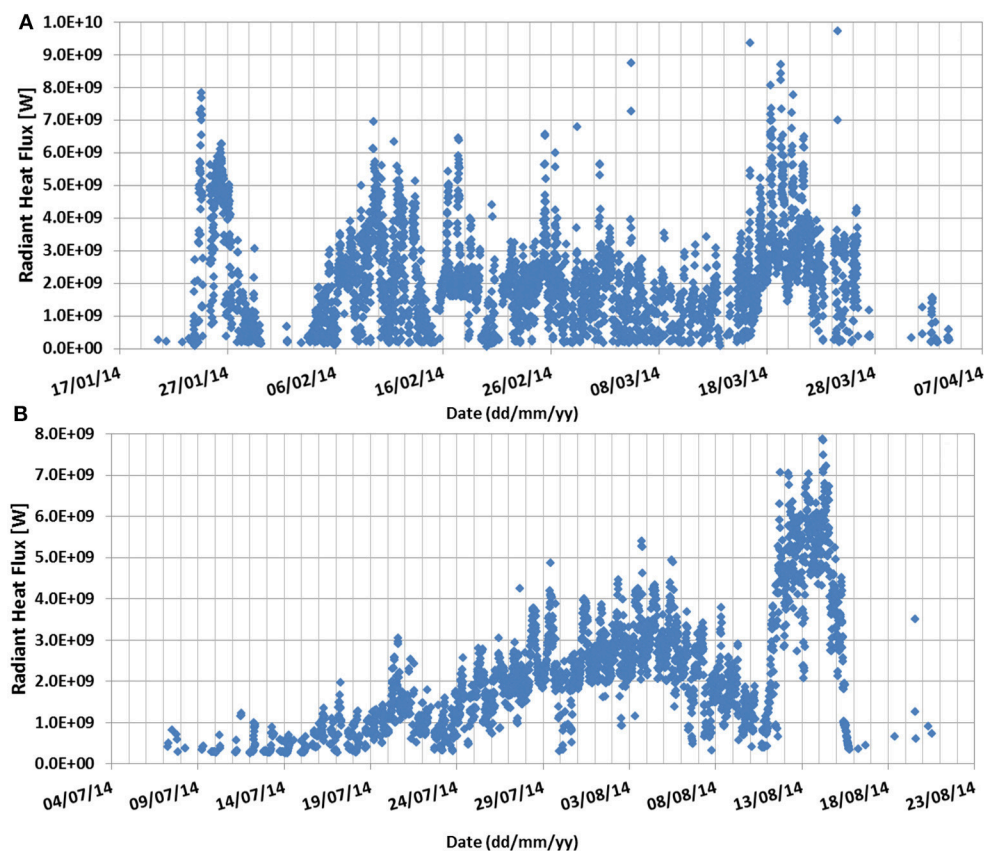


FIGURE 2 | Radiant heat flux curves computed from SEVIRI data for the two long effusive events occurred between 22 January and 7 April 2014 **(A)** and from 7 July to 20 August 2014 **(B)**.

Mapping of Lava Flows and Pyroclastic Deposits

To complement the SEVIRI-derived results, we analyzed the distribution of the 2011–2015 eruptive products thanks to the availability of pre-eruptive and post-eruptive DEMs of Etna volcano. For the pre-eruptive base, we used the last topography of Etna covering the whole deposits of the 2011–2015 eruptions, which goes back to 2005 (Gwinner et al., 2006). It is a DEM at 1 m spatial resolution resulted from a digital photogrammetric mapping, applying the airborne HRSC-AX sensor and photogrammetric processing system (Gwinner et al., 2006). After this, only local updates of the summit area have been derived from Light Detection And Ranging (LIDAR), digital photogrammetry and/or terrestrial laser scanning in 2007, 2010, 2012, 2014, and 2015 (Neri et al., 2008, 2017; Caracciolo D'Ajello et al., 2014; De Beni et al., 2015; Behncke et al., 2016). As post-eruptive base, we considered a topography produced using satellite images from the Pléiades constellation acquired on 18 December 2015.

The Pléiades constellation is composed of two optical satellites launched on December 2011 for Pléiades 1A and on December 2012 for Pléiades 1B, which provide images at 50 cm spatial resolution in stereo and tri-stereo mode. The 3D processing

of the tri-stereo Pléiades 1A imagery was performed using the free and open source MicMac photogrammetric library (Rupnik et al., 2017; <http://micmac.ensg.eu>) developed by the French IGN (Institut Géographique National), and took advantage of field Ground Control Points (GCPs) placed on Mt Etna. MicMac is based on the principles of photogrammetry and consists of three main steps:

- *Tie points recognition and matching between images;*
- *Calibration and orientation*, recognizing relationships between viewpoints and objects;
- *Correlation*, producing dense matching for 3D scene reconstruction.

The best result obtained with the Pléiades images of 18 December 2015 is a 4-meter resolution DEM spanning an area of about 16×15 km, which covers the summit craters and a portion of the south-east flank of the volcano, including the upper part of the Valle del Bove (**Figure 3**). According to our 2015 DEM, the highest point of 3,367 m is on the south-west rim of the NEC, while the SEC and NSEC reach an elevation of 3,336 and 3,325 m, respectively. By subtracting the 2005 DEM from the 2015 one, we obtained the topographic changes due to the volcanic deposits emplaced during the eruptive activity of Etna occurred between 2006 and 2015.

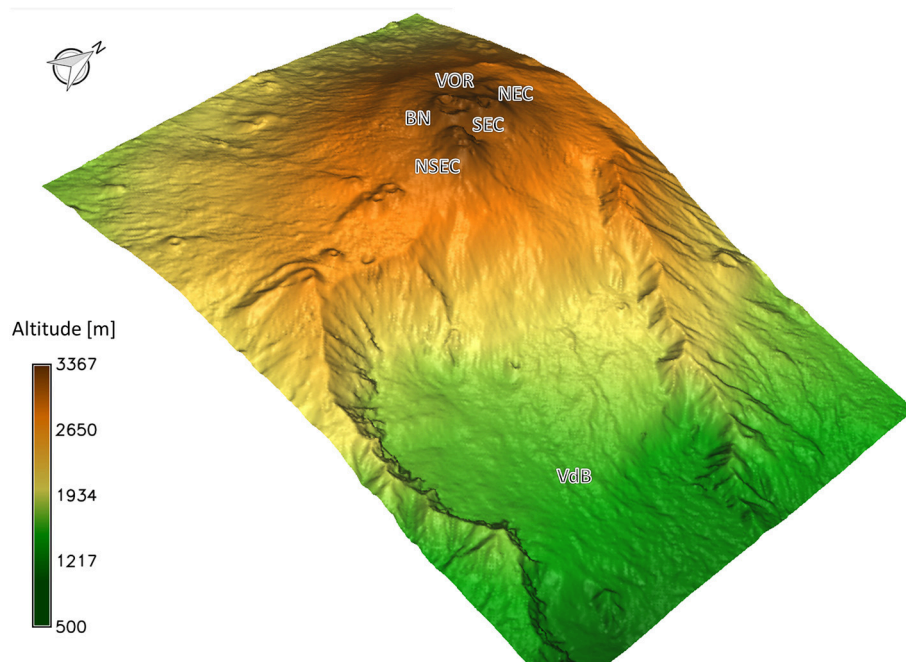


FIGURE 3 | Digital Elevation Model (DEM) of Mount Etna, covering the summit craters and a small portion of the south-east flank of the volcano, obtained by processing tri-stereo Pléiades images acquired on December 18, 2015. NEC, North-East Crater; VOR, Voragine; BN, Bocca Nuova; SEC, South-East Crater; NSEC, New South-East Crater; VdB; Valle del Bove.

RESULTS

Analyzing the thermal activity, we were able to characterize 46 of 53 eruptive events occurred at Etna between 2011 and 2015. **Table 1** reports event number (En), date of the first thermal anomaly detected by HOTSAT, duration, maximum value of the radiative power, MOR and lava volume for each event. In spite of the ash interference and/or cloudy conditions that affected 14 events (gray rows in **Table 1**), volume estimations were computed for 6 of them. Eventually only 7 events were not characterized at all (En: 2, 14, 29, 30, 32, 40, 50), while duration and maximum value of the radiative power were retrieved for the event occurred on 2 December 2013 (En: 44).

We observed that 38 of the 39 events detected between 2011 and 2013 follow the typical waveform associated with lava fountains, characterized by three phases (**Figures 1A,B**). In particular, during 2013 we noticed an increase in explosive behavior visible in the shape of the radiant heat flux curve of some of the events (**Figures 1C,D**), more peaked with a shorter climax and a very rapid cooling, with a loss of more than 10 GW in 15 min, possibly related to the cooling of pyroclastic material rather than lava. From December 15th, 2013 the general radiative heat flux waveform changes, the duration of the events increases and the cooling phase is not as easy to isolate (**Figure 4**).

Volumes, durations and MOR of the events occurred between 2011 and 2015, excluding the two long-lasting effusive periods of 2014, are reported in **Figure 5**. Considering only cloud-free events, erupted lava volumes (**Figure 5A**) vary between a minimum volume of $0.49 \times 10^6 \text{ m}^3$ (erupted on 28 November

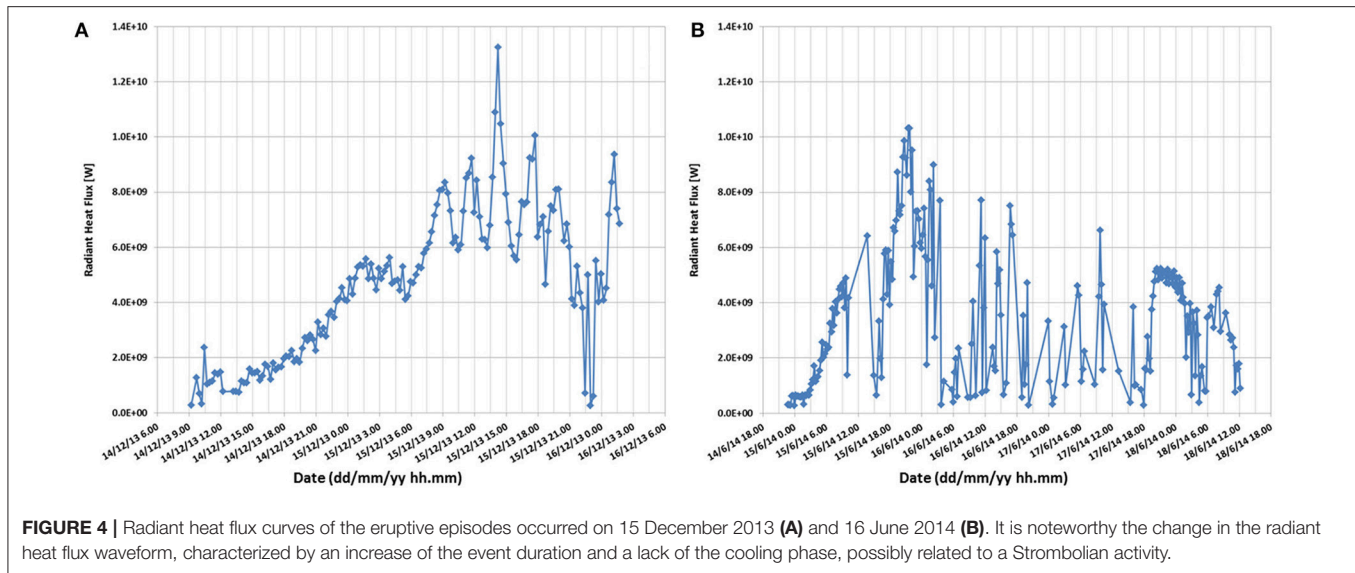
2013, En: 43) and a maximum of $2.86 \times 10^6 \text{ m}^3$ (erupted on 12 August 2011, En: 10). The median and standard deviation are respectively 1.4×10^6 and $0.6 \times 10^6 \text{ m}^3$, for a total volume expressed as dense-rock equivalent (DRE) of $64 \times 10^6 \text{ m}^3$ erupted during 43 events. Durations range from 2.5 h occurred on 23 October 2011 (En: 17) and 12 April 2012 (En: 24) to 3.5 days occurred on 14 June 2014 (En: 48), while MOR (**Figure 5B**) varies between 4.2 (on 14 June 2014, En: 48) and $260 \text{ m}^3 \text{ s}^{-1}$ (on 19 February 2013, En: 26). MOR for each event was obtained by dividing the total volume by the event duration, where the latter was computed by analyzing the radiant heat flux curves from the first thermal anomaly to the beginning of the cooling phase. To highlight the presence of trends or patterns characterizing the temporal distribution of eruption intensities, we calculated the moving average of the MOR time series with a window size set to 5 (orange line in **Figure 5B**).

In order to compute the total volume, we assumed that the eight missing events (En: 2, 14, 29, 30, 32, 40, 44, 50) had median volumes ($1.4 \times 10^6 \text{ m}^3$) obtaining an estimate of $75 \times 10^6 \text{ m}^3$ over 51 events. Applying a correction of 20% for vesicles (according to Behncke et al., 2014) and including the two effusive periods, the cumulative volume, from January 2011 to December 2015, reaches $\sim 106 \pm 22$ million of cubic meters (**Figure 6**). Of these, 50.6 ± 4 million of cubic meters, emitted between May 2012 and October 2014, are well in agreement with the 56.4 million of cubic meters derived from DEM difference (De Beni et al., 2015). Comparing the SEVIRI-derived results with field data (Behncke et al., 2014; De Beni et al., 2015), we found a good fit, generally within the measurement error, with

TABLE 1 | Event number (En), date, duration, maximum value of the radiative power, Mean Output Rate (MOR) and lava volume of eruptive events at Mt Etna from January 2011 to December 2015 as retrieved from SEVIRI data.

Event number	Date (dd/mm/yyyy)	Duration (minutes)	Max radiative power (W)	MOR (m ³ s ⁻¹)	Lava volume (m ³)
1	12/01/2011	255	2.51E+10	101.2	1.55E+06
2	18/02/2011				
3	10/04/2011	495	7.42E+09	29.5	8.77E+05
4	11/05/2011	570	1.39E+10	43.0	1.47E+06
5	09/07/2011	243	1.35E+10	102.3	1.49E+06
6	18/07/2011	240	2.62E+10	148.5	2.14E+06
7	24/07/2011	630	2.33E+10	26.1	9.88E+05
8	30/07/2011	810	1.98E+10	45.7	2.22E+06
9	05/08/2011	270	1.59E+10	98.0	1.59E+06
10	12/08/2011	210	3.00E+10	226.7	2.86E+06
11	20/08/2011	330	1.33E+10	70.8	1.40E+06
12	29/08/2011	255	1.98E+10	113.7	1.74E+06
13	08/09/2011	180	1.43E+10	112.6	1.22E+06
14	19/09/2011				
15	28/09/2011	228	3.73E+09	29.7	4.06E+05
16	08/10/2011	465	1.19E+10	30.2	8.43E+05
17	23/10/2011	150	1.44E+10	145.7	1.31E+06
18	15/11/2011	273	2.26E+10	110.4	1.81E+06
19	05/01/2012	318	9.25E+09	78.3	1.49E+06
20	09/02/2012	690	4.78E+09	21.0	8.71E+05
21	04/03/2012	210	3.41E+10	202.4	2.55E+06
22	18/03/2012	210	2.77E+10	170.6	2.15E+06
23	01/04/2012	240	1.78E+09	113.9	1.64E+06
24	12/04/2012	150	3.52E+10	190.0	1.71E+06
25	24/04/2012	255	3.32E+10	171.2	2.62E+06
26	19/02/2013	165	2.73E+10	260.6	2.58E+06
27	20/02/2013	195	1.78E+10	140.2	1.64E+06
28	20/02/2013	165	1.85E+10	72.7	7.20E+05
29	21/02/2013				
30	23/02/2013				
31	28/02/2013	180	1.11E+10	108.3	1.17E+06
32	05/03/2013				
33	16/03/2013	375	2.62E+09	65.3	1.47E+06
34	03/04/2013	255	2.48E+10	169.9	2.60E+06
35	12/04/2013	2,100	1.85E+10	11.0	1.39E+06
36	18/04/2013	585	1.61E+10	43.0	1.51E+06
37	20/04/2013	1,005	1.73E+10	19.6	1.18E+06
38	27/04/2013	285	1.74E+10	117.0	2.00E+06
39	26/10/2013	645	1.27E+09	31.5	1.22E+06
40	11/11/2013				
41	16/11/2013	540	1.50E+09	37.3	1.21E+06
42	23/11/2013	285	2.56E+09	38.7	6.62E+05
43	28/11/2013	420	6.10E+09	19.6	4.94E+05
44	02/12/2013	1,410	8.87E+09		
45	15/12/2013	2,431	1.32E+10	6.2	9.08E+05
46	29/12/2013	930	9.65E+09	20.6	1.15E+06
47	22/01/2014	102,330	8.70E+09	1.5	9.30E+06
48	14/06/2014	5,148	1.03E+10	4.2	1.29E+06
49	07/07/2014	63,765	7.80E+09	1.7	6.57E+06
50	28/12/2014				
51	31/01/2015	3,465	1.49E+10	6.5	1.35E+06
52	11/05/2015	5,085	1.46E+10	4.5	1.37E+06
53	06/12/2015	2,970	7.64E+09	5.6	9.95E+05

Gray filled rows highlight events affected by ash interference after fountaining and/or cloudy conditions. Orange filled rows refer to the two longest effusive periods.



the volume difference ranging from $0.12 \times 10^6 \text{ m}^3$ (En: 35) and $1.49 \times 10^6 \text{ m}^3$ (En: 36) with an average difference in the volumes of $0.62 \times 10^6 \text{ m}^3$.

We also explored the chance to provide an upper bound to the SEVIRI-derived cumulative volume by using a topographic approach, i.e., by subtracting the 2005 DEM from the 2015 one. In this way we estimated the distribution and volume of volcanic deposits emitted between 2006 and 2015. To minimize the errors introduced by the fact that the two DEMs were derived from different data sources, we first resampled the 2005 DEM to the same spatial resolution of the 2015 DEM (4 m) and improved their coregistration so that the histogram of the elevation differences was centered on zero (Figure 7). Positive values of the bar chart represent the cells where the volcanic deposits emplaced.

The volcanic deposits emplaced between 2006 and 2015 cover an area of $\sim 12.6 \times 10^6 \text{ m}^2$, with a maximum length of $\sim 6.8 \text{ km}$ due to the lava flow emplacement of the 2008–2009 flank eruption (Figure 8). The minimum, median, and average thicknesses, computed from DEMs difference, are 1.01, 13.62, and 22.84 m, respectively. The maximum thickness of 214 m is obtained at the NSEC cone.

The total volume of products, calculated by integration of the thickness distribution over the area covered, is $287 \times 10^6 \text{ m}^3$, with an uncertainty of $\sim 37 \times 10^6 \text{ m}^3$, corresponding to 13% of the entire volume. The uncertainty was computed by multiplying the area ($\sim 12.6 \times 10^6 \text{ m}^2$) by the residual vertical accuracy outside the margins of the deposits, i.e., the standard deviation ($\sim 2.95 \text{ m}$) of the height difference between the DEMs in the area not covered by deposits. The NSEC cone covers an area of $\sim 0.53 \times 10^6 \text{ m}^2$ with a volume of $55 \pm 1.5 \times 10^6 \text{ m}^3$.

DISCUSSION AND CONCLUSIONS

The 5 years spanning from January 2011 to December 2015 at Etna were analyzed through SEVIRI images. Thanks the frequent

revisit time, i.e., 15 min, SEVIRI represents the unique space sensor able to detect and characterize the short-lived activity (a few hours for each event) as that occurred at Etna during 2011–2013.

Radiant heat flux curves apparent in SEVIRI images permitted to compute durations, volumes, and intensities, cataloguing almost all the events (46 of 53) and to discriminate among fountaining activity (e.g., Figures 1A,B) with an information about the degree of explosivity (e.g., Figures 1C,D), Strombolian activity (e.g., Figure 4) and long effusive periods (Figure 2). A statistical analysis on SEVIRI-derived results, excluding the two longest effusive events of 2014, shows a Gaussian distribution slightly right skewed of the estimated volumes peaked on 1.4 million of cubic meters (Figure 9A), while the durations follow the typical features of a Pareto distribution with a large portion of events (76%) lasting around 500 min (Figure 9B). Distribution of MOR underlines the temporal non-stationarity of eruption intensity, mainly decreasing from February 2013, and reaching the minimum values since 2014 (Figure 5B). This highlights that eruptive events occurred with a higher intensity in the first period (2011–2012) than in the following 3 years of activity (2013–2015). It should be noted that our analysis does not take into account the eruptive events occurred on 28 December 2014 (because of the presence of a thick layer of clouds that prevented the observation from satellite) and the eruptive activity occurred at the VOR crater on 3–5 December 2015 (Bonaccorso and Calvari, 2017).

By differencing the 2005 and 2015 DEMs and excluding the volume of the NSEC cone, we obtained a 10-year volume of $\sim 232 \times 10^6 \text{ m}^3$, which is below the recent erupted volumes on decadal scale at Mt Etna ($\sim 300 \times 10^6 \text{ m}^3$ from Harris et al., 2011), interrupting its stable and resilient output trend. By further subtracting published products retrieved from LIDAR analysis in 2007 and 2010 (Neri et al., 2008; Behncke et al., 2016), we found ~ 131 million of cubic meters of eruptive products emitted since 2011, which is still about $\sim 25 \times 10^6 \text{ m}^3$ higher than the volumes

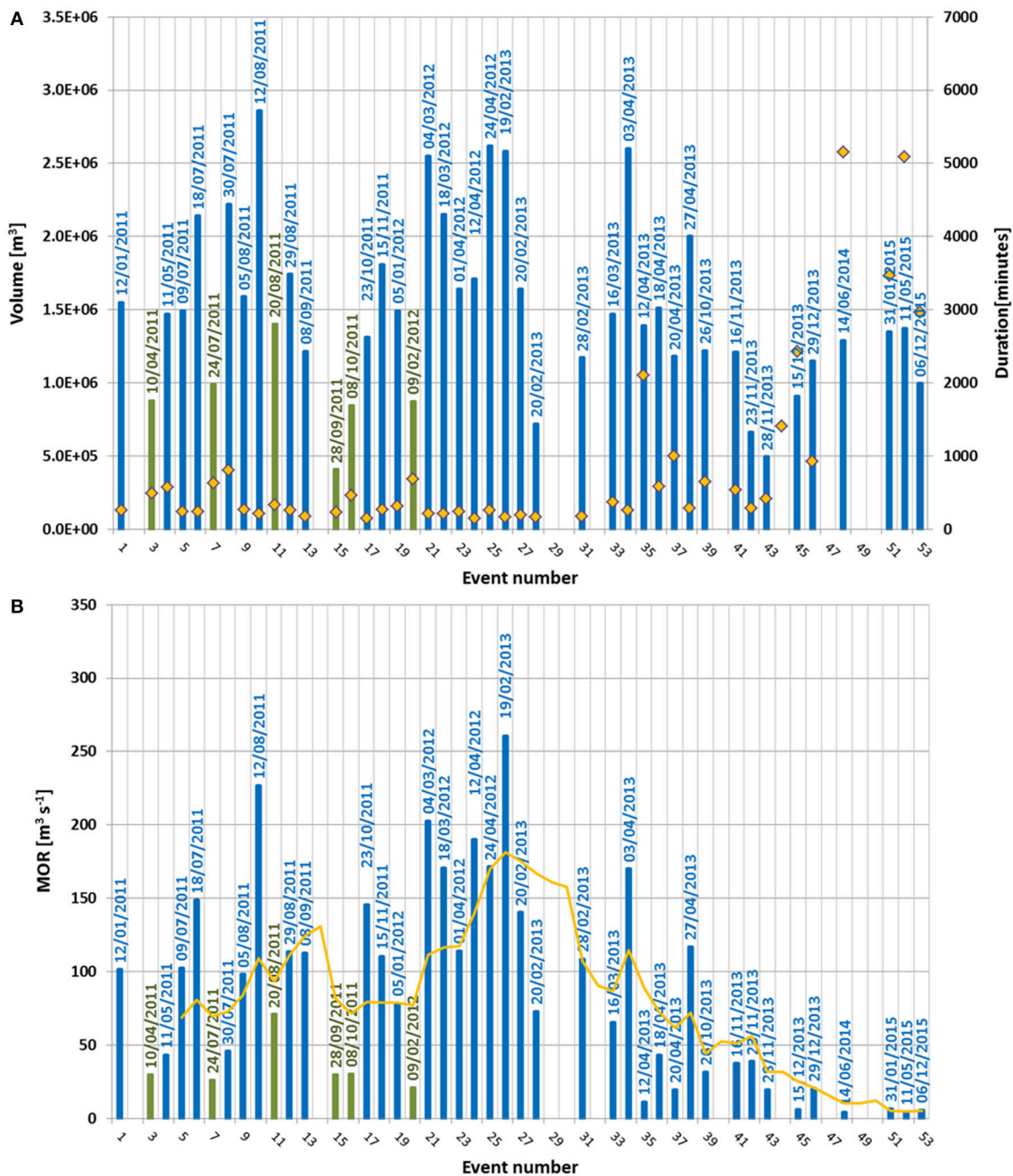


FIGURE 5 | Volumes (blue bars for cloud-free events, green bars for cloud-contaminated events) and durations (orange diamonds) of the events occurred between 2011 and 2015, excluding the two long-lasting effusive periods of 2014 (A). The MOR (blue bars for cloud-free events, green bars for cloud-contaminated events) and 5-period moving average of the MOR time series (orange line) show the temporal non-stationarity of eruption intensity, mainly decreasing from February 2013, and reaching the minimum values since 2014 (B).

derived by SEVIRI. This difference, ranging between 10 and 30% of the total volume, is most likely due to loose materials as the pyroclastic fallout deposits in the same area where the lavas were emplaced and/or to the presence of tephra-covered snow.

Our study revealed a decreasing trend in eruption intensity (according to the volume of erupted products) beginning from

2013 and reaching lower values (around $5 \text{ m}^3 \text{ s}^{-1}$) in 2014 and 2015. This trend was confirmed also in the growth of the NSEC cone that gained only 5 million of cubic meters from December 2014 to December 2015, against $50 \times 10^6 \text{ m}^3$ observed from January 2011 to October 2014 (De Beni et al., 2015). In particular, the plot of cumulative volume (Figure 6) allows us to identify five

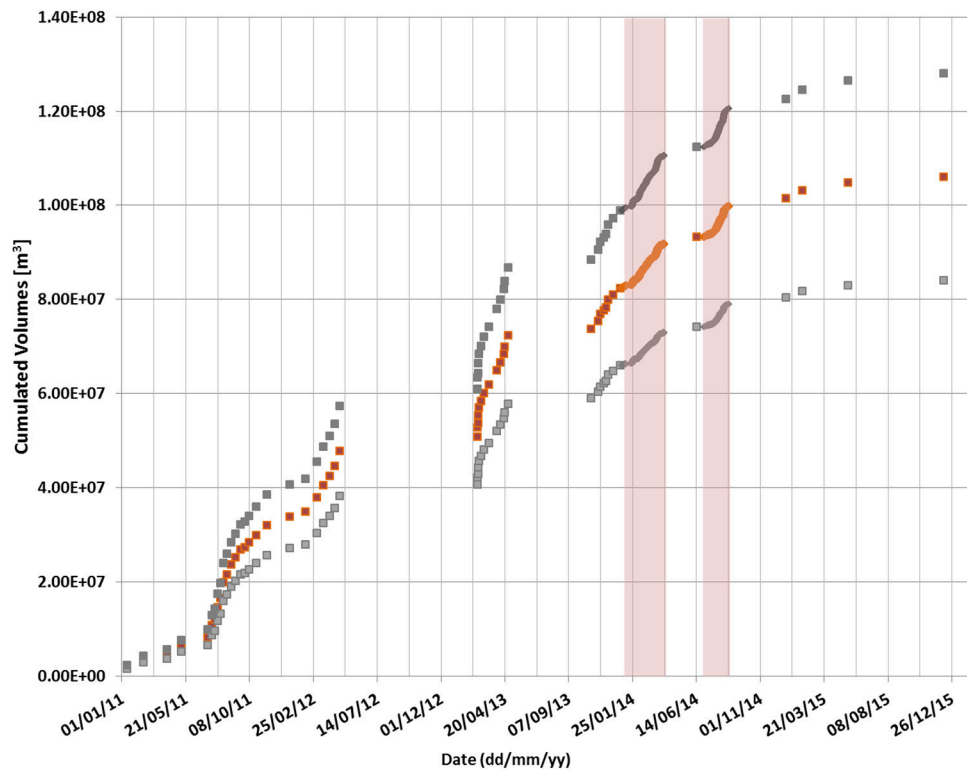


FIGURE 6 | SEVIRI-derived cumulative volume (orange square dots) with the minimum and maximum estimates (gray square dots) computed from January 2011 to December 2015. The red bars highlight the two long-lasting effusive periods of 2014.

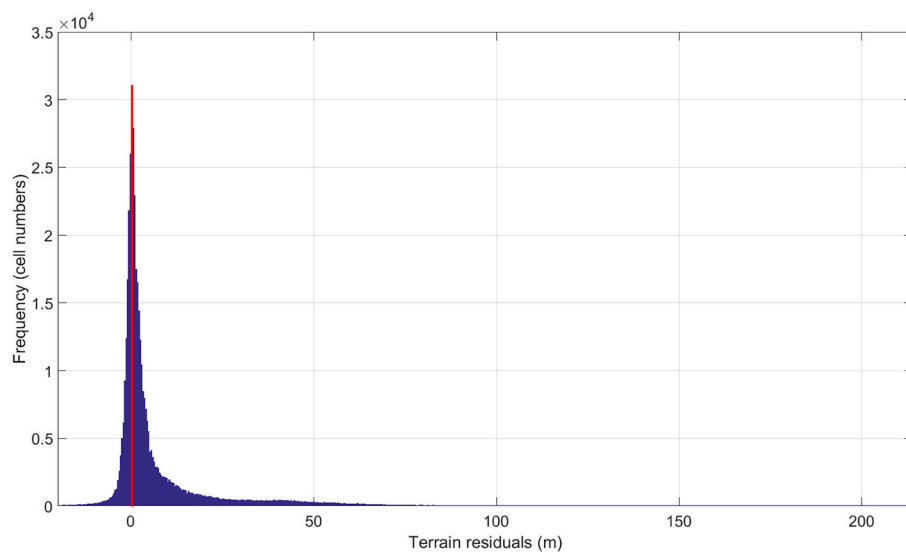


FIGURE 7 | Histogram plot of change in elevation obtained by differencing the 2015 and 2005 DEMs after improvement of the coregistration. The peak centered on zero proves their accurate alignment.

different phases in the observed period: (i) an initial phase, from 12 January to 9 July 2011, with a low TADR ($0.41 \pm 0.08 \text{ m}^3 \text{ s}^{-1}$); (ii) a growth phase, from 18 July 2011 to 24 April 2012, with a

TADR of $1.53 \pm 0.31 \text{ m}^3 \text{ s}^{-1}$; (iii) a peak phase, from 19 February 2013 to 27 April 2013, with a TADR of $3.68 \pm 0.74 \text{ m}^3 \text{ s}^{-1}$; (iv) a waning phase, from 26 October 2013 to 7 July 2014, with a

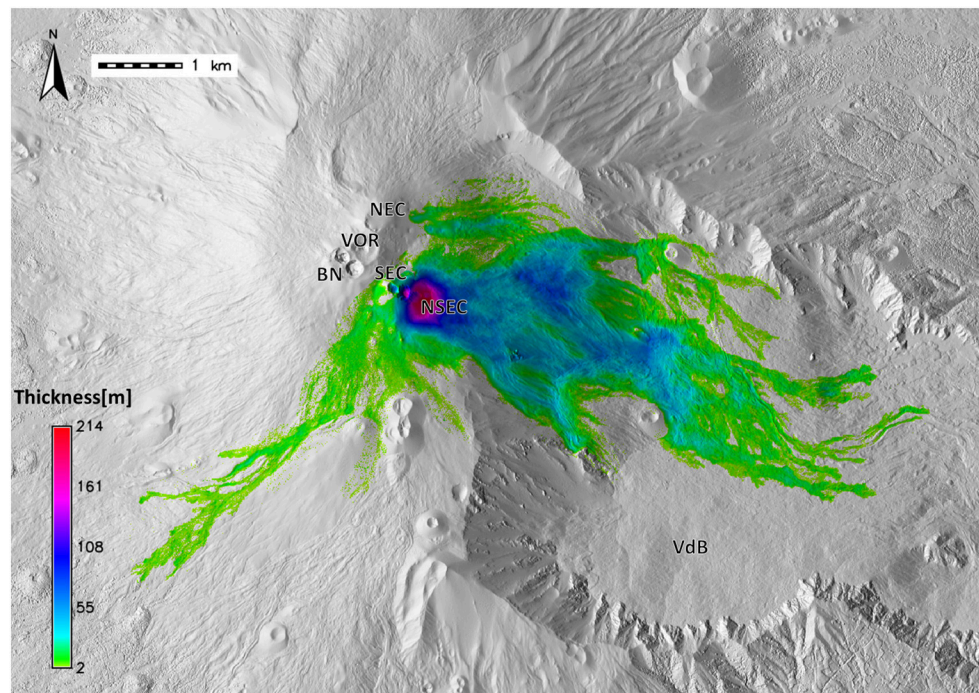


FIGURE 8 | Topographic changes due to the volcanic deposits emplaced during the eruptive activity of Etna occurred between 2006 and 2015. The colors indicate flow thickness. The total area covered is $\sim 12.6 \times 10^6 \text{ m}^2$; the maximum thickness of 214 m is obtained in correspondence of the NSEC cone. The base map is the shaded relief of the 2005 DEM. NEC, North-East Crater; VOR, Voragine; BN, Bocca Nuova; SEC, South-East Crater; NSEC, New South-East Crater; VdB, Valle del Bove.

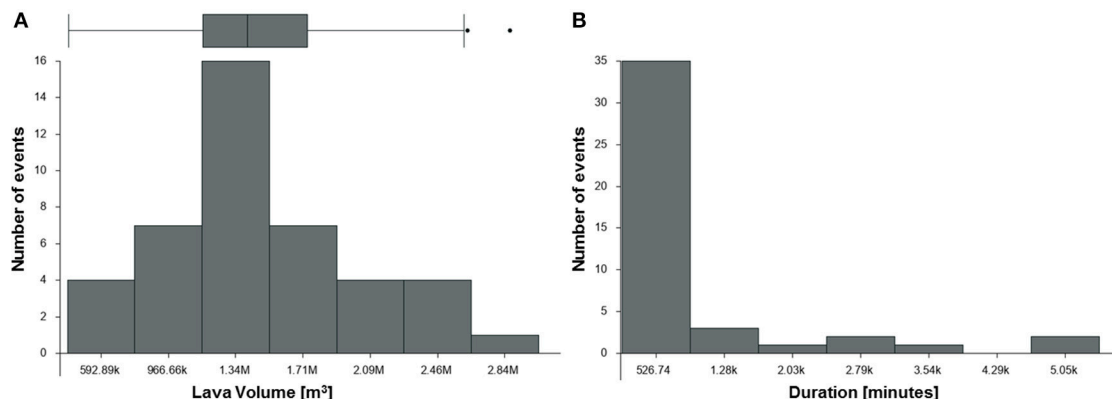


FIGURE 9 | Statistical analysis on SEVIRI-derived results, excluding the two longer effusive events of 2014. The distribution of lava volumes against the number of events is a skewed Gaussian peaked on 1.34 millions of cubic meters, with quartiles $1.15 \times 10^6 \text{ m}^3$ (25%), $1.4 \times 10^6 \text{ m}^3$ (50%), $1.73 \times 10^6 \text{ m}^3$ (75%) and outlier fences at $0.28 \times 10^6 \text{ m}^3$ and $2.6 \times 10^6 \text{ m}^3$ as illustrated in the box plot (A). The durations follow a Pareto distribution with 76% of events lasting around 500 min (B).

TADR of $1.00 \pm 0.20 \text{ m}^3 \text{ s}^{-1}$; (v) a final phase, from 28 December 2014 to 8 December 2015, with an extremely low TADR ($0.15 \pm 0.03 \text{ m}^3 \text{ s}^{-1}$).

In terms of long-term output, we find that $106 \pm 22 \times 10^6 \text{ m}^3$ of lava was erupted in almost 5 years, which results in a time-averaged rate of $0.68 \pm 0.14 \text{ m}^3 \text{ s}^{-1}$. This estimate falls within the range between 0.6 and $0.9 \text{ m}^3 \text{ s}^{-1}$ that characterizes the high eruption rate phase of Etna beginning in 1971 (Harris

et al., 2011). However it interrupts the steady state output rate of $0.9 \text{ m}^3 \text{ s}^{-1}$ started in 2000 (Harris et al., 2011; Ganci et al., 2012a).

AUTHOR CONTRIBUTIONS

GG and AC mainly wrote the manuscript with contributions from all authors. GG processed SEVIRI data and extracted the topography from Pléiades images. AC computed DEM

differences and performed statistics on it. GB performed the statistical analysis on SEVIRI-derived results with the contribution of AH and VZ. CD coordinated the research. All authors contributed ideas and input to the research of the paper.

ACKNOWLEDGMENTS

Thanks are due to the European Organisation for the Exploitation of Meteorological Satellites (EUMETSAT) for Spinning Enhanced Visible and InfraRed Imager (SEVIRI) data (www.eumetsat.int). Pléiades data were available through

the Space Volcano Observatory with Pléiades (SVOP) project coordinated by Pierre Briole (http://volcano.terre.fr/svo_projects). We are grateful to Olivier Galland, Luc Girod and Christopher Nuth for their assistance with the use of the MicMac software. The editor Clive Oppenheimer, the chief editor Valerio Acocella and the three reviewers are acknowledged for their constructive and supportive comments that helped us to improve the manuscript. This work was developed within the framework of TecnoLab, the Laboratory for Technological Advance in Volcano Geophysics of the INGV in Catania (Italy) and was partially supported from the DPC-INGV 2012–2021 Agreement.

REFERENCES

- Acocella, V., Neri, M., Behncke, B., Bonforte, A., Del Negro, C., and Ganci, G. (2016). Why does a mature volcano need new vents? the case of the new southeast crater at Etna. *Front. Earth Sci.* 4:67. doi: 10.3389/feart.2016.00067
- Behncke, B. A., Fornaciai, M., Neri, M., Favalli, M., Ganci, G., and Mazzarini, F. (2016). Lidar surveys reveal eruptive volumes and rates at Etna 2007–2010. *Geophys. Res. Lett.* 43, 4270–4278. doi: 10.1002/2016GL068495
- Behncke, B., Branca, S., Corsaro, R. A., De Beni, E., Miraglia, L., and Proietti, C. (2014). The 2011–2012 summit activity of Mount Etna: Birth, growth and products of the new SE crater. *J. Volcanol. Geother. Res.* 270, 10–21. doi: 10.1016/j.jvolgeores.2013.11.012
- Bonaccorso, A., and Calvari, S. (2013). Major effusive eruptions and recent lava fountains: balance between expected and erupted magma volumes at Etna volcano. *Geophys. Res. Lett.* 40, 6069–6073. doi: 10.1002/2013GL058291
- Bonaccorso, A., and Calvari, S. (2017). A new approach to investigate an eruptive paroxysmal sequence using camera and strainmeter networks: lessons from the 3–5 December 2015 activity at Etna volcano. *Earth Planet. Sci. Lett.* 475, 231–241. doi: 10.1016/j.epsl.2017.07.020
- Cappello, A., Bilotta, G., Neri, M., and Del Negro, C. (2013). Probabilistic modelling of future volcanic eruptions at Mount Etna. *J. Geophys. Res. Solid Earth* 118, 1925–1935. doi: 10.1002/jgrb.50190
- Cappello, A., Ganci, G., Calvari, S., Pérez, N. M., Hernández, P. A., Silva, S. V., et al. (2016). Lava flow hazard modeling during the 2014–2015 Fogo eruption, Cape Verde. *J. Geophys. Res. Solid Earth* 121, 2290–2303. doi: 10.1002/2015JB012666
- Caracciolo D'Ajello, F., Nicolosi, I., Carluccio, R., Chiappini, S., De Ritis, R., Giuntini, A., et al. (2014). High resolution aeromagnetic anomaly map of Mount Etna volcano, Southern Italy. *Volcanol. Geotherm. Res.* 277, 36–40. doi: 10.1016/j.jvolgeores.2014.03.008
- De Beni, E., Behncke, B., Branca, S., Nicolosi, I., Carluccio, R., D'Ajello Caracciolo, F., et al. (2015). The continuing story of Etna's New Southeast Crater (2012–2014): evolution and volume calculations based on field surveys and aerophotogrammetry. *J. Volcanol. Geoth. Res.* 303, 175–186. doi: 10.1016/j.jvolgeores.2015.07.021
- Del Negro, C., Cappello, A., and Ganci, G. (2016). Quantifying lava flow hazards in response to effusive eruption. *Geol. Soc. Am. Bull.* 128, 752–763. doi: 10.1130/B31364.1
- Del Negro, C., Cappello, A., Neri, M., Bilotta, G., Hérault, A., and Ganci, G. (2013). Lava flow hazards at Mount Etna: constraints imposed by eruptive history and numerical simulations. *Sci. Rep.* 3:3493. doi: 10.1038/srep03493
- Ganci, G., Bilotta, G., Cappello, A., Hérault, A., and Del Negro, C. (2016). "HOTSAT: a multiplatform system for the satellite thermal monitoring of volcanic activity," in *Detecting Modelling and Responding to Effusive Eruptions*, eds A. Harris, T. De Groeve, F. Garel, and S. A. Carn (London: Geological Society), 426.
- Ganci, G., Harris, A. J. L., Del Negro, C., Guehenneux, Y., Cappello, A., Labazuy, P., et al. (2012a). A year of lava fountaining at Etna: volumes from SEVIRI. *Geophys. Res. Lett.* 39:L06305. doi: 10.1029/2012GL051026
- Ganci, G., James, M. R., Calvari, S., and Del Negro, C. (2013). Separating the thermal fingerprints of lava flows and simultaneous lava fountaining using ground-based thermal camera and SEVIRI measurements. *Geophys. Res. Lett.* 40, 5058–5063. doi: 10.1002/grl.50983
- Ganci, G., Vicari, A., Bonfiglio, S., Gallo, G., and Del Negro, C. (2011a). A texon-based cloud detection algorithm for MSG-SEVIRI multispectral images. *Geomat. Nat. Hazard Risk* 2, 1947–5705. doi: 10.1080/19475705.2011.578263
- Ganci, G., Vicari, A., Cappello, A., and Del Negro, C. (2012b). An emergent strategy for volcano hazard assessment: from thermal satellite monitoring to lava flow modeling. *Remote. Sens. Environ.* 119, 197–207. doi: 10.1016/j.rse.2011.12.021
- Ganci, G., Vicari, A., Fortuna, L., and Del Negro, C. (2011b). The HOTSAT volcano monitoring system based on a combined use of SEVIRI and MODIS multispectral data. *Ann. Geophys.* 54:2011. doi: 10.4401/ag-5338
- Garel, F., Kaminski, E., Tait, S., and Limare, A. (2012). An experimental study of the surface thermal signature of hot subaerial isoviscous gravity currents: implications for thermal monitoring of lava flows and domes. *J. Geophys. Res.* 117:B02205. doi: 10.1029/2011JB008698
- Gwinner, K., M., Coltelli, J., Flohrer, R., Jaumann, K. D., Matza, M., Marsella, T., et al. (2006). "The HRSC-AX Mt. Etna project: high-resolution orthoimages and 1 m DEM at regional scale," In *Proceedings ISPRS Archives - Volume XXXVI Part 1, 2006, From Sensors to Imagery* (Paris), T05–23.
- Harris, A. J. L., Blake, S., Rothery, D., and Stevens, N. (1997). A chronology of the 1991 to 1993 Mount Etna eruption using advanced very high resolution radiometer data: implications for real-time thermal volcano monitoring. *J. Geophys. Res.* 102, 7985–8003.
- Harris, A. J. L., Dehn, J., and Calvari, S. (2007). Lava effusion rate definition and measurement: a review. *Bull. Volcanol.* 70:1. doi: 10.1007/s00445-007-0120-y
- Harris, A. J. L., Steffke, A., Calvari, S., and Spampinato, L. (2011). Thirty years of satellite-derived lava discharge rates at Etna: implications for steady volumetric output. *J. Geophys. Res.* 116:B08204. doi: 10.1029/2011JB008237
- Harris, A. J. L., Vaughan, R. A., and Rothery, D. A. (1995). Volcano detection and monitoring using AVHRR data: the Krafla eruption, 1984. *Int. J. Remote Sens.* 16, 1001–1020.
- Neri, M., De Maio, M., Crepaldi, S., Suozzi, E., Lavy, M., Marchionatti, F., et al. (2017). Topographic maps of Mount Etna's summit craters, updated to december 2015. *J. Maps* 13, 674–683. doi: 10.1080/17445647.2017.1352041
- Neri, M., Mazzarini, F., Tarquini, S., Bisson, M., Isola, I., Behncke, B., et al. (2008). The changing face of Mount Etna's summit area documented with Lidar technology. *Geophys. Res. Lett.* 35:L09305. doi: 10.1029/2008GL033740
- Rupnik, E., Daakir, M., and Pierrot Deseilligny, M. (2017). MicMac – a free, open-source solution for photogrammetry. *Open Geospatial Data* 2:14. doi: 10.1186/s40965-017-0027-2
- Stevens, N. F., Wadge, G., and Murray, J. B. (1999). Lava flow volume and morphology from digitised contour maps: a case study at Mount Etna, Sicily. *Geomorphology* 28, 251–261. doi: 10.1016/S0169-555X(98)00115-9
- Vicari, A., Ganci, G., Behncke, B., Cappello, A., Neri, M., and Del Negro, C. (2011). Near-real-time forecasting of lava flow hazards during the 12–13 January 2011 Etna eruption. *Geophys. Res. Lett.* 38:L13317. doi: 10.1029/2011GL047545

- Wadge, G., Walker, G. P. L., and Guest, J. E. (1975). The output of the Etna volcano. *Nature* 255, 385–387.
- Wooster, M., Zhukov, B., and Oertel, D. (2003). Fire radiative energy release for quantitative study of biomass burning: derivation from the BIRD experimental satellite and comparison to MODIS fire products. *Remote Sens. Environ.* 86, 83–107. doi: 10.1016/S0034-4257(03)00070-1
- Wright, R., Blake, S., Harris, A., and Rothery, D. (2001). A simple explanation for the space-based calculation of lava eruption rates. *Earth Planet. Sci. Lett.* 192, 223–233. doi: 10.1016/S0012-821X(01)00443-5

Conflict of Interest Statement: The authors declare that the research was conducted in the absence of any commercial or financial relationships that could be construed as a potential conflict of interest.

Copyright © 2018 Ganci, Cappello, Bilotta, Herault, Zago and Del Negro. This is an open-access article distributed under the terms of the Creative Commons Attribution License (CC BY). The use, distribution or reproduction in other forums is permitted, provided the original author(s) and the copyright owner are credited and that the original publication in this journal is cited, in accordance with accepted academic practice. No use, distribution or reproduction is permitted which does not comply with these terms.



Understanding the SO₂ Degassing Budget of Mt Etna's Paroxysms: First Clues From the December 2015 Sequence

Roberto D'Aleo^{1*}, Marcello Bitetto¹, Dario Delle Donne¹, Mauro Coltelli², Diego Coppola³, Brendan McCormick Kilbride⁴, Emilio Pecora², Maurizio Ripepe⁵, Lois Claire Salem⁴, Giancarlo Tamburello⁶ and Alessandro Aiuppa^{1,7}

¹ Dipartimento DiSTeM, Università Degli Studi di Palermo, Palermo, Italy, ² Istituto Nazionale di Geofisica e Vulcanologia, Osservatorio Etneo, Catania, Italy, ³ Dipartimento di Scienze della Terra, Università Degli Studi di Torino, Turin, Italy, ⁴ COMET, Department of Earth Sciences, University of Cambridge, Cambridge, United Kingdom, ⁵ Dipartimento di Scienze Della Terra, Università Degli Studi di Firenze, Florence, Italy, ⁶ Istituto Nazionale di Geofisica e Vulcanologia, Bologna, Italy, ⁷ Istituto Nazionale di Geofisica e Vulcanologia, Palermo, Italy

OPEN ACCESS

Edited by:

Peter William Webley,
University of Alaska Fairbanks,
United States

Reviewed by:

Tom D. Pering,
University of Sheffield,
United Kingdom
Cynthia J. Ebinger,
Tulane University, United States

*Correspondence:

Roberto D'Aleo
roberto.daleo01@unipa.it

Specialty section:

This article was submitted to
Volcanology,
a section of the journal
Frontiers in Earth Science

Received: 14 February 2018

Accepted: 10 December 2018

Published: 14 January 2019

Citation:

D'Aleo R, Bitetto M, Delle Donne D, Coltelli M, Coppola D, McCormick Kilbride B, Pecora E, Ripepe M, Salem LC, Tamburello G and Aiuppa A (2019) Understanding the SO₂ Degassing Budget of Mt Etna's Paroxysms: First Clues From the December 2015 Sequence. *Front. Earth Sci.* 6:239. doi: 10.3389/feart.2018.00239

The persistent open-vent activity of basaltic volcanoes is periodically interrupted by spectacular but hazardous paroxysmal explosions. The rapid transition from quiescence to explosive eruption poses a significant challenge for volcanic hazard assessment and mitigation, and improving our understanding of the processes that trigger these paroxysmal events is critical. Although magmatic gas is unquestionably the driver, direct measurements of a paroxysm's gas flux budget have remained challenging, to date. A particularly violent paroxysmal sequence took place on Etna on December 2015, intermittently involving all summit craters, especially the Voragine (VOR) that had previously displayed no activity for several years. Here, we characterize the volcano's SO₂ degassing budget prior to, during and after this paroxysmal sequence, using ground-based (UV-Camera) and satellite (OMI) observations, complemented with ground- and space-borne thermal measurements. We make use of the high spatial resolution of UV-cameras to resolve SO₂ emissions from the erupting VOR crater for the first time, and to characterize temporal switches in degassing activity from VOR to the nearby New Southeast Crater (NSEC). Our data show that onset of paroxysmal activity on December 3–5 was marked by visible escalation in VOR SO₂ fluxes (4,700–8,900 tons/day), in satellite-derived thermal emissions (2,000 MW vs. ~2–11 MW in July–November 2015), and in OMI-derived daily SO₂ masses (5.4 ± 0.7 to 10.0 ± 1.3 kilotonnes, kt; 0.5 kt was the average in the pre-eruptive period). Switch in volcanic activity from VOR to NSEC on December 6 was detected by increasing SO₂ fluxes at the NSEC crater, and by decaying SO₂ emissions at VOR, until activity termination on December 19. Taken together, our observations infer the total degassed SO₂ mass for the entire VOR paroxysmal sequence at $21,000 \pm 2,730$ t, corresponding to complete degassing of $\sim 1.9 \pm 0.3$ Mm³ of magma, or significantly less than the measured erupted magma volumes (5.1–12 Mm³). From this mismatch we propose

that only a small fraction of the erupted magma was actually emplaced in the shallow plumbing system during (or shortly prior) the paroxysmal sequence. Rather, the majority of the erupted magma was likely stored conduit magma, having gone through extensive degassing for days to weeks prior to the paroxysm.

Keywords: volcanic SO₂, Etna, UV camera, OMI, basaltic paroxysms, thermal remote sensing

INTRODUCTION

Open-vent mafic volcanoes are among the most persistent and spectacular forms of active volcanism on our planet (Rose et al., 2013). Apart from being prodigious sources of magmatic volatiles to the Earth's atmosphere during passive (quiescent) degassing (Shinohara, 2013; Carn et al., 2017), these basaltic volcanoes are also the most frequently erupting (Global Volcanism Program, 2013). Although their eruptions are most commonly effusive in nature, explosive paroxysmal eruptions do also periodically occur, ranging in size and intensity from Hawaiian-Strombolian (Volcanic Explosivity Index, VEI: 1–2) to Plinian (VEI: 5–6) in the most extreme events (Williams and Self, 1983; Coltelli et al., 1998; Houghton et al., 2004; Pérez et al., 2009).

Rapid transitions from quiescent behavior to violent eruptions pose a significant challenge for eruption forecasting and hazard management at open-vent basaltic volcanoes, and developing a deeper understanding of the processes that trigger and sustain paroxysms, or influence their magnitude and intensity, is critical (Manga et al., 2017). Magmatic volatiles are known to play a central role in the generation of these basaltic paroxysms (e.g., Aiuppa et al., 2010). Proposed mechanisms include the periodic collapse of gas-rich magmatic “foams” residing at the upper levels of crustal magma storage systems (Allard et al., 2005; Carbone et al., 2015; Chouet and Dawson, 2015) and recharging of relatively degassed shallow magmas with gas-rich magmas from greater depth (e.g., Albert et al., 2016; Pompilio et al., 2017). Improving our understanding of these, or alternative, mechanisms depends on the integration of several methods, and especially real-time observations of gas emissions.

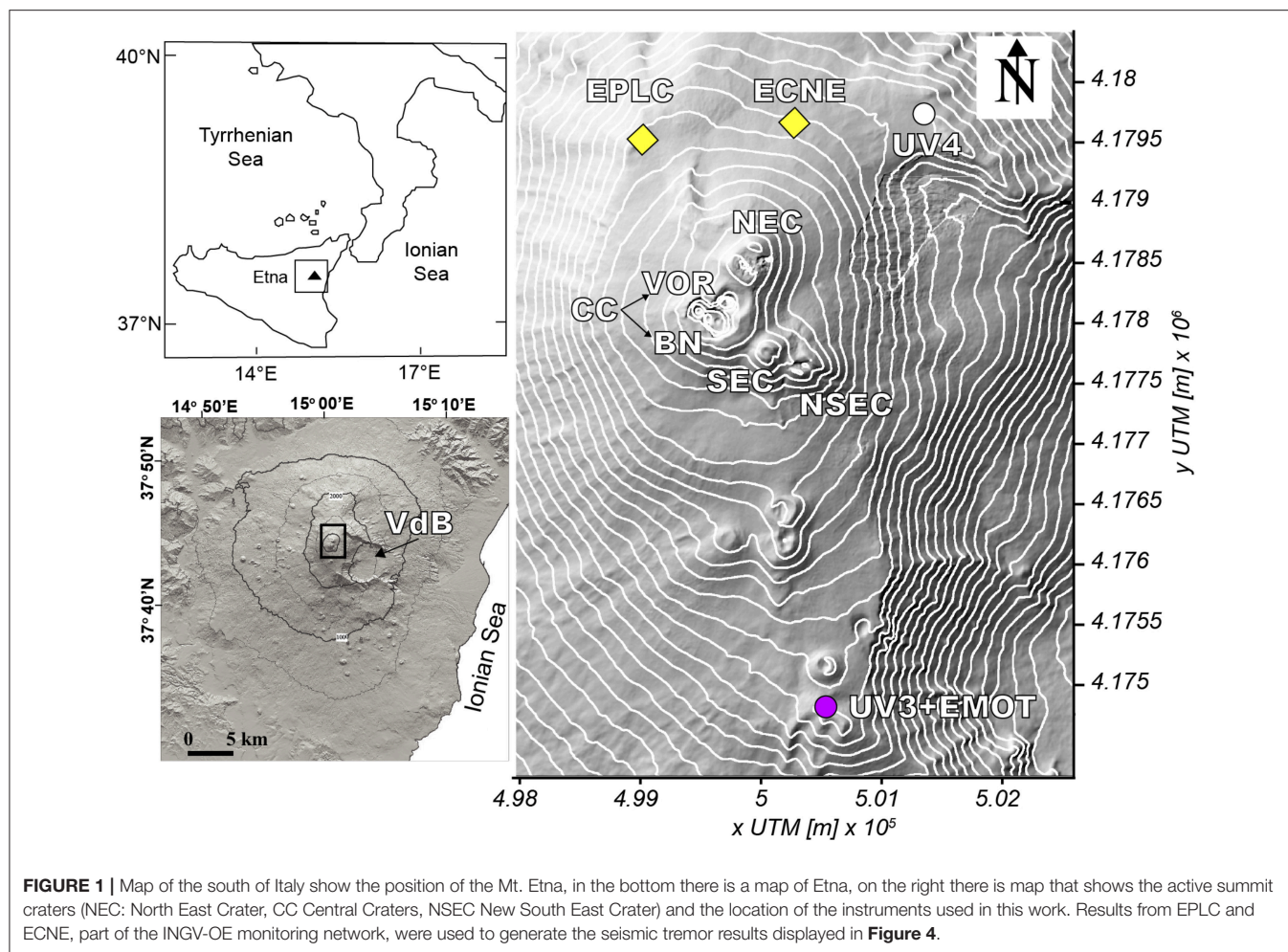
Some of the most frequent and violent basaltic paroxysmal explosions in nature occur on Mt. Etna volcano, in Sicily. Since the late 1990s, roughly ~200 paroxysmal explosive events have occurred at Mt. Etna, frequently clustered in cycles of discrete lava fountaining events initially at the Southeast crater (SEC) (during 1996–2008; Allard et al., 2006; Behncke et al., 2006; Bonaccorso et al., 2011) and latterly at the New Southeast crater (NSEC) (2011–present; Behncke et al., 2014; De Beni et al., 2015). Paroxysmal events are exceptionally well characterized in terms of eruptive dynamics (Harris and Neri, 2002; Dubosclard et al., 2004; Marchetti et al., 2009; Andronico and Corsaro, 2011; Scollo et al., 2012; Olivieri et al., 2013) and composition, texture and volume of erupted materials (Corsaro and Pompilio, 2004; Polacci et al., 2006; Kahl et al., 2015). Interpretation of their associated geophysical signals has led to increasingly refined models for their source region and triggering mechanisms (Alparone et al., 2003; Calvari et al., 2011; Bonaccorso and Calvari, 2013; Patanè et al., 2013; Bonaccorso, 2014; Spampinato

et al., 2015; Gambino et al., 2016). The composition of magmatic gases in the co-eruptive clouds has also been measured (Allard et al., 2005; La Spina et al., 2015).

One major limitation of our current understanding of the mechanisms driving Etna's (and basaltic, in general) paroxysms is the poorly constrained syn-explosive gas output (e.g., the gas flux and total gas volume emitted during the paroxysm). In contrast to quiescent emissions, which are relatively easy to quantify by ground-based remote sensing (e.g., Mather et al., 2006; Burton et al., 2009; Galle et al., 2010; Allard et al., 2016), measuring the gas output from paroxysmal explosions is more challenging. The intensity of activity demands the use of optical remote sensing over *in situ* measurements, yet significant ash emissions can render the plume opaque to proximal sensors, and eruption column heights of a few kilometers make for challenging viewing geometries for near-source ground-based remote sensing networks. Optical remote sensing of dispersing gas plumes from space is a valuable alternative approach, particularly as the eruptive gas plumes disperse downwind over tens to hundreds of kilometers (Carn et al., 2016), but the relatively low temporal/spatial satellite resolution may prevent gas from individual paroxysms to be resolved.

In this study, we apply a suite of complementary methods to calculate a comprehensive gas emissions budget for a notably intense paroxysmal eruption sequence on Mt Etna volcano, Sicily, in December 2015 (**Figure 1**). While satellite observations of paroxysmal eruptions are now routinely made (Carn et al., 2016) and ground-based remote sensing studies have quantified SO₂ emissions budgets for open-vent basaltic volcanoes during lower intensity activity (i.e., quiescent/passive degassing + low-level Strombolian, e.g., Dalton et al., 2010; Tamburello et al., 2012; Pering et al., 2014), to our knowledge this is the first attempt to report the gas budget of an Etna's major paroxysmal episode.

To this aim, we combine UV camera measurements (D'Aleo et al., 2016) with complementary satellite-based observations of the explosive SO₂ release during the paroxysm(s), obtained from the Ozone Monitoring Instrument (OMI; Levelt et al., 2006, 2017; Carn et al., 2017). From these, we quantify the pre-, syn-, and post-paroxysmal SO₂ emissions, and estimate the degassing magma volumes required to supply these emissions. Comparison between SO₂-based degassing magma volumes and direct erupted magma measurements (Bonaccorso and Calvari, 2017; Pompilio et al., 2017) is used to derive constraints on the paroxysms' magmatic volatile source and mechanisms. To assist interpretation of the results, we also use seismic tremor data (Alparone et al., 2007), ground-based thermal radiance measurements (Coltelli et al., 2017) and infrared satellite images acquired by the Moderate Resolution



Imaging Spectroradiometer (MODIS) (Wright et al., 2002; Wright and Flynn, 2004; Rothery et al., 2005; Wright and Pilger, 2008; Coppola et al., 2013, 2016). Thermal data, in particular, are increasingly used to characterize magma circulation (convection) at very shallow depth during the quiescent (e.g., in the absence of effusion) activity of open-vent volcanoes, and are thus very complementary to SO₂ (Coppola et al., 2013; Werner et al., 2017; Aiuppa et al., 2018). We argue that our combined satellite- and ground-based approach could be more widely applied to studies of basaltic volcanism, and forms a useful comparison to indirectly quantified magmatic gas budgets for paroxysms, e.g., the petrological method (combining erupted volumes with pre-eruptive magma volatile content measured in melt inclusions) (e.g., Roggensack et al., 1997).

MATERIALS AND METHODS

Etna's Recent Activity

Since January 2011, Etna's eruptive activity has been characterized by 48 episodic events of lava fountaining from the NSEC, forming both ash-rich eruptive plumes (rising to 11 km a.s.l.) and lava flows flowing eastward and remaining confined within

the Valle del Bove (VdB) depression (**Figure 1**). Between January and May 2015, strombolian activity eventually resumed (though intermittently) at VOR. This crater (one of the Etna's Central Craters CCs), although the oldest of those presently active on the volcano, had exhibited strong gas emissions but no eruptions since the intense 1998–1999 episode that included a sub-plinian explosion on 22 July 1998 (Aloisi et al., 2002). While SO₂ degassing associated to NSEC activity has been discussed earlier (D'Aleo et al., 2016), VOR reactivation in 2015, and particularly the activity build-up in late December (see below), first opened the possibility to characterize SO₂ degassing processes at the volcano's CCs.

Etna's Eruptive Activity in June–December 2015

Volcanic activity progressively escalated at VOR in the second half of 2015, eventually culminating into a violent paroxysmal sequence in early December (**Figure 2**). This sequence (Vulpiani et al., 2016; Corsaro et al., 2017; Pompilio et al., 2017) was composed of individual lava fountain episodes similar in duration (~1–2 h), magnitude (~10⁹–10¹⁰ kg of erupted tephra) and fountain height (~1–4 km) to Etna's earlier paroxysms, but

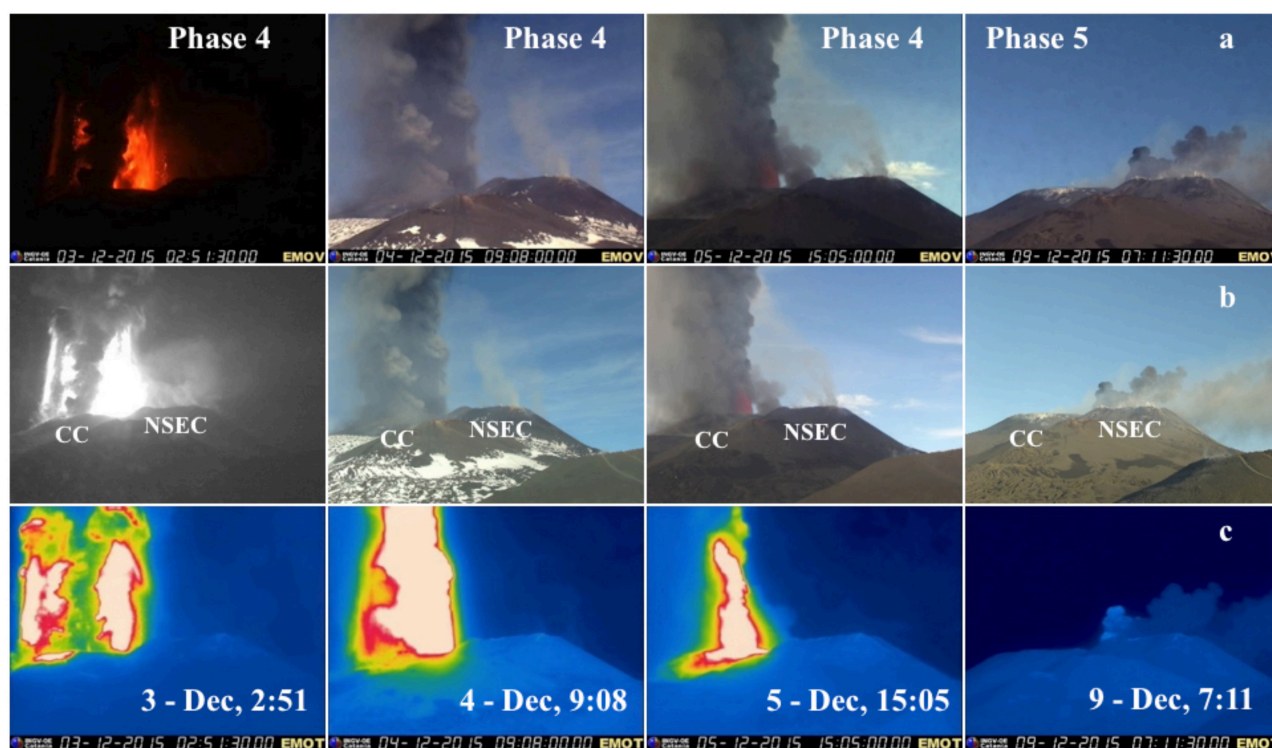


FIGURE 2 | Visible (a,b) and thermal (c) images of Etna's paroxysmal activity from Central Crater (Voragine in this case) on December 3,4,5 (Phase 4). All images taken from the INGV-OE Montagnola multi-parametric Station (see **Figure 1** for location), using (a) EMOV (b) EMHD and (c) EMOT cameras.

was also exceptional for (i) the unusually rapid progression of eruptive episodes, with 4 violent lava fountain events in <2 days; (ii) the eruptive ash column reaching up to 12–15 km height; (iii) the nearly simultaneous reactivation of several summit craters; and particularly (iv) the first paroxysmal events at the Voragine crater (VOR) in more than a decade.

Etna's activity in June–December 2015 is divided into five phases, whose chronology is summarized below.

Phase 1 (June–Mid October): Quiescence

Etna remained relatively quiet between June and mid October 2015, with continuous passive gas emissions, and occasional reddish ash emissions from the Northeast Crater (NEC) (18–20 July) and VOR (20 August). Occasional, dilute ash puffs were observed until 12–18 October, when weak emissions of reddish ash at VOR became more continuous.

Phase 2 (19 October–30 November): Resuming Strombolian Activity at VOR

Mild explosive activity resumed inside the VOR crater on the morning of October 19 (Corsaro et al., 2017), and intensified in the following days. On 19 November, numerous explosions were observed in rapid succession (4–6 events in a few seconds). On November 25, weak strombolian activity at the NSEC began, while activity of the VOR continued without any evident change in intensity until the end of the month.

Phase 3 (1–2 December): Acceleration of Strombolian Activity at VOR

On 1–2 December, frequent and strong explosions were observed at VOR with ejecta rising tens of meters above the crater rim. Explosive activity from a small pit crater of the NSEC, accompanied by weak ash emissions, was also observed. On 2 December from 20:40 UTC, explosive activity at the VOR increased progressively, culminating in the early hours of 3 December in the first paroxysmal eruption.

Phase 4 (3–5 December): Paroxysmal Activity at VOR

A succession of four eruptive episodes was produced by VOR in <3 days during *Phase 4* (**Figure 2**). These episodes were each characterized by paroxysmal phases of short duration ~47–97 min, as derived from Doppler-radar recordings (Donnadieu et al., 2016) and thermal/visible images recorded by INGV video cameras. The eruptive style was similar to the majority of the 230 episodes that have occurred at Etna's summit craters since 1979. The four paroxysmal events of 3–5 December all exhibited an initial phase of strombolian explosions that progressively increased in intensity before a sharply transition into a continuously jetting lava fountain. Each fountain formed a buoyant volcanic plume at the top of the gas-thrust region, while the largest volcanic clasts (spatter and bombs) were ejected and deposited near the vent, forming rootless lava flows filling VOR and BN craters.

The first episode (I; **Figure 2** left panels) occurred on 3 December, after a rapid increase of strombolian explosions begun on 2 December at 20:00 UTC. The paroxysmal phase occurred from 2:08 to 3:28 UTC (duration, 80 min) and was characterized by a transition from strombolian activity to lava fountaining with an accompanying ash column. At 2:20 UTC, the area of incandescent clast fallout increased, peaking at 2:30 UTC when it covered both BN and the crater's slope in the VdB. A strong jet was maintained until 3:12 UTC, when it started to oscillate, gradually reducing to low lava fountaining and finally strombolian explosions after 3:28 UTC.

Episode II (**Figure 2**; second sets of panels from left) occurred on the morning of 4 December from 9:07 to 10:10 (63 min) following several hours of strombolian activity. The transition to lava fountaining, again with an ash column, occurred remarkably rapidly, within a few minutes, and produced a spectacular mushroom-shaped column similar to a classic plinian umbrella. After reaching peak intensity, paroxysmal activity decreased very slowly up to 9:40 UTC, when the fountain started to oscillate and gradually became low lava fountaining (10:10 UTC), finally waning to strombolian activity at 10:25 UTC.

Strombolian explosions continued until the evening of 4 December, when lava fountaining resumed at around 20:00 UTC (Episode III), reaching a climax at 20:27 UTC and terminating at 21:14 UTC. This event was shorter (47 min) and probably associated with a lower ash column. Activity switched to mild strombolian explosions at around 21:30 UTC, which continued throughout the night.

On 5 December (**Figure 2**; second sets of panels from right), after a long phase of stable strombolian activity, the intensity of the strombolian explosions increased from 13:30 UTC, and the final paroxysmal phase (Episode IV) occurred, from 14:48 UTC to 16:25 UTC (97 min duration). The transition to lava fountaining, again with an ash column, occurred in about 10 min. The fountaining became discontinuous from about 15:25 UTC, reducing the most powerful and continuous part of the episode to less than half an hour. From 17:30 UTC, activity switched to mild strombolian explosions that continued into the early hours of 6 December, alternating with increasingly frequent ash puffing.

The overall duration of the paroxysmal phases was about 5 h, in which lava fountaining produced incandescent jets reaching up to 1.7 km above the vent (Bonaccorso and Calvari, 2017). The first two episodes were accompanied by very high eruptive columns (~14–15 km a.s.l.), while in the following two episodes the eruption columns reached only ~10–12 km (Vulpiani et al., 2016; Corsaro et al., 2017). Estimates of mass discharge rate and total erupted mass, obtained from observation of lava fountains and ash columns using either camera images, radar recording or satellite data, show a spread of values (see **Table 1**; data from Vulpiani et al., 2016; Bonaccorso and Calvari, 2017; Corsaro et al., 2017), and do not closely match the limited available field measurements of lava volumes filling the craters and tephra deposits further afield (including material that traveled hundreds of km, and thus fell over the sea). Although the volume output of the four eruptive episodes is not yet accurately known, the available evidence does consistently suggest that episodes I and II were the most intense.

Phase 5 (6—End of December) Waning Phase: Activity Switch at NSEC, and Ash Emissions at NEC

After the last paroxysmal episode, strombolian activity at VOR progressively decreased. On December 6 at 02:00 UTC, after a few hours of quiescence, *Phase 5* started with a switching of eruptive activity to the NSEC (**Figure 2**; right panels). *Phase 5* was characterized by intense strombolian activity concentrated at the pit crater located on the eastern flank of the NSEC, and by effusive activity in the VdB (~2 Mm³ of lava released) during December 6–9 (Corsaro et al., 2017). From 10 December, ash emissions gradually waned and disappeared completely by mid-December.

SO₂ Fluxes: UV Cameras

Etna's volcanic SO₂ flux was measured from the ground using a permanent network of 2 stand-alone UV cameras run by University of Palermo (D'Aleo et al., 2016). These camera systems have been operational since 2014 and are located at Montagnola (UV3) and Pizzi Deneri Observatory (UV4) (**Figure 1**), see D'Aleo et al. (2016) for further details. The network has been deployed within the context of the FP 7 Project BRIDGE (<http://www.bridge.unipa.it/>) of the European Research Council (ERC).

Each UV camera system is equipped with two JAI digital cameras (JAI CM 140 GR, with 10-bit digitization and 1392 × 1040 pixels) fitted with two Edmund Optics pass-band filters at 310 nm and 330 nm, respectively. From the contrast in camera pixel brightness in each set of co-acquired 310 and 330 nm images, the 2D distribution of SO₂ in a volcanic plume is derived and, by processing of consecutive sets of images, the SO₂ flux (Mori and Burton, 2006; Burton et al., 2015). Each camera system also features a visible camera and one ocean optics USB2000+ spectrometer (for calibration of camera-derived absorbance images, see also Lübcke et al., 2013). At the UV3 site, images (UV, visible) and spectra are acquired for 5 h each day from 8 am to 1 pm Local Time, the period of maximum illumination and minimum cloud cover. Acquired data are collected and archived in a rack computer. The UV4 camera system is powered by batteries and equipped with a jetway embedded PC and runs 5 h per day. Each camera mounts a 9 mm Uka Optics UV lens with a field of view (FOV) of 45°. This FOV is selected to provide sufficient spatial resolution (up to 3 meters) to resolve degassing from New South East Crater (NSEC) and Central Craters (CC) (from UV3), and North East Crater (NEC), CC and NSEC (from UV4).

At each site, the two UV cameras capture sequential images of the volcanic plume with 0.5 Hz acquisition rate and ~5 m spatial resolution. Images are then post-processed as described in Kantzas et al. (2010) using an automatic routine version (Delle Donne et al., 2017) of the Vulcamera software (Tamburello et al., 2011, 2012). This yields, for each degassing crater (D'Aleo et al., 2016), time-series of SO₂ integrated column amounts (ICA) along a plume cross-section. These SO₂ ICAs are finally converted into a flux using simultaneous records of plume speed calculated directly from the camera data using an Optical Flow methodology based on the Lukas/Kanade algorithm (Lucas and Kanade, 1981; Bruhn et al., 2005) and integrated in Vulcamera.

Errors on UV camera-derived SO₂ fluxes have recently been quoted at ±18.7% (Holland et al., 2011),

TABLE 1 | Gas and magma budget estimates for the five phases of the June–December 2015 activity phase.

	Phase duration (days)	Cumulative SO ₂ mass (tons)	Cumulative paroxysmal gas mass (tons)	Cumulative paroxysmal gas volume (m ³)	Magma degassing volume (from SO ₂) (Mm ³)	Mean magma degassing rate (from SO ₂) (m ³ /s)	TADR (m ³ /s)	Magma volume (from TDAR) (Mm ³)	Erupted magma volume (Mm ³)
Phases 1–2 (jun–nov)									
TOT (UV Cam)	100	8 ± 0.8·10 ⁴	-	-	7.1 ± 1.1	6.1 ± 0.9	5 ± 1·10 ⁻³ ± 1	0.1 ± 0.03	?
CC (UV Cam)		2.3 ± 0.2·10 ⁴	-	-	2.1 ± 0.3	1.8 ± 0.3			
NEC (UV Cam)		4.4 ± 0.4·10 ⁴	-	-	3.9 ± 0.6	3.4 ± 0.5			
NSEC (UV Cam)		1.3 ± 0.1·10 ⁴	-	-	1.11 ± 0.2	0.9 ± 0.1			
OMI		3.7 ± 0.5·10 ⁴	-	-	3.2 ± 0.6	2.8 ± 0.5			
Phase 3 (1–2 dic)									
TOT (UV Cam)	2	6.7 ± 0.7·10 ³	-	-	0.6 ± 0.1	25.5 ± 3.8	0.22 ± 0.07	0.04 ± 0.01	
CC (UV Cam)		6.7 ± 0.7·10 ³	-	-	0.6 ± 0.1	25.5 ± 3.8			
NSEC (UV Cam)		0	-	-	-	-			
OMI		6.±0.8·10 ²	-	-	-	-			
Phase 4 (3–5 dic)									
TOT (UV Cam)	3	2.25 ± 0.22·10 ⁴	2.7 ± 1.2·10 ⁶	1.5 ± 6.5·10 ¹⁰	2.0 ± 0.3	57.3 ± 8.6	1.009 ± 0.3	0.2 ± 0.06	5.1–12
CC (UV Cam)		1.44 ± 0.14·10 ⁴	1.7 ± 7.8·10 ⁶	9.4 ± 4.2·10 ⁹	1.3 ± 0.2	36.6 ± 5.5			
NSEC (UV Cam)		8.15 ± 0.82·10 ³	9.8 ± 44·10 ⁵	5.3 ± 2.4·10 ⁹	0.7 ± 0.1	20.7 ± 3.1			
OMI		2.10 ± 0.27·10 ⁴	2.5 ± 1.2·10 ⁶	1.4 ± 6.6·10 ¹⁰	1.9 ± 0.3	53.3 ± 9.6	16 ± 0.6	1.7 ± 0.6	~2 ± 0.3
Phase 5 (6 dic–9dic)									
TOT (UV Cam)	4	6.45 ± 0.64·10 ³	7.8 ± 3.5·10 ⁵	4.2 ± 1.9·10 ⁹	0.6 ± 0.1	12.3 ± 1.9			
CC (UV Cam)		2.98 ± 0.29·10 ³	-	-	0.3 ± 0.04	5.7 ± 0.9			
NSEC (UV Cam)		3.47 ± 0.34·10 ³	4.2 ± 1.9·10 ⁵	2.2 ± 1·10 ⁹	0.3 ± 0.05	6.6 ± 1			
OMI		1.10 ± 0.14·10 ⁴	1.3 ± 6.4·10 ⁵	7.2 ± 3.4·10 ⁸	1.0 ± 0.2	21.6 ± 3.9	0.05 ± 0.02	0.04 ± 0.01	?
Phase 5 (10 dic–19dic)									
TOT (UV Cam)	9	1.03 ± 0.10·10 ⁴	-	-	0.9 ± 0.2	8.7 ± 1.3			
CC (UV Cam)		4.61 ± 0.46·10 ³	-	-	0.4 ± 0.1	3.9 ± 0.6			
NSEC (UV Cam)		5.68 ± 0.56·10 ³	-	-	0.5 ± 0.1	4.8 ± 0.7			
OMI		5.47 ± 0.71·10 ³	-	-	-	-			

The cumulative SO₂ masses (column 2) are obtained by summing up the daily averaged total (TOT) SO₂ fluxes, or the SO₂ fluxes from individual craters (CC, Central Crater; NEC, North-east crater; NSEC, New South-east crater) during the specific phase (all obtained from the UV Camera: UV Cam). The corresponding OMI-based results are shown in the table (lines labeled "OMI"). The cumulative SO₂ masses are used (from equation 2) to calculate the magma degassing volumes (Mm³) shown in column (5). The mean magma degassing rates [m³/s; column (6)] are obtained by dividing (5) by phase duration (1), converted in seconds. For the paroxysmal phases only (phases 4 and 5), the cumulative SO₂ masses are converted into cumulative gas masses (tons) and volumes (Mm³) assuming the magmatic gas in the lava fountain comprises ~0.8 ± 0.3 SO₂ mol. % (Allard et al., 2005; La Spina et al., 2015), and using the ideal gas (at T = 1100 °C and P = 0.1 MPa). The mean Time Averaged lava Discharge Rate [TADR; column (7)] is calculated averaging (for each phase) the TADR values obtained from equation 3. The corresponding Cumulative magma volume is also shown in [column (8)]. Ranges for erupted magma volumes are from the literature (Mulpiani et al., 2016; Bonaccorso and Calvari, 2017; Corsaro et al., 2017; Neeri et al., 2017; Pompilio et al., 2017).

$\pm 15\%$ (Tamburello et al., 2012). Use of optical-flow algorithms (Bruhn et al., 2005) to derive plume speed are thought to reduce uncertainty to $\pm 10\%$ (Kern et al., 2015), and this value is taken as representative for errors associated with the SO₂ fluxes presented here.

The 2015 UV camera dataset is unfortunately not continuous. Due to logistical challenges (e.g., very high snow cover and extremely low temperatures in winter), the UV4 camera system is only maintained during summer-early autumn; the NEC SO₂ flux dataset thus only extends from mid-June to mid-October 2015. The UV3 camera system sits in a robust housing (a hut, containing several multi-parametric instruments from INGV-OE). However, technical problems (including icing of the outer quartz window and un-sticking of the optical lenses from the cameras during quick temperature changes) together with the frequent cloud cover over the volcano's summit resulted in non-continuous SO₂ flux measurements for the Central Craters (VOR + Bocca Nuova) and the NSEC. Although many of these technical issues have now been solved, the 2015 dataset demonstrates the challenges in maintaining a permanent UV camera system on a high-altitude volcano with occasionally extreme meteorological conditions.

Satellite-Based SO₂ Observations From OMI

The Ozone Monitoring Instrument (OMI) is a hyperspectral ultraviolet/visible spectrometer carried aboard the NASA satellite Aura (Levelt et al., 2006, 2017). OMI is one of several UV sensors used in monitoring global atmospheric SO₂ concentrations, but it is arguably the most sensitive and effective, offering good spatial resolution (13×24 km at nadir), a wide spectral range (270–500 nm, with resolution of 0.45 nm) and contiguous daily coverage of the Earth. These factors are particularly beneficial in the daily monitoring of volcanic SO₂ emissions, both during eruptions and in the intervals of passive degassing that may separate eruptions, and numerous studies have exploited OMI data for long-term studies of volcanic degassing at individual volcanoes and on a global basis (e.g., Carn et al., 2008, 2013, 2017; McCormick et al., 2012, 2015; Flower and Carn, 2015; Fioletov et al., 2016; Flower et al., 2016). Recently, a new SO₂ retrieval algorithm based on principal component analysis has been developed that dramatically reduces the noise in the OMI SO₂ data (Li et al., 2017). A new dataset, optimized for the study of volcanic emissions, and designated OMSO2VOLCANO is publicly available from the NASA Goddard Earth Sciences (GES) Data and Information Services Center (DISC; http://disc.sci.gsfc.nasa.gov/Aura/data-holdings/OMI/omso2_v003.html). SO₂ column amounts are provided for a set of SO₂ vertical profiles, distributed around a center of mass altitude (CMA). We use the lower tropospheric SO₂ data (CMA of 3 km) for the interval before the onset of the paroxysmal eruption, and either middle troposphere (CMA of 8 km) or lower stratospheric data (CMA of 18 km) throughout the paroxysm, based on auxiliary plume height data (e.g., Corsaro et al., 2017). OMI data can be analyzed using OMIPLOT, a collection of bespoke software routines written in IDL (Carn et al., 2015).

Here, we use OMI observations to compute a time-series of daily SO₂ mass loading over Etna for the paroxysmal interval in December 2015, and several months of preceding activity. The pixels in each OMI instantaneous field-of-view (IFOV, or “scene”) that contain SO₂ are identified and the column concentration of SO₂ in each pixel, reported in DU, is combined with pixel area and converted to a mass. We obtain a total scene mass loading by summing the mass of all SO₂ pixels, and the resulting quantity is typically taken to be the daily SO₂ mass released by the volcano, since OMI makes one daily overpass of each point on the Earth's surface. Under certain conditions, e.g. low windspeed or slow SO₂ loss rates, it is possible that OMI could observe newly-emitted SO₂ in addition to relict SO₂ emitted on preceding days. In this study, we consider this unlikely to be a significant problem: local wind speeds at Etna plume altitudes (roughly, 4 to 10 km) are sufficiently high—usually > 10 m/s based on NCEP2 Reanalysis Data (Palma, 2013) to carry SO₂ rapidly downwind, which we tend to see in SO₂ imagery (e.g., drifting plumes can be tracked downwind in consecutive OMI orbits). Moreover, the emissions that concern us in this study are mostly restricted to the free troposphere and as such would tend to have lifetime on the order of 1–2 days particularly for particle-rich volcanic plumes (Eatough et al., 1994; Oppenheimer et al., 1998; Faloona et al., 2009). To be certain of only including fresh SO₂ in our daily mass loadings calculations, we examine each OMI scene manually, and compute separate mass loading for discrete drifting SO₂ clouds within each image.

The temporal information required to convert SO₂ mass loadings to emission rates is usually unavailable, since the satellite obtains an instantaneous snapshot of activity at the time of overpass. Where high quality atmospheric wind speeds and estimates of SO₂ lifetime are available, mass loadings can be converted into emission rates (e.g., Carn et al., 2013; Lopez et al., 2013) though some of these methods require particular plume geometries to be successful. In this study, we favor the use of daily mass loadings rather than drawing on auxiliary data to compute emission rates from OMI observations, particularly because the key interval of interest for the satellite observations is the paroxysmal period of late November and early December 2017, where plume geometries are unfavorable for emission rate calculations, and the pulsatory nature of the paroxysmal eruption and emissions are not necessarily well-represented by emission rates averaged to tons per day (cf. per-cloud SO₂ mass loadings).

Our reported daily mass loadings should be considered as minima, given the influence of the OMI Row Anomaly (ORA, Carn et al., 2016; Flower et al., 2016). Since 2009, certain rows of the OMI swath have been rendered unusable due to a blockage in the instrument's field of view. This obscures parts of the plume, leading to an underestimate, and on certain days the affected rows may be located squarely across a target volcano and the downwind dispersal area, obscuring the entirety of the plume. In practice this means that SO₂ mass loadings may be underestimated on certain days, and moreover that gaps of 2–3 days between OMI observations are now not uncommon. Another potential problem in the use of tropospheric SO₂ data is meteorological cloud cover obscuring lower altitude volcanic plumes. We include a time-series of mean scene

reflectivity (**Figure S1**) here as a proxy for cloud cover during the OMI observations, and filtered out pixels where cloud fraction (computed from reflectivity) exceeds 30%. Relative to tropical volcanoes, cloud cover is anticipated to be a much less significant problem at Etna and based on the reflectivity time series is not considered likely to majorly impact our results. Factors such as ash interference and plume opacity also affect OMI measurements, and lead to some SO₂ mass underestimation. In the best measurement condition, Yang et al. (2007) estimated an error of 20% on derived SO₂ mass loadings. Recently (Torres et al., 2018) showed that improved processing algorithms may reduce errors to as low as 13%.

Satellite-Based Thermal Data

Thermal data acquired by MODIS were analyzed using the automated, near real time volcanic hot-spot detection system MIROVA (Coppola et al., 2016; www.mirovaweb.it). MIROVA uses middle infrared radiance (MIR) measured by the two MODIS sensors, carried on Terra and Aqua NASA's satellites, respectively. These satellites, scanning the Earth surface four times per day, allow monitoring of volcanic thermal activity globally on a daily basis (Wright et al., 2002; Wright and Flynn, 2004; Rothery et al., 2005; Wright and Pilger, 2008; Coppola et al., 2013, 2016).

The hot-spot detection algorithm includes spectral and spatial analysis of the original MODIS granules, and is designed to detect small to large-scale thermal anomalies (from < 1 MW to >40 GW), and thus capture a large variety of volcanic activity (Coppola et al., 2016). Starting from hot spot pixels detected by MIROVA, we use the Wooster et al. (2003) formulation to retrieve the volcanic radiant power (VRP, W):

$$\text{VRP} = 1.89 \times 10^7 \times (L_{\text{MIR}} - L_{\text{MIRbk}}) \quad (1)$$

where L_{MIR} and L_{MIRbk} are the MIR radiances ($\text{W} \cdot \text{m}^{-2} \cdot \text{sr}^{-1} \cdot \mu\text{m}^{-1}$) characterizing the single hot spot pixel and the background. According to (Wooster et al., 2003), the coefficient 1.89×10^7 ($\text{m}^2 \cdot \text{sr} \cdot \mu\text{m}$) allows estimating VRP with an error of $\pm 30\%$ for any hot surfaces having an integrated temperature between 600 and 1,500 K.

Ground-Based Thermal Data

Volcanic activity at Mt. Etna is continuously monitored in real-time by INGV-OE using a network of video-surveillance cameras (five thermal, nine visible) located on the southern, eastern and western flanks of the volcano (Andò and Pecora, 2006; Behncke et al., 2006, 2009). In this study, we use images recorded by EMOT, EMOV and EMHD cameras, all hosted at La Montagnola Multiparametric Station, 3 km SE from the vent (**Figure 1**) and radiometric data recorded by ENT camera located in Nicolosi, 15 km south of the summit craters. These cameras provided the best quality information and images (**Figure 2**) during the 3–9 December paroxysmal sequence. Images acquired by these cameras are sent to a receiver in Catania through microwave, WiFi, 2 GHz video transmitter and/or cable. All images are digitized and archived on computers in AVI format, with each video clip representing 5 min.

EMOT is equipped with an A320 M Flir Thermovision camera, while ENT with an A40 M Flir Thermovision camera. Both record in the 7.5 and 13 μm spectral range, providing 320×240 pixel images with a spatial resolution of 1.3 mrad. The A320 M and A40 M have thermal sensitivities of 70 mK at 30°C and 80 mK at 25°C, respectively. Thermal images are converted on board the ENT camera to output the peak temperature found in a region of interest, centered on the zone affected by eruptive activity. This value is transmitted at 1 Hz to the acquisition center in Nicolosi. Thermal images and thermal data, recorded between 0 and 500°C, are processed in real-time by a dedicated software (NewSaraterm) developed with LabVIEW™ 8.0 to detect ash-rich eruptive columns, explosive, and effusive activity (Behncke et al., 2009). This software calculates, with a median filter, the daily thermal offset and extracts for each measurement the difference between the measured value and the dynamic thermal offset. NewSaraterm is set to transmit alert messages to the INGV-OE Operative Center anytime when prefigured thresholds are exceeded. Temperatures displayed in the video frames are much lower than the true temperatures at the target, because of the distance between the camera location and the target (the summit craters), environmental factors such as air humidity, pressure, air temperature, and the presence of an additional protective lens on the camera (Sawyer and Burton, 2006). The temperatures discussed here are thus apparent, not absolute, as they have not been corrected for the aforementioned factors.

EMOV is a Sony DXC 950 P visible camera equipped with a professional Canon YH 19 x 6.7 KTS lens, while EMHD uses a VIVOTEK IP8172P camera with a 1/2.5" Progressive CMOS image sensor and maximum resolution of 2560×1920 . The lens is a varifocal KOWA LMVZ3510M-IR 1/2" P-IRIS CS-MOUNT lens. The Focal Length is 3.5–10 mm and the Aperture is F 1.6 (wide) \sim F 2.7 (tele). The Field of View is: $33^\circ \sim 93^\circ$ (horizontal), $24^\circ \sim 68^\circ$ (vertical) and $40^\circ \sim 119^\circ$ (diagonal). Minimum Illumination is 0.05 Lux @ F1.6 (Color) and 0.001 Lux @ F1.6 (B/W).

Seismic Data

We use seismic data from EPLC and ECNE seismic stations (**Figure 2**), part of the INGV permanent multi-parametric monitoring network. These stations are characterized by a Broadband Nanometrics Trillium with an eigen-period of 40 s and a sensitivity of 1,500 V*s / m. Seismic signal is sampled at 100 Hz with a 24 bit resolution using Nanometrics Trident digitizers. Tremor is then calculated as RMS (root mean square) amplitude in the 0.5–5.5 Hz frequency band and using a moving window of 10 s.

RESULTS

UV Camera-Based SO₂ Fluxes

Figure 3 shows examples of SO₂ flux records (30 min each) taken by the UV camera network in 3 distinct measurement days: (a) 14 July, (b) 2 December, and (c) 6 December. These examples are selected to illustrate some of the characteristics of our SO₂ flux measurements, but cannot be taken as

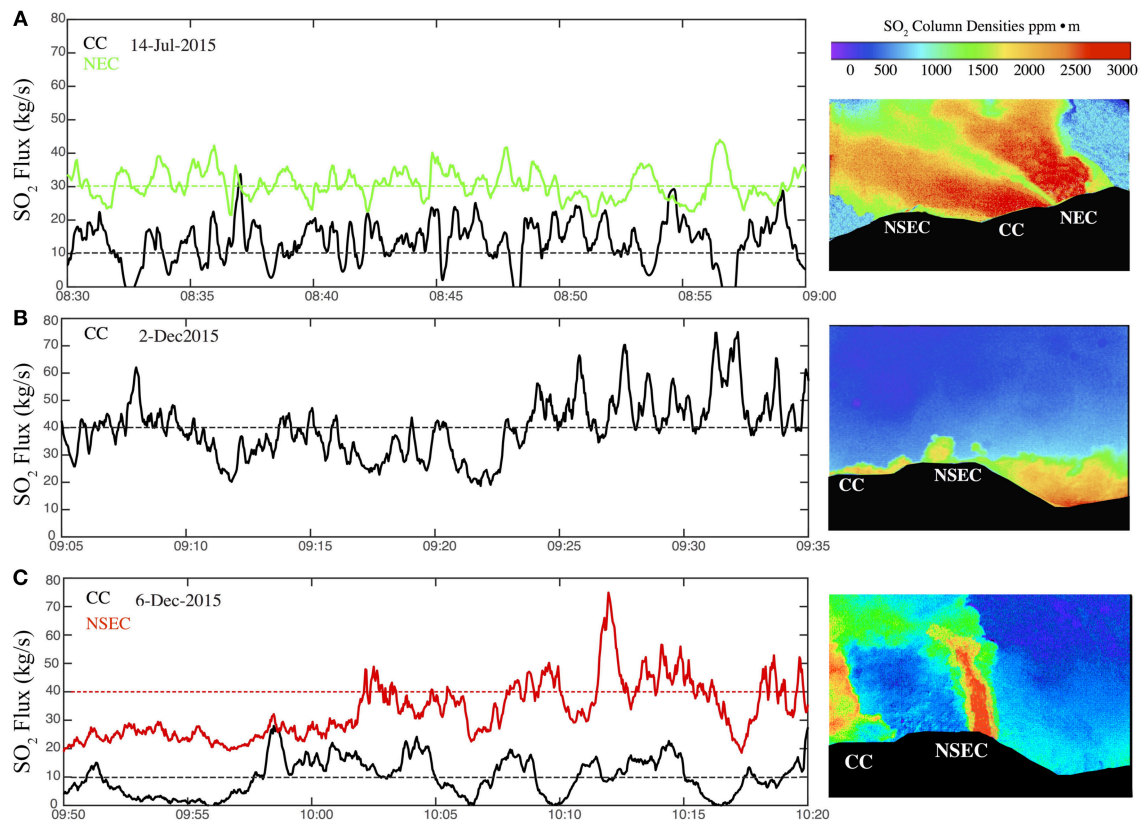


FIGURE 3 | Examples of SO₂ flux records (30 min each) taken by the uv camera network in 3 distinct measurement days. The horizontal dashed lines indicate the mean SO₂ flux values. For each time-series (measurement day), a snapshot of a representative absorbance image (outputted by the camera system) is also shown to illustrate typical plume geometries (CC: Central Craters, NEC: Northeast crater; NSEC: New Southeast crater). **(A)** July 14 results obtained from UV4; **(B)** December 2 results obtained from UV3; **(C)** December 6 results obtained from UV3.

an exhaustive representation of the highly variable degassing behaviors seen at Etna's different vents during the monitored period.

The 14 July dataset (**Figure 3A**) is taken as representative of background, quiescent degassing activity during *Phase 1* (see section Etna's Eruptive Activity in June-December 2015). Both time-series and image show that, during *Phase 1*, the NEC is the dominant gas source on the volcano, the CCs are moderately degassing, while the NSEC exhibits low degassing.

The 2 December observations (**Figure 3B**) illustrate a visible acceleration in SO₂ degassing from the CCs in *Phase 3* (see section Etna's Eruptive Activity in June-December 2015), as a prelude to the ensuing paroxysmal sequence which started only a few hours later.

Paroxysmal activity from VOR during *Phase 4* is fully captured only in the morning of December 4. The UV-camera SO₂ flux record taken during a ~4 h period encompassing paroxysmal activity is illustrated in **Figure 4**. The three other VOR paroxysms occurred either during the night-time (episodes I and III on December 3 and 4, respectively; **Figure 2**) or during the daytime but outside the UV3 operational time window (episode IV on December 5; **Figure 2**). Our SO₂ fluxes for December 3 and 5

thus essentially reflect degassing prior to or after the paroxysms (see below; **Figure 5**).

Figure 4 illustrates our December 4th example (**Figure 4**), corresponding to the second lava fountaining event of VOR (episode II, from 08:41 to 10:03; **Figure 2**). The pseudo-color images in the top panel (**Figure 4a**) illustrate the 2D distribution of SO₂ in the basal (gas thrust) portion of the eruptive cloud. These figures show a dense, tall SO₂-rich plume rapidly dispersing to the left of the camera's FOV (toward S-SW). Based on comparison with OMI data (see below), we are confident that, in the basal portion of the eruptive column (just right above the crater rim), where our integration cross-section is taken to derive the SO₂ fluxes, the largest fraction of the plume is still captured in the camera's FOV. The SO₂ flux time-series (**Figure 4c**) demonstrates ramping up SO₂ release in the 2 h before the paroxysm, from ~100 ± 10 kg/s at 7:00 to ~400 ± 40 kg/s at the paroxysm onset (08:41 U.T.C.). After onset of the lava-fountaining phase, visible cameras (**Figure 4b**) detect significant ash injection in the atmosphere. At the same time, the SO₂ flux (**Figure 4c**) abruptly decreases, from ~400 ± 40 kg/s to ~50 ± 5 kg/s within ~20 min (note degradation of pseudo-color images, **Figure 4a**), while tremor and thermal radiance still

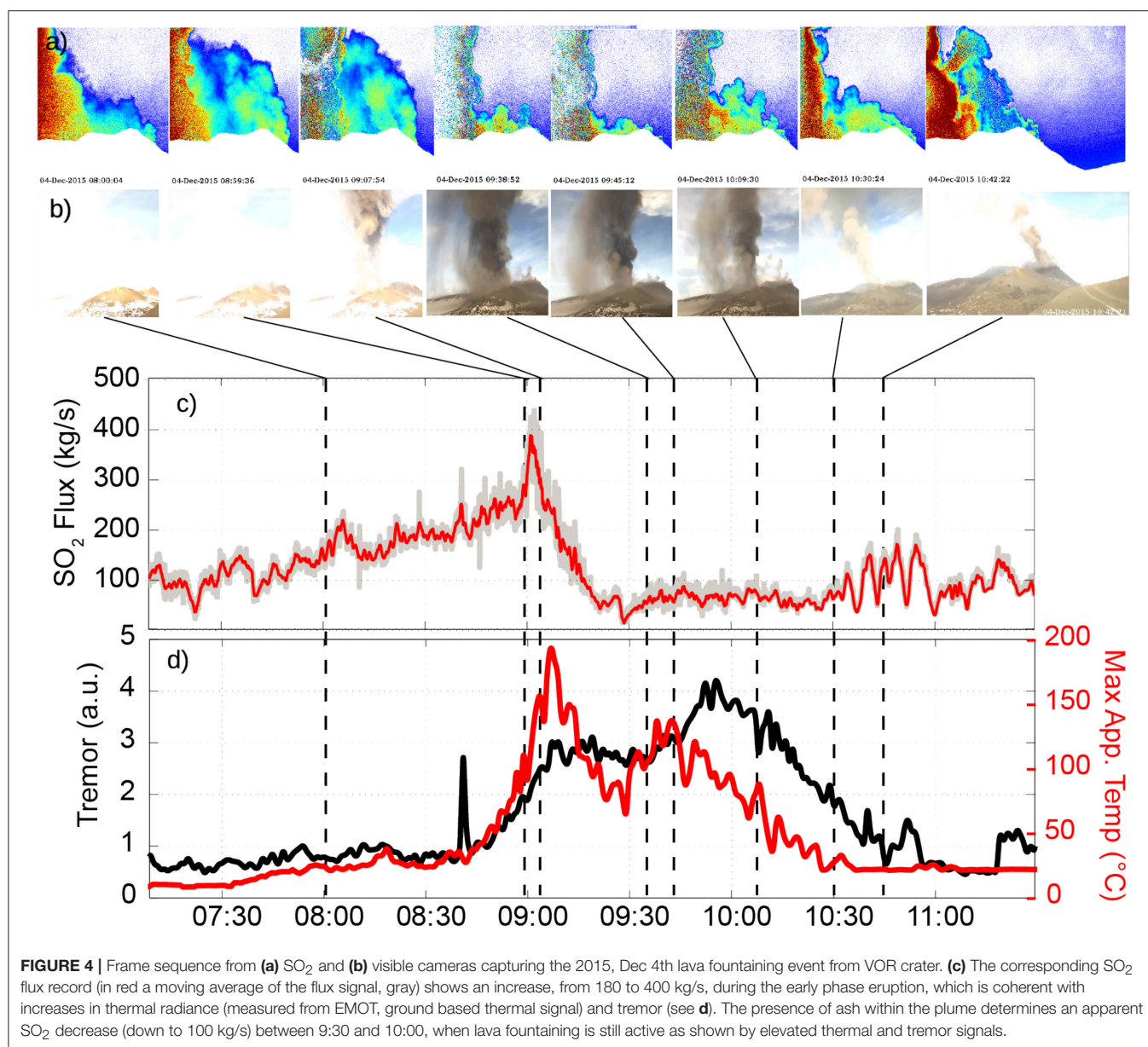


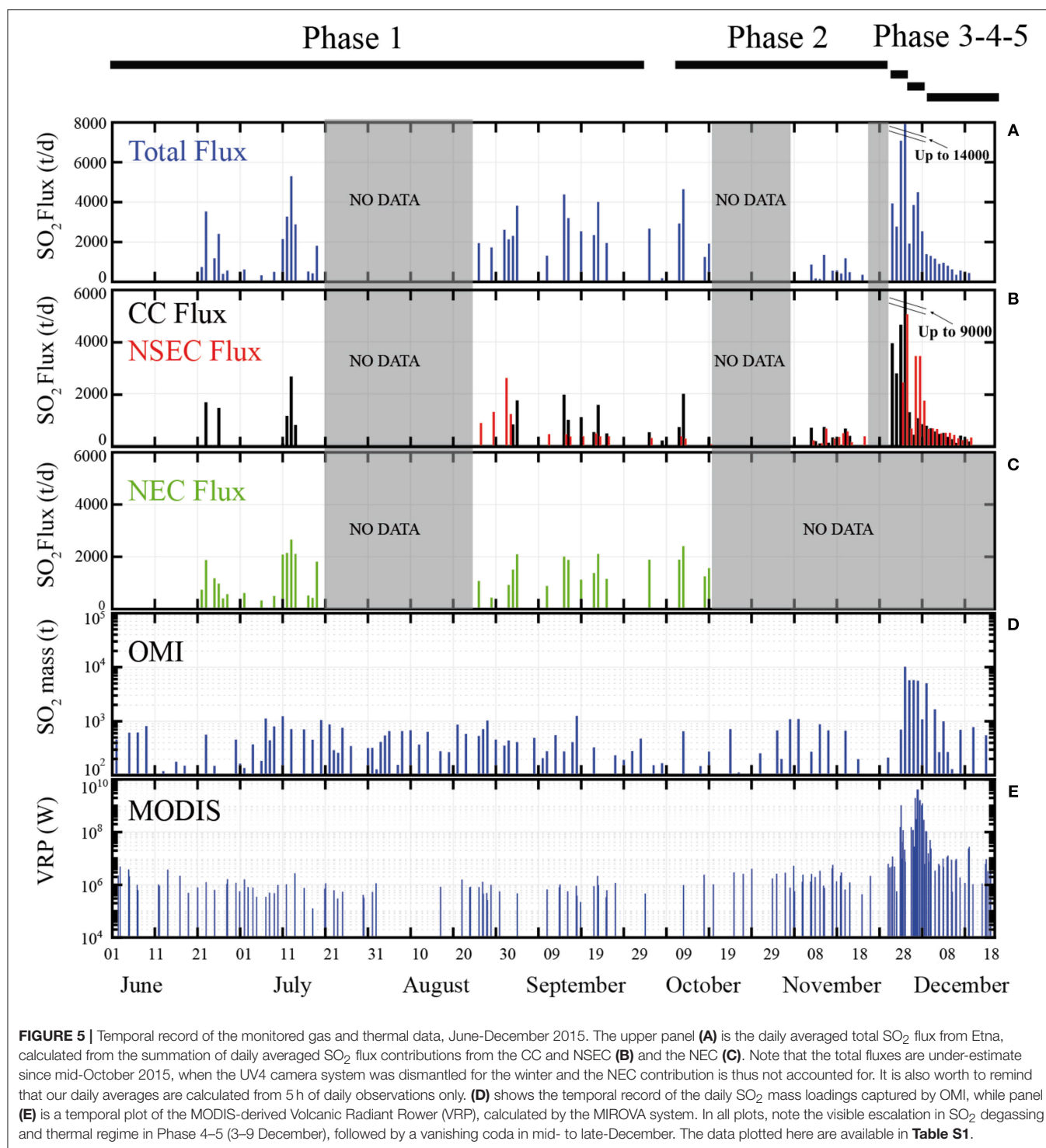
FIGURE 4 | Frame sequence from (a) SO₂ and (b) visible cameras capturing the 2015, Dec 4th lava fountaining event from VOR crater. (c) The corresponding SO₂ flux record (in red a moving average of the flux signal, gray) shows an increase, from 180 to 400 kg/s, during the early phase eruption, which is coherent with increases in thermal radiance (measured from EMOT, ground based thermal signal) and tremor (see d). The presence of ash within the plume determines an apparent SO₂ decrease (down to 100 kg/s) between 9:30 and 10:00, when lava fountaining is still active as shown by elevated thermal and tremor signals.

show relatively high and stationary intensities (Figure 4d). The presence of ash in the FOV is known to prevent reliable UV camera measurement since it increases plume opacity and leads to strongly underestimated SO₂ column densities (Andres and Schmid, 2001). Assuming stationary SO₂ emission during lava fountaining at ~400 kg/s (as observed prior to the onset), we can tentatively infer a factor 87% SO₂ underestimation due to ash in the plume. After ~10:30 U.T.C., the SO₂ flux oscillates around high (~150 kg/s) values during the paroxysm's waning phase.

A typical dataset for a *Phase 5* measurement day (December 6) shows increased degassing from the erupting NSEC crater, and vigorous (though reduced, relative to *Phase IV*) degassing from the CCs (Figure 3C).

In the attempt to characterize Etna's SO₂ degassing behavior in the ~6 month temporal window culminating in the December 2015 paroxysmal sequence, we calculate, for each available measurement day, the daily averaged SO₂ flux, by simply taking the arithmetic mean of data in each 5 h-long daily acquisition (see Table 1). Results are illustrated in the synoptic temporal plot of Figures 5A–C, which also summarizes the results of satellite-based SO₂ (Figure 5D) and thermal (Figure 5E) observations (see below).

In spite of the several data gaps, caused by adverse weather conditions and technical problems (see section Etna's Eruptive Activity in June–December 2015 and Table 1), the ground-based SO₂ flux time-series (Figures 5A–C) documents the temporal evolution of Etna's degassing activity. This is indicated by



changes in the Total SO₂ flux (**Figure 5A**) and in the vent-resolved SO₂ flux contributions from NEC (**Figure 5B**), NSEC, and CC (VOR+BN) (**Figure 5C**). We find that, in *phase 1* (July–October), the Total (NEC+CC+NSEC) SO₂ flux oscillates around a ~2,500 t/d average, with the NEC (mean, ~52%) and the CC (mean, ~40%) being the primary SO₂ sources and

the NSEC contributing only ~8% of the gas on average. The CC SO₂ flux systematically remains $< 2500 \pm 250$ tons/day (**Figure 5B**). *Phase 2* (19 October–30 November), characterized by resumed strombolian activity at VOR, is unfortunately very poorly covered by our observations (note that, from *Phase 2* onward, the Total SO₂ flux accounts for the contribution of

CC+ NSEC only, because UV4 was no longer operative, meaning that NEC emissions were not quantified). Corsaro et al. (2017), based on results of the INGV-OE permanent scanning-DOAS network (Salerno et al., 2009), report a SO₂ flux increases to 2,500–4,000 tons/day during this phase of escalating strombolian activity at VOR. Intensification of eruptive-degassing activity at VOR is consistent with our UV camera records for *Phase* 3 (1–2 December; 3,900 and 2,700 tons/day, respectively; see

Figures 5B, 6b). No appreciable SO₂ is detected at the NSEC during this period (**Figure 6c**).

The onset of paroxysmal activity at VOR, *Phase* 4 (3–5 December), marks a sizeable increase in the CC (4,580–8,900 tons/day), NSEC (2,600–4,900 tons/day), and Total (~7,100–13,900 tons/day) SO₂ flux (**Figure 6**). It is useful to recall that, since only episode II (December 4 morning paroxysm; **Figure 4**) matches with the UV camera acquisition interval, the SO₂

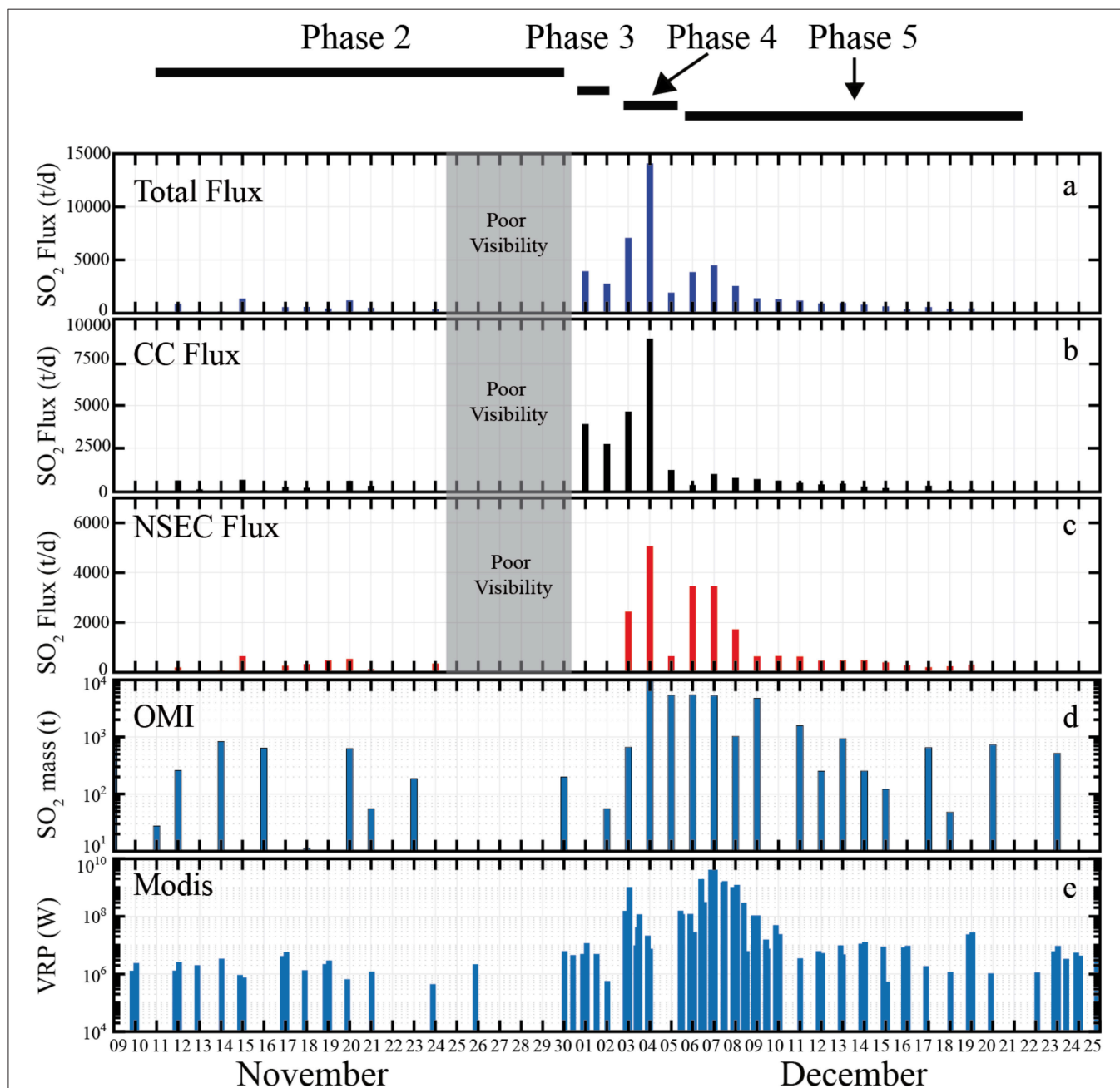
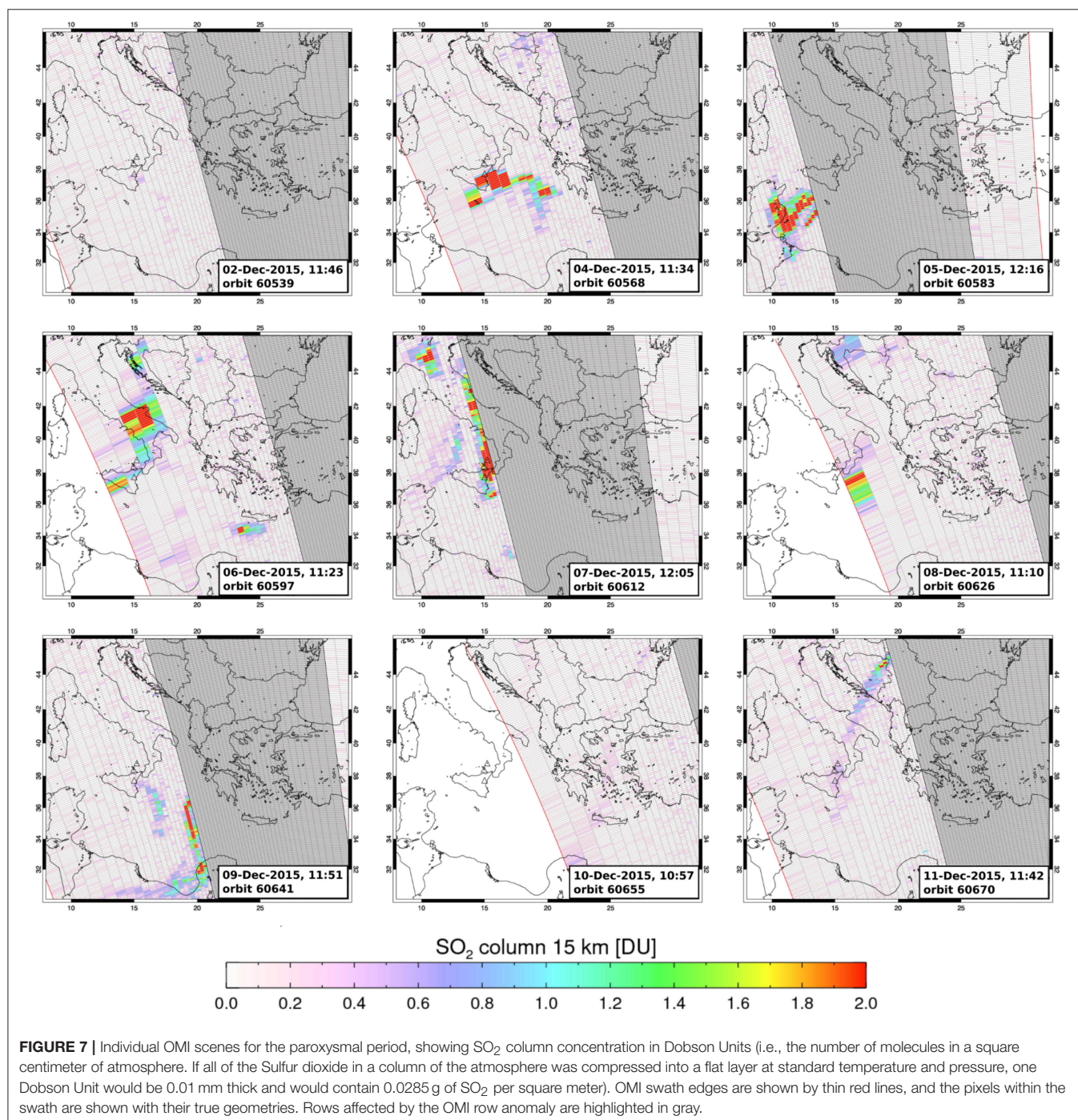


FIGURE 6 | A detail of Figure 5, showing the temporal evolution of gas and thermal signals in November-December 2015. **(a)** Shows ground based SO₂ flux from UV camera, panel **(b,c)** shows the contribution of Central Craters (CC) and New South East Craters. Between 25 and 30 November extremely weather condition. **(d)** shows SO₂ mass loadings captured by OMI, panel **(e)** is a temporal plot of the MODIS-derived Volcanic Radiant Rower (VRP), calculated by the MIROVA system.

increases on December 3 and 5 reflect heightened degassing in between the paroxysms themselves. During December 6–8, the onset of *Phase 5*, volcanic activity switched from VOR to NSEC (see section Material and Methods) as illustrated by increased SO₂ fluxes at NSEC (up to 3,500 t/d, and by an abrupt decline of VOR SO₂ emissions (compare **Figures 6b,c**). An exponential decay of SO₂ emissions from all craters is observed in the waning phase of the paroxysmal sequence (10–18 December) (**Figures 5, 6**).

OMI-Based SO₂ Observations

Example of SO₂ mass loading maps on OMI scene from some selected days are shown in **Figure 7**. The OMI-derived daily SO₂ mass loading over Etna varies widely during *Phases 1–3*, but remains systematically below 1,200 tons (**Figure 5D**). The wide range observed (from <100 to ~1,200 tons) is likely to reflect daily variations in the passive degassing flux from Etna, but also variations in OMI's detection of the prevailing low-altitude and low mass SO₂ clouds during this period of lower intensity



activity. Increases in daily cloud cover or in the position of the ORA-affected portion of OMI's swath relative to Etna can both hamper accurate quantification of SO₂ mass and small plumes during lower intensity volcanic activity suffer disproportionately. That OMI did not observe SO₂ mass >1,200 tons in any overpass reflects the general low level activity of Etna during this passive degassing interval.

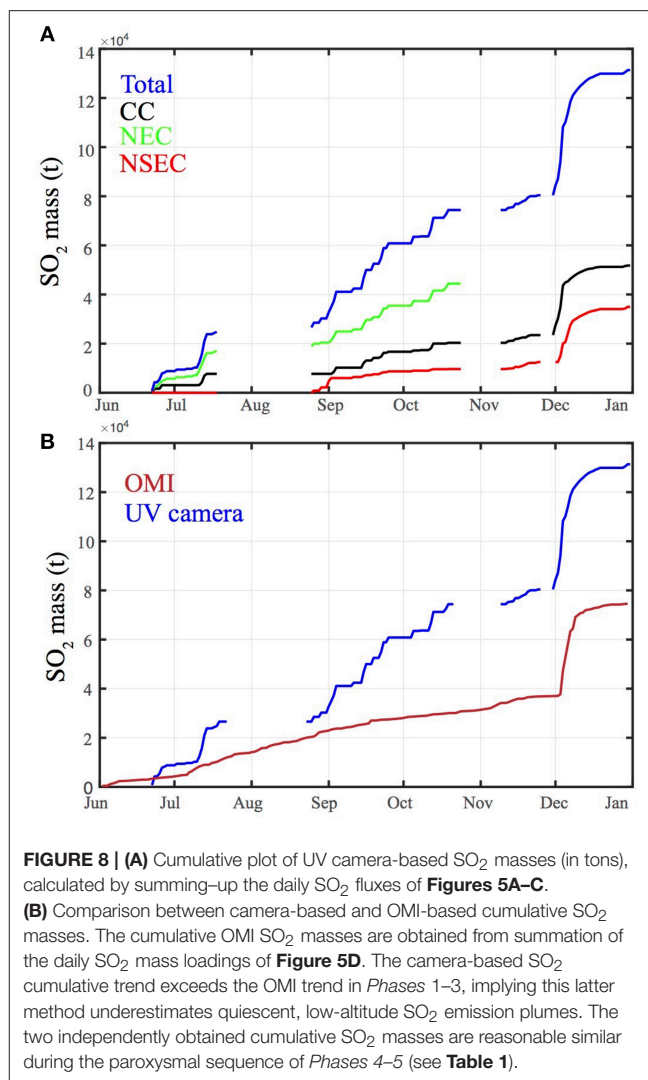
Onset of the *Phase 4* paroxysmal activity marks a sizeable increase in daily SO₂ mass loading on December 4 (~9,600 tons), indicating substantial SO₂ injection in the higher atmosphere during the first two more vigorous VOR episodes. SO₂ mass loading persists at high levels (~5,300 tons) over the next three consecutive days (5–7 December). During *Phase 5*, the high SO₂ mass loading on December 9 reflects degassing from the erupting NSEC, but declines to pre-paroxysm levels (<1,000 tons) by December 12.

The heightened SO₂ degassing behavior of Etna in December 2015 is clearly illustrated by the plot of **Figure 8**, which compares the cumulative masses of degassed SO₂ derived from space (OMI) and from ground (UV Camera).

Satellite Thermal Data

Between 01 July and 31 December 2015, 145 thermal anomalies are detected over Mt. Etna by the MODIS-MIROVA system (Coppola et al., 2016) (**Figures 5E, 9A**). The radiant heat flux spans from 0.15 MW to 4,151 MW (on 7 December 2015) with about 80% of the data below 10 MW (**Figure 9B**). Visual inspection of all the images allows us to discard thermal anomalies due to fires (located at more than 5 km from the summit), as well as to filter out thermal data affected by cloud/plume contamination or acquired under poor geometrical conditions (satellite zenith angle > 45°). The resulting dataset consists of 101 alerts (red line in **Figure 9A**), yielding a total radiant energy of 5.22×10^{14} J over the analyzed time window.

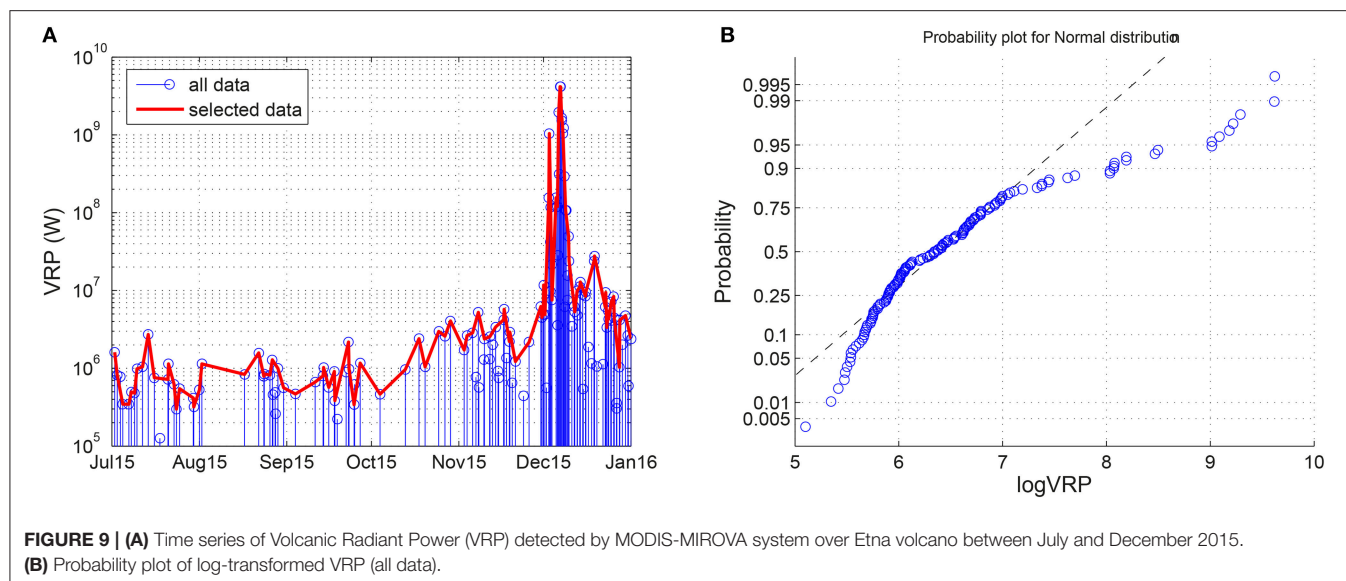
Between July and late September, during *Phase 1*, the radiant power is very low and relatively stable at around 1 MW (**Figure 9A**). However, thermal anomalies increase gradually during late October–November (*Phase 2*), to reach 5 MW, on 28 October 28, and 11 MW on 11 November 2015. On December 2 (*Phase 3*) at 21:00 (UTC), a sharp VRP increase at 155 MW coincides with the first VOR paroxysmal episode. The paroxysm itself generates a peak VRP of 1,037 MW on 3 December at 01:15 (UTC). In the following 2 days, the volcanic plume often obscures and attenuates thermal anomalies, thus precluding clear view observations of paroxysmal episodes 2–4. From December 6 (*Phase 5*), a new phase of increased thermal activity was detected by MIROVA, in response to lava effusion from the base of the NSEC. This phase is accompanied by a clear view of the Etna's summit area, and culminated on 7 December (00:50 UTC) with VRP reaching the maximum value of 4,151 MW (**Figure 9A**). Cessation of lava effusive activity in the evening of December 8 is marked by a VRP decline below 100 MW (**Figures 5E, 9A**). Thermal anomalies progressively declined throughout the following days, dropping to 3 MW by 31 December 2015.



DISCUSSION

Basaltic explosive eruptions are manifestly fuelled by magmatic volatiles (Vergnolle and Mangan, 2000; Taddeucci et al., 2015), so that direct measurements of volatile release during basaltic paroxysms are key to refining models for their trigger mechanisms, which are still debated (Gonnermann and Manga, 2003; Parfitt, 2004; Manga et al., 2017). Although only the third magmatic volatile in order of abundance, SO₂ is the easiest to measure remotely (Oppenheimer et al., 2011), and thus represents an obvious target for gas observations during a paroxysm. However, while the SO₂ budget for individual strombolian explosions is relatively straightforward to characterize (Mori and Burton, 2009; Kazahaya et al., 2011), SO₂ flux measurements during the far more violent (and ash-richer) lava fountain eruptive clouds have remained challenging, to date.

On Etna, the inter-annual time-averaged SO₂ flux is exceptionally well-characterized (Caltabiano et al., 1994, 2004;



Allard, 1997; Allard et al., 2006), and is known to be dominated by persistent passive degassing from the summit craters. In contrast, the SO₂ flux sustained by the brief but very intense paroxysmal episodes is thought to constitute only a small fraction of the long-term total emission budget. Quantifying this paroxysmal flux would nonetheless have profound implications for constraining the dynamics and trigger mechanisms of the paroxysms. It is well established that Etna's SO₂ flux peaks (typically at >10,000 tons/day) during paroxysmal episodes (Caltabiano et al., 2004; Spampinato et al., 2015), but the explosive gas output from the erupting crater has proven difficult to resolve from the background quiescent emissions that persist at the other craters. Recently, we demonstrated the use of a novel network of UV cameras to obtain spatially resolved SO₂ flux emission data from Etna's individual craters (D'Aleo et al., 2016). As a matter of fact, UV cameras offer improved spatial resolution over traditional spectroscopic techniques (COSPEC and scanning DOAS) that typically target a distal plume several km away from the summit area, where the two gas contributions (from the paroxysm and passive degassing) have already merged into a single aggregate plume (Salerno et al., 2009).

Our gas and thermal observations (Figures 5–9) here contribute novel constraints on degassing processes associated with Etna's December 2015 paroxysmal sequence. We show that, during the two days before the onset of the paroxysmal sequence (in Phase 3), SO₂ degassing intensifies at the VOR (up to 3,500 tons/day, Figure 6). The SO₂ flux results presented in Corsaro et al. (2017) imply that this SO₂ flux increase (~2,600–4,300 tons/day) persisted during Phase 2 too (19 October–30 November), and therefore accompanied the entire sequence of escalating strombolian activity at VOR that occurred prior to the paroxysms. The onset of paroxysmal activity at VOR on 3 December sees a further escalation in UV camera-derived SO₂ fluxes, and is also marked by an abrupt increase in OMI-derived SO₂ loadings over Etna (Figures 5–7) and in radiant power (Figure 9). This anomalous SO₂ output and thermal

regime persists throughout the entire VOR (Phase 4) and NSEC (Phase 5) paroxysmal sequence, and then slowly decreases after 10 December, with SO₂ and thermal emissions decaying to pre-paroxysm values by the end of the month.

Our results overall provide four sets of new information: (i) the SO₂ flux during, prior and after a lava fountaining episode is measured for the first time, at high-temporal resolution (Figure 4; see section SO₂ Flux Budget for an Individual Lava Fountain); (ii) the total SO₂ budget from the eruptive sequence is fully reconstructed from both ground and space (Figure 8), leading to calculation of the associated degassing magma volumes (see section SO₂ budget for the Etna's 2015 paroxysmal sequence, and calculation of magma volume fluxes); (iii) a systematic inter-comparison study between UV Camera and OMI (see section UV Camera vs. OMI) and gas- and thermal-based magma volumes (see section Magma Volume Fluxes From Satellite Thermal Data) is undertaken.

SO₂ Flux Budget for an Individual Lava Fountain

Our 4 December 2015 dataset (Figure 4) is, to the best of our knowledge, the first example of an high-frequency (0.5 Hz) SO₂ flux record during a paroxysmal episode at Etna (VOR episode II). This dataset demonstrates both advantages and challenges in UV camera sensing of basaltic paroxysmal activities. Our results show that SO₂ release escalates for ~1 h period prior to Etna's paroxysmal activity, peaking at ~400 kg/s at the paroxysm onset. This confirms escalating transport in the shallow conduits of gas, or perhaps of an effervescent gas-magma mixture, as the paroxysm's driver(s). Temporal SO₂ flux fluctuations broadly correlated with seismic tremor and thermal amplitude (Figure 4), but are also modulated by ash content. In the most intense phase of the lava fountain (as marked by the peak in seismic tremor), the SO₂ flux declines, implying severe SO₂ underestimation during ash-rich periods, when plume opacity increases. In the VOR episode II example, rapid dispersion of the eruptive cloud

toward SSW is an additional issue, and implies that only part of the column is contained in the cameras' FOV (this effect is minimized by taking the integration cross-section right at the crater rim edge, where the majority of the plume is captured). With these limitations in mind, we calculate by integration that 1220 ± 122 tons of SO₂ is explosively released during <2 h of vigorous VOR episode II (average flux, 169 ± 17 kg/s). To put this context, this SO₂ mass corresponds to what normally released by the volcano in one full day of background quiescent activity (e.g., *Phase 1* in 2015).

In a typical Etna lava fountain, SO₂ comprises $\sim 0.8 \pm 0.3$ mol. % of the gas phase (Allard et al., 2005; La Spina et al., 2015). From this and the paroxysmal SO₂ mass of 1220 ± 122 tons (above), we estimate the total magmatic gas output for VOR episode II to be $8 \pm 3.6 \cdot 10^8$ m³. In this calculation, we assume $T = 1100$ °C, $P = 0.1$ MPa, molecular weight = ~ 20.9 g/mol (for a 90 mol. % H₂O gas composition; La Spina et al., 2015) and 45% uncertainty (based on error propagation on SO₂ mass and chemical composition uncertainties). For comparison, Bonaccorso and Calvari (2017) calculated, based on processing of thermal camera images, a total fluid volume for this event of the same order of magnitude (1.5×10^9 m³ of total fluid, with pyroclastic materials accounting for a trivial fraction of this volume, ~ 0.2 %).

SO₂ Budget for the Etna's 2015 Paroxysmal Sequence, and Calculation of Magma Volume Fluxes

VOR episodes I, III and IV (see section Etna's Eruptive Activity in June–December 2015) unfortunately occurred outside the daily UV camera acquisition hours, so that their volatile budget cannot be constrained from measurements on ground. The elevated SO₂ fluxes observed on December 3 and 5 (Figure 6), therefore, are reflecting heightened quiescent (or weakly explosive) degassing in the periods between one paroxysmal episode and the successive.

We therefore place constraint on the total explosive SO₂ release during the entire VOR sequence by using OMI record, which clearly peaks during *Phase 4* (Figures 5, 6). OMI data are likely to fully capture eruptive gas emissions injected into the higher atmosphere, while being less sensitive to Etna's low-altitude quiescent emissions (we consider the average daily SO₂ mass loading of $\sim 500 \pm 65$ tons in July–October 2015 as representative of these background emissions) (see section UV Camera vs. OMI). Figure 8 enables us to estimate the cumulative SO₂ mass released by the Etna's 2015 paroxysmal sequence. By summing up the SO₂ mass loadings seen by OMI during December 3–6, we find a cumulative SO₂ mass of $\sim 21,000 \pm 2,730$ tons (Figure 8, Table 1). Thus, using this total eruptive mass (and the parameters as above for the composition and T–P conditions of the eruptive plume), we infer the total magmatic gas output for the entire *Phase 4* (VOR episodes I–V) at $14 \pm 0.6 \cdot 10^9$ m³. This is in the same order of magnitude of the total calculated erupted volume of fluid of Bonaccorso and Calvari (2017) ($5.9 \cdot 10^9$ m³). Given the impact of the row anomaly on OMI mass loading measurements, this is likely to be a minimum estimate for the total gas output of *Phase 4*.

A similar approach can be used to quantify the SO₂ degassing budget for the NSEC activity of *Phase 5* (Table 1). Although OMI observes a composite plume from Etna, and cannot by itself distinguish the relative contributions of the distinct summit craters, the decrease in Central Crater flux measured by our UV camera network in *Phase 5* gives us confidence that the SO₂ mass dings measured by OMI are dominated by NSEC emissions. Using OMI data, we calculate that $\sim 11,000 \pm 1,430$ tons of SO₂ may have been explosively released by the NSEC during 6–9 December, from which we estimate (at same composition, temperature and pressure as above) a total magmatic gas output of $\sim 7.2 \pm 3.4 \cdot 10^9$ m³, or ~ 2 times less than during *Phase 4*. Again, given the influence of the ORA obscuring part of the plume detected by OMI, this is likely to be a minimum estimate of gas output.

One equally important exercise is to use the above-inferred erupted SO₂ masses to calculate the volumes of degassing magmas required to produce them (e.g., the magma volume necessary to provide the gaseous content to drive the fountaining). In order to convert the SO₂ masses (M_{SO_2}) into volumes of magma (V_e) needed to justify them, we use the same relation as in Allard (1997):

$$V_e = \frac{M_{\text{SO}_2}}{2[S] \cdot \rho \cdot (1 - x)} \quad (2)$$

where $[S]$ is the weight fraction of elemental sulfur degassed per unit mass of magma (3,000 mg/kg, from glass inclusion record; Métrich et al., 2004), ρ is typical basalt density (2700 kg/m³) and x is magma crystallinity (0.3; see Pompilio et al., 2017). We infer the uncertainty on the estimated magma volumes to be 15–18%, based on errors on either UV-camera (10%) or OMI-derived (13%) masses, and uncertainty in initial sulfur content in magma (5%). We caution these 15–18% errors are likely to correspond to minimum uncertainties, because melt-inclusion information on pre-eruptive S contents for this specific 2015 activity phase is currently unavailable, and because best-guess values for “typical” density and crystallinity of Etna's magmas are assumed throughout.

Using equation (2) and OMI-based SO₂ masses, we find that a degassing magma volume of only $\sim 1.9 \pm 0.3$ Mm³ (Table 1) is required to justify SO₂ emissions during VOR activity (*Phase 4*). This is well below the erupted pyroclastic volume for 3–5 December, for which available estimates range between 5.1 Mm³ (Vulpiani et al., 2016; Pompilio et al., 2017), 7.1–7.2 Mm³ (Corsaro et al., 2017; Neri et al., 2017) and 12 Mm³ (Bonaccorso and Calvari, 2017) (Table 1). We consider this mismatch as only partially justifiable by OMI underestimating the real SO₂ emissions, and interpret it instead as an evidence for that only a small fraction (8–33 %) of the erupted magma was actually emplaced above the SO₂ degassing depth (~ 3 km below the summit; Spilliaert et al., 2006) during the VOR paroxysm(s). We argue thus that a large (77–92 %) fraction of the erupted magma was already degassed (SO₂-poor) at the time of the paroxysm(s), likely because it had remained stored in the shallow (< 3 km) VOR conduit for days before the paroxysm. This interpretation is well consistent with textural

and compositional features of *Phase 4* ash particles (Pompilio et al., 2017), whose heterogeneity indicates coexistence in the VOR conduit of variably degassed/crystalline/viscous magma volumes that had been emplaced somewhere between hours to several days before. We calculate that, at the average magma shallow emplacement rate of 0.2 ± 0.02 to 0.4 ± 0.04 Mm³/day (implicit in the SO₂ flux release of 2600 ± 260 to 4300 ± 430 tons/day in *Phases 2–3*) (Table 1), 9 to 45 days would have been required to accumulate, in the VOR conduits, the missing magma volume (the difference between the erupted and the syn-eruptive degassing magma). This 9–45 day interval is consistent with the total duration of the VOR activity observed from 19 October (43 days in total).

We conclude that the VOR paroxysmal phase in December 2015 was likely driven by progressive re-mobilization and eruption of degassed conduit magma, emplaced days to even >1 month before the onset of eruption. The ascent of fresh magma, perhaps corresponding to our syn-paroxysm $\sim 1.9 \pm 0.3$ Mm³ magma volume, is the most likely trigger for destabilization of resident conduit magma, as invoked on completely independent basis by Pompilio et al. (2017). We finally argue that this mechanism may not be exclusive to the VOR paroxysmal sequence in 2015. For instance, a similar mismatch was observed for the ensuing NSEC activity between the co-paroxysmal degassing magma volume ($\sim 0.6 \pm 0.1$ Mm³) and the erupted ($\sim 2 \pm 0.3$ Mm³) magma volume (Table 1).

UV Camera vs. OMI

Our 2015 dataset also allows testing the level of agreement between ground-based and satellite-derived SO₂ emission observations (Figure 8). Inter-comparison studies between ground- and satellite-based measurements of SO₂ emissions are relatively sparse, and due to differences in sensitivity to SO₂ and the spatial/temporal duration and resolution of each measurement type, strong quantitative agreement is limited to certain ideal cases, e.g., estimates of long-term emissions budgets where short-term variability of SO₂ fluxes are suppressed (Carn et al., 2017).

In our specific Etna example, we caution that direct comparison between UV camera and OMI datasets is challenging, since the two measurement types target volcanic SO₂ emissions on distinct temporal/spatial timescales and good quantitative correlation is therefore unlikely. UV camera SO₂ measurements have very high temporal/spatial resolution, but observations are limited to only 5 h per day. Whether or not these 5 h of observations can confidently be extrapolated to quantify the total SO₂ mass degassed in a daily—to become then comparable to the daily SO₂ mass loadings delivered by OMI—depends on how dynamic and changeable the volcano's activity state is. While the operation is probably relatively safe in “calm” days of quiescent degassing (e.g., our *Phase 1*), it becomes more problematic when the volcano behavior changes dramatically within a day, as during the *Phase 4–5* paroxysmal sequence. For example, measurements taken on December 4 encompass 2 h of intense fountaining and vigorous degassing that raise the mean SO₂ flux at 160 ± 16 kg/s. This, if extrapolated over the entire measurement day, would lead

to a daily output of $\sim 14,000 \pm 1,400$ tons, exceeding the OMI SO₂ mass measured on the following day ($\sim 5,400 \pm 780$ tons). In contrast, on December 3 and 5, the paroxysmal episodes occurred outside the UV camera measurement interval. Since the UV-derived mean fluxes (respectively, ~ 82 and ~ 22 kg/s) thus miss the paroxysmal gas contributions, their extrapolated masses (7,080 and 1,917 tons) do likely under-estimate the real daily SO₂ output, and are unsurprisingly lower than the OMI-derived mass loading ($10,000 \pm 1,300$ and $5,500 \pm 720$ tons for December 3 and 5, respectively). We thus find it more prudent to use OMI data for calculation of total eruptive gas masses and degassing magma volumes (see section SO₂ budget for the Etna's 2015 Paroxysmal Sequence, and Calculation of Magma Volume Fluxes). Still, we note that eruptive gas masses and degassing magma volumes obtained from UV Camera data for *Phase 4* are remarkably close (Table 1), implying that the above discussed effects cancel out over the entire paroxysmal sequence (3 days).

On the other hand, our results suggest OMI may underestimate more sluggish SO₂ quiescent emissions, at least in the conditions of our *Phase 1–2* (see Figure 8). Over the 3 months period covered by *Phase 1*, for example, the cumulative mass loadings derived from OMI are nearly one order of magnitude lower than those measured on ground from the UV camera (Table 1). The sensitivity of ultraviolet satellite observations to atmospheric SO₂ are strongly altitude dependent, and underestimates of SO₂ mass loadings are relatively common for lower tropospheric plumes due to higher SO₂ detection limits (e.g., McCormick et al., 2012; Carn et al., 2013).

We conclude that ground-based and satellite-based SO₂ flux observations are complementary in monitoring basaltic volcanoes. While UV-camera measurements are more effective in monitoring quiescent emissions, and perhaps more useful to capture pre-paroxysm escalation in degassing activity (see Figure 4, and results in Corsaro et al., 2017), satellites become invaluable during paroxysmal explosive eruptions. Over longer intervals (timescales of several months), the SO₂ degassing histories registered by the two independent monitoring tools show similar overall trends (Figure 8).

Magma Volume Fluxes From Satellite Thermal Data

Satellite thermal IR data also potentially offer the opportunity to quantify the volumes of magma reaching the surface, before, during and after the paroxysmal sequence. The conversion between thermal and volumetric fluxes is based on the observed relationships between effusion rates and active lava flow areas [see Harris and Baloga (2009) for a review]. Various approaches have been proposed to adapt this methodology to satellite thermal data (i.e., Harris et al., 1998; Wright et al., 2001; Coppola et al., 2013), all aimed at calibration of a simple linear relationship between space-based radiant flux (for example the VRP) and the Time Averaged lava Discharge Rate (TADR).

The relationship can be written as:

$$\text{TADR} = \text{VRP}/C_{\text{rad}} \quad (3)$$

where c_{rad} is a conversion coefficient empirically calculated (e.g., Coppola et al., 2013) or based on cooling models of active lava flows (e.g., Harris and Ripepe, 2007).

Here we used the values for c_{rad} calibrated during previous effusive eruptions of Mt. Etna (Coppola et al., 2013, 2016), that indicate a range between $2 \cdot 10^8$ J/m³ and $3.6 \cdot 10^8$ J/m³. According to equation (3), these two values allow us to estimate a maximum and minimum TADR, and consequently a range of erupted lava volumes. This methodology provides results in excellent agreement with field estimates (cf. Harris et al., 2007, 2011) and, once calibrated (as for at Etna), it allows us to assess erupted volume during effusive activity within $\pm 30\%$ uncertainty (Coppola et al., 2016, 2017).

On the other hand, it is important to highlight some limitations and assumptions of the thermal proxy, if applied to periods that include different types of volcanic activity (such as at Etna in late 2015):

- 1) A volume calculated using the thermal approach is based on the implicit assumption that the heat flux is generated by an active lava flow (cf. Coppola et al., 2013). Consequently, the model breaks down when the lava is not extruded but instead retained in the vent, as in the case of lava lakes or open-vent activity. In such circumstances, the thermal proxy provides a minimum estimate of the magma circulation (convection) at very shallow depth, rather than effusion rates, as long as the top of the magma column is sufficiently shallow to produce thermal anomalies on the surface (Werner et al., 2017; Aiuppa et al., 2018);
- 2) The coefficient c_{rad} is expressly calibrated for effusive (lava-flow-forming) eruptions (Coppola et al., 2016), and it does not necessarily work during explosive eruptions (i.e., paroxysms). During explosive eruptions, the heat flux detected by satellite is sourced by the lava fountains themselves and by the accumulation of intra-crateric material forming reomorphical lava bodies. In these cases, the relationship between erupted volumes and thermal energy is strongly altered by the complexity of the mixed heat source (lava fountains and reomorphical flows). In addition, the thermal approach does not allow us to estimate the volumes of tephra produced by explosive activity;
- 3) Accurate processing requires filtering out data contaminated by clouds, and/or acquired with extreme viewing angles. Alternatively, the maximum daily or weekly average (considering all data) can produce appropriate but less accurate estimates.

The application of equation (3) to the selected MIROVA dataset allows calculating a total volume of lava equal to 2.0 ± 0.6 Mm³ (Figure 10). However, based on the observed activity the interpretation of the calculated volume is subdivided according to the distinct phases of activity:

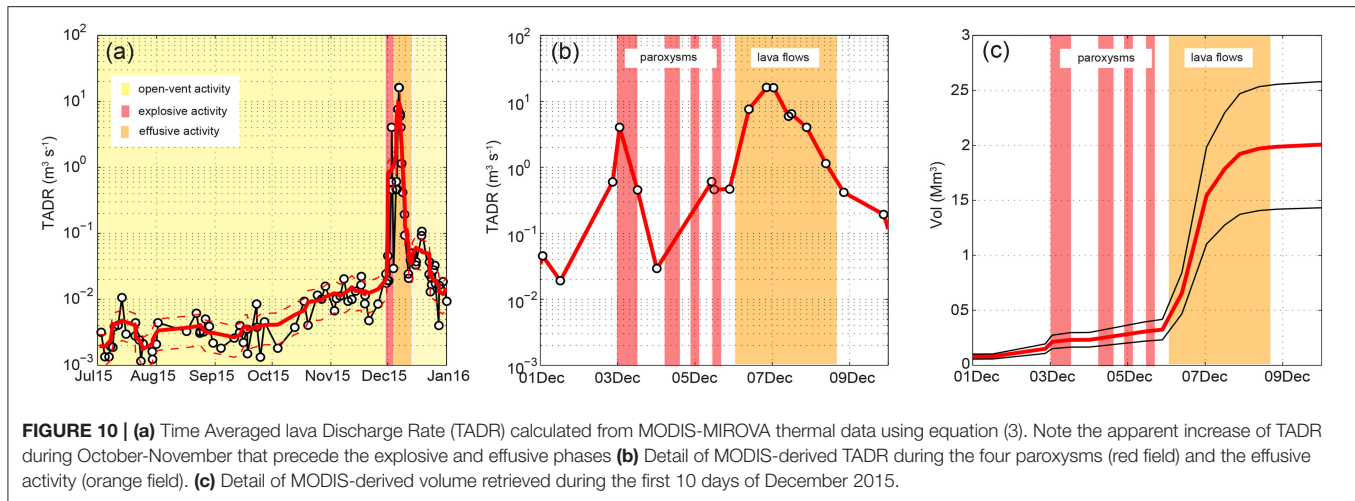
- *Phases 1–3* (01 July– 02 December 2015). During this phase we calculate that $\sim 0.1 \pm 0.03$ Mm³ of magma reached the bottom of the summit craters, before being recycled back into Etna's shallow plumbing system (Table 1). Thus, the average TADR

(0.005 m³/s) represents the fraction of the total degassing magma flux that actually reached the surface and radiated heat into the atmosphere. However, most of the degassing magma remains some tens or hundreds of meters below the surface (or more), and therefore does not contribute to the surface thermal anomaly. It is unsurprising that, if we use a cumulative degassed SO₂ mass of $80,000 \pm 8,000$ tons (Table 1) for this period (time-averaged SO₂ flux of $\sim 1,700 \pm 221$ tons/day), in combination with eq. 2, we obtain a much higher magma degassing volume ($\sim 7 \pm 1.1$ Mm³; magma degassing rate, $\sim 6 \pm 0.9$ m³/s; Table 1). Notably, between October and November 2015, the thermal-derived magma flux reaching the surface has gradually increased, likely reflecting the shallowing of the top of the magma column that preceded the onset of the paroxysmal phase (Figure 10). The beginning of intense strombolian activity, observed on 2 December at 21:00 (UTC) was marked by a TADR equal to 0.6 ± 0.2 m³/s that could represent a transition between open-vent passive degassing to explosive/effusive activity.

- *Phase 4* (03–05 December 2015). In <48 h, four consecutive paroxysms occurred at the summit craters of Etna. The plumes generated by this explosive activity often masked the thermal anomalies associated with the lava fountains and the incandescent material accumulated inside the VOR and BN craters. The thermal proxy applied during this phase indicates a minimum volume of $\sim 0.2 \pm 0.06$ Mm³ (Table 1), but this figure severely underestimates both the SO₂-based ($\sim 1.9 \pm 0.3$ Mm³) and erupted (5.1 – 12 Mm³) volumes (Table 1);
- *Phase 5* (06–08 December 2015). During this phase, three small lava flows were emitted from a vent that opened at the base of the NSEC crater (Corsaro et al., 2017). The maximum TADR (16 ± 0.6 m³/s) was reached in the night between 6 and 7 December, when the lava flow reached a maximum extent of ~ 3.5 km. Based on MODIS data we estimate a total volume of $\sim 1.7 \pm 0.6$ Mm³ which agrees well with independent field estimates (2.0 ± 0.3 Mm³; Corsaro et al., 2017).

Implications for Other Basaltic Systems

Our results indicate that integrating multidisciplinary information from both ground and space, and including gas, thermal and seismic records, is key to unveiling the complexities of the trigger mechanisms of basaltic paroxysms. The advent of high-rate UV Camera observations is now opening the way to real-time monitoring the volcanic SO₂ flux behavior at the quiescence-to-explosive transition (Figure 4). Our Etna results, although preliminary, suggest that individual lava fountain episodes can be preceded by detectable SO₂ flux escalation (Figure 4). We stress that similar high-temporal resolution SO₂ flux time-series, possibly streamed in real-time by permanent UV Camera systems, are now urgently needed at other basaltic systems. At volcanic systems with multiple active vents (such as Etna and many others), the high spatial resolution offered by UV Cameras is vital to resolving explosive from passive gas emissions, and thus to



obtaining accurate gas-based estimates of gas/magma budgets for individual explosions and/or paroxysmal sequences. However, comparison with independently derived gas/magma budgets, from satellites (both SO₂ and thermal) and from measurements of erupted pyroclastic materials on ground, is key to interpretation.

CONCLUSIONS

We combine ground- and satellite-based information to characterize, with unprecedented detail, the SO₂ degassing behavior associated with an Etna's paroxysmal sequence. The high-temporal/spatial resolution of UV Cameras allows us to obtain the first (at least to our knowledge) high-rate (0.5 Hz) records of the SO₂ flux during a basaltic lava fountaining episode. Our results demonstrate a factor ~ 4 SO₂ flux escalation prior to the fountain's onset (when SO₂ peaks at $\sim 400 \pm 40$ kg/s), confirming that magmatic volatiles are drivers of these events. We also constrain the total magmatic gas output during such a paroxysm at $8 \pm 3.6 \cdot 10^8$ m³. We anticipate that these SO₂-based estimates for the magmatic phase volume will now serve for better initializing/constraining models for the generation of basaltic explosive events.

Based on satellite-based OMI observations, we estimate that at least $21,000 \pm 2,730$ tons of SO₂ may have been injected into the atmosphere during the entire VOR paroxysmal sequence, corresponding to a total magmatic gas output of $14 \pm 0.6 \cdot 10^9$ m³. We also infer that the degassing magma required to generate the $\sim 21,000 \pm 2,730$ tons of SO₂ is $\sim 1.9 \pm 0.3$ Mm³, or much less than the 5.1–12 Mm³ erupted volume. This mismatch is used to derive novel constraints of mechanisms governing the generation of the paroxysms. In particular, we suggest that a large fraction of magma erupted during the December 3–5 VOR paroxysms was shallow stored conduit magma, emplaced and degassed in the days (9 to 45) before the sequence onset. The paroxysmal sequence was also associated with an abrupt increase in thermal radiance, as observed by MODIS. Analysis of these data reveals a magma source of $\sim 0.2 \pm 0.06$ Mm³, suggesting that the thermal

proxy considerably underestimates the paroxysmal pyroclastic volume.

Our study also brings additional evidence for the ability of UV Camera systems to resolve switch in activity between different vents. In the December 2015 example, VOR paroxysms are followed by an activity switch to the NSEC, fully captured by the UV camera network. Based on OMI records, the NSEC activity released at least $\sim 7.2 \pm 3.4 \cdot 10^9$ m³ of gas, or a factor of 2 less than VOR activity. The MODIS thermal data constrain a magmatic infrared radiation source with a volume of 1.7 ± 0.6 Mm³, fitting well the lava erupted volume of $\sim 2 \pm 0.3$ Mm³. Inverting MODIS data to lava volumes is more accurate during episodes with some effusive activity.

AUTHOR CONTRIBUTIONS

AA, MB, DD, GT, and RD conceived the idea. RD, MB, DD, GT, MC, and EP conducted the field experiments. RD, DD, DC, BM, LS, MC, and EP processed the data. AA, RD, DC, BM, EP, MC, and MR drafted the manuscript with help from all co-authors.

FUNDING

The research leading to these results has received funding from the European Research Council under the European Union's Seventh Framework Program (FP7/2007/2013)/ERC grant agreement n 305377 (PI, AA).

ACKNOWLEDGMENTS

We wish to thank E. Privitera (Director of INGV-OE) and the INGV-OE staff for support to installation and maintenance of the UV3 camera system. The INGV-OE Unità Funzionale Sismologia is particularly acknowledged for providing seismic tremor data. Ente Parco dell'Etna is acknowledged for granting access to the volcano summit.

SUPPLEMENTARY MATERIAL

The Supplementary Material for this article can be found online at: <https://www.frontiersin.org/articles/10.3389/feart.2018.00239/full#supplementary-material>

Table S1 | Data.csv contains the data used to generate **Figure 5** (per-orbit SO₂ mass loading from OMI, daily mean SO₂ emission rate from the UV camera network, and per-orbit radiant power from MODIS and the ground-based thermal

camera network). Further data used in this study are available from the authors upon request. The satellite- and ground-based SO₂ data we present herein will ultimately be stored in a bespoke gas emissions data repository, currently being developed as a collaboration between the International Earth Data Alliance (IEDA) and the Deep Carbon Observatory DECADE programme (<http://decade.iedadata.org/>).

Figure S1 | Time series of **(A)** mean reflectivity (in %) and **(B)** the daily SO₂ mass burden (in tons) measured by OMI.

REFERENCES

- Aiuppa, A., Cannata, A., Cannavò, F., Di Grazia, G., Ferrari, F., Giudice, G., et al. (2010). Patterns in the recent 2007–2008 activity of mount etna volcano investigated by integrated geophysical and geochemical observations. *Geochem. Geophys. Geosyst.* 11, 1–13. doi: 10.1029/2010GC003168
- Aiuppa, A., de Moor, M. J., Arellano, S., Coppola, D., Francoforte, V., Galle, B., et al. (2018). Tracking formation of a lava lake from ground and space: masaya volcano (Nicaragua), 2014–2017. *Geochem. Geophys. Geosyst.* 19, 496–515. doi: 10.1002/2017GC007227
- Albert, H., Costa, F., and Martí, J. (2016). Years to weeks of seismic unrest and magmatic intrusions precede monogenetic eruptions. *Geology* 44, 211–214. doi: 10.1130/G37239.1
- Allard, P. (1997). Endogenous magma degassing and storage at mount etna. *Geophys. Res. Lett.* 24, 2219–2222. doi: 10.1029/97GL02101
- Allard, P., Behncke, B., D'Amico, S., Neri, M., and Gambino, S. (2006). Mount etna 1993–2005: anatomy of an evolving eruptive cycle. *Earth-Sci. Rev.* 78, 85–114. doi: 10.1016/j.earscirev.2006.04.002
- Allard, P., Burton, M., and Muré, F. (2005). Spectroscopic evidence for a lava fountain driven by previously accumulated magmatic gas. *Nature* 433, 407–410. doi: 10.1038/nature03246
- Allard, P., Burton, M., Sawyer, G., and Bani, P. (2016). Degassing dynamics of basaltic lava lake at a top-ranking volatile emitter: ambrym volcano, vanuatu arc. *Earth Planet. Sci. Lett.* 448, 69–80. doi: 10.1016/j.epsl.2016.05.014
- Aloisi, M., D'Agostino, M., Dean, K. G., Mostaccio, A., and Neri, G. (2002). Satellite and PUFF simulation of the eruptive cloud generated by the Mount Etna paroxysm of 22 July 1998. *J. Geophys. Res. Solid Earth* 107, ECV 9–1–ECV 9–12. doi: 10.1029/2001JB000630
- Alparone, A., Andronico, D., Sgroi, T., Ferrari, F., Lodato, L., and Reitano, D. (2007). Alert system to mitigate tephra fallout hazards at Mt. Etna volcano, Italy. *Nat. Hazards* 43, 333–350. doi: 10.1007/s11069-007-9120-7
- Alparone, S., Andronico, D., Lodato, L., and Sgroi, T. (2003). Relationship between tremor and volcanic activity during the Southeast crater eruption on Mount Etna in early 2000. *J. Geophys. Res. Solid Earth* 108, 1–13. doi: 10.1029/2002JB001866
- Andò, B., and Pecora, E. (2006). An advanced video-based system for monitoring active volcanoes. *Comput. Geosci.* 32, 85–91. doi: 10.1016/j.cageo.2005.05.004
- Andres, R. J., and Schmid, J. W. (2001). The effects of volcanic ash on COSPEC measurements. *J. Volcanol. Geotherm. Res.* 108, 237–244. doi: 10.1016/S0377-0273(00)00288-2
- Andronico, D., and Corsaro, R. A. (2011). Lava fountains during the episodic eruption of South-East Crater (Mt. Etna), 2000: insights into magma-gas dynamics within the shallow volcano plumbing system. *Bull. Volcanol.* 73, 1165–1178. doi: 10.1007/s00445-011-0467-y
- Behncke, B., Branca, S., Corsaro, R. A., De Beni, E., Miraglia, L., and Proietti, C. (2014). The 2011–2012 summit activity of Mount Etna: birth, growth and products of the new SE crater. *J. Volcanol. Geotherm. Res.* 270, 10–21. doi: 10.1016/j.jvolgeores.2013.11.012
- Behncke, B., Falsaperla, S., and Pecora, E. (2009). Complex magma dynamics at Mount Etna revealed by seismic, thermal, and volcanological data. *J. Geophys. Res. Solid Earth* 114:B03211. doi: 10.1029/2008JB005882
- Behncke, B., Neri, M., Pecora, E., and Zanon, V. (2006). The exceptional activity and growth of the southeast crater, Mount Etna (Italy), between 1996 and 2001. *Bull. Volcanol.* 69, 149–173. doi: 10.1007/s00445-006-0061-x
- Bonaccorso, A. (2014). Eruptive processes leading to the most explosive lava fountain at Etna volcano: the 23 November 2013 episode. *Geophys. Res. Lett.* 41, 4912–4919. doi: 10.1002/2014GL060623
- Bonaccorso, A., Bonforte, A., Calvari, S., Del Negro, C., Di Grazia, G., Ganci, G., et al. (2011). The initial phases of the 2008–2009 Mount Etna eruption: a multidisciplinary approach for hazard assessment. *J. Geophys. Res. Solid Earth* 116, 1–19. doi: 10.1029/2010JB007906
- Bonaccorso, A., and Calvari, S. (2013). Major effusive eruptions and recent lava fountains: Balance between expected and erupted magma volumes at Etna volcano. *Geophys. Res. Lett.* 40, 6069–6073. doi: 10.1002/2013GL058291
- Bonaccorso, A., and Calvari, S. (2017). A new approach to investigate an eruptive paroxysmal sequence using camera and strainmeter networks: lessons from the 3–5 December 2015 activity at Etna volcano. *Earth Planet. Sci. Lett.* 475, 231–241. doi: 10.1016/j.epsl.2017.07.020
- Bruhn, A., Weickert, J., and Schörr, C. (2005). Lucas / Kanade Meets Horn / Schunck : combining local and global optic flow methods. *Int. J. Comput. Vis.* 61, 211–231. doi: 10.1023/B:VISI.0000045324.43199.43
- Burton, M. R., Caltabiano, T., Muré, F., Salerno, G., and Randazzo, D. (2009). SO₂ flux from Stromboli during the 2007 eruption: results from the FLAME network and traverse measurements. *J. Volcanol. Geotherm. Res.* 182, 214–220. doi: 10.1016/j.jvolgeores.2008.11.025
- Burton, M. R., Salerno, G. G., D'Auria, L., Caltabiano, T., Muré, F., and Maugeri, R. (2015). SO₂ flux monitoring at stromboli with the new permanent INGV SO₂ camera system: a comparison with the FLAME network and seismological data. *J. Volcanol. Geotherm. Res.* 300, 95–102. doi: 10.1016/j.jvolgeores.2015.02.006
- Caltabiano, T., Burton, M., Giammanco, S., Allard, P., Bruno, N., Muré, F., et al. (2004). "Volcanic gas emissions from the summit craters and flanks of Mt. Etna, 1987–2000," in *Mt. Etna: Volcano Laboratory*, eds A. Bonaccorso, S. Calvari, M. Coltelli, C. Del Negro, and S. Falsaperla (Washington, DC: American Geophysical Union), 111–128. doi: 10.1029/GM143
- Caltabiano, T., Romano, R., and Budetta, G. (1994). SO₂ flux measurements at Mount Etna (Sicily). *J. Geophys. Res. Atmos.* 99, 12809–12819. doi: 10.1029/94JD00224
- Calvari, S., Salerno, G. G., Spampinato, L., Gouhier, M., La Spina, A., Pecora, E., et al. (2011). An unloading foam model to constrain Etna's 11–13 January 2011 lava fountaining episode. *J. Geophys. Res. Solid Earth* 116, 1–18. doi: 10.1029/2011JB008407
- Carbone, D., Zuccarello, L., Messina, A., Scollo, S., and Rymer, H. (2015). Balancing bulk gas accumulation and gas output before and during lava fountaining episodes at Mt. Etna. *Sci. Rep.* 5:18049. doi: 10.1038/srep18049
- Carn, S. A., Clarisse, L., and Prata, A. J. (2016). Multi-decadal satellite measurements of global volcanic degassing. *J. Volcanol. Geotherm. Res.* 311, 99–134. doi: 10.1016/j.jvolgeores.2016.01.002
- Carn, S. A., Fioletov, V. E., McLinden, C. A., Li, C., and Krotkov, N. A. (2017). A decade of global volcanic SO₂ emissions measured from space. *Sci. Rep.* 7, 1–12. doi: 10.1038/srep44095
- Carn, S. A., Krotkov, N. A., Yang, K., and Krueger, A. J. (2013). Measuring global volcanic degassing with the ozone monitoring instrument (OMI). *Geol. Soc. London Spec. Publ.* 380, 229–257. doi: 10.1144/SP380.12
- Carn, S. A., Krueger, A. J., Arellano, S., Krotkov, N. A., and Yang, K. (2008). Daily monitoring of ecuadorian volcanic degassing from space. *J. Volcanol. Geotherm. Res.* 176, 141–150. doi: 10.1016/j.jvolgeores.2008.01.029
- Carn, S. A., Yang, K., Prata, A. J., and Krotkov, N. A. (2015). Extending the long-term record of volcanic SO₂ emissions with the ozone mapping

- and profiler suite nadir mapper. *Geophys. Res. Lett.* 42, 925–932. doi: 10.1002/2014GL062437
- Chouet, B., and Dawson, P. (2015). Seismic source dynamics of gas-piston activity at Kilauea Volcano Hawai'i. *J. Geophys. Res. Solid Earth* 120, 2525–2560. doi: 10.1002/2014JB011789
- Coltelli, M., Carlo, P., Del, and Vezzoli, L. (1998). Discovery of a Plinian basaltic eruption of Roman age at Etna volcano, Italy. *Geology* 26, 1095–1098. doi: 10.1130/0091-7613(1998)026<1095:DOAPBE>2.3.CO;2
- Coltelli, M., d'Aranno, J. P., de Bonis, R., Guerrero Tello, F. J., Marsella, M., Nardinocchi, C., et al. (2017). The use of surveillance cameras for the rapid mapping of lava flows: an application to Mount Etna Volcano. *Remote Sens.* 9:192. doi: 10.3390/rs9030192
- Coppola, D., Di Muro, A., Peltier, A., Villeneuve, N., Ferrazzini, V., Favalli, M., et al. (2017). Shallow system rejuvenation and magma discharge trends at piton de la Fournaise volcano (La Réunion Island). *Earth Planet. Sci. Lett.* 463, 13–24. doi: 10.1016/j.epsl.2017.01.024
- Coppola, D., Laiolo, M., Cigolini, C., Delle Donne, D., and Ripepe, M. (2016). Enhanced volcanic hot-spot detection using MODIS IR data: results from the MIROVA system. *Geol. Soc. London Spec. Publ.* 426, 181–205. doi: 10.1144/SP426.5
- Coppola, D., Laiolo, M., Piscopo, D., and Cigolini, C. (2013). Rheological control on the radiant density of active lava flows and domes. *J. Volcanol. Geoth. Res.* 249, 39–48. doi: 10.1016/j.jvolgeores.2012.09.005
- Corsaro, R. A., Andronico, D., Behncke, B., Branca, S., Caltabiano, T., Ciancitto, F., et al. (2017). Monitoring the December 2015 summit eruptions of Mt. Etna (Italy): implications on eruptive dynamics. *J. Volcanol. Geotherm. Res.* 341, 53–69. doi: 10.1016/j.jvolgeores.2017.04.018
- Corsaro, R. A., and Pompilio, M. (2004). "Dynamics of magmas at mount etna," in *Mt. Etna: Volcano Laboratory*, eds A. Bonaccorso, S. Calvari, M. Coltelli, C. Del Negro, and S. Falsaperla (Washington, DC: American Geophysical Union), 91–110. doi: 10.1029/GM143
- D'Aleo, R., Bitetto, M., Donne, D. D., Tamburello, G., Battaglia, A., Coltelli, M., et al. (2016). Spatially resolved SO₂ flux emissions from Mt Etna. *Geophys. Res. Lett.* 43, 7511–7519. doi: 10.1002/2016GL069938
- Dalton, M. P., Waite, G. P., Watson, I. M., and Nadeau, P. A. (2010). Multiparameter quantification of gas release during weak strombolian eruptions at Pacaya Volcano, Guatemala. *Geophys. Res. Lett.* 37:L09303. doi: 10.1029/2010GL042617
- De Beni, E., Behncke, B., Branca, S., Nicolosi, I., Carluccio, R., D'Ajello Caracciolo, F., et al. (2015). The continuing story of Etna's new southeast crater (2012–2014): evolution and volume calculations based on field surveys and aerophotogrammetry. *J. Volcanol. Geotherm. Res.* 303, 175–186. doi: 10.1016/j.jvolgeores.2015.07.021
- Delle Donne, D., Tamburello, G., Aiuppa, A., Bitetto, M., Lacanna, G., D'Aleo, R., et al. (2017). Exploring the explosive-effusive transition using permanent ultra-violet cameras. *J. Geophys. Res. Solid Earth* 122, 4377–4394. doi: 10.1002/2017JB014027
- Donnadieu, F., Freville, P., Hervier, C., Coltelli, M., Scollo, S., Prestifilippo, M., et al. (2016). Near-source Doppler radar monitoring of tephra plumes at Etna. *J. Volcanol. Geotherm. Res.* 312, 26–39. doi: 10.1016/j.jvolgeores.2016.01.009
- Dubosclard, G., Donnadieu, F., Allard, P., Cordesses, R., Hervier, C., Coltelli, M., et al. (2004). Doppler radar sounding of volcanic eruption dynamics at Mount Etna. *Bull. Volcanol.* 66, 443–456. doi: 10.1007/s00445-003-0324-8
- Eatough, D. J., Caka, F. M., and Farber, R. J. (1994). The conversion of SO₂ to sulfate in the atmosphere. *Isr. J. Chem.* 34, 301–314. doi: 10.1002/ijch.199400034
- Faloona, I., Conley, S. A., Blomquist, B., Clarke, A. D., Kapustin, V., Howell, S., et al. (2009). Sulfur dioxide in the tropical marine boundary layer: dry deposition and heterogeneous oxidation observed during the Pacific atmospheric sulfur experiment. *J. Atmos. Chem.* 63, 13–32. doi: 10.1007/s10874-010-9155-0
- Fioletov, V. E., McLinden, C. A., Krotkov, N., Li, C., Joiner, J., Theys, N., et al. (2016). A global catalogue of large SO₂ sources and emissions derived from the ozone monitoring instrument. *Atmos. Chem. Phys.* 16:11497. doi: 10.5194/acp-16-11497-2016
- Flower, V. J. B., and Carn, S. A. (2015). Characterising volcanic cycles at soufriere hills volcano, montserrat: time series analysis of multi-parameter satellite data. *J. Volcanol. Geotherm. Res.* 304, 82–93. doi: 10.1016/j.jvolgeores.2015.07.035
- Flower, V. J. B., Oommen, T., and Carn, S. A. (2016). Improving global detection of volcanic eruptions using the Ozone Monitoring Instrument (OMI). *Atmos. Meas. Tech.* 9:5487. doi: 10.5194/amt-9-5487-2016
- Galle, B., Johansson, M., Rivera, C., Zhang, Y., Kihlman, M., Kern, C., et al. (2010). Network for observation of volcanic and atmospheric change (NOVAC)—a global network for volcanic gas monitoring: network layout and instrument description. *J. Geophys. Res.* 115:D05304. doi: 10.1029/2009JD011823
- Gambino, S., Cannata, A., Cannavò, F., La Spina, A., Palano, M., Sciutto, M., et al. (2016). The unusual 28 December 2014 dike-fed paroxysm at Mount Etna: timing and mechanism from a multidisciplinary perspective. *J. Geophys. Res. Solid Earth* 121, 2037–2053. doi: 10.1002/2015JB012379
- Global Volcanism Program (2013). *Volcanoes of the World*, v. 4.6.5, eds Venzke, E. (Smithsonian Institution). <https://dx.doi.org/10.5479/si.GVP.VOTW4-2013> doi: 10.5479/si.GVP.VOTW4-2013 (Accessed 22 Jan, 2018).
- Gonnermann, H. M., and Manga, M. (2003). Explosive volcanism may not be an inevitable consequence of magma fragmentation. *Nature* 426, 432–435. doi: 10.1038/nature02138
- Harris, A., and Ripepe, M. (2007). Synergy of multiple geophysical approaches to unravel explosive eruption conduit and source dynamics - a case study from Stromboli. *Chemie. Der. Erde. Geochem.* 67, 1–35. doi: 10.1016/j.chemer.2007.01.003
- Harris, A., Steffke, A., Calvari, S., and Spampinato, L. (2011). Thirty years of satellite-derived lava discharge rates at Etna: Implications for steady volumetric output. *J. Geophys. Res. Solid Earth* 116:B08204. doi: 10.1029/2011JB008237
- Harris, A. J. L., and Baloga, S. M. (2009). Lava discharge rates from satellite-measured heat flux. *Geophys. Res. Lett.* 36:L19302. doi: 10.1029/2009GL039717
- Harris, A. J. L., Dehn, J., and Calvari, S. (2007). Lava effusion rate definition and measurement: a review. *Bull. Volcanol.* 70:1. doi: 10.1007/s00445-007-0120-y
- Harris, A. J. L., Flynn, L. P., Keszthelyi, L., Mouginis-Mark, P. J., Rowland, S. K., and Resing, J. A. (1998). Calculation of lava effusion rates from Landsat TM data. *Bull. Volcanol.* 60, 52–71. doi: 10.1007/s004450050216
- Harris, A. J. L., and Neri, M. (2002). Volumetric observations during paroxysmal eruptions at Mount Etna: pressurized drainage of a shallow chamber or pulsed supply? *J. Volcanol. Geotherm. Res.* 116, 79–95. doi: 10.1016/S0377-0273(02)00212-3
- Holland, A. S. P., Watson, I. M., Phillips, J.-C., Caricchi, L., and Dalton, M. P. (2011). Degassing processes during lava dome growth: insights from santiaguito lava dome, guatemala. *J. Volcanol. Geoth. Res.* 202, 153–166. doi: 10.1016/j.jvolgeores.2011.02.004
- Houghton, B. F., Wilson, C. J. N., Del Carlo, P., Coltelli, M., Sable, J. E., and Carey, R. (2004). The influence of conduit processes on changes in style of basaltic plinian eruptions: Tarawera 1886 and Etna 122 BC. *J. Volcanol. Geotherm. Res.* 137, 1–14. doi: 10.1016/j.jvolgeores.2004.05.009
- Kahl, M., Chakraborty, S., Pompilio, M., and Costa, F. (2015). Constraints on the nature and evolution of the magma plumbing system of Mt. Etna volcano (1991–2008) from a combined thermodynamic and kinetic modelling of the compositional record of minerals. *J. Petrol.* 56, 2025–2068. doi: 10.1093/petrology/egv063
- Kantzas, E. P., McGonigle, J. S., Tamburello, G., Aiuppa, A., and Bryant, R. G. (2010). Protocols for UV camera volcanic SO₂ measurements. *J. Volcanol. Geotherm. Res.* 194, 55–60. doi: 10.1016/j.jvolgeores.2010.05.003
- Kazahaya, R., Mori, T., Takeo, M., Ohminato, T., Urabe, T., and Maeda, Y. (2011). Relation between single very long period pulses and volcanic gas emissions at Mt. Asama, Japan. *Geophys. Res. Lett.* 38:L11307. doi: 10.1029/2011GL047555
- Kern, C., Sutton, J., Elias, T., Lee, L., Kamibayashi, K., Antolik, L., et al. (2015). An automated SO₂ camera system for continuous, real-time monitoring of gas emissions from Kilauea Volcano's summit Overlook Crater. *J. Volcanol. Geotherm. Res.* 300, 81–94. doi: 10.1016/j.jvolgeores.2014.12.004
- La Spina, A., Burton, M., Allard, P., Alparone, S., and Muré, F. (2015). Open-path FTIR spectroscopy of magma degassing processes during eight lava fountains on Mount Etna. *Earth Planet. Sci. Lett.* 413, 123–134. doi: 10.1016/j.epsl.2014.12.038
- Levelt, P., Joiner, J., Tamminen, J., Veefkind, P., Bhartia, P. K., Stein Zweers, D., et al. (2017). The ozone monitoring instrument: overview of twelve years in space. *Atmos. Chem. Phys. Discuss.* 2017, 1–61. doi: 10.5194/acp-2017-487

- Levelt, P. F., Oord, G. H. J., van den, Dobber, M. R., Malkki, A., Visser, H., Vries, J., et al. (2006). The ozone monitoring instrument. *IEEE Trans. Geosci. Remote Sens.* 44, 1093–1101. doi: 10.1109/TGRS.2006.872333
- Li, C., Krotkov, N. A., Carn, S., Zhang, Y., Spurr, R. J. D., and Joiner, J. (2017). New-generation NASA Aura Ozone Monitoring Instrument (OMI) volcanic SO₂ dataset: Algorithm description, initial results, and continuation with the Suomi-NPP Ozone Mapping and Profiler Suite (OMPS). *Atmos. Meas. Tech.* 10, 445–458. doi: 10.5194/amt-10-445-2017
- Lopez, T., Carn, S., Werner, C., Fee, D., Kelly, P., Doukas, M., et al. (2013). Evaluation of Redoubt Volcano's sulfur dioxide emissions by the ozone monitoring instrument. *J. Volcanol. Geotherm. Res.* 259, 290–307. doi: 10.1016/j.jvolgeores.2012.03.002
- Lübcke, P., Bobrowski, N., Illing, S., Kern, C., Alvarez Nieves, J. M., Vogel, L., et al. (2013). On the absolute calibration of SO₂ cameras. *Atmos. Meas. Tech.* 6, 677–696. doi: 10.5194/amt-6-677-2013
- Lucas, B. D., and Kanade, T. (1981). An iterative image registration technique with an application to stereo vision. *IJCAI*, 81, 674–679.
- Manga, M., Simon, A., Carn, K., Cashman, V., Amanda, B., Clarke, C. B., et al. (2017). *Volcanic Eruptions and Their Repose, Unrest, Precursors, and Timing*. Washington, DC: The National Academies Press.
- Marchetti, E., Ripepe, M., Olivieri, G., Caffo, S., and Privitera, E. (2009). Infrasonic evidences for branched conduit dynamics at Mt. Etna volcano, Italy. *Geophys. Res. Lett.* 36:L19308. doi: 10.1029/2009GL040070
- Mather, T. A., Pyle, D. M., Tsanev, V. I., McGonigle, A. J. S., Oppenheimer, C., and Allen, A. G. (2006). A reassessment of current volcanic emissions from the central american arc with specific examples from Nicaragua. *J. Volcanol. Geotherm. Res.* 149, 297–311. doi: 10.1016/j.jvolgeores.2005.07.021
- McCormick, B., Popp, C., Andrews, B., and Cottrell, E. (2015). Ten years of satellite observations reveal highly variable sulphur dioxide emissions at Anatahan Volcano, Mariana Islands. *J. Geophys. Res.* 120, 7258–7282. doi: 10.1002/2014JD022856
- McCormick, B. T., Edmonds, M., Mather, T. A., and Carn, S. A. (2012). First synoptic analysis of volcanic degassing in Papua New Guinea. *Geochem. Geophys. Geosyst.* 13, 1–21. doi: 10.1029/2011GC003945
- Métrich, N., Allard, P., Spilliaert, N., Andronico, D., and Burton, M. (2004). 2001 flank eruption of the alkali- and volatile-rich primitive basalt responsible for Mount Etna's evolution in the last three decades. *Earth Planet. Sci. Lett.* 228, 1–17. doi: 10.1016/j.epsl.2004.09.036
- Mori, T., and Burton, M. (2006). The SO₂ camera: A simple, fast and cheap method for ground-based imaging of SO₂ in volcanic plumes. *Geophys. Res. Lett.* 33, 1–5. doi: 10.1029/2006GL027916
- Mori, T., and Burton, M. (2009). Quantification of the gas mass emitted during single explosions on Stromboli with the SO₂ imaging camera. *J. Volcanol. Geotherm. Res.* 188, 395–400. doi: 10.1016/j.jvolgeores.2009.10.005
- Neri, M., De Maio, M., Crepaldi, S., Suozzi, E., Lavy, M., Marchionatti, F., et al. (2017). Topographic maps of Mount Etna's summit craters, updated to December 2015. *J. Maps* 13, 674–683. doi: 10.1080/17445647.2017.1352041
- Oppenheimer, C., Francis, P., Burton, M., Maciejewski, A. J. H., and Boardman, L. (1998). Remote measurement of volcanic gases by fourier transform infrared spectroscopy. *Appl. Phys. B. Lasers Opt.* 67, 505–515. doi: 10.1007/s003400050536
- Oppenheimer, C., Scaillet, B., and Martin, R. S. (2011). Sulfur degassing from volcanoes: source conditions, surveillance, plume chemistry and earth system impacts. *Rev. Min. Geochem.* 73, 363–421. doi: 10.2138/rmg.2011.73.13
- Palma, J. L. (2013). *Wind Reanalysis*. Available online at <https://vhub.org/resources/windre>.
- Parfitt, A. E. A. (2004). Discussion of the mechanisms of explosive basaltic eruptions. *J. Volcanol. Geotherm. Res.* 134, 77–107. doi: 10.1016/j.jvolgeores.2004.01.002
- Patanè, D., Aiuppa, A., Aloisi, M., Behncke, B., Cannata, A., Coltelli, M., et al. (2013). Insights into magma and fluid transfer at Mount Etna by a multiparametric approach: a model of the events leading to the 2011 eruptive cycle. *J. Geophys. Res. Solid Earth* 118, 3519–3539. doi: 10.1002/jgrb.50248
- Pérez, W., Freundt, A., Kutterolf, S., and Schmincke, H. U. (2009). The Masaya triple layer: a 2100 year old basaltic multi-episodic Plinian eruption from the Masaya caldera complex (Nicaragua). *J. Volcanol. Geotherm. Res.* 179, 191–205. doi: 10.1016/j.jvolgeores.2008.10.015
- Pering, T. D., Tamburello, G., McGonigle, A. J., Hanna, E., and Aiuppa, A. (2014). Correlation of oscillatory behaviour in matlab using wavelets. *Comput. Geosci.* 70, 206–212. doi: 10.1016/j.cageo.2014.06.006
- Polacci, M., Corsaro, R. A., and Andronico, D. (2006). Coupled textural and compositional characterization of basaltic scoria: Insights into the transition from strombolian to fire fountain activity at Mount Etna, Italy. *Geology* 34, 201–204. doi: 10.1130/G22318.1
- Pompilio, M., Bertagnini, A., Del Carlo, P., and Di Roberto, A. (2017). Magma dynamics within a basaltic conduit revealed by textural and compositional features of erupted ash: the December 2015 Mt. Etna paroxysms. *Sci. Rep.* 7:4805. doi: 10.1038/s41598-017-05065-x
- Roggensack, K., Hervig, R. L., McKnight, S. B., and Williams, S. N. (1997). Explosive basaltic volcanism from cerro negro volcano: influence of volatiles on eruptive style. *Science* 277, 1639–1642. doi: 10.1126/science.277.5332.1639
- Rose, W. I., Palma, J. L., Delgado Granados, H., and Varley, N. (2013). “Open-vent volcanism and related hazards: Overview,” in *Understanding Open-Vent Volcanism and Related Hazards*, eds. W. I. Rose, J. L. Palma, H. D. Granados, and N. Varley (Boulder: Geological Society of America), 7–9. doi: 10.1130/2013.2498(00)
- Rothery, D. A., Coppola, D., and Saunders, C. (2005). Analysis of volcanic activity patterns using MODIS thermal alerts. *Bull. Volcanol.* 67, 539–556. doi: 10.1007/s00445-004-0393-3
- Salerno, G. G., Burton, M. R., Oppenheimer, C., Caltabiano, T., Randazzo, D., Bruno, N., et al. (2009). Three-years of SO₂ flux measurements of Mt. Etna using an automated UV scanner array: comparison with conventional traverses and uncertainties in flux retrieval. *J. Volcanol. Geotherm. Res.* 183, 76–83. doi: 10.1016/j.jvolgeores.2009.02.013
- Sawyer, G. M., and Burton, M. R. (2006). Effects of a volcanic plume on thermal imaging data. *Geophys. Res. Lett.* 33:L14311. doi: 10.1029/2005GL025320
- Scollo, S., Kahn, R. A., Nelson, D. L., Coltelli, M., Diner, D. J., Garay, M. J., et al. (2012). MISR observations of Etna volcanic plumes. *J. Geophys. Res. Atmos.* 117, 1–13. doi: 10.1029/2011JD016625
- Shinohara, H. (2013). Volatile flux from subduction zone volcanoes: insights from a detailed evaluation of the fluxes from volcanoes in japan. *J. Volcanol. Geotherm. Res.* 268, 46–63. doi: 10.1016/j.jvolgeores.2013.10.007
- Spampinato, L., Sciutto, M., Cannata, A., Cannavò, F., La Spina, A., Palano, M., et al. (2015). Multiparametric study of the February–April 2013 paroxysmal phase of Mt. Etna New South-East crater. *Geochem. Geophys. Geosyst.* 16, 1932–1949. doi: 10.1002/2015GC005795
- Spilliaert, N., Métrich, N., and Allard, P. (2006). S–Cl–F degassing pattern of water-rich alkali basalt: modelling and relationship with eruption styles on Mount Etna volcano. *Earth Planet. Sci. Lett.* 248, 772–786. doi: 10.1016/j.epsl.2006.06.031
- Taddeucci, J., Alatorre-Ibarguengoitia, M. A., Palladino, D. M., Scarlato, P., and Camaldo, C. (2015). High-speed imaging of strombolian eruptions: gas-pyroclast dynamics in initial volcanic jets. *Geophys. Res. Lett.* 42, 6253–6260. doi: 10.1002/2015GL064874
- Tamburello, G., Aiuppa, A., Kantzas, E. P., McGonigle, A. J. S., and Ripepe, M. (2012). Passive vs. active degassing modes at an open-vent volcano (Stromboli, Italy). *Earth Planet. Sci. Lett.* 359–360, 106–116. doi: 10.1016/j.epsl.2012.09.050
- Tamburello, G., Kantzas, E. P., McGonigle, A. J. S., Aiuppa, A., and Giudice, G. (2011). UV camera measurements of fumarole field degassing (La Fossa crater, Vulcano Island). *J. Volcanol. Geotherm. Res.* 199, 47–52. doi: 10.1016/j.jvolgeores.2010.10.004
- Torres, O., Bhartiya, P. K., Jethva, H., and Ahn, C. (2018). Impact of the ozone monitoring instrument row anomaly on the long-term record of aerosol products. *Atmos. Meas. Tech.* 11, 2701–2715. doi: 10.5194/amt-11-2701-2018
- Ulivieri, G., Ripepe, M., and Marchetti, E. (2013). Infrasound reveals transition to oscillatory discharge regime during lava fountaining: implication for early-warning. *Geophys. Res. Lett.* 40, 3008–3013. doi: 10.1002/grl.50592
- Vergnolle, S., and Mangan, M. T. (2000). “Hawaiian and Strombolian eruptions,” in *Encyclopedia of Volcanoes*, eds. H. Sigurdsson, B. Houghton, S. R. McNutt, H. Rymer, and J. Stix (San Diego, CA: Academic Press), 447–461.
- Vulpiani, G., Ripepe, M., and Valade, S. (2016). Mass discharge rate retrieval combining weather radar and thermal camera observations. *J. Geophys. Res. Solid Earth* 121, 5679–5695. doi: 10.1002/2016JB013191

- Werner, C., Kern, C., Coppola, D., Lyons, J. J., Kelly, P. J., Wallace, K. L., et al. (2017). Magmatic degassing, lava dome extrusion, and explosions from Mount Cleveland volcano, Alaska, 2011–2015: insight into the continuous nature of volcanic activity over multi-year timescales. *J. Volcanol. Geotherm. Res.* 337, 98–110. doi: 10.1016/j.jvolgeores.2017.03.001
- Williams, S. N., and Self, S. (1983). The October 1902 plinian eruption of Santa Maria volcano, Guatemala. *J. Volcanol. Geotherm. Res.* 16, 33–56. doi: 10.1016/0377-0273(83)90083-5
- Wooster, M. J., Zhukov, B., and Oertel, D. (2003). Fire radiative energy for quantitative study of biomass burning: derivation from the BIRD experimental satellite and comparison to MODIS fire products. *Remote Sens. Environ.* 86, 83–107. doi: 10.1016/S0034-4257(03)00070-1
- Wright, R., Flynn, L., Garbeil, H., Harris, A., and Pilger, E. (2002). Automated volcanic eruption detection using MODIS. *Remote Sens. Environ.* 82, 135–155. doi: 10.1016/S0034-4257(02)00030-5
- Wright, R., and Flynn, L. P. (2004). Space-based estimate of the volcanic heat flux into the atmosphere during 2001 and 2002. *Geology* 32, 189–192. doi: 10.1130/G20239.1
- Wright, R., Flynn, L. P., and Harris, A. J. (2001). Evolution of lava flow-fields at Mount Etna, 27–28 October 1999, observed by Landsat 7 ETM+. *Bull. Volcanol.* 63, 1–7. doi: 10.1007/s004450100124
- Wright, R., and Pilger, E. (2008). Satellite observations reveal little inter-annual variability in the radiant flux from the Mount Erebus lava lake. *J. Volcanol. Geotherm. Res.* 177, 687–694. doi: 10.1016/j.jvolgeores.2008.03.005
- Yang, K., Krotkov, N. A., Krueger, A. J., Carn, S. A., Bhartia, P. K., and Levelt, P. F. (2007). Retrieval of large volcanic SO₂ columns from the aura ozone monitoring instrument: comparison and limitations. *J. Geophys. Res. Atmos.* 112. doi: 10.1029/2007JD008825

Conflict of Interest Statement: The authors declare that the research was conducted in the absence of any commercial or financial relationships that could be construed as a potential conflict of interest.

Copyright © 2019 D'Aleo, Bitetto, Delle Donne, Coltelli, Coppola, McCormick Kilbride, Pecora, Ripepe, Salem, Tamburello and Aiuppa. This is an open-access article distributed under the terms of the Creative Commons Attribution License (CC BY). The use, distribution or reproduction in other forums is permitted, provided the original author(s) and the copyright owner(s) are credited and that the original publication in this journal is cited, in accordance with accepted academic practice. No use, distribution or reproduction is permitted which does not comply with these terms.



Mass Eruption Rates of Tephra Plumes During the 2011–2015 Lava Fountain Paroxysms at Mt. Etna From Doppler Radar Retrievals

Valentin Freret-Lorgeril¹, Franck Donnadieu^{1,2*}, Simona Scollo³, Ariel Provost¹, Patrick Fréville², Yannick Guéhenneux², Claude Hervier², Michele Prestifilippo³ and Mauro Coltelli³

¹ Université Clermont Auvergne, CNRS, IRD, OPGC, Laboratoire Magmas et Volcans, Clermont-Ferrand, France, ² Université Clermont-Auvergne, CNRS, UMS 833, OPGC, Aubière, France, ³ Istituto Nazionale di Geofisica e Vulcanologia, Osservatorio Etna, Sezione di Catania, Catania, Italy

OPEN ACCESS

Edited by:

Clive Oppenheimer,
University of Cambridge,
United Kingdom

Reviewed by:

Lea Scharff,
Universität Hamburg, Germany
Alessandro Tibaldi,
Università degli Studi di Milano
Bicocca, Italy

*Correspondence:

Franck Donnadieu
f.donnadieu@opgc.fr

Specialty section:

This article was submitted to
Volcanology,
a section of the journal
Frontiers in Earth Science

Received: 05 March 2018

Accepted: 22 May 2018

Published: 26 June 2018

Citation:

Freret-Lorgeril V, Donnadieu F,
Scollo S, Provost A, Fréville P,
Guéhenneux Y, Hervier C,
Prestifilippo M and Coltelli M (2018)
Mass Eruption Rates of Tephra
Plumes During the 2011–2015 Lava
Fountain Paroxysms at Mt. Etna From
Doppler Radar Retrievals.
Front. Earth Sci. 6:73.
doi: 10.3389/feart.2018.00073

Real-time estimation of eruptive source parameters during explosive volcanic eruptions is a major challenge in terms of hazard evaluation and risk assessment as these inputs are essential for tephra dispersal models to forecast the impact of ash plumes and tephra deposits. In this aim, taking advantage of the 23.5 cm wavelength Doppler radar (VOLDORAD 2B) monitoring Etna volcano, we analyzed 47 paroxysms produced between 2011 and 2015, characterized by lava fountains generating tephra plumes that reached up to 15 km a.s.l. Range gating of the radar beam allows the identification of the active summit craters in real-time, no matter the meteorological conditions. The radar echoes help to mark (i) the onset of the paroxysm when unstable lava fountains, taking over Strombolian activity, continuously supply the developing tephra plume, then (ii) the transition to stable fountains (climax), and (iii) the end of the climax, therefore providing paroxysm durations. We developed a new methodology to retrieve in real-time a Mass Eruption Rate (MER) proxy from the radar echo power and maximum Doppler velocity measured near the emission source. The increase in MER proxies is found to precede by several minutes the time variations of plume heights inferred from visible and X-Band radar imagery. A calibration of the MER proxy against ascent models based on observed plume heights leads to radar-derived climax MER from 2.96×10^4 to 3.26×10^6 kg s⁻¹. The Total Erupted Mass (TEM) of tephra was computed by integrating over beam volumes and paroxysm duration, allowing quantitative comparisons of the relative amounts of emitted tephra among the different paroxysms. When the climactic phase can be identified, it is found to frequently release 76% of the TEM. Calibrated TEMs are found to be larger than those retrieved by satellite and X-band radar observations, deposit analyses, ground-based infrared imagery, or dispersion modeling. Our methodology, potentially applicable to every Doppler radar, provides mass load parameters that represent a powerful all-weather tool for the quantitative monitoring and real-time hazard assessment of tephra plumes at Etna or any other volcano with radar monitoring.

Keywords: Etna, paroxysmal activity, Lava fountains, Doppler radar, mass eruption rate, total erupted mass

INTRODUCTION

Quantifying the so-called eruptive source parameters (Bonadonna et al., 2015) of tephra plumes is critical for hazard assessment of explosive volcanic eruptions and associated risk mitigation, as well as for a better understanding of the dynamics of eruption columns and plumes. The different eruptive source parameters are: the location of the eruptive vent, the start time and duration of an eruption, the plume height, the Mass Eruption Rate (MER), and the Total Grain Size Distribution (TGSD). These parameters are used by the Volcanic Ash Advisory Centers (VAACs) to initialize Volcanic Ash Dispersion and Transportation Models (VATDMs) in near real-time. A particularly challenging objective is to measure the MER in real-time. It is generally derived from empirical relationships between observed top heights of strong plumes and corresponding MERs inferred from scaling laws (Wilson et al., 1978; Sparks et al., 1997; Mastin et al., 2009). However, Mastin et al. (2009) and Degruyter and Bonadonna (2012) have reported that such empirical relationships between plume heights and MERs are subject to high uncertainties. MERs estimated from post-eruption deposits analyses themselves hold uncertainties highly dependent upon the selected methodology (Andronico et al., 2014a; Bonadonna et al., 2015; Spanu et al., 2016).

A way to operationally retrieve, i.e., in (near) real-time, the eruptive source parameters is to use remote sensing techniques. Radars represent particularly robust tools for real-time assessment of source parameters owing to their relatively high spatial resolution and acquisition rate, their all-weather detection capacity near the emission source allowing early warning and quantification. Fixed-beam transportable Doppler radars with high time resolution were for instance used to monitor and study the dynamics of Strombolian and mild Vulcanian activity, using either 23.5-cm wavelength radars mostly sensitive to lapilli- and block-sized tephra (Dubosclard et al., 1999, 2004; Gouhier and Donnadieu, 2010, 2011; Donnadieu et al., 2011; Valade et al., 2012), or 1-cm wavelength micro rain radars well suited for lapilli and coarse ash detection (Seyfried and Hort, 1999; Hort et al., 2003; Scharff et al., 2015; Hort and Scharff, 2016). Strong Vulcanian to Plinian eruptions have also been surveyed with 5-cm (Harris and Rose, 1983) and 3-cm wavelength scanning weather radars (Marzano et al., 2013; Maki et al., 2016; Vulpiani et al., 2016). Those radars have shown their capabilities and strength to study the dynamics of tephra plumes in real time and to provide estimates of (some of) the source parameters *a posteriori*, although generally with a lack of output parameters cross-validation.

At Etna (**Figure 1A**), one of the most active European volcanoes, the repetitive explosive activity and the risks associated with tephra plumes has led the Istituto Nazionale di Geofisica e Vulcanologia, Osservatorio Etneo (INGV-OE) to improve its monitoring network to better anticipate and measure Etna's ash emissions (Scollo et al., 2015). The network is based on the use of different remote sensing measurements

and VATDMs runs daily using fixed eruptive scenarios (e.g., Scollo et al., 2009, 2010). In this context, a 23.5 cm-wavelength Doppler radar (VOLDORAD 2B) has been integrated into the INGV-OE monitoring network since 2009 (Donnadieu, 2012; Donnadieu et al., 2016). This radar recorded 43 out of 45 paroxysmal episodes from the New Southeast Crater (NSEC) between 2011 and 2013, and 4 from the Voragine Crater (VOR) in December 2015, totaling 47 paroxysms between January 2011 and December 2015 (**Figure 1B**). Two paroxysms were missed on 19 July 2011 and 20 February 2013 due to power outage and radar maintenance. Paroxysms at Etna are powerful events lasting several hours and characterized by lava fountains generating high eruption columns accompanied or not by the emission of lava flows (Andronico et al., 2014a; Corsaro et al., 2017). The plumes typically reach 9–15 km above sea level, produce downwind fallout of lapilli (and sometimes bombs) up to several kilometers from the vents and ash fallout up to 400 km away from the volcano (Andronico et al., 2015). Considering that the mild Strombolian activity preceding the paroxysmal activity may last a few hours to a few days, and that the transition to a sustained tephra plume is currently not accurately predictable, it is crucial to quantify the evolution of the source parameters in near real-time.

Yet, measuring the whole set of eruptive source parameters of an eruption is not trivial. Indeed, in addition to the aforementioned observables, the Total Grain Size Distribution is also required (Bonadonna et al., 2015). The latter parameter is often incompletely estimated due to the limitations of tephra sampling near the summit craters. Indeed, the aforementioned paroxysms have two distinct fallout contributions. On the one hand, lava fountains are composed of dense ballistics and wind-pushed lighter blocks and lapilli that fall close to the source (i.e., <5 km). Despite the fact that they likely represent the dominant part of the total erupted mass, they are rarely sampled because the deposits are hardly distinguishable from those of previous eruptions and owing to recurrent fallout in the hardly accessible Valle del Bove (Andronico et al., 2014a; Spanu et al., 2016). On the other hand, lapilli and ash constituting the developing tephra plumes are often wind-drifted toward Southeast above the Ionian Sea, again preventing sampling. Incomplete deposit sampling leads, in turn, to high uncertainties on the retrieved Total Erupted Masses (TEMs), from which, the mean MERs are derived (Andronico et al., 2014a).

In this paper, we first describe the VOLDORAD 2B monitoring system and utilize the Doppler radar retrievals to qualitatively describe common features of the eruption dynamics during paroxysmal episodes of Etna between 2011 and 2015. We then present a new methodology to compute a proxy for the erupted mass only from the measured radar parameters. This methodology has potentially powerful application in real-time monitoring at Etna, but also at any volcano monitored by Doppler radars. Calibration of the mass proxy with plume ascent models parameterized with observed plume heights and with results from other methods leads to MER (potentially in real-time) and TEM estimates. Results are then discussed in the last section.

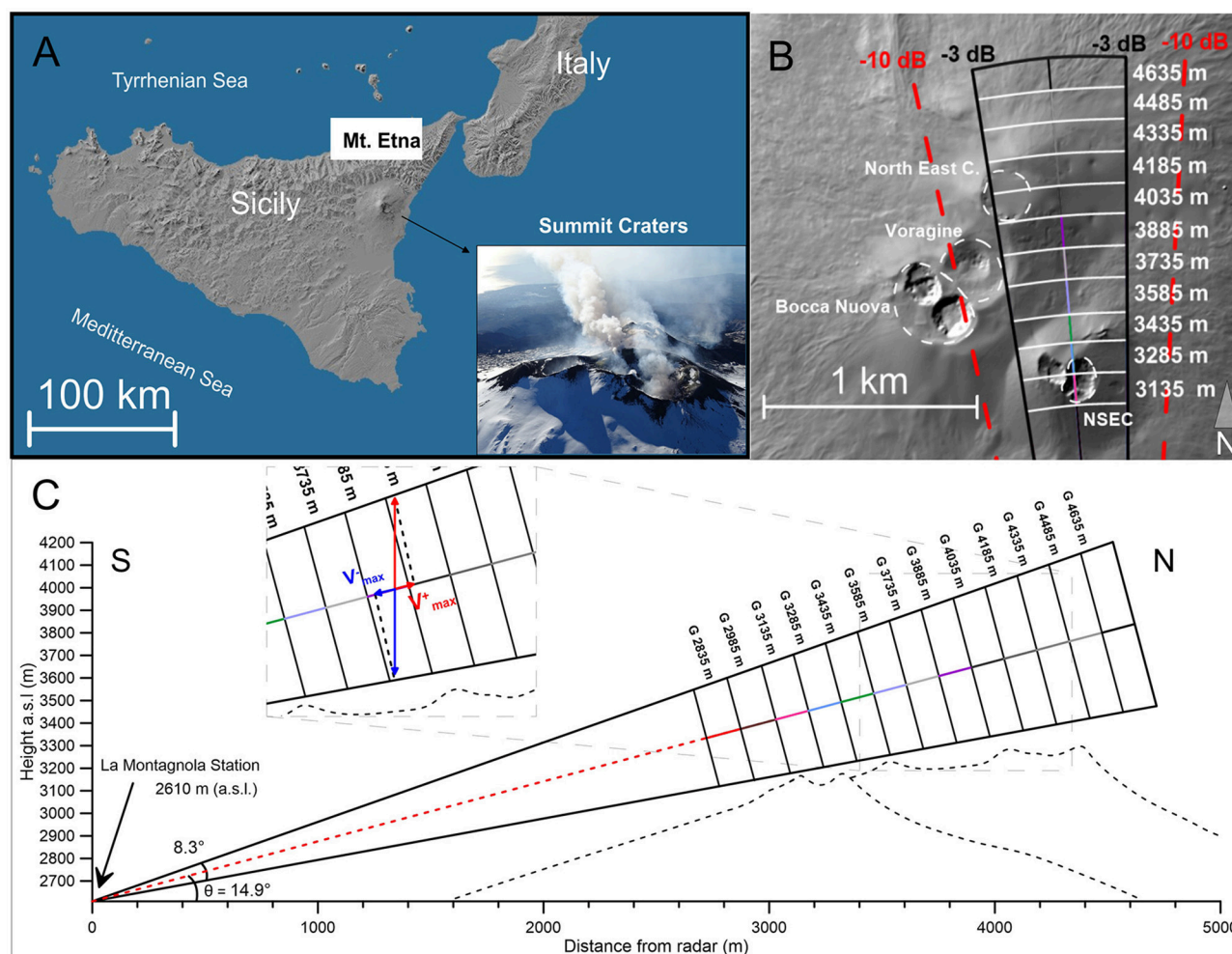


FIGURE 1 | (A) Mount Etna location and photograph of the summit crater (courtesy of Boris Behncke). Geometry of radar beam above Etna's summit craters: probed volumes are drawn at -3 dB, i.e., at half the power in the beam axis, and dashed lines indicate beam limit at -10 dB; **(B)** top view (after Oct. 10 2012); **(C)** S-N cross-section view (aperture angle of 8.3° in elevation at -3 dB): before December 16 2013, 11 range gates (3,135–4,635 m) were monitored and 13 gates (2,685–4,485 m) after this date. Inset: for range gates above the emission source, the positive (v_{max}^+) and negative (v_{max}^-) radial velocities measured along-beam mainly stem from ascending and falling tephra, respectively.

MATERIALS AND METHODS

The VOLDORAD 2B Monitoring System

Dubosclard et al. (1999, 2004) carried out pioneering surveys at Etna using a transportable L-band fixed-beam radar showing the high potential of radars to quantitatively monitor explosive activity near the emission source. They found in particular a correlation between tremor amplitude and echo power and ejecta initial velocities. In 2009, a similar 23.5-cm wavelength radar, VOLDORAD 2B, was set up at La Montagnola station on Etna (2,610 m a.s.l.) with its fixed beam pointing to a zone right above the summit craters 3 km northward (Figures 1A,C). Since then, it has been continuously monitoring the tephra emissions in volumes close to the summit craters (Donnadieu, 2012; Donnadieu et al., 2015, 2016). The 23.5 cm wavelength is well suited for the detection of lapilli and blocks/bombs

allowing to probe inside the tephra column regardless of weather conditions. The high sampling rate (about 5 Hz) allows the real-time quantification and provides insight into the dynamics of the eruption column at time scales of individual explosions to that of entire eruptive/inter-eruptive periods. The radar beam is divided into successively probed 150 m-deep volumes (range gates) extending 1.2 km above the summit craters area along the N-S direction of the beam. This range gating provides spatial information on the explosive activity, allowing for instance the identification of the active crater or craters during simultaneous activity (Donnadieu, 2012). From 2009 to October 10, 2012, the radar beam aimed above the summit vent with azimuth and elevation (θ) angles of 347.5° and 13° , respectively. After this date, the radar antenna was rotated to about 355.2° in azimuth and 14.9° in elevation (Figure 1B) to better record the activity of the NSEC. On December 16 2013, two more

proximal range gates were added, passing the number of recorded volumes ranging from 11 (3,135–4,635 m) to 13 (2,835–4,635 m; **Figures 1B,C**). VOLDORAD 2B simultaneously records the amplitude of the echo power backscattered by the tephra and their radial velocity (measured along-beam using the Doppler effect) in each range gate. Displays of radar parameters, the power spectral distribution as a function of radial velocities, are called Doppler spectra. Velocity component toward the radar are negative, and positive away from it (Sauvageot, 1992). For the range gates located above the emission source, the power associated with positive and negative radial velocities mainly stem from ascending and falling tephra respectively (**Figure 1C**). Out of the time series of power and velocity parameters retrieved from the Doppler spectra (e.g., Dubosclard et al., 2004), two are most useful to quantify the mass loading of explosive activity, as explored in a following section: (i) the total power $P(t)$ backscattered by tephra in each probed volume, which is directly related to the quantity and size of particles crossing the radar beam; and (ii) the maximum positive Doppler velocity $v_{max}^+(t)$ as it can be geometrically related to the ejection velocities $V(t)$ assuming vertical jets (Dubosclard et al., 1999, 2004; Donnadieu, 2012; Scharff et al., 2015):

$$V(t) = \frac{v_{max}^+(t)}{\sin(\theta)} \quad (1)$$

with θ the elevation angle of the radar beam (**Figure 1**). As θ was changed on 10 October 2012 from about 13° to 14.9° , $V(t) \approx 4.45v_{max}^+(t)$ for the 2011–2012 paroxysms, and $V(t) \approx 3.89v_{max}^+(t)$ afterwards, including the 2013–2015 paroxysms.

Plume Top Height Measurements

In order to retrieve absolute MERs from the radar parameters, we have used independently the MER obtained from the column height observations. In fact, the link between plume heights and mass eruption rates is one of the most studied among volcanic source parameters relationships (Mastin et al., 2009). Scollo et al. (2014) proposed a methodology to retrieve column heights at Etna from image analyses of the ECV visible camera (in Catania, 27 km away from Etna's summit craters), with an error of ± 500 m (Scollo et al., 2015). The method limitations include night and bad weather conditions preventing the use of this visible camera, and the maximum altitude of 9 km above sea level. In this case, the ECV measurements may be supplemented by satellite imageries to retrieve the maximum column height using the Dark Pixel procedure that assumes a thermal equilibrium between the plume top and the atmosphere (Wen and Rose, 1994; Prata and Grant, 2001; Corradini et al., 2016).

When available, we have also used DPX4 X-band weather-radar data of the Italian civil protection, in addition to other remote sensor data (i.e., satellite and visible imagery) estimating the plume heights during the 23 November 2013 NSEC paroxysm and the December 2015 VOR Crater paroxysms (Corradini et al., 2016; Vulpiani et al., 2016).

The Radar Mass Eruption Rate Proxy

Several recent works using scanning weather radars aimed at estimating mass loading parameters of explosive eruptions.

Marzano et al. (2006) produced a procedure to retrieve ash mass load parameters (i.e., VARR model) using an electromagnetic scattering model and Dual-polarization radar observables. Their work was applied to Etna paroxysmal activity in 2013 (Corradini et al., 2016; Montopoli, 2016) and in December 2015 (Vulpiani et al., 2016) using the volume information of the X-Band (3 cm wavelength) weather radar located at Catania airport (30 km south from the Etna's summit), with a 3-D scan time resolution of 10 min.

Taking advantage of the higher time (<0.1 s) and spatial (120 m) resolution of a fixed-beam radar similar to VOLDORAD 2B pointing right above the emission source, Gouhier and Donnadieu (2008) developed an inversion method based on the Mie Scattering Theory to retrieve the ejecta mass of individual outbursts during Strombolian activity at Etna in 2001. Because of their short emission time, Strombolian explosions were treated as quasi-instantaneous releases of particles in which all ejecta could be captured in the large volumes of the fixed beam during the recorded peak of echo power.

The continuous monitoring of Etna with the VOLDORAD 2B radar at high space-time resolution (150 m, 0.2 s) offers a good opportunity to estimate the mass load parameters of Etna paroxysms. However, the lack of accurate physical characterization of proximal tephra (i.e., from the lava fountaining) in terms of shape, size and density weakens assumptions on inputs to scattering simulations, in particular the particle size distribution, and brings out large uncertainty in the mass load outputs. Therefore, in the following, we present a new approach based on a simple analytical model to compute the tephra mass loading parameters from a mass proxy directly retrieved from Doppler radar observables above the vent, and then calibrated against values measured by other methods. Interestingly, this methodology does not require an accurate particle size distribution and is applicable to the most frequent cases of eruptions in which the tephra emission duration is longer than the time needed for tephra to cross the beam. It also has obvious application to improve real-time monitoring and hazard assessment of tephra plumes.

As our goal is to calibrate a (relative) mass proxy directly related to radar observables, the physical model does not need to mimic the complexity of the particle dynamics during the eruption but only to correlate with the MER evolution. In our simplified eruption model, spherical particles with a unique diameter D (in m), constant with time, cross the beam vertically at velocity $V(t)$ (in m s^{-1}) assumed equal to the maximum ejection velocity, and constant over the beam crossing height (**Figure 2**).

The number of ascending particles dN inside the volume probed during the radar sampling period dt between two successive measurements is therefore defined by:

$$dN = n(t) [S V(t) dt] \quad (2)$$

where $n(t)$ is the number of particles per unit volume (m^{-3}), and S is the entering surface area (m^2) of the jet into the beam, no matter its shape.

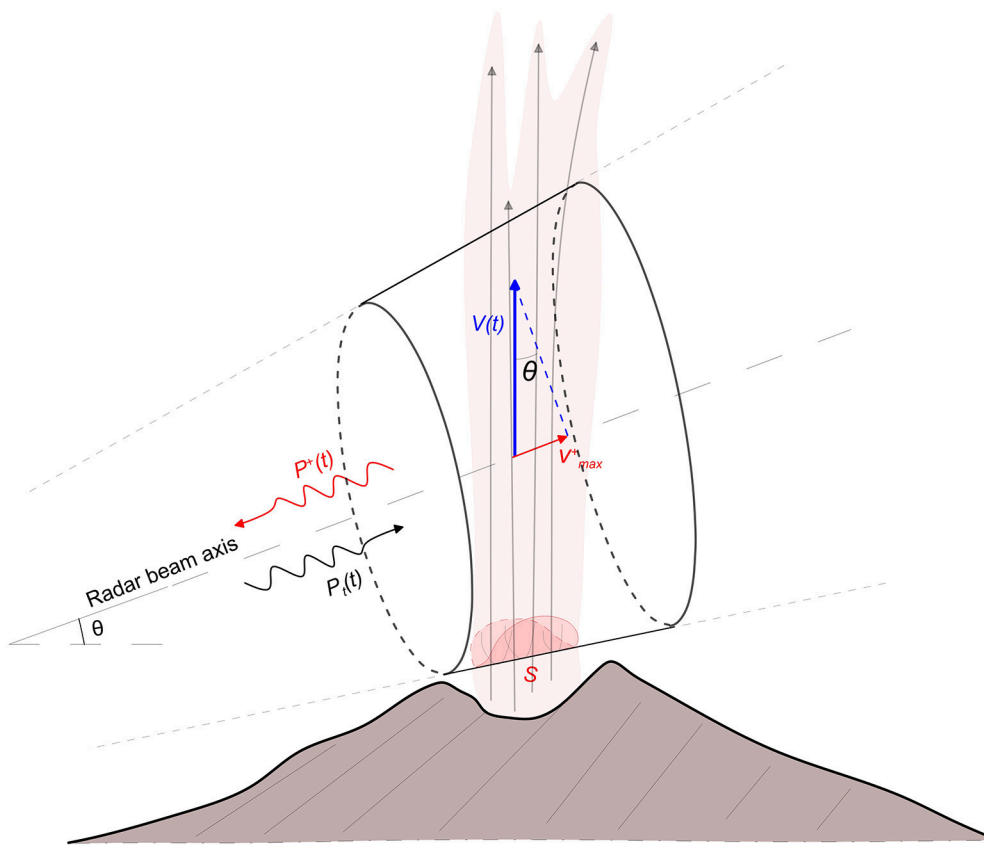


FIGURE 2 | Sketch of the physical model to compute the mass eruption rate from the power and velocity parameters measured by the radar. S defines the (arbitrary) entry surface of the ejecta at the bottom of the radar beam. $V(t)$ is the ejected tephra velocity in the beam, assumed vertical, and v_{\max}^+ its component along-beam, as measured by the radar. θ is the radar beam elevation angle. $P_t(t)$ is the peak power transmitted into the atmosphere by the radar, and $P^+(t)$ the power backscattered from ejecta having a positive radial velocity, supposedly ascending vertically, in a range gate above the emission source.

Assuming spheres of density ρ (kg m^{-3}), the total particle mass over time M (kg) is:

$$M = \frac{\pi}{6} \rho S D^3 \int_{t_1}^{t_2} n(t) V(t) dt \quad (3)$$

Under the Rayleigh assumptions ($D < \lambda/4$ in Gouhier and Donnadieu, 2008; where λ is the 23.5 cm-wavelength of our radar), the power ($P^+(t)$, in mW) backscattered by ascending spheres homogeneously distributed inside a probed beam volume above the emission source can be obtained from the radar equation (e.g., Sauvageot, 1992):

$$P^+(t) = \gamma D^6 n(t) \quad (4)$$

γ being a constant (mW m^{-3}) gathering known parameters specific to the radar.

The combination of Equations (1–4) leads to the time-integrated mass of tephra M (kg) expelled through the probed

volume between times t_1 and t_2 :

$$M = \frac{\pi \rho S}{6 \gamma (\sin \theta) D^3} \int_{t_1}^{t_2} P^+(t) v_{\max}^+(t) dt = C \times M^* \quad (5)$$

where M^* is the above integral and C ($\text{kg mW}^{-1} \text{m}^{-1}$) the constant factor before it.

Under the complete Mie scattering theory, where the Rayleigh approximation (Equation 4) is no more valid, $P^+(t)$ is found to increase with D according to a more complicated power law formulation. Following the scattering model of Gouhier and Donnadieu (2008), and for blocks larger than 9 cm, the time-integrated mass M (kg) becomes:

$$M = \frac{\pi \rho D^3}{6 h (\sin \theta) 7.474 \times 10^{-10} D^{2.359}} \int_{t_1}^{t_2} P^+(t) v_{\max}^+(t) dt = C' \times M^* \quad (6)$$

where h is the vertical length of the given probed volume (in m). As in Equation 5, the first factor can be grouped into a constant C' ($\text{kg mW}^{-1} \text{m}^{-1}$).

While most parameters are known (γ , θ) or could be roughly estimated (ρ , S), the radar-sensitive mean diameter D can

hardly be estimated, especially during an eruption, despite its dominant weight in the relationship owing to the power law. For this reason, our approach aims at calibrating the constants C (and hence C') against results from other methods in order to obtain absolute radar-derived mass load, as explained later. Most interestingly, the integral factor represents a Radar proxy for the mass of tephra M^* depending only on radar power and velocity measurements. A proxy for the total erupted mass of tephra (TEM^*) can be obtained by integrating the radar mass proxy M^* over the total duration of the paroxysm and over all range gates capturing ascending tephra above the crater. It is also straight forward to compute an average Mass Eruption Rate proxy (MER^*) from the number of samples n recorded at acquisition intervals $dt = 0.23$ s in a probed volume above the emission source:

$$\overline{MER}^* = \frac{M^*}{n \, dt} \quad (7)$$

Time series of the radar-derived MER proxy can thus be computed at high rate (MER^*), potentially at each acquisition time (i.e., at rate $1/dt$ using $n = 1$), to inform in real-time on the eruption intensity evolution including during overcast weather preventing visual observations. MER^* thus provides an useful tool to improve the real-time monitoring and forecasting volcanic ash dispersal and fallout during lava fountain paroxysms at Etna.

Because the range resolution (150 m) is usually smaller than the lava fountain width, several range gates commonly dominate the echoes amplitude and are used for the aforementioned spatial integration of the mass or MER proxy: 3,135 and 3,285 m for the NSEC paroxysms, 3,885, 4,035, and 4,185 m for the VOR paroxysms in December 2015, and 4,035 and 4,185 m for the Northeast Crater. These are the range gates above the erupting crater, as seen from the sounding geometry (Figures 1B,C).

In the next section, we illustrate the use of the radar mass proxy to infer on the dynamics during an explosive eruption at Etna.

RESULTS

Eruption Dynamics During Etna's Paroxysmal Activity

First, paroxysmal eruptions at Mount Etna present a similar succession of eruptive phases (Bonaccorso et al., 2011, 2013; Behncke et al., 2014; Calvari et al., 2014). The first phase corresponds to a discrete Strombolian activity lasting hours to several days (Behncke et al., 2014), which is not well captured by the radar at the very beginning of the paroxysm owing to tephra emissions mostly confined inside the crater and the lack of sustained plume above the crater rims.

Secondly, the number and intensity of explosions increase and a transition toward an unsteady lava fountain regime occurs (phase 2 in Figure 3, 15–20 min). This period of increasing intensity might represent the evacuation of the partially degassed conduit magma from the previous eruption as it becomes pushed out of the conduit (Calvari et al., 2011) and replaced by newer magma richer in gas. As new magma progressively fills up the entire conduit, the flow regime transitions from slug flow to churn flow leading to an unstable lava fountaining (Ulivieri et al., 2013). This unsteady phase can be characterized by a shoulder (first bump) in the radar signals, well observed during strong paroxysms like those on 23 February 2013 and 23 November 2013 for example (Figures 3B,C).

Then, two main types of paroxysms can be distinguished during the following third eruptive phase. The 27 Type-A paroxysms (57.4% of the total) are characterized by a clearly sustained climax phase lasting 44.19 ± 5.30 min in average (Figures 3B,C and Table 1). In type-B paroxysms (42.6% of the total), the climax phase is not always well defined, suggesting a lava fountain regime remaining unstable (Figure 3A). Over 20 Type-B paroxysms, only 8 (40%) present identifiable sustained phases during 44.25 ± 17.89 min in average (Type-B1, Table 1). The 12 (60%) other paroxysms are characterized by highly variable tephra emission (Type-B2).

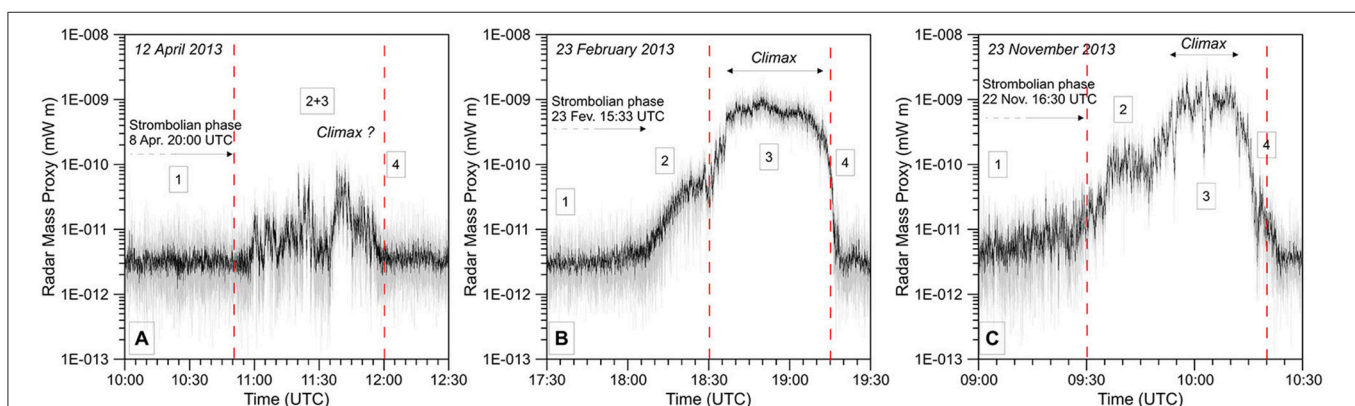


FIGURE 3 | Raw (gray) and 2.5-s running average (black) time series of the Radar Mass proxy recorded during lava fountain paroxysms of Etna's NSEC on 12 April 2013 (A), 23 November 2013 (B), and 23 February 2013 (C). Radar-inferred eruption phases are numbered: (1) Strombolian activity, (2) Strombolian to lava fountain transition, (3) climax phase, and (4) waning phase including a sudden drop in activity marking the end of the lava fountain. Dashed red lines correspond to the onset and end times of the lava fountains according to De Beni et al. (2015).

TABLE 1 | Statistical values of the retrieved mass proxies of Mount Etna paroxysmal activity recorded by VOLDORAD 2B.

		TYPE-B	TYPE-A	ALL
Number		20	27	47
Duration Δt (min)	Min	49	33	33
	Max	531	711	711
	Average	180.70	152.67	164.60
	Standard error of the mean	30.09	29.16	20.96
TEM* (mW m)	Min	2.19E-07	1.63E-07	1.63E-07
	Max	2.70E-06	9.60E-06	9.60E-06
	Average	7.58E-07	2.33E-06	1.66E-06
	Standard error of the mean	1.30E-07	5.10E-07	3.17E-07
Total MER* (mW m s ⁻¹)	Min	2.15E-11	2.10E-11	2.10E-11
	Max	4.25E-10	1.76E-09	1.76E-09
	Average	1.05E-10	3.45E-10	2.43E-10
	Standard error of the mean	2.39E-11	8.05E-11	5.01E-11
Δt climax (min)	Min	10	12	10
	Max	166	122	166
	Average	44.25	44.19	44.19
	Standard error of the mean	17.89	5.30	5.62
		TYPE-B2	TYPE-A	ALL
Number		8	27	35
Climax M* (mW m)	Min	1.49E-07	1.19E-07	1.19E-07
	Max	2.49E-06	7.86E-06	7.86E-06
	Average	5.94E-07	1.83E-06	1.55E-06
	Standard error of the mean	2.72E-07	3.87E-07	3.16E-07
Climax MER* (mW m s ⁻¹)	Min	3.63E-11	3.26E-11	3.26E-11
	Max	1.12E-09	3.95E-09	3.95E-09
	Average	3.31E-10	9.18E-10	7.84E-10
	Standard error of the mean	1.21E-10	2.07E-10	1.66E-10
TEM* ratio	Min	47.81	49.45	47.81
	Max	92.04	95.68	95.68
	Average	71.19	77.85	76.32
	Standard deviation	14.20	11.76	12.46
MER* ratio	Min	23.25	12.23	12.23
	Max	59.29	66.20	66.20
	Average	45.21	42.73	43.29
	Standard deviation	11.54	11.91	11.70

Finally, the fourth phase (**Figure 3**) is characterized by a relatively rapid decrease in the radar signal (between 7 and 70 min) with respect to the eruption duration, with an average of 25.4 min during which the lava fountain stops and is replaced by ash emission not well captured by VOLDORAD 2B. Four long-lasting paroxysms present outlier values of decrease time lasting 126 and 289 min (episodes E20, E40, E41, and E43 in Appendix 1).

Average velocities during the climax phase range between 55 and 200 m s⁻¹ (Appendix 1), with a mean of 125 ± 6 m s⁻¹. However, ejection velocities can reach much higher velocities for a few seconds, 360 m s⁻¹ at the highest over all the paroxysms (short peaks up to 432 m s⁻¹). Ejection velocities exceeding 400 m s⁻¹ had previously been measured at Etna using the same type of radar during the Laghetto eruption in July 2001 (Donnadieu et al., 2005). Maximum velocities measured by radar are generally higher than those estimated from infrared. For example, Calvari et al. (2011) and Bonaccorso et al. (2014) estimated maximum ejection velocity of 125 and 258 m s⁻¹ compared to maximum radar ejection velocities of 368 (average of 188 m s⁻¹) and 378 m s⁻¹ (average of 184 m s⁻¹) on 12 January 2011 and 23 November 2013, respectively. TEM* calculated for all paroxysms (Appendix 1; **Figure 4**) range over nearly two orders of magnitude, from 1.63×10^{-7} (20 February 2013, NSEC paroxysm) to 9.60×10^{-6} mW m (3 December 2015, VOR paroxysm).

However, in **Figure 3**, it is important to notice that the pyroclastic emission during a paroxysmal activity is highly variable as a function of time, and variations are also different among the paroxysms. Indeed, ratios shown in histograms of **Figures 5A,B** indicate that the climax most frequently releases about 80 to 90% of the TEM (modal class) with an average of 76%. Likewise, the MER* averaged over the whole paroxysm most frequently represents about 43% of the climax MER* (**Figure 5 and Table 1**).

Paroxysms after October 2012 show average mass parameters (i.e., TEM* and MER* in **Figures 5A,B**), during the climax and during the total duration of the events, about twice the averages between 2011 and 2012. This can be a result of a better beam sampling of the lava fountains after the antenna rotation toward the NSEC in October 2012 (**Figure 5A,B**). Nevertheless, both mass load parameters are homogeneously distributed over nearly two orders of magnitude, indistinctly before (2011–2012) and after (2013–2015) the antenna rotation, with good correlations (e.g., R^2 of 0.98 and 0.94 in **Figures 5A,B**).

Behncke et al. (2014) and De Beni et al. (2015) estimated proximal pyroclastic bulk volumes forming the NSEC of about 19×10^6 m³ during 25 paroxysms in 2011–2012 and 27×10^6 m³ during 25 events in 2013–2014. Among the last 25 events, 19 presented observed strong lava fountains. The 6 non paroxysmal events occurred between December 2013 and August 2014 and were marked by intense Strombolian (detected by VOLDORAD 2B) and effusive activity. Thus, considering the paroxysms after October 2012, the volume ratio between the two periods is about 1.86. This value

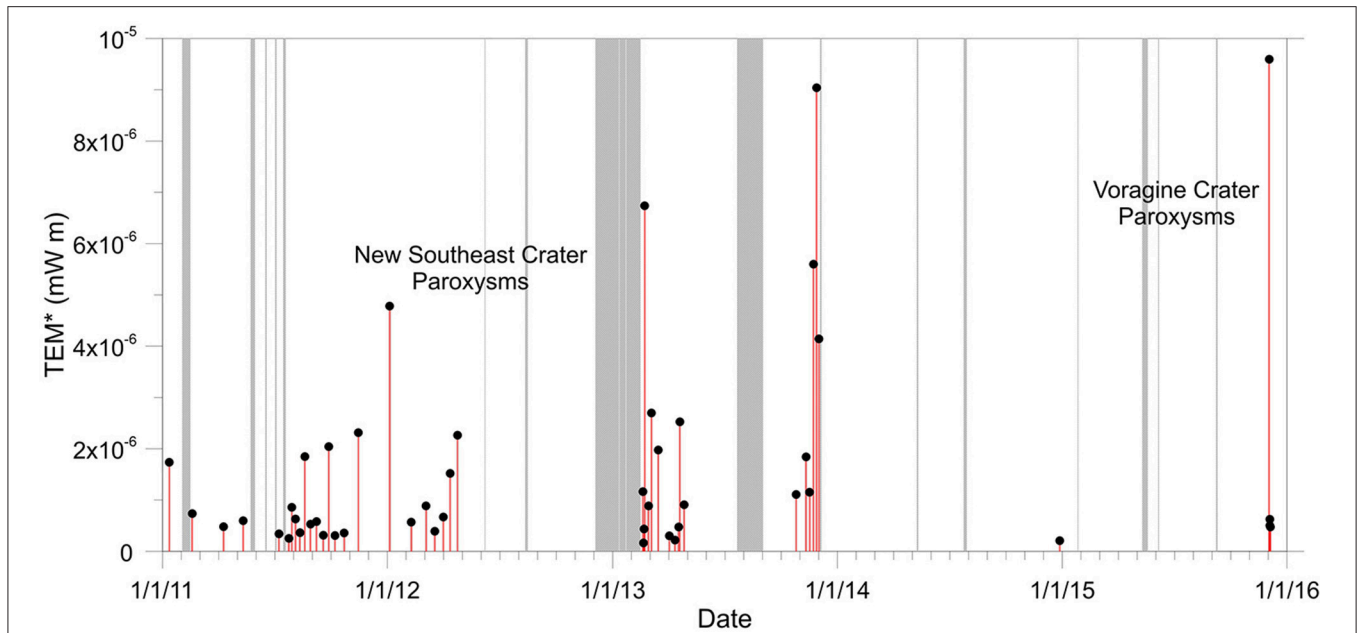


FIGURE 4 | Radar-derived proxy for the total mass of tephra (TEM^*) emitted by each detected paroxysm of Etna between January 2011 and December 2015, showing periods of grouped eruptive episodes. Gray areas indicate the periods of power outages.

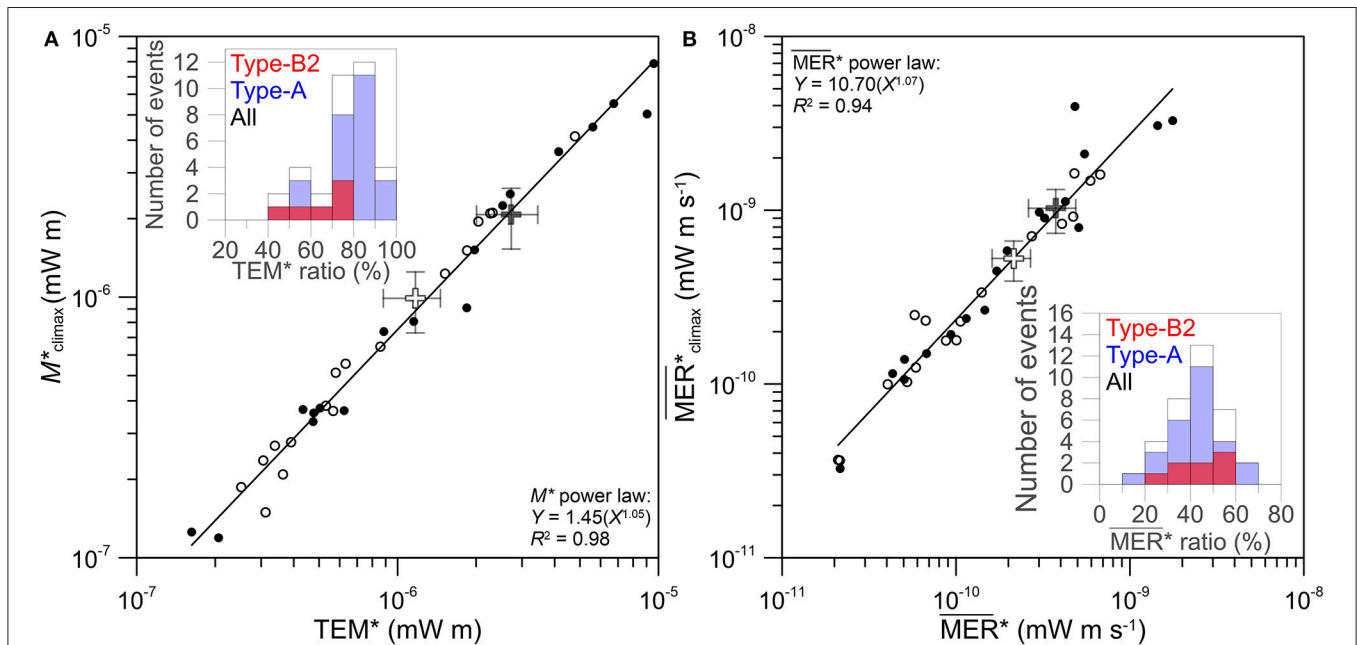


FIGURE 5 | **(A)** Correlation between the relative masses of tephra emitted during the climax (M^*_{climax}) and during whole paroxysmal episodes (TEM^*), as inferred from radar records of the 2011–2012 (open circles) and 2013–2015 (black circles) paroxysms. The open and black crosses corresponds to the average values for both periods. Error bars corresponds to the standard error of the mean. Inset: Histogram of the tephra mass proportion released during the climax, as deduced from M^* . **(B)** Correlation between Mass Eruption Rate Proxies averaged over climax duration (MER^*_{climax}) and over whole paroxysmal duration (MER^*). Inset: Histograms of the ratio of Mass Eruption Rate (MER^*) averaged over the whole paroxysm duration relative to that of the climax. Paroxysms typology is also shown: B2-type (red bars), A-type (blue bars) and all (black outline).

is in agreement with the previous factor two of average radar proxies in **Figures 5A,B**. The last paroxysmal episode of the NSEC 2011–2014 eruptive activity occurred on 28

December 2013. The latter event is not taken into account to estimate the bulk volumes forming the NSEC (De Beni et al., 2015).

Plume Top Height and Radar Mass Proxy

Plume top heights are strongly controlled by the MER and cross-winds (Morton et al., 1956; Sparks et al., 1997; Bursik, 2001; Mastin et al., 2009). Taking advantage of the capacity of VOLDORAD 2B to efficiently monitor the MER at high rate in real-time and given the ample variations in mass eruption rate observed during lava fountain paroxysms at Etna (**Figure 3**), we here investigate the relationship of plume heights and the radar-derived MER*.

Figure 6 shows times series of radar mass proxy and observed plume top height evolution over the course of four paroxysmal episodes: those on 12 August 2011, 12 April 2012, and 23 November 2013 of the NSEC, and that on 3 December 2015 of VOR crater. For the 12 August 2011 event, heights were measured from the visible camera (ECV), from satellite imagery and from radar. As expected, during each paroxysm, plume top height variations closely follow the radar mass proxy.

For the 12 August 2011, 12 April 2012, 23 November 2013, and 3 December 2015 events, the start of the sudden increase in activity leading to the climax phases according to the radar data occurs 15–21 min before the tephra plumes reach their first maximum heights (**Figures 6B–D**). From this, to reach 6.3 km (**Figure 6A**), 4.3 km (**Figure 6B**), 7.8 km (**Figure 6C**), and 12.8 km (**Figure 6D**) above the vent, the estimated upward velocities of the tephra plumes are calculated to be 4.97, 4.84, 8.67, and 10.67 m s⁻¹ at the very beginning of the climax phase, respectively.

For the 12 August 2011 paroxysm, the plume maximum heights increase significantly before the ascending phase leading to the climax seen in the radar mass. This can be due to the lack of momentum in the waxing phase of this particular weak emission bringing the plume to its top height mainly by simple buoyant upraise before the weak climax has started. The antenna azimuth before October 2012 might also have led to incomplete sampling of weak paroxysms such as the 12 August 2011 (TEM* of 3.64×10^{-7} mW m) compared to stronger ones like the 12 April 2012 (TEM* of 1.52×10^{-6} mW m).

Tephra Mass Load Estimates

Although temporal offsets and their variation as a function of time remain to be explained in detail in terms of phenomenology and environmental factors, the evolution of the plume top height during a paroxysm appears closely related to the radar-derived MER proxy. Plume height is an essential input to VATDMs in order to assess hazards from explosive eruptions. The implementation of this capacity of VOLDORAD 2B to provide a relative MER (i.e., a proxy) in real-time and at high rate, in addition to ejection velocities, would already be a step forward in the monitoring of Etna.

However, absolute MER estimates derived from the MER* are of even greater added value. According to Equation (5), converting the radar mass proxy into an absolute mass in kg requires knowledge of parameters constitutive of constant C. However, particle diameters

near the source are mostly unconstrained. A way to calibrate C is to compare radar MER proxies with mass eruption rates (MER in kg s⁻¹) from empirical laws based on correlation with plume top heights (H in km), such as in Mastin et al. (2009):

$$H = 0.304\text{MER}^{0.241} \quad (8)$$

However, the latter equation is based on a dataset that is biased by the high proportion of strong eruptions, which hence suffers from a lack of more frequent and smaller ones (Woodhouse et al., 2013). Thus, the scaling law of Mastin et al. (2009) does not appear best suited to tephra plumes associated with a MER < 10⁶ kg s⁻¹, also more sensitive to atmospheric conditions common during fountain-fed tephra plumes of Etna.

Therefore, we secondly compared with the model of Degruyter and Bonadonna (2012) using wind velocity profiles across tephra plume heights:

$$\text{MER} = \pi \frac{\rho_{a0}}{g'} \left(\frac{2^{5/2} \alpha^2 \bar{N}^3}{z_1^4} H^4 + \frac{\beta^2 \bar{N}^2 \bar{v}}{6} H^3 \right) \quad (9)$$

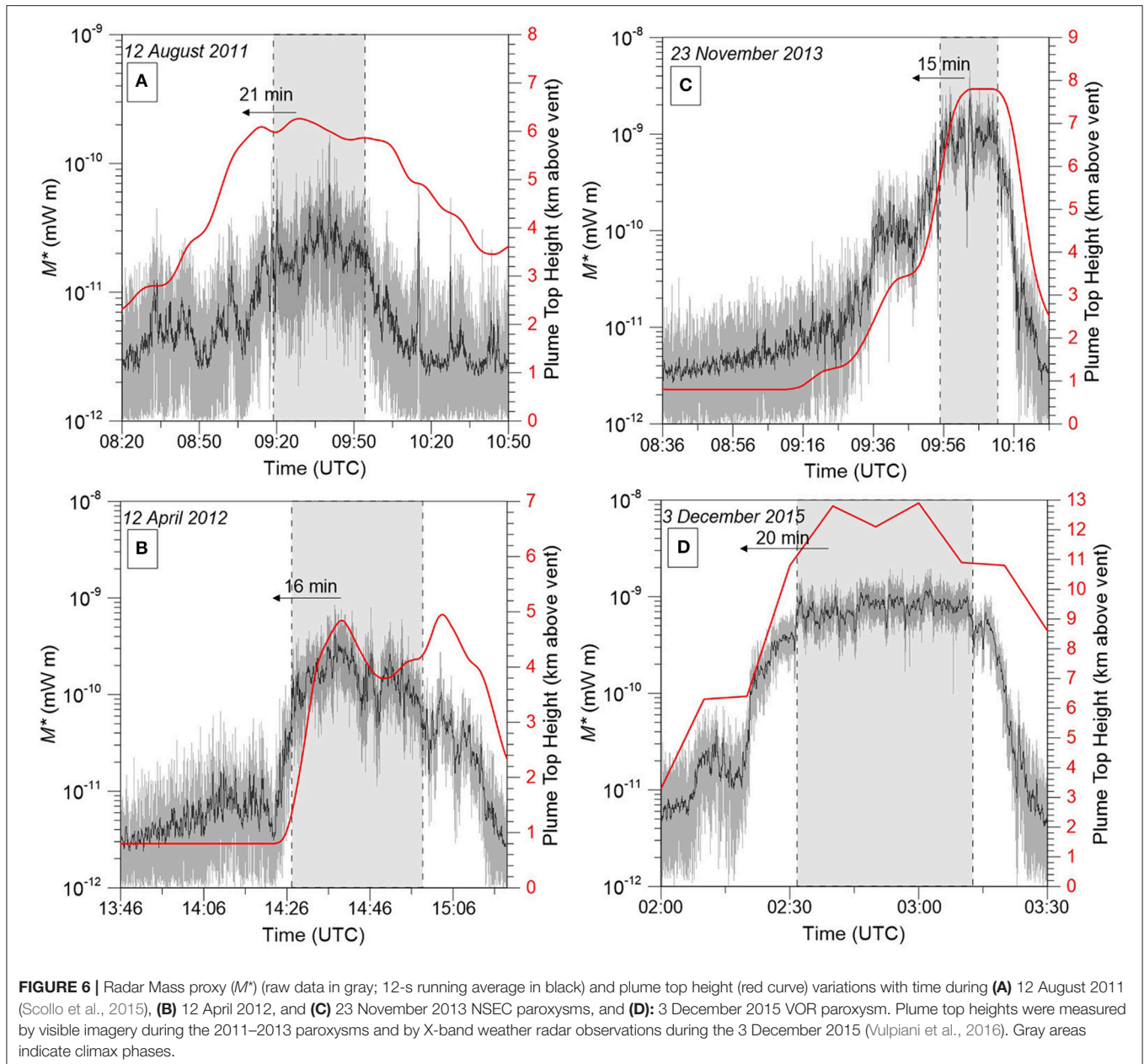
where ρ_{a0} is the reference atmosphere density (in kg m⁻³), g' is the reduced gravity at the source vent (in m s⁻²) and \bar{N} is the buoyancy frequency (equals to 1.065×10^{-2} s⁻¹ for a standard atmosphere). α is the radial entrainment coefficient set at 0.1 (Degruyter and Bonadonna, 2012). β is the wind entrainment coefficient. We used $\beta = 0.5$, a value that diminishes the error associated with downwind plume trajectories (Aubry et al., 2017).

Finally, \bar{v} is the wind velocity across the plume height z (in m):

$$\bar{v} = \frac{1}{H} \int_0^H v(z) dz \quad (10)$$

Vertical wind profiles were taken from radio soundings operated at the LICT station in the Northwest of Sicily (<http://weather.uwyo.edu/upperair/sounding.html>).

Figure 7A shows the 1 min-averaged Radar MER proxies calculated 5 min before the plume maximum height measurements from visible and satellite imagery during 19 paroxysms of NSEC. Quantitatively, a systematic approach is used to calibrate the MER proxies with a constant C (Equation 5). We consider all data points falling within the plume height-MER model domain of Degruyter and Bonadonna (2012, Equation 9) limited by the vertical profile wind conditions of 0 m/s and highest winds at Etna during the 23 February 2013 paroxysms. The constant needed to reach the highest percentage (i.e., 90% in **Figure 7B**) of data fitting between the models and the MER proxies is equal to 8.25×10^{14} kg mW⁻¹ m⁻¹. Altogether, the MER proxies as a function of observed plume top heights by visible, satellite and X-band radar imagery are scattered on either side of the Mastin et al. (2009)'s statistical law (Equation 8, **Figure 7A**). Although there is a moderate correlation ($R^2 = 0.58$), a best-fit



power law $H \propto \text{MER}^{1/4}$ is found with an elegant power coefficient of $1/4$ well-fitting with the theory (Morton et al., 1956).

Using **Table 1** and Appendix 1, the above calibration leads to radar-derived MER for the climax phases from 2.96×10^4 to $3.26 \times 10^6 \text{ kg s}^{-1}$ with an average of $6.47 \times 10^5 \text{ kg s}^{-1}$. In comparison, average MERs during the whole duration of each 2011–2015 Etna's paroxysms span from 1.73×10^4 to $1.45 \times 10^6 \text{ kg s}^{-1}$ (**Figure 8**). About two thirds of the paroxysms show an average MER between 1.73×10^4 and $2 \times 10^5 \text{ kg s}^{-1}$ (57% with average MERs $\leq 10^5 \text{ kg s}^{-1}$, inset in **Figure 8**), the remaining third spreads from 2 to $6 \times 10^5 \text{ kg s}^{-1}$ with a modal value between 3.5 and $4 \times$

10^5 kg s^{-1} . The two strongest average MERs corresponds to the 23 February 2013 (NSEC) and 3 December 2015 (VOR) paroxysms with values of 1.19 and $1.45 \times 10^6 \text{ kg s}^{-1}$, respectively.

First order TEMs can be calculated from the calibrated MERs from VOLDORAD 2B data at Etna: they range from 1.34×10^8 to $7.92 \times 10^9 \text{ kg}$ with an average of $1.37 \times 10^9 \text{ kg}$, while the climax erupted masses span from 9.82×10^7 to $6.49 \times 10^9 \text{ kg}$ with an average value of $1.28 \times 10^9 \text{ kg}$. Given the radar wavelength, estimated TEMs mainly concern lapilli and block/bombs in the eruptive column. Behncke et al. (2014) have reported a NSEC growth between 2011 and the end of 2012 of about $19 \times 10^6 \text{ m}^3$ (bulk volume) due to the

proximal fallout. The sum of radar-derived TEMs during the same period leads to a total eruptive bulk volume of detected pyroclasts of $16.1 \times 10^6 \text{ m}^3$. The total erupted bulk volume of detected pyroclasts over all 2013 paroxysms is equal to $26.4 \times 10^6 \text{ m}^3$. This value is also similar to the contribution of proximal fallout, building the NSEC between 2013 and 2014, estimated to $27.0 \pm 0.8 \times 10^6 \text{ m}^3$ (De Beni et al., 2015). The mean particle density of $1,300 \text{ kg m}^{-3}$ taken to calculate such bulk volumes characterizes the mixture of light (410 kg m^{-3} , Andronico et al., 2015) and dense block/bombs (close to $2,700 \text{ kg m}^{-3}$, Bonadonna and Phillips, 2003), and light scoriaceous lapilli (about 600 kg m^{-3} ; Bonny, 2012) emitted during the paroxysms.

In the next section, we discuss the uncertainties related to the radar mass proxy calibration and the potential benefits of its implementation in real-time for operational monitoring of volcanic activity.

DISCUSSION

Uncertainties and Implications on Mass Load Parameters

The tephra plume radar sampling has changed on October 2012 because of the antenna rotation eastwards. This might have led

to mass load underestimates from radar retrievals of the 2011–2012 lava fountains generating vertical tephra columns. Also, the beam sampling suits better the NSEC lava fountains than the December 2015 VOR paroxysms because the Voragine Crater is more offset from the beam axis (Figure 1B). The above sampling issues could be highlighted by the three data points falling on the results of Equation 9 based on a 0 m s^{-1} wind profile (Figure 7). Those points correspond to the 9 July 2011, 1 April 2012 NSEC paroxysms (open circles in Figure 7) and the 3 December 2015 VOR paroxysm (black square).

However, the MER^* of all events show consistent distribution trends within a range of two orders of magnitude, whichever the active crater and/or the eruptive periods (Figures 5, 7A). This suggests that the difference in sounding conditions is not a major source of error at first order in mass load estimates from radar parameters. This strengthens our radar-derived mass-proxy methodology to quantitatively characterize the lava fountain paroxysmal episodes of Mount Etna and the high variability of their intensity. Specific environmental conditions such as strong cross wind away from the beam axis, or highly fluctuating wind strength/direction, or strongly bent fountain emission might represent a more significant source of error, underestimating the MER, and these cases should be considered with caution when radar monitoring data are used in real-time for hazard assessment.

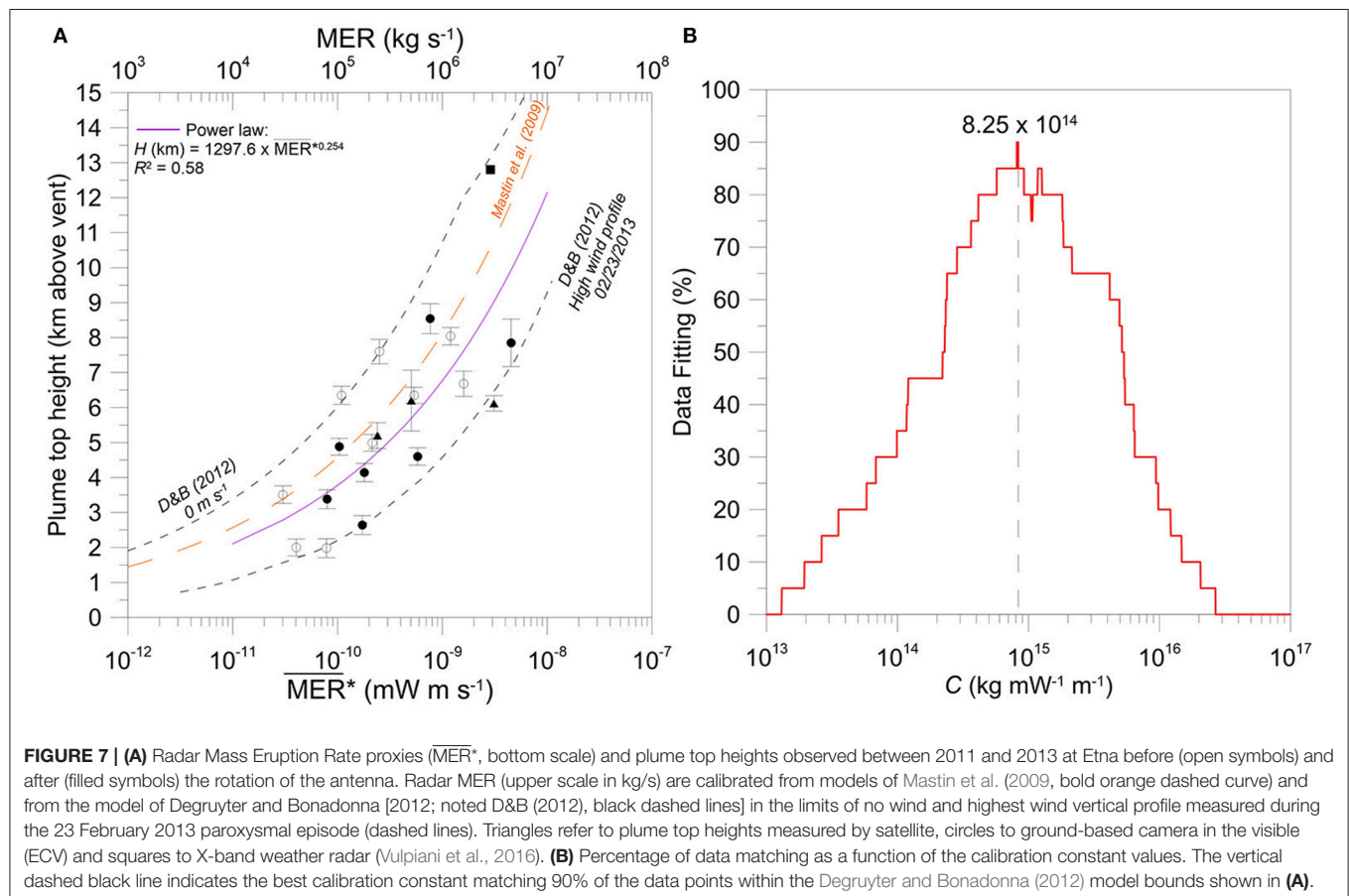


FIGURE 7 | (A) Radar Mass Eruption Rate proxies (MER^* , bottom scale) and plume top heights observed between 2011 and 2013 at Etna before (open symbols) and after (filled symbols) the rotation of the antenna. Radar MER (upper scale in kg/s) are calibrated from models of Mastin et al. (2009, bold orange dashed curve) and from the model of Degruyter and Bonadonna [2012; noted D&B (2012), black dashed lines] in the limits of no wind and highest wind vertical profile measured during the 23 February 2013 paroxysmal episode (dashed lines). Triangles refer to plume top heights measured by satellite, circles to ground-based camera in the visible (ECV) and squares to X-band weather radar (Vulpiani et al., 2016). **(B)** Percentage of data matching as a function of the calibration constant values. The vertical dashed black line indicates the best calibration constant matching 90% of the data points within the Degruyter and Bonadonna (2012) model bounds shown in (A).

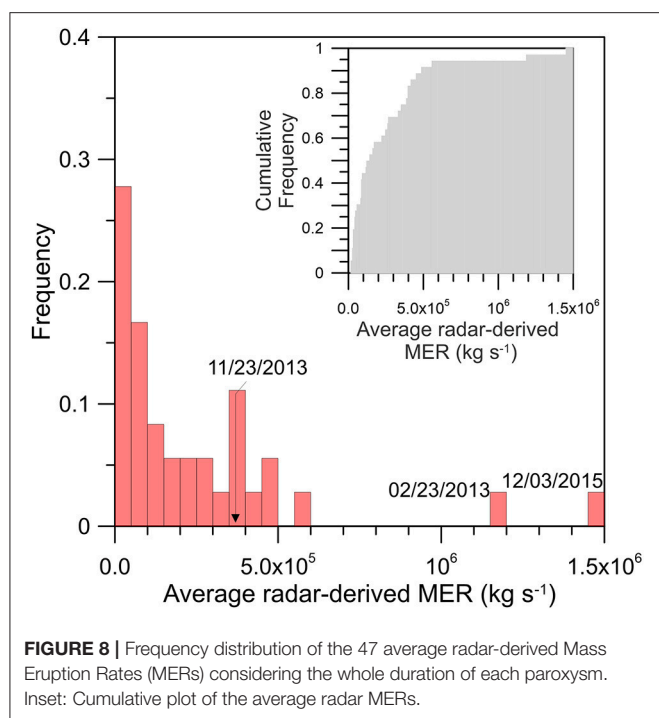


FIGURE 8 | Frequency distribution of the 47 average radar-derived Mass Eruption Rates (MERs) considering the whole duration of each paroxysm. Inset: Cumulative plot of the average radar MERs.

The calibration of the radar-derived MER provides, even in the absence of constraints on plume height, mass loading parameters that could be used by the INGV-OE to routinely initialize VATDMs. Assuming the particle size distribution does not vary significantly among events, MER* can also be used to directly compare the relative intensity of an ongoing paroxysm with previous ones. In addition to the currently implemented automatic detection and warning of onset and ending of a paroxysmal episode, and the real-time provision of near-source ejection velocities, VOLDORAD 2B could now be further used to automatically locate the active crater by means of the range gating and maximum echoes, and to estimate MER of tephra in real-time with high time resolution. The time series of released mass and hence the mass eruption rate show high variability during an event (Figures 3, 5, 6). This highlights the need to take into account the variations of eruption source parameters during the lava fountains of Etna, in particular the mass-loading parameters, in order to better assess tephra plume hazards. The fact that the MER proxies follow closely the variation of the plume top heights reflects the control of tephra plume ascent by the dynamics of the lava fountains and eruptive column (Figure 6).

The MER for instance is known to strongly control plume height (Mastin et al., 2009). Yet, the average MER is often obtained *a posteriori* and considered constant, being usually deduced from the total erupted mass inferred from post-eruption deposit analyses and eruption duration. As shown in Figure 5B, the MERs corresponding to the whole paroxysm durations are underestimating by a factor 2.6 the climax MER, and hence potentially the maximum plume height derived from deposit analyses, whereas 76% of the

TEM in average is released during the climax (Table 1). Figures 5A,B emphasize the high contribution of the climax phase in terms of tephra mass load, still assuming that the particle size distribution remains the same during an event.

Thus, the main eruption source parameters are available to operationally initialize dispersion models and constantly reevaluate their input parameters. In fact, by not taking into account cross wind considerations, Mastin et al. (2009) results are supposed to underestimate the MERs for a given plume top height (Degruyter and Bonadonna, 2012). The systematic procedure used to infer a calibration constant of 8.25×10^{14} kg mW⁻¹ m⁻¹ highlights the spread of our data. Shifting the calibration constant value by a factor of 2 would leave only 80% of the data points inside the Degruyter and Bonadonna (2012) model bounds (Figure 7B). In the case of only 50% matching, the constant varies by a factor of 4–6 toward lower and upper bounds, respectively. Hence, the variation of the calibration constant to obtain absolute MERs, in agreement with Equation 8 and 9, is still reasonable compared to the uncertainty of Mastin et al. (2009)'s formulation (a factor of four within a 50% confidence interval). However, there is still no information concerning the grain size distribution inside lava fountains. The coarsest part of the Total Grain Size Distribution released during Etna's paroxysmal episodes, which falls within the first 5 km from the vents, is rarely sampled (Andronico et al., 2014b; Spanu et al., 2016). Hence, the variability in eruption intensity and fragmentation could lead to different values of the calibration constant *C*, which is also related to the density and size of detected tephra.

Multi-Method Integration

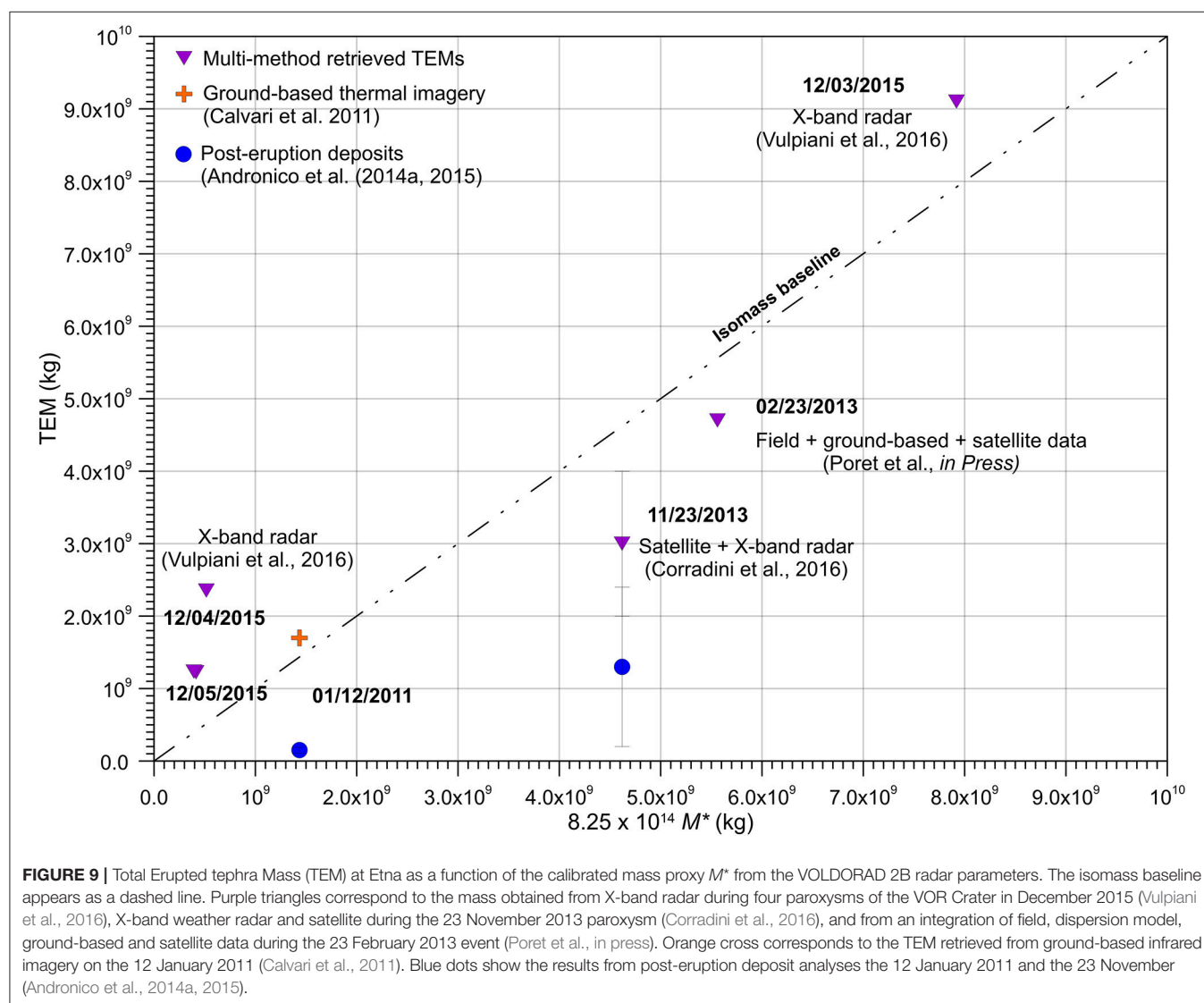
Eruption Source Parameters are essential to initialize VATDMs in order to forecast the impact of tephra plumes and mitigate related risks. The TGSD is a particularly important parameter to estimate and is not provided by our methodology using instead a calibration of the radar mass proxy against other methods. Owing to the scattering theory, electromagnetic methods are mostly sensitive to a given range of particle sizes as a function of their wavelength. Methods such as satellite-based infrared observations, like SEVIRI in the thermal infrared spectral range (Corradini et al., 2016) discriminate fine ash transported in the atmosphere from micron size up to 20 μm (Wen and Rose, 1994). Samples collected in the field are generally upper limited to centimeter-sized lapilli. The X-band weather radar (DPX4; 3 cm-wavelength) in Catania also used to monitor fountain-fed plumes of Etna is mostly sensitive to particles ranging from 25 μm up to lapilli-sized tephra (Marzano et al., 2012). Comparatively, VOLDORAD 2B Doppler radar (23.5 cm wavelength) is mostly sensitive to cm-sized lapilli up to pluridecimetric blocks and bombs. Thus, each technique provides mass load outputs reflecting the mass proportion of the TGSD fraction for which it is the most sensitive. Unsurprisingly, mass estimates should differ among methods, providing for instance TEM underestimates. The mass proportion of each fraction of the TGSD, however, is poorly known. The mass fraction of block-sized particles

in the total, despite its presumably very significant proportion (Spanu et al., 2016), is generally not taken into account. This fraction is well captured by VOLDORAD 2B close to the emission source and mass estimates could be largely improved by integrating its measurements. Behncke et al. (2014) estimated the proportion of distal pyroclastic emission from 2011 to 2012 paroxysms of about $3 \times 10^6 \text{ m}^3$. Such a value corresponds to 14% of the total pyroclastic emission building the NSEC (i.e., the paroxysmal proportion being equal to $19 \times 10^6 \text{ m}^3$). Accordingly, it means that VOLDORAD 2B, by its detection of the lava fountain, is able to detect the maximum total erupted mass from Etna's paroxysmal episodes.

Figure 9 shows the reasonable good agreement between the calibrated TEMs from our radar data and the TEMs retrieved from X-band weather radar, ground-based and satellite-based infrared imagery, and from post-eruption deposit analyses.

Data points scatter across the isomass baseline with 71% of estimates by remote sensing methods within a factor of 3 of our calibrated radar TEMs. Data points falling above the isomass baseline correspond to less material detected by VOLDORAD 2B. These include mainly the VOR Crater paroxysms (3–5 December 2013) and, to a lower degree, the 12 January 2011 NSEC paroxysm. However, those paroxysms, as suggested before, could have been less well sampled, and hence their TEM underestimated by VOLDORAD 2B in Figure 9, owing to activity location offset. This means, therefore, that VOLDORAD 2B TEMs are supposed to be always larger than those found by X-band radar, ground-based and satellite-based infrared data.

In addition, TEMs retrieved from post-eruption deposits by Andronico et al. (2014a, 2015) for the 23 November 2013 and the 12 January 2011 are 2 to 10 times weaker than the remote sensing ones. This is probably due to the lack



of tephra sampling in the first 5–6 km from the NSEC. In fact, Spanu et al. (2016) have shown that a lack of sampling inside the first km from the Southeast Crater, after the 24 November 2006 paroxysm, can lead to a loss of 30% of the TEM. Moreover, Andronico et al. (2014a, 2015) do not consider the deposits on the pyroclastic cone that were instead evaluated by Behncke et al. (2014). Mainly for this reason, we suggest that the total mass derived from deposits should rather be called Plume Erupted Mass instead of Total Erupted Mass of tephra, and this, in the case of a paroxysmal activity involving a fountain-fed plume. Given the particle size overlap among methods, the total grain size distribution could be determined through a multi-frequency combination of remote sensing methods and field sampling, and used in dispersal models (Poret et al., in press). Future efforts should aim at this objective. Indeed, a comparison between radar-inferred TEMs and those obtained by post-eruption deposits could be useful to investigate the issue of partitioning of proximal fallout recorded by VOLDORAD 2B relative to the distal ash mass fraction sampled up to 400 km away from Etna (Andronico et al., 2015).

Finally, the methodology of the radar mass proxy could be transportable to other radars used for the monitoring of other volcanoes. In particular, several scanning Weather Doppler radars are able to measure the above-vent radial velocities and echo power, in addition to detect the whole eruptive column and their internal properties (example of the VARR of Marzano et al., 2006). Weather-radar estimates at the source could be improved thanks to our methodology being independent of the detected particle diameters. Moreover, in terms of multi-method integration, our estimates of near-source ejection velocities from the VOLDORAD data base (Donnadieu et al., 2015) could be used to refine as well the DPX4-inferred MER estimates of the Voragine paroxysms, as suggested by Vulpiani et al. (2016).

CONCLUSIONS

Forty-seven out of the 49 paroxysmal episodes of fountain-fed tephra plumes produced by Etna between January 2011 and December 2015 were analyzed using the high rate data of the 23.5-cm wavelength Doppler radar (VOLDORAD 2B) monitoring the explosive activity of the summit craters. A methodology has been developed to compute a radar mass proxy, and hence a Mass Eruption Rate proxy. In addition to the estimation of near-source ejection velocities with a high time resolution, the radar mass proxies allow to study the dynamics of Etna's paroxysms. Although there is limitation of the full sampling of lava fountains in 2011–2012 and 2015 because of the detection angle of the radar beam, each derived mass parameter during the climax phases and the total duration of the paroxysms seem correlated, and this, no matter the detection limits. Paroxysmal episodes of Etna present highly variable volcanic emission as a function of time but the tephra mass released during the climax phases most commonly represent more than 70% of the total erupted mass.

By calibrating the radar MER proxy with models relating MER to plume height, TEMs and MERs are found to correlate with TEM inferred from independent remote sensors. Eventually, the developed mass proxy methodology allows the real-time assessment of eruption source parameters at Etna, but also at any volcano monitored by Doppler radars. These eruption source parameters include vent location, event duration, near-source ejection velocities, MER evaluation and expected plume top height at first order. This could be integrated into the 24/7 procedure operational during volcanic crises at Mount Etna. Given the lack of information on the total grain size distribution, synergetic efforts should now aim to combine sensors working at different wavelength (radars, ground-based, and satellite imagery) with field deposits analyses to refine the MER and complete TEM during the next paroxysmal activity at Etna, as well as to investigate the partitioning between proximal and distal tephra.

AUTHOR CONTRIBUTIONS

VF-L processed the Doppler radar data. VF-L and FD interpreted the data and wrote the manuscript. SS and MP processed the plume top heights data retrieved by visible imagery. AP developed the original physical model behind the mass proxy methodology. SS and MC provided INGV-OE monitoring data and helped with the writing process of the manuscript. PF, CH, YG, and MP were in charge of radar data acquisition and formatting.

ACKNOWLEDGMENTS

VOLDORAD 2B radar measurements on Etna are carried out in the frame of a collaborative research agreement between the Observatoire de Physique du Globe de Clermont-Ferrand (OPGC, Université Clermont Auvergne, Clermont-Ferrand, France), the French CNRS, and the Istituto Nazionale di Geofisica e Vulcanologia, Osservatorio Etneo, sezione di Catania (INGV-OE). This study used the open-access data bases of OPGC—Université Clermont Auvergne, with support from the EU EPOS and EUROVOLC programs and the French SNOV: VOLDORAD (<http://voldorad.opgc.fr/>) for the Doppler radar data on Etna, and HOTVOLC for the satellite MSG-SEVIRI data. The X-band weather-radar data were provided by the Civil Protection Department (Rome). This study also benefited from funding by the European Union FP7MED-SUV project (Grant agreement 308665), the European Science Foundation in the framework of the Research Networking Programme MeMoVolc, and the TerMex-MISTRALS program of the French CNRS-INSU.

SUPPLEMENTARY MATERIAL

The Supplementary Material for this article can be found online at: <https://www.frontiersin.org/articles/10.3389/feart.2018.00073/full#supplementary-material>

REFERENCES

- Andronico, D., Scillo, S., and Cristaldi, A. (2015). Unexpected hazards from tephra fallout at Mt Etna: the 23 November 2013 lava fountain. *J. Volcanol. Geotherm. Res.* 304, 118–125. doi: 10.1016/j.jvolgeores.2015.08.007
- Andronico, D., Scillo, S., Cristaldi, A., and Lo Castro, M. D. (2014a). Representivity of incompletely sampled fall deposits in estimating eruption source parameters: a test using the 12–13 January 2011 lava fountain deposit from Mt. Etna volcano, Italy. *Bull. Volcanol.* 76:861. doi: 10.1007/s00445-014-0861-3
- Andronico, D., Scillo, S., Lo Castro, M. D., Cristaldi, A., Lodato, L., and Taddeucci, J. (2014b). Eruption dynamics and tephra dispersal from the 24 November 2006 paroxysm at South-East Crater, Mt Etna, Italy. *J. Volcanol. Geotherm. Res.* 274, 78–91. doi: 10.1016/j.jvolgeores.2014.01.009
- Aubry, T. J., Carazzo, G., and Jellinek, A. M. (2017). Turbulent entrainment into volcanic plumes: new constraints from laboratory experiments on buoyant jets rising in a stratified crossflow. *Geophys. Res. Lett.* 44, 10198–10207. doi: 10.1002/2017GL075069
- Behncke, B., Branca, S., Corsaro, R. A., De Beni, E., Miraglia, L., and Proietti, C. (2014). The 2011–2012 summit activity of Mount Etna: birth, growth and products of the new SE crater. *J. Volcanol. Geotherm. Res.* 270, 10–21. doi: 10.1016/j.jvolgeores.2013.11.012
- Bonaccorso, A., Caltabiano, T., Currenti, G., Del Negro, C., Gambino, S., Ganci, G., et al. (2011). Dynamics of a lava fountain revealed by geophysical, geochemical and thermal satellite measurements: the case of the 10 April 2011 Mt Etna eruption. *Geophys. Res. Lett.* 38:L24307. doi: 10.1029/2011GL049637
- Bonaccorso, A., Calvari, S., Currenti, G., Del Negro, C., Ganci, G., Linde, A., et al. (2013). From source to surface: dynamics of Etna's lava fountains investigated by continuous strain, magnetic, ground and satellite thermal data. *Bull. Volcanol.* 75:690. doi: 10.1007/s00445-013-0690-9
- Bonaccorso, A., Calvari, S., Linde, A., and Sacks, S. (2014). Eruptive processes leading to the most explosive lava fountain at Etna volcano: the 23 November 2013 episode. *Geophys. Res. Lett.* 41, 4912–4919. doi: 10.1002/2014GL060623
- Bonadonna, C., Biass, S., and Costa, A. (2015). Physical characterization of explosive volcanic eruptions based on tephra deposits: propagation of uncertainties and sensitivity analysis. *J. Volcanol. Geotherm. Res.* 296, 80–100. doi: 10.1016/j.jvolgeores.2015.03.009
- Bonadonna, C., and Phillips, J. C. (2003). Sedimentation from strong volcanic plumes. *J. Geophys. Res.* 108, 1–28. doi: 10.1029/2002JB002034
- Bonny, E. (2012). *Study of the Ash Plumes From Etna Volcano: a Perspective From Doppler Radar and Deposits Analysis*. Dissertation/master's thesis, Blaise Pascal University, Clermont-Ferrand.
- Bursik, M. (2001). Effect of wind on the rise height of volcanic plumes. *Geophys. Res. Lett.* 18, 3621–3624. doi: 10.1029/2001GL013393
- Calvari, S., Bonaccorso, A., and Pellegrino, A. (2011). *Investigation on the Lava Fountain Events Occurred at Etna between 2011 and 2013. Conferenza A. Rittman: 2014 October 31*, Nicolosi.
- Calvari, S., Salerno, G. G., Spampinato, L., Gouhier, M., La Spina, A., Pecora, E., et al. (2014). An unloading foam model to constrain Etna's 11–13 January 2011 lava fountaining episode. *J. Geophys. Res.* 116, 1–18. doi: 10.1029/2011JB008407
- Corradini, S., Montopoli, M., Guerrieri, L., Ricci, M., Scillo, S., Merucci, L., et al. (2016). A multi-sensor approach for volcanic ash cloud retrieval and eruption characterization: the 23 November 2013 Etna Lava fountain. *Remote Sens.* 8:58. doi: 10.3390/rs8010058
- Corsaro, R. A., Andronico, D., Behncke, B., Branca, S., Caltabiano, T., Ciancitto, F., et al. (2017). Monitoring the December 2015 summit eruption of Mt. Etna (Italy): Implications on eruptive dynamics. *J. Volcanol. Geotherm. Res.* 341, 53–69. doi: 10.1016/j.jvolgeores.2017.04.018
- De Beni, E., Behncke, B., Branca, S., Nicolosi, I., Carluccio, R., D'Ajello Caracciolo, F., et al. (2015). The continuing story of Etna's New Southeast Crater (2012–2014): evolution and volume calculations based on field surveys and aerophotogrammetry. *J. Volcanol. Geotherm. Res.* 303, 175–186. doi: 10.1016/j.jvolgeores.2015.07.021
- Degruyter, W., and Bonadonna, C. (2012). Improving on mass flow rate estimates of volcanic eruptions. *Geophys. Res. Lett.* 39:L16308. doi: 10.1029/2012GL052566
- Donnadieu, F. (2012). “Volcanological applications of Doppler radars: a review and examples from a transportable pulse radar in L-band,” in *Doppler Radar Observations - Weather Radar, Wind Profiler, Ionospheric Radar, and Other Advanced Applications*, eds J. Bech and J. L. Chau (Rijeka: InTech), 409–446.
- Donnadieu, F., Duboscclard, G., Cordesses, R., Druitt, T. H., Hervier, C., Kornprobst, J., et al. (2005). Remotely monitoring volcanic activity with ground-based Doppler radar. *EOS Trans.* 86, 201–204. doi: 10.1029/2005EO210001
- Donnadieu, F., Freville, P., Hervier, C., Coltelli, M., Scillo, S., Prestifilippo, M., et al. (2016). Near-source Doppler radar monitoring of tephra plumes at Etna. *J. Volcanol. Geotherm. Res.* 312, 26–39. doi: 10.1016/j.jvolgeores.2016.01.009
- Donnadieu, F., Freville, P., Rivet, S., Hervier, C., and Cacaull, P. (2015). *The Volcano Doppler Radar Data Base of Etna (VOLDORAD 2B)*. Université Clermont Auvergne – CNRS. Available online at: <http://www.obs.univ-bpclermont.fr/SO/televolc/voldorad/bddtr.php>
- Donnadieu, F., Valade, S., and Moune, S. (2011). Three dimensional transport speed of wind-drifted ash plumes using ground-based radar. *Geophys. Res. Lett.* 38, 1–5. doi: 10.1029/2011GL049001
- Duboscclard, G., Cordesses, R., Allard, P., Hervier, C., Coltelli, M., and Kornprobst, J. (1999). First testing of a volcano Doppler radar (Voldorad) at Mount Etna, Italy. *Geophys. Res. Lett.* 26, 3389–3392. doi: 10.1029/1999GL008371
- Duboscclard, G., Donnadieu, F., Allard, P., Cordesses, R., Hervier, C., Coltelli, M., et al. (2004). Doppler radar sounding of volcanic eruption dynamics at Mount Etna. *Bull. Volcanol.* 66, 443–456. doi: 10.1007/s00445-003-0324-8
- Gouhier, M., and Donnadieu, F. (2008). Mass estimations of ejecta from Strombolian explosions by inversion of Doppler radar measurements. *J. Geophys. Res.* 113:B10202. doi: 10.1029/2007JB005383
- Gouhier, M., and Donnadieu, F. (2010). The geometry of Strombolian explosions: insights from Doppler radar measurements. *Geophys. J. Int.* 183, 1376–1391. doi: 10.1111/j.1365-246X.2010.04829.x
- Gouhier, M., and Donnadieu, F. (2011). Systematic retrieval of ejecta velocities and gas fluxes at Etna volcano using L-Band Doppler radar. *Bull. Volcanol.* 73, 1139–1145. doi: 10.1007/s00445-011-0500-1
- Harris, D. M., and Rose, W. I. (1983). Estimating particle sizes, concentrations, and total mass of ash in volcanic clouds using weather radar. *J. Geophys. Res.* 88, 969–983. doi: 10.1029/JC088iC15p10969
- Hort, M., and Scharff, L. (2016). “Detection of airborne volcanic ash using radar,” in *Volcanic Ash*, eds S. Mackie, K. Cashman, H. Ricketts, A. Rust, and M. Watson (Oxford; Cambridge: Elsevier BV), 131–160.
- Hort, M., Seyfried, R., and Vöge, M. (2003). Radar Doppler velocimetry of volcanic eruptions; theoretical considerations and quantitative documentation of changes in eruptive behaviour at Stromboli volcano, Italy. *Geophys. J. Int.* 154, 515–532. doi: 10.1046/j.1365-246X.2003.01982.x
- Maki, M., Iguchi, M., Maesaka, T., Miwa, T., Tanada, T., Kozono, T., et al. (2016). Preliminary results of weather radar observations of sakurajima volcanic smoke. *J. Disaster Res.* 11, 15–30. doi: 10.20965/jdr.2016.p0015
- Marzano, F. S., Barbieri, S., Vulpiani, G., and Rose, W. I. (2006). Volcanic ash cloud retrieval by ground-based microwave weather radar. *IEEE Trans. Geosci. Remote Sens.* 44, 3235–3246. doi: 10.1109/TGRS.2006.879116
- Marzano, F. S., Picciotti, E., Montopoli, M., and Vulpiani, G. (2013). Inside volcanic clouds: remote sensing of ash plumes using microwave weather radars. *Bull. Am. Meteorol. Soc.* 94, 1567–1586. doi: 10.1175/BAMS-D-11-00160.1
- Marzano, F. S., Picciotti, E., Vulpiani, G., and Montopoli, M. (2012). Synthetic signatures of volcanic ash cloud particles from X-Band dual-polarization radar. *IEEE Trans. Geosci. Remote Sens.* 50, 193–211. doi: 10.1109/TGRS.2011.2159225
- Mastin, L. G., Guffanti, M., Servranckx, R., Webley, P., Barsotti, S., Dean, K., et al. (2009). A multidisciplinary effort to assign realistic source parameters to models of volcanic ash-cloud transport and dispersion during eruptions. *J. Volcanol. Geotherm. Res.* 186, 10–21. doi: 10.1016/j.jvolgeores.2009.01.008
- Montopoli, M. (2016). Velocity profiles inside volcanic clouds from three-dimensional scanning microwave dual polarization Doppler radars. *J. Geophys. Res. Atmos.* 121, 7881–7900. doi: 10.1002/2015JD023464
- Morton, B., Taylor, G., and Turner, J. (1956). Gravitational turbulent convection from maintained and instantaneous sources. *Proc. R. Soc. Lond.* 234, 1–23. doi: 10.1098/rspa.1956.0011.

- Poret, M., Costa, A., Andronico, D., Scollo, S., Gouhier, M., and Cristaldi, A. (in press). Modeling eruption source parameters by integrating field, ground-based and satellite-based measurements: the case of the 23 February 2013 Etna paroxysm. *J. Geophys. Res. Solid Earth*. doi: 10.1002/2017JB015163
- Prata, A. J., and Grant, I. F. (2001). Retrieval of microphysical and morphological properties of volcanic ash plumes from satellite data: application to Mt. Ruapehu, New Zealand. *Q. J. R. Meteorol. Soc.* 127, 2153–2179. doi: 10.1002/qj.49712757615
- Sauvageot, H. (1992). *Radar Meteorology*, Artech House. Boston, MA.
- Scharff, L., Hort, M., and Varley, N. R. (2015). Pulsed Vulcanian explosions: a characterization of eruption dynamics using Doppler radar. *Geology* 43, 995–998. doi: 10.1130/G36705.1
- Scollo, S., Boselli, A., Coltelli, M., Leto, G., Pisani, G., Prestifilippo, M., et al. (2015). Volcanic ash concentration during the 12 August 2011 Etna eruption. *Geophys. Res. Lett.* 42, 2634–2641. doi: 10.1002/2015GL063027
- Scollo, S., Prestifilippo, M., Coltelli, M., Peterson, R. A., and Spata, G. (2010). A statistical approach to evaluate the tephra deposit and ash concentration from PUFF model forecasts. *J. Volcanol. Geotherm. Res.* 200, 129–142. doi: 10.1016/j.jvolgeores.2010.12.004
- Scollo, S., Prestifilippo, M., Pecora, E., Corradini, S., Merucci, L., Spata, G., et al. (2014). Height estimation of the 2011–2013 Etna lava fountains. *Ann. Geophys.* 57:S0214. doi: 10.4401/ag-6396
- Scollo, S., Prestifilippo, M., Spata, G., D'Agostino, M., and Coltelli, M. (2009). Monitoring and forecasting Etna volcanic plumes. *Nat. Hazards Earth Syst. Sci.* 9, 1573–1585. doi: 10.5194/nhess-9-1573-2009
- Seyfried, R., and Hort, M. (1999). Continuous monitoring of volcanic eruption dynamics: a review of various techniques and new results from a frequency-modulated radar Doppler system. *Bull. Volcanol.* 60, 624–639. doi: 10.1007/s004450050256
- Spanu, A., de' Micheli Vitturi, M., and Barsotti, S. (2016). Reconstructing eruptive source parameters from tephra deposit: a numerical study of medium-sized explosive eruptions at Etna volcano. *Bull. Volcanol.* 78:59. doi: 10.1007/s00445-016-1051-2
- Sparks, R. S. J., Bursik, M. I., Carey, S. N., Gilbert, J. S., Glaze, L. S., Sigurdsson, H., et al. (1997). *Volcanic Plumes*. Chichester: Wiley.
- Ulivieri, G., Ripepe, M., and Marchetti, E. (2013). Infrasound reveals transition to oscillatory discharge regime during lava fountaining: implication for early warning. *Geophys. Res. Lett.* 40, 1–6. doi: 10.1002/grl.50592
- Valade, S., Donnadieu, F., Lesage, P., Mora, M. M., Harris, A., and Alvarado, G. E. (2012). Explosion mechanisms at Arenal volcano, Costa Rica: an interpretation from integration of seismic and Doppler radar data. *J. Geophys. Res.* 117:B01309. doi: 10.1029/2011JB008623
- Vulpiani, G., Ripepe, M., and Valade, S. (2016). Mass discharge rate retrieval combining weather radar and thermal camera observations. *J. Geophys. Res. Solid Earth* 121, 5679–5695. doi: 10.1002/2016JB013191
- Wen, S., and Rose, W. I. (1994). Retrieval of sizes and total masses of particles in volcanic clouds using AVHRR bands 4 and 5. *J. Geophys. Res.* 99, 5421–5431. doi: 10.1029/93JD03340
- Wilson, L., Sparks, R. S. J., Huang, T. C., and Watkins, N. D. (1978). The control of volcanic column heights by eruption energetics and dynamics. *J. Geophys. Res.* 83, 1829–1836. doi: 10.1029/JB083iB04p01829
- Woodhouse, M. J., Hogg, A. J., Phillips, J. C., and Sparks, R. S. J. (2013). Interaction between volcanic plumes and wind during the 2010 Eyjafjallajökull eruption, Iceland. *J. Geophys. Res.* 118, 92–109. doi: 10.1029/2012JB009592

Conflict of Interest Statement: The authors declare that the research was conducted in the absence of any commercial or financial relationships that could be construed as a potential conflict of interest.

Copyright © 2018 Freret-Lorgeril, Donnadieu, Scollo, Provost, Fréville, Guéhenneux, Hervier, Prestifilippo and Coltelli. This is an open-access article distributed under the terms of the Creative Commons Attribution License (CC BY). The use, distribution or reproduction in other forums is permitted, provided the original author(s) and the copyright owner are credited and that the original publication in this journal is cited, in accordance with accepted academic practice. No use, distribution or reproduction is permitted which does not comply with these terms.



First Volcanic Plume Measurements by an Elastic/Raman Lidar Close to the Etna Summit Craters

Antonella Boselli¹, Simona Scollo^{2*}, Giuseppe Leto³, Ricardo Zanmar Sanchez³, Alessia Sannino⁴, Xuan Wang⁵, Mauro Coltelli² and Nicola Spinelli⁴

¹ Consiglio Nazionale delle Ricerche, Istituto di Metodologie per l'Analisi Ambientale, CNR-IMAA, Tito Scalo, Italy, ² Istituto Nazionale di Geofisica e Vulcanologia, Osservatorio Etno, Catania, Italy, ³ Istituto Nazionale di Astrofisica – Osservatorio Astrofisico di Catania, Rome, Italy, ⁴ Dipartimento di Fisica – Università di Napoli “Federico II”, Consorzio Nazionale Interuniversitario per le Scienze Fisiche della Materia (CNSIM), Naples, Italy, ⁵ Dipartimento di Fisica, Consiglio Nazionale delle Ricerche, Istituto Superconduttori, Materiali Innovativi e Dispositivi, CNR-SPIN, Università di Napoli “Federico II”, Naples, Italy

OPEN ACCESS

Edited by:

Clive Oppenheimer,
University of Cambridge,
United Kingdom

Reviewed by:

Corrado Cimarelli,
Ludwig-Maximilians-Universität
München, Germany
Matthias Tesche,
University of Hertfordshire,
United Kingdom

*Correspondence:

Simona Scollo
simona.scollo@ingv.it;
simona.scollo@ct.ingv.it

Specialty section:

This article was submitted to
Volcanology,
a section of the journal
Frontiers in Earth Science

Received: 28 February 2018

Accepted: 10 August 2018

Published: 24 September 2018

Citation:

Boselli A, Scollo S, Leto G,
Sanchez RZ, Sannino A, Wang X,
Coltelli M and Spinelli N (2018) First
Volcanic Plume Measurements by an
Elastic/Raman Lidar Close to the Etna
Summit Craters.
Front. Earth Sci. 6:125.
doi: 10.3389/feart.2018.00125

Volcanic emissions represent a well-known hazard mainly for aviation safety that can be reduced with real time observations and characterization of eruptive activity. In order to mitigate risks from volcanic ash, Lidar observations allow to perform immediate and accurate detection of volcanic plumes, quantify volcanic ash concentration in atmosphere and characterize optical properties of volcanic particles, improving modeling of volcanic ash clouds and their potential impact. From 14 to 17 December, 2013, Mt. Etna, in Italy, showed an intense Strombolian activity from the New South East Crater (NSEC). Lidar measurements were performed in Catania, pointing at a thin volcanic plume, clearly visible and dispersed from the summit craters toward the South East. Real-time Lidar observations captured the complex dynamics of the volcanic plume along with the pulsatory nature of the explosive activity and allowed to analyze the geometrical, optical and microphysical properties of the volcanic ash. Both the aerosol backscattering (β_A) and the extinction coefficient (α_A) profiles at 355 nm, and their ratio [the Lidar Ratio (LR)] were measured near the volcanic source using an Elastic/Raman Lidar system. Moreover, calibrated particle linear depolarization values (δ_A) were obtained from Lidar profiles measured in the parallel and cross polarized channels at 355 nm, thus allowing to characterize the particle shape. The β_A , LR, and δ_A values were used to estimate the ash concentration (γ) profiles in the volcanic plume. This is the first study of optical properties of volcanic particles through Elastic/Raman measurements near volcanic summit craters and one of few studies which quantify the impact of weak eruptive activity in atmosphere, demonstrating that ash concentration from this type of activity was lower than the safety concentration threshold established by the International Civil Aviation Organization.

Keywords: Etna, volcanic aerosol, Elastic/Raman Lidar, optical properties, ash concentration

INTRODUCTION

The amount and composition of silicate particles and gasses emitted during volcanic eruptions are the result of very complex processes (Robock and Oppenheimer, 2003) which depend on different variables, such as chemistry of magma and mechanisms of its ejection and removals. During explosive eruptions, silicate particles and gasses mainly made of water vapor, carbon, and

sulfur dioxides, are continuously released in the atmosphere (Sparks et al., 1997). Volcanic aerosols interact with the Earth's dynamic atmosphere affecting both terrestrial and marine ecosystems, human health, and microphysical processes in clouds and climate (Delmelle et al., 2002; Delmelle, 2003; Horwell, 2007; Ayris and Delmelle, 2012; Witt et al., 2017). Eruption produced aerosol strongly influence air quality especially in regions close to active volcanoes, nonetheless these effects may also be found many kilometers away from the volcanic vent at a regional scale (e.g., Azzopardi et al., 2013; Ayris et al., 2014). Volcanic emissions also represent a serious hazard to aviation safety because of the well-known damages to airplane engines and the drop of atmospheric visibility (Miller and Casadevall, 2000; Guffanti et al., 2005; Weinzierl et al., 2012; Kueppers et al., 2014; Song et al., 2014).

The volcanic plume impact reduction, which is nowadays a mandatory and scientifically recognized need (Bonadonna et al., 2012), can be better understood only with real-time observations. Real-time observations provide a unique opportunity to follow the volcanic process evolution, characterizing the eruption intensity variation over time (Bonadonna et al., 2015; Scollo et al., 2015). Furthermore, the knowledge of the atmospheric particles content may be very useful to define the eruption style and discriminate sulfate and/or water vapor dominated plumes that is very important to understand their atmospheric contribution, having the erupted particles many implications in climate and environmental effects (Scollo et al., 2012a,b). In this respect, remote sensing instruments can improve the monitoring capability of volcanic ash dispersion and fallout, helping the data interpretation and optimization for a real-time alert and rapid warning dissemination (Ripepe et al., 2013; Corradini et al., 2016). Results of real time observations are also useful to improve volcanic ash forecasts (Scollo et al., 2015).

Among the remote sensing techniques, Lidar represents one of the most efficient techniques in the atmospheric studies, since it gives reliable information on the characteristics of particles and gas with high spatial and temporal resolution. During the 2010 Eyjafjallajökull volcano eruption (Bonadonna et al., 2011; Gudmundsson et al., 2012; Stevenson et al., 2012), Lidar systems demonstrated their potentiality to study the volcanic emissions impact on a continental scale giving quantitative data about the presence of the volcanic cloud and its layering and optical characteristics (Ansmann et al., 2010, 2011; Marenco and Hogan, 2011; Marenco et al., 2011; Papayannis et al., 2012; Sicard et al., 2012; Navas-Guzmán et al., 2013; Pappalardo et al., 2013; Trickl et al., 2013; Balis et al., 2016). During the Eyjafjallajökull eruption, near real time data were available from ground based Lidar of the European Aerosol Research Lidar NETwork (EARLINET), giving large scale information on both particle content and ash concentration.

Mount Etna in Italy is one of the most active volcanoes of the world and, for this reason it is regularly monitored mainly by several ground-based instruments (e.g., Scollo et al., 2014). Recently, the Lidar technique has been routinely used

to monitor Etna's explosive activity successfully giving unique information on the aerosol properties above the volcano (Scollo et al., 2012a; Mereu et al., 2018). Most of the papers concerning Lidar monitoring of volcanic plume analyzed the properties of aged volcanic particles transported over long distances in the troposphere and stratosphere (Sassen et al., 2007; Wang et al., 2008; Miffre et al., 2011; Kokkalis et al., 2013) while Lidar measurements of fresh volcanic ash in the proximity of active craters are still limited. The main limitation in using Lidar techniques is the decrease of the signal dynamic due to the presence of high optical depth layers. However, this constraint is mainly related to large explosive eruptions, which are not so frequent at Etna. Nonetheless, low concentration plumes produced by small intensity explosive eruptions could contaminate the air space over the near international airport in Catania, located only 26 km away from Etna summit's craters. Low intensity activity is not considered dangerous for aviation safety because the amount of associated ash would be considered not harmful for aircrafts. However, so far no measurement ever proved that the ash concentration associated to this type of activity is lower than the safety concentration threshold established by the International Civil Aviation Organization (ICAO, 2010).

The elastic backscatter Lidars are the most common and low cost systems able to measure geometrical features of an aerosol layer in the atmosphere and the aerosol backscatter coefficient. Lidars with Raman capabilities give a better characterization of the aerosol properties by simultaneously measuring the aerosol backscattering and extinction profiles. This allows to directly determining the extinction-to-backscatter ratio profile, also called LR. The LR parameter depends on the shape, size, and chemical composition of the aerosol (Ackermann, 1998; Müller et al., 2007), and it is useful to characterize the aerosol typology. Theoretical and experimental values of these parameters are reported in the literature for different aerosol types but studies of LR of freshly ejected volcanic ash are still few. Raman measurements carried out during the 2010 Eyjafjallajökull eruption showed, for example, LR values ranging between 50 and 82 steradians (sr) (Ansmann et al., 2010; Marenco and Hogan, 2011; Hervo et al., 2012; Mona et al., 2012). LR reported values, measured over Europe many kilometers away from the volcano, can change with time and distance from it and are indicative of a modification of the volcanic plume composition during the transport in the troposphere. Nevertheless, to the best of our knowledge, measurements of LR of volcanic ash performed shortly after its emission are not yet available at Etna.

A direct measurement of LR has been reported here as proxy from Etna at about 25 km away from the summit craters. The LR data measurements on freshly ejected volcanic aerosol offer great potential for sensitivity studies in transport and climatological model applications, hence, represent a reference value for Lidar applications to volcanic emissions. In this paper, we present the results of Elastic/Raman Lidar measurements carried out during the 16 December, 2013 Etna explosive activity and we show the measurements of volcanic plume optical parameters detected near the summit craters.

MATERIALS AND METHODS

Volcanological Data

The Istituto Nazionale di Geofisica e Vulcanologia, Osservatorio Etneo (INGV-OE) performs daily forecast of volcanic ash for some eruptive Etna scenarios using automatic procedures that download weather forecast data from meteorological mesoscale models, run models of tephra dispersal, plot hazard maps of volcanic ash dispersal and deposition for certain scenarios and publish the results on the Italian Civil Protection dedicated web-site (Scollo et al., 2009). The system has been working since 2009 and, furthermore, since 2012 forecasts include also the Maltese area, in the frame of the VAMOS SEGURO (Volcanic Ash Monitoring and Forecasting between Sicilia and Malta arEa and sharingG of the resUlts foR aviatiOn safety) project¹. Moreover, INGV-OE has several cameras recording images in the visible and infrared bands; they are located in Catania (ECV, 27 km from the summit craters), Milo (EMV, 11 km from the summit craters), Nicolosi (ENV and ENT, 15 km from the summit craters), Schiena dell'Asino (ESV, 5 km SE from the summit craters), Monte Cagliato (EMCT, 8 km E from the summit craters), and La Montagnola (EMOV and EMOT, 3 km SE from the summit craters). The images of those cameras are used by the volcanologist on duty to monitor any variation of volcanic activity and estimate the eruption column height (Scollo et al., 2014).

Lidar System

An innovative Lidar system was developed in the frame of the VAMOS SEGURO project, with the aim of studying and forecasting volcanic ash plumes from Etna. The Lidar, named Aerosol Multi-Wavelength Polarization Lidar Experiment (AMPLE) and developed by the Consorzio Interuniversitario per le Scienze Fisiche della Materia (CNISM), is a compact multi-wavelength Elastic/Raman scanning system with depolarization capability, suitable for mobile measurements and able to carry out 4-D (space and time) imaging of volcanic particles distributions, their optical properties and microphysical characterization. The AMPLE Lidar is equipped with a doubled and tripled Nd:YAG diode-pumped laser with a repetition rate of 1 kHz and average optical power of 0.6 W at 355 nm, 1.5 W at 532 nm, and 1 W at 1,064 nm. The relative high repetition rate laser source increases the detectable signal dynamic range allowing to perform measurements even in the case of high density aerosol load, such as those ejected during massive explosive eruptions or heavy dust storm events. The receiving system is based on a 25 cm modified Cassegrain telescope. The detection system is able to measure both the elastic Lidar returns at 355 nm (parallel and cross-polarized signals) and the N₂ Raman Lidar echoes at 386 nm. Due to its modular configuration the system has been upgraded on 2016 with channels at 532 nm (parallel and cross-polarized signals) and the N₂ Raman channel at 607 nm. Each detected signal is acquired by a multi-channel scaler with a raw spatial resolution of 15 m.

¹<http://www.vamosseguero.eu>

In order to verify the accuracy of parameter measured by AMPLE Lidar system inter comparison measurements were performed with the EARLINET (European Aerosol Research Lidar Network) (Bösenberg et al., 2001, 2003) Lidar system MALIA (Multi-wavelength Aerosol Lidar Apparatus) located in Naples. MALIA is periodically calibrated for depolarization measurements through the technique proposed by Freudenthaler et al. (2009). Calibration methods and results are detailed in Wang et al. (2015). At present, the AMPLE system is part of the EARLINET network² and it is devoted to special measurement campaigns at Etna volcano. The Lidar system was operated at the Istituto Nazionale di Astrofisica in Catania about 25 km away from the summit craters. Lidar derived aerosol properties are studied in terms of the boundaries of the observed layers, aerosol extinction (α_A), and backscattering (β_A) coefficients profiles, their ratio (LR), and calibrated particle linear depolarization ratio (δ_A).

The α_A coefficient was retrieved by means of the method introduced by Ansmann et al. (1990) from N₂ Raman Lidar signal measured at 386 nm during night-time. The retrieval of the β_A coefficient at 355 nm from night-time observations was performed by using the Raman method (Ansmann et al., 1992) based on simultaneous detection of both elastic and N₂ Raman Lidar echoes. In a different way, the retrieval of the β_A coefficient at 355 nm from daytime measurements was obtained by using the Klett–Fernald algorithm (Klett, 1981; Fernald, 1984). The Elastic/Raman technique provides an independent estimation of β_A and α_A vertical profiles; in this way the LR can be directly measured along the beam path. This parameter is essential in the optical properties retrieval and it is generally assumed to be known in the inversion procedure using the Klett–Fernald algorithm requiring a hypothesis on the LR value. The LR values choice should be carefully evaluated to prevent large uncertainty on the retrieved value of the backscattering coefficient. In our analysis the uncertainty due to a LR assumption was removed. For daytime observations, we fixed the LR values having as references the values of LR determined by the nearest time Raman measurements. The δ_A values were obtained from the elastic Lidar profiles measured in the parallel and cross-polarized channels at 355 nm according to Biele et al. (2000) and Freudenthaler et al. (2009) inversion procedures. The depolarization of aerosol can be used to discriminate aerosol shape and to identify the presence of non-spherical particles with higher depolarization ratios (Gasteiger et al., 2011) in the atmospheric sample sounded by the Lidar. In our analysis the polarization Lidar technique was used to recognize the volcanic product and to distinguish the particles shape and thermodynamic phase in the emitted plume.

Due to the different gain of the detection channels or to the different optical transmission efficiency, the δ_A calibration is essential since the uncertainty related to the particle depolarization ratio retrieval affects the accuracy of the derived parameters.

In order to calibrate the Lidar depolarization channels, we used a two-step procedure. The first step is the correction of

²<https://www.earlinet.org>

gain ratio by means of a depolarizer plate placed in the receiver. The depolarizer plate makes the return light unpolarised and let us to calibrate the difference of gain between parallel and cross-polarized channels. However, since the light emitted from a laser is not completely polarized, optical components drawbacks also add depolarisation to the signal so calibration by depolarizer plate is not enough.

The second step is the correction of the depolarization caused by transmitting and receiving optical systems using pure molecular scattering. Since the depolarization ratio of atmospheric molecules is determined in the Lidar system using very narrow filters, pure molecular scattering profile (Behrendt and Nakamura, 2002) is used to calibrate the depolarization of AMPLE.

Finally, ash mass concentration (γ) was evaluated using the δ_A and LR profiles, measured in the observed plume and following the methodology of Tesche et al. (2009) and Ansmann et al. (2011) detailed in the work of Pisani et al. (2012), already applied by Scollo et al. (2012b, 2015).

RESULTS

The December 14th–17th 2013 Etna Eruption

Etna eruptions are mainly produced from the summit craters (e.g., Alparone et al., 2003; Behncke et al., 2006; Scollo et al., 2013) and from some fractures opened on the volcano flanks (e.g., Rittmann, 1973; Branca and Del Carlo, 2005). In late 2009 a new crater, the New South East Crater (NSEC), formed at the base of the eastern flank of the South East Crater (SEC) (e.g., Calvari et al., 2011) and became one of the most active and biggest crater in the recent eruptive story of Etna (Behncke et al., 2014) with 25 eruptive episodes between January 2011 and April 2012. The explosive activity of the SEC was mainly characterized by powerful lava fountains forming eruption columns that often reached the tropopause (Scollo et al., 2014).

The 14–17 December eruption at Etna was preceded by Strombolian activity accompanied by a gradual increase of volcanic tremors until 2 December, when the last lava fountain event of 2013 occurred (INGV-OE, 2013a). Ash emission and intense Strombolian activity characterized the period between 14 and 17 December, 2013 (INGV-OE, 2013b). This activity was well-recorded by the INGV-OE video surveillance system. On 14 December, there was a resumption of the explosive activity from the NSEC at 08:24 GMT with an ash emission event forming a thin volcanic plume reaching about 2 km a.s.l. high. After this explosion, a small vent opened on the edge of the NSEC, producing Strombolian activity forming a weak volcanic plume that was dispersed toward the East-South East. The activation of a new lava flow directed toward the Valle del Bove was observed at about 22:23 GMT. In the early morning of 15 December, two new vents opened on the NSEC flank at about 05:10 and 05:33 GMT, while Strombolian activity persisted with variable intensity. Both the explosive and effusive activity went on until 16 December when, at about 13:30 GMT, a new eruptive fracture opened on the lower part of the North-East flank (**Figure 1a**)

that also formed a small lava flow well-visible during the night (**Figure 1b**). Explosive activity was clearly detected at 14:50 and 15:36 GMT from both the EMOV and EMOT cameras, located at about 2,500 m a.s.l., while the ECV camera showed a cloud cover above Catania (**Figures 1c–h**). **Figure 2** shows the eruptive activity observed by EMOH, EMOT, and EMCT cameras during Lidar measurements. The videos highlighted two lava flows and a weak decrease of the explosive activity during the evening. The clockwise variations of tephra fallout, as it is shown by INGV-OE volcanic ash forecasts (Scollo et al., 2009), interested the South East and South flanks (**Figure 3**) of the volcano. Ash fallout reported in Acitrezza, Acicastello, and Catania³ and formed a thin tephra deposit. The explosive activity ended during the first hours of 17 December, 2013, while the lava flow finally stopped during the night between 18 and 19 December, 2013.

Lidar Data

Several zenith Lidar observations, with 1 min integration time, were performed on 16 December, 2013 when an eruptive cloud of ash, driven by winds in the South direction (**Figure 3**), was visible in Catania. Long time measurement at 355 nm were continuously performed from 10:45 to 17:33 GMT; during this time period three measurements lasting 30 min using a depolarizer for calibration of the depolarization were carried out. The analysis of each Lidar profile measured during the morning revealed fast moving atmospheric clouds mainly composed of water vapor ($\delta_A < 5\%$) at lower altitude ($< 1,400$ m), while a slightly depolarizing layer ($5\% < \delta_A < 10\%$) was visible between about 1,400 and 2,000 m, suggesting the presence of irregular particles in the atmosphere. The upper layer was stable in the altitude range. This detected layer could result from water vapor cloud and volcanic ash mixture. In the data inversion procedure for this layer, we used a LR of 50 sr, as determined by the closest Elastic/Raman measurement. Nevertheless, below 1,400 m we used a smaller LR value (30 sr), according to low cloud presence together with a contribution of volcanic particles. Diurnal observations showed a decrease with time in the measured backscattering below 2,000 m; this is probably due to the waning of the explosive activity at the NSEC as also qualitatively visible in the images taken by video cameras. After 15:36 GMT, a new layer with $\delta_A > 10\%$ was clearly visible in the backscatter profiles between 3 and 4 km. This new layer might be interpreted as volcanic ash coming from the new eruptive fracture opened on the lower North-East Side of the NSEC flank, producing a small lava flow detected by camera and visual observations. In **Figure 4** the map of the range corrected Lidar signals (RCS) for those measurements performed on 16 December, 2013 from 16:30 to 17:30 GMT, with a spatial resolution of 15 m and a temporal resolution of 60 s, is reported. The figure highlights both the first layer due to diurnal emission below 2 km of altitude and the second more depolarizing volcanic layer between 3 and 4 km.

Raman measurements were performed since 16:30 GMT and allowed to detect, for the first time, the LR profiles of the volcanic

³www.ct.ingv.it

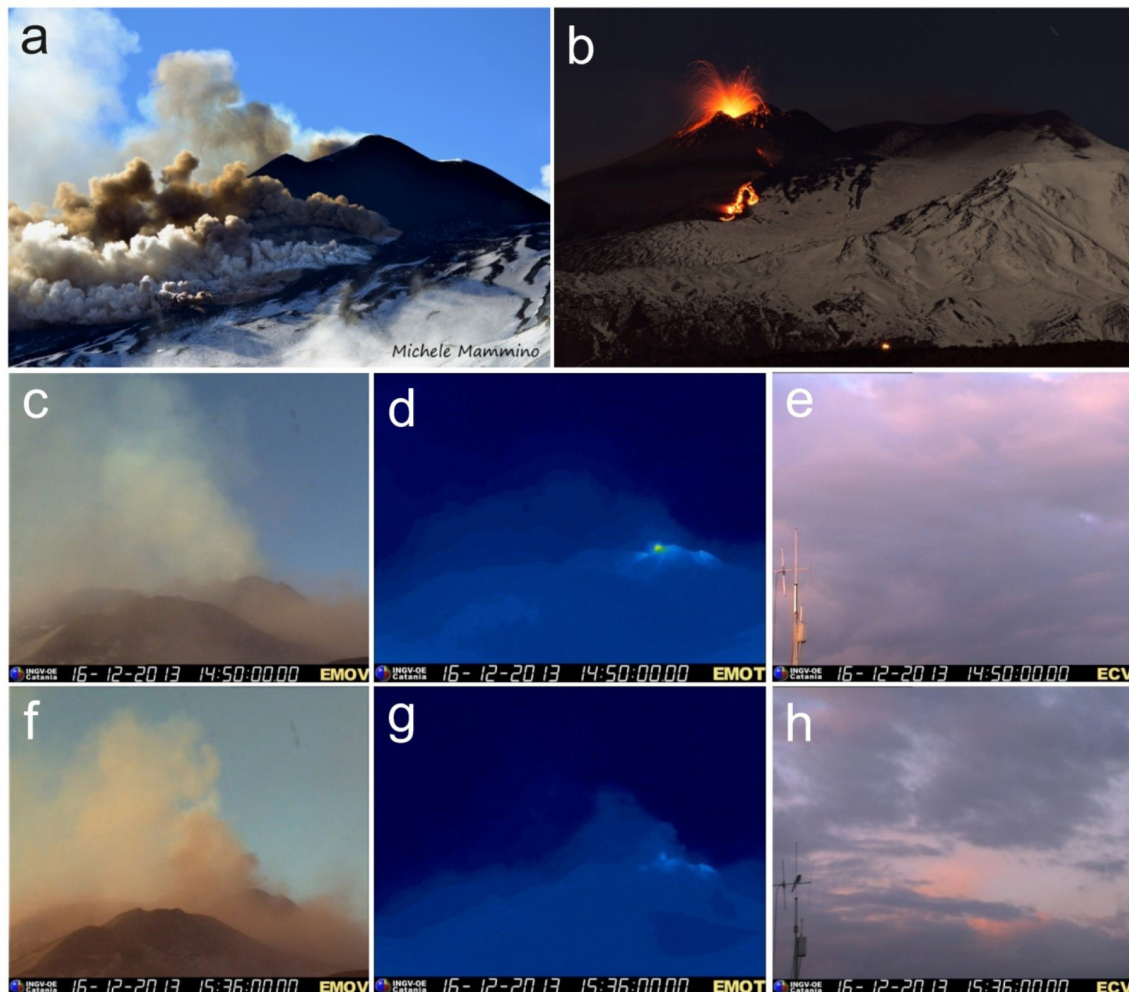


FIGURE 1 | Explosive activity during 16 December, 2016. **(a)** Photo of the eruptive fissures opened at about 13:00 GMT taken by Michele Mammino; **(b)** Photo of the lava flow coming from the same fracture taken by Francesco Mangiaglia; strombolian activity retrieved at 14:50 GMT by **(c)** EMOV, **(d)** EMOT and **(e)** ECV cameras; and at 15:36 GMT retrieved by **(f)** EMOV, **(g)** EMOT, and **(h)** ECV cameras.

plume near Mount Etna's summit craters. **Figure 5** reports the Lidar profiles of β_A , α_A , LR, and δ_A obtained from measurements carried out at 17:00 GMT. In order to enhance the signal to noise ratio, the Lidar profiles were reported with 15 min integration time; moreover, a binning procedure was performed on lidar signals in the data analysis, therefore the vertical resolution was reduced to 60 m for β_A and δ_A profiles, while it was 180 m for α_A and LR profiles. Lidar measurements highlight two different signatures of fresh volcanic ash in the altitude ranges between 3,000–3,400 m and 3,400–4,100 m. The δ_A mean values in these layers resulted 49.7 and 43.5%, respectively. The very high δ_A values measured along the vertical profile (up to $75 \pm 19\%$) correspond to ash with highly irregular shape. This result could reflect the fragmentation of hot basaltic magma with low viscosity that produces juvenile ash with elongated shape cooling in the atmosphere.

Larger concentrations of ash particles were detected in the higher range of altitude ($5.5 \times 10^{-4} \text{ g/m}^3$) with respect to the

values in the lower one ($2.3 \times 10^{-4} \text{ g/m}^3$). This is in agreement with larger LR mean values in the higher layer (53 sr) compared to the one measured in the lower layer (35 sr). LR and δ_A measured values were in agreement with the volcanic ash classification scheme at 355 nm showing LR values higher than 40 sr and δ_A higher than 33%, as reported by Groß et al. (2015). These values clearly indicate the presence of non-spherical particles and suggest a large fraction of glass and mineral aerosols. The δ_A values, measured in the plume developed in the afternoon, are different from the values measured in the morning at lower altitude; this suggests a different shape of volcanic particles and reflects the increase of explosive activity in the afternoon.

The LR, δ_A , and γ_A averaged values in the layers resulting from the afternoon measurements of 16 December, 2013 are reported in **Table 1**. The mean properties inside each layer changed during the time, highlighting a temporal evolution of the vertical distribution of the aerosol load and possible changes in its composition. The δ_A values of the higher layer rapidly

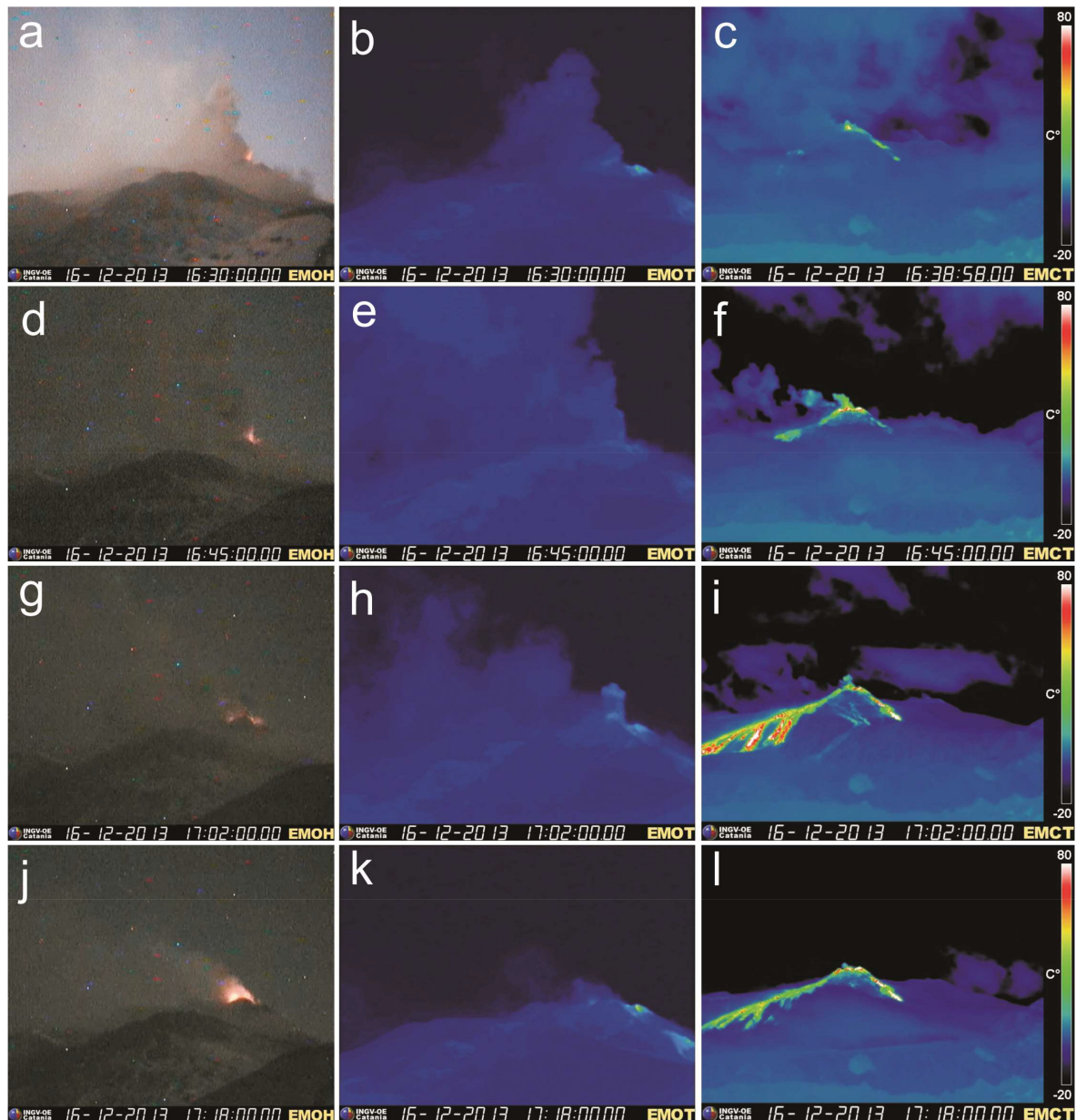


FIGURE 2 | Explosive activity retrieved by EMOH (a,d,g,j), EMOT (b,e,h,k), and EMCT (c,f,i,l) cameras on 16 December, 2013 during the Lidar measurements.

increased with time going up to 44%, while, LR resulted in about 48 sr due to the presence of volcanic ash in the layer and it did not change with time after the 16:45 GMT. The lack of significant variability of the LR in the observed volcanic plume suggests the presence of the same type of aerosol. Despite the high depolarizing nature of the observed plume, the multiple scattering influence in our measurement was not relevant due to both the short distance of the plume from the Lidar and the low values of the optical depth (OD) measured in the plume < 0.1 .

In the Planetary Boundary Layer (PBL) whose top height was located at 1,100 m of altitude during the time measurements,

we observed a slightly decrease in the LR values with time, which suggests a change in the dominant aerosol typology. The observed behavior could be related to the contribution of the diurnal ash, located in the range 1,400–2,000 m, which feels across the PBL and mixed up with local marine aerosol. The mixed aerosol in the PBL shows lower δ_A values thus suggesting a more pronounced spherical particle shape. Finally, the larger LR values obtained in the range 1,100–3,000 m fit well with the higher values obtained in volcanic ash plumes (Groß et al., 2012), when volcanic sulfate particles were mixed with anthropogenic particles (Navas-Guzmán et al., 2013).

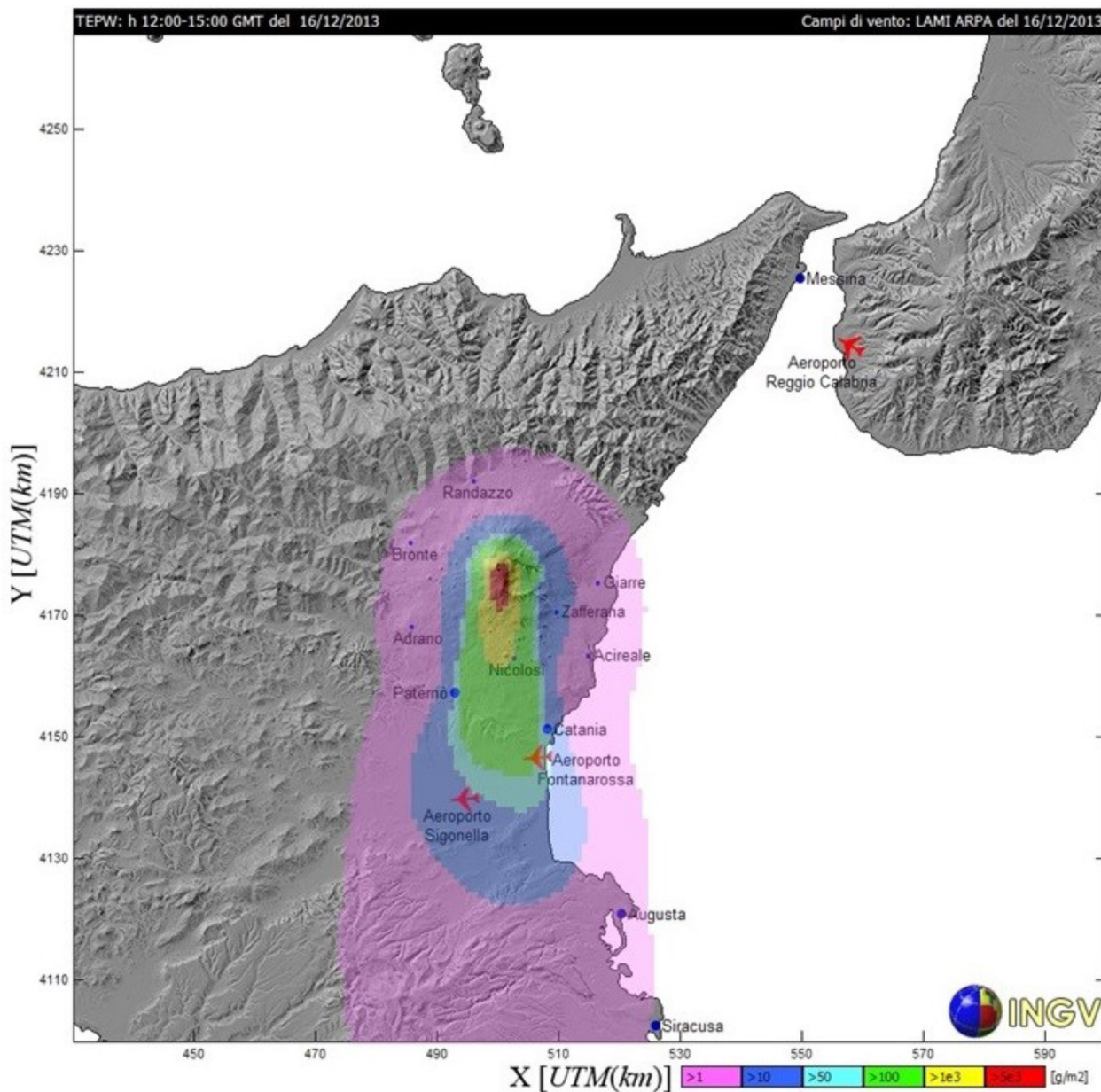


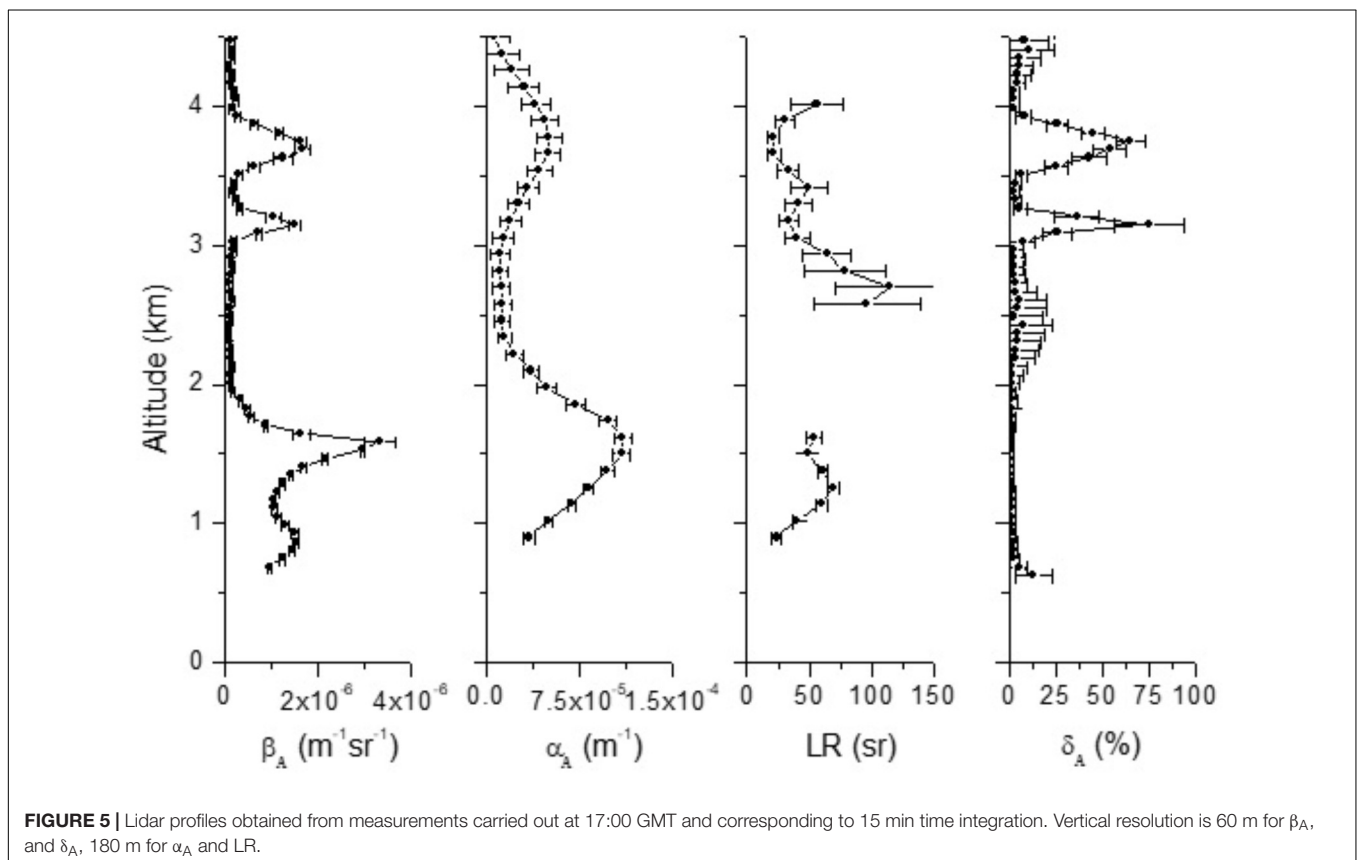
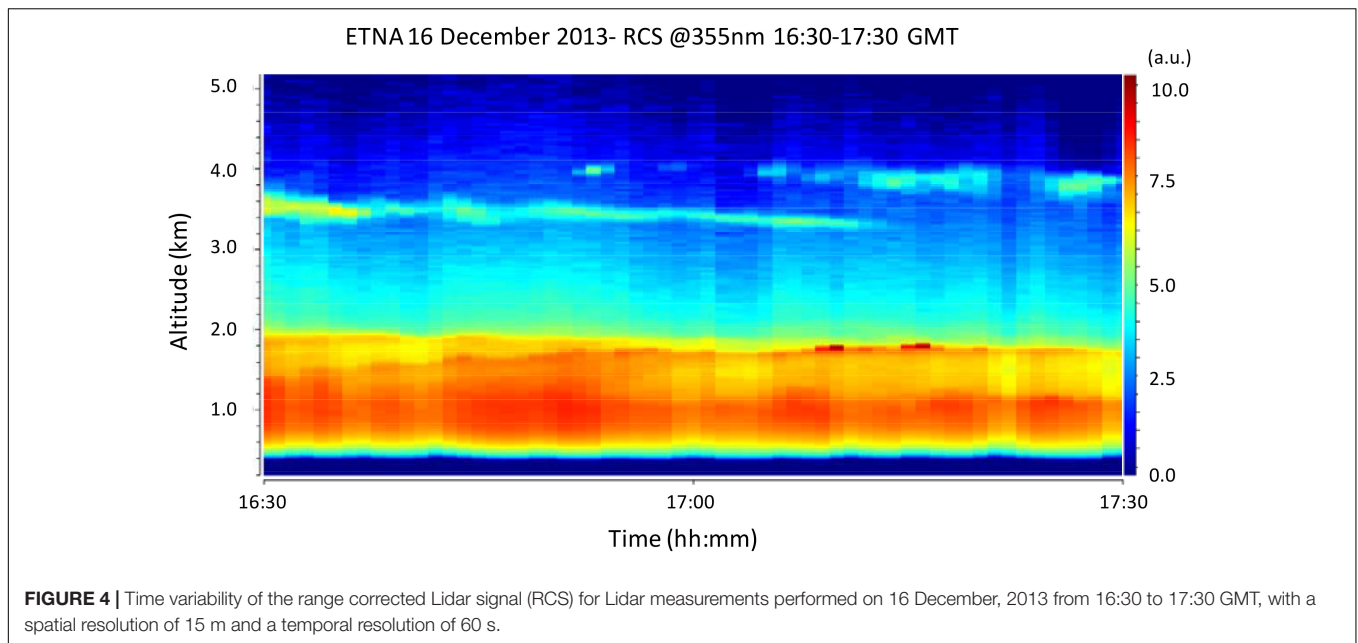
FIGURE 3 | Forecast of tephra fallout carried out by INGV-OE on 16 December at 12:00 GMT.

DISCUSSION AND CONCLUSION

Lidar data acquired on 16 December, 2013 have shown how Lidar observations can provide real time detection of volcanic plume emission and can be very useful for monitoring its evolution with time. Lidar measurements were able to capture the complex dynamics of the eruptive event by tracking the variations of ash emissions during the explosive activity with time. Data highlighted two different phases of the eruptive activity: from 10:45 to 15:05 GMT we observed a volcanic layer which was related to the explosive activity that occurred early

in the morning while in the afternoon, after 15:36 GMT, Lidar measurements captured particles coming from both the explosive activity and the eruptive fracture developed at about 13:30 GMT. The combination of values and variation of the backscatter coefficient and the LR and the aerosol depolarization ratio also showed variations on particles features in the atmosphere.

Vertical profiles of aerosol backscattering coefficient were able to track in time the decrease of the explosive activity of the fissure developed late in the morning and located at the North East side of the NSEC. Aerosol depolarization ratio δ_A allowed to evaluate the sphericity of the volcanic cloud particles. Its variation with



time suggests a modification of the aerosol shape probably related to physical interactions between volcanic ash particles and water vapor, a dominant component during most explosive volcanic eruptions, strongly affecting the microphysical evolution of ash (Latham et al., 2011). In fact, ash uptakes water efficiently via

adsorption and nucleates into cloud drops, whose more spherical shape can justify the observed values of δ_A . Larger δ_A values obtained in the afternoon measurement in an upper plume clearly indicate the presence of non-spherical particles and suggest the presence of a larger fraction of glass and mineral aerosols.

TABLE 1 | Timetable of aerosol parameters [Lidar Ratio (LR), aerosol depolarization δ_A , and concentration γ] averaged in the observed layers.

Time (hh:mm) GMT	Range (m)	LR (sr)		δ (%)		γ (mg/m ³) $\times 10^{-2}$	
16:30–16:45	<1100	51.5 \pm 3.5		2.04 \pm 0.20		1.5 \pm 0.2	
	1100–2000	75.3 \pm 2.5		1.07 \pm 0.09		0.5 \pm 0.2	
	2000–3000	57.1 \pm 29.0		0.89 \pm 0.13		0.04 \pm 0.09	
	3000–4100	45.1 \pm 4.1		12.19 \pm 1.10		10.7 \pm 4.4	
16:45–17:00	<1100	48.5 \pm 4.0		2.52 \pm 0.20		2.4 \pm 0.3	
	1100–2000	70.6 \pm 2.8		1.57 \pm 0.07		2.8 \pm 0.3	
	2000–3000	72.3 \pm 24		5.69 \pm 0.75		1.9 \pm 0.2	
	3000–3500	30.1 \pm 6.7	48.2 \pm 7.0*	15.54 \pm 2.10	18.87 \pm 2.44*	13.0 \pm 4.5	13.9 \pm 5.0*
	3500–4100	58.2 \pm 17.1		26.06 \pm 3.72		16.0 \pm 5.9	
17:00–17:15	<1100	48.3 \pm 3.3		2.05 \pm 0.12		2.1 \pm 0.3	
	1100–2000	71.8 \pm 2.3		1.24 \pm 0.05		1.1 \pm 0.2	
	2000–3000	69.9 \pm 16.0		3.91 \pm 0.49		1.0 \pm 0.2	
	3000–3400	34.9 \pm 3.6	46.8 \pm 6.2*	49.67 \pm 8.99	46.34 \pm 9.05*	22.8 \pm 6.8	40.3 \pm 12.6*
	3400–4100	53.3 \pm 16.2		43.47 \pm 9.56		55.0 \pm 17.7	
17:15–17:30	<1100	44.3 \pm 3.7		2.97 \pm 0.11		4.3 \pm 0.6	
	1100–2000	78.3 \pm 3.8		2.31 \pm 0.24		4.7 \pm 0.5	
	2000–3000	75.3 \pm 24.0		13.32 \pm 0.51		4.6 \pm 0.4	
	3000–4100	48.1 \pm 5.6		44.13 \pm 4.76		38.8 \pm 13.8	

Values with * correspond to values averaged in the range 3000–4100 m.

Mean LR values, measured for the first time near the Etna summit craters, matched with values reported in the literature for volcanic ash when volcanic sulfate particles are mixed with anthropogenic particles (Navas-Guzmán et al., 2013). The obtained results suggest a large amount of SO₂ released from the volcano in the ash, according to SO₂ flux emitted from Etna that reached peak values greater than 15,000 t/d on 16 December (INGV – Bollettino settimanale Etna del 24/12/2013 Rep. N° 52/2013). The SO₂ presence in the plume is also confirmed by the IASI and GOME 2 satellite images⁴ in the UV – visible and infrared wavelengths, respectively.

Daily forecasts run by INGV-OE confirmed the movement of the volcanic plume from South East toward the South in the night between 15 and 16 December. The airspace around Etna was accordingly closed in the evening of 15 December 2013 and dozens of departures were canceled at the international airport in Catania, with several flights diverted toward Palermo airport. However, Lidar measurements carried out at the INAF, in Catania, only 10 km far from the airport, showed the highest concentration value of 5.5×10^{-4} g/m³, measured at altitudes between 3,000 and 4,000 m, i.e., below the risk threshold for aircrafts (2×10^{-3} g/m³).

It should be noted that our study is based on observations carried out using a one wavelength Lidar system with Elastic/Raman and polarization capability. Due to the lack of multi-wavelengths observations, important parameters for particles characterization have not been estimated. Particle shape information derived from the aerosol depolarization values in combination with aerosol optical properties measured at many wavelengths allow the aerosol microphysical characterization and

both size distribution and mass concentration retrieval. The extended observation capability of the system, upgraded in 2016 with the implementation of the 532 nm channels (parallel and cross-polarized) and the corresponding N₂ Raman channel at 607 nm, has already allowed us to improve our capability to evaluate optical particles near active craters. Lidar measurements carried out near active volcanoes are, however, uncommon although they could really improve our understanding on plume transport and evolution of volcanic particles. The elastic channel at 1,064 nm will be implemented in the next future opening new prospects for the use of Lidars in the volcanic plume survey.

AUTHOR CONTRIBUTIONS

AB and SS were responsible for the conceptual design of the work and lead the writing and compilation of figures and tables. SS and MC are responsible of volcanological observations. GL, SS, and RS performed the Lidar measurements, AS, AB, XW, and NS performed the Lidar data analysis and interpretation. GL and SS manage the Lidar system at Etna. All authors have given substantial contributions to the discussion of the article and approved the submitted version of the manuscript and thereby agreed to be accountable for all aspects of the work, ensuring that questions related to the accuracy or integrity of any part of the work are appropriately investigated and resolved.

FUNDING

The financial support for EARLINET-ASOS by the European Commission in the Sixth Framework Programme under grant

⁴<http://sacs.aeronomie.be>

RICA-025991 and for ACTRIS in the Seventh Framework Programme under Grant Agreement No. 262254 are gratefully acknowledged. This work was funded by the VAMOS SEGURO project, Programma di Cooperazione Transfrontaliera Italia – Malta 2007–2013, A1.2.3-62, Obiettivo Specifico 2.3.

REFERENCES

- Ackermann, J. (1998). The extinction-to-backscatter ratio of tropospheric aerosol: a numerical study. *J. Atmos. Oceanic Technol.* 15, 1043–1050. doi: 10.1175/1520-0426(1998)015<1043:TETBRO>2.0.CO;2
- Alparone, S., Andronico, D., Lodato, L., and Sgroi, T. (2003). Relationship between tremor and volcanic activity during the Southeast Crater eruption on Mount Etna in early 2000. *J. Geophys. Res.* 108:2241. doi: 10.1029/2002JB001866
- Ansmann, A., Riebesell, M., Wandinger, U., Weitkamp, C., Voss, E., Lahmann, W., et al. (1992). Combined raman elastic-backscatter LIDAR for vertical profiling of moisture, aerosol extinction, backscatter, and LIDAR ratio. *Appl. Phys. B* 55:18. doi: 10.1007/BF00348608
- Ansmann, A., Riebesell, M., and Weitkamp, C. (1990). Measurement of atmospheric aerosol extinction profiles with a Raman lidar. *Opt. Lett.* 15, 746–748. doi: 10.1364/OL.15.000746
- Ansmann, A., Tesche, M., Groß, S., Freudenthaler, V., Seifert, P., Hiebsch, A., et al. (2010). The 16 April 2010 major volcanic ash plume over central Europe: EARLINET lidar and AERONET photometer observations at Leipzig and Munich, Germany. *Geophys. Res. Lett.* 37:L13810. doi: 10.1029/2010GL043809
- Ansmann, A., Tesche, M., Groß, S., Freudenthaler, V., Seifert, P., Hiebsch, A., et al. (2011). Ash and fine-mode particle mass profiles from EARLINET-AERONET observations over central Europe after the eruptions of the Eyjafjallajökull volcano in 2010. *J. Geophys. Res. Atmos.* 116:L13810. doi: 10.1029/2010GL043809
- Ayris, P. M., and Delmelle, P. (2012). The immediate environmental effects of tephra emission. *Bull. Volcanol.* 74, 1905–1936. doi: 10.1007/s00445-012-0654-5
- Ayris, P. M., Delmelle, P., Cimarelli, C., Maters, E. C., Suzuki, Y. J., and Dingwell, D. B. (2014). HCl uptake by volcanic ash in the high temperature eruption plume: mechanistic insights. *Geochimica et Cosmochimica Acta* 144, 188–201. doi: 10.1016/j.gca.2014.08.028
- Azzopardi, F., Raymond, E., Prestifilippo, M., Scollo, S., and Coltelli, M. (2013). The effect of Etna volcanic ash clouds on the maltese islands. *J. Volcanol. Geother. Res.* 260, 13–26. doi: 10.1016/j.jvolgeores.2013.04.019
- Balis, D., Koukouli, M. E., Siomos, N., Dimopoulos, S., Mona, L., Pappalardo, G., et al. (2016). Validation of ash optical depth and layer height retrieved from passive satellite sensors using EARLINET and airborne lidar data: the case of the Eyjafjallajökull eruption. *Atmos. Chem. Phys.* 16, 5705–5720. doi: 10.5194/acp-16-5705-2016
- Behncke, B., Branca, S., Corsaro, R. A., De Beni, E., Miraglia, L., and Proietti, C. (2014). The 2011–2012 summit activity of Mount Etna: birth, growth and products of the new SE crater. *J. Volcanol. Geotherm. Res.* 270, 10–21. doi: 10.1016/j.jvolgeores.2013.11.012
- Behncke, B., Neri, M., Pecora, E., and Zanon, V. (2006). The exceptional activity and growth of the Southeast Crater, Mount Etna (Italy), between 1996 and 2001. *Bull. Volcanol.* 69, 149–173. doi: 10.1007/s00445-006-0061-x
- Behrendt, A., and Nakamura, T. (2002). Calculation of the calibration constant of polarization lidar and its dependency on atmospheric temperature. *Opt. Express* 10, 805–817. doi: 10.1364/OE.10.000805
- Biele, J., Beyerle, G., and Baumgarten, G. (2000). Polarization lidar: corrections of instrumental effects. *Opt. Express* 7, 427–435. doi: 10.1364/OE.7.000427
- Bonadonna, C., Folch, A., Loughlin, S., and Puempel, H. (2012). Future developments in modelling and monitoring of volcanic ash clouds: outcomes from the first IAVCEI-WMO workshop on Ash dispersal forecast and civil aviation. *Bull. Volcanol.* 74, 1–10. doi: 10.1007/s00445-011-0508-6
- Bonadonna, C., Genco, R., Gouhier, M., Pistolesi, M., Cioni, R., Alfano, F., et al. (2011). Tephra sedimentation during the 2010 Eyjafjallajökull eruption (Iceland) from deposit, radar, and satellite observations. *J. Geophys. Res. Solid Earth* 116:B12202. doi: 10.1029/2011JB008462
- Bonadonna, C., Pistolesi, M., Cioni, R., Degruyter, W., Elisondo, M., and Baumann, V. (2015). Dynamics of wind-affected volcanic plumes: the example of the 2011 Cordón Caulle eruption, Chile. *J. Geophys. Res. Solid Earth* 120, 2242–2261. doi: 10.1002/2014JB011478
- Bösenberg, J., Ansmann, A., Baldasano, J. M., Balis, D., Böckmann, C., Calpini, B., et al. (2001). “EARLINET: a european aerosol research lidar network in advanced in laser remote sensing, of the atmosphere,” in *Selected Papers of the 20th International Laser Radar Conference*, eds A. Dabas, C. Loth, and J. Pelon (Palaiseau: Ecole Polytechnique), 155–158.
- Bösenberg, J., Matthias, V., Amodeo, A., Amoiridis, V., Ansmann, A., Baldasano, J. M., et al. (2003). A European aerosol research lidar network to establish an aerosol climatology. *Max Planck Institut für Meteorol. Tech. Rep.* 348, 135–137.
- Branca, S., and Del Carlo, P. (2005). Types of eruptions of Etna volcano AD 1670–2003: implications for short-term eruptive behavior. *Bull. Volcanol.* 67, 732–742. doi: 10.1007/s00445-005-0412-z
- Calvari, S., Salerno, G. G., Spampinato, L., Gouhier, M., La Spina, A., Pecora, E., et al. (2011). An unloading foam model to constrain Etna’s 11–13 January 2011 lava fountaining episode. *J. Geophys. Res.* 116:B11207. doi: 10.1029/2011JB008407
- Corradini, S., Montopoli, M., Guerrieri, L., Ricci, M., Scollo, S., and Merucci, L. (2016). A multi-sensor approach for volcanic ash cloud retrieval and Eruption characterization: the 23 November 2013 Etna Lava fountain. *Remote Sens.* 8:58. doi: 10.3390/rs8010058
- Delmelle, P. (2003). Environmental impacts of tropospheric volcanic gas plumes. *Geol. Soc. Lond. Spec. Pub.* 213, 381–399. doi: 10.1144/GSL.SP.2003.213.01.23
- Delmelle, P., Stix, J., Baxter, P., Garcia-Alvarez, J., and Barquero, J. (2002). Atmospheric dispersion, environmental effects and potential health hazard associated with the low altitude gas plume of Masaya volcano. *Nicaragua. Bull. Volcanol.* 64, 423–434. doi: 10.1007/s00445-002-0221-6
- Fernald, F. G. (1984). Analysis of the atmospheric lidar observations; some comments. *Appl. Opt.* 23, 652–653. doi: 10.1364/AO.23.000652
- Freudenthaler, V., Esselborn, M., Wiegner, M., Heese, B., Tesche, M., Ansmann, A., et al. (2009). Depolarization ratio profiling at several wavelengths in pure Saharan dust during SAMUM 2006. *Tellus* 61B, 165–179. doi: 10.1111/j.1600-0889.2008.00396.x
- Gasteiger, J., Groß, S., Freudenthaler, V., and Wiegner, M. (2011). Volcanic ash from Iceland over Munich: mass concentration retrieved from ground-based remote sensing measurements. *Atmos. Chem. Phys.* 11:2209e2223. doi: 10.5194/acp-11-2209-2011
- Groß, S., Freudenthaler, V., Wiegner, M., Gasteiger, J., Geiß, A., and Schnell, F. (2012). Dual-wavelength linear depolarization ratio of volcanic aerosols: Lidar measurements of the Eyjafjallajökull plume over Maisach, Germany. *Atmos. Environ.* 48, 85–96. doi: 10.1016/j.atmosenv.2011.06.017
- Groß, S., Freudenthaler, V., Wirth, M., and Weinzierl, B. (2015). Towards an aerosol classification scheme for future EarthCARE lidar observations and implications for research needs. *Atmos. Sci. Lett.* 16, 77–82. doi: 10.1002/asl2.524
- Gudmundsson, M. T., Thordarson, T., Hoskuldsson, A., Larsen, G., Björnsson, H., Prata, F. J., et al. (2012). Ash generation and distribution from the Aprile May 2010 eruption of Eyjafjallajökull. *Icel. Sci. Rep.* 2:572. doi: 10.1038/srep00572
- Guffanti, M., Ewert, J. W., Gallina, G. M., Bluth, G. J. S., and Swanson, G. L. (2005). Volcanic-ash hazard to aviation during the 2003–2004 eruptive activity of

ACKNOWLEDGMENTS

We thank Michele Prestifilippo who maintains the forecasting system of volcanic ash dispersal at INGV-OE. We also thank Emilio Biale and Michele Prestifilippo for the use of images coming from the INGV-OE camera network.

- anatahan volcano, commonwealth of the Northern Mariana Islands. *J. Volcanol. Geoth. Res.* 146, 241–255. doi: 10.1016/j.jvolgeores.2004.12.011
- Hervo, M., Quennehen, B., Kristiansen, N. I., Boulon, J., Stohl, A., Fréville, P., et al. (2012). Physical and optical properties of 2010 Eyjafjallajökull volcanic eruption aerosol: ground-based, Lidar and airborne measurements in France. *Atmos. Chem. Phys.* 12, 1721–1736. doi: 10.5194/acp-12-1721-2012
- Horwell, C. J. (2007). Grain size analysis of volcanic ash for the rapid assessment of respiratory health hazard. *J. Environ. Monit.* 9, 1107–1115. doi: 10.1039/b710583p
- INGV-OE (2013a). *BollettinoEtna20131202*. Rep. 50/2013. Available at: <http://www.ct.ingv.it/it/rapporti/multidisciplinari.html?start=465>
- INGV-OE (2013b). *BollettinoEtna20131217*. Rep. 51/2013. Available at: <http://www.ct.ingv.it/it/rapporti/multidisciplinari.html?start=465>
- Klett, J. D. (1981). Stable analytical inversion solution for processing lidar returns. *Appl. Opt.* 20, 211–220. doi: 10.1364/AO.20.000211
- Kokkalis, P., Papayannis, A., Amiridis, V., Mamouri, R. E., Veselovskii, I., Kolgotin, A., et al. (2013). Optical, microphysical, mass and geometrical properties of aged volcanic particles observed over Athens, Greece, during the Eyjafjallajökull eruption in April 2010 through synergy of Raman lidar and sunphotometer measurements. *Atmos. Chem. Phys.* 13, 9303–9320. doi: 10.5194/acp-13-9303-2013
- Kueppers, U., Cimarelli, C., Hess, K., Taddeucci, J., Wadsworth, F. B., and Dingwell, D. B. (2014). The thermal stability of Eyjafjallajökull ash versus turbine ingestion test sands. *J. Appl. Volcanol.* 3:4. doi: 10.1186/2191-5040-3-4
- Latham, T. L., Kumar, P., Nenes, A., Dufek, J., Sokolik, I. N., Trail, M., et al. (2011). Hygroscopic properties of volcanic ash. *Geophys. Res. Lett.* 38:L11802. doi: 10.1029/2011GL047298
- Marenco, F., and Hogan, R. J. (2011). Determining the contribution of volcanic ash and boundary layer aerosol in backscatter lidar returns: a three-component atmosphere approach. *J. Geophys. Res. Atmos.* 116:D00U06. doi: 10.1029/2010jd015415
- Marenco, F., Johnson, B., Turnbull, K., Newman, S., Haywood, J., Webster, H., et al. (2011). Airborne lidar observations of the 2010 Eyjafjallajökull volcanic ash plume. *J. Geophys. Res.* 116:D00U05. doi: 10.1029/2011JD016396
- Mereu, L., Scollo, S., Mori, S., Boselli, A., and Leto, G. (2018). Maximum-likelihood retrieval of volcanic ash concentration and particle size from ground-based scanning Lidar. *IEEE Trans. Geosci. Remote Sens.* 1–19. doi: 10.1109/TGRS.2018.2826839
- Miffre, A., David, G., Thomas, B., Rairoux, P., Fjaeraa, A. M., Kristiansen, N. I., et al. (2011). Volcanic aerosol optical properties and phase partitioning behavior after long-range advection characterized by UV-Lidar measurements. *Atmos. Environ.* 48, 76–84. doi: 10.1016/j.atmosenv.2011.03.057
- Miller, T. P., and Casadevall, T. J. (2000). “Volcanic ash hazards to aviation,” in *Encyclopedia of Volcanoes*, eds H. Sigurdsson, B. F. Houghton, S. R. McNutt, H. Rymer, and J. Stix (San Diego: Academic Press), 915–930.
- Mona, L., Amodeo, A., D’Amico, G., Giunta, A., Madonna, F., and Pappalardo, G. (2012). Multi-wavelength raman lidar observations of the Eyjafjallajökull volcanic cloud over Potenza, southern Italy. *Atmos. Chem. Phys.* 12:2229e2244. doi: 10.5194/acp-12-2229-2012
- Müller, D., Ansmann, A., Mattis, I., Tesche, M., Wandinger, U., Althausen, D., et al. (2007). Aerosol-type-dependent lidar ratios observed with Raman lidar. *J. Geophys. Res. Atmos.* 112:D16202. doi: 10.1029/2006JD008292
- Navas-Guzmán, F., Muller, D., Bravo-Aranda, J. A., Guerrero-Rascado, J. L., Granados-Munoz, M. J., Perez-Ramírez, D., et al. (2013). Eruption of the Eyjafjallajökull Volcano in spring 2010: multiwavelength Raman lidar measurements of sulphate particles in the lower troposphere. *J. Geophys. Res. Atmos.* 118, 1804–1813. doi: 10.1002/jgrd.50116
- Papayannis, A., Mamouri, R. E., Amiridis, V., Giannakaki, E., Veselovskii, P., Kokkalis, I., et al. (2012). Optical properties and vertical extension of aged ash layers over the Eastern Mediterranean as observed by Raman lidars during the Eyjafjallajökull eruption in May 2010. *Atmos. Environ.* 48, 56–65. doi: 10.1016/j.atmosenv.2011.08.037
- Pappalardo, G., Mona, L., D’Amico, G., Wandinger, U., Adam, M., Amodeo, A., et al. (2013). A Four-dimensional distribution of the 2010 Eyjafjallajökull volcanic cloud over Europe observed by EARLINET. *Atmos. Chem. Phys.* 13, 4429–4450. doi: 10.5194/acp-13-4429-2013
- Pisani, G., Boselli, A., Coltelli, M., Leto, G., Pica, G., Scollo, S., et al. (2012). Lidar calibrated depolarization measurement of fresh volcanic ash from Mt. Etna. *Atmos. Environ.* 62, 34–40. doi: 10.1016/j.atmosenv.2012.08.015
- Ripepe, M., Bonadonna, C., Folch, A., Delle Donne, D., Lacanna, G., Marchetti, E., et al. (2013). Ash-plume dynamics and eruption source parameters by infrasound and thermal imagery: the 2010 Eyjafjallajökull eruption. *Earth Planet. Sci. Lett.* 366, 112–121. doi: 10.1016/j.epsl.2013.02.005
- Rittmann, A. (1973). Structure and evolution of Mount Etna. *Philos. Trans. R. Soc. Lond. A* 274, 5–16. doi: 10.1098/rsta.1973.0021
- Robock, A., and Oppenheimer, C. (eds) (2003). *Volcanism and the Earth's Atmosphere. Geophysical Monograph* 139. Washington, DC: American Geophysical Union, doi: 10.1029/GM139
- Sassen, K., Zhu, J., Webley, P., Dean, K., and Cobb, P. (2007). Volcanic ash plume identification using polarization lidar: augustine eruption, Alaska. *Geophys. Res. Lett.* 34:L08803. doi: 10.1029/2006GL027237
- Scollo, S., Boselli, A., Coltelli, M., Leto, G., Pisani, G., Prestifilippo, M., et al. (2015). Volcanic ash concentration during the 12 August 2011 Etna eruption. *Geophys. Res. Lett.* 42, 2634–2641. doi: 10.1002/2015GL063027
- Scollo, S., Coltelli, M., Bonadonna, C., and Del Carlo, P. (2013). Tephra hazard assessment at Mt. Etna (Italy). *Nat. Hazards Earth Syst. Sci.* 13, 3221–3233. doi: 10.5194/nhess-13-3221-2013
- Scollo, S., Boselli, A., Coltelli, M., Leto, G., Pisani, G., Spinelli, N., et al. (2012a). Monitoring Etna volcanic plumes using a scanning lidar. *Bull. Volcanol.* 74, 2382–2395. doi: 10.1007/s00445-012-0669-y
- Scollo, S., Kahn, R. A., Nelson, D. L., Coltelli, M. D., Diner, J., Garay, M. J., et al. (2012b). MISR observations of Etna volcanic plumes. *J. Geophys. Res.* 117:D06210. doi: 10.1029/2011JD016625
- Scollo, S., Prestifilippo, M., Pecora, E., Corradini, S., Merucci, L., Spata, G., et al. (2014). Eruption column height estimation of the 2011–2013 Etna lava fountains. *Ann. Geophys.* 57, 1–5. doi: 10.4401/ag-6396
- Scollo, S., Prestifilippo, M., Spata, G., D’Agostino, M., and Coltelli, M. (2009). Monitoring and forecasting Etna volcanic plumes. *Nat. Hazards Earth Syst. Sci.* 9, 1573–1585. doi: 10.5194/nhess-9-1573-2009
- Sicard, M., Guerrero-Rascado, J. L., Navas-Guzmán, F., Preißler, J., Molero, F., Tomás, S., et al. (2012). Monitoring of the Eyjafjallajökull volcanic aerosol plume over the Iberian Peninsula by means of four EARLINET lidar stations. *Atmos. Chem. Phys.* 12, 3115–3130. doi: 10.5194/acp-12-3115-2012
- Song, W., Hess, K., Damby, D. E., Wadsworth, F. B., Lavallée, Y., Cimarelli, C., et al. (2014). Fusion characteristics of volcanic ash relevant to aviation hazards. *Geophys. Res. Lett.* 41, 2326–2333. doi: 10.1002/2013GL059182
- Sparks, R. S. J., Bursik, M. I., Carey, S. N., Gilbert, J. S., Glaze, L. S., Sigurdsson, H., et al. (1997). *Observations and Interpretation of Volcanic Plumes*, in *Volcanic Plumes*. Chichester: John Wiley, 117–140.
- Stevenson, J. A., Loughlin, S., Rae, C., Thordarson, T., Milodowski, A. E., Gilbert, J. S., et al. (2012). Distal deposition of tephra from the Eyjafjallajökull 2010 summit eruption. *J. Geophys. Res. Solid Earth* 117:B00C10. doi: 10.1029/2011JB008904
- Tesche, M., Ansmann, A., Müller, D., Althausen, D., Engelmann, R., Freudenthaler, V., et al. (2009). Separation of dust and smoke profiles over cape verde by using multiwavelength Raman and polarization lidars during SAMUM 2008. *J. Geophys. Res.* 114:D13202. doi: 10.1029/2009JD011862
- Trickl, T., Giehl, H., Jäger, H., and Vogelmann, H. (2013). 35 yr of stratospheric aerosol measurements at Garmisch-Partenkirchen: from Fuego to Eyjafjallajökull, and beyond. *Atmos. Chem. Phys.* 13, 5205–5225. doi: 10.5194/acp-13-5205-2013
- Wang, X., Boselli, A., D’Avino, L., Pisani, G., Spinelli, N., Amodeo, A., et al. (2008). Volcanic dust characterization by EARLINET during Etna’s eruptions in 2001–2002. *Atm. Environ.* 42, 893–905. doi: 10.1016/j.atmosenv.2007.10.020
- Wang, X., Boselli, A., Sannino, A., Song, C., Spinelli, N., Yiming Zhao, Y., et al. (2015). Calibration of multi-wavelength raman polarization lidar. *EPJ Web Conf.* 89:01002. doi: 10.1051/epjconf/20158901002
- Weinzierl, B., Sauer, D., Minikina, A., Reitebuch, O., Dahlkötter, F., Mayer, B., et al. (2012). On the visibility of airborne volcanic ash and mineral dust from the pilot’s perspective in flight. *Phys. Chem. Earth Parts A/B/C* 45–46, 87–102. doi: 10.1016/j.pce.2012.04.003

Witt, V., Ayris, P. M., Damby, D. E., Cimarelli, C., Kueppers, U., and Dingwell, D. B. (2017). Volcanic ash supports a diverse bacterial community in a marine mesocosm. *Geobiology* 15, 453–463. doi: 10.1111/gbi.12231

Conflict of Interest Statement: The authors declare that the research was conducted in the absence of any commercial or financial relationships that could be construed as a potential conflict of interest.

Copyright © 2018 Boselli, Scollo, Leto, Sanchez, Sannino, Wang, Coltelli and Spinelli. This is an open-access article distributed under the terms of the Creative Commons Attribution License (CC BY). The use, distribution or reproduction in other forums is permitted, provided the original author(s) and the copyright owner(s) are credited and that the original publication in this journal is cited, in accordance with accepted academic practice. No use, distribution or reproduction is permitted which does not comply with these terms.



Tephra From the 3 March 2015 Sustained Column Related to Explosive Lava Fountain Activity at Volcán Villarrica (Chile)

Jorge E. Romero^{1*}, Franco Vera², Margherita Polacci³, Daniele Morgavi⁴, Fabio Arzilli³, Mohammad Ayaz Alam¹, Jorge E. Bustillos⁵, Alicia Guevara⁶, Jeffrey B. Johnson⁷, José L. Palma², Mike Burton³, Evelyn Cuenca⁵ and Werner Keller⁸

¹ Departamento de Geología, Facultad de Ingeniería, Universidad de Atacama, Copiapó, Chile, ² Department of Earth Science, Faculty of Chemical Science, University of Concepción, Concepción, Chile, ³ School of Earth and Environmental Sciences, University of Manchester, Manchester, United Kingdom, ⁴ Department of Physics and Geology, University of Perugia, Perugia, Italy, ⁵ Escuela de Geología, Universidad Central de Ecuador, Quito, Ecuador, ⁶ Departamento de Metalurgia Extractiva, Escuela Politécnica Nacional, Quito, Ecuador, ⁷ Department of Geosciences, Boise State University, Boise, ID, United States, ⁸ Proyecto de Observación Volcán Villarrica (POVI), Fundación Volcanes de Chile, Santiago, Chile

OPEN ACCESS

Edited by:

Sonia Calvari,
Istituto Nazionale di Geofisica e
Vulcanologia (INGV), Italy

Reviewed by:

Victoria C. Smith,
University of Oxford, United Kingdom
Jon J. Major,
United States Geological Survey,
United States

*Correspondence:

Jorge E. Romero
jorge_eduardorm@gmail.com

Specialty section:

This article was submitted to
Volcanology,
a section of the journal
Frontiers in Earth Science

Received: 14 April 2018

Accepted: 29 June 2018

Published: 24 July 2018

Citation:

Romero JE, Vera F, Polacci M,
Morgavi D, Arzilli F, Alam MA,
Bustillos JE, Guevara A, Johnson JB,
Palma JL, Burton M, Cuenca E and
Keller W (2018) Tephra From the 3
March 2015 Sustained Column
Related to Explosive Lava Fountain
Activity at Volcán Villarrica (Chile).
Front. Earth Sci. 6:98.
doi: 10.3389/feart.2018.00098

Exceptionally intense lava fountains at open conduit volcanoes are infrequent, hazardous and little-warned events. Studying their tephra falls may reveal conduit dynamics, eruption source parameters and fragmentation mechanisms. Villarrica Volcano (Southern Andes of Chile) has sustained persistent open conduit activity, associated with a dynamic lava lake since at least 1984–85. Increased seismicity and degassing in August 2014 were followed by Strombolian activity starting in February 2015 and culminated with a 1.5 km-high lava fountain on 3 March 2015. This eruption produced tephra fallout, spatter agglutination, clastogenic lavas and mixed avalanche deposits. Here we characterized for first time Villarrica's 3 March 2015 tephra fall deposits produced by lava fountain and its rapid transition to sustained eruption column, providing valuable information on paroxysmal activity in open conduit volcanoes. Tephra was dispersed southeast of the crater in a narrow, elongated, nearly-elliptic area. Minimum observed tephra loading was estimated to be 80–120 g/m² at crosswind locations, while maximum load estimation was about 11,500 g/m², at 7–9 km distance from the vent. At 6–8 km downwind, the tephra fall deposit consisted of a single black scoria layer; fall varied from a lapilli blanket at medial distances (9–19 km) to a few individual particles at distal sites (20–43 km). All samples are vitrophyric and contain plagioclase (3–30%), clinopyroxene (2–5%), olivine (1–4%) and orthopyroxene (<1%) phenocrysts. We estimate that 1.4 × 10⁹ kg, equivalent to ~2.4 × 10⁶ m³ of basaltic andesite tephra (52.7–54.7 SiO₂ wt. %), were erupted within a period of about 16 min at a mass eruption rate of ~1.5 × 10⁶ kg/s. The sustained eruption column height was estimated at ~10.8 km, with magnitude and intensity of 2.11 and 9.13 respectively. We propose that a rejuvenated, volatile-rich magmatic intrusion probably triggered paroxysmal activity. The Villarrica

eruption is classified as a short-lived, large-scale lava fountain, similar to analogous historical events at Mt. Etna and Kilauea. As evident by devastating twentieth century Villarrica eruptions which also developed similar lava fountains, this eruption style should be considered as frequent and a potential source of volcanic hazard in the future.

Keywords: lava fountain, tephra fall, eruption parameters, Villarrica Volcano, Southern Andes

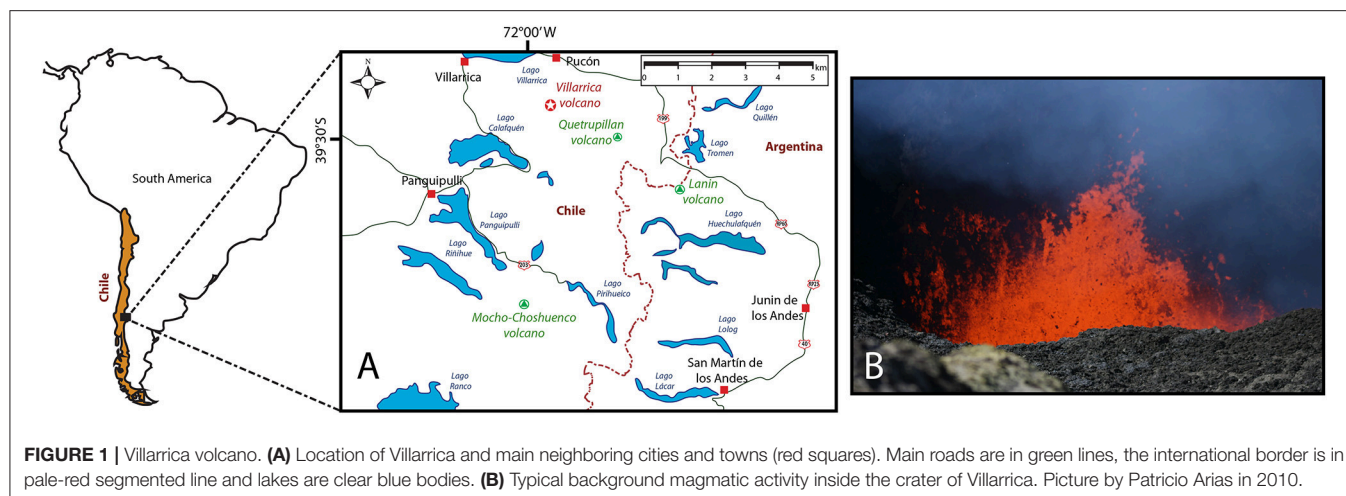
INTRODUCTION

Lava fountains (also known as “fire fountains”) are powerful, continuous but normally short-lived gas jets (from less than one to a few hours) caused by fast-rising bubbly melt or the ascent of a bubble foam layer coming from depth (Parfitt, 2004). They typically emit lava fragments to heights extending tens to hundreds of meters (Bonaccorso et al., 2011). Most lava fountains reach 500–600 m above the crater (e.g., Houghton and Gonnermann, 2008; Taddeucci et al., 2015), but the highest reach ~2.0 km and are infrequent, violent and short-lived (e.g., Bonaccorso et al., 2014; Andronico et al., 2015). Their evolution is commonly initiated by Strombolian activity (resumption phase) followed by lava fountaining, and typically the formation of an eruption column (paroxysmal phase), which ends with the waning of the eruption (conclusive phase) (Andronico et al., 2015). As fountaining episodes are more frequent at open, passively degassing volcanic systems like that of Villarrica volcano, their onset can be sudden, sometimes with little to no advance warning or signals in monitoring data (Ruth et al., 2016). A population living close to an open-vent volcano may underestimate the scale of hazards, thus zonation should reflect potential hazards from both small and large eruptions, even if low-level activity appears dominant (Rose et al., 2013). Tephra fall from lava fountains threatens critical infrastructure and human activities around the volcano (e.g., Allard et al., 2005; Andronico et al., 2008, 2014a,b, 2015; Carracedo et al., 2012). A study of tephra fall deposits from lava fountains and paroxysmal phases, especially when they are exceptionally intense, is an essential tool for early assessment of conduit dynamics, hazards and impacts (e.g., Polacci et al., 2006; Gurioli et al., 2008; Andronico and Corsaro, 2011; Stovall et al., 2011; Corsaro and Miraglia, 2014; Ruth and Calder, 2014; Ruth et al., 2016) and provides critical information for better understanding of volcanic activity.

Villarrica Volcano (39°25'S, 71°57' W; 2847 m high; **Figure 1A**) has been active since middle Pleistocene (Moreno and Clavero, 2006; Lohmar et al., 2012; Morgado et al., 2015), and is the most active stratovolcano of the Southern Andes Volcanic Zone (SVZ, Petit-Breuilh and Lobato, 1994; González-Ferrán, 1995). It has sourced about 100 small eruptions between AD 1384 and AD 1971 (Van Daele et al., 2014), among them at least 60 eruptions since AD 1558 (Petit-Breuilh and Lobato, 1994). The latest eruptions have been mostly effusive and slightly explosive, namely Hawaiian to Strombolian. Small lava fountains (heights up to ~30 m) are frequent at Villarrica and have been observed during periods of elevated activity, a result of vigorous seething magma involving a greater concentration

of gas bubbles of likely larger size and higher velocity as they reach the surface of the lava lake (Calder et al., 2004; Palma et al., 2008). However, episodes with higher lava fountains (200–600 m) accompanied by successively taller eruption columns from 3 to 15 km above the vent, were observed during the eruptions of 1 and 31 January, 1948–1949, 2 March 1964 and 29 December 1971. Most of these eruptions triggered lava effusion, mixed (ice and pyroclast) avalanche generation and massive lahars, killing a total of 100 people and causing major disruption of human activities and damage to infrastructure (González-Ferrán, 1995; Naranjo and Moreno, 2004). Despite their significant impacts, including damage to agricultural fields and public and private infrastructure in Pucon (González-Ferrán, 1995), tephra deposits from these historical events have not been studied properly. The most recent explosive eruption occurred in 1984–85, when lava flows overtopped the summit crater rim. Since then, open-conduit dynamics associated with continuous shallow magmatic activity has been observed inside the crater at the summit of the volcano (**Figure 1B**), including continuous outgassing and “puffing,” roiling magma, small lava fountains, Strombolian explosions, gas jetting, and sloshing lava (Palma et al., 2008). Between August and December 1999, Villarrica showed a significant increase in seismic activity and lava lake activity increased as explosions occurred and destroyed the lava lake crust on at least 4 occasions (Calder et al., 2004). At least two instances of lava lake ascent in 2001 and 2004–05 are associated with increased volcanic activity, producing spatter explosions and small Strombolian eruptions affecting the crater perimeter (Calder et al., 2004; Palma et al., 2008). From 2005 to January 2015 most activity consisted of continuous outgassing, small Strombolian explosions, gas jetting and some small ash emissions due to sporadic collapse of material accumulated in the internal walls of the crater.

A new eruptive cycle with vigorous Strombolian activity began in February and preceded the highest historical lava fountain event of the volcano (1500 m high) on 3 March 2015. Activity started at ~03:08 h local time and terminated at about 03:26 h. This short-lived eruption produced heavy tephra fall to the east and clastogenic scoria flows, predominantly on the northern and eastern flanks of the volcano, due to spatter coalescence (Johnson and Palma, 2015). Although previous field observations have described the nature of pyroclastic products from this eruption (e.g., Bertin et al., 2015), detailed studies are required to better understand the eruptive parameters, triggering mechanisms and conduit dynamics Development of the 3 March 2015 lava fountain and the main features of the erupted tephra (distribution, mass,



grain size, textural, and composition), together with eruption source parameters, have been investigated to determine their critical importance for tephra fall risk assessment. Tephra properties have been compared with texture and geochemical composition of samples collected from the crater rim of Villarrica erupted on 9 and 15 December 2015 and 13 February 2017.

ERUPTION CHRONOLOGY

Since April 2012, the surface activity of Villarrica has exhibited deepening of the active lava lake which persisted at a depth of 120–130 m below the crater rim up to February 2015 (Romero et al., 2016a; Johnson et al., 2018). Unrest initiated in August 2014, when the number of long-period (LP) seismic events increased and higher SO₂ fluxes (up to 5,000 tons/day) were recorded up until a few days before the eruption (Giacomozzi et al., 2015). On 12 December 2014, gas jetting (strong exhalations of gas) was caught on video operated by the Proyecto Volcan Villarrica (POVI) (<http://www.povi.cl/2014.html>). These signs of unrest were accompanied by a change in the gas emissions, from low CO₂/SO₂ ratios (0.65–2.7) during November 2014–January 2015 to CO₂/SO₂ ratios up to 9, while the H₂O/CO₂ ratio simultaneously declined (Aiuppa et al., 2017). During early February 2015, an abrupt increase in radiated infrasound power was observed coincident with increased vigor of Strombolian activity sourced from two small vents within the lava lake and material ejected beyond the summit crater (Johnson and Palma, 2015; **Figure 2A**). Ash venting and ballistics ejection, in addition to increase of seismic events and the real-time seismic amplitude measurement (RSAM), caused authorities to increase the volcanic alert level. A dramatic increase of LP seismicity >4,000 events between 1 and 16 February 2015, and a sustained increase in thermal anomalies (Inostroza et al., 2015) was coincident with an exponential increase in thermal radiance $Wm^{-2}sr^{-1}\mu m^{-1}$, as reported by near-real-time thermal monitoring of global hotspots (MODVOLC; <http://modis.higp.hawaii.edu/>) and Middle InfraRed Observation of

Volcanic Activity Project (MIROVA; www.mirova.it). Ground deformation patterns were not observed through GPS network or interferograms prior to eruption (Córdova et al., 2015; Delgado et al., 2017).

Infrasound resonance observations suggest that the lava lake began to rise from about 70 m depth on 27 February to the flared upper part of the Villarrica crater, at depth ~ 50 m, before oscillating at that level between 1 and 3 March (Johnson et al., 2018). On 3 March, Strombolian activity initiated at 2:37 local time (UTC+3) with ballistics reaching >100 m height (**Figure 2B**). The maximum reduced displacement of seismic tremor increased from 30 to 400 cm^2 , and was followed by the beginning of a lava fountain phase at 3:08 local time consisting in a 1.5 km-high lava fountain (**Figure 2C**). Vigorous eruptive activity began at 03:10 and resulted in a 6–8 km-high sustained eruption column, which lasted for 16 min; the entire eruption lasted about 55 min (SERNAGEOMIN, 2015; **Figures 2D–F**). Thermal radiance reached a peak value of $81.8 \text{ W m}^{-2} \text{ sr}^{-1} \mu\text{m}^{-1}$ $\text{W m}^{-2} \text{ sr}^{-1} \mu\text{m}^{-1}$. According to isochrons derived from GOES 13 satellite imagery, the eruptive plume drift speed was 8.57 m/s and the cloud had an estimated lowermost temperature of $\sim 40^\circ\text{C}$ (<http://satellite.cptec.inpe.br/>).

Vera and Palma (2017) identified four clearly distinguishable types of volcanic deposits at a distance <3 km from the vent: (a) up to 5-m-thick agglutinated spatters, covering ca. 3×10^5 m² and radially distributed from the crater; (b) black, rugged clastogenic lavas formed due to spatter coalescence descending on the north flank (**Figure 2G**) and covering ca. 5×10^4 m²; (c) a series of mixed-avalanche deposits which consisted of radially dispersed elongated deposits formed by a few centimeter-thick external crust of scoria and lithics with a central core of snow and ice up to a few meters (**Figure 2H**); and (d) a blanket of ash to lapilli sized scoria covering the east and southeast flank of the volcano (**Figure 2I**). Bertin et al. (2015) correlated the aerodynamic and breadcrust bombs to the spatter deposit, while describing low-density and high-vesicularity scoria as a typical product of the tephra fall deposit. Due to glacier melting

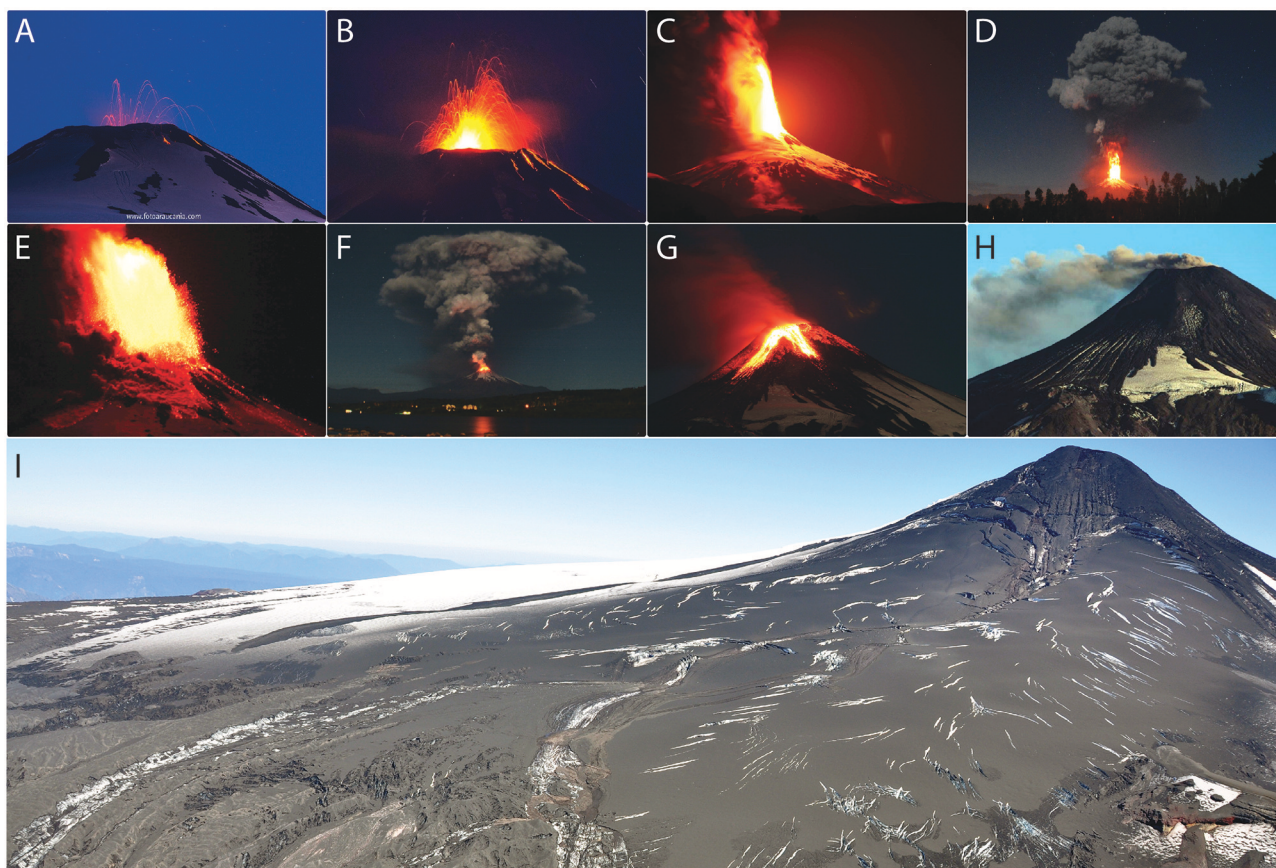


FIGURE 2 | Chronology of the 3 March 2015 lava fountain episode. **(A)** Strombolian activity on 20 February 2015 (Diego Spatafore). **(B)** A rising of the lava lake level produced increased Strombolian activity on 3 March 2015 (Martini Fotografia). **(C)** Lava fountain activity since 03.08 local time on 3 March. **(D)** Paroxysmal tephra column at 03.20 local time (Nicolás Gallo). **(E)** Reduction of the lava fountain height at 03.22 local time. **(F)** Tephra column at 03.22 local time (José Rodríguez). **(G)** Clastogenic lavas seen after the end of the paroxysmal eruption. **(H)** Aspect of the mixed avalanche deposits and ash emissions on 18 March 2015. **(I)** Tephra fall deposit on the east-southeast flank of the volcano on 3 March (Daniel Basualto). Pictures **(C,E,G,H)** taken by Anselmo Durán.

(indicated by profuse water vapor production over the glacier in **Figure 2E**), a consequence of a-, b-, and d-type-deposits, lahars descended through Correntoso, Zanjón Seco-Carmelito, Pedregoso, and Turbio rivers draining the volcano (Flores and Amigo, 2015; Johnson and Palma, 2015).

Following the 3 March 2015 eruption there was a notable deficit in infrasound generation and the summit crater was temporarily plugged with a carapace of lava. Gradual collapse of the summit lava led to the resumption of typical open-vent activity by the end of March. Subsequent activities, until the end of April 2015, consisted of ash emissions and incandescence. About 1 month after the eruption, GPS stations detected an uplift (1 cm/month) ~ 2.5 km southeast of the vent, with an apparent source at a depth of 4.5–5.2 km, which could be well correlated with volcano-tectonic (VT) seismicity (Córdova et al., 2015). InSAR interferograms that span mid-April to mid-May 2015 showed a persistent uplift of 4–6 cm about 5 km southeast of the volcano with a modeled source located at a depth of ~ 4.2 km and a cumulative volume change of $7.5 \times 10^6 \text{ m}^3$ (Delgado et al., 2017). This uplift was perhaps caused by refilling of the

magma reservoir after the eruption or a pressurization of the magma chamber caused by degassing (Delgado et al., 2017). Until February 2017, vent activity was characterized by variations in the magma column level, minor Strombolian activity erupting scoria and spatter a few tens of meters above the crater level, and ash emissions associated with partial collapse of the crater walls.

MATERIALS AND METHODS

Fieldwork

During the fieldwork in April 2017 and January 2018, mass per unit area (kg/m^2) loads of tephra fall deposit were measured at 29 locations, together with the maximum particle size at 21 locations. Mass loadings were measured *in-situ*, but in order to rectify results for any existence of humidity in samples, random samples were selected and were measured again in laboratory and results show $<1\%$ wt. content in water. Thus, 1% mass was discounted for correction of tephra loads reported in **Supplementary Table 1**. Clast size measurements were made

using three axis measurements and the average of the three largest particles per site (**Supplementary Table 1**). Mass loading measurements were made at flat sites with minimal effect of wind reworking or the influence of trees (shadow effect). Representative surfaces of 50×100 , 50×50 , and 25×25 cm² were selected, depending on the amount of tephra found in a particular site. All sampled particles from the eruption were cleaned of foreign inorganic particle or organic matter, and dry weights were measured with a digital scale. The mass loading data were used for the construction of an isomass map of the fall deposits (**Figure 3A**), while satellite images were useful for the reconstruction of tephra dispersal patterns. On the basis of the proximity to the source and tephra load on the ground, the deposits were divided into proximal (6–8 km downwind; 12 data points), medial (9–19 km downwind; 11 data points) and distal (20–43 km downwind; 6 data points). No far distal (>43 km) data were collected during this study. An estimation of the total mass (TM) of the deposit was obtained by integrating tephra load over isomass area following both the Exponential Thinning (Pyle, 1989) and Weibull (Bonadonna and Costa, 2012) methods.

Laboratory

Prior to characterization, tephra was dried at 35°C for 48 h. Grain-size analysis was carried out through dry manual sieving from 2,000 μ m to 32 μ m (–1 to 5 phi; fine lapilli to extremely fine ash) at steps of 1 phi (using seven meshes and one recipient for finer residuals). These size analyses allowed us to better describe magmatic fragmentation processes and to identify any potential contamination of tephra by ashes deposited subsequently. The relative density of juvenile particles was measured on 38 clasts and four sample types (7 from mixed avalanche deposit, 21 from scoria lapilli fallout, 3 from lava spatter and 7 from scoria bombs), using a distilled water pycnometer. Mean and standard deviation values were obtained from these samples. Representative samples from the four particle types were used for thin section preparation (thickness to 30 μ m) and observation under polarizing microscope for petrographic and mineralogical description at the Department of Geology of the University of Atacama, Copiapó (Chile). Both particle density and petrographic description were used to investigate the textural variation (i.e., crystallinity and vesicularity) of different particles in order to assess conduit dynamics. A Tescan-Vega (Bruker) Scanning Electron Microscope with Energy Dispersive Spectroscopy (SEM-EDS), operating at 15.0 kV and with a zoom of 20–250 x, was used for a qualitative description of juvenile textures at the Department of Extractive Metallurgy of the National Polytechnic School of Ecuador (DEMEX-EPN). Terminology from Parcheta et al. (2013) has been used on scoria vesicularity for descriptions, such as vesicle number density (VND) and vesicle size distribution (VSD). These observations informed an interpretation of quenching of pyroclastic fragments. The X-Ray intensities obtained through EDS semi-quantitative geochemical characterization directly on glass were converted to weight percent of oxides, which permitted constraints on nature of the magma feeding the 2015–2017 activity at Villarrica.

THE 3 MARCH 2015 TEPHRA FALL DEPOSITS

Distribution and Stratigraphy

Tephra dispersion mainly occurred southeast ($\sim 120^\circ$ azimuth) of the crater in a narrow, elongated, nearby-elliptic area (**Figure 3A**). Minimum loads of about 80–120 g/m², were observed at crosswind locations, where the mass of the deposit rapidly decreases to minimum values away from the downwind axis. In contrast, higher load values coincided with the dispersal axis and they diminished slowly from the source. Maximum loads of about 11,500 g/m² were observed at a distance of 7–9 km from the source. A good correlation was observed in the plot of tephra load (kg/m²) vs. square root area (km) for both Weibull and Exponential fits (**Figure 3B**). On the other hand, the largest particles of the deposit were distributed in semi-elliptic isopleths trending southeast, decreasing rapidly from 6 cm to 1 cm diameter between 7 and 20 km away from the vent (**Figure 3C**).

At proximal locations, in the immediate vicinity of the crater (<1 km) the deposit stratigraphy consisted of non-welded agglutinated spatter bombs (**Figure 4A**) up to several meters in thickness (10–15 m), where meter-sized aerodynamic fusiform bombs were also found (**Figure 4B**). At proximal to medial locations, the tephra fall deposit consisted of a single black basaltic scoria layer, inversely graded and formed by medium-to-coarse lapilli and bombs (particle size > 4 mm) (**Figures 4C,D**), with a total thickness of 3–5 cm, corresponding to respective loads of 6 and 11 kg/m². A progressive decrease in deposit thickness is observed from medial to distal deposits, where it varies from a 2 to 3 cm thick, medium- to coarse-lapilli blanket (particle size 4–32 mm; **Figure 4E**) to a single-particle medium-size lapilli blanket (4–8 mm; **Figure 4F**), where the thickness of the deposit was the same as the size of the smallest axis of these particles. Distal deposits were full of fine- to medium-size lapilli (**Figure 4G**), with ash at the bottom of the deposit. At farther distances (>40 km), only individual fine lapilli (2–5 mm) particles were found without the formation of a homogeneous tephra layer (**Figure 4H**). In those deposits, lapilli were partially cemented by the subsequent ash fallout from the eruption of Calbuco Volcano on 22–23 April 2015, which deposited a few mm of tephra in the area near to the international road (CH-199) and Mamuil-Malal mountain pass (see Romero et al., 2016b for details). Ash deposits were not detected at San Martín de Los Andes or Junin de los Andes in Argentina (Clarín, 2015).

Characteristics of Tephra

All samples are compound by well sorted coarse ash to lapilli and they vary from unimodal (samples at sites 20 and 32) to bimodal (sites 14 and 36) in their grain size distribution. Frequent modes are at 750 μ m (site 20), 1,500 μ m (sites 14, 32, and 36), 187 μ m (site 14), and 94 μ m (site 36) (**Figure 5A**). The second mode of fine material at Mamuil-Malal (sample at site 36) has been correlated to ash from the Calbuco eruption, as confirmed by microscopic inspection of the sample.

Densest particles corresponded to spatter (2.10 ± 0.11 g/cm³), followed by scoria bombs (1.68 ± 0.34 g/cm³), and the mixed

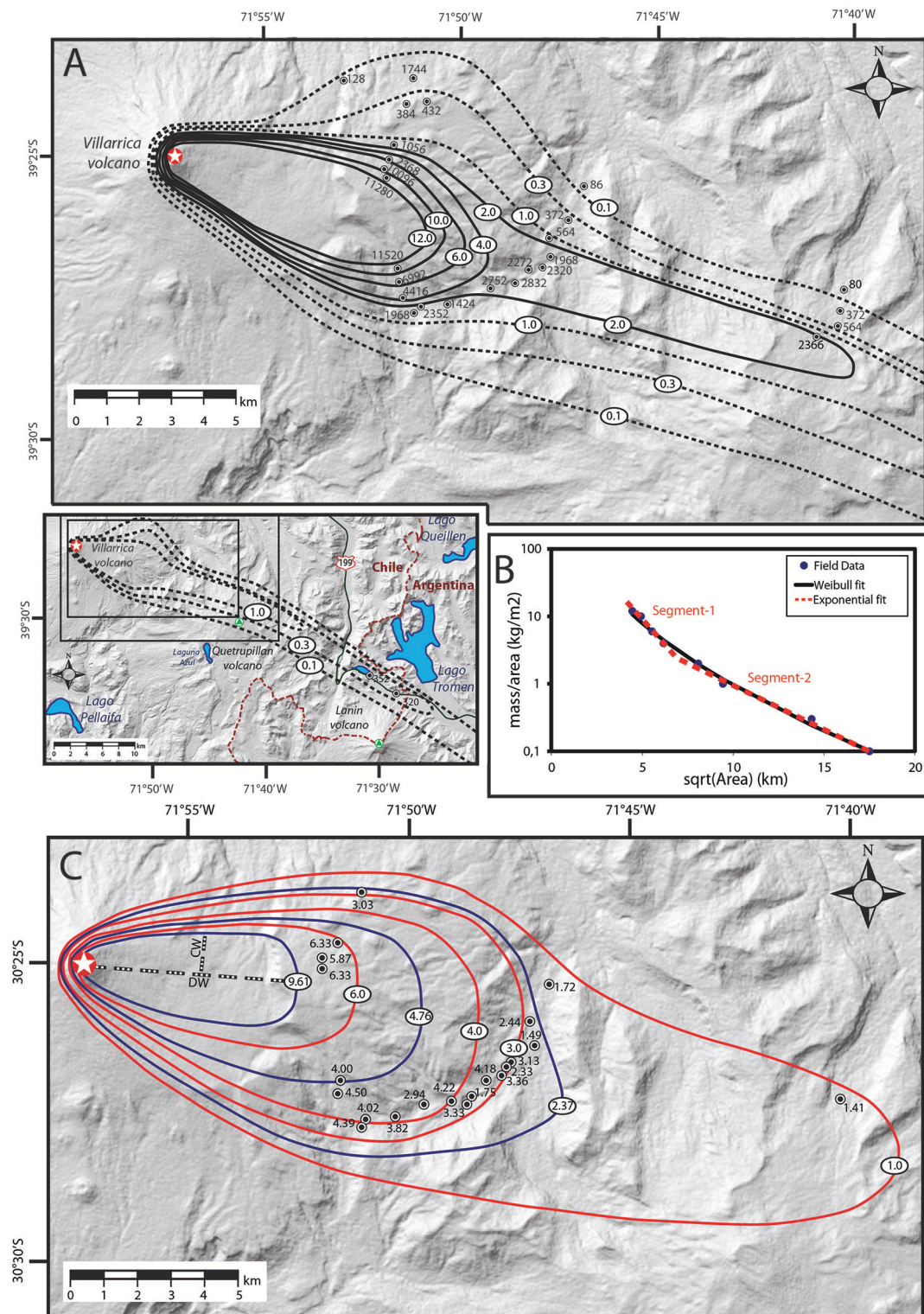


FIGURE 3 | Distribution of the tephra fall deposit. **(A)** Isomass map. Load values on isopachs are expressed in kg/m², while field data are released in g/m² for detailed observation. Dotted lines represent isomass curves with uncertainty. **(B)** Load (kg/m²) v/s square root area (km) plot for the tephra fall deposit. Both Weibull and Exponential (two-segment) best fits are plotted. **(C)** Isolepth map. Clast diameters are in cm, and the red curves are based on field data. Blue curves are result from interpolation and were used for the calculation of column heights following the method of Carey and Sparks (1986). DW and CW represent example downwind and crosswind axes, as these were used for the earlier procedure.

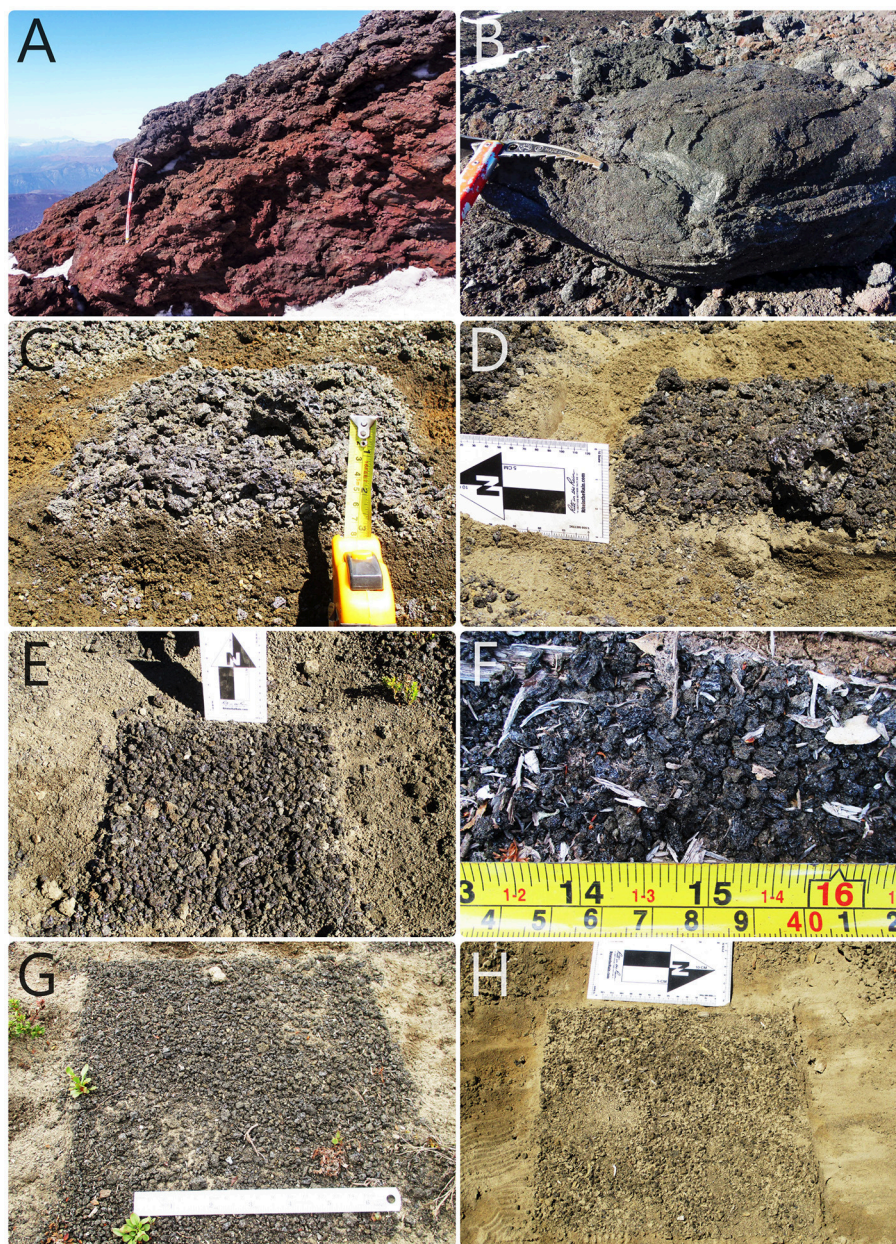
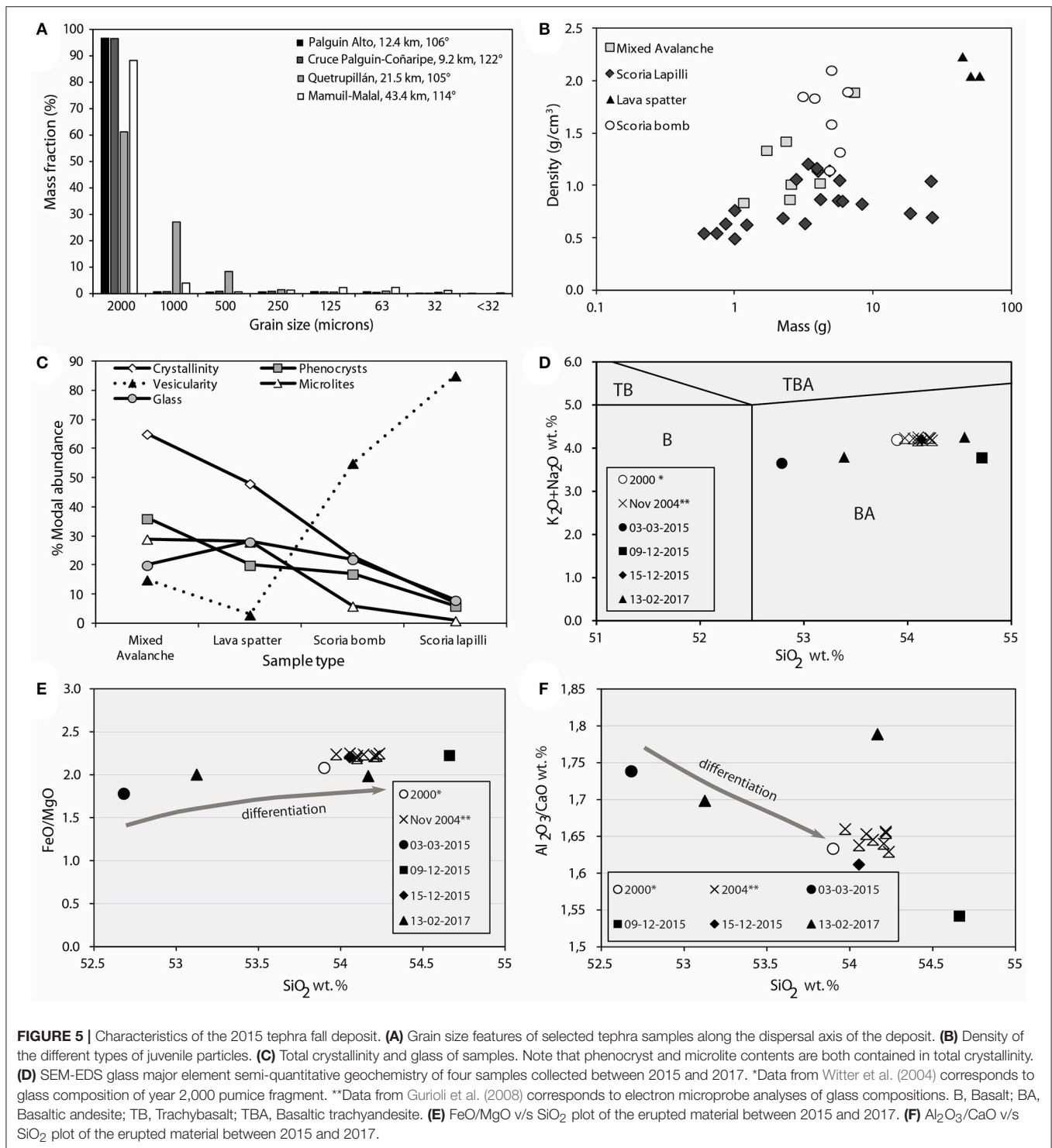


FIGURE 4 | Field features of the tephra fall deposit. **(A)** Non-welded agglutination of spatters close to the summit of Villarrica (photo by Franco Vera). Ax pick is 66 cm long. **(B)** Metric-sized fusiform bomb in the upper flanks of the volcano (photo by Franco Vera). **(C,D)** Proximal, reverse graded tephra fall deposit at 6 and 7 km distance east-northeast from the vent, respectively. Decimetre-sized scoria bombs are found on top. **(E)** Medial deposit found 8 km southeast the vent. Note that the clast size is smaller (medium to coarse lapilli) than at proximal distances, and bombs are relatively scarce on top. **(F)** Medial deposit 13 km east-northeast from the vent, exclusively consisting of medium-sized scoria lapilli. **(G,H)** Distal deposits with fine to medium sized scoria lapilli at 21 and 43 km distance, east-southeast from the vent. Scale length in G is 16.5 cm. Pictures **(B–H)** by Jorge Romero and Franco Vera.

avalanche pyroclasts ($1.20 \pm 0.38 \text{ g/cm}^3$); the lowest density samples corresponded to air fall lapilli ($0.84 \pm 0.23 \text{ g/cm}^3$) (**Figure 5B**). All the samples are vitrophyric in texture, with a mineral assemblage of plagioclase (Plg; 3–30%), clinopyroxene (Cpx; 2–5%), olivine (Ol; 1–4%) phenocrysts, and scarce orthopyroxene (Opx; <1%). Occasionally, glomeroporphyrict clots contain subhedral to euhedral Plg, Cpx, and Ol. Plg

phenocrysts (size between 0.05 and 2.0 mm) show sieved texture, polysynthetic twinning and rounded frames by crystal resorption (**Supplementary Figure 1A**). Cpx phenocrysts were anhedral to subhedral (rarely euhedral), with size between 0.1 and 1.7 mm and simple twinning (**Supplementary Figure 1B**), while Ol phenocrysts are anhedral to subhedral with size between 0.05 and 0.6 mm (**Supplementary Figure 1C**). The total amount



of phenocrysts varies from 6 to 36%, however 1 to 29% of microlites are observed; thus, the whole-rock crystallinity (phenocrysts; microlites) varies from 7 to 65% (Figure 5C). The mixed avalanche pyroclasts are highly crystalline (65%), followed by the lava spatter (48%) and the scoria bombs (23%), while the lapilli fragments had lower crystallinities (7%) (Figure 5C).

Vesicularity varies largely from 3 to 85%, with subangular to rounded (low to high sphericity) vesicles, which are elongated in some cases.

During the paroxysmal eruption of 3 March 2015, three airfall scoria textures were observed. The first had fluidal shape and smooth curvilinear surface with spherical vesicles

<200 μm in size (**Supplementary Figure 2A**), the second was characterized by blocky morphology, with spherical to sub-spherical vesicles with size with size > 200 and < 500 μm (**Supplementary Figure 2B**), while the third had blocky morphology but elongated vesicles with fibrous walls with size up to 250 μm (**Supplementary Figure 2C**). These scorias had vesicularity of 70–90% by volume and crystal fraction was very low (<3%). Samples collected at the crater rim on 9 and 15 December 2015 showed blocky morphology but also extremely vesicular morphology (ca. 90%), with slightly low VND and narrow VSD (100–250 μm), respectively (**Supplementary Figures 2D,E**). However, the 13 February 2017 sample, also collected at the crater rim, had a texture similar to that observed in the second type of scoria ejected during the paroxysmal eruption (**Supplementary Figure 2F**). Geochemical compositions of juvenile particles range from 52.68 to 54.66 SiO₂ wt.%, and are thus classified as basaltic andesite (**Figure 5D**; **Supplementary Table 2**) from the medium-K series (K₂O from 0.40 to 0.62 wt. %). The samples that were erupted during 9 and 15 December 2015 and 13 February 2017 are more evolved when compared with the 3 March 2015 products.

Total Mass, Volume, and Eruption Source Parameters

The total mass (TM) of the deposit is estimated to 6.9×10^8 kg using the exponential model (**Figure 3B**) with a single segment. Mass increases to 1.6×10^9 kg, when two segments are integrated. A higher mass was obtained with the Weibull fit integration (**Figure 3B**), reaching 2.0×10^9 kg. The correlation (R^2 -squared root) fit between these distributions and the field data varied from 0.989 to 0.997 for the single Exponential and the Weibull models respectively. The average TM derived from all methods was 1.4×10^9 kg. Using an average deposit density of 567

kg/m³, obtained from the average density of 8 bulk proximal-to-distal tephra samples (**Supplementary Table 3**), we calculate bulk volumes between 1.2 and 3.4×10^6 m³ and an average of 2.3×10^6 m³, similarly to results of Bertin et al. (2015). The dense rock equivalent (DRE) of the total mass is 4.9×10^5 m³ using an assumed basaltic melt density of 2850 kg/m³. TM is used to estimate the mass eruption rate (MER) using the eruption duration of the paroxysmal phase whose duration is estimated at 16 min. MER values from 7.6×10^5 to 2.10×10^6 kg/s were used for the TM spectrum retrieved by different integration methods (**Table 1**). An average MER of 1.48×10^6 kg/s implies a column height of about 8.6 km according to the model of (Mastin et al., 2009) (**Table 1**). Application of the Carey and Sparks (1986) method for the estimation of the eruption column height using isopleths (**Figure 3C**) yields a column height of 10.8 km (**Table 2**). The magnitude and intensity of the eruption is inferred through MER values using the equations of Pyle (2015) resulting in magnitude and intensity values of 2.11 and 9.13 respectively (**Table 1**). Such characteristics are in agreement with a VEI 2-3 eruption in the classification scheme of Newhall and Self (1982).

DISCUSSION AND CONCLUSIONS

Data Reliability

Tephra mass/volume estimates are subject to different sources of uncertainty, such as tephra reworking, field data quality, contouring of isomass maps and integration models (e.g., Engwell et al., 2013; Biassé et al., 2014; Klawonn et al., 2014; Bonadonna et al., 2015). Although fieldwork for the present work was conducted more than 2 years after the eruption, the tephra fall deposit remained in a relatively unaltered state in most of the locations and no signs of erosion were apparent. Deposits consisted of uniform blankets of tephra without any sign of water dissection or aeolian sedimentary structures (**Figure 4**).

TABLE 1 | Volume estimates and eruption source parameters of the 3 March 2015 lava fountain eruption from Villarrica volcano.

Method	Fitting parameters	Correlation (R)	Total mass (kg)	Volume non-DRE (m ³)	Volume DRE (m ³)	Mass eruption rate (kg/s)	Magnitude (M)	Column height, H _T (m)	Intensity (I)
Exponential - 1 segment	b _T = 1.093	0.989	6.87×10^8	1.15×10^6	2.41×10^5	7.16×10^5	1.84	7,225	8.85
	T ₀ = 43.96								
Exponential - 2 segment	b _{TTP} = 0.587; b _{TDP} = 1.289	0.994	1.56×10^9	2.61×10^6	5.46×10^5	1.62×10^6	2.19	8,928	9.21
	T _{0P} = 245.2; T _{0D} = 20.78								
Weibull	ϑ = 186.065; λ = 1.953; η = 0.703	0.997	2.02×10^9	3.38×10^6	7.08×10^5	2.10×10^6	2.30	9,550	9.32
	Average		1.42×10^9	2.38×10^6	4.98×10^5	1.48×10^6	2.11	8,568	9.13

DRE is Dense rock equivalent; $M = \log_{10} TM - 7$ (Pyle, 2015) $H_T = 0.220 \cdot MER^{0.259}$ (Mastin et al., 2009); $I = \log_{10} MER + 3$ (Pyle, 2015). Exponential thinning function is integrated as follows: $TM = (13.08 \cdot M_0 \cdot (b_T^2)) \cdot 10^6$; M_0 is the maximum mass measured in the field, while b_T^2 is the distance from the vent where the mass of the deposit has decreased to half of the total. p and d are referred to proximal and distal. Weibull function is integrated as follows: $TM = 2(\vartheta \cdot 10^6) \cdot (\lambda^2/n)$ where λ is the characteristic decay scale of the deposit (km), ϑ represents mass scale and n is a shape parameter.

TABLE 2 | Isopleth data obtained from field data interpolation, through the method of Carey and Sparks (1986).

Diameter (cm)	DW (km)	CW (km)	H _T (m)
2.37	15.09	4.18	10,390
4.76	9.75	2.38	12,140
9.61	6.12	1.20	9,990
		Average	10,840

DW, Downwind axis; CW, Crosswind axis; HT, Column height.

The largest source of uncertainty comes from the border-conditions on the isomass map (0.1 kg/m^2) in addition to bias in contouring due to limited field data. Uncertainty of contouring has been assessed for the integration of erupted volumes through isopach maps by Klawonn et al. (2014) but no reports are available for mass integration from isomass maps. However, both procedures are equivalent and uncertainties vary between 7 and 30% at well-sampled deposits (with field data at proximal, medial and distal areas) and for maps governed by extreme values (proximal and distal), respectively. Thus the maximum uncertainty in the mass estimation should be no larger than 30%. In addition, column heights estimated through the Carey and Sparks (1986) method are sensitive to the nature of the measured clasts, especially when these are susceptible to breakage during impact to the ground. To minimize this potential source of error, three largest particles were measured at each site. The best clast characterization has been reported to be the geometric mean of the three orthogonal axes with approximation of the minimum ellipsoid. However, discrepancies associated with the choice of number of particle axis are considered to be larger than the discrepancies associated with the number of clasts analyzed (Bonadonna et al., 2013). According to Blass and Bonadonna (2011) the average uncertainty is within 20% for all averaging techniques and contours considered. Nonetheless, the estimated values for column height are slightly larger (10.8 vs. 8.6 km; $\sim 15\%$ difference) using isopleths compared to MER or direct observation (SERNAGEOMIN, 2015). Estimates obtained through imagery analysis yield 11–12 km above the crater (Romero et al., 2016a), which is up to 10% larger than our estimates. However, this value should be considered as slightly overestimated due to the lack of side-views of the column, as all the pictures were taken from front view. In fact, the reported mean column height value of 10.8 km is between values estimated from imagery analyses and eyewitness estimates. Thus column-height uncertainty is about 10–15%. Uncertainty is also present in petrological and geochemical characterization. For instance, thin section description through polarizing microscope may have an uncertainty of 1–2% in the quantification of crystal and vesicle abundance and competence of the analyst.

Conduit Dynamics

The 3 March 2015 paroxysm products are characterized by a lower SiO_2 content ($\sim 52.7 \text{ wt. \%}$) than are lava lake products ($\sim 54.7 \text{ wt. \%}$) (Figures 5D–F). The compositional trend observed at Villarrica (Figure 5E) was also observed during the 2,000 cyclic activity at Etna volcano, where Strombolian

activity was found compositionally slightly more evolved than lava fountain scoria at Etna (Polacci et al., 2006). This means that the magma erupted during the 3 March 2015 paroxysmal event at Villarrica was less-differentiated (more primitive). Similar observations have been done by Aiuppa et al. (2009) during the transition from Strombolian to effusive activity at Stromboli volcano between February and April 2007. Furthermore, paroxysm products show a higher $\text{Al}_2\text{O}_3/\text{CaO}$ ratio than that of lava lake (Figure 5F). This evidence confirms that the most explosive pyroclastic eruptions of Villarrica are characterized by a high $\text{Al}_2\text{O}_3/\text{CaO}$ ratio (Hickey-Vargas et al., 1989, 2004; López-Escobar and Moreno, 1994). Our chemical data support the observation of Aiuppa et al. (2017), who conclude that the 3 March 2015 paroxysmal eruption of Villarrica was sourced by an intrusion of deep (20–35 MPa), primitive, volatile-rich magma. Such a trigger has been described previously as a typical mechanism for the generation of lava fountains and is known in the literature as the “foam collapse model” (Jaupart and Vergnolle, 1989), as opposed to the “rise-speed-dependent model” (Parfitt, 2004), which assumes that an eruption is triggered by syneruptive bubble exsolution accompanying magma rising in the conduit as the volume fraction of bubbles exceeds that of maximum packing.

The higher SiO_2 content of lava lake products may be explained by convective conduit dynamics (Witter et al., 2004) during pre-eruptive (years to days) and post-paroxysmal (i.e., days and months after 3 March 2015 eruption) stages, where bubbly flow controls the bursting of lava lake and magma degassing (Figure 6A). The progressive increase of geophysical signals (i.e., increasing seismicity, thermal anomalies and rising of CO_2/SO_2 degassing) together with the rise of lava lake and Strombolian activity is interpreted as a higher participation of primitive magma within the conduit and a slug flow type volatile transport on 2 March 2015 (Figure 6B). A full involvement of primitive, low viscosity foamy basaltic-andesite magma during the 3 March 2015 eruption is believed to have produced both lava fountain and sustained tephra column during the paroxysmal eruption (Figure 6C).

Tephra with unimodal grain-size distribution, which commonly are coarse-grained and better sorted than those for bimodal distributions are a typical feature of “dry” or “magmatic” explosivity (Houghton and Gonnermann, 2008). Tephra having bimodal grain-size distributions could be related to synsedimentary processes of sorting within the eruption column (e.g., Houghton et al., 2004). Particularly, sample at site14 which has a bimodal grain-size distribution, was collected fairly close to the north border of the deposit where surface crosswind may have played a role in grain-size selection. The eruption of different types of scoria can be explained by their textural features. For instance, blocky scoria containing two populations of sub-spherical bubbles, such as those seen during the paroxysmal eruption and then during the activity of 9 December 2015 and 13 February 2017, have previously been interpreted as coming from a waning discharge through ponded lava during increased outgassing (Parcheta et al., 2013; Figure 6A). The simultaneous eruption of scoria with

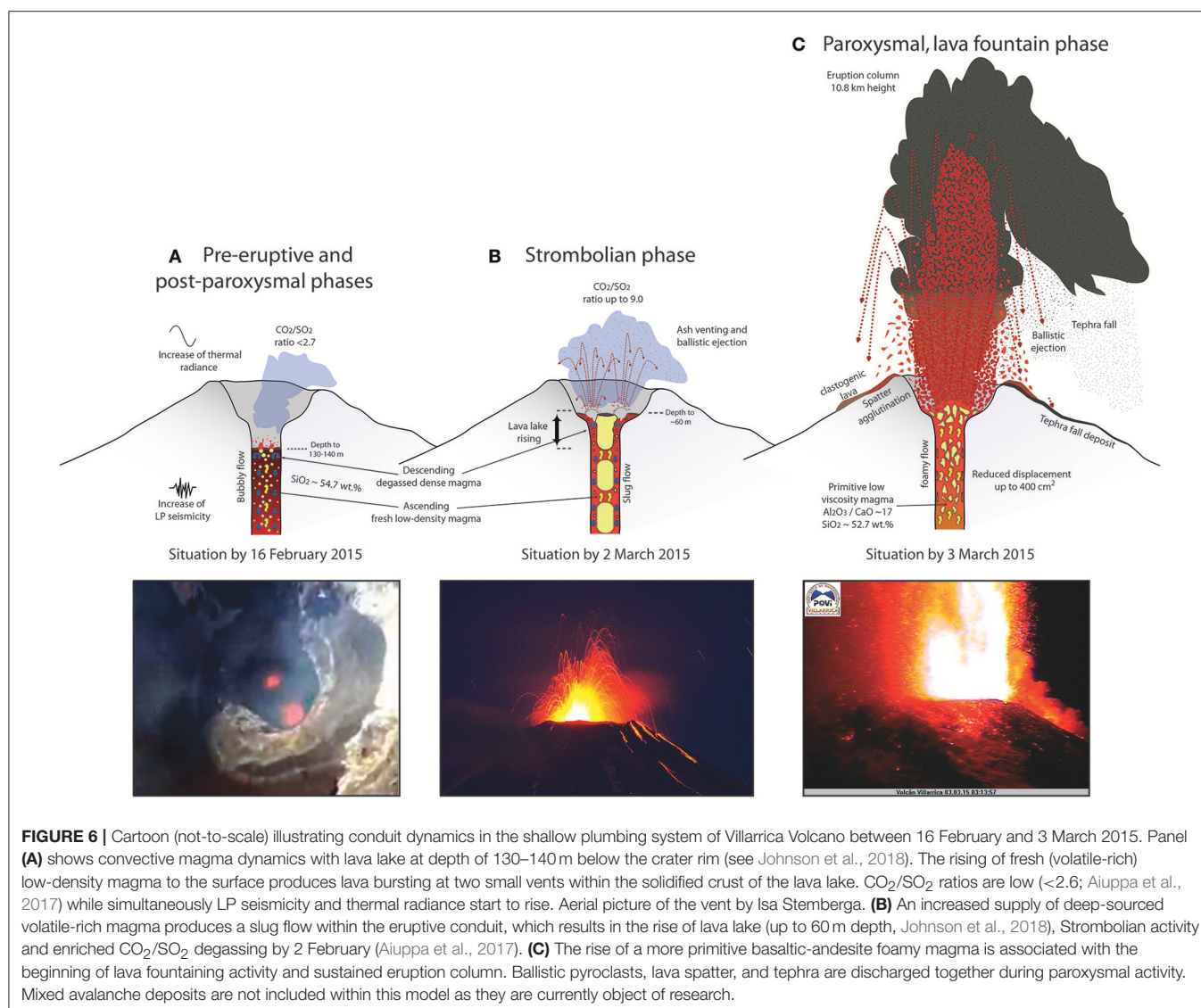


FIGURE 6 | Cartoon (not-to-scale) illustrating conduit dynamics in the shallow plumbing system of Villarrica Volcano between 16 February and 3 March 2015. Panel (A) shows convective magma dynamics with lava lake at depth of 130–140 m below the crater rim (see Johnson et al., 2018). The rising of fresh (volatile-rich) low-density magma to the surface produces lava bursting at two small vents within the solidified crust of the lava lake. CO₂/SO₂ ratios are low (<2.6; Aiuppa et al., 2017) while simultaneously LP seismicity and thermal radiance start to rise. Aerial picture of the vent by Isa Stemmerga. (B) An increased supply of deep-sourced volatile-rich magma produces a slug flow within the eruptive conduit, which results in the rise of lava lake (up to 60 m depth, Johnson et al., 2018), Strombolian activity and enriched CO₂/SO₂ degassing by 2 February (Aiuppa et al., 2017). (C) The rise of a more primitive basaltic-andesite foamy magma is associated with the beginning of lava fountaining activity and sustained eruption column. Ballistic pyroclasts, lava spatter, and tephra are discharged together during paroxysmal activity. Mixed avalanche deposits are not included within this model as they are currently object of research.

spherical-shaped vesicles and scoria with stretched vesicles has been interpreted as the result of a violent eruptive phase triggered by the ascent of a fresher, crystal-poor, and highly vesicular magma (Di Traglia et al., 2009; Figure 6C). However, this does not rule out the possibility that stretched vesicles may result from shearing due to magma ascent close to the conduit margins (e.g., Polacci et al., 2001, 2003; Parcheta et al., 2013; Figure 6C). We interpret the bimodality of vesicle shapes as the simultaneous eruption of scoria coming from the margin and central part of the lava fountain during the paroxysmal event of 3 March 2015, and/or during the transition from Strombolian activity to a lava-fountain event as observed for other basaltic volcanoes (e.g., Wolff and Sumner, 2000; Taddeucci et al., 2015; Figures 6B,C).

Total vesicularity was higher in samples favored by a quick subaerial quenching process (i.e., scoria), suggesting a rapid loss of volatile content. Total crystallinity, on the other hand, was lower in these rocks. Glass content also slightly increased with

vesicularity, but the overall glass content decreased as vesicles occupied a larger space in the whole sample. In addition, we observed a direct relation between the dispersal of erupted products and vesicularity, as more vesicular pyroclasts were deposited at greater distances from the vent due to their lower density. This relationship between vesicle-to-melt ratio, vesicle number density and vesicle size has been previously studied in lava fountains and it has been suggested that these textural properties are controlled by the length of residence time within the fountain (Stovall et al., 2011).

Lessons From the March 2015 Lava Fountain

Single paroxysmal events related to lava fountain activity generally last a few hours and erupt 10⁸ to 10⁹ kg of tephra (Taddeucci et al., 2015), which is well in agreement with the estimates presented here for the 3 March 2015 eruption. In fact, the triggering, initiation and size of the Villarrica lava fountain

seems to be typical for this volcano and other analog volcanoes. Lava fountain height, eruption column height and MER values calculated here are comparable, for instance, to the eruptive parameters obtained for the largest-scale lava fountain events at Mt. Etna (e.g., 24 September 1986, 5 January 1990, 22 July 1998 and the climax MER of paroxysmal events between 2011 and 2015; see Andronico et al., 2015; Freret-Lorgeril et al., 2018 for details). In addition, the erupted volume is very similar to that from the Kilauea Iki Crater eruption (1959), which was the highest historical lava fountain event registered in Hawaii (height up to 580 m and erupted a total non-DRE volume between 2.1 and $5.8 \times 10^6 \text{ m}^3$; Stovall et al., 2011; Klawonn et al., 2014) and slightly larger than the DRE tephra volume estimated for 2012–13 Tolbachik fissure eruptions (about $4.0 \times 10^5 \text{ m}^3$; Belousov et al., 2015). In contrast, the violent Strombolian activity of Llaima volcano in 2008–2009 had lower intensity/MER values ($\sim 1.6 \times 10^4 \text{ kg/s}$) and lava-fountain-related column did not become sustained for the whole eruption duration, even though it produced equivalent peak thermal radiance values ($89.5 \text{ W m}^{-2} \text{ sr}^{-1} \mu\text{m}^{-1}$ $\text{W m}^{-2} \text{ sr}^{-1} \mu\text{m}^{-1}$; Romero et al., 2013) and a similar tephra fall volume ($\sim 1.31 \times 10^6 \text{ m}^3$) and composition (basaltic andesite) (Ruth and Calder, 2014). This suggests that the 3 March eruption of Villarrica is an example of a high-intensity end member of lava fountain-related paroxysmal events. In addition, a rapid initiation of the paroxysmal eruption column following the lava fountain onset (~ 2 min) with an unexpected increase in volcanic hazard is here reported. This is a challenging aspect for volcanologists and civil protection authorities at active volcanoes having similar volcanic activity.

The historical record confirms that the volcanic phenomena observed during the 2015 Villarrica eruption are not isolated but frequent and constitute a major source of volcanic hazard (e.g., Van Daele et al., 2014). In this view, fresh knowledge acquired through the study of the 2015 eruption needs to be supplemented with historical accounts in order to improve measures for hazard mitigation during future eruptions. For example, probabilistic tephra fall hazard assessment and tephra fall accumulation maps, derived from historical events, would be helpful to forecast on the medium-to longer-term the impact of future tephra fall events at Villarrica.

AUTHOR CONTRIBUTIONS

JR and FV undertook the fieldtrips and tephra sampling. JR, JB, AG, and EC analyzed tephra samples in laboratory. The paper was primarily written by JR. MP, DM, FA, MA, JP, MB, and JJ analyzed and discussed data and contributed to paper writing. However they are conducting complementary research to this work. WK provided samples from the crater rim after the main 2015 eruption, and also audiovisual registry from the eruption.

REFERENCES

Aiuppa, A., Bitetto, M., Francofonte, V., Velasquez, G., Bucarey-Parra, C., Giudice, G., et al. (2017). A CO_2 -gas precursor to the March 2015

FUNDING

This study was partially supported by the NSF-GEO-NERC grant Quantifying disequilibrium processes in basaltic volcanism (Reference: NE/N018575/1). Partial support for JJ was made possible through National Science Foundation EAR grant 0838562.

ACKNOWLEDGMENTS

Authors would like to thank Robinson Garrido, Victoria Ramirez, and Nicolás Luengo for their assistance during field work. They are grateful to Diego Spatafore, Anselmo Durán, Martini Fotografía, José Rodríguez, Nicolás Gallo, Isa Stemberga, Patricio Arias, and Daniel Basualto (OVDAS) for the photos and to the staff of Sol y Luna, for accommodation at Pucón and transport to the volcano. Thin sections were prepared and studied at the Department of Geology of the Universidad de Atacama. SEM-EDS analyses were carried out at the DEMEX-EPN, Ecuador. Original data are available upon request. The fruitful and constructive reviews of two referees, in addition to the editorial handling of Dr. Sonia Calvari and Dr. Valerio Acocella, greatly improved the original version of this manuscript.

SUPPLEMENTARY MATERIAL

The Supplementary Material for this article can be found online at: <https://www.frontiersin.org/articles/10.3389/feart.2018.00098/full#supplementary-material>

Supplementary Figure 1 | Thin sections of juvenile products erupted by 3 March 2015 seen at cross polarized light (left) and plane polarized light (right). (A) corresponds to the scoria bomb, (B) to the scoria lapilli and (C) to the mixed avalanche juvenile fragment.

Supplementary Figure 2 | Scanning electron microscope (SEM) images. Yellow scale bars are $500 \mu\text{m}$ in length. (A–C) are three different basaltic-andesitic scoria (tachylite) morphologies erupted by 3 March 2015 (A—smooth curvilinear surface, B—blocky morphology with spherical vesicles and C—blocky morphology with elongated vesicles plus fibrous walls). (D–F) are blocky tachylite erupted by 9 December 2015, 15 December 2015 and 13 February 2017, respectively.

Supplementary Table 1 | Field data with the location of sample points, tephra loads, and maximum scoria size measured. D means distance from the vent.

Supplementary Table 2 | SEM-EDS semi-quantitative geochemical glass composition of samples from Villarrica volcano. The X-Ray intensities directly obtained on glass were converted to wt. % of oxides. Notice that MnO and P_2O_5 are not recognized within this method. Total values are uncorrected.

Supplementary Table 3 | Apparent density calculations on 7 bulk tephra deposit samples collected at the field locations labeled (see **Supplementary Table 1**). Average density is representative of the whole deposit as samples were collected at proximal, medial and distal locations. The samples 13A and 13B were collected at a distance of 10 m of difference for comparison control purpose.

Villarrica volcano eruption. *Geochim. Geophys. Geosys.* 18, 2120–2132. doi: 10.1002/2017GC006892

Aiuppa, A., Federico, C., Giudice, G., Giuffrida, G., Guida, R., Gurrieri, S., et al. (2009). The 2007 eruption of Stromboli volcano: insights from real-time

- measurement of the volcanic gas plume CO₂/SO₂ ratio. *J. Volcanol. Geotherm. Res.* 182, 221–230. doi: 10.1016/j.jvolgeores.2008.09.013
- Allard, P., Burton, M., and Muré, F. (2005). Spectroscopic evidence for a lava fountain driven by previously accumulated magmatic gas. *Nature* 433, 407–410. doi: 10.1038/nature03246
- Andronico, D., and Corsaro, R. A. (2011). Lava fountains during the episodic eruption of South-East Crater (Mt. Etna), 2000: insights into magma-gas dynamics within the shallow volcano plumbing system. *Bull. Volcanol.* 73, 1165–1178. doi: 10.1007/s00445-011-0467-y
- Andronico, D., Cristaldi, A., and Scollo, S. (2008). The 4–5 September 2007 lava fountain at South-East Crater of Mt Etna, Italy. *J. Volcanol. Geotherm. Res.* 173, 325–328. doi: 10.1016/j.jvolgeores.2008.02.004
- Andronico, D., Scollo, S., Castro, M. D. L., Cristaldi, A., Lodato, L., and Taddeucci, J. (2014a). Eruption dynamics and tephra dispersal from the 24 November 2006 paroxysm at South-East Crater, Mt Etna, Italy. *J. Volcanol. Geotherm. Res.* 274, 78–91. doi: 10.1016/j.jvolgeores.2014.01.009
- Andronico, D., Scollo, S., and Cristaldi, A. (2015). Unexpected hazards from tephra fallout at Mt Etna: The 23 November 2013 lava fountain. *J. Volcanol. Geotherm. Res.* 304, 118–125. doi: 10.1016/j.jvolgeores.2015.08.007
- Andronico, D., Scollo, S., Cristaldi, A., and Castro, M. D. L. (2014b). Representivity of incompletely sampled fall deposits in estimating eruption source parameters: a test using the 12–13 January 2011 lava fountain deposit from Mt. Etna volcano, Italy. *Bull. Volcanol.* 76:861. doi: 10.1007/s00445-014-0861-3
- Belousov, A., Belousova, M., Edwards, B., Volynets, A., and Melnikov, D. (2015). Overview of the precursors and dynamics of the 2012–13 basaltic fissure eruption of Tolbachik Volcano, Kamchatka, Russia. *J. Volcanol. Geotherm. Res.* 307, 22–37. doi: 10.1016/j.jvolgeores.2015.06.013
- Bertin, D., Amigo, A., and Bertin, L. (2015). Erupción del volcán Villarrica 2015: Productos emitidos y volumen involucrado. *XIV Congreso Geológico Chileno* (La Serena).
- Biass, S., and Bonadonna, C. (2011). A quantitative uncertainty assessment of eruptive parameters derived from tephra deposits: the example of two large eruptions of Cotopaxi volcano, Ecuador. *Bull. Volcanol.* 73, 73–90. doi: 10.1007/s00445-010-0404-5
- Biasse, S., Bagheri, G., Aeberhard, W., and Bonadonna, C. (2014). TError: towards a better quantification of the uncertainty propagated during the characterization of tephra deposits. *Stat. Volcanol.* 1, 1–27. doi: 10.5038/2163-338X.1.2
- Bonaccorso, A., Caltabiano, T., Currenti, G., Del Negro, C., Gambino, S., Ganci, G., et al. (2011). Dynamics of a lava fountain revealed by geophysical, geochemical and thermal satellite measurements: The case of the 10 April 2011 Mt Etna eruption. *Geophys. Res. Lett.* 38. doi: 10.1029/2011GL049637
- Bonaccorso, A., Calvari, S., Linde, A., and Sacks, S. (2014). Eruptive processes leading to the most explosive lava fountain at Etna volcano: the 23 November 2013 episode. *Geophys. Res. Lett.* 41, 4912–4919. doi: 10.1002/2014GL060623
- Bonadonna, C., Biass, S., and Costa, A. (2015). Physical characterization of explosive volcanic eruptions based on tephra deposits: propagation of uncertainties and sensitivity analysis. *J. Volcanol. Geotherm. Res.* 296, 80–100. doi: 10.1016/j.jvolgeores.2015.03.009
- Bonadonna, C., Cioni, R., Pistolesi, M., Connor, C. B., Scollo, S., Pioli, L., et al. (2013). Determination of the largest clast sizes of tephra deposits for the characterization of explosive eruptions: a study of the IAVCEI commission on tephra hazard modelling. *Bull. Volcanol.* 75:680. doi: 10.1007/s00445-012-0680-3
- Bonadonna, C., and Costa, A. (2012). Estimating the volume of tephra deposits: a new simple strategy. *Geology* 40, 415–418. doi: 10.1130/G32769.1
- Calder, E., Harris, A., Peña, P., Pilger, E., Flynn, L., Fuentealba, G., et al. (2004). Combined thermal and seismic analysis of the Villarrica volcano lava lake, Chile. *Rev. Geol.* 31, 259–272. doi: 10.4067/S0716-02082004000200005
- Carey, S., and Sparks, R. S. J. (1986). Quantitative models of the fallout and dispersal of tephra from volcanic eruption columns. *Bull. Volcanol.* 48, 109–125. doi: 10.1007/BF01046546
- Carracedo, M., Sarrionandia, F., Arostegui, J., Eguiluz, L., and Ibarguchi, J. G. (2012). The transition of spatter to lava-like body in lava fountain deposits: features and examples from the Cabezo Segura volcano (Calatrava, Spain). *J. Volcanol. Geotherm. Res.* 227–228, 1–14. doi: 10.1016/j.jvolgeores.2012.02.016
- Clarín (2015). *Un volcán Reavivó el Fantasma de las cenizas en la Patagonia*. Clarín.com – Sociedad. Available online at: <https://www.clarin.com/sociedad/>
- volcan-villarrica-cenizas-patagonia_0_rk-j_XqDQg.html (Accessed March 17, 2018).
- Córdova, L., Alarcón, A., Mardones, C., Cardona, C., Gil, F., Rojas, G., et al. (2015). “Monitoreo de la Deformación en Volcanes Chilenos Mediante Técnica GPS, Resultados Asociados a la Actividad de Los Volcanes Laguna del Maule, Copahue y Villarrica,” in *XIV Congreso Geológico Chileno* (La Serena: Colegio de Geólogos de Chile).
- Corsaro, R. A., and Miraglia, L. (2014). The transition from summit to flank activity at Mt. Etna, Sicily (Italy): Inferences from the petrology of products erupted in 2007–2009. *J. Volcanol. Geotherm. Res.* 275, 51–60. doi: 10.1016/j.jvolgeores.2014.02.009
- Delgado, F., Pritchard, M. E., Ebmeier, S., González, P., and Lara, L. (2017). Recent unrest (2002–2015) imaged by space geodesy at the highest risk Chilean volcanoes: villarrica, Llaima, and Calbuco (Southern Andes). *J. Volcanol. Geotherm. Res.* 344, 270–288. doi: 10.1016/j.jvolgeores.2017.05.020
- Di Traglia, F., Cimarelli, C., De Rita, D., and Torrente, D. G. (2009). Changing eruptive styles in basaltic explosive volcanism: examples from Croscat complex scoria cone, Garrotxa Volcanic Field (NE Iberian Peninsula). *J. Volcanol. Geotherm. Res.* 180, 89–109. doi: 10.1016/j.jvolgeores.2008.10.020
- Engwell, S. L., Sparks, R. S. J., and Aspinall, W. P. (2013). Quantifying uncertainties in the measurement of tephra fall thickness. *J. Appl. Volcanol.* 2:5. doi: 10.1186/2191-5040-2-5
- Flores, F., and Amigo, A. (2015). “Dinámica de Flujos Laháricos Asociados a la Erupción del 3 de Marzo del Volcán Villarrica,” in *XIV Congreso Geológico Chileno* (La Serena: Colegio de Geólogos).
- Freret-Logeril, V., Donnadiou, F., Scollo, S., Provost, A., Fréville, P., Guéhenneux, Y., et al. (2018). Mass Eruption Rates of tephra plumes during the 2011–2015 lava fountain paroxysms at Mt. Etna from Doppler radar retrievals. *Front. Earth Sci.* 6:73. doi: 10.3389/feart.2018.00073
- Giacomozzi, R. M., Parra, C. B., Herrera, C. E., Valencia, G. G., and Lara, L. (2015). “Flujos de Dióxido de Azufre (SO₂) del Volcán Villarrica, Período 2012–2015,” in *XIV Congreso Geológico Chileno* (La Serena: Colegio de Geólogos).
- González-Ferrán, O. (1995). Volcanes de Chile. Instituto Geográfico Militar: Santiago. 640.
- Gurioli, L., Harris, A. J., Houghton, B. F., Polacci, M., and Ripepe, M. (2008). Textural and geophysical characterization of explosive basaltic activity at Villarrica volcano. *J. Volcanol. Geotherm. Res.* 113:B08206. doi: 10.1029/2007JB005328
- Hickey-Vargas, R., López-Escobar, L., Moreno, H., Clavero, J., Lara, L., and Sun, M. (2004). Magmatic evolution of the villarrica volcano,” in *Villarrica Volcano* (39.5° S), eds L. E. Lara, and J. Clavero (Santiago: Servicio Nacional de Geología y Minería), 39–45.
- Hickey-Vargas, R., Moreno, H., López-Escobar, L., and Frey, F. (1989). Geochemical variations in Andean basaltic and silicic lavas from the Villarrica-Lanín volcanic chain (39.5 °S): an evaluation of source heterogeneity, fractional crystallization and crustal assimilation. *Contribut. Mineral. Petrol.* 103, 361–386. doi: 10.1007/BF00402922
- Houghton, B. F., and Gonnermann, H. M. (2008). Basaltic explosive volcanism: constraints from deposits and models. *Chem. Erde Geochem.* 68, 117–140. doi: 10.1016/j.chemer.2008.04.002
- Houghton, B. F., Wilson, C. J. N., Fierstein, J., and Hildreth, W. (2004). Complex proximal deposition during the Plinian eruptions of 1912 at Novarupta, Alaska. *Bull. Volcanol.* 66, 95–133. doi: 10.1007/s00445-003-0297-7
- Inostroza, M., Aguilera, F., González, C., Layana, S., and Chocobar, J. (2015). “Variaciones en la anomalía termal del volcán Villarrica asociados al pulso eruptivo de Marzo 2015: Interpretaciones mediante imágenes Landsat ETM+y OLI,” in *XIV Congreso Geológico Chileno* (La Serena).
- Jaupart, C., and Vergnolle, S. (1989). The generation and collapse of foam layer at the roof of a basaltic magma chamber. *J. Fluid Mech.* 203, 347–380. doi: 10.1017/S0022112089001497
- Johnson, J. B., Watson, L. M., Palma, J. L., Dunham, E. M., and Anderson, J. F. (2018). Forecasting the eruption of an open-vent volcano using resonant infrasound tones. *Geophys. Res. Lett.* 45, 2213–2220. doi: 10.1002/2017GL076506
- Johnson, J., and Palma, J. L. (2015). Lahar infrasound associated with Volcán Villarrica's 3 March 2015 eruption. *Geophys. Res. Lett.* 42, 6324–6331. doi: 10.1002/2015GL065024

- Klawonn, M., Houghton, B. F., Swanson, D. A., Fagents, S. A., Wessel, P., and Wolfe, C. J. (2014). From field data to volumes: constraining uncertainties in pyroclastic eruption parameters. *Bull. Volcanol.* 76:839. doi: 10.1007/s00445-014-0839-1
- Lohmar, S., Parada, M. A., Gutiérrez, F., Robin, C., and Gerbe, M. C. (2012). Mineralogical and numerical approaches to establish the pre-eruptive conditions of the mafic Licán Ignimbrite, Villarrica Volcano (Chilean Southern Andes). *J. Volcanol. Geotherm. Res.* 235–236, 55–69. doi: 10.1016/j.jvolgeores.2012.05.006
- López-Escobar, L., and Moreno, H. (1994). *Contribution to the Knowledge of the Postglacial Geochemical Evolution of the Villarrica volcano*. Southern Andes, 39°25'S. VII Congreso Geológico Chileno (Concepción, October 1994), Universidad de Concepción, 1091–1094.
- Master, L. G., Guffanti, M., Servranckx, R., Webley, P., Barsotti, S., Dean, K., et al. (2009). A multidisciplinary effort to assign realistic source parameters to models of volcanic ash-cloud transport and dispersion during eruptions. *J. Volcanol. Geotherm. Res.* 186, 10–21. doi: 10.1016/j.jvolgeores.2009.01.008
- Moreno, H., and Clavero, J. (2006). *Geología del Volcán Villarrica, Regiones de la Araucanía y de Los Lagos*. Carta Geológica de Chile, Serie Geología Básica No. 98, Santiago: Servicio Nacional de Geología y Minería.
- Morgado, E., Parada, M. A., Contreras, C., Castruccio, A., Gutiérrez, F., and McGee, L. E. (2015). Contrasting records from mantle to surface of Holocene lavas of two nearby arc volcanic complexes: Caburgua-Huelemolle Small Eruptive Centers and Villarrica Volcano, Southern Chile. *J. Volcanol. Geotherm. Res.* 306, 1–16. doi: 10.1016/j.jvolgeores.2015.09.023
- Naranjo, J. A., and Moreno, H. (2004). “Laharic debris – flows from Villarrica Volcano,” in *Villarrica Volcano (39.5°S), Southern Andes*, eds L. E. Lara and J. Clavero (Chile: Boletín Servicio Nacional de Geología y Minería), 28–38.
- Newhall, C., and Self, S. (1982). The volcanic explosivity index (VEI): An estimate of explosive magnitude for historical volcanism. *J. Geophys. Res.* 87, 1231–1238. doi: 10.1029/JC087iC02p01231
- Palma, J. L., Calder, E. S., Basualto, D., Blake, S., and Rothery, D. A. (2008). Correlations between SO₂ flux, seismicity, and outgassing activity at the open vent of Villarrica volcano, Chile. *J. Geophys. Res. Solid Earth* 113:B10201. doi: 10.1029/2008JB005577
- Parcheta, C. E., Houghton, B. F., and Swanson, D. A. (2013). Contrasting patterns of vesiculation in low, intermediate, and high Hawaiian fountains: a case study of the 1969 Mauna Ulu eruption. *J. Volcanol. Geotherm. Res.* 255, 79–89. doi: 10.1016/j.jvolgeores.2013.01.016
- Parfitt, E. A. (2004). A discussion of the mechanisms of explosive basaltic eruptions. *J. Volcanol. Geotherm. Res.* 134, 77–107. doi: 10.1016/j.jvolgeores.2004.01.002
- Petit-Breuilh, M. E., and Lobato, J. (1994). *Análisis Comparativo de la Cronología Eruptiva Histórica de los volcanes Llaima y Villarrica (38–39°S)*. VII Congreso Geológico Chileno (Concepción, October 1994), Universidad de Concepción, 366–370.
- Polacci, M., Corsaro, R. A., and Andronico, D. (2006). Coupled textural and compositional characterization of basaltic scoria: insights into the transition from Strombolian to fire fountain activity at Mount Etna, Italy. *Geology* 34, 201–204. doi: 10.1130/G22318.1
- Polacci, M., Papale, P., and Rosi, M. (2001). Textural heterogeneities in pumices from the climatic eruption of Mount Pinatubo, 15 June 1991, and implication for magma ascent dynamics. *Bull. Volcanol.* 63, 83–97. doi: 10.1007/s004450000123
- Polacci, M., Pioli, L., and Rosi, M. (2003). The Plinian phase of the Campanian Ignimbrite eruption (Phlegrean Fields, Italy): evidence from density measurements and textural characterization of pumice. *Bull. Volcanol.* 65, 418–432. doi: 10.1007/s00445-002-0268-4
- Pyle, D. M. (1989). The thickness, volume and grain size of tephra fall deposits. *Bull. Volcanol.* 51, 1–15. doi: 10.1007/BF01086757
- Pyle, D. M. (2015). “Sizes of volcanic eruptions,” in *The Encyclopedia of Volcanoes, 2nd Edn*, eds H. Sigurdsson, B. Houghton, S. McNutt, H. Rymer, and J. Stix (London: Encyclopedia of Volcanoes, Academic Press), 263–269.
- Romero, J. E., Keller, W., and Marfull, V. (2013). Short chronological analysis of the 2007–2009 eruptive cycle and its nested cones formation at Llaima volcano. *J. Technol. Possibilism* 2, 1–9. Available online at: <http://www.revistas.usach.cl/ojs/index.php/jotp/article/download/1395/1301>
- Romero, J., Keller, W., Díaz-Alvarado, J., Polacci, M., and Inostroza, F. (2016a). *The 3 March 2015 Eruption of Villarrica Volcano, Southern Andes of Chile: Overview of deposits and impacts*. Encuentro del Centro Internacional de Ciencias de la Tierra (E-ICES 11). International Center for Earth Science (ICES), Comisión Nacional de Energía Atómica (CNEA), Facultad de Exactas y Naturales, Facultad de Ciencias Políticas y Sociales, Universidad Nacional de Cuyo, Mendoza, Argentina.
- Romero, J. E., Morgavi, D., Arzilli, F., Daga, R., Caselli, A., Reckziegel, F., et al. (2016b). Eruption dynamics of the 22–23 April 2015 Calbuco Volcano (Southern Chile): Analyses of tephra fall deposits. *J. Volcanol. Geotherm. Res.* 317, 15–29. doi: 10.1016/j.jvolgeores.2016.02.027
- Rose, W. I., Palma, J. L., Delgado Granados, H., and Varley, N. (2013). “Open-vent volcanism and related hazards: overview,” in *Understanding Open-Vent Volcanism and Related Hazards: Geological Society of America Special Paper*, eds W. I. Rose, J. L. Palma, H. Delgado Granados, and N. Varley, vii–xiii.
- Ruth, D. C., and Calder, E. S. (2014). Plate tephra: preserved bubble walls from large slug bursts during violent Strombolian eruptions. *Geology* 42, 11–14. doi: 10.1130/G34859.1
- Ruth, D. C., Cottrell, E., Cortés, J. A., Kelley, K. A., and Calder, E. S. (2016). From passive degassing to violent strombolian eruption: the case of the 2008 eruption of Llaima volcano, Chile. *J. Petrol.* 57, 1833–1864. doi: 10.1093/petrology/egw063
- SERNAGEOMIN (2015). *Informe de Resumen Crisis Volcán Villarrica, Febrero-Marzo 2015*. Red Nacional de Vigilancia Volcánica, OVDAS, Servicio Nacional de Geología y Minería (Santiago), 17.
- Stovall, W. K., Houghton, B. F., Gonnermann, H., Fagents, S. A., and Swanson, D. A. (2011). Eruption dynamics of Hawaiian-style fountains: the case study of episode 1 of the Kilauea Iki 1959 eruption. *Bull. Volcanol.* 73, 511–529.
- Taddeucci, J., Edmonds, M., Houghton, B., James, M. R., and Vergnolle, S. (2015). “Hawaiian and Strombolian eruptions,” in *Encyclopedia of Volcanoes*, eds H. Sigurdsson, B. F. Houghton, S. R. McNutt, H. Rymer, J. Stix (London: Academic Press) 485–503.
- Van Daele, M., Moernaut, J., Silversmit, G., Schmidt, S., Fontijn, K., Heirman, K., et al. (2014). The 600 yr eruptive history of Villarrica Volcano (Chile) revealed by annually laminated lake sediments. *GSA Bull.* 126:481. doi: 10.1130/B30798.1
- Vera, F., and Palma, J. L. (2017). “Avalanchas mixtas y depósitos proximales generados en la erupción de 2015 del Volcán Villarrica y su interacción con la cubierta glacial,” in *VIII Encuentro Nacional de Estudiantes de Geología* (Copiapó: Universidad de Atacama).
- Witter, J., Kress, V., Delmelle, P., and Stix, J. (2004). Volatile degassing, petrology, and magma dynamics of the Villarrica lava lake, Southern Chile. *J. Volcanol. Geotherm. Res.* 134, 303–337. doi: 10.1016/j.jvolgeores.2004.03.002
- Wolff, J. A., and Sumner, J. M. (2000). “Lava fountains and their products,” in *Encyclopedia of Volcanoes*, eds H. Sigurdsson, B. F. Houghton, S. R. McNutt, H. Rymer, and J. Stix (London: Academic Press), 321–331.

Conflict of Interest Statement: The authors declare that the research was conducted in the absence of any commercial or financial relationships that could be construed as a potential conflict of interest.

Copyright © 2018 Romero, Vera, Polacci, Morgavi, Arzilli, Alam, Bustillos, Guevara, Johnson, Palma, Burton, Cuenca and Keller. This is an open-access article distributed under the terms of the Creative Commons Attribution License (CC BY). The use, distribution or reproduction in other forums is permitted, provided the original author(s) and the copyright owner(s) are credited and that the original publication in this journal is cited, in accordance with accepted academic practice. No use, distribution or reproduction is permitted which does not comply with these terms.



Magma Budget From Lava and Tephra Volumes Erupted During the 25-26 October 2013 Lava Fountain at Mt Etna

Daniele Andronico^{1*}, Boris Behncke¹, Emanuela De Beni¹, Antonino Cristaldi¹, Simona Scollo¹, Manuela Lopez² and Maria D. Lo Castro¹

¹ Istituto Nazionale di Geofisica e Vulcanologia, Osservatorio Etno, Catania, Italy, ² Istituto Nazionale di Geofisica e Vulcanologia, Palermo, Italy

OPEN ACCESS

Edited by:

Clive Oppenheimer,
University of Cambridge,
United Kingdom

Reviewed by:

Marco Viccaro,
Università degli Studi di Catania, Italy
Luis E. Lara,
Sernageomin, Chile

*Correspondence:

Daniele Andronico
daniele.andronico@ingv.it

Specialty section:

This article was submitted to
Volcanology,
a section of the journal
Frontiers in Earth Science

Received: 15 March 2018

Accepted: 30 July 2018

Published: 23 August 2018

Citation:

Andronico D, Behncke B, De Beni E, Cristaldi A, Scollo S, Lopez M and Lo Castro MD (2018) Magma Budget From Lava and Tephra Volumes Erupted During the 25-26 October 2013 Lava Fountain at Mt Etna. *Front. Earth Sci.* 6:116. doi: 10.3389/feart.2018.00116

Determining the volume of the various types of products of a highly frequent active volcano can be very difficult, especially if most of them are deposited on a growing volcanic cone. The New South-East Crater (NSEC) of Mt Etna, Italy, may be considered one of the best case studies because of tens of paroxysmal episodes which it produced in the last few years. On 25-26 October 2013, a lava fountain at the NSEC produced magma jets up to 500 m high, a maximum ~8 km high column, a multilobate lava flow field 1.3–1.5 km long, and almost 30 m of growth in height of the NSEC cone. Mapping of explosive and effusive deposits allowed us to calculate the total volume of erupted products, including lava flows, proximal, and distal tephra fallout, and the amount of coarse pyroclastics on the cone. The estimation of the latter products was also confirmed subtracting digital elevation models (DEMs) obtained at different stages of the NSEC growth. Results show that the volume of tephra fallout away from the cone was only <5 % of the total erupted magma, while the total volume of pyroclasts (distal plus proximal fallout) was about a third of the lava volume. Our analysis suggests that, at least for the studied event, three fourth of the involved magma was already partially degassed and thus emitted as lava flows. Hence, the main distinctive character of lava fountains at Etna, i.e., formation of eruption column and propagation of tephra-laden volcanic plumes to tens of km away from the volcano, would not contribute significantly to the final budget of erupted magma of the 25-26 October 2013 eruption. We therefore propose that the same magma dynamics, i.e., similar magma distribution, probably occur also during most of the common lava fountain episodes. Finally, we infer that quantifying the magma budget from lava and tephra volumes erupted during the 25-26 October lava fountain can give new insights into the mechanisms driving the eruptive behavior of Etna during paroxysmal activity from the summit craters, and provide useful indications also in terms of volcanic hazard.

Keywords: Mt Etna, lava fountain, erupted volume, lava flows, tephra, magma budget, effusion rate, digital elevation models

INTRODUCTION

The simultaneous occurrence of intense explosive and effusive activity—often in brief, paroxysmal eruptive episodes—has been observed at a number of basaltic volcanoes, such as Pacaya (Rose et al., 2013) and Fuego in Guatemala (Lyons et al., 2010), Klyuchevskoy in Kamchatka (Zharinov and Demyanchuk, 2016), Manam in Papua New-Guinea (Tupper et al., 2007), Pavlof in Alaska (Waythomas et al., 2014), Llaima in Chile (Romero et al., 2013), and Mt Etna in Italy (Behncke et al., 2006; Calvari et al., 2018). However, the exact volumetric contribution of lava flows vs. proximal vs. distal tephra deposits has thus far not been precisely evaluated for any of these volcanoes, although it potentially bears significant implications for volcanic hazard assessments.

The New South-East Crater (NSEC) of Etna (**Figure 1**) is a young and still growing volcanic cone, which formed by accumulation of lava and proximal pyroclastics (**Figure 2a**; Behncke et al., 2014). These products were mostly emplaced around a primordial pit-shaped vent located on the eastern flank of the South-East Crater (SEC; Andronico et al., 2013, 2014a,b), one of the summit craters of Etna, between 2011 and 2013, when 48 paroxysmal episodes or “paroxysms” took place (Corsaro et al., 2017; Giuffrida and Viccaro, 2017). Eruptive activity after 2013 has led to the coalescence of the NSEC with the SEC, while most recently, in the spring of 2017, effusive and Strombolian activity from new vents caused the growth of a small cone in between, and on top of, the two craters (Andronico et al., 2017).

The 25–26 October 2013 lava fountain followed a quiescent interval of 6 months after a paroxysmal episode on 27 April 2013; it also opened a new “episodic eruption,” the third in the period 2011–2013 (Andronico et al., 2014b), consisting of a sequence of 8 paroxysmal episodes, the last of which ended on 1 January 2014. Rather fine weather conditions allowed continuous observation of the 25–26 October eruptive activity: while lava flows were confined to a radius of 1.5 km from the NSEC, the more coarse-grained, cone-building fraction of pyroclastics (hereafter proximal tephra) was mostly deposited on the southern half of the NSEC cone (significantly contributing to its growth; **Figure 2b**), and distal tephra fallout (hereafter distal tephra) was dispersed up to several tens of kilometers distance from Etna. Remote sensing measurements, furthermore, retrieved aerosol particle size dispersal to far as Lampedusa, more than 350 km downwind (Sellitto et al., 2016).

Both effusive and explosive products were mapped and sampled within the first few days after the end of the eruption. This mapping allowed to quantify for the first time the relationships between effusive and explosive activity in terms of magma volume. In fact, although we consider the 25–26 October episode as a unique eruptive event, during paroxysmal episodes effusive and explosive activity occur from closed-space vents, reflecting the different types of magma erupted, i.e., degassed (lava flows) vs. gas-rich (tephra).

Here we consider dense rock equivalent (DRE) values for volumes and Mass Eruption Rates (MER) estimated for the output of lava and tephra (both distal and proximal), in order to discuss the magma dynamics and its partition in the shallow

plumbing system during the 25–26 October 2013 lava fountain. By detailing the effusive and explosive contribution of volcanics, we take an in-depth look at the mechanisms that may drive the eruptive behavior of Etna during a paroxysmal episode from one of its summit craters.

THE 2011–2013 PAROXYSMAL ACTIVITY

Eruptive activity at Etna characteristically occurs either as eruptions from vents on the flanks of the volcano (Neri et al., 2011), or eruptions from one or more of the four summit craters, NSEC, SEC, Voragine (VOR), Bocca Nuova (BN), and Northeast Crater (NEC). Summit eruptions are often long-lived, and especially in recent decades occur in the form of multiple sequences of paroxysmal eruptive episodes. This type of activity has been very common in recent years at Etna and particularly at the SEC in 1998–2008 (~130 episodes; e.g., Andronico et al., 2014a) and the NSEC thereafter, when both craters displayed “episodic eruptions,” i.e., sequences of paroxysmal episodes (Andronico and Corsaro, 2011). These events are characterized by powerful Strombolian to lava fountaining activity, accompanied by the formation of eruption columns (with tephra fallout extending over distances of several tens, and rarely, hundreds, of kilometers from the volcano) and spawning of lava flows onto the upper slopes of Etna (e.g., Alparone et al., 2003; Andronico et al., 2014a; Behncke et al., 2014; De Beni et al., 2015).

On 12 January 2011, summit activity resumed at Etna after 3 years of mild explosive activity mainly consisting of Strombolian bursts and ash emissions (Andronico et al., 2013). The last paroxysmal episode, in fact, had occurred on 10 May 2008 at the SEC (Andronico et al., 2008b), 3 days before the beginning of the 2008–2009 flank eruption (e.g., Aloisi et al., 2009). The 12 January episode opened a sequence of paroxysmal episodes consisting of 25 lava fountains up to 24 April 2012 (Andronico et al., 2014b; Behncke et al., 2014). Two shorter paroxysmal sequences occurred also in 2013 (De Beni et al., 2015), exactly between 19 February and 27 April (13 episodes), and between 25 October and 30 December (8 episodes).

As reported in several papers (e.g., Alparone et al., 2003), each paroxysmal episode may be subdivided into three eruption phases. The *resumption phase* is marked by the onset of increasingly intense explosive activity at the summit vents of the cone, which typically is accompanied by the opening of one or more lower effusive vents producing low-rate lava emission. The transition from powerful Strombolian activity to sustained lava fountaining leads to the *paroxysmal phase*, the most critical phase being characterized by the formation of an eruption column for several kilometers above the vent and an exponential increase in the effusion rate at the effusive vent(s). Finally, the rapid decline of all eruptive phenomena up to their total cessation represents the *conclusive phase* of the paroxysmal episode.

Episode after episode, the 2011–2012 sequence built the NSEC cone on the eastern flank of the SEC. On this side, a WNW–ESE trending eruptive vent-fissure repeatedly opened during the paroxysmal activity, feeding virtually all of the lava

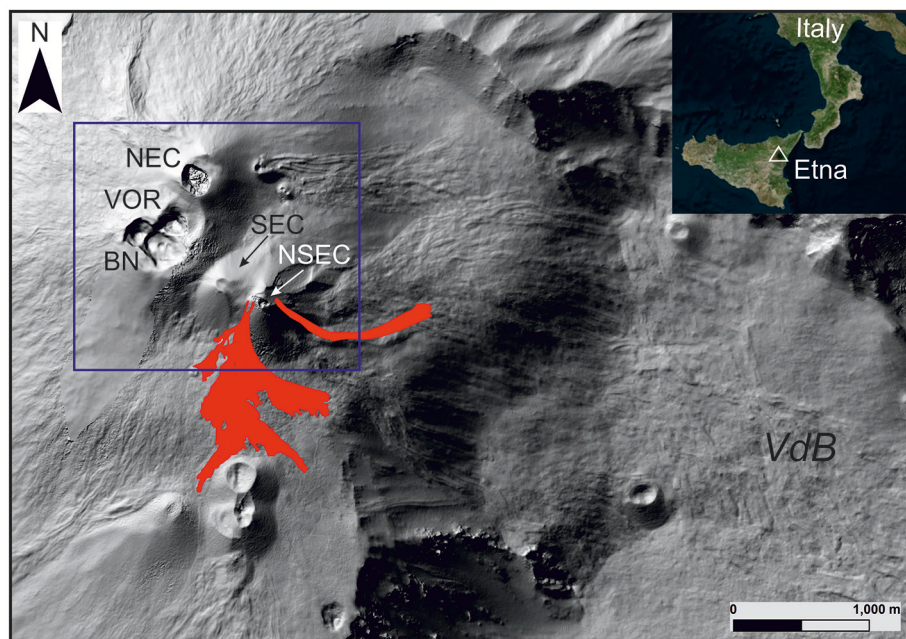


FIGURE 1 | Shaded relief of Mount Etna summit area. The blue square encloses the summit craters: NSEC, New South-East Crater; SEC, South-East Crater, BN, Bocca Nuova; VOR, Voragine; NEC, North-East Crater; VdB, Valle del Bove. Red polygons are the 25-26 October lava flows. Top right inset: map of southern Italy showing the location of Sicily.

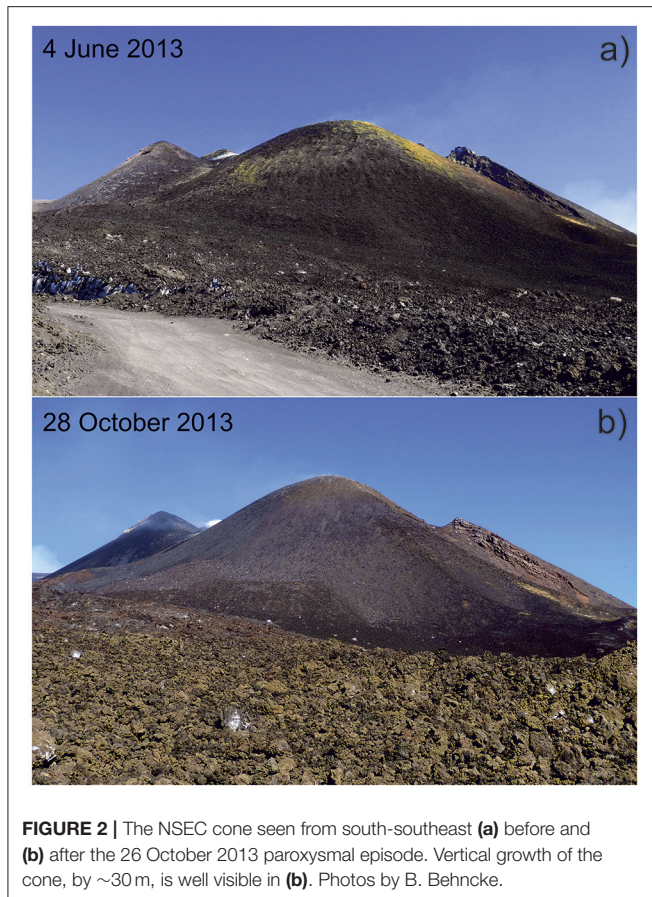
flows down toward the Valle del Bove. The 25 episodes in 2011-2012 were initially characterized by a low occurrence frequency, which then increased in the period July-September 2011 with episodes recurring every 5-10 days. Moreover, the 2011-12 paroxysmal activity produced tephra fallout deposits of similar order of magnitude in terms of mass loading and areal extension.

During the two sequences in 2013, the NSEC started to produce almost regularly lava flows also toward NE (February-April) and SE (October-December). Furthermore, the 2013 activity was characterized by episodes strongly varying in intensity. The 23 February and 23 November 2013 episodes are among the most intense summit paroxysms observed in the recent history of Etna: they produced tephra fallout up to 400 km from the volcano (Poret et al., 2018a,b). Conversely, the last 2 episodes in December 2013 consisted of prevalently powerful Strombolian activity alternating with rather discontinuous fountaining.

THE 25-26 OCTOBER 2013 PAROXYSMAL EPISODE

After about 6 weeks of sporadic ash emissions and weak Strombolian activity from the NSEC, since the morning of 25 October 2013 the video-camera monitoring system and the seismic surveillance networks of the Istituto Nazionale di Geofisica e Vulcanologia, Osservatorio Etneo—Sezione di Catania (INGV-OE) recorded a gradual buildup in Strombolian activity accompanied by a marked rise of the volcanic tremor

amplitude. On the early morning of 26 October, the Strombolian explosions blended into a continuous lava fountain about 250 m tall (Figures 3a,b), and an eruption column started to rise (Figures 3c, 4a,b) above the summit of the volcano before being bent toward WSW by the wind (Figure 3d). Initially this plume consisted mostly of gas, but as the activity intensified, the amount of pyroclastics in the eruption column increased, causing tephra fallout on the slopes of the volcano and beyond (Figure 5). At 06:21 GMT (=local time-2) on 26 October 2013 vigorous ash emissions at the nearby Northeast Crater, the tallest of Etna's four summit craters at 3,329 m above sea level (a.s.l.) (Figures 1, 3b, 4c,d, 5), accompanied the magma jets from the NSEC (Figures 4b,e,f), while occasional explosions occurred also at the Bocca Nuova crater (Figures 1, 4g-i). Lava fountaining continued at gradually increasing intensity up to about 500 m in height but without significant variations over the next few hours, while the eruption column rose to up to ~8 km a.s.l. (Corradini et al., 2018) and then started to diminish at about 10:00 GMT. The *paroxysmal phase* (Alparone et al., 2003) of the whole episode, i.e., the time during which we observed the volcanic plume fed by the eruption column extending away from the volcano, lasted ~8 h, with the most intense activity occurring between 06:00 and 09:00 GMT. Shortly after 02:00 GMT on 26 October, lava had started to spill through a notch in the southwestern rim of the NSEC, feeding a flow that expanded downslope to the southern base of the cone, and then bifurcated into two main lobes on the relatively flat terrain to its south and southeast. The effusion rate increased notably at 04:00 GMT, when a portion of the crater rim collapsed and widened the notch through which the lava was overflowing.



In the ensuing waning activity, lava overflowed the southeastern rim of the crater, feeding a flow that slowly advanced through a deep trench that had been carved out of the flank of the cone during the previous paroxysmal eruptive episode, on 27 April 2013. This flow eventually reached a length of 1.3 km, burying a part of a lava flow emitted on 27 April. Meanwhile, lava fountaining at the NSEC passed into violent Strombolian activity, often producing powerful explosions caused by the bursting of huge lava blisters, which sent sprays of meter-sized incandescent bombs up to several hundred meters high; most of these bombs were observed to fall onto the northern base of the NSEC cone. By 13:00 GMT, eruptive activity was essentially over, although renewed Strombolian activity occurred in the evening before the eruptive episode ended for good shortly before midnight on 26 October.

The 25–26 October episode brought a few surprises, activity at the NSEC was accompanied by prolonged ash emission at the NEC and episodic explosive bursts at the Bocca Nuova. The breaching of the south rim of the NSEC also opened a path southward for lava flows during this and following episodes. However, the effusive and explosive activity did not show any evident qualitative differences in terms of eruptive style with respect to other paroxysmal episodes, apart from the relatively long duration of its *paroxysmal phase*.

METHODS

During a field survey carried out on 28 October 2013, GPS measurements were performed along the lava flow boundaries to map the lava flows, and at the NSEC in order to update existing maps of the crater and its cone. In particular, 36 thickness measurements were acquired along the lava boundary of the main lava field located on the south flank; 4.5 km of the lava flow boundary were mapped in track mode (i.e., about 60% of the lava flow field). GNSS receivers were connected (via cable) to a binocular laser rangefinder (for details: De Beni and Proietti, 2010; Behncke et al., 2014; www.leica-geosystems.com) for the absolute positioning and dimensioning of inaccessible targets like the summit of the NSEC. The northern portion of the south lava branch, the east branch and the NSEC cone were instead mapped by integrating GPS measurements, field observations and analyses of ground and aerial visible photography. Moreover, the crater rim shape and the fractures along the south-east and north-east flanks of the NSEC were drawn thanks to a satellite image (<http://earthobservatory.nasa.gov/NaturalHazards>). Joining thickness measurements and camera observations carried out in the field, we subdivided the lava field in different sectors characterized by homogenous thicknesses expressed as minimum and maximum values. The volume was calculated as area per thickness for each sector, we finally summed all the values obtaining the minimum and maximum values of the total lava flow volume.

To compare the erupted magma volumes of the studied episode to previous paroxysmal activity, we completely revisited the data provided by two photogrammetric surveys in May 2012 and October 2014. In particular, we drew the base of the NSEC cone *ex novo* as it was after the 25–26 October episode, then we selected each lava flow emplaced on the cone and calculated the lava volume on the cone and subtracted this volume from the NSEC cone in order to obtain the volume of proximal pyroclastics constituting the cone.

When mapping the fallout deposit, 13 tephra samples (NSEC261013-1 to 13), representative of the whole area covered, were collected on measured surfaces between 0.7 and 90 km from the NSEC. This allowed us to cover proximal to very distal outcrops based on increasing distances of mass per unit area and grain-size of the fallout deposit (Andronico et al., 2014b). Ten of the samples were dried in oven to quantify the ground load per m², draw an isomass map and measure grain-sizes by CAMSIZER® (Lo Castro and Andronico, 2008). Further, using a binocular stereoscopic microscope (Nikon SMZ1500) we evaluated the ash componentry of two, differently grain-sized samples by counting 500 clasts for each one in the modal classes 0.250–0.5 and 0.125–0.250 mm on the coarser (NSEC261013-3) and the finer (NSEC261013-5), respectively.

Of the fallout deposit, we estimated the Total Erupted Mass (TEM) by averaging the values from four different methods, i.e., the model following the exponential thinning decay (Pyle, 1989), and its extended version (Fierstein and Nathenson, 1992), power law fit (Bonadonna and Houghton, 2005), and Weibull distribution (Bonadonna and Costa, 2012).

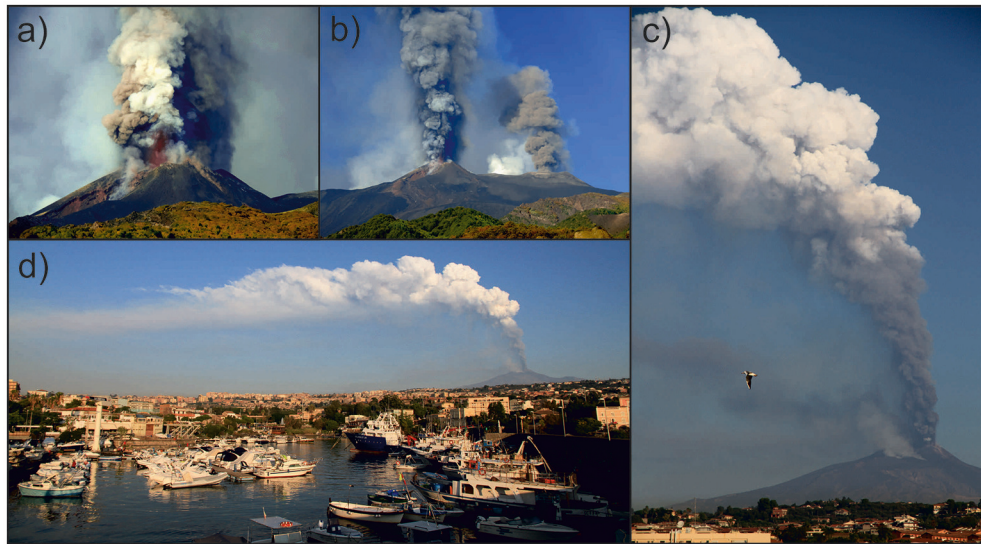


FIGURE 3 | Images showing the evolution of the eruption plume of the 25–26 October 2013 paroxysm between 07:00 and 12:00 of 26 October. **(a)** Lava fountaining and associated steam, ash and tephra plumes; **(b)** fountaining jets at the NSEC (left) and coeval dense ash plume from the NEC (right); **(c)** the dark gray eruption column rising above the NSEC and culminating into a whitish, gas-enriched volcanic plume viewed from S; **(d)** eruption plume extending to the west of the volcano viewed from the Ognina harbor in Catania. Photos by B. Behnke **(a,b)** and D. Andronico **(c,d)**.

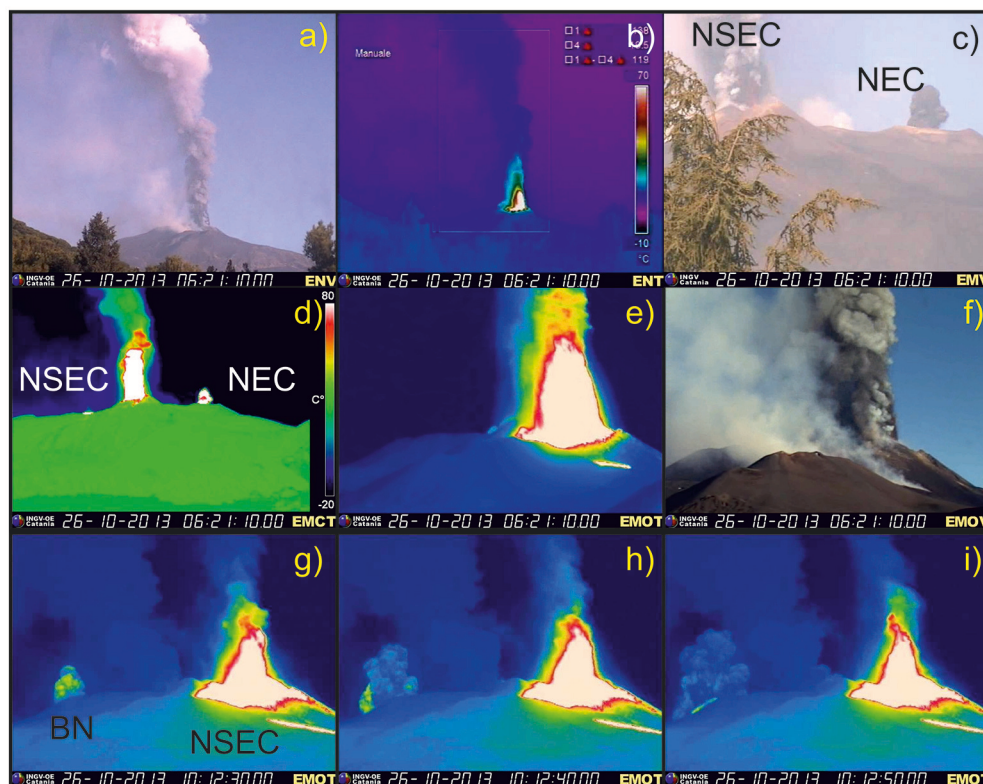


FIGURE 4 | **(a)** Lava fountaining activity as recorded by the INGV video-surveillance network: **(a)** Nicolosi visible camera (ENV), **(b)** Nicolosi thermal camera (ENT), **(c)** Milo visible camera (EMV) **(d)** Monte Cagliato thermal (EMCT), **(e)** Montagnola thermal camera (EMOT), **(f)** Montagnola visible camera (EMOV); **(g,h,i)** sequence of frames showing an explosion at the Bocca Nuova Crater (EMOT). Nicolosi and Montagnola cameras are recording from the S, the Milo camera from the SE and the Monte Cagliato from the E. Times are GMT (local time: + 2 h). Frames **(a,b,c,d,e,f)** show the same eruption time (06:21).

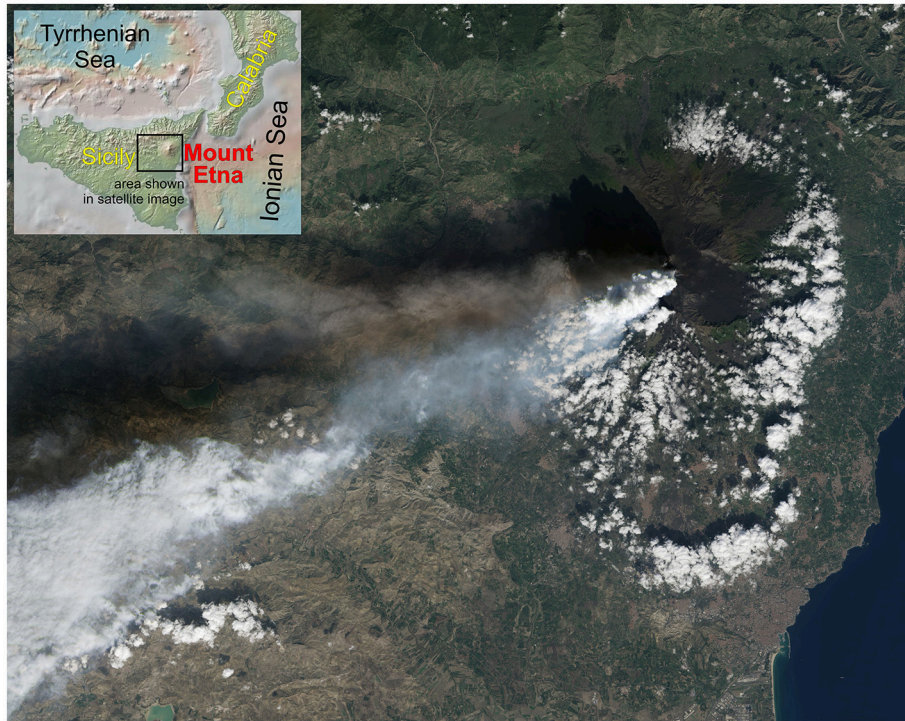


FIGURE 5 | Natural-color image collected by Landsat 8, showing the whitish eruption plume from the NSEC dispersed toward ~WSW of 26 October, 2013 at 11:38 (local time). The darker, shorter volcanic plume above the NSEC plume is emitted from the Northeast Crater and is traveling at a lower elevation than the NSEC plume. NASA Earth Observatory image by Jesse Allen and Robert Simmon, using Landsat data from the USGS Earth Explorer. Area of the image is shown in the index map at upper left. Photograph © 2013, at https://eoimages.gsfc.nasa.gov/images/imagerecords/82000/82287/etna_oli_2013299_lrg.jpg.

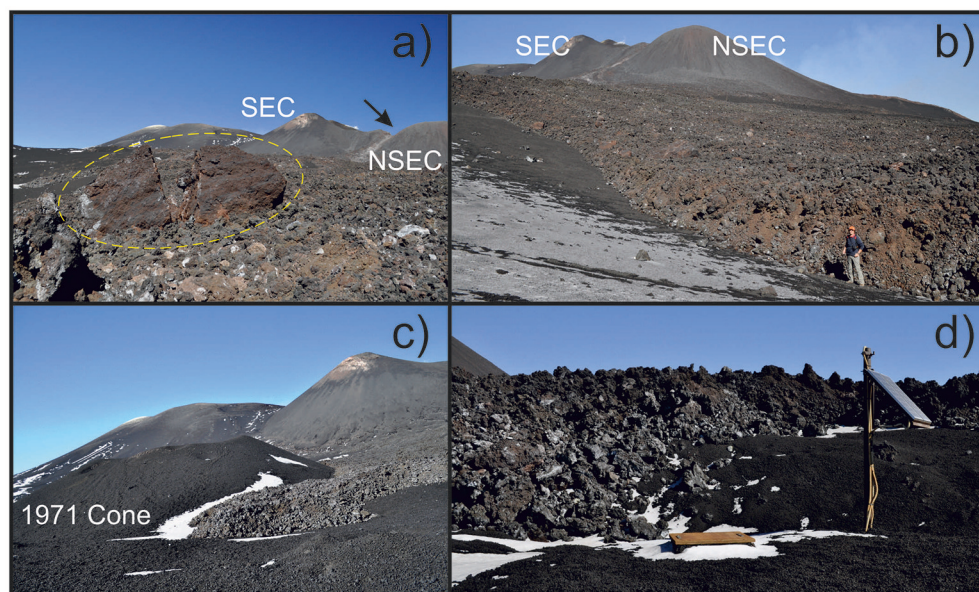


FIGURE 6 | (a) Mega-block of sub-decametric size (dotted yellow line) that collapsed from the rim crater of the NSEC and was rafted downslope by the S lava flows during the 25–26 October 2013 paroxysm. (b) The main lava flow lobe propagating toward South, in the background the peaks of the SEC and NSEC (on the left and right, respectively); see person at top right for scale; (c) the lava flow surrounding the 1971 cone; (d) the southern lava flow threatening the TdF seismic station. Photos by D. Andronico.

To evaluate the density of lava and tephra, we used values of vesicularity from the literature. In particular, a range of vesicularity has been assumed for lava due to the difficulty of establishing a single value (e.g., Gaonac'h et al., 1996; Herd and Pinkerton, 1997; Harris et al., 2007), that is an average porosity of 20%. As well as for lava, a wide range exists also for tephra density. In this case, in fact, the density values may vary significantly based on the grain-size of the clasts. Fine-grained clasts (e.g., ash particles) have poor or almost no porosity, while lapilli may display a rather broad range of vesicularity. At Etna, however, the commonly low thickness of tephra fallout deposits constrains us to measure the weight per unit area instead of the thickness at selected sites. Therefore, the total mass obtained for the total deposit provides its DRE volume simply subdividing the TEM (in kg) by the density of magma (2.7 g/cm^3).

Evaluating an average density for the NSEC cone, instead, is a major challenge due to its rather high heterogeneity, since it is constituted mostly by tephra ranging in grain-size from large clasts (up to meter-sized bombs) to lapilli and ash particles (with varying degrees of compaction and welding) and minor intercalated lava flows. For the purposes of our work, we collected 10 decimeter-sized fragments taken from a portion of the crater rim that collapsed and was rafted downslope during the effusive activity (Figure 6a), and we assumed them to be representative of the cone for providing density measurements. These fragments were dried, weighted, waterproofed with plastic wraps and finally immersed in water, resulting in weights and volumes ranging between 113 and 857 g, and 120 and 700 cm^3 , respectively, which is equal to clasts from 8 to 18 cm (in dimension). By measuring the excess water volume, we obtained a mean value of density of 1.22 g/cm^3 , providing a vesicularity of $\sim 55\%$ for the cone. This value agrees well enough with the density value estimated by Mulas et al. (2016) for the 1669 Monti Rossi cone, considering it as consisting of coarse lapilli and bombs (without lava intercalations), of 1.8 g/cm^3 . So far, in this paper we adopted the value of 50% in order to compare our volume estimation with the value used by Behncke et al. (2014) and De Beni et al. (2015) to evaluate the growth of the NSEC in the period 2011–13. Due to the irregular packing of volcanic particles (strongly varying in size and density) which compose the NSEC, we believe that this value can be considered reasonably realistic though conservative, unless new estimates of volcanic cone density will be published.

RESULTS

Growth of the Cone During Paroxysmal Events

The cone of the NSEC grew over a pre-existing subsidence depression formed between 2007 and 2009 and significantly enlarged due to minor explosive activity in 2010 (Andronico et al., 2013); its growth has been then documented by repeated GPS surveys starting from 2011 (Behncke et al., 2014). The NSEC at the time of our study was mostly composed of large welded scoriaceous bombs and blocks; on 26 October, some sizeable blocks (3–5 m) were torn from the crater rim and carried along by the southern lava flow close to the 2002–03 cones (Figures 6a,b). These blocks permitted insights into the structure of the inner portion of the crater rim, consisting of scoria, spatter, and ash layers of reddish-brown color. In Table 1 we reported the values of the cone volumes for the 2011–12 and 2013 sequences. The volume of the cone was estimated at $19 \times 10^6 \text{ m}^3$ by Behncke et al. (2014) after the 2011–12 lava fountaining episodes, i.e., $0.76 \times 10^6 \text{ m}^3$ per episode. Furthermore, the difference between the May 2012 and October 2014 DEMs (De Beni et al., 2015), when 22 paroxysmal events and a few Strombolian-effusive episodes took place, provides a volume increase for the NSEC of $27.0 \pm 0.8 \times 10^6 \text{ m}^3$. However, considering that the base of the cone

TABLE 2 | Volcanological parameters of the 25–26 October 2013 lava fountain episode.

Type of deposit	Bulk volume	DRE volume	MGER DRE
	10^6 m^3	10^6 m^3	m^3/s
Cone	0.90*	0.45	15.63
Tephra	/	0.083	2.89
Lava	1.84	1.47	51.11
Total DRE volume		2.01	
Total MER			69.63

We reported: the bulk volume increase of the cone, the bulk lava volume, and the dense rock equivalent (DRE) volume plus the correspondent magma eruption rate (MGER) for both cone (assuming 50 % vesicularity), tephra fallout (30 %) and lava flow (20 %) deposits. The value marked by the apex () has been assumed by averaging the volume increases of the 2011–13 episodes. The average DRE MGER value from effusive and explosive deposits is $69.63 \text{ m}^3/\text{s}$.*

TABLE 1 | Volcanological parameters of the NSEC cone during the 2011–12 and 2013 lava fountaining sequences.

Paroxysmal sequence(s)	Number of episodes	Total cone volume	Cone volume increase per episode	DRE total cone volume	DRE cone volume increase per episode	MGER DRE total cone
		10^6 m^3	10^6 m^3	10^6 m^3	10^6 m^3	m^3/s
2011–12	25	19	0.76	9.5	0.38	68.54
2013	19	20.48	1.08	10.24	0.54	57.56
2011–12+2013	44	39.48	0.90	19.74	0.45	62.37

We reported: the bulk values and the correspondent dense rock equivalent (DRE) values (assuming 50 % vesicularity) of the whole cone volume, the average volume increase for a single episode of each sequence, the average values of the two sequences, and the magma eruption rate (MGER) of the DRE total cone volume (single sequence and average of the sum of the two cones).

was smaller on 26 October 2013 than the base on October 2014, as deduced from field observation and GPS measurements, we calculate a volume of $23.28 \pm 1.57 \times 10^6 \text{ m}^3$ for the scoria cone in October 2013. By subtracting the volume of the lava flows emplaced over the cone in that period, we obtained a total volume for the NSEC of $20.48 \pm 1.69 \times 10^6 \text{ m}^3$. Dividing this value per the number of events, we derived an average increase of the cone volume of $1.08 \pm 0.08 \times 10^6 \text{ m}^3$ for each paroxysm. By averaging the previous two estimates, we assume that, from 2011 to 2013 the NSEC has grown by $0.90 \times 10^6 \text{ m}^3$ during each paroxysm, a value we consider representative also for the volume increase caused by the 25–26 October 2013 episode (Table 2).

Distal Tephra Fallout Deposit

During the *paroxysmal phase*, on 26 October, tephra fallout extended to at least 130 km distance from the vent, beyond the southern coast of Sicily (Figure 7a). The dispersal area of the tephra was quite symmetrical and the deposit well-visible on the ground due to almost constant direction of wind above the volcano from ENE to WSW during the eruption. The load on unit area declined very rapidly orthogonally to the dispersal axis. Adrano, Centuripe (~10 km WSW from Adrano), Caltanissetta and, to a lesser degree, Enna were the towns most affected by tephra fallout (principally ash); small amounts of fine-grained ash reached also the urban settlements of Leonforte and Montedoro.

Along the dispersal axis, in the proximal area (at ~1.4 km from the NSEC), the fallout deposit formed a 3-cm thick bed made of coarse ash to prevalently fine, black and iridescent, poorly porphyritic, vesicular scoriaceous lapilli (85% of particles in the range 1–8 mm) with scattered pluridecimeteric scoria (Figure 8a), amounting to a mass load of 22.25 kg/m^2 . At medial sites (~5 km distant), we measured 4.7 kg/m^2 of mostly fine lapilli forming a continuous <2 cm-thick layer on the ground. Further away, the tephra fall dropped to 0.4 kg/m^2 in Adrano (16 km distant), where we found a continuous, thin layer of medium-sized ash (~85% of clasts sized between 0.25 and 1 mm; Figure 8b). Finally, at distal sites the fallout consisted of fine to medium ash particles, ~99% of which were <0.25 mm in Caltanissetta (~90 km from the vent).

Laterally away from the fallout axis, the tephra cover became rapidly discontinuous; for example, close to Torre del Filosofo (~1 km from the NSEC; Figure 7b), the deposit consisted of scattered 5–10 cm-sized scoria, with larger clots up to 40 cm, while we measured 0.16 and 0.087 kg/m^2 of tephra at only 2 km N and 3.3 km ~S (Figure 8c), respectively, off-axis from the Adrano sample (16 km from the vent). Furthermore, within <1 km from the NSEC, we found a low number of spindle- to fusiform-shaped bombs with diameters mostly around 20–40 cm.

The two different analyzed grain-size classes of ash show comparable componentry in both samples, the ash being almost totally composed of juvenile particles (~97% both), mainly sideromelane (87.2% in the coarser sample and 91% in the finer) with minor percentages of tachylite (9.8% and 5.8%, respectively). The few present lithics are mostly gray-dark to gray lava particles and secondarily reddish clasts, while crystals (mainly plagioclase) are negligible (0.2 and 1.6%, respectively).

The fallout deposit was estimated having a TEM of $2.25 \pm 0.76 \times 10^8 \text{ kg}$, which is equivalent to a mean MER of $7.81 \times 10^3 \text{ kg/s}$ providing a DRE magma volume of $8.33 \times 10^4 \text{ m}^3$ (assuming an average density value of 2700 kg/m^3 ; Harris et al., 2010) (Table 2).

Lava Flows

On early 26 October, lava overflowed from the crater above the NSEC cone in three spots, two on the SW crater rim and one on the E rim (Figure 7b). The first overflow from the SW rim fed a narrow lava tongue that spilled southward, broadening on the flat terrain at the southern base of the cone and expanding into several lobes. Later, as lava fountaining intensified the effusion rate increased, leading to the breaching of the crater rim in the place where the lava was overflowing (Figures 6a,b), and to a second overflow a few tens of meters further west, which fed a rather narrow lava flow that spilled down the south flank of the cone for about 100 m before uniting with the earlier lava flow.

The resulting lava flow-field to the south of the NSEC expanded into four main lobes (Figure 7b): one toward SW, stopping at the base of the small 1971 cinder cone (Figure 6c); another circled the NW base of the 2002–2003 cone (stopping short of the “Torre del Filosofo” monitoring station that fortuitously survived, only to be destroyed by the next lava fountaining episode, on 11 November 2013; Figure 6d) and coming then to a halt near the N base of the prehistoric cone Monte Frumento Supino; the third advanced SSE near the NE base of the 2002–2003 cone; finally, the fourth went toward SE, reaching the site of the monitoring station “Belvedere” on the rim of the Valle del Bove. The most advanced lava front, near Monte Frumento Supino, was about 1.5 km from the NSEC. The eastern lava flow was emitted at a late stage of the paroxysm, and spilled down through a deep notch formed on 27 April 2013 in the flank of the NSEC cone, largely covering a lava flow emitted at that date, and stopping at a distance of about 1.3 km from the crater.

Based on the minimum and maximum values of thicknesses, we estimate an average total volume of lava emitted on 26 October 2013 of $1.84 \pm 0.44 \times 10^6 \text{ m}^3$ (Table 2), 86% of which constitutes the main southern lava flow-field.

DISCUSSION

How Representative Is the 25–26 October 2013 Eruption Within the Paroxysmal Activity of Etna?

In order to ascertain the representativeness of the 25–26 October eruption among the almost 200 paroxysms that occurred in 1998–2015 from the SEC and NSEC, in the following we compare physical parameters, textural features and observations on lava and tephra deposits with previous, well-studied paroxysmal episodes at Etna and particularly with the 2011–12 and 2013 sequences (Table 1). Our study shows that the paroxysmal phase of the 25–26 October lava fountain lasted ~8 h, producing $1.84 \pm 0.44 \times 10^6 \text{ m}^3$ of lava flows, and $2.25 \times 0.76 \times 10^8 \text{ kg}$ of distal tephra as fallout deposit (corresponding to a mean MER of $7.81 \times 10^3 \text{ kg/s}$). Lava flows reached a maximum length of 1.5 km from the vent, extending for 0.59 km^2 at a mean effusion rate

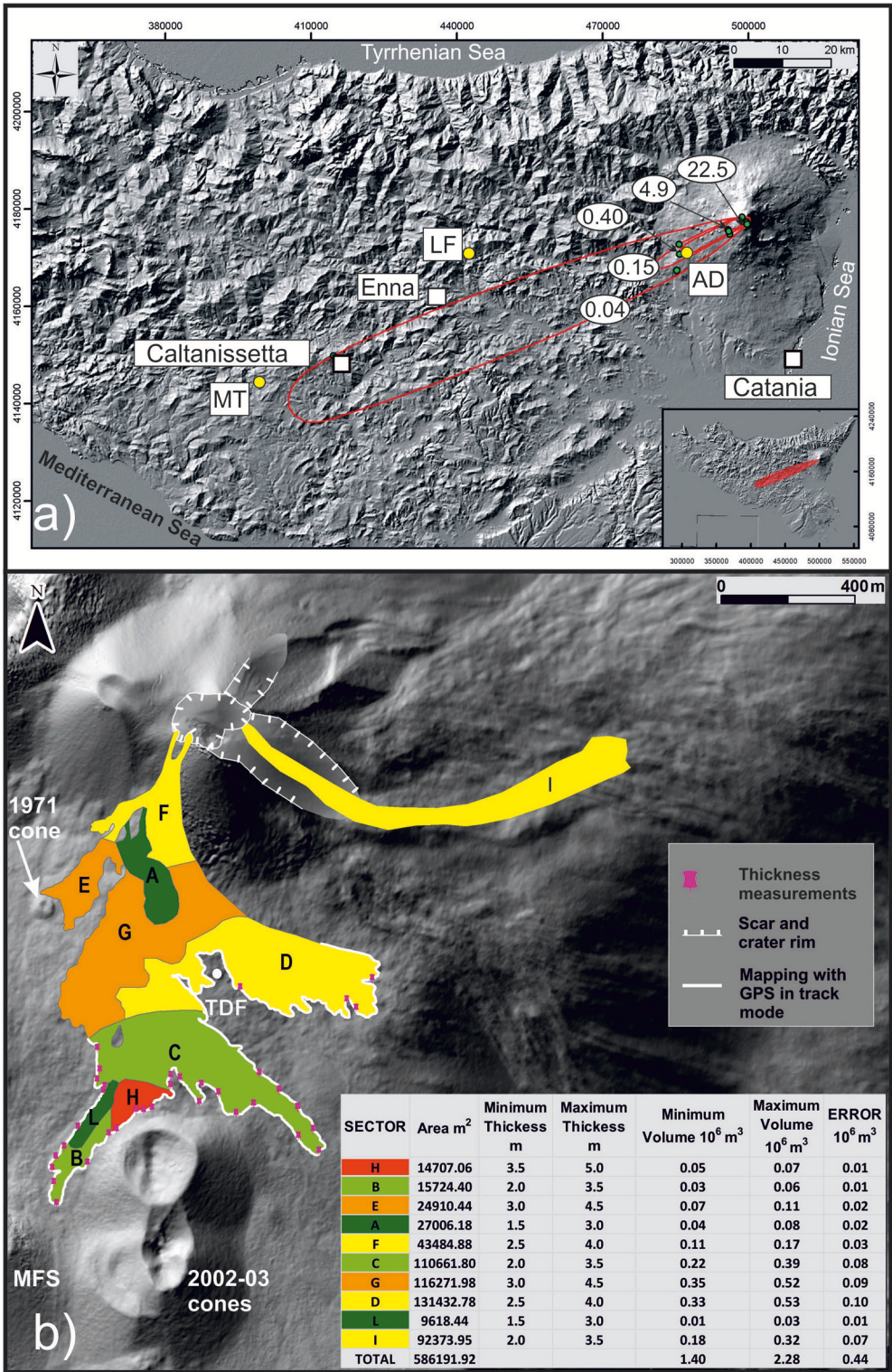


FIGURE 7 | Mapping of the volcanic deposits erupted during the 25-26 lava fountain 2013 episode. **(a)** Tephra fallout on the shaded relief of Sicily; the red lines are the isomasses in kg per square meter (values in full white circles). Full white squares are the main cities in this part of Sicily (Catania, Enna e Caltanissetta). Full yellow circles indicate some localities affected by the fallout (AD, Adrano; LF, Leonforte; MT, Montedoro). The bottom right inset shows the fallout deposit drawn over the map showing all of Sicily. **(b)** The NSEC cone and the associated lava flows on the shaded relief of Mount Etna volcano. TDF is the location of a former alpine shelter buried under recent tephra and lava, MFS is Monte Frumento Supino.



FIGURE 8 | The tephra deposit associated with the 25–26 October 2013 distal fallout. **(a)** Proximal lapilli layer and 40-cm sized scoria deposited at about 1 km of distance from the NSEC; **(b)** continuous layer of ash deposit along the dispersal axis at 16 km distant in Adrano; **(c)** lateral outcrop showing a scattered ash deposit in Adrano. Photos by D. Andronico.

of $\sim 65 \text{ m}^3/\text{s}$. During the paroxysmal activity, lava jets reached a maximum height of 500 m and the eruption column is estimated to have risen to up to $\sim 8 \text{ km a.s.l.}$ (i.e., $\sim 4.7 \text{ km}$ above the NSEC).

Paroxysmal Phase Length

The 25–26 October episode produced magma jets rising on average between 300 and 400 m (and maximum height of 500 m), a height range commonly observed for lava fountains at Etna (Carbone et al., 2015). However, the 8 h duration of the *paroxysmal phase* (characterized by continuous fountaining) was much longer than usual. Lava fountain episodes exceeding 3 h, in fact, were only 12, 13 and 20%, respectively, of the total number of episodes during the 2000 (64 episodes; Alparone et al., 2003), 2011–12 (25 episodes; Behncke et al., 2014), and 2013 (20 episodes; De Beni et al., 2015) sequences. In particular, the *paroxysmal phase* duration is much longer than during the 2011–12 (from 0.5 to 4.5 h with mean duration of 1.54 h) and the 2013 episodes (from 0.2 to 8 h with mean duration of 2.6 h for 19 episodes).

Cone Growth

For the cone constructed during the 25 episodes of the 2011–12 sequence from the NSEC, Behncke et al. (2014) evaluated by field surveys a growth of $\sim 190 \text{ m}$ and a DRE volume of $9.5 \times 10^6 \text{ m}^3$ (proximal tephra; vesicularity of 50%). These values are on average equivalent to a DRE volume of $0.38 \times 10^6 \text{ m}^3$ per episode (Table 1). We also derived a DRE volume for the 2013 cone (De Beni et al., 2015) of $20.48 \times 10^6 \text{ m}^3$, corresponding to a DRE volume of $0.54 \times 10^6 \text{ m}^3$ per episode (averaging 19 of the 21 episodes). By elaborating DEMs from different periods, for the 25–26 October activity we assume, in terms of erupted DRE volume, the average of the 2011–13 period (44 episodes) of $0.45 \times 10^6 \text{ m}^3$ (Table 1). Such a value is in good agreement with any average episode of the 2011–12 (slightly higher) and of the 2013 sequences (lower), which was mostly characterized by large-scale fountaining episodes (e.g., Andronico et al., 2015; Poret et al., 2018a,b in revision).

Distal Tephra

The distal tephra fallout was characterized by a TEM of $2.25 \pm 0.76 \times 10^8 \text{ kg}$, which is equivalent to a mean MER of $7.81 \times 10^3 \text{ kg/s}$. These values are slightly lower than the 4–5 September 2007 ($3.9 \times 10^8 \text{ kg}$ – $1.1 \times 10^4 \text{ kg/s}$) and 12–13 January 2011 ($1.5 \times 10^8 \text{ kg}$ – $2.5 \pm 0.7 \times 10^4 \text{ kg/s}$) lava fountaining episodes (Andronico et al., 2008a, 2014b), but a little higher than those calculated for the 24 November 2006 paroxysm ($1.9 \times 10^8 \text{ kg}$ – $5 \times 10^3 \text{ kg/s}$; Andronico et al., 2014a), characterized by alternating powerful Strombolian activity and pulsating fountaining. Physical parameters, therefore, would suggest that, during its 8 h of *paroxysmal activity*, the style and intensity of the 25–26 October 2013 eruption was that of a small-scale lava fountain (Andronico et al., 2015). Expressed in DRE magma volume they provided TEM and MER equivalent to $0.083 \times 10^6 \text{ m}^3$ and $2.89 \text{ m}^3/\text{s}$ respectively (Table 2).

The componentry analysis shows that nearly all of the ash-sized products ($\sim 97\%$) were constituted by juvenile material (of which sideromelane particles were $>87\%$). In agreement with the physical parameters, such high values are common during fountaining activity (e.g., Andronico et al., 2008a) as it is well suggested by the steady eruptive dynamics without any evidence of significant variations in the magma flux throughout the long *paroxysmal phase*, i.e., absence of significant syn-eruptive phenomena (like inner sliding and collapses within the eruptive conduit). This also permits to establish that the tephra forming the distal fallout is almost all represented by new, fresh magma.

Lava Flows

The 25–26 October 2013 lava flows show unusual geometric features when compared with other lavas of the 2011–2013 effusive activity (Behncke et al., 2014; De Beni et al., 2015). The morphology of the two lava fields reflects the different slopes of the NSEC cone, i.e., the smooth south flank and steep east flank, over which lava flows propagated from the respective vents up to only 1.3 and 1.5 km in around 8 h, covering a total area of 0.59 km^2 (Table 3) with average thicknesses of 3 m. In spite of the longer paroxysmal phase, the 25–26 October lava-covered area is comparable to areas measured for the lava flows emitted during the sequences in 2011–12 (25 episodes) and 2013 (11 episodes), which were respectively between 0.29 and 1.32 km^2 .

(mean value of 0.76 km^2) and between 0.02 and 1.3 km^2 (mean value of 0.55 km^2) (data estimated from Behncke et al., 2014 and De Beni et al., 2015) (Table 3). Conversely, the lava flow length is significantly lower than the mean length measured in 2011–12 (2.94 km for 25 episodes) and 2013 (2.06 for 11 episodes). The DRE volume of lava emitted on 25–26 October 2013 is $1.47 \times 10^6 \text{ m}^3$ (Table 2), higher than the mean DRE values of the 2011–12 and 2013 sequences of $0.90 \times 10^6 \text{ m}^3$ (averaged for 25 episodes) and $1.04 \times 10^6 \text{ m}^3$ (19 episodes), respectively (Table 4).

The 25–26 October lava flows were emitted at a DRE effusion rate of $51.11 \text{ m}^3/\text{s}$ (Table 2), a value much lower than episodes during the 2011–2013 sequences, where the mean effusion rates are estimated $161.62 \text{ m}^3/\text{s}$ in 2011–12 (25 episodes) and $88.72 \text{ m}^3/\text{s}$ in 2013 (19 episodes) (Table 4).

Comparison between the 25–26 October event and selected events or averaged values of the physical parameters/durations of the 2000, 2011–12, and 2013 sequences shows that the study event has a similar areal extent and DRE volume on the one hand, and minor lava flow length and DRE effusion rate on the other hand (compared to the 2011–13 paroxysmal sequences). Conversely, the fallout deposit erupted as distal tephra is only slightly smaller than other studied deposits, and the volume increase of the cone during this event is comparable to the average volume increase derived from the 2011–2013 sequences. However, the longer duration of the paroxysmal phase along with a significant lower DRE effusion rate during the 25–26 October event seem to indicate a relatively slow emplacement of the lava flows. We infer that their limited capability of advancing could be related to the low content of gas in the lava, possibly fed from a residual, degassed magma batch inherited from the first paroxysmal sequence in 2013, which started on 19 February and ended on 27 April. We conclude that, although eruptive style and

dynamics are fully overlapping and comparable with previous events, the 25–26 October 2013 event is a small-scale paroxysmal episode as confirmed by the longer duration of the paroxysmal phase associated with a lower magma output.

Magma Budget Estimation From Explosive and Effusive Deposits

In general, the estimation of the magma budget provided by a volcano during its history is a good proxy for understanding its magma dynamics, how the feeding system works (e.g., Wadge et al., 2006), and how magma (degassed or undegassed) is transferred to the surface (Allard, 1997). The peculiarity of a volcano, which erupts as frequently and often displays episodic eruptions as Etna, also bears significant implications for volcanic hazard assessments. Estimating the magma budget available during paroxysmal events, in particular from the SEC or NSEC, and as long as this value is constant or at least similar within the same paroxysmal sequences, may be therefore crucial for assessing their potential impact with time on the territory. In other terms, how much is the magma erupted as tephra (distal plus proximal) and lava? Does the ratio between these two amounts change or remain constant as suggested by recent studies based on the analysis of borehole dilatometers (Bonaccorso et al., 2014)? While the lava flows may be evaluated both using standard methods (mainly direct mapping and subtraction of DEMs extracted from remote sensing data; Coltelli et al., 2007; Behncke et al., 2014) and new techniques such as infrared data from geostationary sensors (Ganci et al., 2012) and near real-time production of DEMs (De Beni et al. under review), calculating the portion of magma fragmented “explosively” is more difficult. The most common models used for the fallout deposits, in fact, do not sufficiently take into account the

TABLE 3 | Volcanological parameters of the NSEC cone during the 2011–12 and 2013 lava fountaining sequences, and the single 25–26 October 2013 paroxysm.

Paroxysmal sequence(s)	Number of episodes	Total lava covered area	Total lava length	Lava covered area per episode	Lava length per episode
		Km^2	Km	Km^2	km
2011–12	25	18.95	73.4	0.76	2.94
2013	11	6.02	22.7	0.55	2.06
2011–12+2013	36	24.97	96.1	0.69	2.67
25–26 October 2013	1			0.59	1.4

We reported: the total lava covered area and total lava length for the two sequences, and the average values per episode.

TABLE 4 | Volcanological parameters of the NSEC cone during the 2011–12 and 2013 lava fountaining sequences, and the single 25–26 October 2013 paroxysm.

Paroxysmal sequence(s)	Number of episodes	Total lava volume	DRE total lava volume	Lava volume per episode	DRE lava volume per episode	MGER DRE total lava volume
		10^6 m^3	10^6 m^3	10^6 m^3	10^6 m^3	m^3/s
2011–12	25	28	22.40	1.12	0.90	161.62
2013	19	19.73	15.78	1.04	0.83	88.72
2011–12+2013	44	47.73	38.18	1.08	0.87	120.64
25–26 October 2013	1			1.84	1.47	51.11

We reported: the total lava volume (bulk and dense rock equivalent-DRE) and the correspondent average values per episode.

coarse-grained tephra which does not enter into convection within the eruption column. Conversely, during low- to mid-intensity explosive eruptions, like lava fountaining and powerful Strombolian events at Etna, which typically produce low, <10 km-high eruption columns a.s.l., the contribution of very coarse clasts that coevally fall back into and closely around the active vent of a rapidly growing scoria cone is significant.

Considering the contribution of proximal tephra and lava flows emitted during the 2011–12 and 2013 sequences, we quantified the average DRE magma volume erupted for episode. For the 25 episodes of the 2011–12 sequence, we obtain a total DRE volume of $31.9 \times 10^6 \text{ m}^3$, i.e., $1.28 \times 10^6 \text{ m}^3$ per episode, a value similar to the mean DRE volume of $1.47 \times 10^6 \text{ m}^3$ estimated averaging 19 of 25 episodes by Ganci et al. (2012) using a geostationary sensor (SEVIRI). Considering 138,600 s for the combined duration of the paroxysmal activity of all eruptive episodes (Behncke et al., 2014), we obtain a total mean DRE magma eruption rate (MGER) of $\sim 230.16 \text{ m}^3/\text{s}$, i.e., $68.54 \times 10^6 \text{ m}^3/\text{s}$ and $161.62 \times 10^6 \text{ m}^3/\text{s}$ the contributions from the cone and the lava, respectively, without including the magma volume erupted as distal tephra. By the same calculation averaging 19 of the 21 episodes in 2013, we derived a DRE volume of lava plus cone of $3.00 \times 10^7 \text{ m}^3$, and a DRE MGER of $168.47 \text{ m}^3/\text{s}$.

Considering the 25–26 October activity, in terms of DRE erupted volumes we estimated $15.63 \text{ m}^3/\text{s}$ for the cone and $51.11 \text{ m}^3/\text{s}$ for the lava flows, respectively (Table 2). Such estimations indicate that the cone increase was on average a fourth than during the 2011–13 episodes (Table 1), while the lava output value is almost a third of the mean value obtained for the 2011–12 episodes from Behncke et al. (2014), and \sim half the value obtained for 19 of 21 episodes in 2013 by De Beni et al. (2015) (Table 4), suggesting that the lava effusion from the studied episode occurred at a lower rate compared to the averaged values of the 2011–13 paroxysmal activity. In addition, we obtained $0.083 \times 10^6 \text{ m}^3$ of magma DRE volume erupted as distal tephra, which accounts for a further DRE MGER of $2.89 \text{ m}^3/\text{s}$ (Table 2); for the 2011–12 lava fountains, this parameter was only approximately estimated by Behncke et al. (2014) and not calculated by Ganci et al. (2012). Summing together proximal tephra, lava flows, and distal tephra, for the 25–26 October paroxysmal activity we have a total mean DRE MGER of $69.63 \text{ m}^3/\text{s}$ (Table 5). This value is significantly lower than 230.16 and $146.28 \text{ m}^3/\text{s}$ derived by Behncke et al. (2014) and De Beni et al. (2015) for the 2011–12

and 2013 episodic activity (lava and cone contribution without distal tephra).

Magma Dynamics During Paroxysmal Activity at Etna

In the literature, the eruptive mechanism invoked for describing sustained lava fountains from the summit craters of Etna (e.g., Allard et al., 2005; Andronico and Corsaro, 2011) is the separate ascent of a bubble foam layer related to a gas-melt separation. This is the collapsing foam model, which implies the accumulation of volatiles at the top of the plumbing system, the formation of a foam layer (e.g., Jaupart and Vergnolle, 1988, 1989; Vergnolle and Jaupart, 1990), and its dramatic collapse emptying the magma reservoir. Allard et al. (2005) postulated that the 14 June 2000 lava fountain at Etna was supplied by a shallow magma body on top of which “repeated growth and collapse of a bubble foam may have triggered periodic lava fountaining.” They also measured distinct chemical compositions of the gas driving the magma jets and the lava flows, suggesting somehow the separation from the parcel already stored in the shallow reservoir resulting into the emission of fragmented magma and degassed magma by distinct vents. Polacci et al. (2006) inferred that the foam collapse process may be followed and accompanied by syneruptive, although minor, volatile degassing. Consequently, the occurrence of lava fountaining suggests in general the availability of a pressurized volume of magma (composed of solid, liquid and abundant volatiles) in the shallow reservoir.

The 25–26 October lava fountain had a longer duration but lower mean MGER than the respective mean values calculated for the 2011–12 and 2013 sequences. Volcanological data, camera recordings and direct observations show that the intensity of the paroxysmal activity was relatively low. Noteworthy, most of the magma emitted was discharged as lava flows and proximal tephra. The distal tephra, in fact, represents only around 4% of the total erupted DRE volume, while the total volume of pyroclasts (proximal plus distal tephra) is lower (around 36%) than the magma volume erupted as lava flow (Table 1). This means that approximately three-quarters (i.e., 73%) of the magma was emitted as lava flows, i.e., it was already degassed and/or crystallized for the most part. The remaining >25 % of magma was erupted explosively, and mostly (>80 %) fragmented and

TABLE 5 | Volcanological parameters of the NSEC cone during the 2011–12 and 2013 lava fountaining sequences, and the single 25–26 October 2013 paroxysm.

Paroxysmal sequence(s)	MGER DRE total cone volume	MGER DRE total lava volume	Total MGER DRE (cone+lava)	Total MGER DRE (cone+lava+tephra)
	m^3/s	m^3/s	m^3/s	m^3/s
2011–12	68.54	161.62	230.16	
2013	57.56	88.72	146.28	
2011–12+2013	62.37	106.74	169.11	
25–26 October 2013	15.63	51.11	66.74	69.63

We reported: the MGER DRE total cone volume, the MGER DRE total lava volume, the sum of the previous values and the MGER DRE tephra (see Table 2). DRE, dense rock equivalent; MGER, magma eruption rate.

deposited as coarse tephra clasts above the NSEC cone. **Figure 9** summarizes the DRE magma volume (%) distribution as derived from our work in terms of lava, distal tephra and proximal tephra deposits.

In other terms, on 26 October 2013 the fraction of magma erupted as tephra and transported in convection above the NSEC was rather small compared to the magma emitted as lava flows and cone-building tephra. The importance of the extruded lava mass and of the effusive process in general is also suggested by the detachment of blocks from the NSEC summit and carriage downward. Noteworthy, the presence of a dark eruption column above the volcano which then becomes progressively lighter-colored for tens of km away from Etna could be related to high amounts of water vapor (**Figures 3c,d**), but foremost points to a relatively low discharge of tephra, the fine-grained part of which diluted in the atmosphere.

Although the eruption column that typically accompanies the common lava fountains at Etna is the most striking eruptive phenomenon, and possibly the one, which distinguishes this activity from the “fire-fountaining” activity at Hawaiian volcanoes, its contribution in terms of magma volume, at least for the studied event (but probably also for other small-scale lava fountain episodes), was only a small fraction of the total budget of erupted magma.

In conclusion, we infer that before 25 October, as already proposed for past episodic eruptions (Andronico and Corsaro, 2011; Behncke et al., 2014), a cooling magma batch was resident below the NSEC. This batch was extruded for the most part as lava flows, possibly as result of degassing during the 6-months-long residence in the shallow plumbing system since the previous paroxysmal episode on 27 April. However, it opened the plumbing system to the rise of more gas-rich magma, which was erupted during the following five lava fountains episodes (e.g., the exceptionally powerful 23 November 2013 episode; Bonaccorso et al., 2014; Poret et al., 2018a) up to 2 December 2013, plus two powerful Strombolian events in the following month. Similarly, for the 64 paroxysmal episodes that occurred in January–June 2000, Andronico and Corsaro (2011) showed that the ascent of new, more primitive and volatile-rich magma triggered the start of this long episodic eruption, progressively intruding into the SEC reservoir and mixing with the resident and more evolved magma, finally determining the composition of erupted volcanics. Noteworthy, in the case of the 2000 sequence, the more primitive magma was emitted only during the last events.

The latter hypothesis is also in agreement with two recent studies from Viccaro et al. (2014) and Giuffrida et al. (2018) about the triggering mechanisms of paroxysmal episodes at Etna. Viccaro et al. (2014) infer that textures and compositional zoning in selected plagioclase crystals of lavas can explain the relations between the duration of the paroxysms and dynamics of pre-eruptive magmatic processes at depth. They proposed a recharge by more mafic, gas-rich magma in case of prolonged, ramp-shaped tremor increase, and conversely a prominent role of gas injections into the residing system when recording a sudden increase of the seismic amplitude before the climax of the eruption. The 25–26 October 2013 episode,

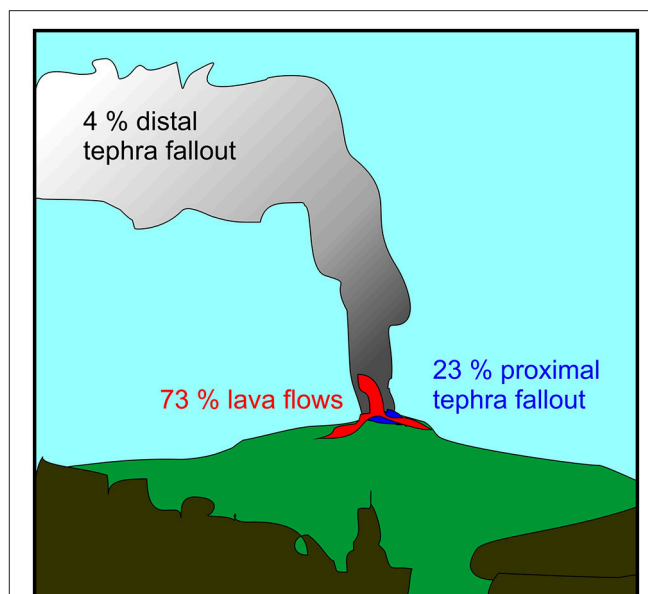


FIGURE 9 | Schematic diagram of proposed magma (DRE %) distribution in terms of lava, distal tephra and proximal tephra deposits erupted during the 25–26 October 2013 lava fountain at Etna.

indeed, shows intermediate features between the previous end-members, because the tremor increase accompanying the initial Strombolian phase was neither long nor short, while the paroxysmal phase was clearly longer than usual. At the same time, by studying lithium gradients in plagioclase crystals, Giuffrida et al. (2018) suggest that, during the 2011–2013 paroxysmal episodes, the fast recharge of gas-rich magma would have caused the re-activation of the magmatic system after quiet eruptive periods, thus enhancing powerful eruptions. We therefore cannot exclude the presence of two distinct mechanisms which concurred to open a short sequence of 8 paroxysmal events after 6 months of quiescence. We finally suggest that the rise of a new mafic, gas-rich magma batch triggered the 25–26 October episode and provoked the extrusion of degassed resident magma, accompanied by the resumption of the Strombolian activity and sustaining a long-lasting *paroxysmal phase*.

CONCLUDING REMARKS

The ascent of magma during paroxysmal eruptions and its partition to produce disproportionate values of lava/tephra ratios as well as a wide range of MERs have been never properly investigated and debated at Etna. In spite of various research on single paroxysmal episodes in recent years, to date only this study quantifies, on the base of field data, the DRE magma volumes erupted as proximal tephra, distal tephra, and lava flows. The 25–26 October 2013 lava fountain deposited a proximal tephra deposit of $0.45 \times 10^6 \text{ m}^3$ on top of the NSEC cone (causing $\sim 30 \text{ m}$ growth of the cone), dispersed a distal tephra fallout deposit of $\sim 0.083 \times 10^6 \text{ m}^3$, and emitted $\sim 1.47 \times 10^6 \text{ m}^3$ of lava flows. Considering 8 h of paroxysmal

activity, the mean rate at which all the erupted magma was supplied is $69.63 \text{ m}^3/\text{s}$. The estimation of the total mass and the relative percentages of lava and tephra may address the evaluation of the eruption dynamics during paroxysmal episodes at Etna, and gain insights into the wide spectrum of eruption intensity (MER) and style (powerful Strombolian to large-scale lava fountain events) observed in the last years at the summit craters. Most importantly, our study highlights that, at least for ordinary paroxysmal episodes, the magma budget distribution is strongly balanced in favor of lava flows and proximal tephra (accumulating around the NSEC cone and enhancing its fast growth), while the distal tephra fallout seems to have a rather modest importance in quantitative terms (i.e., only $<5\%$ of the total erupted magma). A similar distribution of magma (predominant output of lava flows/coarse tephra around the cone than distal tephra) is coherent with the eruptive behavior observed during the paroxysmal phase of most of the lava fountain episodes at Etna, i.e., the start of lava fountaining and formation of the eruption column, which are accompanied by high-rate lava effusion.

In the future, further and more reliable estimations of the different contributions of magma discharged as lava and tephra during paroxysmal events are desirable. The application of new measurement techniques (like drones and ground-based photogrammetry) is likely to allow swift calculation of detailed and reliable volume values, not only of lava flows but also of the proximal tephra which accumulates on top of the cone; for example, by subtraction of DEMs focused on the NSEC cone just before and after an eruption. Moreover, coeval and punctual geochemical measurements of the gas plumes are recommended to correlate the total SO_2 flux and *in situ* measurements of gas phases (e.g., SO_2 , HCL, HF, and their relative ratios) with the eruptive activity, thus allowing to validate the total volume of erupted magma and possibly, its partitioning in terms of lava and tephra.

Understanding the relationships between effusive and explosive deposits (i.e., degassed vs. gas-rich magma) erupted during single paroxysms, finally, may be greatly useful to predict the evolution of such episodic eruptions and their likely conclusion, and thus also to improve the assessment of the

potential volcanic hazard from future tephra fallout over the densely populated slopes of Etna.

AUTHOR CONTRIBUTIONS

DA conceived the research and drafted the article. DA and BB made field observations during the whole duration of the lava fountain. DA carried out survey to map the tephra fallout from the proximal area to the volcanic slope, and collected representative samples. BB and ED carried out field campaigns to map the lava flow field. ED produced the cartographic maps for the lava and tephra deposits, and elaborated the obtained maps to calculate the volume of the cone and of the lava deposits. AC analyzed the products of the tephra fallout in the laboratory. SS estimated the volume of the tephra fallout. ML surveyed the distal fallout deposit and collected the relative ash samples. MLC collaborated during the laboratory analysis of the tephra samples. All authors discussed the results and reviewed the manuscript, strictly collaborating for the interpretation of the results obtained. BB also gave a substantial contribution to the draft of the manuscript.

FUNDING

Osservatorio Etneo—Sezione di Catania Istituto Nazionale di Geofisica e Vulcanologia.

ACKNOWLEDGMENTS

We are strongly indebted with the INGV staff, which maintained the video-camera network during the period of the eruption, and in particular our colleagues who were in the field to make observations from different viewpoints at different time during its long paroxysmal phase. Finally, we are really indebted to reviewers, Prof. Marco Viccaro and Dr. Luis E. Lara, whose criticism and observations gave more clarity to the paper. We also thank the Editor, Prof. Clive Oppenheimer, for his continuous support and the Chief Editor, Prof. Valerio Acocella, for the final editing to the revised paper that has given greater completeness and self-sustainability to our work.

REFERENCES

- Allard, P. (1997). Endogenous magma degassing and storage at Mount Etna. *Geophys. Res. Lett.* 24, 2219–2222.
- Allard, P., Burton, M., and Murè, F. (2005). Spectroscopic evidence for a lava fountain driven by previously accumulated magmatic gas. *Nature* 433, 407–410. doi: 10.1038/nature03246
- Aloisi, M., Bonaccorso, A., Cannavò, F., Gambino, S., Mattia, M., Puglisi, G., et al. (2009). A new dike intrusion style for the Mount Etna May 2008 eruption modelled through continuous tilt and GPS data. *Terra Nova* 21, 316–321. doi: 10.1111/j.1365-3121.2009.00889.x
- Alparone, S., Andronico, D., Lodato, L., and Sgroi, T. (2003). Relationship between tremor and volcanic activity during the Southeast Crater eruption on Mount Etna in early 2000. *J. Geophys. Res.* 108:B52241. doi: 10.1029/2002JB001866
- Andronico, D., Coltelli, M., Cristaldi, A., Lo Castro, D., and Scollo, S. (2008b). *Il Parossismo del 10 Maggio 2008 al Cratere di SE: Caratteristiche del Deposito di Caduta*. INGV Internal Report No UFVG2008/043
- Andronico, D., and Corsaro, R. A. (2011). Lava fountains during the episodic eruption of South-east Crater (Mt. Etna), 2000: insights into magma-gas dynamics within the shallow volcano plumbing system. *Bull. Volcanol.* 73, 1165–1178.
- Andronico, D., Corsaro, R. A., Cristaldi, A., Lo Castro, M. D., Messina, L., Scollo, S., et al. (2017). *L'attività Esplosiva del Cratere di SE tra il 15 e il 18 Marzo 2017: Dispersione del Deposito Distale di Caduta E Caratteristiche Tessiturali Delle Ceneri Eruttate*. Rapporto interno N. 005/2017. Available online at: <http://www.ct.ingv.it>
- Andronico, D., Cristaldi, A., and Scollo, S. (2008a). The 4–5 September 2007 lava fountain at South-East Crater of Mt Etna, Italy. *J. Volcanol. Geotherm. Res.* 173, 325–328. doi: 10.1016/j.jvolgeores.2008.02.004

- Andronico, D., Lo Castro, M. D., Sciotto, M., and Spina, L. (2013). The 2010 ash emissions at the summit craters of Mt Etna: relationship with seismo-acoustic signals. *J. Geophys. Res. Solid Earth*. 118, 51–70. doi: 10.1029/2012JB009895
- Andronico, D., Scollo, S., and Cristaldi, A. (2015). Unexpected hazards from tephra fallouts at Mt Etna: the 23 November 2013 lava fountain. *J. Volcanol. Geotherm. Res.* 304, 118–125. doi: 10.1016/j.jvolgeores.2015.08.007
- Andronico, D., Scollo, S., Cristaldi, A., and Lo Castro, M. D. (2014b). Representivity of incompletely sampled fall deposits in estimating eruption source parameters: a test using the 12–13 January 2011 lava fountain deposit from Mt. Etna volcano. *Bull. Volcanol.* 76:861. doi: 10.1007/s00445-014-0861-3
- Andronico, D., Scollo, S., Lo Castro, M. D., Cristaldi, A., Lodato, L., and Taddeucci, J. (2014a). Eruption dynamics and tephra dispersal from the 24 November 2006 paroxysm at South-East Crater, Mt Etna, Italy. *J. Volcanol. Geotherm. Res.* 274, 78–91. doi: 10.1016/j.jvolgeores.2014.01.009
- Behncke, B., Branca, S., Corsaro, R. A., De Beni, E., Miraglia, L., and Proietti, C. (2014). The 2011–2012 summit activity of Mount Etna: birth, growth and products of the new SE crater. *J. Volcanol. Geotherm. Res.* 270, 10–21. doi: 10.1016/j.jvolgeores.2013.11.012
- Behncke, B., Neri, M., Pecora, E., and Zanon, V. (2006). The exceptional activity and growth of the Southeast Crater, Mount Etna (Italy), between 1996 and 2001. *Bull. Volcanol.* 69, 149–173. doi: 10.1007/s00445-006-0061-x
- Bonaccorso, A., Calvari, S., Linde, A., and Sacks, S. (2014). Eruptive processes leading to the most explosive lava fountain at Etna volcano: the 23 November 2013 episode. *Geophys. Res. Lett.* 41, 4912–4919. doi: 10.1002/2014GL060623
- Bonadonna, C., and Costa, A. (2012). Estimating the volume of tephra deposits: a new simple strategy. *Geology* 40, 415–418. doi: 10.1130/G32769.1
- Bonadonna, C., and Houghton, B. F. (2005). Total grain-size distribution and volume of tephra-fallout deposits. *Bull. Volcanol.* 67, 441–456. doi: 10.1007/s00445-004-0386
- Calvari, S., Cannavò, F., Bonaccorso, A., Spampinato, L., and Pellegrino, A. (2018). Paroxysmal explosions, lava fountains and ash plumes at Etna volcano: eruptive processes and hazard implications. *Front. Earth Sci.* 6:107. doi: 10.3389/feart.2018.00107
- Carbone, D., Zuccarello, L., Messina, A., Scollo, S., and Rymer, H. (2015). Balancing bulk gas accumulation and gas output before and during lava fountaining episodes at Mt. Etna. *Sci. Rep.* 5:18049. doi: 10.1038/srep18049
- Coltelli, M., Proietti, C., Branca, S., Marsella, M., Andronico, D., and Lodato, L. (2007). Analysis of the 2001 lava flow eruption of Mt. Etna from three-dimensional mapping. *J. Geophys. Res.* 112:F02029. doi: 10.1029/2006JF000598
- Corradini, S., Guerrieri, L., Lombardo, V., Merucci, L., Musacchio, M., Prestifilippo, M., et al. (2018). Proximal monitoring of the 2011–2015 Etna lava fountains using MSG-SEVIRI data. *Geosciences* 8:140. doi: 10.3390/geosciences8040140
- Corsaro, R. A., Andronico, D., Behncke, B., Branca, S., De Beni, E., Caltabiano, T., et al. (2017). Monitoring the December 2015 summit eruptions of Mt. Etna (Italy): implications on eruptive dynamics. *J. Volcanol. Geotherm. Res.* 341, 53–69. doi: 10.1016/j.jvolgeores.2017.04.018
- De Beni, E., Behncke, B., Branca, S., Nicolosi, I., Carluccio, R., D'Aiello Caracciolo, F., et al. (2015). The continuing story of Etna's New Southeast Crater (2012–2014): evolution and volume calculations based on field surveys and aerophotogrammetry. *J. Volcanol. Geotherm. Res.* 303, 175–186. doi: 10.1016/j.jvolgeores.2015.07.021
- De Beni, E., and Proietti, C. (2010). *Un Geodatabase a Supporto Della Mappatura Sinergetica di Colate Laviche al Monte Etna*. INGV Rapporti Tecnici. Available online at: <http://istitutoingv.it/l-ingv/produzione-scientifica/rapporti-tecnici-ingv/archivio/rapporti-tecnici-2010/2010-10-25.5202754525>
- Fierstein, J., and Nathenson, M. (1992). Another look at the calculation of fallout tephra volumes. *Bull. Volcanol.* 54, 156–167. doi: 10.1007/BF00278005
- Ganci, G., Harris, A. J. L., Del Negro, C., Guehenneux, Y., Cappello, A., Labazuy, P., et al. (2012). A year of lava fountaining at Etna: volumes from SEVIRI. *Geophys. Res. Lett.* 39:L06305. doi: 10.1029/2012GL051026
- Gaonac'h, H., Stix, J., and Lovejoy, S. (1996). Scaling effects on vesicle shape, size and heterogeneity of lavas from Mount Etna. *J. Volcanol. Geotherm. Res.* 74, 131–153. doi: 10.1016/S0377-0273(96)00045-5
- Giuffrida, M., and Viccaro, M. (2017). Three years (2011–2013) of eruptive activity at Mt. Etna: working modes and timescales of the modern volcano plumbing system from micro-analytical studies of crystals. *Earth Sci. Rev.* 171, 289–322. doi: 10.1016/j.earscirev.2017.06.003
- Giuffrida, M., Viccaro, M., and Ottolini, L. (2018). Ultrafast syn-eruptive degassing and ascent trigger high-energy basic eruptions. *Sci. Rep.* 8:147. doi: 10.1038/s41598-017-18580-8
- Harris, A. J. L., Dehn, J., and Calvari, S. (2007). Lava effusion rate definition and measurement: a review. *Bull. Volcanol.* 70, 1–22. doi: 10.1007/s00445-007-0120-y
- Harris, A. J. L., Favalli, M., Steffke, A., Fornaciai, A., and Boschi, E. (2010). A relation between lava discharge rate, thermal insulation, and flow area set using lidar data. *Geophys. Res. Lett.* 37:L20308. doi: 10.1029/2010GL044683
- Herd, R. A., and Pinkerton, H. (1997). Bubble coalescence in basaltic lava: its impact on the evolution of bubble populations. *J. Volcanol. Geotherm. Res.* 75, 137–157. doi: 10.1016/S0377-0273(96)00039-X
- Jaupart, C., and Vergnolle, S. (1988). Laboratory models of Hawaiian and Strombolian eruptions. *Nature* 33, 58–60.
- Jaupart, C., and Vergnolle, S. (1989). The generation and collapse of foam layer at the roof of a basaltic magma chamber. *J. Fluid. Mech.* 203, 347–380.
- Lo Castro, M. D., and Andronico, D. (2008). *Operazioni di Base per la Misura Della Distribuzione Granulometrica di Particelle Vulcaniche Tramite il CAMSIZER*. Rapporti Tecnici INGV. 79, 1–35. Available online at: <https://www.earth-prints.org/bitstream/2122/5614/1/rapporto79.pdf>
- Lyons, J. J., Waite, G. P., Rose, W. I., and Chigna, G. (2010). Patterns in open vent, Strombolian behavior at Fuego volcano, Guatemala, 2005–2007. *Bull. Volcanol.* 72, 1–15. doi: 10.1007/s00445-009-0305-7
- Mulas, M., Cioni, R., Andronico, D., and Mundula, F. (2016). The explosive activity of the 1669 Monti Rossi eruption at Mt. Etna (Italy). *J. Volcanol. Geotherm. Res.* 303, 25–40. doi: 10.1016/j.jvolgeores.2016.10.012
- Neri, M., Accolla, V., Behncke, B., Giammanco, S., Mazzarini, F., and Rust, D. (2011). Structural analysis of the eruptive fissures at Mount Etna (Italy). *Ann. Geophys.* 54, 464–479. doi: 10.4401/ag-5332
- Polacci, M., Corsaro, R., and Andronico, D. (2006). Coupled textural and compositional characterization of basaltic scoria: insights into the transition from Strombolian to fire fountain activity at Mount Etna, Italy. *Geology* 34, 201–204. doi: 10.1130/G223181.1
- Poret, M., Corradini, S., Merucci, L., Costa, A., Andronico, D., Montopoli, M., et al. (2018a). Reconstructing volcanic plume evolution integrating satellite and ground-based data: application to the 23 November 2013 Etna eruption. *Atmos. Chem. Phys.* 18, 4695–4714. doi: 10.5194/acp-18-4695-2018
- Poret, M., Costa, A., Andronico, D., Scollo, S., Gouhier, M., and Cristaldi, A. (2018b). Modelling eruption source parameters by integrating field, ground-based and satellite-based measurements: the case of the 23rd February 2013 Etna paroxysm. *J. Geophys. Res.* 123, 1–24. doi: 10.1029/2017JB015163
- Pyle, D. M. (1989). The thickness, volume and grain size of tephra fall deposits. *Bull. Volcanol.* 51, 1–15.
- Romero, J. E., Keller, W., and Marfull, V. (2013). Short chronological analysis of the 2007–2009 eruptive cycle and its nested cones formation at Llaima volcano. *J. Technol. Possib.* 2, 1–9. Available online at: <http://www.revistas.usach.cl/ojs/index.php/jotp/article/view/1395/1301>
- Rose, W. I., Palma, J. L., Escobar-Wolf, R., and Matias Gomez, R. O. (2013). A 50 yr eruption of a basaltic composite cone: Pacaya, Guatemala. *Geol. Soc. Am. Spec. Pap.* 498, 1–21. doi: 10.1130/2013.2498(01)
- Sellitto, P., di Sarra, A., Corradini, S., Boichu, M., Herbin, H., Dubuisson, P., et al. (2016). Synergistic use of Lagrangian dispersion and radiative transfer modelling with satellite and surface remote sensing measurements for the investigation of volcanic plumes: the Mount Etna eruption of 25–27 October 2013. *Atmos. Chem. Phys.* 16, 6841–6861. doi: 10.5194/acp-16-6841-2016
- Tupper, A., Itikarai, I., Richards, M., Prata, F., Carn, S., and Rosenfeld, D. (2007). Facing the challenges of the international airways volcano watch: the 2004/05 eruptions of Manam, Papua New Guinea. *Weather Forecast.* 22, 175–191. doi: 10.1175/WAF974.1
- Vergnolle, S., and Jaupart, C. (1990). The dynamics of degassing at Kilauea volcano, Hawaii. *J. Geophys. Res.* 95, 2793–2809.
- Viccaro, M., Garozzo, I., Cannata, A., Di Grazia, G., and Gresta, S. (2014). Gas burst vs. gas-rich magma recharge: a multidisciplinary study to reveal factors controlling triggering of the recent paroxysmal eruptions at Mt. Etna. *J. Volcanol. Geotherm. Res.* 278, 1–13. doi: 10.1016/j.jvolgeores.2014.04.001

- Wadge, G., Oramas Dorta, D., and Cole, P. D. (2006). The magma budget of Volcán Arenal, Costa Rica from 1980 to 2004. *J. Volcanol. Geotherm. Res.* 157, 60–74. doi: 10.1016/j.jvolgeores.2006.03.037
- Waythomas, C. F., Haney, M. M., Fee, D., Schneider, D. J., and Wech, A. (2014). The 2013 eruption of Pavlof Volcano, Alaska: a spatter eruption at an ice- and snow-clad volcano. *Bull. Volcanol.* 76:862. doi: 10.1007/s00445-014-0862-2
- Zharinov, N. A., and Demyanchuk, Y. V. (2016). Summit eruptions of Klyuchevskoi volcano, Kamchatka in the early 21st century, 2003–2013. *J. Volcanol. Seismol.* 10, 1–17. doi: 10.1134/S0742046316010061

Conflict of Interest Statement: The authors declare that the research was conducted in the absence of any commercial or financial relationships that could be construed as a potential conflict of interest.

Copyright © 2018 Andronico, Behncke, De Beni, Cristaldi, Scollo, Lopez and Lo Castro. This is an open-access article distributed under the terms of the Creative Commons Attribution License (CC BY). The use, distribution or reproduction in other forums is permitted, provided the original author(s) and the copyright owner(s) are credited and that the original publication in this journal is cited, in accordance with accepted academic practice. No use, distribution or reproduction is permitted which does not comply with these terms.



Assessing Impact to Infrastructures Due to Tephra Fallout From Öräfajökull Volcano (Iceland) by Using a Scenario-Based Approach and a Numerical Model

Sara Barsotti^{1*}, Dario Ingi Di Rienzo^{1,2}, Thorvaldur Thordarson², Bogi Brynjar Björnsson¹ and Sigrún Karlsdóttir¹

¹ Icelandic Meteorological Office, Reykjavík, Iceland, ² Faculty of Earth Sciences, University of Iceland, Reykjavík, Iceland

OPEN ACCESS

Edited by:

Sonia Calvari,
Istituto Nazionale di Geofisica e
Vulcanologia (INGV), Italy

Reviewed by:

Marco Viccaro,
Università degli Studi di Catania, Italy
Eisuke Fujita,
National Research Institute for Earth
Science and Disaster Prevention,
Japan

*Correspondence:

Sara Barsotti
sara@vedur.is

Specialty section:

This article was submitted to
Volcanology,
a section of the journal
Frontiers in Earth Science

Received: 02 June 2018

Accepted: 19 October 2018

Published: 13 November 2018

Citation:

Barsotti S, Di Rienzo DI,
Thordarson T, Björnsson BB and
Karlsdóttir S (2018) Assessing Impact
to Infrastructures Due to Tephra
Fallout From Öräfajökull Volcano
(Iceland) by Using a Scenario-Based
Approach and a Numerical Model.
Front. Earth Sci. 6:196.
doi: 10.3389/feart.2018.00196

Mt. Öräfajökull is one of the most dangerous volcanoes in Iceland with potential for a VEI6 eruption and the generation of many severe associated hazards. It is not a frequently erupting volcano with two eruptions in the last 1100 years, in 1362 and 1727–28. During the 1362 eruption 10 km³ of freshly fallen tephra was emitted, the eruption plume reached the stratosphere and was dispersed offshore toward mainland Europe. In this study we investigate the possible impact due to tephra fallout to critical infrastructures in Iceland namely – roads, airports, electrical power-lines – in case of a new eruption at Öräfajökull of similar intensity as in 1362. The analysis is done by running several times the VOL-CALPUFF dispersal model to simulate the dispersal of ash in the atmosphere and its deposition on the ground. The resulting maps show the probability of exceeding critical thickness of the tephra fall. Critical infrastructures have been added to the analysis to get a quantitative assessment of the potential impact. The results indicate that in case of an event similar to the 1362 eruption, the tephra fallout could be expected over most of the country, with higher likelihood on the eastern side. The tephra fallout is likely to have a severe impact in the proximity of the volcano, generating a deposit with a load of up to 1000 kg/m². The likelihood of failure for more than 160 km of the electrical power-line and for critical driving conditions on about 900 km of the main ring road is between 50 and 100%. The probability that the tephra fall will affect three of the main domestic airports is higher than 50%. An eruption of this magnitude is likely to affect commuting and communication between the greater Reykjavík area, where the government resides, and the rest of the country. Our analysis also reveals the limitations of current knowledge and understanding of the Öräfajökull volcano and highlights the need for further studies on past activity to better characterize its future behavior.

Keywords: Öräfajökull volcano, Iceland, tephra fallout, 1362 eruption, hazard assessment, numerical model, critical infrastructure

INTRODUCTION

There are about 30 active volcanic systems in Iceland and about half of those have featured tephra-producing eruptions (Thordarson and Höskuldsson, 2008). Volcanic eruptions are common in Iceland and have a recurrence interval of 2–5 years (Thordarson and Larsen, 2007). Basaltic eruptions are the most common volcanic events, and among them explosive within-glacier eruptions are most frequent because the most active central volcanoes are capped by glaciers (e.g., Katla, Grímsvötn, Bárðarbunga). Less frequent are explosive eruptions featuring more evolved magmas, such as dacite and rhyolite, that typify central volcanoes such as Öraefajökull and Hekla (Larsen and Eiríksson, 2008a,b). Highly active volcanic systems, as Hekla, Katla, Bárðarbunga and Grímsvötn, have explosive eruptions rates of 82, 97, 90, and 95%, respectively (CIV, 2017). Volcanogenic floods (Pagneux et al., 2015 and references herein), lava flows (Thordarson and Höskuldsson, 2008; Thordarson, 2013), tephra fallout (Larsen, 2002; Óladóttir et al., 2011; Janebo et al., 2016; Gudnason et al., 2017, 2018), lightnings (Bennett et al., 2010; Behnke et al., 2014), pyroclastic flows (Walker, 1962; Jørgensen, 1987; Thordarson and Höskuldsson, 2007; Tomlinson et al., 2010), are all phenomena associated with past eruptions in Iceland. Tephra dispersal and fallout is by far the most widespread hazard affecting local as well as distal regions. Ash clouds and tephra fallout can cause severe health issues (Baxter, 1990; Horwell and Baxter, 2006), affect important infrastructure like as electrical supply systems (Wilson et al., 2012), the national and international transportation network (Guffanti et al., 2009; Wilson et al., 2012), sensitive buildings (Spence et al., 2005), human health and life stock, vegetation and eco-system (Thorarinsson, 1979; Wilson et al., 2012; Ágústadóttir, 2015).

It was during the infamous eruption at Eyjafjallajökull in 2010 when a persistent northwesterly winds carried the ash-rich plume toward Europe for more than a month (Baerbel et al., 2012; Gudmundsson et al., 2012). On that occasion a prolonged closure of the European airspace resulted in severe economic impact estimated to be € 1.3 billion in the first week of the eruption (Bolić and Sivčev, 2011). The southernmost tip of Iceland experienced heavy tephra fallout, which impacted the local residence in various ways. Situation of low visibility happened often during the eruption as well as in its aftermath because of resuspension of ash (Petersen, 2010; Karlsdóttir et al., 2012). Air quality was often poor and affected the health of population living closest to the volcano (Carlsen et al., 2012). Relocation of life stock became essential due to heavy tephra fallout (Karlsdóttir et al., 2012; Thorvaldsdóttir and Sigbjörnsson, 2015). Specific investigations were done during the Eyjafjallajökull eruption to assess the effect of ash contamination on electrical power plants (Rarik, 2010). Eruptions at Hekla volcano have also been investigated to assess their effect on the environment and eco-system (e.g., Frogner et al., 2006). Heavy tephra and lapilli fallout during the eruption at Heimaey (Vestmannaeyjar Island) in 1973 destroyed and damaged several houses (Williams, 1983; Spence et al., 2005; Gudmundsson et al., 2008), some of those were restored after extensive cleaning effort to remove the tephra fall deposit.

In the period 2013–2016 the Icelandic Government, together with the International Civil Aviation Organization (ICAO), supported several projects aimed at assessing in a quantitative manner the long-term volcanic hazard in Iceland, to be used for more in-depth risk analysis. A specific component of these projects was the investigation of the impact of tephra fallout in Iceland for both medium-size, more frequent, and large, less frequent, explosive eruptions. Öraefajökull volcano was selected as the low probability but high-impact scenario.

Here, we focus on the AD 1362 Öraefajökull event as the most extreme scenario for a regional tephra fallout hazard and a preliminary risk assessment. The sparse eruption records for Öraefajökull introduces uncertainties in the volcanological scenario considered and we address this issue by using a numerical model to investigate the sensitivity of model results to variations in the volcanological input parameters.

The results of this study are presented through probabilistic hazard maps. These type of maps have become a commonly practiced representation of volcanic hazards and helps with the visualization of the footprint of the volcanic phenomena that may impact the surroundings of a volcano (Haynes et al., 2007; Nave et al., 2012; Calder et al., 2015; Thompson et al., 2015). Different types of hazard maps exist in literature. They can be produced on the basis of geological data, historical records and/or numerical model results (Calder et al., 2015; Loughlin et al., 2017). They can refer to a past eruption, to a specific hypothetical eruptive scenario or to a distribution of scenarios. If based on numerical results they can show the results from a single specific simulation (deterministic map) or from a multitude of scenarios. In the latter case the maps are often representing the impact of a specific hazard as a spatial probability and we refer to them as “probabilistic hazard maps.” Hazard maps are often used by volcano monitoring institutions to inform their stakeholders (e.g., decision makers institutions, general public, emergency managers, land-plan managers) about areas prone to be affected by specific hazards in case of an eruption. On a map it is easy to visualize extent of borders plus location of sensitive infrastructures, roads, towns and villages and, therefore, put the hazards into a spatial context that can be perceived more effectively by the users. Volcanic hazard maps have been produced for several volcanoes using numerical models and are applied for long-term hazard and risk assessment at particular volcanoes. For example, hazard maps have been produced for pyroclastic density currents at Mt. Vesuvius and Napolitean area (Esposti Ongaro et al., 2002, 2012; Sandri et al., 2018); for lava flows at Etna (Favalli et al., 2005; Tarquini and Favalli, 2013), Nyiragongo volcano (Favalli et al., 2009) and Lanzarote (Felpeto et al., 2001); for volcanogenic floods at Öraefajökull volcano (Pagneux et al., 2015). Probabilistic hazard maps for tephra fallout have been produced for Mt. Etna (Scollo et al., 2013), Campi Flegrei (Costa et al., 2009), Tarawera volcano (Bonadonna et al., 2005), Indonesian volcanoes (Jenkins et al., 2012), Santorini volcano (Jenkins et al., 2015). Most recently probabilistic maps for hazard due to ejection of ballistic have been produced for Mt. Chihshin in North Taiwan (Nurmawati and Konstantinou, 2018).

Here, we have produced probabilistic hazard maps to investigate the potential impact at a national level of a VEI6

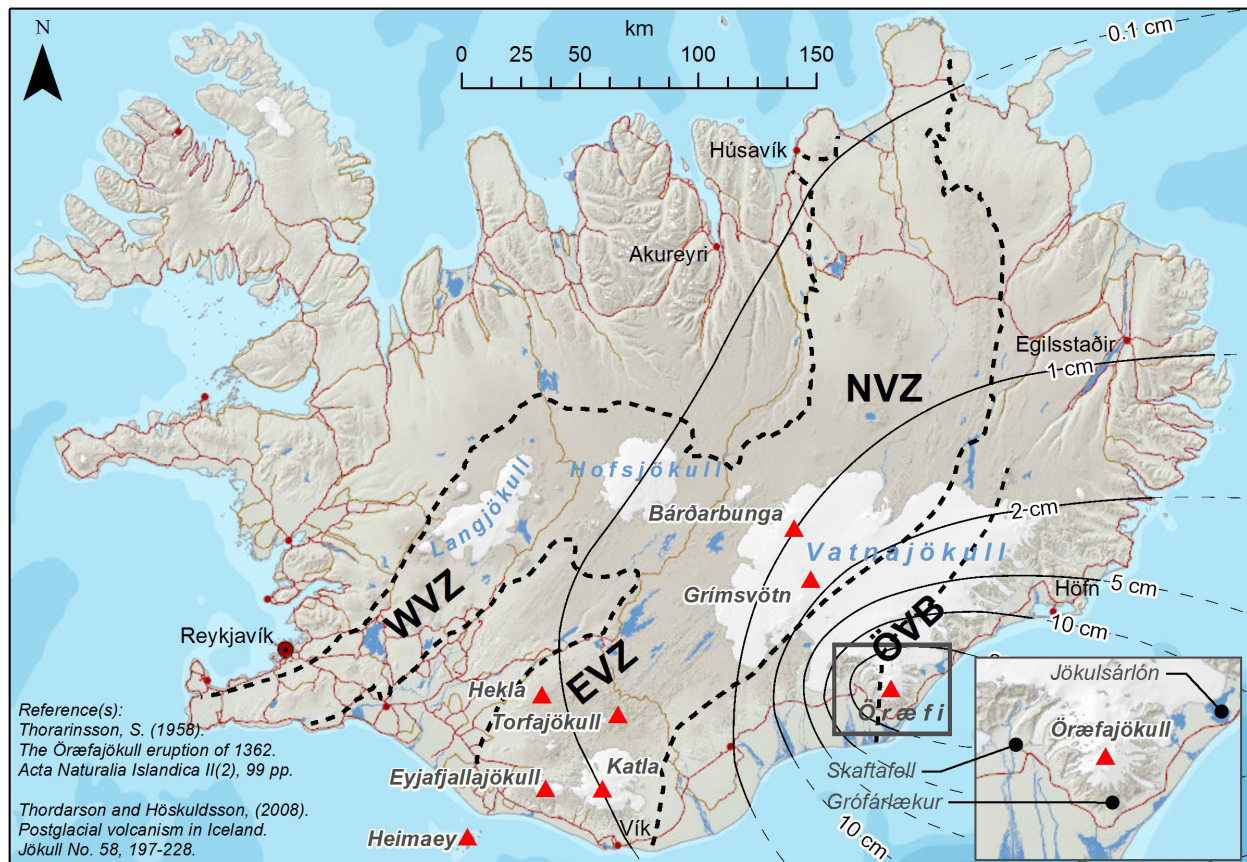


FIGURE 1 | Map showing the locations of Örfajökull volcano and the main sites mentioned in the text. On top of it the reconstructed deposit for the 1362 AD eruption is displayed.

(Newhall and Self, 1982) eruption at Örfajökull. The impact of tephra fallout on infrastructures is calculated via a numerical model that simulates the atmospheric dispersal of tephra and its deposition. GIS-referenced layers with information on the powerline network, roads, airports are included to assess potential disruptions to services and commuters. Possibly, these results will support the national authorities in planning and designing mitigation actions that are necessary to reduce the risks posed by a future eruption at Örfajökull. A more complete hazard assessment should also include the investigation of smaller eruptions (VEI4) as they appear to be most frequent events at Örfajökull as reported in Section “Geological Background.” The choice to look first at a VEI6 eruption was dictated by the need to quantify the potential damage the worst case scenario would cause to the society nowadays. The indications provided by the Icelandic Civil Protection addressed this research and supported the worst case scenario as the reference scenario for Örfajökull.

Geological Background

Örfajökull is an ice-capped stratovolcano located in South-East Iceland on the southern margin of Vatnajökull glacier (Thordarson and Larsen, 2007; Gudmundsson et al., 2008;

Sharma et al., 2008; Larsen et al., 2015). It is about 20 km in diameter with a 3 by 4 km ice-filled caldera which rises to a summit of 2110 m a.s.l. (Figure 1). The volcano is part of the intraplate Örfajökull Volcanic Belt, situated to the east of the current plate margins and possibly represents an embryonic rift (e.g., Thordarson and Larsen, 2007; Thordarson and Höskuldsson, 2008).

The Örfajökull central volcano has featured two explosive eruptions in historical times (e.g., Thorarinnsson, 1958). The most recent was a small icelandite eruption of VEI4 in 1727–1728 CE (e.g., Larsen et al., 1999; Larsen et al., 2015). This was preceded by a much larger rhyolitic Plinian (VEI6) eruption in 1362 CE. Studies on the tephra stratigraphy in soils around the volcano have revealed five prehistoric silicic explosive eruptions at Örfajökull and all are assumed to be smaller in magnitude and intensity than the 1362 CE event (Gudmundsson, 1998; Larsen et al., 2015).

In Iceland VEI6 events are infrequent and only three such events are known during the Holocene: the before mentioned 1362 CE event at Örfajökull along with the two largest Holocene silicic explosive eruptions in Iceland, the 3 ka H3 and 4.2 ka H4 events at the Hekla volcanic system (e.g., Larsen and Thorarinnsson, 1977; Stevenson et al., 2015).

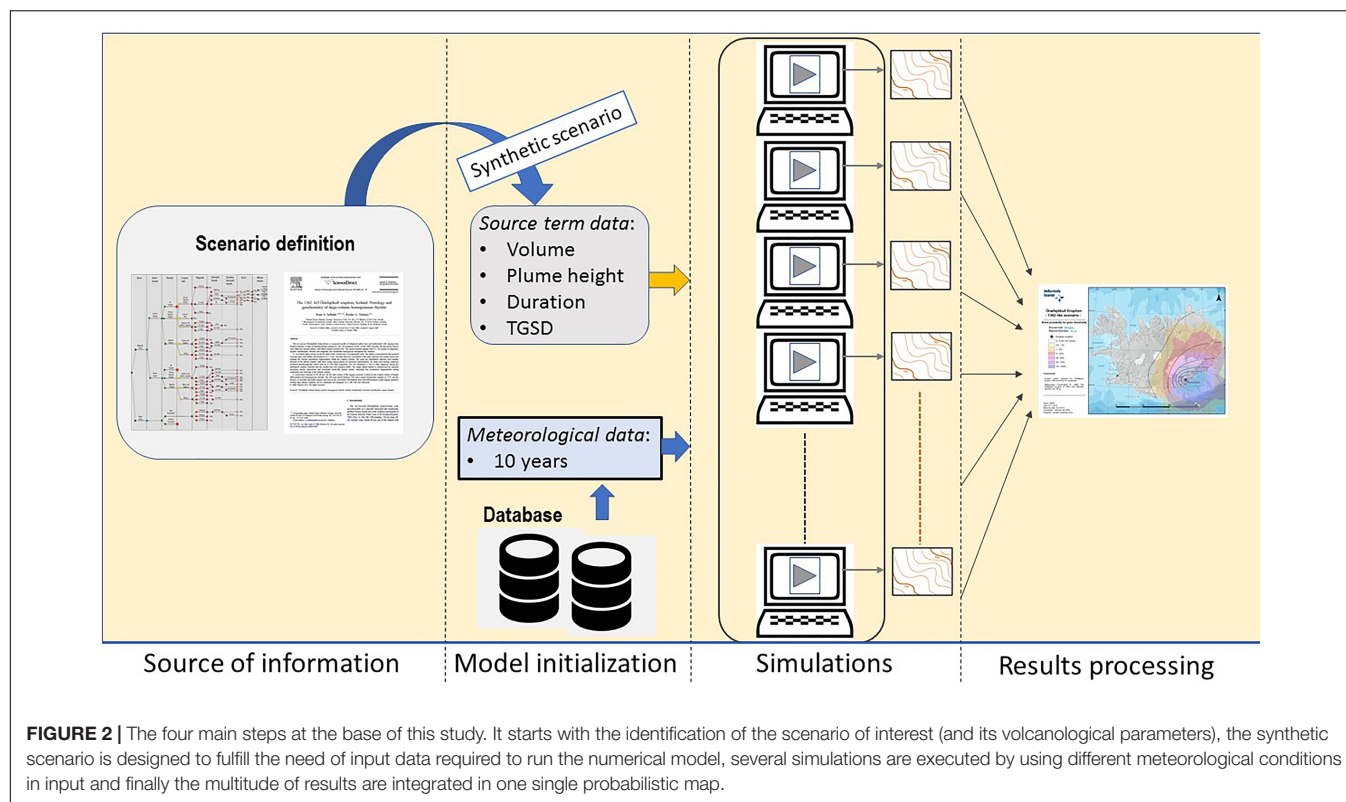


TABLE 1 | Volcanological parameters characterizing the 1362 eruption at Öraefajökull as reported in Thorarinsson, 1958.

Volcano	Volume uncompacted (km ³)	Tephra mass (kg)	Duration (h)	Plume height (km a.s.l.)	Reference eruption
Öraefajökull	~10	~4.8 × 10 ¹²	18–24	25–35	1362

The 1362 CE Öraefajökull eruption is the largest rhyolitic eruption in Iceland since settlement in the 9th Century, with an estimated volume of freshly fallen tephra of 10 or ~6 km³ of compacted tephra and about 2 km³ when calculated as dense rock (Thorarinsson, 1958). Sharma et al. (2008) obtained a smaller volume of 2.3 km³ assumed to equal 1.2 km³ calculated as dense rock. Early stage pyroclastic density currents and intercalated jökulhlaups, along with the subsequent tephra fall, inundated the then prosperous farming district “Litla Hérað” causing fatalities (e.g., Thorarinsson, 1958; Jónsson and Valdimar, 2007; Thordarson and Höskuldsson, 2007). The reconstructed tephra dispersal is shown in **Figure 1**, where isopachs (i.e., lines of

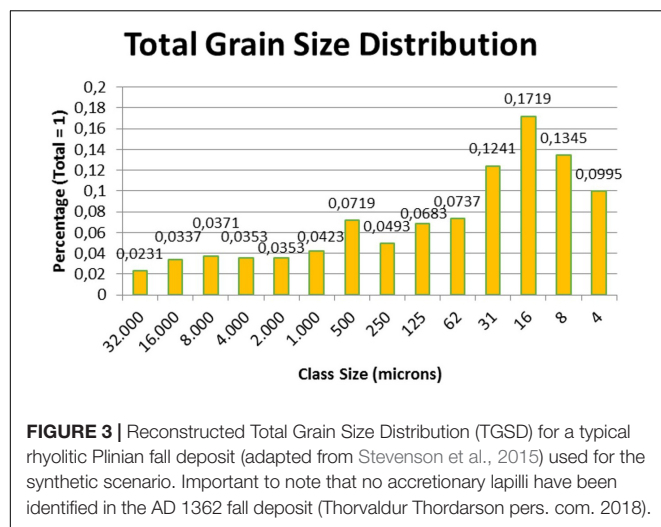
equal thickness) for the 1362 eruptions are shown as black lines, and the dashed lines indicate the inferred dispersal over the sea. About half of the country received >1 mm of ash as a consequence of the tephra fall from this eruption. Close to the volcano up to 20 cm of ash has been accumulated over an area of 1000 km², peaks in the deposit thickness are found in Grófarlækur (40 cm) at about 10 km from the summit volcano (Thorarinsson, 1958) and between Hnappavellir and Fagurhólmsmýri where the thickness reached 2 m (Jónsson and Valdimar, 2007; Sharma et al., 2008) (**Figure 1**). Tephra from Öraefajökull has been identified in Western Europe (e.g., Pilcher et al., 2005) and in Greenland ice-cores (e.g., Palais et al., 1991).

The magma erupted in 1362 is a medium-K alkali rhyolite that is extremely homogeneous in composition. It is thought to be extracted from the topmost portion of a compositionally stratified magma storage zone, although there is no geophysical indication of any upper crustal (<15 km depth) magma storage zone beneath Öraefajökull at present. In contrast to the East Volcanic Zone and other rift zone rhyolites, which demonstrably are generated by partial melting of hydrated metabasaltic crust (e.g., Sigmarsson et al., 1992), the Öraefajökull and other silicic magmas generated by intraplate volcanoes are inferred to have evolved from a more mafic parent via fractional crystallization

TABLE 2 | Estimation of total mass emitted during the 1362 eruption by using different ways to interpolate the isopachs drawn by Thorarinsson (1958).

	Total mass	Volume DRE
Thorarinsson, 1958	4.8 × 10 ¹² kg	2 km ³
Thorarinsson GIS simple	4.29 × 10 ¹² kg	1.79 km ³
Thorarinsson GIS interpolation	6.96 × 10 ¹² kg	2.9 km ³
Model	2.75 × 10 ¹³ kg	5.5 km ³

The mass estimated to match the reconstructed deposit with the modeled results is also shown.



(e.g., Selbekk and Tronnes, 2007; Martin and Sigmarsson, 2007; Sigmarsson et al., 2008).

Recent Unrest

From September 2017 Öraefajökull volcano has showed clear indications of unrest. The reinvigoration of the geothermal activity beneath the volcano was corroborated by elevated seismicity, gas release and the formation of a cauldron in the middle of the caldera. Consequently, the Icelandic Meteorological Office raised the color code for Öraefajökull to yellow¹ in November 2017. The aviation color code was turned back to green on 4th May, 2018 when the main monitoring parameters indicated a stable situation with no immediate hazard to the aviation. However, given the persistent potential for local hazards, the Icelandic Civil Protection decided to maintain the level of Uncertainty for Öraefajökull (IMO, 2018a).

In the period November 2017 to May 2018, a priority has been placed on improving the real-time monitoring around Öraefajökull. At the same time, hazard, and risk assessments performed for glacial outbursts originating from this volcano (Pagneux et al., 2015) were provided to the Department of Civil Protection and Emergency Management of the National Commissioner of the Icelandic Police to finalize the evacuation plans for the Öraefi district (NCIP, 2017). The preliminary study on tephra fallout and its potential impact on infrastructures at a national level, here presented, was also finalized.

At the time of writing the seismicity is elevated and higher than in November 2017. The deformation data (from both cGPS and InSAR analysis) reveal clear indication of an on going inflation process likely due to injection of new magma at depth (IMO, 2018b).

MATERIALS AND METHODS

The methodology used for the hazard assessment in this study is shown in **Figure 2**. It consists of four main steps: (1) identification

¹<http://en.vedur.is/about-imo/news/a-new-ice-cauldron-in-oraefajokull-volcano>

of the scenario of interest (this can be defined on the basis of an Event Tree outcome or from literature); (2) initialization of VOL-CALPUFF model (Barsotti et al., 2008) by using a *synthetic scenario* (selected eruption source parameters to be used as a model input) as well as a range of meteorological scenarios; (3) execution of several numerical runs by using different starting times; (4) statistical processing of the results from multiple runs. The obtained probabilities, as visualized in the final maps, are those called “conditional probabilities,” i.e., conditioned to the occurrence of that specific eruptive scenario.

Scenario Definition

Available publications (Thorarinsson, 1958; Jónsson and Valdimar, 2007; Thordarson and Höskuldsson, 2007; Sharma et al., 2008), provide the general framework for the eruption source parameters used in the dispersal simulations. Calculating the total mass emitted during the Plinian phase of the eruption is a first order estimate because large portion of tephra fell onto the sea (see **Figure 1**). Using the values given in Thorarinsson (1958) the total mass is estimated to be 4.8×10^{12} kg (**Table 1**).

A GIS referenced reconstruction of the original map by Thorarinsson (1958) is used to recalculate the erupted tephra mass by (1) assuming a constant thickness between the different isopachs and (2) by interpolating between two successive isopachs assuming a linear trend. These two estimates give an erupted tephra mass of 4.29×10^{12} and 6.96×10^{12} kg, where the latter is about factor of 1.5 larger than that obtained from Thorarinsson (1958) data (see **Table 2**).

TABLE 3 | Tephra fallout conditions investigated to cause insulator flashover and pole and line damages for wet and dry ash (as reported in Wilson et al., 2012).

Dry ash	Deposit thickness <5 mm	Deposit thickness >5 mm
Insulator flashover (line voltage <33 kV)	Low	Low
Insulator flashover (line voltage >33 kV)	Low	Low
Wet ash	Deposit thickness <5 mm	Deposit thickness >5 mm
Insulator flashover (line voltage <33 kV)	High	High
Insulator flashover (line voltage >33 kV)	Medium	High
Dry ash	Deposit thickness <100 mm	Deposit thickness >100 mm
Electrical tower and pole damage	Low	Medium
Electrical line damage	Low	Medium
Wet ash	Deposit thickness <5 mm	Deposit thickness >5 mm
Electrical tower and pole damage	Low-medium	Medium-high
Electrical line damage	Low-medium	High

In order to run a dispersal model several input parameters need to be defined. VOL-CALPUFF model requires initial values of parameters like the vertical exit velocity of the volcanic mixture, the vent radius, the total grain size distribution (TGSD). As we currently have no information on the values for these variables, they are obtained via iteration by running VOL-CALPUFF model with a range of input values for the above mentioned variables. The output values selected are those that produced the best fit between the modeled and the observed deposit distribution as well as the eruption column heights. In an attempt to reproduce the scenario reported in **Table 1** and to match the isopachs as depicted in Thorarinsson (1958), the VOL-CALPUFF dispersal model was run multiple times using a vent radius from 150 to 300 m; a gas mass fraction from 1 to 5% and three different TGSDs (one peaked at $\phi = -3$, one peaked at $\phi = 0$ and a bi-modal distribution with two peaks at $\phi = -3$ and $\phi = 2$, respectively). By a comparison of the model results and the original isopach map and by constraining the top plume height between 24 and 34 km, the best fit was obtained by using the following input parameters:

1. Vertical velocity: 300 m/s
2. Vent radius: 300 m

3. Gas mass fraction: 3%
4. Total grain size distribution: bi-modal (see **Figure 3**).
5. Mass flow rate: 4.24×10^8 kg/s
6. Duration of the emission: 18 h

A forward run of the plume model with these input parameters produced the following values for plume height and tephra emitted mass (to compare with values reported in **Table 1**):

1. Plume height: 23.5–37 km a.s.l.
2. Total erupted tephra mass: 2.75×10^{13} kg

This synthetic scenarios is in a reasonable agreement with anticipated duration of the Plinian phase and plume height. However, there is a larger discrepancy in terms of mass. The new numerical simulation results suggest that in order to match the original isopachs, the DRE volume is 5.5 km^3 . This volume is 2.75 times larger than that provided by Thorarinsson, and 1.9 times larger than the value calculated with the GIS interpolation (**Table 2**). Considering the huge uncertainties affecting the meteorological conditions during the eruption, the real extension of the deposit and the few observational data available, we considered valuable in this study to use those input parameters obtained through the matching procedure to perform the probabilistic assessment.

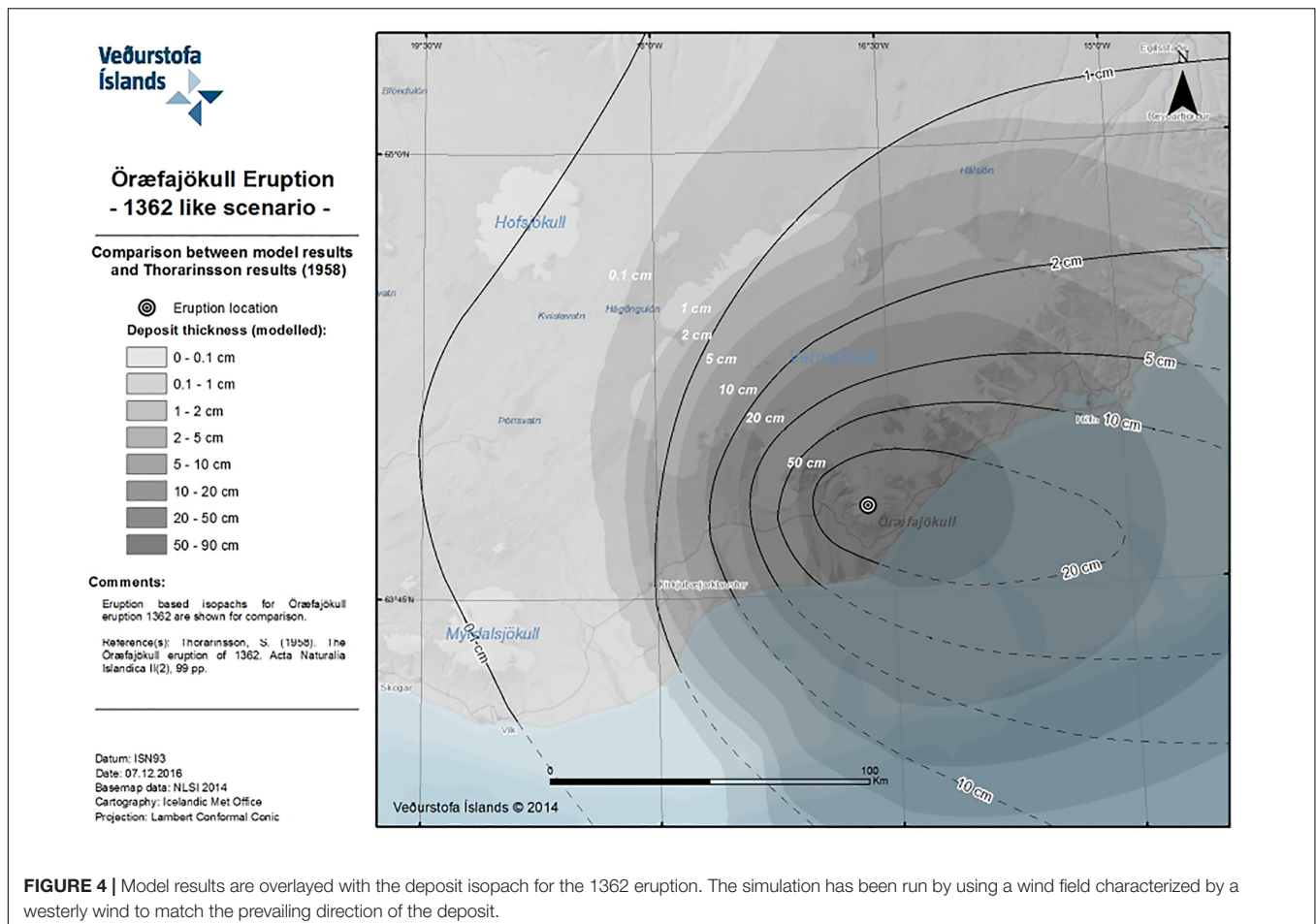


FIGURE 4 | Model results are overlaid with the deposit isopach for the 1362 eruption. The simulation has been run by using a wind field characterized by a westerly wind to match the prevailing direction of the deposit.

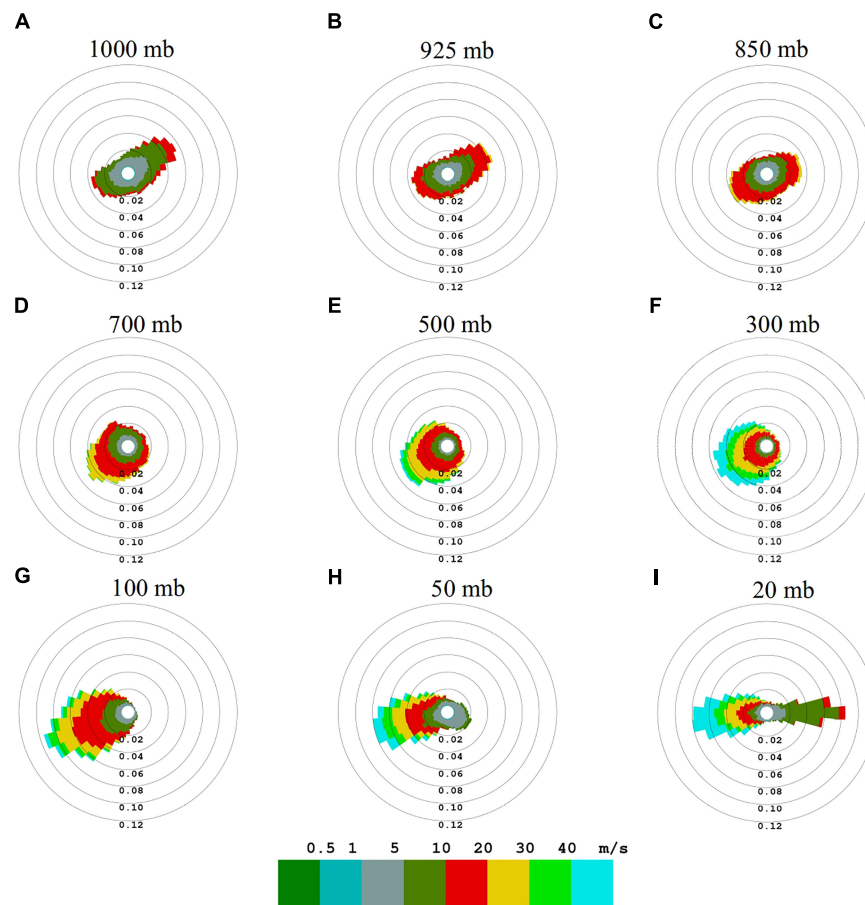


FIGURE 5 | The nine windroses show the wind direction (the sectors correspond to the direction from which the wind blows) and speed (different colors) at different altitudes over Vatnajökull glacier. 1000 mb corresponding roughly to the ground level up to 20 mb corresponding about to 24000 m asl. Ten years of ECMWF data (1980–1990) have been processed to produce these windroses.

The tephra dispersal from the synthetic scenario is compared with the isopachs reconstructed for the real event in **Figure 4**. The gray filled contours are the model results whereas the solid black lines are the deposit isopachs as reconstructed by Thorarinsson (1958). A westerly wind has been selected to run the dispersal and match the general feature of the deposit pattern. For the same simulation (i.e., by assuming the same input condition) the model reproduced a super-buoyant plume with height of 30.6 km above the vent.

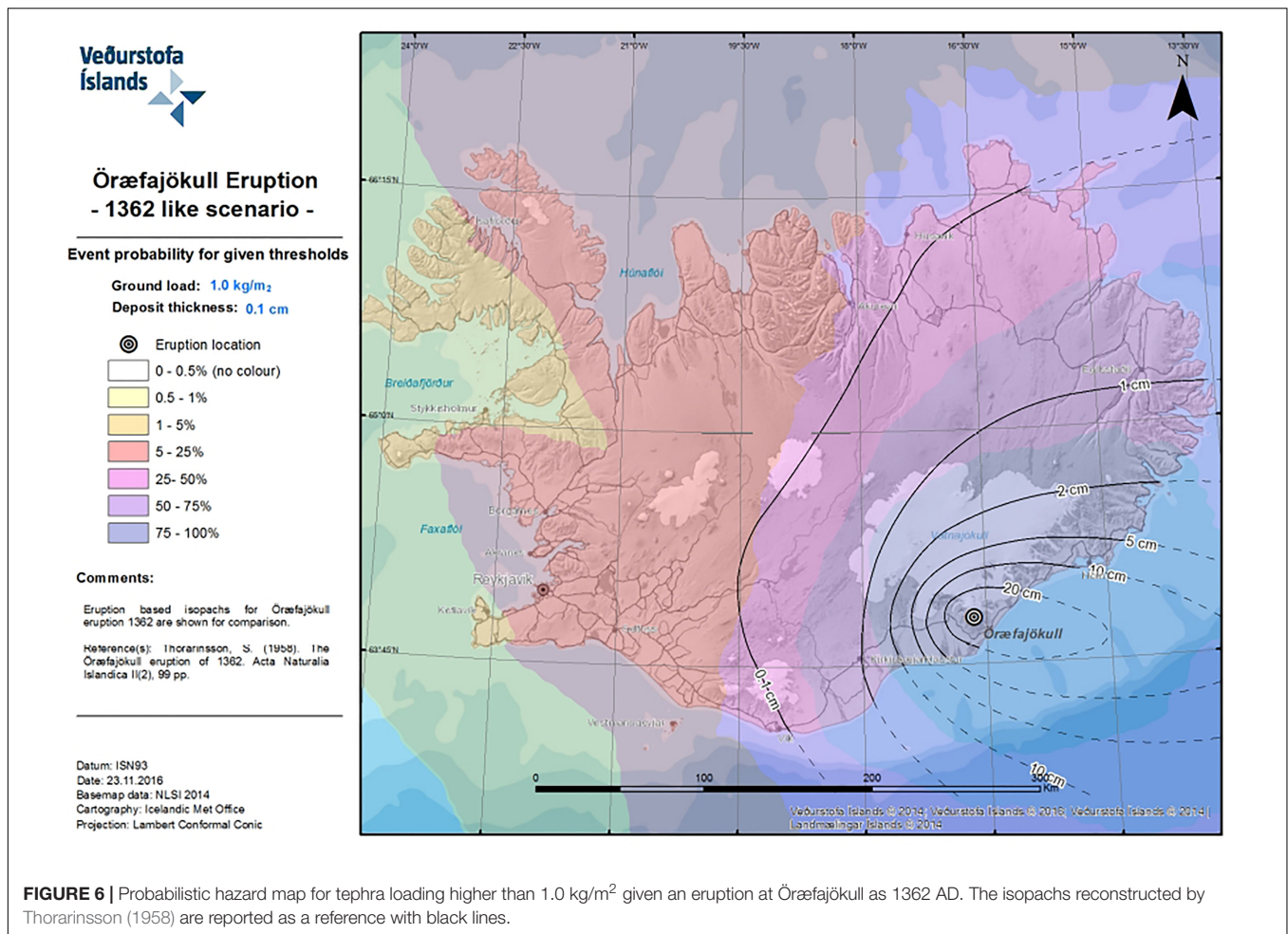
Numerical Approach

The Numerical Model

Plume ascent is described solving plume theory equations (Bursik, 2001) to compute column height as a function of volcanological source input data and wind field parameters. The latter are relevant for simulating weak plumes that are strongly affected by wind shearing. During plume ascent the heaviest particles fall from the column and a lighter mixture continues its upward motion, entraining air up to a null-vertical velocity altitude where only lateral dispersion takes place. The plume initially decelerates due to higher density compared with

surrounding atmosphere, but due to heating of entrained air (mixed by turbulent motions) the mixture can eventually become lighter than air. Buoyancy effect can cause the mixture to accelerate upward until an equilibrium is achieved.

The dispersal code VOL-CALPUFF originates from the CALPUFF model and it has been modified to reproduce some processes specific of a volcanic eruption, e.g., plume rise phase and the dispersal of a distribution of solid particles. It is a hybrid model in which the plume rise phase is described with a Eulerian approach, whereas the ash cloud transport is solved in a Lagrangian framework. Along the plume and at its top the material is released as a series of diffusing packets (puffs) containing an initially assigned amount of particulate matter which varies during the transport due to gravitational fallout. Since its development the VOL-CALPUFF model has been applied mostly at Mt. Etna to reconstruct past explosive events (Barsotti and Neri, 2008; Barsotti et al., 2008), as an ash dispersal forecasting tool (Barsotti et al., 2008) and to estimate potential hazards posed by volcanic ash to human health and ground infrastructures (Barsotti et al., 2010). In the past years VOL-CALPUFF has been also applied to other active volcanoes to



produce forecasting maps of ash dispersal during eruptive crises at Redoubt Volcano (Alaska) in 2009, Eyjafjallajökull (Iceland) and Mount Merapi (Indonesia) in 2010 (Barsotti et al., 2011; Spinetti et al., 2013) and Grímsvötn (Iceland) in 2011.

Monte Carlo Simulations

Numerical models can be used to investigate the behavior of a specific process process (Kavanagh et al., 2018) as for example dispersal of ash (Bonadonna et al., 2011; Folch, 2012), lava flow invasion (Del Negro et al., 2005; Favalli et al., 2005, 2009), maximum distances of pyroclastic flow (Esposti Ongaro et al., 2012; Dufek, 2016). Each simulation needs specific input conditions to characterize the volcanological scenarios to be investigated. For volcanic ash dispersal simulation the eruptive source parameters (ESP) as plume height, particle size distribution, mass flow rate need to be quantified (Mastin et al., 2009). As we do not know in advance about the next eruptive conditions, like the weather and the ESP, a way to treat this uncertainty is to reflect this into a probabilistic analysis. Looking into a range of eruptive scenarios it is possible to get a statistics that would investigate and reflect the uncertainty in the assumption made analyzing a single scenario. By running the model with several sets of starting conditions enables us to

estimate the probability that a specific area will be affected by a certain type of hazard. A method widely used to achieve such a result is called Monte Carlo approach and is based exactly on the assumption that a model could be executed multiple times for as many initial conditions as required for producing an ensemble modeling (Sparks and Aspinall, 2013). The application of this approach for a probabilistic analysis of a simulated volcanic process can be found in Cioni et al. (2003), Hurst and Smith (2004), Bonadonna et al. (2005), Macedonio et al. (2008), Costa et al. (2009), Barsotti et al. (2010), Scaini et al. (2012, 2014), Scollo et al. (2013), Biass et al. (2014), Bonasia et al. (2014).

A Monte Carlo simulation is performed for this study by running several times the dispersal model VOL-CALPUFF for a fixed volcanological scenario (the 1362 AD reference eruption) and by using several years of meteorological data. Each simulation is performed using the same input data given in Section “Scenario Definition.” The simulations are initiated with different starting date and times of the day, over a period of 10 years. This is done to ensure the randomness of the analysis and to avoid bias in the results due to the daily variations of the atmospheric parameters as we only investigate the effect of the wind field statistics on the tephra dispersal. The potential variability associated with the uncertainty in the volcanological

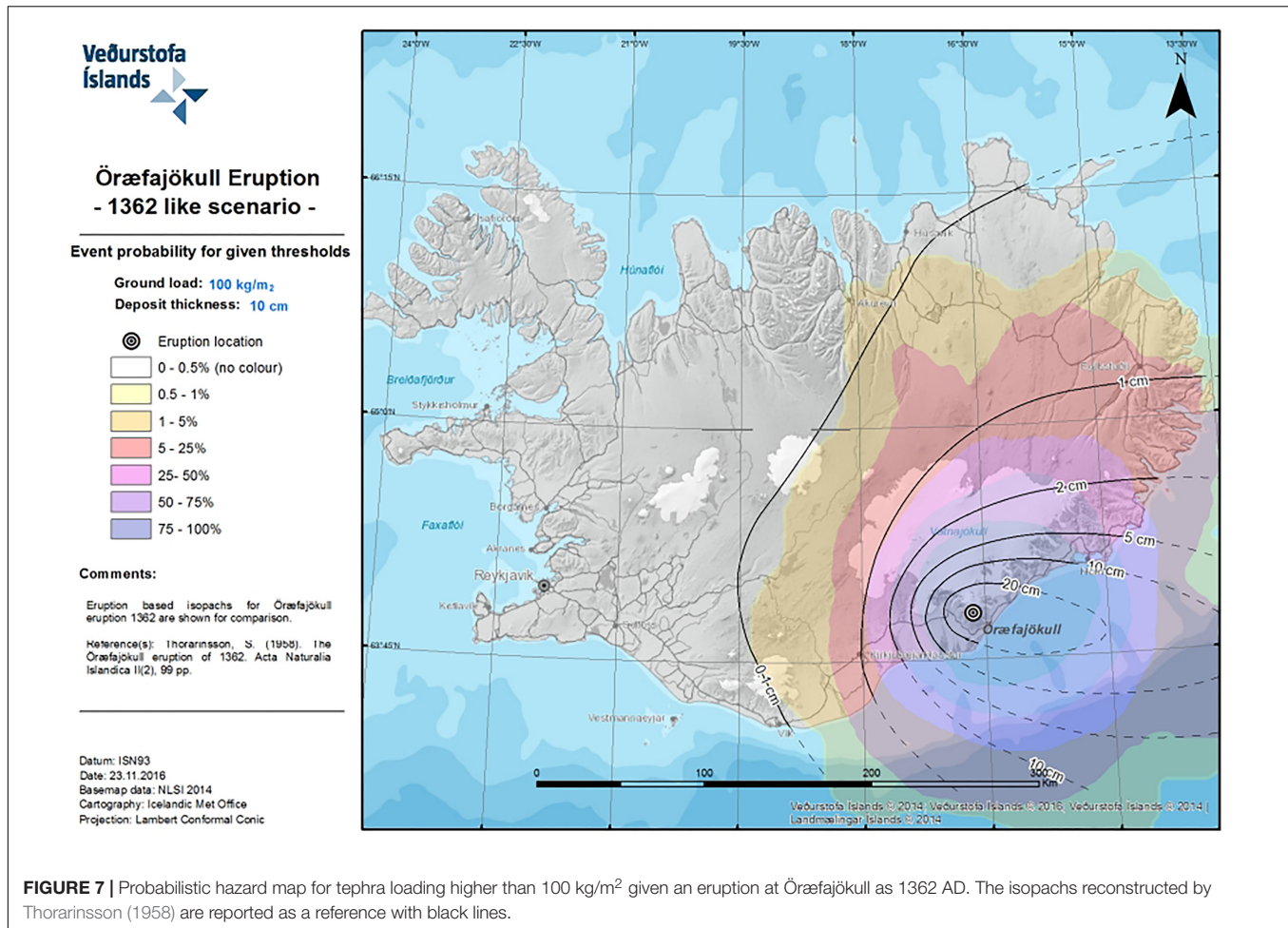


FIGURE 7 | Probabilistic hazard map for tephra loading higher than 100 kg/m² given an eruption at Öraefajökull as 1362 AD. The isopachs reconstructed by Thorarinnsson (1958) are reported as a reference with black lines.

scenario is not considered. A total of 500 simulations were performed in order to obtain a convergence for the modeled tephra dispersal distribution.

Forecast data produced by the European Centre of Medium-range Weather Forecast is used to run the VOL-CALPUFF model. The meteorological data for the probabilistic maps have been downloaded from the ERA-INTERIM archive and cover a period of 10 years, from 1980 to 1991. This dataset is produced by re-analyzing the forecast, i.e., by assimilating the observational data into the original weather forecast (Dee et al., 2011). This means that this dataset provides a quite complete and verified description of the 3D atmospheric fields over the period of interest. On the other side the horizontal resolution of the meteorological data is of 0.7° (i.e., about 35 and 77 km in the longitude and latitude respectively), making the spatial resolution of this dataset a bit coarse for the domain considered in this project. The statistics for the investigated area around Öraefajökull produced by using the ECMWF data over this time period is shown in Figure 5.

In Figure 5 each windrose shows the direction of provenance for the wind field, identified by the sector, and the wind velocity, identified by the color. Each windrose is produced for a specific altitude expressed in pressure from 1000 mb (surface level) to

20 mb (~25 km). At low levels (1000 mb, a in Figure 5) the wind is weak, with wind velocity between 5 and 10 m/s. The prevailing direction at this altitude is location dependent, and has a NE component over Vatnajökull. Higher up in the atmosphere the wind field is more uniform and less affected by the surface topography. The velocity tends to increase moving higher up to 300 mb (9–10 km, f in Figure 5). Further up the wind velocity decreases to increase again at 20 mb (i in Figure 5) where there is a clear W-E directionality, with Easterly winds weaker than Westerly ones.

Impact of Tephra on Infrastructure

Tephra can have wide type of impacts either nearby and far away the volcano. As reported in literature, at ground level volcanic tephra can cause:

1. health issues (Baxter, 1990; Horwell and Baxter, 2006);
2. roofs/building collapse (Spence et al., 2005);
3. poor visibility conditions (Blong, 1996);
4. dangerous road conditions (Wilson et al., 2012; Blake et al., 2017);
5. contamination of water reservoirs and vegetation (Wilson et al., 2012; Ágústssdóttir, 2015);

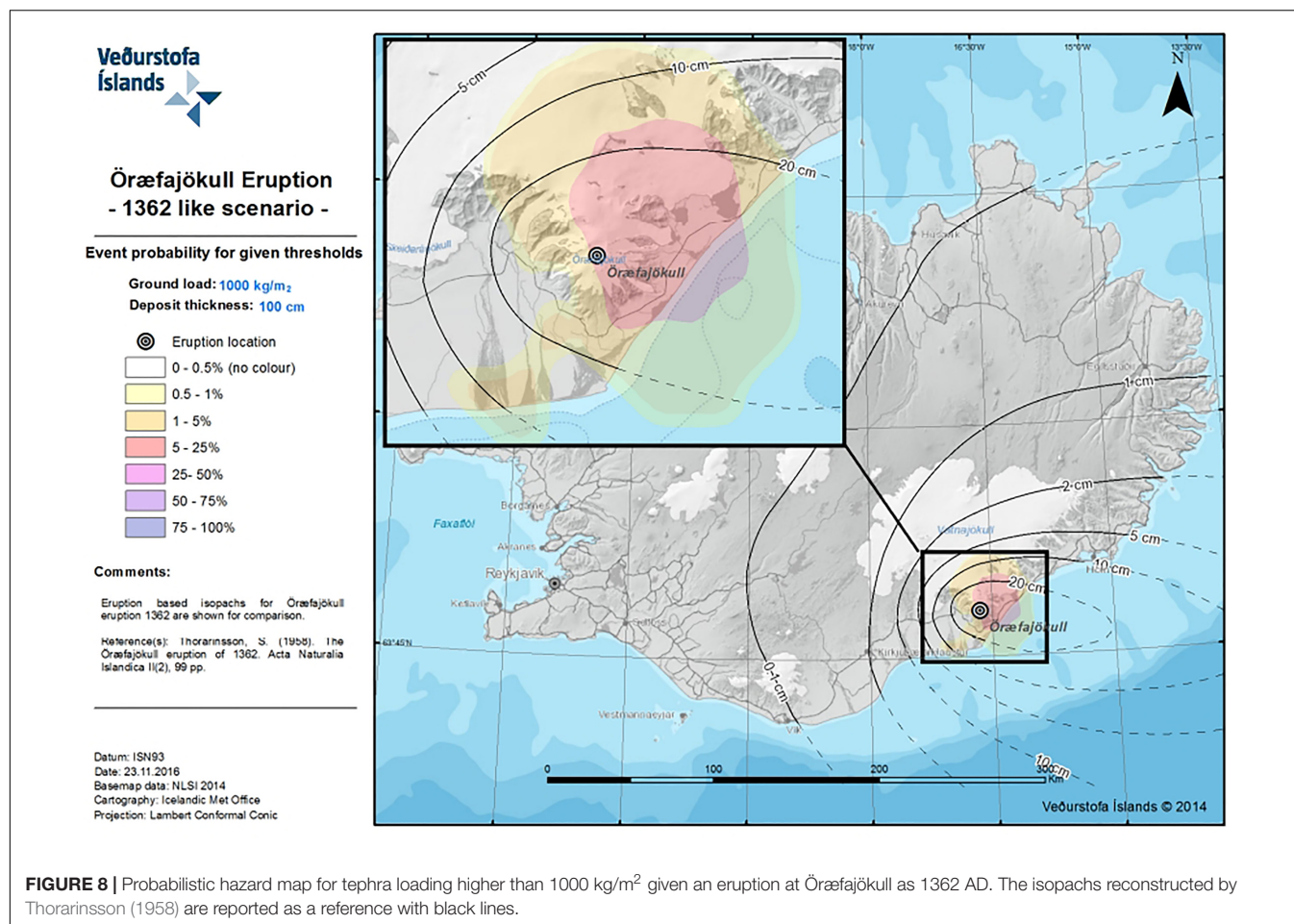


TABLE 4 | Likelihood of receiving specific amounts of tephra is calculated for five main towns in the country.

Town	Probability to exceed 1 kg/m ²	Probability to exceed 10 kg/m ²	Probability to exceed 100 kg/m ²	Distance from Öraefajökull central volcano (km)
Akureyri	25.4189	10.2073	1.17319	200
Reykjavík	5.714	1.429	0	259
Egilsstaðir	61.4466	49.1621	7.01942	177
Vík	35.2207	11.6758	0	134
Höfn	97.8526	94.8986	72.9586	76

6. damages to electrical infrastructures (Bebbington et al., 2008; Wardman et al., 2012; Wilson et al., 2012);
7. transportation system disruptions (Casadevall, 1994; Guffanti et al., 2009; Wilson et al., 2012);
8. impact on telecommunication networks (Wilson et al., 2012).

Composition of the tephra, its grain-size distribution and presence of precipitation might enhance some of these hazards, as for example roof collapse conditions, damages to electrical infrastructure and contamination of water and vegetation. Wet

tephra can reach higher load due to the contribution of rain that remains trapped in the deposit (Macedonio and Costa, 2012). This means that tephra fallout might have a different impact on buildings if it rains during or shortly after the eruption. Similarly, wet conditions might affect the conduction properties of tephra enhancing its effect in flashover events (Wilson et al., 2012). Finally silicic tephra can be strongly toxic for humans, pollute water supplies and poison grazing animals (Thorarinsson, 1979; Cronin et al., 2003).

Here, we investigate the potential impact of tephra fall on three key infrastructures, because if damaged, it can result in prolonged disruptions to the local population. The primary/direct hazards due to tephra fall onto airports, roads and power-lines are here considered.

Roads

Tephra on roads is an issue for traffic safety. It can result in the reduction of tire friction, obscure road markings, cause blockage of engine air intake filters and reduce the visibility for drivers. Few studies have properly investigated the thresholds of tephra fall capable to trigger critical driving conditions. Recently, Blake et al. (2017) presented results of laboratory experiments on how the properties of tephra fall (thickness, particle composition, particle size) along with precipitation can compromise skid resistance.

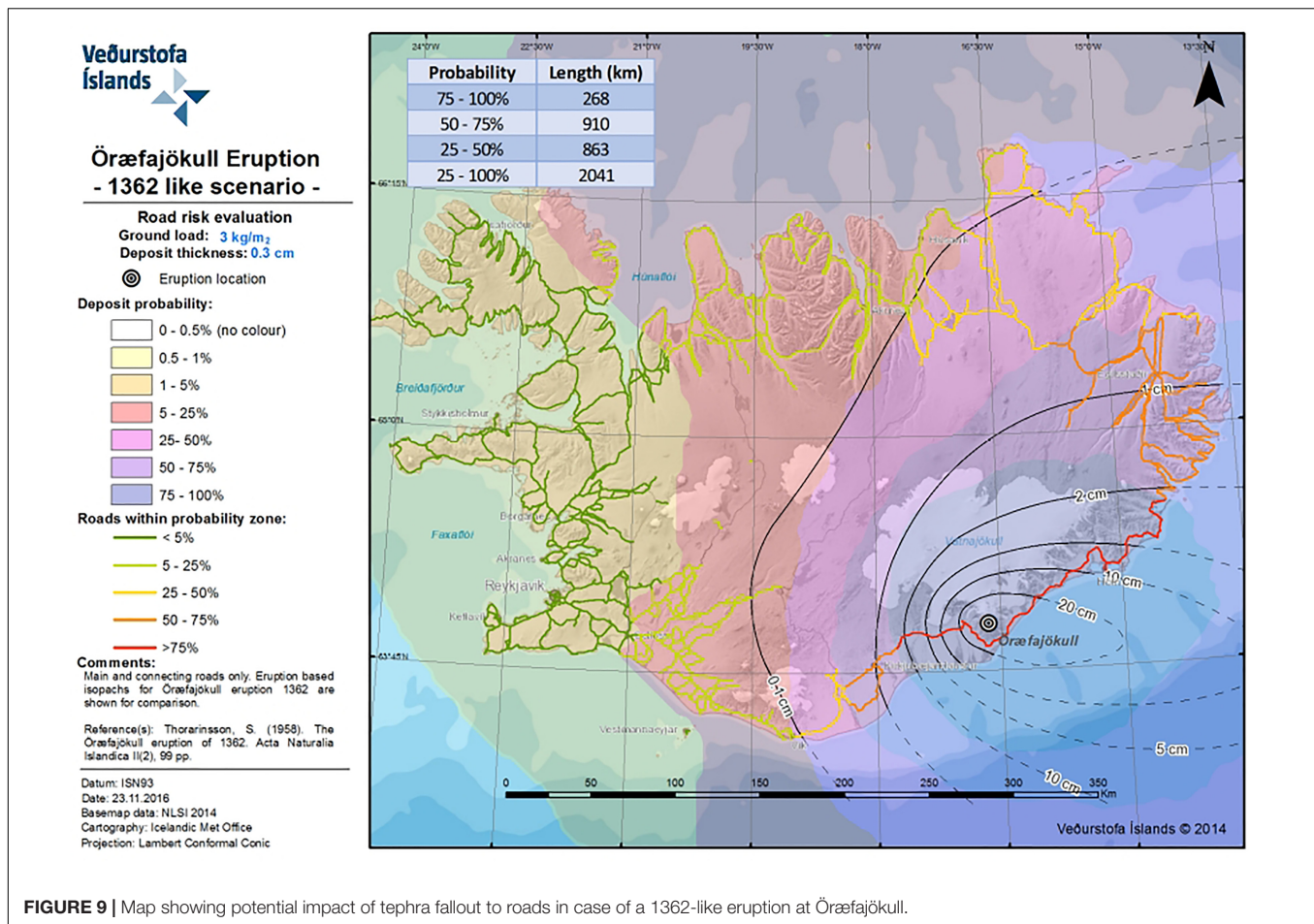


FIGURE 9 | Map showing potential impact of tephra fallout to roads in case of a 1362-like eruption at Örfajökull.

These results showed that for a 1 mm-thick fallout the skid resistance is below the “difficult site” safety levels. In case of thicker deposit (>5 mm) the conditions are more favorable, with skid resistance above the “safe” value. The study concludes that tephra fall thickness of 5 mm is the critical limit for which mitigation actions need to be taken to guarantee safe driving conditions on roads. At the same time Blake et al. (2017) presents a list of road disruptions occurred at volcanoes worldwide and shows how in several cases deposit several-10s-of-mm-thick have also been causing difficulties to the ground transportation. In this study we use a threshold value of 3 mm to represent disruptive conditions on the roads.

Airport

As reported in Guffanti et al. (2009) and Prata and Tupper (2009) the primary hazard to airports is ashfall, which can cause loss of visibility, create slippery runways, infiltrate communication and electrical systems, interrupt ground services, and damage buildings and parked airplanes. The skid resistance analysis performed by Blake et al. (2017) can be partly applied to airfield and runways, even though no clear thresholds exist for this environment with each airport operating authorities responsible for maintaining the runways functional and secure. Some critical conditions described for roads can be also applied to airfield

and runways with few-mm ash deposit- to be considered a condition that can be critical for safe operations. Here, we use a threshold value of 1 mm to investigate the impact on airports.

Power Lines

Several papers discuss the vulnerability of electrical infrastructure to volcanic ash (Bebbington et al., 2008; Wardman et al., 2012; Wilson et al., 2012) and are used to identify correlation between specific thresholds of ash thickness and the level of impact (low, medium, and high) it would have on electrical infrastructure (Wilson et al., 2012). Critical infrastructure as power-lines have been investigated for damages due to:

- o insulator flashover;
- o electrical tower and pole damage;
- o electrical line damage.

The effect of tephra fall on this type of infrastructure depends on three main factors: the grain-size, the tephra load and presence of precipitation (wet deposition).

In this study we only look into those critical conditions associated with fine tephra because, as shown in **Figure 3**, this is the assumption we use for an eruption at Örfajökull.

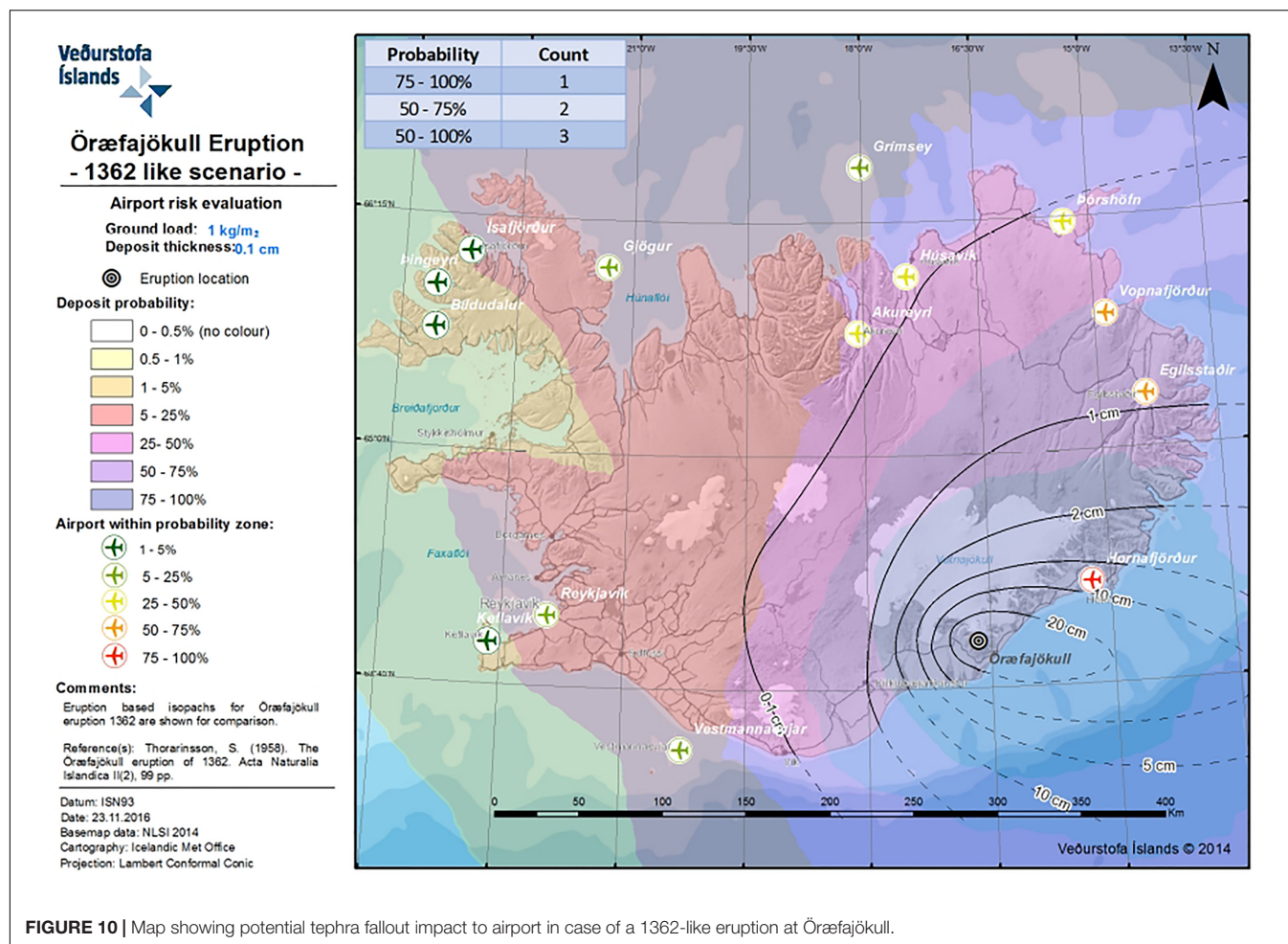


Table 3 summarizes the results as reported in the mentioned paper for fine tephra. For a deposit larger than 5 mm in wet conditions there is a high likelihood of insulator flashover. Damages to tower, poles and lines are highly likely for thicknesses larger than 100 mm in dry conditions and 5 mm in wet conditions. In the following analysis we have been considering the likelihood to get deposit larger than 10 and 100 mm in dry conditions. The assumption is that these limits can be considered as of danger in wet condition for a fully wet deposit (i.e., all the voids in the deposit are full of water).

RESULTS

Probabilistic Hazard Maps

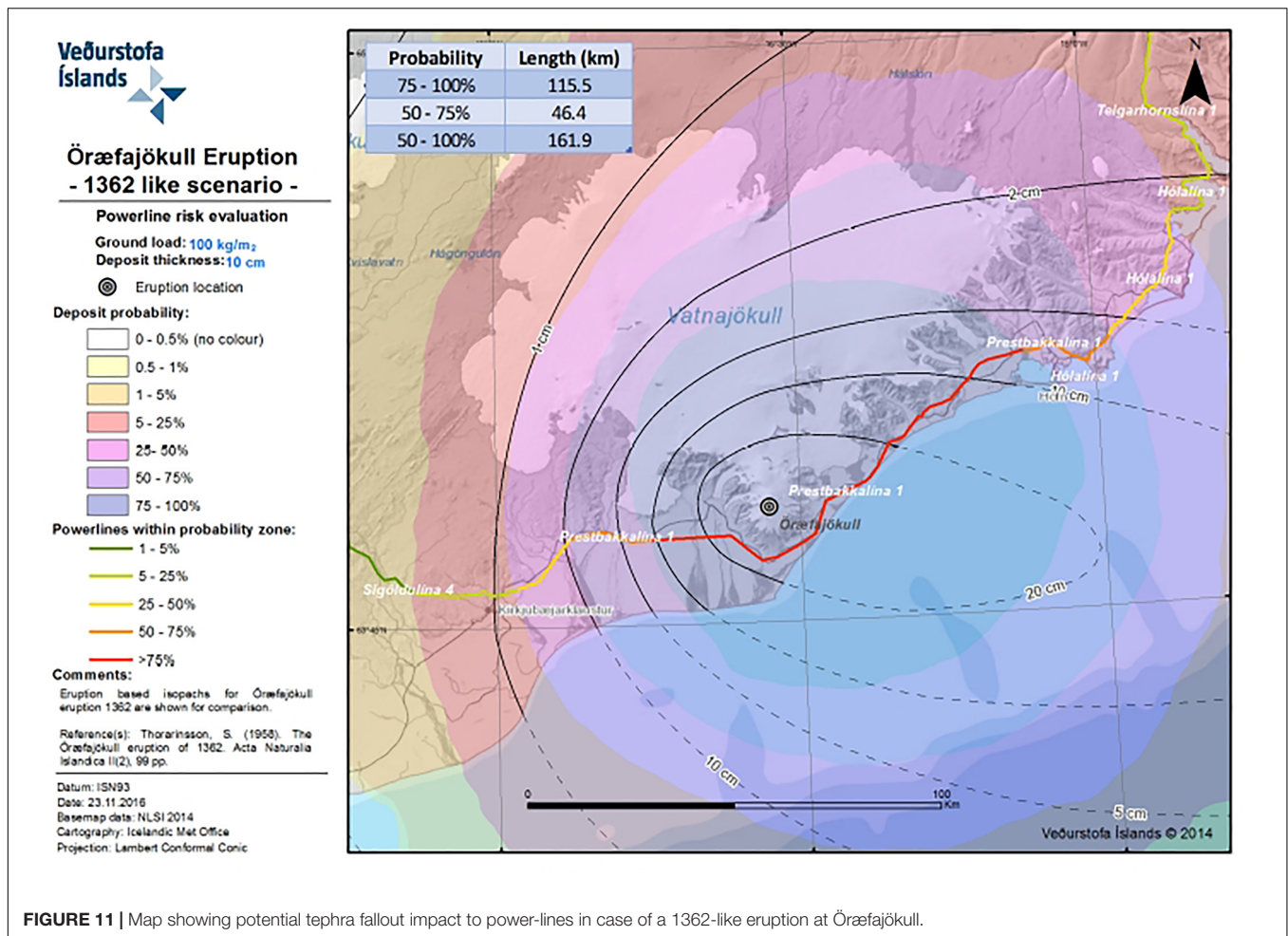
We performed numerical simulations of volcanic tephra dispersal by using VOL-CALPUFF code. The simulations yielded tephra thicknesses and concentrations data points over Iceland. We then generated probabilistic hazard maps for tephra loading at given thresholds by adopting a Monte Carlo approach. Here, we present three probabilistic hazard maps (Figures 6–8) for tephra loading thresholds of 1.0 kg/m² (equivalent to about 0.1 cm

under the assumption of a deposit of 1000 kg/m³), 100 kg/m² (equivalent to about 10 cm) and 1000 kg/m² (equivalent to about 1 m).

Comparison of these three maps reveals that the higher deposit load threshold investigated, the smaller is the area likely interested by this load. This is because in each simulation the thick deposit impacts a proximal area around the volcano, whereas thinner deposit can spread over a larger domain. In addition, in all maps there is a general eastward trend that reflects the meteorological statistics, as shown in Figure 5. At high altitudes the stronger westerly wind dominates the distribution of tephra toward the East.

In Figure 6 the isoline of 0.1 cm thickness produced by Thorarinnsson (1958) falls entirely within the 25–50% probability of reaching this deposit thickness. All the country, apart from the northern part of the Westfjords, has at least a 5% probability of exceeding a ground load threshold of 1 kg/m².

In Figure 7 the isoline of 10 cm produced by Thorarinnsson (1958) falls entirely within the 75–100% probability of reaching this deposit thickness. About half of the country has at least a probability of 1% of exceeding a ground load of 100 kg/m². This area includes eastern and South-Eastern



Iceland, most of the highlands and parts of the North-East.

In **Figure 8** the likelihood of exceeding a threshold of 1000 kg/m² is confined to a small area closest to the volcano edifice. Part of the proximal area enclosed within the 20 cm isoline falls within the 5–25% probability of reaching a deposit thickness of 1 m.

The potential impact of tephra fallout can also be investigated at specific locations by performing an analysis site by site. For example **Table 4** shows the likelihood of exceeding specific tephra ground loads at five key population centers in Iceland (**Figure 1**). All of these population centers have a likelihood higher than 5% of experiencing tephra fallout deposit exceeding a thickness of 1 mm. Höfn (97.8%) and Egilsstaðir (61.4%) are the most vulnerable centers as they are closest to the volcano. Höfn can experience very high loads (10 and 100 kg/m²) and the likelihood is about 95 and 73%, respectively.

Reykjavík is the less exposed town due to its distance from the volcano and mainly because it is located upwind the dominant wind direction. Akureyri (in the North), despite its long distance, is showing intermediate values.

Impact Maps

An analysis to investigate how these results translate into an impact assessment has been done by quantifying the level of disruption due to tephra fallout on roads, airports, and powerline network. The type of disruption has been defined with regards to: (1) kilometers of roads potentially exposed to critical driving conditions, (2) number of airports potentially affected by tephra fallout on the runways, and (3) kilometers of powerline potentially affected by tephra fallout that can cause either flashover and physical damage to the lines. For each of this infrastructure a map has been created and the results are shown in **Figures 9–11**.

When looking at the possible disruption to road traffic (**Figure 9**) we can see that up to 268 km of the main road system (either paved and unpaved according to the National Land Survey IS50V database v3.4, 2012) could be affected by tephra fallout thicker than 3 mm with a likelihood between 75 and 100% (red road sector). There is a 25% likelihood that more than 2000 km of the road network can be affected by this condition (the yellow, orange, and red road sector). The main road extending from Vík, in the

South, to Húsavík, in the North, passing through the East part of the country will be impassable (see **Figure 1** for site locations).

The analysis performed for the airports network includes all the main airports in the country for which flights are regularly scheduled (as reported from the National Land Survey IS50V database v3.4, 2012). The analysis reveals that the airport in Hornafjörður will be affected by a deposit thicker than 1 mm with a probability between 75 and 100%. The likelihood for two more airports (Egilsstaðir and Vopnafjörður) to receive this amount of tephra is between 50 and 75%. These three airports are located in the Eastern sector of the country. The international airport of Akureyri shows a likelihood between 25 and 50%, whereas the domestic airport in Reykjavík is calculated to have a likelihood between 5 and 25%. The International airport of Keflavík has potential to be affected by tephra fallout from Öraefajökull volcano with a likelihood between 1 and 5%. All the main airports of Iceland (14 in total) have >0% likelihood to be affected by tephra fallout capable to create disruption to the operations of landing and taking off.

Figure 11 shows a zoomed domain around Öraefajökull, as the main impact on the power line network is assessed to be quite proximal to the volcano. Only the network owned by the principal Icelandic provider Landsnet, which operates >33 kV powerage line, has been considered here. For this investigation a threshold of 100 mm of ash has been adopted, as given in **Tables 3, 4**. We assume this condition, corresponding to a load of about 100 kg/m², to correspond to critical conditions for powerlines. The results show that up to 115 km of powerline network will be exposed to such a load with likelihood of 75 to 100%. This is the part of the powerline passing nearby the volcano at a minimum distance of about 9.5 km (red line sector). Additional 45 km will be exposed to such load with a likelihood between 50 and 75%. So that overall more than 160 km of the powerline network can be damaged by an eruption at Öraefajökull and the likelihood for such an occurrence is greater than 50%. Almost the entire powerline network feeding the Öraefi district is vulnerable to these effects.

DISCUSSION AND CONCLUSION

An eruption at Öraefajökull is likely to have a significant impact in Iceland, its nearby Nordic countries and, Europe. As evidence shows, such an eruption can produce pyroclastic density currents that will inundate the communities at the base of the volcano, glacial outbursts can also cover a substantial area (possibly >300 km²) around the volcano. On top of that a heavy tephra fallout is expected to occur over a period of about 1 day (e.g., Thorarinsson, 1958; Jónsson and Valdimar, 2007; Thordarson and Höskuldsson, 2007; Gudmundsson et al., 2008).

The volcanological scenario selected for this study represents the worst case scenario known to have happened at Öraefajökull,

the 1362 AD eruption. The model results and the probabilistic hazard maps clearly indicate how, in case of a similar event, the associated tephra fallout might have effects all over the country. However, the location of the volcano, in the southernmost tip of the island, together with the prevailing westerly wind at high altitude favor the tephra fallout and ash dispersal to occur mainly toward the East. This will possibly represent a serious issue for the air traffic over the European air space, as occurred in 2010 when Eyjafjallajökull volcano erupted (Reichardt et al., 2018).

This study highlights two main issues: firstly, there are no places in the country completely safe from receiving ash generated from an eruption like 1362 at Öraefajökull (**Figure 6**); second, the tephra fallout can have a very severe impact in the proximity of the volcano with up to 1000 kg/m² of ash expected up to a distance of only 25 km the vent (**Figure 9**). Most of the main towns in Iceland have likelihood higher than 1% to receive an amount of ash larger than 10 kg/m² (**Table 4**).

The impact analysis performed for three different types of infrastructures (roads, airports, and power lines) reveals the vulnerability of the country in case of such an eruption. **Figure 9**, which shows the kilometers of road network potentially affected by critical driving conditions, suggests that the entire Eastern part of the country will be hardly reached by car either through the Southern and the Northern ring road section. The main town of Egilsstaðir and the very popular localities of Höfn, Skaftafell and Jökulsarlón will be cut off the main viable connections, with important implications for either inhabitants and tourists potentially trapped in the area due to very low visibility conditions and unsafe driving conditions of paved roads.

The results show also that the likelihood for the airports in Hornafjörður (next to Höfn) and Egilsstaðir to be disrupted by the tephra fallout is >50% (**Figure 10**). Consequently, connection with the Eastern part of the country via air or road will be very difficult and dangerous during and shortly after the eruption. An eruption like 1362 will affect the communication and commuting toward the East part of the country and the Greater Reykjavík area (i.e., the capital and its surroundings).

Failure of the electricity provision can be expected due to damages to powerlines during and shortly after the eruption (**Figure 11**). These data need to be seriously evaluated when planning for mitigation actions and evacuation plans. The impact of a similar scenario would be even more dramatic if an eruption will take place during the winter time, when the daylight time is very short and the need for electricity to illuminate is higher and essential for the daily activities of the society and its economy.

The results shown so far are just the beginning of a long study that is needed to fully address the volcanic hazard at Öraefajökull volcano, but still enough to identify the potential critical scenario that could raise if it will erupt again with a similar intensity as in 1362. The unrest phase declared in November 2017 has been putting emphasis on the need of a proper multi-hazard assessment for Öraefajökull and this study is a contribution to it.

AUTHOR CONTRIBUTIONS

SB worked on the definition of the volcanological scenarios, performed the simulations, processed the data and wrote the interpretation, and discussion of the results. DDR worked on the volcanological scenarios and performed part of the simulations, processed the data and contributed to the discussion of the results. DDR, BBB contributed to the interpretation of the results, used GIS to recalculate the masses, and prepared all the graphical maps. TT worked on the definition of the volcanological scenarios and contributed to the discussion of the results. SK contributed to the discussion and interpretation of the results.

REFERENCES

- Ágústssdóttir, A. M. (2015). Ecosystem approach for natural hazard mitigation of volcanic tephra in Iceland: building resilience and sustainability. *Nat. Hazards* 78, 1669–1691. doi: 10.1007/s11069-015-1795-6
- Baerbel, L., Arnau, F., Martin, H., and Volker, M. (2012). Volcanic ash over Europe during the eruption of Eyjafjallajökull on Iceland, April–May 2010. *Atmos. Environ.* 48, 1–8. doi: 10.1016/j.atmosenv.2011.03.054
- Barsotti, S., Andronico, D., Neri, A., Del Carlo, P., Baxter, P. J., Aspinall, T., et al. (2010). Quantitative assessment of volcanic ash hazards for health and infrastructure at Mt. Etna (Italy) by numerical simulation. *J. Volcanol. Geother. Res.* 192, 85–96. doi: 10.1016/j.jvolgeores.2010.02.011
- Barsotti, S., Bignami, C., Buongiorno, M. F., Corradini, S., Doumaz, F., Guerrieri, L., et al. (2011). SAFER response to eyjafjallajökull and merapi volcanic eruptions. In *Let's embrace space'Space Research Achievements Under the 7th Framework Programme*, ed. European Commission, DG Enterprise and Industry, (Belgium: European Commission, DG Enterprise and Industry)
- Barsotti, S., and Neri, A. (2008). The vol-calpuff model for atmospheric ash dispersal: 2. application to the weak mount etna plume of july 2001. *J. Geophys. Res.* 113:B03209. doi: 10.1029/2006JB004624
- Barsotti, S., Neri, A., and Scire, J. S. (2008). The vol-calpuff model for atmospheric ash dispersal: 1. Approach and physical formulation. *J. Geophys. Res.* 113:B03208. doi: 10.1029/2006JB004623
- Baxter, P. (1990). Medical effects of volcanic eruptions. *Bull. Volcanol.* (1990) 52, 532. doi: 10.1007/BF00301534
- Bebbington, M., Cronin, S. J., Chapman, I., and Turnera, M. B. (2008). Quantifying volcanic ash fall hazard to electricity infrastructure. *J. Volcanol. Geother. Res.* 177:4. doi: 10.1016/j.jvolgeores.2008.07.023
- Behnke, S. A., Thomas, R. J., Edens, H. E., Krehbiel, P. R., and Rison, W. (2014). The 2010 eruption of Eyjafjallajökull: lightning and plume charge structure. *J. Geophys. Res. Atmos.* 119, 833–859. doi: 10.1002/2013JD020781
- Bennett, A. J., Odams, P., Edwards, D., and Arason, P. (2010). Monitoring of lightning from the April–May 2010 Eyjafjallajökull volcanic eruption using a very low frequency lightning location network. *Environ. Res. Lett.* 5:044013. doi: 10.1088/1748-9326/5/4/044013
- Biass, S., Scaini, C., Bonadonna, C., Folch, A., Smith, K., and Höskuldsson, A. (2014). A multi-scale risk assessment for tephra fallout and airborne concentration from multiple Icelandic volcanoes – Part 1: hazard assessment. *Nat. Hazards Earth Syst. Sci.* 14, 2265–2287. doi: 10.5194/nhess-14-2265-2014
- Blake, D. M., Wilson, T. M., Cole, J. W., Deligne, N. I., and Lindsay, J. M. (2017). Impact of volcanic ash on road and airfield surface skid resistance. *Sustainability* 9:1389. doi: 10.3390/su9081389
- Blong, R. J. (1996). “Volcanic hazards risk assessment,” in *Monitoring and Mitigation of Volcano Hazards*, eds R. Scarpa and R. I. Tilling (Berlin: Springer).
- Bolić, T., and Sivčev, Ž. (2011). Eruption of Eyjafjallajökull in Iceland: experience of European air traffic management. *Transp. Res. Rec.* 2214, 136–143. doi: 10.3141/2214-17
- Bonadonna, C., Connor, C. B., Houghton, B. F., Connor, L., Byrne, M., Laing, A., et al. (2005). Probabilistic modeling of tephra dispersal: hazard assessment of

FUNDING

This study has been benefiting from the GOSVÁ project (2012–2018) funded by the Icelandic Government together with the International Civil Aviation Organization (ICAO).

ACKNOWLEDGMENTS

A great thank goes to the Steering Committee of the project for fruitful and constructive discussion. Marco Viccaro, the reviewer and the Chief Editor Valerio Acocella are kindly thanked for their help in improving the paper.

- a multiphase rhyolitic eruption at Tarawera, New Zealand. *J. Geophys. Res.* 110:B03203. doi: 10.1029/2003JB002896
- Bonadonna, C., FolchSusan, A., and Puempel, L. (2011). Future developments in modelling and monitoring of volcanic ash clouds: outcomes from the first IAVCEI-WMO workshop on Ash Dispersal Forecast and Civil Aviation. *Bull. Volcanol.* 74, 1–10. doi: 10.1007/s00445-011-0508-6
- Bonasia, R., Scaini, C., Capra, L., et al. (2014). Long-range hazard assessment of volcanic ash dispersal for a Plinian eruptive scenario at Popocatepetl volcano (Mexico): implications for civil aviation safety. *Bull. Volcanol.* 76:789. doi: 10.1007/s00445-013-0789-z
- Bursik, M. (2001). Effect of wind on the rise height of volcanic plumes. *Geophys. Res. Lett.* 28, 3621–3624. doi: 10.1029/2001GL013393
- Calder, E., Wagner, K., and Ogburn, S. E. (2015). *Volcanic Hazard Maps in Global Volcanic Hazards and Risk*. Cambridge: Cambridge University Press, 335–342. doi: 10.1017/CBO9781316276273.022
- Carlsen, H. K., Hauksdóttir, A., Valdimarsdóttir, U. A., Gíslason, T., Einarsdóttir, G., Runolfsson, H., et al. (2012). Health effects following the Eyjafjallajökull volcanic eruption: a cohort study. *BMJ Open* 2:e001851. doi: 10.1136/bmjopen-2012-001851
- Casadevall, T. J. (1994). The 1989–1990 eruption of redoubt volcano, alaska: impacts on aircraft operations. *J. Volcanol. Geother. Res.* 62, 301–316. doi: 10.1016/0377-0273(94)90038-8
- Cioni, R., Longo, A., Macedonio, G., Santacroce, R., Sbrana, A., Sulpizio, R., et al. (2003). Assessing pyroclastic fall hazard through field data and numerical simulations: example from Vesuvius. *J. Geophys. Res.* 108:2063. doi: 10.1029/2001JB000642
- Costa, A., Dell'Erba, F., Di Vito, M. A., Isaia, R., Macedonio, G., Orsi, G., et al. (2009). Tephra fallout hazard assessment at the Campi Flegrei caldera (Italy). *Bull. Volcanol.* 71:259. doi: 10.1007/s00445-008-0220-3
- Cronin, S. J., Neall, V. E., Lecointre, J. A., Hedley, M. J., and Loganathan, P. (2003). Environmental hazards of fluoride in volcanic ash: a case study from Ruapehu volcano, New Zealand. *J. Volcanol. Geother. Res.* 121, 271–291. doi: 10.1016/S0377-0273(02)00465-1
- Dee, D. P., Uppala, S. M., Simmons, A. J., Berrisford, P., Poli, P., Kobayashi, S., et al. (2011). The ERA-Interim reanalysis: configuration and performance of the data assimilation system. *Q. J. R. Meteorol. Soc.* 137, 553–597. doi: 10.1002/qj.828
- Del Negro, C., Fortuna, L., and Vicari, A. (2005). Modelling lava flows by Cellular Nonlinear Networks (CNN): preliminary results. *Nonlinear Process. Geophys.* 12, 505–513. doi: 10.5194/npg-12-505-2005
- Dufek, J. (2016). The fluid mechanics of pyroclastic density currents. *Ann. Rev. Fluid Mech.* 48, 459–485. doi: 10.1146/annurev-fluid-122414-034252
- Esposti Ongaro, T., Clarke, A. B., Voight, B., Neri, A., and Widiwijayanti, C. (2012). Multiphase flow dynamics of pyroclastic density currents during the May 18, 1980 lateral blast of Mount St. Helens. *J. Geophys. Res. Solid Earth* 117:B06208. doi: 10.1029/2011JB009081
- Esposti Ongaro, T., Neri, A., Todesco, M., Macedonio, G. (2002). Pyroclastic flow hazard assessment at Vesuvius (Italy) by using numerical modeling. II. Analysis of flow variables. *Bull. Volcanol.* 64, 178–191. doi: 10.1007/s00445-001-0190-1
- Favalli, M., Chirico, G. D., and Papale, P. (2009). Lava flow hazard at Nyiragongo volcano, D.R.C. *Bull. Volcanol.* 71, 363–374. doi: 10.1007/s00445-008-0233-y

- Favalli, M., Pareschi, M. T., Neri, A., and Isola, I. (2005). Forecasting lava flow paths by a stochastic approach. *Geophys. Res. Lett.* 32:L03305. doi: 10.1029/2004GL021718
- Felpeito, A., Araña, V., Ortiz, R. et al. (2001). Assessment and Modelling of Lava Flow Hazard on Lanzarote (Canary Islands). *Nat. Hazards* 23, 247–257. doi: 10.1023/A:1011112330766
- Folch, A. (2012). A review of tephra transport and dispersal models: Evolution, current status, and future perspectives. *J. Volcanol. Geother. Res.* 235–236, 96–115. doi: 10.1016/j.jvolgeores.2012.05.020
- Frogner, K. P., Roger, B. H., and Sigurdur, R. G. (2006). A diverse ecosystem response to volcanic aerosols. *Chem. Geol.* 231, 57–66. doi: 10.1016/j.chemgeo.2005.12.008
- Gudmundsson, H. (1998). *Holocene Glacier fluctuations and Tephrochronology of the Öraefi district, Iceland*. PhD, School of Geosciences, the University of Edinburgh, Edinburgh.
- Gudmundsson, M. T., Guðrún, L., Ármann, H., and Ágúst, G. G. (2008). Volcanic hazards in Iceland. *JÖKULL* 58, 251–268.
- Gudmundsson, M. T., Thordarson, T., Höskuldsson, Á., Larsen, G., Björnsson, H., Prata, A. J., Oddsson B., Magnússon, E., et al. (2012). Ash generation and distribution from the April–May 2010 eruption of Eyjafjallajökull, Iceland. *Sci. Rep.* 2:572. doi: 10.1038/srep00572
- Gudnason, J., Thordarson, T., Houghton, B., and Larsen, G. (2017). The opening subplinian phase of the Hekla 1991 eruption: properties of the tephra fall deposit. *Bull. Volcanol.* 79:34. doi: 10.1007/s00445-017-1118-8
- Gudnason, J., Thordarson, T., Houghton, B. F., and Larsen, G. (2018). The 1845 Hekla eruption: grain-size characteristics of a tephra layer. *J. Volcanol. Geother. Res.* 350, 33–46. doi: 10.1016/j.jvolgeores.2017.11.025
- Guffanti, M., Mayberry, G. C., and Casadevall, T. J. (2009). Volcanic hazards to airports. *Nat. Hazards* 51, 287–302. doi: 10.1007/s11069-008-9254-2
- Haynes, K., Barclay, J., and Pidgeon, N. (2007). Volcanic hazard communication using maps: an evaluation of their effectiveness. *Bull. Volcanol.* 70:123. doi: 10.1007/s00445-007-0124-7
- Horwell, C. J., and Baxter, P. J. (2006). The respiratory health hazards of volcanic ash: a review for volcanic risk mitigation. *Bull. Volcanol.* 69, 1–24. doi: 10.1007/s00445-006-0052-y
- Hurst, T., and Smith, W. (2004). A monte carlo methodology for modelling ashfall hazards. *J. Volcanol. Geother. Res.* 138:15. doi: 10.1016/j.jvolgeores.2004.08.001
- IMO (2018a). *IMO and The Icelandic Civil Protection Agency Reassess the Status for Öraefajökull*. Available at: <http://en.vedur.is/about-imo/news/the-imo-and-the-icelandic-civil-protection-agency-reassess-the-status-for-oraefajokull>
- IMO (2018b). *Status of Öraefajökull Volcano*. Available at: <http://en.vedur.is/about-imo/news/status-of-oraefajokull-volcano>
- Janebo, M. H., Thordarson, T., Houghton, B. F., et al. (2016). Dispersal of key subplinian–Plinian tephra from Hekla volcano, Iceland: implications for eruption source parameters. *Bull. Volcanol.* 78:66. doi: 10.1007/s00445-016-1059-7
- Jenkins, S., Barsotti, S., Hincks, T. K., Neri, A., Phillips, J. C., Sparks, R. S. J., et al. (2015). Rapid emergency assessment of ash and gas hazard for future eruptions at Santorini Volcano, Greece. *J. Appl. Volcanol. Soc. Volcanoes* 2015:16. doi: 10.1186/s13617-015-0033-y
- Jenkins, S., Magill, C., McAneney, J., Blong, R. (2012). Regional ash fall hazard I: a probabilistic assessment methodology. *Bull. Volcanol.* 74:1699. doi: 10.1007/s00445-012-0627-8
- Jónsson, P., and Valdimar, K. (2007). *Eyðing Bæjar í Öraefasveit í Öraefajökulsgosinu 1362*. BS ritgerð við Jarðvísindadeild HÍ, Iceland.
- Jørgensen, K. A. (1987). Mineralogy and petrology of alkaline granophyric xenoliths from the Thorsmörk ignimbrite, southern Iceland. *Lithos* 20, 153–168. doi: 10.1016/0024-4937(87)90004-1
- Karlsdóttir S., Gylfason, Á. G., Höskuldsson, Á., Brandsdóttir, B., Ilyinskaya, E., Gudmundsson, M. T., et al. (2012). *The 2010 Eyjafjallajökull eruption, Iceland*. ICAO report, ISBN 978-9979-9975-4-2
- Kavanagh, J. L., Engwell, S. L., and Martin, S. A. (2018). A review of laboratory and numerical modelling in volcanology. *Solid Earth* 9, 531–571. doi: 10.5194/se-9-531-2018
- Larsen, G. (2002). “A brief overview of eruptions from ice-covered and ice-capped volcanic systems in Iceland during the past 11 centuries: frequency, periodicity and implications,” in *Volcano-Ice Interactions on Earth and Mars*, eds J. L. Smellie and M. G. Chapman (London: Geological Society, Special Publications 202), 81–90.
- Larsen, G., and Eiríksson, J. (2008a). Holocene tephra archives and tephrochronology in Iceland: a brief review. *Jökull* 58, 229–250.
- Larsen, G., Dugmore, A., and Newton, A. (1999). Geochemistry of historical-age silicic tephra in Iceland. *Holocene* 9, 463–471. doi: 10.1191/095968399669624108
- Larsen, G., and Eiríksson, J. (2008b). Late Quaternary terrestrial tephrochronology of Iceland—frequency of explosive eruptions, type and of tephra deposits. *J. Quat. Sci.* 23, 109–120. doi: 10.1002/jqs.1129
- Larsen, G., and Thorarinnsson, S. (1977). H4 and other acidic Hekla tephra layers. *Jökull* 27, 28–46.
- Larsen, G., Gudmundsson, M. T., Vogfjörð, K., Ilyinskaya, E., Oddsson, B., Pagneux, E. (2015). “The Öraefajökull volcanic system,” in *Catalogue of Icelandic Volcanoes*. IMO, UI, CPD-NCIP, eds Ilyinskaya, Larsen, and Gudmundsson (Reykjavik: University of Iceland).
- Loughlin, S., Barsotti, S., Bonadonna, C., Calder, E. (2017). “Geophysical risk: volcanic activity,” in *Science for Disaster Risk Management: Knowing Better and Losing Less*, eds K. Poljanšek, M. Marin Ferrer, T. De Groeve, I. Clark, 3.2. (Luxembourg: EUR 28034 EN, Publications Office of the European Union) doi: 10.2788/688605
- Macedonio, A., Costa, A., and Folch, A. (2008). Ash fallout scenarios at Vesuvius: Numerical simulations and implications for hazard assessment. *J. Volcanol. Geother. Res.* 178, 366–377. doi: 10.1016/j.jvolgeores.2008.08.014
- Macedonio, G., and Costa, A. (2012). Brief communication “rain effect on the load of tephra deposits”. *Nat. Hazards Earth Syst. Sci.* 12:1229. doi: 10.5194/nhess-12-1229-2012
- Martin, E., and Sigmarsson, O. (2007). Crustal thermal state and origin of silicic magma in Iceland: the case of Torfajökull, Ljósufjöll and Snæfellsjökull volcanoes. *Contrib. Min. Petrol.* 153:593. doi: 10.1007/s00410-006-0165-5
- Masterin, L. G., Guffanti, M., Servranckx, R., Webley, P., Barsotti, S., Dean, K., et al., (2009). A multidisciplinary effort to assign realistic source parameters to models of volcanic ash-cloud transport and dispersion during eruptions. *J. Volcanol. Geotherm. Res.* 186, 10–21. doi: 10.1016/j.jvolgeores.2009.01.008
- Nave, R., Isaia, R., Vilardo, G., and Barclay J. (2012). Re-assessing volcanic hazard maps for improving volcanic risk communication: application to Stromboli Island, Italy. *J. Maps* 6, 260–269. doi: 10.4113/jom.2010.1061
- NCIP (2017). *Emergency Evacuation Plan for Öraefajökull*. Available at: <https://www.almannavarnir.is/english/english-news/emergency-evacuation-for-oraefajokull/>
- Newhall, C. G., and Self, S. (1982). The volcanic explosivity index (VEI) an estimate of explosive magnitude for historical volcanism. *J. Geophys. Res.* 87, 1231–1238. doi: 10.1029/JC087iC02p01231
- Nurmawati, A., and Konstantinou, K. I. (2018). Hazard assessment of volcanic ballistic impacts at Mt Chihshin, Tatun Volcano Group, northern Taiwan. *Nat. Hazards* 92:77. doi: 10.1007/s11069-018-3192-4
- Óladóttir, B. A., Larsen, G., and Sigmarsson, O. (2011). Holocene volcanic activity at Grímsvötn, Bárðarbunga and Kverkfjöll subglacial centres beneath Vatnajökull, Iceland. *Bull. Volcanol.* 73, 1187–1208. doi: 10.1007/s00445-011-0461-4
- Pagneux, E., Gudmundsson, M. T., Karlsdóttir, S., and Roberts, M. J. (eds.). (2015). *Volcanogenic Floods in Iceland: An Assessment of Hazards and Risks at Öraefajökull and on the Markarfljót outwash Plain*. Reykjavik: IMO, IES-UI, NCIP-DCPEM.
- Palais, J. M., Taylor, K., Mayewski, P. A., and Grootes, P. (1991). *Volcanic Ash from the 1362 A.D. Öraefajökull Eruption (Iceland) in the Greenland Ice Sheet*. Earth Science Faculty Scholarship. Orono, ME: University of Maine.
- Petersen, G. N. (2010). A short meteorological overview of the Eyjafjallajökull eruption 14 April–23 May 2010. *Weather* 65, 203–207. doi: 10.1002/wea.634
- Pilcher, J., Bradley, R. S., Francus, P., and Andreson, L. (2005). A Holocene tephra record from the Lofoten Islands, Arctic Norway. *Boreas* 34, 136–156. doi: 10.1111/j.1502-3885.2005.tb01011.x
- Prata, A. J., and Tupper, A. (2009). Aviation hazards from volcanoes: the state of the science. *Natur. Hazards* 51:239. doi: 10.1007/s11069-009-9415-y
- Rarik (2010). *Yearly Report*. Available at: https://rafhladan.is/bitstream/handle/10802/13208/Arsskyrsla_RARIK_2010.pdf?sequence=9

- Reichardt, U., Ulfarsson, G. F., and Pétursdóttir, G. (2018). Volcanic ash and aviation: recommendations to improve preparedness for extreme events. *Transp. Res. Part A Policy Pract.* 113, 101–113. doi: 10.1016/j.tra.2018.03.024
- Sandri, L., Tierz, P., Costa, A., and Marzocchi, W. (2018). Probabilistic hazard from pyroclastic density currents in the Neapolitan area (Southern Italy). *J. Geophys. Res. Solid Earth* 123, 3474–3500. doi: 10.1002/2017JB014890
- Scaini, C., Folch, A., and Navarro, M. (2012). Tephra hazard assessment at Concepción Volcano, Nicaragua. *J. Volcanol. Geother. Res.* 219–220, 41–51. doi: 10.1016/j.jvolgeores.2012.01.007
- Scaini, C., Biass, S., Galderisi, A., Bonadonna, C., Folch, A., Smith, K., et al. (2014). A multi-scale risk assessment for tephra fallout and airborne concentration from multiple Icelandic volcanoes – Part 2: Vulnerability and impact. *Nat. Hazards Earth Syst. Sci.* 14, 2289–2312. doi: 10.5194/nhess-14-2289-2014
- Scollo, S., Coltelli, M., Bonadonna, C., and Del Carlo, P. (2013). Tephra hazard assessment at Mt. Etna (Italy). *Natur. Hazards Earth Syst. Sci.* 13, 3221–3233. doi: 10.5194/nhess-13-3221-2013
- Selbekk, R. S., and Tronnes, R. G. (2007). The 1362 AD Öraefajökull eruption, Iceland: petrology and geochemistry of large-homogeneous rhyolite. *J. Volcanol. Geother. Res.* 160, 42–58. doi: 10.1016/j.jvolgeores.2006.08.005
- Sharma, K., Self, S., Blake, S., Thordarson, T., and Larsen, G. (2008). The AD 1362 Öraefajökull eruption, S.E. Iceland: physical volcanology and volatile release. *J. Volcanol. Geother. Res.* 178, 719–739. doi: 10.1016/j.jvolgeores.2008.08.003
- Sigmarrsson, O., MacLennan, J., and Carpentier, M. (2008). Geochemistry of igneous rocks in Iceland: a review. *JÖKULL* 58, 139–160.
- Sigmarrsson, O., Condomines, M., and Fourcade, S. (1992). Mantle and crustal contribution in the genesis of Recent basalts from off-rift zones in Iceland: constraints from Th, Sr and O isotopes. *Earth Planet. Sci. Lett.* 110, 149–162. doi: 10.1016/0012-821X(92)90045-W
- Sparks, R. S. J., and Aspinall, W. (2013). “Volcanic activity: frontiers and challenges in forecasting, prediction and risk assessment, in *The State of the Planet: Frontiers and Challenges in Geophysics*, eds Sparks and Hawkesworth, (Hoboken: Blackwell)
- Spence, R. J. S., Kelman, I., Baxter, P. J., Zuccaro, G., and Petrazzuoli, S. (2005). Residential building and occupant vulnerability to tephra fall. *Natur. Hazards Earth Syst. Sci.* 5, 477–494. doi: 10.5194/nhess-5-477-2005
- Spinetti, C., Barsotti, S., Neri, A., Buongiorno, M. F., Doumaz, F., and Nannipieri, L. (2013). Investigation of the complex dynamics and structure of the 2010 Eyjafjallajökull volcanic ash cloud using multispectral images and numerical simulations. *J. Geophys. Res. Atmos.* 118, 4729–4747. doi: 10.1002/jgrd.50328
- Stevenson, J., Larsen, G., and Thordarson, T. (2015). Physical volcanology of the prehistoric Hekla 3 and Hekla 4 eruptions, Iceland. EGU General Assembly. *Geophys. Res. Abstr.* 17:EGU2015–EGU4207.
- Tarquini, S., and Favalli, M. (2013). Uncertainties in lava flow hazard maps derived from numerical simulations: the case study of Mount Etna. *J. Volcanol. Geother. Res.* 260, 90–102. doi: 10.1016/j.jvolgeores.2013.04.017
- Thompson, M. A., Lindsay, J. M., and Gaillard, J. (2015). The influence of probabilistic volcanic hazard map properties on hazard communication. *J. Appl. Volcanol.* 4:6. doi: 10.1186/s13617-015-0023-0
- Thorarinsson, S. (1958). The Öraefajökull eruption of 1362. *Acta Natur. Island* 2, 6–99.
- Thorarinsson, S. (1979). “On the damage caused by volcanic eruptions with special reference to tephra and gases,” in *Volcanic Activity and Human Geology*, eds P. D. Sheets, and D. K. Grayson (New York, NY: Academic press), 125–159.
- Thordarson, T. (2013). “Hraun,” in *Nattúruvá á Íslandi: Eldgos og Jarðskjálftar: Viðlagatrygging Íslands/Háskólaútgáfan*, eds J. Sólves, F. Sigmundsson and B. Bessason (Reykjavik: Háskólaútgáfan), 105–129.
- Thordarson, T., and Höskuldsson, Á. (2007). *The Eruption of Öraefajökull 1362 and the Destruction of the District Herad, SE Iceland*. Shimabara: Cities on Volcanoes 5.
- Thordarson, T., and Höskuldsson, Á. (2008). Postglacial volcanism in Iceland, *Jökull* 58, 197–228.
- Thordarson, T., and Larsen, G. (2007). Volcanism in Iceland in historical time: volcano types, eruption styles and eruptive history. *J. Geodynam.* 43, 118–152. doi: 10.1016/j.jog.2006.09.005
- Thorvaldsdóttir, S., and Sigbjörnsson, R. (2015). Framing the 2010 Eyjafjallajökull volcanic eruption from a farming-disaster perspective. *Nat. Hazards* 77:1619. doi: 10.1007/s11069-015-1667-0
- Tomlinson, E. L., Thordarson, T., Müller, W., Thirlwall, M., and Menzies, M. A. (2010). Microanalysis of tephra by LA-ICP-MS — Strategies, advantages and limitations assessed using the Thorsmörk ignimbrite (Southern Iceland), *Chem. Geol.* 279, 73–89. doi: 10.1016/j.chemgeo.2010.09.013
- Walker, G. P. L. (1962). Tertiary welded tuffs in Eastern Iceland. *Quart. J. Geol. Soc.* 118, 275–290. doi: 10.1144/gsjgs.118.1.0275
- Wardman, J. B., Wilson, T., Bodger, P. S., Cole, J. W., and Johnston, D. M. (2012). Investigating the electrical conductivity of volcanic ash and its effect on HV power systems. *Phys. Chem. Earth* 45–46, 128–145. doi: 10.1016/j.pce.2011.09.003
- Williams, R. S. (1983). *Man Against Volcano: The Eruption on Heimaey*. Vestmannaeyjar: United States Department Of The Interior Geological Survey Usgs: INF-75-22. doi: 10.3133/70039211
- Wilson, T. M., Stewart, C., Sword-Daniels, V., Leonard, G. S., Johnston, D. M., Cole, J. W., Wardman, J., et al. (2012). Volcanic ash impacts on critical infrastructure. *Phys. Chem. Earth* 45–46, 5–23. doi: 10.1016/j.pce.2011.06.006

Conflict of Interest Statement: The authors declare that the research was conducted in the absence of any commercial or financial relationships that could be construed as a potential conflict of interest.

Copyright © 2018 Barsotti, Di Rienzo, Thordarson, Björnsson and Karlsdóttir. This is an open-access article distributed under the terms of the Creative Commons Attribution License (CC BY). The use, distribution or reproduction in other forums is permitted, provided the original author(s) and the copyright owner(s) are credited and that the original publication in this journal is cited, in accordance with accepted academic practice. No use, distribution or reproduction is permitted which does not comply with these terms.



Paroxysmal Explosions, Lava Fountains and Ash Plumes at Etna Volcano: Eruptive Processes and Hazard Implications

Sonia Calvari^{1*}, Flavio Cannavò¹, Alessandro Bonaccorso¹, Letizia Spampinato¹ and Alessandra G. Pellegrino^{1,2}

¹ Istituto Nazionale di Geofisica e Vulcanologia - Osservatorio Etneo (INGV-OE), Sezione di Catania, Catania, Italy,

² Dipartimento di Scienze Biologiche Geologiche e Ambientali, Università degli Studi di Catania, Catania, Italy

OPEN ACCESS

Edited by:

Roberto Sulpizio,
Università degli Studi di Bari Aldo
Moro, Italy

Reviewed by:

Geoff Kilgour,
GNS Science, New Zealand
Susanna Jenkins,
Earth Observatory of Singapore,
Singapore

*Correspondence:

Sonia Calvari
sonia.calvari@ingv.it

Specialty section:

This article was submitted to
Volcanology,
a section of the journal
Frontiers in Earth Science

Received: 06 April 2018

Accepted: 13 July 2018

Published: 15 August 2018

Citation:

Calvari S, Cannavò F, Bonaccorso A,
Spampinato L and Pellegrino AG
(2018) Paroxysmal Explosions, Lava
Fountains and Ash Plumes at Etna
Volcano: Eruptive Processes and
Hazard Implications.
Front. Earth Sci. 6:107.
doi: 10.3389/feart.2018.00107

Lava fountains have a major impact on the local population since they cause ash plumes that spread several kilometers above and hundreds of kilometers away from the crater. Ash fallout is responsible for disrupting airports and traffic on the motorways well beyond the area of the volcano itself, as well as affecting the stability of buildings and causing public health issues. It is thus a primary scientific target to forecast the impact of this activity on local communities on the basis of parameters recorded by the monitoring network. Between 2011 and 2015, 49 paroxysmal explosive episodes occurred at two of Mt Etna's five summit craters: the New South-East Crater (NSEC) and the Voragine (VOR). In this paper, we examine the features of the 40 episodes occurring at the NSEC during 2011–2013, and of the 4 events at VOR in December 2015. We study these paroxysms using geophysical monitoring data, characterize the episodes, and analyse all available data statistically. Our main results are two empirical relationships allowing us to forecast the maximum elevation of the ash plume from the average height of the lava fountain, useful for hazard assessment and risk mitigation. For Etna, and using the examples described in this paper, we can infer that wind speed $<10 \text{ m s}^{-1}$ generally results in strong to intermediate plumes rising vertically above the crater, whereas wind speed $>10 \text{ m s}^{-1}$ is normally associated with weak plumes, bent-over along the wind direction and reaching lower elevations.

Keywords: Etna volcano, paroxysmal explosive activity, lava fountains, ash plume, thermal cameras

INTRODUCTION

Lava fountains are a mixture of liquid clots and droplets (the pyroclasts) and magmatic gases (H_2O , CO_2 , SO_2 , CH_4 , N_2O , HCl , HF , and CO , in order of decreasing abundance; Allard et al., 2005). They are generated when large volumes of volatiles rapidly exsolve from the magma during its ascent and decompression along the conduit (Wilson et al., 1995). The mixture of gas and pyroclasts emerges from the vent as a jet (Wilson et al., 1995), expanding vertically into an eruptive column, where three main regions can be identified. The lowest portion is the gas-thrust region, and comprises the lava fountains (Sparks et al., 1997; Bonaccorso and Calvari, 2017). Measured ascent velocities

in this region are normally greater than 15 m s^{-1} (Patrick, 2007; Patrick et al., 2007; Sahetapy-Engel and Harris, 2009), and for Etna vary between 33 and 125 m s^{-1} (Calvari et al., 2011; Carbone et al., 2015; Giuffrida et al., 2018), but values of 170, 227, and 405 m s^{-1} have been measured at Montserrat, Sakurajima, and Stromboli volcanoes, respectively (Clarke et al., 2002; Taddeucci et al., 2012; Tournigand et al., 2017). Above the gas-thrust is the convective region, where atmospheric mixing occurs (Sparks et al., 1997; Bombrun et al., 2018), causing a decrease in ascent velocity and lateral wind transport (Carey and Sparks, 1986). The uppermost portion is the umbrella region, where the volcanic plume reaches the zone of neutral buoyancy and spreads out laterally (Carey and Sparks, 1986; Bonadonna and Phillips, 2003). Within the buoyant umbrella region, plume rise rates are less than 15 m s^{-1} (Patrick, 2007; Patrick et al., 2007). Volcanic plume dynamics depend closely on the interaction with the atmospheric wind field. They are classified as strong or weak depending on whether the characteristic plume rise velocity is greater or much smaller than the cross wind speed, respectively (Carey and Sparks, 1986). Thus, strong plumes vertically rise (**Figure 1A**), while weak plumes tend to bend over in the downwind direction (**Figure 1C**) which then start spreading sub-horizontally around the neutral buoyancy level (Carey and Sparks, 1986; Bonadonna and Phillips, 2003). The plume shape has significant effects on the forecast of the fallout area, which is ideally distributed all around the vent in the case of a strong plume and zero wind, and elongated downwind for a weak plume and strong wind. The stronger the wind, the narrower the resulting fallout region from the plume (Andronico et al., 2009). Interestingly enough, the wind speed has important effects not just on the fine-grained portion of the plume, but even on the bombs and ballistics, being able to transport large ejecta for several kilometers down wind, causing damage to cars, solar panels, and windows (Andronico et al., 2015). It is difficult to univocally forecast plume height because it is related to the conditions and properties of the erupting system, such as magma discharge rate (Carey and Sparks, 1986), exsolved volatiles from magma, magma/water interaction (Schmith et al., 2018), and vent geometry (either elongated fissure or near-circular conduit; Wilson and Head, 1981; Wilson et al., 1995). Given that discharge rate and ultimately erupted volume have been measured from the lava fountain height (Calvari et al., 2011; Carbone et al., 2015; Bonaccorso and Calvari, 2017), there must be a direct connection between lava fountain height and maximum plume elevation, although this last parameter is also affected by wind speed (e.g., Bonadonna et al., 2015).

Paroxysmal explosive basaltic activity, especially when occurring at frequently erupting volcanoes, can have a strong impact on the population, air traffic and public health (Andronico et al., 2008, 2009; Martin et al., 2009; Baxter, 2010; Horwell et al., 2017). During 2011–2015, Mt. Etna volcano produced 49 paroxysmal lava fountain episodes, evolving into volcanic plumes that spread for more than 9 km above sea level (a.s.l.) into the atmosphere, and with ash fallout as far as hundreds of km from the vent (e.g., Dellino and Kyriakopoulos, 2003; Azzopardi et al., 2013; Athanassiadou, 2016). It is thus of paramount importance to monitor this activity and analyse the

data with the aim of developing routines or tools that might be useful for hazard assessment and impact prediction (Cannavò et al., 2017).

This paper seeks to analyse the data recorded during Etna's recent lava fountaining episodes in order to find possible relationships between measurable parameters. We have used images from the network of fixed thermal and visual cameras installed on the volcano slopes by the Istituto Nazionale di Geofisica e Vulcanologia-Osservatorio Etneo (INGV-OE), and gathered from these several parameters such as lava fountain height, exit velocity, duration of the episode, erupted volume and plume height. Among these, estimates of tephra fall volume are of paramount importance for hazard assessment and risk mitigation during future explosive events, since they are typically based on eruption intensity (eruption rate) and magnitude (total erupted mass; Walker, 1980).

We present an analysis of 44 of the 49 paroxysmal episodes occurring at Etna between 2011 and 2015; the remaining 5 could not be analyzed due to poor visibility from the ground cameras. We have used thermal and visual images recorded by the monitoring network of fixed cameras installed by INGV-OE (Andò and Pecora, 2006; Coltelli et al., 2017) to gather information about the total erupted mass and eruption rate of each episode. We have statistically analyzed the dimensional parameters extracted from the monitoring cameras, such as height of the lava fountain and ash plume vs. time, duration of each episode, erupted volume of pyroclastics (obtained from the camera images) and of lava flows (taken from available published data), time-averaged discharge rate (TADR, here referred only to the pyroclastic portion of the erupted material; Harris et al., 2007) and maximum exit velocities of both the lava fountain and plume. Following Harris et al. (2007), instantaneous effusion rate (IER) is the discharge rate from a vent averaged over a smaller unit of time when compared to TADR, which we consider as averaged over the whole duration of the explosive event. We carried out a rigorous correlation analysis on the measured parameters and tried to find a link among parameters.

ETNA'S ERUPTIVE ACTIVITY

Before 2010, lava fountain episodes at Mt. Etna (**Figures 1, 2**) were an exceptional activity, normally preceding major flank eruptions, such as those in 1991–93, 2000–01, and 2002–03 (Calvari et al., 1994, 2001; Andronico et al., 2005; Andronico and Corsaro, 2011). However, between January 2011 and December 2013, a sequence of 44 such events occurred from a pit on the east flank of the South-East Crater (SEC), one of the four summit craters of Etna (**Figure 2b**). This activity built up a new summit cone (the New South-East Crater, NSEC, **Figure 2b**; Behncke et al., 2014; De Beni et al., 2015), but no major flank eruptions have followed this activity yet. Bonaccorso and Calvari (2013) explained this apparent paradox by the balance between intruded and extruded magma, which at Etna volcano has been found steady during the last 3–4 decades (Wadge and Guest, 1981; Harris et al., 2011, 2012). This steady

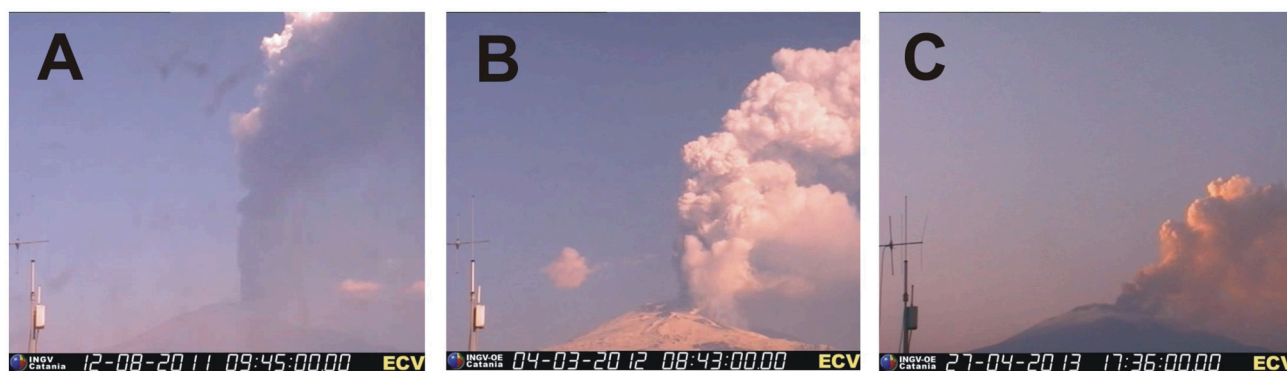


FIGURE 1 | Images taken from the ECV visual camera (see **Table 1** and **Figure 2** for details) showing: **(A)** a strong plume formed during the episode of 12 August 2011 at 09:45; **(B)** an intermediate plume formed during the episode of 4 March 2012 at 08:43; **(C)** a weak plume bending eastward during the episode of 27 April 2013 at 17:36.

output can result either in a few, high-output rate effusive phases, or in several, low-output rate lava fountain events (Bonaccorso and Calvari, 2013). Whatever the cause, it is clear that paroxysmal explosive activity at Etna is becoming increasingly common, thus requiring a greater effort to forecast its possible evolution.

Lava fountains are always associated with ash plumes, often disrupting the air traffic and driveability on the main highway along the east coast of Sicily, where frequent winds blow the ash and cause problems not only to traffic but also public health, agriculture, aviation, and building stability (Andronico et al., 2008; Martin et al., 2009; Baxter, 2010; Horwell et al., 2017). Eruptive columns and ash plumes, associated with the lava fountains, cause a more widespread fallout of ash transported well beyond the boundaries of Sicily and southern Italy and into Greece (Dellino and Kyriakopoulos, 2003) and Malta (Azzopardi et al., 2013).

Lava Fountaining From NSEC, 2011–2013

The 44 lava fountain (LF) episodes at the NSEC between 2011 and 2013 were preceded by deep magma uprising (Del Negro et al., 2013). We distinguished three main phases, separated by two long eruptive pauses (**Table 1**). The first phase lasted from 11 January 2011 to 24 April 2012, and comprised 25 LF events displaying similar features. These are: duration of the Strombolian phase preceding the paroxysmal episode (hours to days); duration of the LF event (hours); maximum height of the LF (800–1,500 m); extension of the lava flow field associated with the explosive event (1–4 km; Behncke et al., 2014); and erupted volume of pyroclastics and lava flows ($\sim 2.5 \times 10^6 \text{ m}^3$; Calvari et al., 2011; Gouhier et al., 2012; Bonaccorso and Calvari, 2013). The first eruptive pause lasted from April 2012 to February 2013 (**Table 1**). During this pause, only mild and intermittent eruptive activity within the Bocca Nuova summit crater (BN; **Figure 2b**) occurred between July and October 2012, producing a small cinder cone and lava flow field within its crater (Cannata et al., 2015; Slatcher et al., 2015; Spampinato et al., 2015). During the period preceding the second LF phase, ground deformation

data from the permanent GPS network revealed an inflation of the volcano due to the pressurization of its plumbing system (e.g., Bruno et al., 2016), whereas gas fluxes showed that no volatile-rich magma was supplied to the shallow (1–2 km below sea level, b.s.l.) volcano feeding system (Spampinato et al., 2015). This suggested that the BN eruptive activity was produced by magma already residing within the shallow plumbing system (Spampinato et al., 2015). A depressurization of the plumbing system was observed when LF activity resumed again in 19 February 2013 (**Table 1**), giving rise to the second eruptive phase that lasted until 27 April 2013, producing 13 additional events (Cannata et al., 2015; Spampinato et al., 2015; Bruno et al., 2016). There was another eruptive pause between April and the end of October 2013, followed by six additional paroxysmal explosive events until the end of that year. This last and third phase was very different from the previous, and comprised the most explosive end-member of the series, occurring on 23 November 2013 (Bonaccorso et al., 2014; Andronico et al., 2015; Carbone et al., 2015; Corradini et al., 2016; Montopoli, 2016). This very short but violent paroxysm produced an exceptionally high LF of over 2.5 km above the crater, and was the only one at the NSEC that did not produce lava flows (Bonaccorso et al., 2014). The third phase also displayed a unique episode (26 October 2013, **Table 1**) during which two craters were erupting together, with the North-East Crater (NEC) producing an ash column that flanked that of the NSEC (Andronico et al., 2018, this volume). As a result of the proximal accumulation of ballistics from the LF around the vent, a new cinder cone (the NSEC) grew on the east flank of the SEC, with a volume of $19 \times 10^6 \text{ m}^3$ (Behncke et al., 2014) by April 2012, and growing up to $50 \times 10^6 \text{ m}^3$ by October 2014 (De Beni et al., 2015). The shallow storage feeding these paroxysmal events, imaged from volcanic tremor and long-period seismic events, is very shallow and located within the volcanic pile between sea level and the ground surface (Cannata et al., 2015) and should represent just the final portion of the uprising path. We know very little about the episode occurring in 2014 (**Table 1**) because of poor weather conditions.

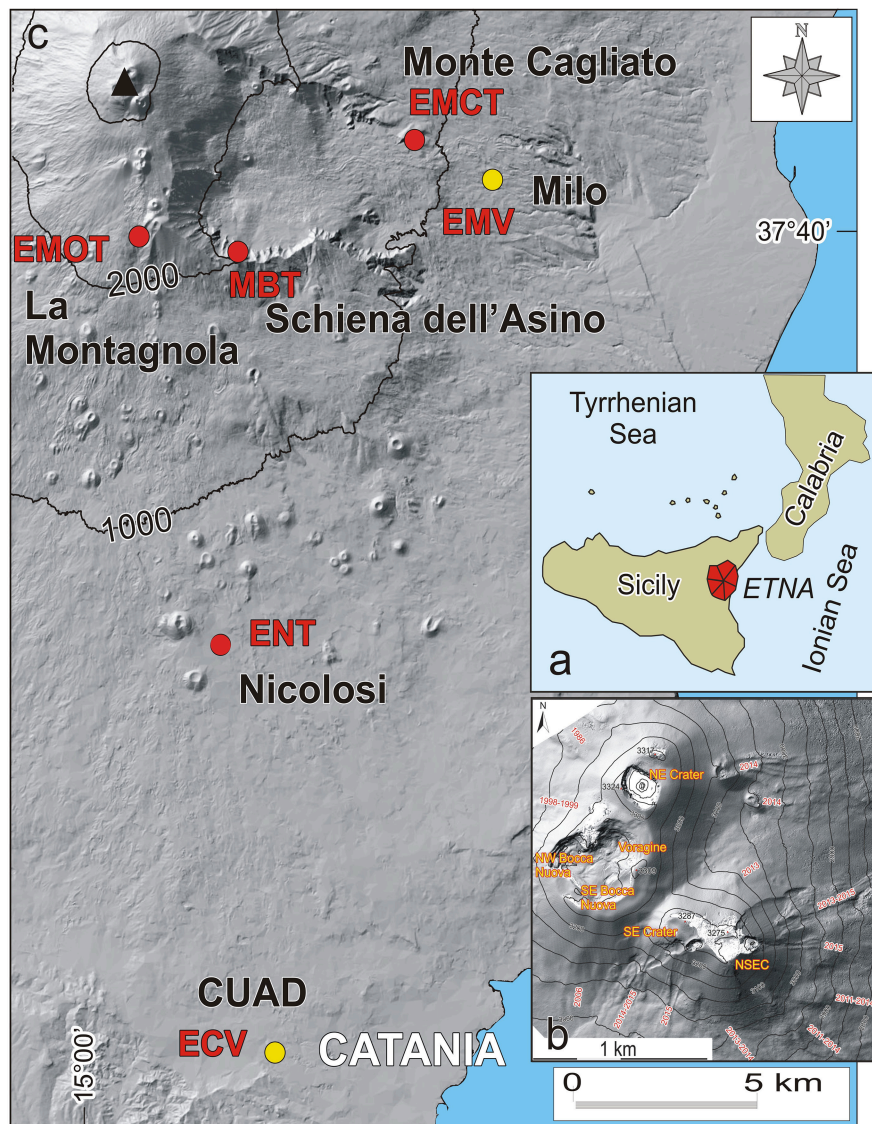


FIGURE 2 | (a) Map of southern Italy, showing the location of Mt. Etna (in red) in the eastern portion of Sicily. (b) Map of Etna's summit craters (modified after Neri et al., 2017), with the NE Crater, Voragine, the NW and SE pits of Bocca Nuova, the SE Crater, and the New SE Crater (NSEC) built up on its east flank since 2011. (c) Map of the SE flank of Etna volcano, modified after Calvari et al. (2011), showing the location of the thermal (red circles) and visual (yellow circles) monitoring cameras used in this paper. The black triangle shows the position of the summit craters, magnified in (b).

Lava Fountain From VOR, 3–5 December 2015

In January 2015, ash plume emissions started from the Voragine crater (VOR), after 16 years quiescence at this crater (Corsaro et al., 2017; Cannata et al., 2018). Explosive activity from this crater increased in intensity and became almost regular since 27 October, climaxing with a sequence of four paroxysmal events between 3 and 5 December (Vulpiani et al., 2016; Bonaccorso and Calvari, 2017; Neri et al., 2017). The four explosive events interrupted the usual trend of inflation observed at Mt. Etna (Aloisi et al., 2017). They were characterized by decreasing LF maximum heights (from 4.1 to 1.1 km), by lack of associated

lava flows, by durations varying between 65 and 114 min, and by a total erupted volume of at least $10 \times 10^6 \text{ m}^3$ dense rock equivalent (Bonaccorso and Calvari, 2017). The eruption columns and ash plume rose vertically with velocities between 150 and 200 m s^{-1} , and the transition from the convective to the umbrella region was observed at $\sim 8 \text{ km}$ height (Vulpiani et al., 2016). In about 10 min the ash plume expanded up to 10–15 km above sea level (a.s.l.; Vulpiani et al., 2016; Corsaro et al., 2017). Tephra fallout accumulated mostly within the summit crater, resulting in a fountain-fed rheomorphic lava of $\sim 7.2 \times 10^6 \text{ m}^3$ (Corsaro et al., 2017; Neri et al., 2017). The strain data constrained the depth of the magmatic source

TABLE 1 | Eruptive parameters obtained from the analysis of the visual and thermal fixed cameras on each of the paroxysmal episodes.

Event number	Date dd/mm/yy	Vent	Inter time (days)	Duration of Strombolian activity (s)	Start of Lava Fountain (hh:mm)	End of Lava Fountain (hh:mm)	Duration of Lava Fountain (s)	Volume of pyro (m ³)	Volume of pyro (%)	Interp. frames	Cameras	TADR (m ³ s ⁻¹)	Hav (m)	Hmax (m)	V _i max (m s ⁻¹)	Duration of lava flow (s)	Lava flow volume (m ³)	Plume type	Max. plume height (m)	V _p max (m s ⁻¹)	Wind speed (m s ⁻¹)
1	12/01/11	NSEC	–	114,000	21:40	23:20	6,000	850,000*	15.4	–	EMOT+ EMV	142	334	830	1.28	21,420	1,685,000 [§]	Strong	9,000*	–	5.76
2	18/02/11	NSEC	37	15,240	12:34	13:05	1,740	95,250	36.1	–	EMOT	55	95	176	1.81	3,240	700,000 [§]	–	–	4.81	
3	10/04/11	NSEC	51	112,320	09:12	13:22	15,000	1,434,400	11.1	–	EMOT	96	308	1,080*	6.67	18,000	1,038,500 [§]	Strong	7,800**	10.00	7.63
4	12/05/11	NSEC	32	304,320	00:20	03:30	8,220	1,107,380	11.4	4	EMOT	135	331	880	7.62	44,760	1,262,000 [§]	Strong	8,200**	25.00	7.13
5	09/07/11	NSEC	58	42,720	13:45	15:28	6,180	678,370	6.6	–	EMOT	110	520	1,131*	8.19	27,780	1,316,000 [§]	Strong	7,99	–	7.99
6	19/07/11	NSEC	10	16,320	00:00	02:10	7,800	941,360	6.4	–	EMOT	121	487	1,040	8.86	13,140	1,599,500 [§]	Weak	–	–	15.05
7	25/07/11	NSEC	6	27,420	01:44	05:50	14,760	1,311,680	14.8	24	EMOT	89	289	823	7.05	19,260	919,000 [§]	Weak	–	–	21.68
8	30/07/11	NSEC	5	60,720	19:16	21:20	7,440	777,510	11.0	2	ENT	105	308	1,000	8.75	20,760	2,026,500 [§]	Intermediate	–	–	12.33
9	05/08/11	NSEC	6	80,700	21:26	23:20	6,840	975,970	4.8	–	EMOT	143	685	1,097*	6.29	26,640	1,499,000 [§]	Strong	–	–	2.78
10	12/08/11	NSEC	7	105,480	08:00	10:18	8,280	815,420	9.7	–	EMOT+ ENT	99	222	900	6.67	20,400	2,303,500 [§]	Strong	9,500 ^{§§}	6.67	3.39
11	20/08/11	NSEC	8	28,800	06:45	07:50	3,120	342,280	8.6	–	EMOT	110	411	994	4.57	29,400	1,580,500 [§]	Strong	9,300**	16.67	8.69
12	29/08/11	NSEC	9	6,900	03:55	05:05	4,200	476,290	8.1	–	EMOT	113	453	1,080*	9.52	13,800	1,359,500 [§]	Strong	7,800**	10.00	3.66
13	08/09/11	NSEC	10	5,100	06:50	08:18	5,280	553,960	9.5	5	EMOT	105	375	983	7.05	10,800	838,000 [§]	Strong	10,900**	6.67	4.12
14	19/09/11	NSEC	11	55,740	12:40	13:45	3,900	501,500	4.8	88	EMOT	129	509	651	9.05	35,520	430,000 [§]	Weak	5,000**	–	21.51
15	28/09/11	NSEC	9	61,200	19:05	19:58	3,180	269,570	15.5	37	EMOT	85	271	1,029	13.33	29,340	393,000 [§]	Strong	–	–	4.46
16	08/10/11	NSEC	10	14,400	12:58	15:40	10,500	–	–	–	–	–	–	–	–	20,760	671,500 [§]	Weak	–	–	–
17	23/10/11	NSEC	15	4,380	18:30	20:16	6,360	524,300	14.6	1	ENT	82	238	550	5.00	9,180	950,500 [§]	Intermediate	6,000 ^{–§§}	5.37	–
18	15/11/11	NSEC	23	10,860	11:15	12:28	4,380	594,480	4.9	–	EMOT	136	590	960	6.29	31,020	1,309,500 [§]	Strong	11,100**	–	3.41
19	05/01/12	NSEC	51	16,800	05:20	06:55	5,700	818,420	16.0	–	ENT	144	464	1,200	8.33	19,380	1,092,000 [§]	Strong	> 9,000 [–]	13.33	1.05
20	08–09/02/12	NSEC	34	263,280	23:50	05:39	22,080	2,105,970	8.7	–	ENT	95	289	750	2.92	46,500	1,110,000 [§]	Strong	9,000 [–]	–	10.37
21	04/03/12	NSEC	25	11,400	06:00	09:31	7,980	1,335,420	11.7	–	ENT	167	444	1,400	14.17	15,240	1,540,000 [§]	Intermediate	9,000 [–]	13.33	3.22
22	18/03/12	NSEC	14	18,000	07:30	10:03	9,180	1,439,050	22.1	–	ENT	157	669	1,700	11.67	16,620	1,360,000 [§]	Strong	> 9,000 [–]	6.67	2.79
23	01/04/12	NSEC	14	6,300	01:45	03:38	6,780	901,100	4.8	–	ENT	133	682	1,500	7.50	11,400	1,000,000 [§]	Strong	–	–	15.00
24	12/04/12	NSEC	11	133,320	12:10	15:16	11,160	929,030	6.5	–	ENT	83	649	1,950	10.00	13,380	1,540,000 [§]	Weak	7,500**	8.33	8.75
25	23–24/04/12	NSEC	11	125,160	23:30	02:20	10,200	641,280	6.4	–	ENT	63	688	1,400	6.67	91,140	1,550,000 [§]	Intermediate	–	–	15.79
26	19/02/13	NSEC	302	6,840	03:48	05:02	4,440	611,340	5.4	–	EMOT	138	634	983*	7.43	3,720	687,500**	Weak	–	–	13.31
27	20/02/13–am	NSEC	1	9,000	00:30	01:40	4,200	529,830	6.1	–	EMOT	126	515	1,057	6.29	12,360	687,500**	Intermediate	–	–	9.39
28	20/02/13–pm	NSEC	0.5	6,180	12:40	13:46	3,960	295,700	20.9	72	EMOT	75	212	810	5.33	84,600	687,500**	Weak	–	–	12.31
29	21/02/13	NSEC	1	13,140	04:00	04:35	2,100	–	–	–	–	–	–	–	–	171,000	687,500**	–	–	–	–
30	23/02/13	NSEC	2	14,400	18:20	19:16	3,360	426,830	4.2	–	ENT	127	590	1,350	10.00	25,560	687,500**	Weak	9,400**	24.68	5.26
31	28/02/13	NSEC	5	6,180	10:00	10:46	2,760	351,930	6.0	–	EMOT	128	534	937*	6.67	37,080	687,500**	Weak	–	–	8.66
32	05–06/03/13	NSEC	5	17,760	23:18	00:15	3,420	456,050	6.2	–	MBT	133	615	938*	6.50	156,000	687,500**	Intermediate	–	–	–
33	16/03/13	NSEC	11	74,580	17:20	18:15	3,300	444,410	8.9	–	EMOT	135	612	926*	4.67	86,400	687,500**	Intermediate	–	–	11.66
34	03/04/13	NSEC	18	7,860	11:20	14:45	10,800	1,512,880	6.1	–	ENT	140	485	1,300	5.00	23,400	2,900,000*	Weak	7,800**	1.58	21.78
35	11–12/04/13	NSEC	8	57,600	18:00	12:05	65,100	1,466,621	15.6	–	EMOT	23	189	375	9.90	72,000	700,000*	Intermediate	7,300**	2.22	15.30
36	18/04/13	NSEC	7	124,200	10:30	13:10	8,220	922,730	7.6	39	EMOT+ EMCT	112	494	1,320	3.81	12,000	3,000,000*	Strong	6,900**	11.67	6.51
37	20/04/13	NSEC	2	86,760	15:06	16:35	5,340	480,500	4.6	23	ENT	90	514	1,100	10.00	75,600	1,300,000*	Strong	–	–	5.87
38	27/04/13	NSEC	7	518,400	16:36	19:37	10,860	1,038,250	10.7	15	ENT	96	312	900	7.50	25,200	900,000*	Weak	8,500**	10.00	10.89
39	26/10/13	NSEC +NEC	182	46,860	01:45	10:30	32,400	3,628,450	4.5	–	EMOT	83	430	1,100	5.90	28,800	1,600,000*	Strong	–	–	1.43

(Continued)

TABLE 1 | Continued

Event number	Date dd/mm/yy	Vent	Inter time (days)	Duration of Strombolian activity (s)	Start of Lava Fountain (hh:mm)	End of Lava Fountain (hh:mm)	Duration of Lava Fountain (s)	Volume of pyro (m ³)	Volume of pyro (%)	Max error (%)	Interp. frames	Cameras	TADR (m ³ s ⁻¹)	Hav (m)	Hmax (m)	V, max (m s ⁻¹)	Duration of lava flow (s)	Lava flow volume (m ³)	Plume type	Max. plume height (m)	V _o max (m s ⁻¹)	Wind speed (m s ⁻¹)
40	11/11/13	NSEC	16	28,500	02:20	10:30	29,400	—	—	—	—	—	—	—	—	—	61,200	1,700,000 ⁺	—	—	—	—
41	16–17/11/13	NSEC	5	158,400	22:41	04:40	21,540	2,409,520	7.9	—	—	ENT	112	416	1,200	10.00	36,720	500,000 ⁺	Strong	—	—	1.42
42	23/11/13	NSEC	7	60,000	08:20	10:25	4,620	789,240	3.5	—	—	ENT	171	1,075	3,400	33.33	30,720	30,000 ⁺	Intermediate	12,600 ^{mm}	13.33	17.19
43	28/11/13	NSEC	5	3,300	20:15	22:39	8,640	944,860	7.4	18	—	ENT	109	348	700	3.33	21,600	700,000 ⁺	Weak	—	—	8.11
44	02/12/13	NSEC	4	1,800	19:00	22:20	12,000	—	—	—	—	—	—	—	—	—	21,600	900,000 ⁺	—	—	—	—
45	28/12/14	NSEC	391	—	17:16	18:42	5,160	—	—	—	—	—	—	—	—	—	—	2,600,000 ⁺	—	—	—	—
46	03/12/15	VOR	340	—	01:50	03:20	5,400	4,190,000 ⁺	1.7	—	—	ENT	776	1,673	4,100	24.58	No lava flows	—	Strong	15,000 [#]	—	2.98
47	04/12/15–am	VOR	1	—	08:41	10:03	4,920	2,760,000 ⁺	2.3	—	—	ENT	561	1,264	2,600	11.25	No lava flows	—	Strong	13,400 [#]	11.67	2.69
48	04/12/15–pm	VOR	0.5	—	20:12	21:17	3,900	1,810,000 ⁺	3.3	—	—	ENT	464	850	2,050	14.17	No lava flows	—	Strong	13,300 [#]	3.72	—
49	05/12/15	VOR	1	—	14:21	16:15	6,840	1,360,000 ⁺	3.9	—	—	EMOT	199	680	1,123	8.57	No lava flows	—	Strong	13,000 [#]	2.06	—

Times are in UT format. NSEC, New South-East Crater; NEC, North-East Crater; TADR, time averaged effusion rate, calculated only for pyroclastics erupted during the lava fountain over the entire duration of each eruptive episode. Cameras labels and locations are in **Table 2** and **Figure 2**. Hav, average height of the lava fountain. Hmax, maximum height of the lava fountain. "Saturated value." Data from Calvari et al. (2011). ° Data from Bonaccorso and Calvari (2017). § Data averaged from Ganci et al. (2012) and Behncke et al. (2014). * Data from De Beni et al. (2015). ° Data from Behncke et al. (2014). ++ Derived from the total volume erupted between 19 February and 16 March 2013 (De Beni et al., 2015) divided by the number (8) of eruptive episodes. ** Data from Scollo et al. (2014). §§ Data from Scollo et al. (2015). ° Data from Guerrieri et al. (2016). # Data from Vulpianti et al. (2016). = Data from this work. Gray lines indicate poor weather conditions and lack of visibility from cameras.

at ~ 1.5 km b.s.l. (Bonaccorso and Calvari, 2017). This is much deeper than the magmatic source at sea level inferred for the lava fountain episodes at the NSEC (Bonaccorso et al., 2013a,b; Cannata et al., 2015). The fast transfer from the deepest levels of the plumbing system of basic, undegassed magmas has been considered as the crucial triggering factor leading to the development of exceptionally violent volcanic phenomena (Cannata et al., 2018). Also the time scale for completely refilling the VOR system and renewing magma is very fast, being as short as a few tens of hours (Pompilio et al., 2017).

CAMERA RECORDED DATA

We have used the thermal and visual cameras from the INGV-OE monitoring network (**Figure 2c**) to acquire information about the duration of the eruptive activity, such as the start and end of the Strombolian activity preceding the paroxysm, of the lava fountain, of the lava flows, exit velocity, as well as the height of lava fountains. **Table 2** reports the characteristics of the cameras used in this study. Additional information can be found in Andò and Pecora (2006) and Coltelli et al. (2017). Details on the time and kind of eruptive activity for each episode, as well as its duration, are listed in **Table 1**, which also contains the erupted volumes of pyroclastics for each event. These have been obtained, following the approaches of Calvari et al. (2011) and Bonaccorso and Calvari (2017), by integrating the height of the LF obtained from the saturated portion of the thermal images over time at 1 min time lapse, and using the formulas:

$$U = (2gH)^{0.5} \quad (1)$$

$$V = U \times A \times t \quad (2)$$

where U is the mean fluid exit velocity at the vent, H is the LF height, g is the gravity acceleration, V is the fluid volume (gas + pyroclastics) erupted by a LF, A is the vent surface area, and t is the duration of the LF. Vent surface area is calculated considering a circular vent with a diameter of 30 m (Calvari et al., 2011) and supposed constant. Considering a circular shape for the vent area, and multiplying the mean fluid exit velocity at the vent by the vent surface area integrated over time, we transformed the 2D view given by the camera obtaining a 3D volume estimation. The images from the thermal cameras (EMOT, ENT, EMCT, and MBT; **Figure 2c**, **Table 2**) have been used to measure the maximum height of the LF, considered as the saturated portion of each image. Saturation varies with respect to distance between 50°C for the most distant camera (ENT, 15 km; **Figure 2c**) to 100°C for the closest (EMOT, 3 km; **Figure 2c**). The error in the height measurement is ± 50 m. We carefully measured the height of the saturated portion, avoiding errors due to clouds interference and to the variable position of the eruptive vent, given that the NSEC, responsible for this eruptive activity, grew by more than 190 m during the lapse of time considered here (Behncke et al., 2014). The heights of the LF at 1 min intervals have then been used to calculate the total fluid erupted volume from Equations (1) and (2), which includes both gas and pyroclastics (Calvari et al., 2011; Bonaccorso and Calvari, 2017). To obtain the volume of pyroclastics from the total volume

TABLE 2 | Characteristics of visual and thermal cameras of the INGV-OE monitoring network used in this paper.

Camera name	Position	Distance from the vent (km)	Vertical FOV (°)	Camera model	Image
EMOT	La Montagnola, 2,600 m a.s.l., south flank	3.0	24	FLIR A40	Thermal
MBT	Schiena dell'Asino, 1,985 m a.s.l., south-east flank	4.9	24	FLIR A40	Thermal
EMCT	Mt. Cagliato, 1,160 m a.s.l., east flank	8.3	25	FLIR A320	Thermal
EMV	Milo, 770 m a.s.l., east flank	10.8	3-47.5	CANON VC-C4R	Visible
ENT	Nicolosi, 730 m a.s.l., south flank	15.0	24	FLIR A40	Thermal
ECV	Catania Nesima, 35 m a.s.l., south flank	26.7	3-47.5	CANON VC-C4R	Visible

See **Figure 2c** for their location.

of erupted fluid (gas + pyroclastics), we have considered 0.18% as the ratio between the volumes of magma and fluids within the eruptive column as typical for Etna's fountains (e.g., Donnadieu et al., 2016). This 0.18% between the pyroclastic portion of the LF and the total erupted fluids (gas + pyroclasts), derives from the average volumetric growth of the NSEC cone during the first 12 paroxysmal episodes. In fact, most of the LF fallout accumulates all around the vent, causing the fast growth of the NSEC cinder cone. The NSEC cone volume was measured by Behncke et al. (2014) on 31 August 2011, after 12 LF episodes from the NSEC, at $\sim 9.5 \times 10^6 \text{ m}^3$ dense rock equivalent (DRE). This volume is $\sim 0.18\%$ of the total volume of fluids (gas + pyroclastics, $\sim 5.4 \times 10^9 \text{ m}^3$) erupted during the first 12 LF events and obtained from Equations (1) and (2). Considering this a constant, we applied the 0.18% to all pyroclastic volume calculations of the LF episodes from the NSEC reported in **Table 1**. For the four paroxysmal episodes of VOR, this value has been calculated individually for each event, showing a significant variability and a general gradual decline (from 0.22 to 0.09%; Bonaccorso and Calvari, 2017). The maximum error on the pyroclastic volume calculation is reported in **Table 1**, and is calculated from the LF height error ($\pm 50 \text{ m}$) and its propagation when using Equations (1) and (2).

The lava flow volumes in **Table 1** are taken from Ganci et al. (2012), Behncke et al. (2014) and De Beni et al. (2015), or are averages of more values when available. TADR is related only to the explosive component of each episode and averaged over the whole duration of the paroxysmal explosive event.

Note that the starting and ending times in **Table 1** (in UT format) have been obtained from careful analysis of the images of the closest cameras (3.0 km from the vent, see **Table 2**), and thus refer to surface expression of the eruptive activity. As such, they could be significantly different from those obtained by geophysical data that refer to changes detected in the source region (e.g., Carbone et al., 2015; Spampinato et al., 2015; Bonaccorso and Calvari, 2017). In addition, given the change from Strombolian to LF activity is generally gradual and characterized by a transitional phase (e.g., Spampinato et al., 2008), we have taken as the starting time of the LF activity the moment when tephra fallout began spreading well outside the crater, in a way to minimize errors in volume calculations. In fact, we have observed that during the transitional phase, the jet of magma is highly collimated, and tephra fallout mainly falls back within the crater, with very little contribution to the volume accumulated on the outer flanks of the cone and beyond.

For four of the 44 eruptive episodes at NSEC between January 2011 and December 2013, we lack data because poor weather conditions hampered camera visibility throughout the entire episode. These are: 8 October 2011, 21 February 2013, 11 November 2013, and 2 December 2013 (**Table 1**). However, in the next section we also considered these episodes when analyzing the relationships between pause interval and total erupted volume. When instead cloud coverage was partial, we have interpolated the missing values. In addition, the 19 September 2011 event (**Table 1**) allowed visibility for only 7 min out of 65, thus in this case most of the erupted volume has been extrapolated on the basis of available data and must be considered a minimum, given that the climax of the LF has been lost. We have analyzed 6333 frames to extract dimensional parameters of the LF. Of these, 352 have been interpolated because of cloud cover, making a 5.6% data interpolated. The amount of interpolated frames for each LF is indicated in **Table 1**. However, it is worth noting that the two events of 18 April 2013 and 20 April 2013 occurred in poor weather conditions, allowing only 1/3 and 2/3 of their duration to be captured by the cameras. These two volumes must be considered as minimums. **Figure 3** displays the first LF episode from NSEC (A) occurring on 12 January 2011 and (B) the first episode from VOR occurred on 3 December 2015, with the outline of the volcano and the two vent positions. Note the very different size of both the LF (in white-red) and eruptive plumes (bluish to pink).

The ECV visual camera (**Figure 2c**, **Table 2**) has been used to extract the growing height of the eruptive plume, following the method proposed by Scollo et al. (2014). They calibrated the ECV images by projecting the plume on a vertical plane passing through the craters and parallel to the wind direction, taken from the daily wind direction forecast, thus obtaining a grid for the plume height estimation with an estimated error on the height of $\pm 0.5 \text{ km}$. The ECV camera has a field of view allowing a maximum height of 9 km a.s.l., thus higher plumes are not visible. Fifteen out of the 44 episodes occurred during daytime and in good weather conditions, also enabling us to analyse the plume height growth together with LF height growth. These data are displayed in **Figure 5**, with the limit of 9 km a.s.l. due to the camera field of view. Note that **Table 1** reports maximum plume heights, thus most of the values greater than 9 km are taken from existing literature.

In summary, we have analyzed the images of 40 eruptive episodes from the NSEC and 4 from VOR in order to obtain:

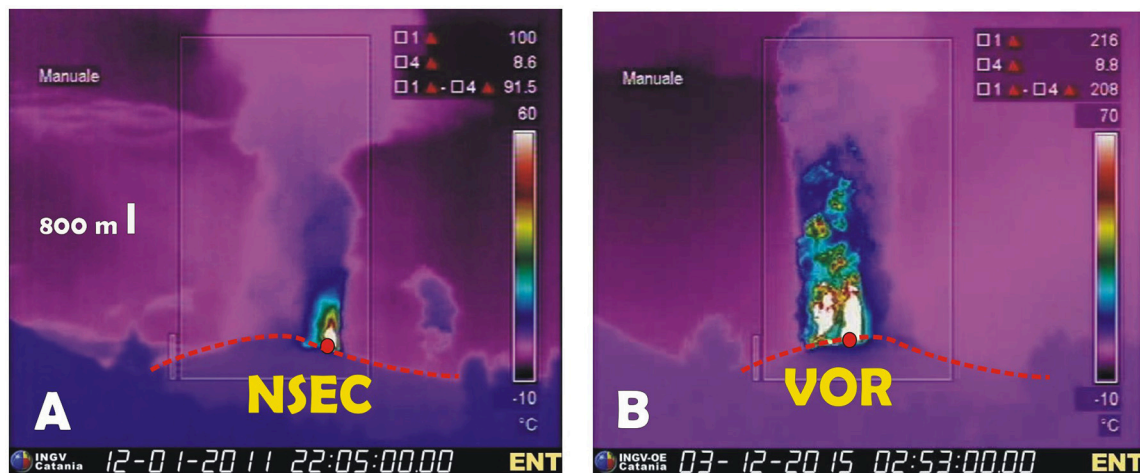


FIGURE 3 | Thermal images from the camera located at Nicolosi, showing (A) the first lava fountain episode from NSEC, occurring on 12 January 2011 and taken at 22:05 UT, and (B) the first lava fountain episode from VOR on 3 December 2015 and taken at 02:53 UT. The red circles show the position of vent, and the red dotted line is the volcano profile. The white vertical bar in A is for scale. The lava fountain portion is in white-red, the ash plume in bluish-pink. Note the different size of the two episodes, with the VOR lava fountain and plume being much taller and wider.

(1) the duration of the Strombolian activity preceding each episode; (2) the duration of the LF; (3) the total volume of erupted pyroclastics; (4) the time-averaged discharge rate (TADR), referred just to the LF portion of each episode and averaged over the entire duration of the paroxysmal explosive phase; (5) the average and (6) maximum LF heights; (7) the maximum exit velocity of LF; (8) the duration of the lava flow output; (9) the plume type; (10) the maximum elevation of the plume (when lower than 9 km) and the plume growth for 15 events displayed in **Figure 5**; (11) the maximum exit velocity of the plume. Plume type is differentiated into a strong plume when vertical, intermediate when slightly inclined ($\sim 70^\circ$) downwind, and weak when markedly bent in a downwind direction (**Figure 1**). These results are listed in **Table 1**. Lava flow volumes and maximum plume heights are taken from available published data as specified in **Table 1**.

STATISTICAL APPROACH

To make the most of the substantial set of paroxysms, we statistically characterized the measured volcanological features with the final aim of analyzing possible correlations among them. Indeed, conducting a correlation analysis that assumes the data follow a normal distribution when, in fact, the data are non-normal, can lead to inaccurate results (e.g., linear correlation analysis is not robust in the presence of non-normality; Kowalski, 1972). To avoid this potential error, we first determined the right distribution of each considered feature. For the analysis, we took into account the following nine features, listed in **Table 1**:

- (1) the inter-time between two consecutive paroxysms;
- (2) the duration of Strombolian activity before the fountaining event;
- (3) the fountain duration;

- (4) the duration of the lava flow accompanying the paroxysm;
- (5) the mean fountain height;
- (6) the maximum fountain height;
- (7) the total volume of lava flow associated with the paroxysm;
- (8) the total volume of erupted pyroclastics;
- (9) the mean wind speed at altitude during the paroxysm.

Each feature was tested for a normal distribution. We used the Shapiro-Wilk (SW) test that is a widely used test of normality in frequency statistics (Shapiro and Wilk, 1965). The null-hypothesis of this test is that the population is normally distributed. The Shapiro-Wilk test is based on the correlation between the data and the corresponding normal scores and performs better than the Kolmogorov-Smirnov (KS) test in recognizing samples from non-normal distributions (Steinskog, 2007). We adopted a confidence level for the test of 5%.

For all the considered features, the test rejected the null-hypothesis of normality, thus we estimated the best distribution among the following ones: t location-scale (Rinne, 2011), inverse Gaussian (Chhikara and Folks, 1989), exponential (Balakrishnan and Basu, 1996), logistic and log-logistic (Balakrishnan, 1992). To this set of alternative distributions, we also added the normal distribution to confirm the SW test outcomes. Each distribution was fitted using maximum likelihood estimation. The Akaike information criterion (AIC) was then applied to choose the distribution that better describes the data. The AIC estimates the relative quality of statistical models for a given dataset (Burnham and Anderson, 2003). Given a collection of models for the data, AIC estimates the quality of each model, relative to each of the other models. Thus, AIC provides a means for model selection. The AIC corrected (AICc) for finite sample sizes is defined as:

$$AICc = -2 \log \left(L(\hat{\theta}) \right) + 2k + (2k + 1)/(n - k - 1) \quad (3)$$

TABLE 3 | Distribution analysis of volcanological features for the set of paroxysms listed in **Table 1**.

Feature	Distribution	I moment (mean)	II moment ^{0.5} (standard deviation)
Paroxysm inter-time	Exponential	38 (days)	38 (days)
Duration of Strombolian phase, pre-LF	Inverse Gaussian	53.5 (h)	179.5 (h)
Lava fountain duration	Log-logistic	2.2 (h)	2.1 (h)
Lava flow duration	Log-logistic	9.2 (h)	14 (h)
Mean lava fountain height	Log-logistic	521 (m)	349 (m)
Maximum lava fountain height	t location-scale	1,003 (m)	–
Volume of lava flow	Logistic	1.11×10^6 (m ³)	0.61×10^6 (m ³)
Volume of pyroclastics	Log-logistic	1.06×10^6 (m ³)	1.21×10^6 (m ³)
Wind speed	Log-normal	–	–

L being the model likelihood of the estimated model parameters ($\hat{\theta}$), k the number of parameters, and n the sample size. For all the estimated best distributions, we calculated the first and second moments when existing and finite. Results are reported in **Table 3**, where it is then possible to read the estimated characteristic scales of the features.

We performed a correlation analysis to infer possible hidden relationships among the considered features. Correlation is a bivariate analysis that measures the strengths of association between two variables and the direction of the relationship. In terms of the strength of relationship, the value of the correlation coefficient varies between $+1$ and -1 . When the value of the correlation coefficient lies around ± 1 , then it is said to be a perfect degree of association between the two variables. As the correlation coefficient value goes toward 0, the relationship between the two variables will be weaker (Hazewinkel, 2001). Commonly, Cohen's standard is used to evaluate the correlation coefficient to determine the strength of the relationship, or the effect size, where correlation coefficients between 0.10 and 0.29 represent a small association, coefficients between 0.30 and 0.49 represent a medium association, and coefficients of 0.50 and above represent a large association or relationship (Cohen, 1988).

There are different types of correlation methodologies. Pearson correlation (parametric test) is the most widely used correlation statistic to measure the degree of the relationship between linearly related variables (Pearson, 1895). For the Pearson correlation, both variables should be normally distributed. Other assumptions include linearity and homoscedasticity. Linearity assumes a straight-line relationship between each of the variables in the analysis and homoscedasticity assumes that data are normally distributed about the regression line (and both variables have a finite variance). These assumptions make the Pearson coefficient unreliable in case of non-normally distributed data. In order to mitigate the distribution effects, we used the Box-Cox transformation (Box and Cox, 1964) to convert the feature distributions into normal ones. In addition, we used the

non-parametric tests of Spearman rank (Spearman, 1904) and Kendall rank (Kendall and Gibbons, 1990) correlations to measure the degree of association between two variables without any assumptions about the distribution of the data.

Based on the statistical analysis of the parameters obtained from analyzing the camera images, considering all the three cited coefficients, the correlation analysis confirms that the only significant/large associations are those for the self-explanatory feature pairs:

- volume of pyroclastics and fountain duration (0.66 of mean correlation);
- mean and maximum fountain heights (0.76 of mean correlation).

Nevertheless, it is important to underline that the above statistical analysis is valid for the considered set of volcanological data and should not be generalized outside the considered time interval without further accurate studies.

LAVA FOUNTAIN AVERAGE HEIGHT VS. PLUME MAXIMUM HEIGHT

We investigated the relationship between the average height of the LF (H_F) and the maximum height that reaches the plume (H_P). The average heights of the LF are derived from the thermal images at 1 min intervals. Regarding the measurement of the maximum heights of the plume, in the current literature the work presenting the most complete and detailed catalog is the one published by Scollo et al. (2014), which reports the height measurements of the plume of 19 LF from 10 April 2011 to 27 April 2013. For each event considered, in their **Table 1** the Authors reported three heights respectively estimated from: (1) ECV camera, which, however, cuts the image to 9 km a.s.l.; (2) the MODIS satellite; (3) the SEVIRI satellite. The heights measured with greater precision are those seen by ECV, which records the peak in elevation when below 9 km. Then, with less precision, is the value obtained by MODIS, which has less frequency of satellite passages (and therefore fewer images; 1 every 15 min with 1 km of spatial resolution in the thermal infrared; Corradini et al., 2016). Finally, with even less precision, is the value obtained by SEVIRI, which has a spatial resolution of 3 km and records images every 15 min (Ganci et al., 2012). To obtain a more robust dataset, we therefore used the values obtained from ECV measurements, when H_P was less than 9 km in height, and for other cases ($H_P > 9$ km) we considered the value from MODIS and alternatively, if this was not available, the value of SEVIRI (**Table 4**). For a few cases (**Table 4**) where ECV camera images saturated at 9 km a.s.l., but with the satellite passage providing a lower height because their passage was temporarily distant from the LF climax, we used the ECV camera height. We did not consider the 19 September 2011 and 08 October 2011 episodes due to cloudy weather. Moreover, for the LF of 12 January 2011, we used the plume height reported in Calvari et al. (2011); for the LF of 23 October 2011, we considered the plume height measured by

SEVIRI and reported in Guerrieri et al. (2015); for the LF of 23 November 2013, we considered the height inferred by Corradini et al. (2016) by using a multi-sensor approach considering different satellite instruments such as Meteosat, MODIS and SEVIRI, and finally for the four events of the VOR of 3–5 December 2015, we used the plume heights reported in Vulpiani et al. (2016), obtained by three radar systems (at C and X band) operated by the Italian Department of Civil Protection (Table 4).

The relationship between H_F and H_P has some limitations. In fact, it considers a heterogeneous set of data because heights from ECV camera saturate at 9 km a.s.l., and in these cases it is necessary to consider this underestimated value or to resort to the satellites that have a greater resolution error, when often their passage in time is not perfectly synchronous with the maximum height reached by the plume. Despite these limitations, the relationship presents an interesting correlation (Figure 4) with a good R^2 of 0.78 for the overall average (Equation 4), and 0.91 for the VOR events only (Equation 5). This provides a useful tool to make a rough forecast of the maximum height reached by the plume once the fountain, well after its initial phase, stabilizes its explosive power and thus its average height, which can be accurately measured in real-time by the cameras monitoring system.

The equations expressing these relationships are:

$$y = 5.26x + 6,830 \quad R^2 = 0.78 \quad (4)$$

$$y = 2.00x + 11,286 \quad R^2 = 0.91 \quad (5)$$

This equals to:

$$H_P = 5.26H_F + 6,830 \quad (\text{NSEC}) \quad (6)$$

$$H_P = 2.00H_F + 11,286 \quad (\text{VOR}) \quad (7)$$

TIME-DEPENDENT RELATION BETWEEN LAVA FOUNTAIN AND PLUME HEIGHTS

For 15 of the 49 eruptive events, occurring during daytime and with good weather conditions, we also managed to obtain the growing height of the plume over time from the analysis of the images recorded by the ECV camera (Table 2). This allows a view of the eruptive plume up to about 9 km a.s.l., estimated using the scheme proposed by Scollo et al. (2014).

The comparison between height of the LF and height of the ash plume is shown in the graphs of Figure 5. Although with the limit of the 9 km caused by the camera field of view, from the analysis of Figure 5 it is possible to observe different behaviors. A first class of events comprises 7 LF (10 April 2011, 20 August 2011, 29 August 2011, 8 September 2011, 18 March 2012, 18 April 2013, and 4 December 2015; Figure 5), where the ash plume stays above the 9 km threshold for most of the duration of the LF. These are all strong plumes (Figure 1A) formed in wind conditions variable between 2.69 and 8.69 m s⁻¹ and with TADR, calculated only for the explosive portion, between 96 and 157 m³ s⁻¹, and with the outsider event of 4 December 2015 which displayed the exceptional value of 561 m³ s⁻¹ (Table 1). A second

TABLE 4 | Episodes (first column) and dates (second column) of lava fountains of NSEC (events from 1 to 42) and VOR (events from 46 to 49) with the mean height of the fountains (H_F) as obtained from the cam analysis in this study (third column) and maximum height of the plume (H_P) (fourth column) as reported in literature with the sensor utilized (fifth column).

Episode	date (dd/mm/yy)	mean H_F (m)	H_P (m)	H_P reference, sensor utilized
1	12/01/11	334	9,000	Calvari et al. (2011), ECV saturated
3	10/04/11	310	7,800	Scollo et al. (2014), Modis
5	09/07/11	520	9,000	Scollo et al. (2014), ECV saturated
10	12/08/11	636	9,000	Scollo et al. (2014), ECV saturated
11	20/08/11	411	9,300	Scollo et al. (2014), Sevir
12	29/08/11	453	9,000	Scollo et al. (2014), ECV saturated
13	08/09/11	375	9,700	Scollo et al. (2014), Modis
17	23/10/11	238	6,000	Guerrieri et al. (2015), Sevir
18	15/11/11	590	11,100	Scollo et al. (2014), Modis
19	05/01/12	644	9,000	Scollo et al. (2014), ECV saturated
20	09/02/12	290	8,000	Scollo et al. (2014), ECV & Sevir
21	04/03/12	450	9,500	Scollo et al. (2014), Modis
22	18/03/12	640	11,000	Scollo et al. (2014), Modis
24	12/04/12	112	7,500	Scollo et al. (2014), ECV
31	28/02/13	534	9,400	Scollo et al. (2014), Sevir
34	03/04/13	485	7,500	Scollo et al. (2014), ECV
35	12/04/13	204	7,500	Scollo et al. (2014), ECV
36	18/04/13	165	9,000	Scollo et al. (2014), ECV saturated
38	27/04/13	312	8,500	Scollo et al. (2014), ECV
42	23/11/13	1,075	12,600	Corradini et al. (2016), Sevir + Modis
46	03/12/15	1,743	15,000	Vulpiani et al. (2016), terrestrial radar
47	04/12/15	1,264	13,400	Vulpiani et al. (2016), terrestrial radar
48	04/12/15	926	13,200	Vulpiani et al. (2016), terrestrial radar
49	05/12/15	682	12,800	Vulpiani et al. (2016), terrestrial radar

class of events comprises the two events of 9 July 2011 and 12 August 2011 (Figure 5), where the plume remained above 9 km for a short period of time (30 and 52 min, respectively) during

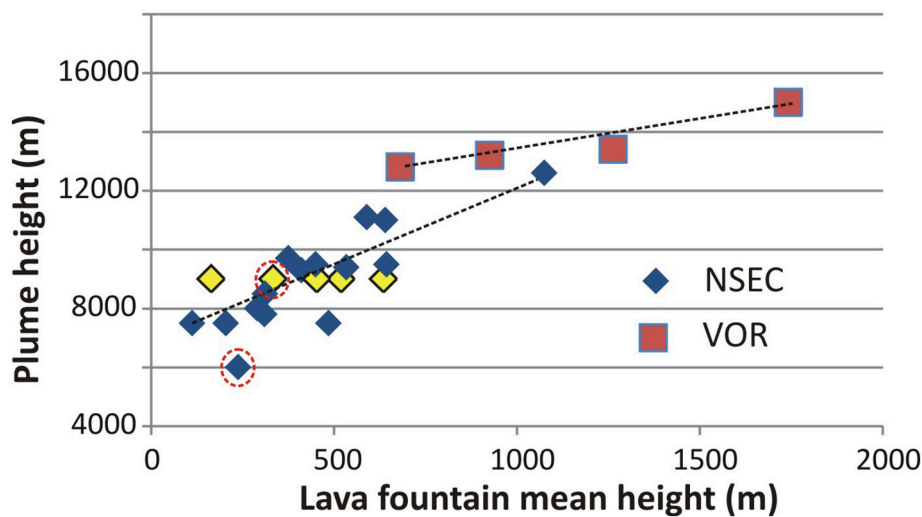
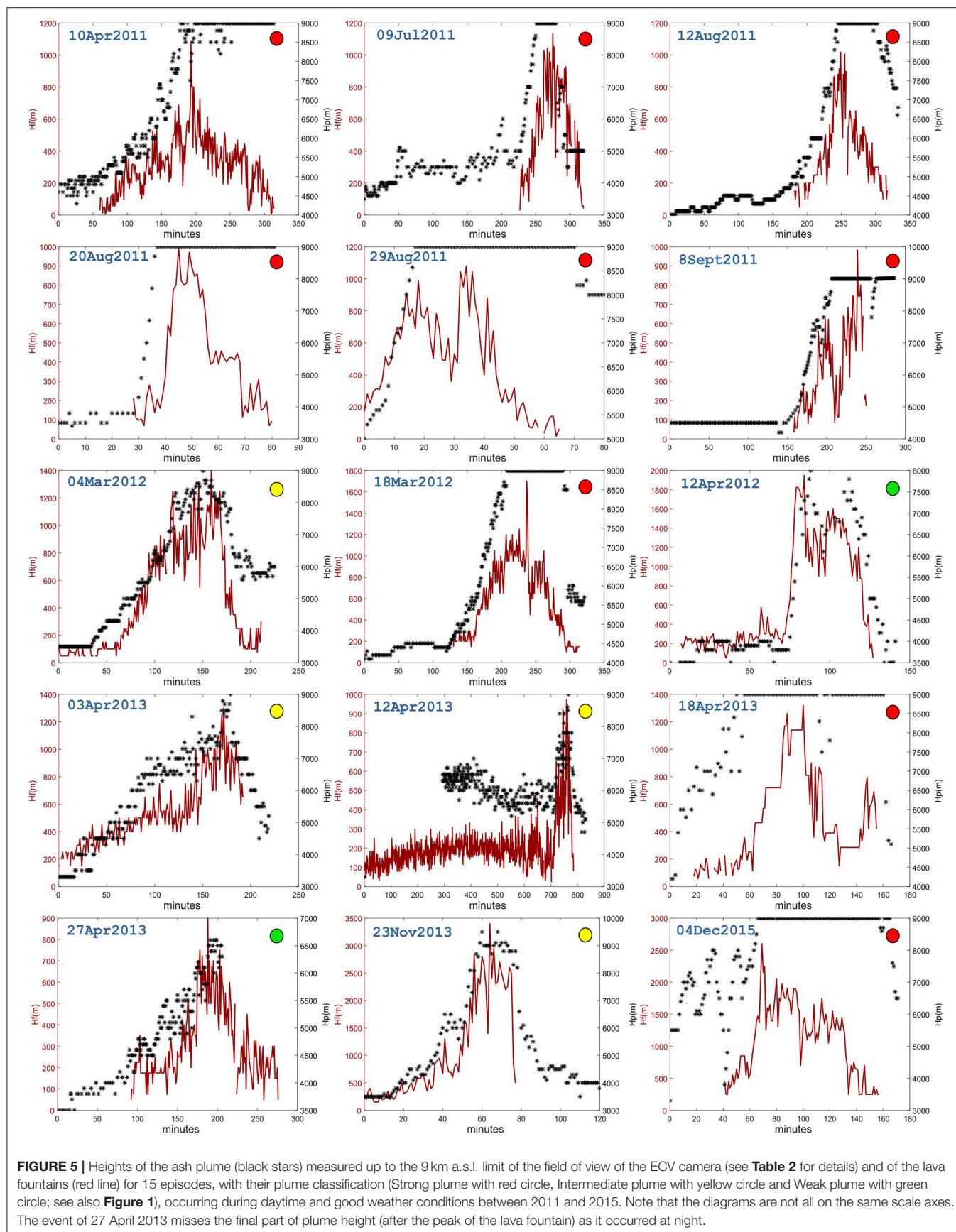


FIGURE 4 | Fountain average height H_F vs. plume height H_P . For the NSEC lava fountains, the H_P values are taken from Scollo et al. (2014) for 19 lava fountains (from 10 April 2011 to 27 April 2013) with the criterion detailed in the text. To this database we added the measurements, highlighted by the red circles, coming from Calvari et al. (2011) for the event of 12 January 2011, and from Guerrieri et al. (2015) for the event of 23 October 2011. The four H_P values of the VOR December 2015 events (red squares) are taken from Vulpiani et al. (2016). The five yellow diamonds show data taken from ECV, with the 9 km a.s.l. limit.

the climax reached by the lava fountains, and decreased soon after and while the LF was still on going. These two events are both strong plumes formed in wind conditions of 3.99 and 7.99 m s^{-1} , and having TADR of 110 and 99 $\text{m}^3 \text{s}^{-1}$, respectively, thus comparable to the range of the first class. A different pattern is shown by the 6 events of 4 March 2012, 12 April 2012, 3 April 2013, 12 April 2013, 27 April 2013, and 23 November 2013, where the height of the ash plume increases and decreases together with the height of the LF (Figure 5). It is worth noting that the 27 April 2013 plume decline after the end of the LF is not reported in Figure 5 because it has been observed from thermal images and not from the ECV camera, given that it occurred during the evening and hence with no visibility from this camera. These are intermediate to weak plumes (Figures 1B,C) formed in wind conditions comprised between 3.22 and 21.78 m s^{-1} and displaying TADR between 23 and 171 $\text{m}^3 \text{s}^{-1}$. Thus, from an overall view of these data, it appears that conditions of strong wind (above $\sim 10 \text{ m s}^{-1}$) or low TADR (below 100 $\text{m}^3 \text{s}^{-1}$), or a combination of these two factors, might favor weak to intermediate plumes that decrease in height soon after or together with the end of the LF. Conversely, conditions of high TADR (above 100 $\text{m}^3 \text{s}^{-1}$) and slight wind (below $\sim 10 \text{ m s}^{-1}$), or a combination of these two factors, involves the formation of strong plumes, with plume heights above 9 km maintained even during the phase of waning LF height (Figure 5).

The effect of wind speed on the plume style is clearly visible when comparing the LF events on 12 May 2011 and on 19 July 2011 (Figure 6). It is worth noting here that wind speed is sampled every 3 h, thus we lack details of wind variability during an event, and we consider it constant throughout a paroxysmal event. The first event occurred in low wind conditions (7.13 m s^{-1}), with LF maximum height of 880 m, and average of $\sim 300 \text{ m}$,

and with a TADR of 135 $\text{m}^3 \text{s}^{-1}$ (Table 1), allowing the gradual development of a strong plume rising vertically from the vent. As the eruptive phase proceeded, we observed at first, between 00:00 and 01:02, intermittent minor ash emissions (Figure 6A) accompanied by a Strombolian to transitional phase, followed between 01:02 and 01:17 by the formation of a weak plume (Figure 6B) inclined westward (left) by about 45°; between 01:18 and 01:26 (Figure 6C) it passed to an intermediate plume with inclination of $\sim 70^\circ$ westward; and from 01:26 to 3:21 giving rise to a strong plume rising vertically from the vent (Figure 6D) and spreading laterally (Figure 6E); between 3.21 and 3:44 the plume again became transitional (Figure 6F) until the end of the eruptive event. An opposite example is given by the event of 19 July 2011, which had a similar TADR (121 $\text{m}^3 \text{s}^{-1}$, Table 1) and a slightly greater vertical extension of the LF height (1,040 m maximum, 487 m average; Table 1), but whose plume formed in conditions of stronger wind (15.05 m s^{-1}). The activity started as pulsating and increasing ash emissions between 00:00 and 00:29 (Figure 6G), passing to weak plume (bent about 45° eastward, Figure 6H) between 00:29 to 01:38 (with LF about 800 m high), and again at pulsating and decreasing ash emissions between 01:38 and 02:18 (Figure 6I), until the end of the event. Thus, Figure 6 displays the importance of wind speed and IER in determining the plume style, passing from no plume to weak, intermediate and then to strong plume with increasing IER (from 43 to 67, 85 and 130 $\text{m}^3 \text{s}^{-1}$, respectively) and in conditions of low wind (7.13 m s^{-1} , Table 1 and Figures 6A–E). Vice-versa, the opposite change occurs when IER vanishes (Figures 6E,F, from 119 to 0 $\text{m}^3 \text{s}^{-1}$). On the contrary, if wind speed is strong (15.05 m s^{-1} in the case of the 19 July 2011 event, Table 1 and Figures 6G–I), then also a powerful LF $\sim 800 \text{ m}$ high (with IER up to 158 $\text{m}^3 \text{s}^{-1}$, Figure 6H) is unable to form a strong plume



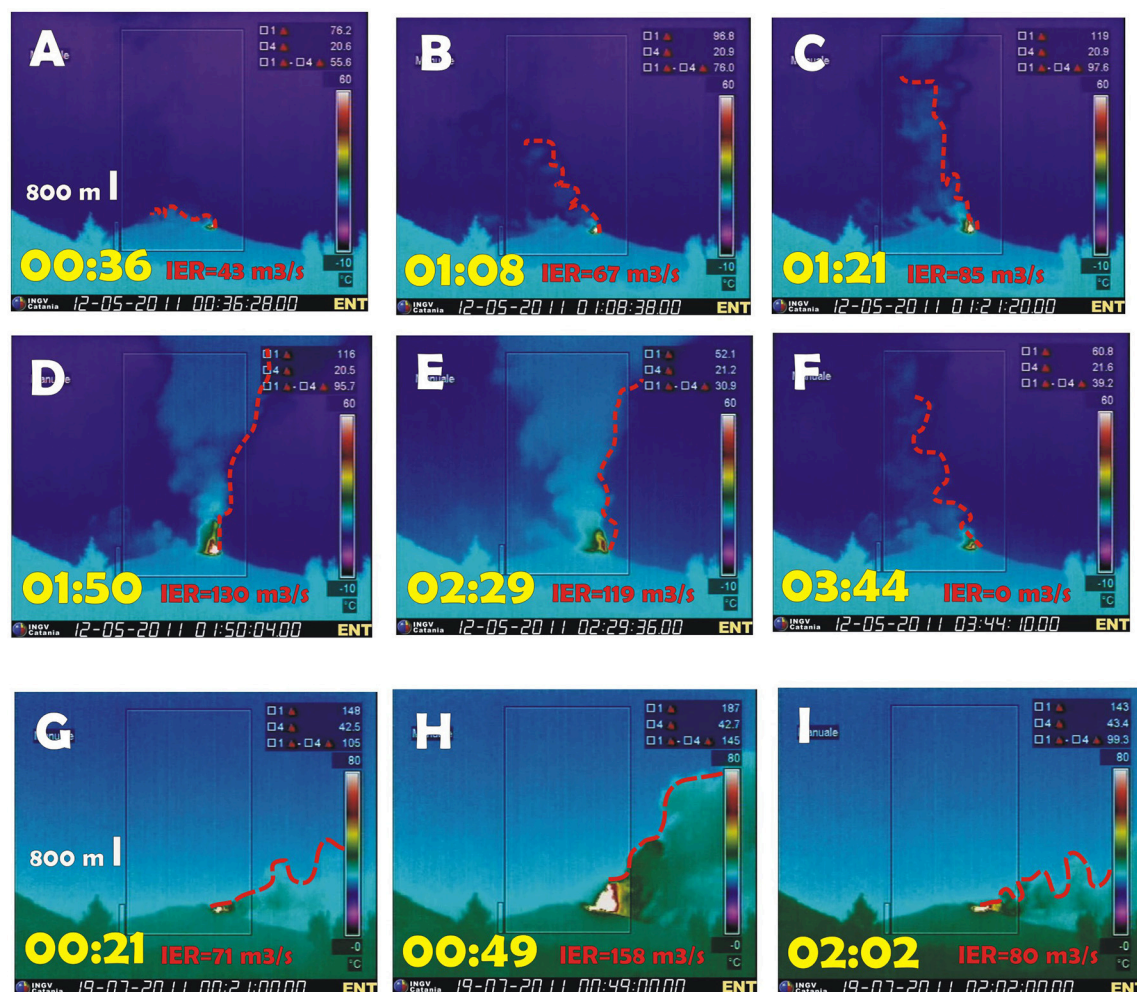


FIGURE 6 | Thermal images recorded by the fixed camera of Nicolosi, south flank of the volcano (ENT, see **Table 2** for details), showing the variability of the plume inclinations (bounded by the red striped line) for the episode of 12 May 2011 (**A–F**), producing a strong plume (**D,E**), and for the episode of 19 July 2011 (**G–I**), giving rise to a weak plume. Eruption parameters are in **Table 1**. In yellow is time (UT), in red Instantaneous Effusion Rate (IER; Harris et al., 2007). The vertical white line in (**A,G**) is for scale. See text for further details.

(**Figures 6G–I**). It is worth noting that the two events reported in **Figure 6** have very similar TADR and durations (averaged over the whole duration of the explosive event, 135 and 121 m³ s⁻¹, and durations of 8,220 and 7,800 s, respectively; **Table 1**) but wind speed is two-fold during the second case (7.13 vs. 15.05 m s⁻¹; **Table 1**).

DISCUSSION

In this paper, we have analyzed 44 paroxysmal explosive events occurring at Mt. Etna between 2011 and 2015, with the aim of analyzing the eruptive process and finding simple relationships among easily measurable parameters that might be useful for hazard assessment and risk mitigation. Using the images recorded by the network of thermal and visual cameras (**Figure 2c**, **Table 2**), we have characterized each event, extracting the parameters listed in **Table 1**. They are: the vent that produced

the event (NSEC, VOR or NEC); duration of the Strombolian phase preceding the LF event; starting and ending time and duration of each LF event; volume of erupted pyroclastics and its maximum error; TADR; maximum and average height of the LF; maximum speed of the LF; the lava flow duration when associated to the explosive event; lava flow volume (taken from available published data, as detailed in **Table 1** caption); plume type (either strong, intermediate or weak, see **Figure 1**); maximum plume heights (from available published data, detailed in **Table 1** caption, or from our measurements using the ECV camera image); maximum velocity of plume growth; and wind speed.

Etna's LFs are significantly different from their Hawaiian counterpart. The main difference is the shape of the vent, which is normally linear (fissure) in Hawaii (e.g., Parcheta et al., 2012), and localized (circular vent or bocca) at Etna (e.g., Calvari et al., 2011). In addition, Hawaiian LFs are normally 200–400 m high

(Head and Wilson, 1987; Wolfe et al., 1988), whereas on Etna we measured LF up to 3–4 km in height during the lapse of time here considered (**Table 1**). It is worth noting that during the explosive activity of Kilauea observed on 17 May 2018, when a summit circular vent was active within the Halemaumau Crater (Patrick et al., 2016), a more than 9 km high ash plume was reported¹. This suggests that, considering all other parameters as steady, a circular vent might promote a greater vertical distribution of the erupted ash when compared to a fissure.

Even more than vent geometry, LF heights depend primarily on the amount of exsolved volatiles (Head and Wilson, 1987), with H₂O being the most abundant (92–96 mol%) and turning to zero as soon as the paroxysm ends (Allard et al., 2005). Etnean magmas are very water-rich basalts, with 3.4 wt% H₂O (Métrich et al., 2004) when compared to their Hawaiian counterpart (0.6–0.8 wt% H₂O; Head and Wilson, 1987), thus confirming that LF height can be used as a reliable indication of exsolved magma gas (water) content (Head and Wilson, 1987).

Using the scheme proposed by Newhall and Self (1982), we have used the erupted volume as the primary parameter for estimating the Volcanic Explosivity Index (VEI) of each event. We have attributed to erupted volumes $<0.5 \times 10^6 \text{ m}^3$ and/or durations of $< 1 \text{ h}$ a VEI = 2; VEI = 4 for volumes greater than $2.0 \times 10^6 \text{ m}^3$ and/or durations $> 3 \text{ h}$; and VEI = 3 for all events in between these two end-members. Most of the explosive events listed in **Table 1** can be classified as eruptions having VEI 3, based on their durations (1–3 h), erupted volumes (between 0.5 and $2 \times 10^6 \text{ m}^3$) and eruptive column height (3–15 km). Only a few (e.g., 18 February 2011) have erupted volumes so small ($\sim 95 \times 10^3 \text{ m}^3$) to be classified as having VEI = 2 (**Table 5**). **Table 5** lists an estimation of VEI for each of the LF events occurring at Etna between 2011 and 2015.

For the events 16, 29, 40, 44, and 45 (**Tables 1, 5**) where no volumes are available, VEI has been suggested on the basis of duration. Observing the results displayed in **Table 5**, the first phase of activity, from 11 January 2011 to 24 April 2012, is characterized by 20 VEI 3 plus 4 VEI 2 and 1 VEI 4 events, indicating a steady-state of the volcano as already proposed by Bonaccorso and Calvari (2013) on the basis of just volume estimations. The second phase, from 19 February to 27 April 2013, is very short and comprises 7 VEI 2 and 6 VEI 3 events, suggesting that a new input of gas-rich magma entered the shallow supply system (Bruno et al., 2016) that emptied during the July–October 2012 mainly effusive BN activity (Cannata et al., 2015; Slatcher et al., 2015; Spampinato et al., 2015). The third phase, from 26 October to December 2013, showed a significant change in the supply system, involving more than one crater (26 October 2013 event, **Table 1**) and comprising the most explosive NSEC event (23 November 2013, **Table 1**) during which no lava flows have been erupted. This phase comprises 3 VEI 4 and 3 VEI 3 events, is more powerful and variable, and forecasts the activation of the deeper storage and of the VOR crater that was

inactive since 1999 (Corsaro et al., 2017; Cannata et al., 2018). The fourth and final phase here considered (3–5 December 2015, **Table 1**) produced 2 VEI 4 and 2 VEI 3 events (**Table 5**) and high volumes erupted in a short time. Also this phase is followed by a mainly effusive eruption, with the degassed magma being quietly erupted by VOR during 17–25 May 2016 (Edwards et al., 2018). Thus, the estimation of VEI over time gives insights on the state of the volcano and its changes, with a steady-state displayed by constant and low VEI (2–3), and significant changes in the supply system marked by an increase in VEI (3–4).

Each paroxysmal event is characterized by three phases, clearly visible in **Figure 5**: (1) an initial gradual increase of the LF heights; (2) a climax; and (3) a sharply declining phase often accompanied by lava flow output, as already observed by Ganci et al. (2012). These phases, following Head and Wilson (1987), reveal: (1) an initial low gas content release, during the eruption of the gas-poor magma resident in the shallow supply system and left over after the end of the previous explosive event; (2) the output of the gas-rich magma pocket intruded into the system and accumulated at depth to form a foam layer (Allard et al., 2005; Calvari et al., 2011); and (3) the exhaustion of the gas within the magma and the fast passage to either strombolian or effusive conditions.

The two sequences described here, produced by the NSEC (40 events) and by VOR (4 events) displayed very different features. **Figure 3** clearly depicts the different size between the first event occurring at the NSEC in 2011 (**Figure 3A**) and the first event of VOR in 2015 (**Figure 3B**), with greater size of both LF and ash plume for the VOR event. In addition, the events from VOR occurred in a very short time (3 days), had TADR comprised between 199 and $776 \text{ m}^3 \text{ s}^{-1}$ and maximum height of the LF between 1,123 and 4,100 m, and durations of 3,900–6,840 s, and did not produce lava flows (**Table 1**). By contrast, the events produced by the NSEC occurred in 3 years, had much lower TADR ($23\text{--}171 \text{ m}^3 \text{ s}^{-1}$) and maximum heights of the LF (176–1,950 m), and greater durations (1,740–65,100 s), were accompanied by lava flow output, with the outsider event of 23 November 2013, which, unlike all other NSEC events, did not erupt lava flows and had LF that reached the huge elevation of 3,400 m above the crater, when all other NSEC events were normally in the range 800–1,200 m (**Table 1**). The two different features are compatible with the different depth of the source region, much deeper for VOR (1.5 km b.s.l.; Bonaccorso and Calvari, 2017) and shallower for NSEC (Bonaccorso et al., 2013a,b; Cannata et al., 2015). The deeper source for VOR also results in a more primitive erupted magma (Corsaro et al., 2017). It is worth noting that VOR erupted just pyroclastics, whereas NSEC had weaker LF generally accompanied by the output of degassed lava flows.

All LF events have displayed an associated ash plume, whose size and shape depends essentially on the interplay between the volume of pyroclastics erupted in the unit of time (IER, here calculated at 1 min intervals; Harris et al., 2007) and the wind speed affecting the summit of the volcano at the time of eruption (Bonadonna and Phillips, 2003). **Table 1** shows that in general at Mt. Etna, low wind speed ($<10 \text{ m s}^{-1}$) results in strong plumes, whereas high wind speed ($>10 \text{ m s}^{-1}$) causes

¹ ANSA (2018). http://www.ansa.it/sito/notizie/mondo/2018/05/17/hawaii-allarme-rosso-per-colonna-di-cenere-dal-vulcano_cd92ade5-4066-445e-bbf2-464833d0db52.html; <https://www.theguardian.com/us-news/2018/may/17/hawaii-kilauea-volcano-erupts-releasing-30000ft-plume-of-ash>.

TABLE 5 | Event numbers (first column) and dates (second column) of lava fountains of NSEC (events from 1 to 45) and VOR (events from 46 to 49).

Event number	Date dd/mm/yy	Vent	Duration of lava fountain (hh:mm)	Volume of pyro (m ³)	TADR (m ³ s ⁻¹)	Hav (m)	Plume height (m)	VEI	Q (kg s ⁻¹)	Hp1 (m a.s.l.) This study	Hp2 (m a.s.l.) Sparks et al. (1997)	Hp3 (m a.s.l.) Woodhouse et al. (2013)
1	12/01/11	NSEC	01:40	850,000*	142	334	9,000*	3	375,417	8,587	6,024	8,180
2	18/02/11	NSEC	00:29	95,250	55	95		2	145,060	7,330	4,709	6,431
3	10/04/11	NSEC	04:10	1,434,400	96	308	7,800**	3	253,411	8,450	5,441	7,406
4	12/05/11	NSEC	02:17	1,107,380	135	331		3	357,001	8,571	5,946	8,077
5	09/07/11	NSEC	01:43	678,370	110	520	8,200**	3	290,888	9,565	5,639	7,669
6	19/07/11	NSEC	02:10	941,360	121	487		3	319,822	9,392	5,779	7,855
7	25/07/11	NSEC	04:06	1,311,680	89	289		3	235,499	8,350	5,339	7,270
8	30/07/11	NSEC	01:04	777,510	105	308		3	276,935	8,450	5,568	7,574
9	05/08/11	NSEC	01:54	975,970	143	685		3	378,117	10,433	6,035	8,195
10	12/08/11	NSEC	02:18	815,420	99	222	9,500 ^{§§}	3	260,972	7,998	5,483	7,461
11	20/08/11	NSEC	00:52	342,280	110	411	9,300**	2	290,716	8,992	5,638	7,668
12	29/08/11	NSEC	01:10	476,290	113	453	7,800**	2	300,518	9,213	5,687	7,733
13	08/09/11	NSEC	01:28	553,960	105	375	10,900**	3	278,031	8,803	5,573	7,582
14	19/09/11	NSEC	01:05	501,500	129	509	5,000**	3	340,766	9,507	5,875	7,982
15	28/09/11	NSEC	00:58	269,570	85	271		2	224,640	8,255	5,274	7,184
16	08/10/11	NSEC	02:55	–	–	–		3?	–	–	–	–
17	23/10/11	NSEC	01:46	524,300	82	238	6,000 ^{°°}	3	218,458	8,082	5,236	7,133
18	15/11/11	NSEC	01:13	594,480	136	590	11,100**	3	359,675	9,933	5,958	8,092
19	05/01/12	NSEC	01:35	818,420	144	464	>9,000 ⁼	3	380,492	9,271	6,045	8,208
20	08-09/02/12	NSEC	06:08	2,105,970	95	289	9,000 ⁼	4	252,754	8,350	5,437	7,401
21	04/03/12	NSEC	02:13	1,335,420	167	444	9,000 ⁼	3	443,468	9,165	6,290	8,533
22	18/03/12	NSEC	02:33	1,439,050	157	669	> 9,000 ⁼	3	415,412	10,349	6,184	8,393
23	01/04/12	NSEC	01:53	901,100	133	682		3	352,201	10,417	5,925	8,049
24	12/04/12	NSEC	03:06	929,030	83	649	7,500**	3	220,602	10,244	5,249	7,151
25	23-24/04/12	NSEC	02:50	641,280	63	688		3	166,607	10,449	4,881	6,661
26	19/02/13	NSEC	01:14	611,340	138	634		3	364,879	10,165	5,980	8,122
27	20/02/13-am	NSEC	01:10	529,830	126	515		3	334,299	9,539	5,846	7,944
28	20/02/13-pm	NSEC	01:06	295,700	75	212		2	197,881	7,945	5,103	6,957
29	21/02/13	NSEC	00:35	–	–	–		2?	–	–	–	–
30	23/02/13	NSEC	00:56	426,830	127	590		2	336,638	9,933	5,856	7,958
31	28/02/13	NSEC	00:46	351,930	128	534	9,400**	2	337,904	9,639	5,862	7,965
32	05-06/03/13	NSEC	00:57	456,050	133	615		2	353,375	10,065	5,930	8,056
33	16/03/13	NSEC	00:55	444,410	135	612		2	356,877	10,049	5,946	8,076
34	03/04/13	NSEC	03:00	1,512,880	140	485	7,800**	3	371,215	9,381	6,007	8,157
35	11-12/04/13	NSEC	18:05	1,466,621	23	189	7,300**	3	59,701	7,824	3,742	5,137
36	18/04/13	NSEC	02:17	922,730	112	494	6,900**	3	297,475	9,428	5,672	7,713
37	20/04/13	NSEC	01:29	480,500	90	514		2	238,452	9,534	5,356	7,293
38	27/04/13	NSEC	03:01	1,038,250	96	312	8,500**	3	253,348	8,471	5,441	7,406
39	26/10/13	NSEC+NEC	09:00	2,672,821	83	430		4	218,610	9,092	5,237	7,135
40	11/11/13	NSEC	08:10	–	–	–		4?	–	–	–	–
41	16-17/11/13	NSEC	05:59	2,409,520	112	416		4	296,436	9,018	5,667	7,706
42	23/11/13	NSEC	01:17	789,240	171	1,075	12,600**	3	452,700	12,485	6,323	8,577
43	28/11/13	NSEC	02:24	944,860	109	348		3	289,801	8,660	5,634	7,662
44	02/12/13	NSEC	03:20	–	–	–		3?	–	–	–	–
45	28/12/14	NSEC	01:26	–	–	–		3?	–	–	–	–
46	03/12/15	VOR	01:30	4,190,000 [°]	776	1,673	15,000 [#]	4	2,056,204	14,632	9,358	12,579
47	04/12/15-am	VOR	01:22	2,760,000 [°]	561	1,264	13,400 [#]	4	1,486,585	13,814	8,604	11,588
48	04/12/15-pm	VOR	01:05	1,810,000 [°]	464	850	13,300 [#]	3	1,229,872	12,986	8,192	11,045
49	05/12/15	VOR	01:54	1,360,000 [°]	199	680	13,000 [#]	3	526,901	12,646	6,577	8,913

NSEC, New South-East Crater; NEC, North-East Crater; VOR, Voragine crater. Duration of the lava fountains and volume of pyroclastics as in **Table 1**. TADR, time averaged effusion rate, calculated only for pyroclastics erupted during the lava fountain over the entire duration of each explosive event. Hav, average height of the lava fountain. *Data from Calvari et al. (2011). °Data from Bonaccorso and Calvari (2017). **Data from Scollo et al. (2014). §§Data from Scollo et al. (2015). °°Data from Guerrieri et al. (2015). +Data from this study. **Data from (Corradini et al., 2016). #Data from Vulpiani et al. (2016). Gray lines indicate poor weather conditions and lack of visibility from cameras. VEI has been calculated from Newhall and Self (1982), see text for details. Q is source mass flux, obtained from TADR and magma density, considered as 2,650 kg m⁻³. Hp1 is the maximum plume height calculated applying (Equations 6 and 7) proposed in this study. Hp2 has been obtained by the equation from Sparks et al. (1997; $H = 1.67 \text{ TADR}^{0.259} \times 1,000$), and Hp3 from Woodhouse et al. (2013; $H = 0.318 \text{ Q}^{0.253} \times 1,000$).

weak plumes, although some exceptions occur. The importance of wind speed is revealed by the examples displayed in **Figure 6**, showing two events with similar duration, TADR and maximum height of the LF, but very different wind speed. **Figure 6** shows that, during a single event formed in conditions of low wind ($<10 \text{ m s}^{-1}$), the passage from weak to intermediate and then to a strong plume occurs at increasing IER (or LF height), and vice-versa (**Figures 6A–F**). By contrast, if a similar event develops in conditions of strong wind ($>10 \text{ m s}^{-1}$), then the resulting plume will be weak (**Figures 6G–I**). This is in agreement with the predictive models of Bursik (2001) and Woodhouse et al. (2013), who found that windy conditions require an order of magnitude increase in the source mass flux to obtain equivalent rise heights.

These results stress that evaluating paroxysmal explosive activity just on the basis of the total mass eruption rate (e.g., Corsaro et al., 2017), which is averaged over the whole duration of the event, only gives a general idea of the strength of an event. In addition, this parameter being calculated once that the eruption is finished, cannot be used for hazard purposes. If these data are made available in real time, for example using an automated routine (e.g., Cannavò et al., 2017), it is extremely important to take into account the IER measured on a much shorter lapse of time (Harris et al., 2007), given that it is ideally the instantaneous release of pyroclastics that, in steady wind conditions, defines the passage from weak to strong plume and vice-versa.

The statistical analysis on the parameters obtained from the analysis of the camera images and listed in **Table 1** confirms that the only significant associations are those for the feature pairs:

- volume of pyroclastics and fountain duration (0.66 of mean correlation);
- Mean and maximum fountain heights (0.76 of mean correlation).

The measurement of maximum plume height is a difficult parameter to obtain, because at present ground cameras have limits due to their field of view (9 km a.s.l. for the ECV camera used in this study, **Table 2**), and satellite data depend on the proximity of the satellite overpass with respect to the climax of the explosive phase, whose duration is usually quite short at Etna (**Table 1**). However, even with all these limits, if we select the available data opportunely as we did in **Table 4**, then it is possible to find a good relation between maximum plume height and average LF height, which is even better if we consider only the explosive events of VOR, during which no lava flows were involved.

In fact, using selected published parameters of H_p (**Table 4**), we were able to find two empirical formulas that relate the maximum height of the plume with the average LF height, and these might be used for forecasting a plume extent as soon as the average height of the lava fountain stabilizes. Equation (6) can be used if the eruptive crater is unknown, because for example of poor weather conditions, or if the erupting crater is the NSEC. In cases of paroxysms fed by VOR, instead it is better to use Equation (7), which also gives a lower error in the estimation of plume height.

For the lower correlation between H_p and H_f observed for the NSEC events, we consider that lava flows, spreading mainly within the Valle del Bove depression on the east flank of the volcano, where winds normally also blow the ash plume, might heat the atmosphere and increase the duration of the ash plume at high elevations. Using the regression line of these data (**Figure 4** and Equations 6 and 7) as a general formula applicable during the earlier phases of a future eruption, we can forecast the maximum elevation that an ash plume may attain as soon as the lava fountain has reached its climax, measuring this elevation from the thermal images recorded by the monitoring cameras. In addition, knowing wind speed and direction, we can immediately forecast the sector of the volcano that will be involved by ash fallout and its extension.

Figure 5 shows that plume formation is often as quick as lava fountain formation, although ash fallout on the flanks of the volcano can be observed with 20–30 min delay, as a function of wind speed. However, weak to intermediate plumes tend to decline rapidly as soon as the paroxysm ends, whereas strong plumes tend to keep the elevation of $>9 \text{ km a.s.l.}$ for most of the duration of the eruptive event, thus increasing the possibility that fine ash transported at high elevations into the atmosphere is dispersed by wind for greater distances.

For Etna, and using the examples described in this paper, we can infer that wind speed $<10 \text{ m s}^{-1}$ generally results in strong to intermediate plumes, whereas wind speed $>10 \text{ m s}^{-1}$ is normally associated with weak plumes. A second parameter, important for defining plume formation, is IER, whose effect is shown in **Figure 6**. An increasing IER in low wind conditions will give rise to weak, intermediate and then strong plumes with elevation greater than 9 km, with the opposite trend observed when IER vanishes. In conditions of strong wind instead, the plume remains below 9 km and we usually observe just weak plumes. More data, especially from satellite combined with simultaneous ground measurements, and especially with frequently measured wind speed data, are necessary to improve our ability to forecast the extension and growth of ash plumes associated with lava fountains on Etna and other volcanoes.

Equations (6) and (7) can be used for hazard purposes to calculate the maximum height that the ash plume will attain. They have the great advantage of being applied as soon as the LF mean height has been reached. We will use Equation (6) for events where is the NSEC erupting, and Equation (7) when the crater involved is VOR. Two other possibilities are to use the formula proposed by Sparks et al. (1997):

$$H = 1.67 \text{TADR}^{0.259} \quad (8)$$

where H is maximum column height (in km) and TADR is mean discharge rate ($\text{m}^3 \text{s}^{-1}$), or a similar equation proposed by Woodhouse et al. (2013):

$$H = 0.318 \text{Q}^{0.253} \quad (9)$$

where Q is source mass flux measured in kilograms per second, obtained from TADR and from magma density, considered as $2,650 \text{ kg m}^3$ (**Table 5**). However, Equations (8) and (9) are

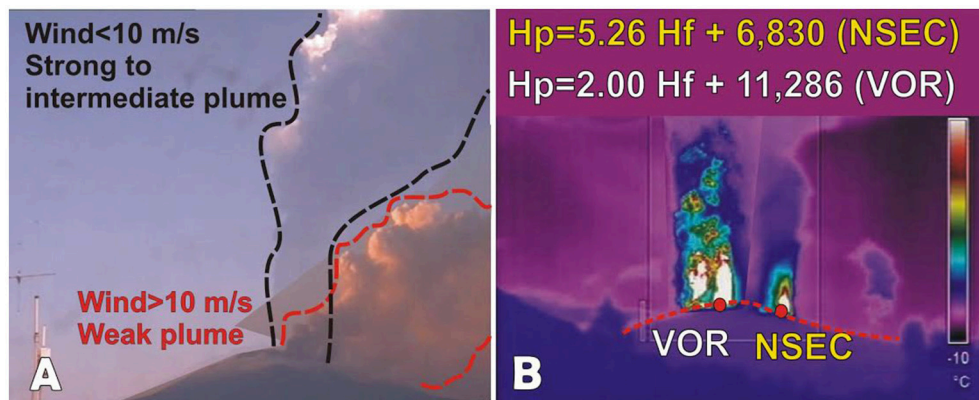


FIGURE 7 | Schemes summarizing the main results obtained in this study. **(A)** At Mt. Etna wind speed greater than 10 m/s produces a weak plume that bends and is elongated along the wind direction (red outline), whereas wind speed below 10 m/s results in strong to intermediate plumes (black outline), causing a lesser impact on the local population (since the ash fallout is mainly concentrated around the crater, although the upper portion of the eruptive column comprising the fine-grained particles is always affected by wind) but a greater effect on aviation (because the elevation of the ash plume is greater). **(B)** We have found two simple relationships between plume (H_p) and lava fountain (H_f) heights that could be used for hazard assessment as soon as the lava fountain average height is reached, expressed by the two equations for VOR (VORagine crater) and for the NSEC (New SE-Crater).

impossible to use for hazard purposes because in order to know the value of TADR or Q , we need to wait until the end of the LF event. **Table 5** presents a comparison between the plume heights from available literature, with those obtained using our Equation (6) for events 1–45 and Equation (7) for the events 46–49 and with values obtained using Equation (8) proposed by Sparks et al. (1997) and Equation (9) proposed by Woodhouse et al. (2013). As reported in **Table 5**, the values from Sparks et al. (1997) mostly result underestimated, whereas those from Woodhouse et al. (2013) are much closer to those obtained from our formulas. However, we must consider that the equation from Sparks et al. (1997) has been obtained using a number of mostly plinian eruptions from several different volcanoes, whereas our equations have been calibrated for Etna. Thus, for hazard purposes, we suggest to interpolate data collected from a single volcano in order to obtain a suitable empirical relationship.

FINAL REMARKS

Etna's LFs are significantly different from their Hawaiian counterpart. The main difference is the shape of the vent, which is normally a fissure in Hawaii, and a circular vent or bocca at Etna. Hawaiian LFs are normally 200–400 m high, whereas on Etna we measured LF up to 3–4 km in height during the lapse of time here considered (**Table 1**). Considering all other parameters as steady, we suggest that a circular vent might promote a greater vertical distribution of the erupted ash when compared to a fissure.

Even more than vent geometry, LF heights depend primarily on the amount of exsolved volatiles, with H_2O being the most abundant (92–96 mol%) and turning to zero as soon as the paroxysm ends. Etnean magmas are very water-rich basalts, with 3.4 wt% H_2O (Métrich et al., 2004) when compared to their Hawaiian counterpart (0.6–0.8 wt% H_2O ; Head and Wilson, 1987), thus confirming that LF height can be used as a reliable

indication of exsolved magma gas (water) content (Head and Wilson, 1987).

In this paper, we have presented an analysis of the images recorded by Etna's web cameras aimed at quantifying the paroxysmal explosive events occurring between 2011 and 2015. The measured parameters are listed in **Table 1** and their range of variability is reported in **Table 3**. The 44 events here described (**Table 1**) can be divided into two groups: the events from the NSEC normally have VEI 2–3 and lower LF heights, longer event duration, and lower TADR than the events produced by VOR. This is consistent with a deeper source region for the VOR events (e.g., Bonaccorso and Calvari, 2017) allowing deeper, more primitive and gas rich magma to rise rapidly along the conduit (Corsaro et al., 2017; Pompilio et al., 2017), resulting in more hazardous VEI 3–4 eruptions.

An analysis of the measured parameters did not find ready correlations between them, if we exclude those that are directly connected. This is probably due to the many variables affecting the impact of each event, with wind speed and IER playing an important role in defining the maximum extension and style of an ash plume. However, from the data presented, we can observe that in general at Mt. Etna wind speed greater than 10 m s^{-1} produces a weak plume that bends and is elongated along the wind direction, whereas wind speed below 10 m s^{-1} results in strong to intermediate plumes, causing a lower impact on the population (because the ash fallout is mainly concentrated around the crater, although the upper portion of the eruptive column comprising the fine-grained particles is always affected by wind, see **Figure 1A**) but a greater effect on aviation (because the elevation of the ash plume is greater).

For Etna, and using the examples described in this paper, we can infer that wind speed $< 10 m s^{-1}$ generally results in strong to intermediate plumes, whereas wind speed $> 10 m s^{-1}$ is normally associated with weak plumes (**Figure 7A**). A second parameter,

important for defining plume formation, is IER (**Figure 6**). An increasing IER in low wind conditions will give rise to weak, intermediate and then strong plumes with elevation greater than 9 km, with the opposite trend observed when IER vanishes. In conditions of strong wind instead, the plume remains below 9 km and we usually observe just weak plumes. We have found a simple relationship between plume and LF heights that could be used for hazard assessment as soon as the LF average height is reached, expressed by the (Equations 6 and 7; **Figure 7B**). The results are better for VOR, because the events produced by this crater did not involve emission of lava flows, thus the whole volume erupted went into the proximal fallout and ash plume. On the contrary, all paroxysms produced by the NSEC, apart from that of 23 November 2013 (Bonaccorso et al., 2014), were associated with lava flow output, thus also involving the emission of degassed magma at the end of each event. In addition, the lava flow spreading mainly within the Valle del Bove, on the east flank of the volcano, where winds normally blow the ash plume, causes heat release and then possibly a plume staying at high elevation for longer time when compared to VOR. More

data are necessary to improve our knowledge of these events and our ability to predict their impact, especially by comparing both satellite and ground data and having more frequent wind speed measurements.

AUTHOR CONTRIBUTIONS

All authors listed have made a substantial, direct and intellectual contribution to the work, and approved it for publication.

ACKNOWLEDGMENTS

We thank T. Caltabiano for extracting wind speed and direction from meteorological data provided by the Hydro-Meteorological Service of the Emilia-Romagna Regional Agency for Environmental Protection (ARPA-SIM), and E. Pecora, E. Biale, and M. Prestifilippo for the camera network maintenance. We thank S. Conway for revising the text. A previous version of the manuscript was significantly improved by the comments of two reviewers.

REFERENCES

- Allard, P., Burton, M., and Muré, F. (2005). Spectroscopic evidence for a lava fountain driven by previously accumulated magmatic gas. *Nature* 433, 407–410. doi: 10.1038/nature03246
- Aloisi, M., Jin, S., Pulvirenti, F., and Scaltrito, A. (2017). The December 2015 Mount Etna eruption: an analysis of inflation/deflation phases and faulting processes. *J. Geodynam.* 107, 34–45. doi: 10.1016/j.jog.2017.03.003
- Andò, B., and Pecora, E. (2006). An advanced video-based system for monitoring active volcanoes. *Comput. Geosci.* 32, 85–91. doi: 10.1016/j.cageo.2005.05.004
- Andronico, D., Behncke, B., De Beni, E., Cristaldi, A., Scollo, S., Lopez, M., et al. (2018). Magma Budget from Lava and Tephra Volumes erupted during the 25–26 October 2013 Lava Fountain at Mt Etna. *Front. Earth Sci.* 6:116. doi: 10.3389/feart.2018.00116
- Andronico, D., Branca, S., Calvari, S., Burton, M. R., Caltabiano, T., Corsaro, R. A., et al. (2005). A multi-disciplinary study of the 2002–03 Etna eruption: insights for into a complex plumbing system. *Bull. Volcanol.* 67, 314–330. doi: 10.1007/s00445-004-0372-8
- Andronico, D., and Corsaro, R. A. (2011). Lava fountains during the episodic eruption of South–East Crater (Mt. Etna), 2000: insights into magma-gas dynamics within the shallow volcano plumbing system. *Bull. Volcanol.* 73, 1165–1178. doi: 10.1007/s00445-011-0467-y
- Andronico, D., Scollo, S., Caruso, S., and Cristaldi, A. (2008). The 2002–03 Etna explosive activity: tephra dispersal and features of the deposits. *J. Geophys. Res.* 113:B04209. doi: 10.1029/2007JB005126
- Andronico, D., Scollo, S., and Cristaldi, A. (2015). Unexpected hazards from tephra fallouts at Mt Etna: the 23 November 2013 lava fountain. *J. Volcanol. Geother. Res.* 304, 118–125. doi: 10.1016/j.jvolgeores.2015.08.007
- Andronico, D., Spinetti, C., Cristaldi, A., and Buongiorno, M. F. (2009). Observations of Mt. Etna volcanic ash plumes in 2006: an integrated approach from ground-based and polar satellite NOAA–AVHRR monitoring system. *J. Volcanol. Geother. Res.* 180, 135–147. doi: 10.1016/j.jvolgeores.2008.11.013
- Athanassiadou, M. (2016). The Mt Etna SO₂ eruption in December 2015 – the view from space. *R. Meteorol. Soc.* 71, 273–279. doi: 10.1002/wea.2794
- Azzopardi, F., Ellul, R., Prestifilippo, M., Scollo, S., and Coltelli, M. (2013). The effect of Etna volcanic ash clouds on the Maltese Islands. *J. Volcanol. Geother. Res.* 260, 13–26. doi: 10.1016/j.jvolgeores.2013.04.019
- Balakrishnan, N. (1992). *Handbook of the Logistic Distribution*. New York, NY: Marcel Dekker.
- Balakrishnan, N., and Basu, A. P. (1996). *The Exponential Distribution: Theory, Methods, and Applications*. New York, NY: Gordon and Breach.
- Baxter P. J. (2010). “Impacts of eruptions on human health,” in *Encyclopedia of Volcanoes*, eds H. Sigurdsson, B. Houghton, S. McNutt, H. Rymer, and J. Stix (San Diego, CA: Academic Press), 1035–1043.
- Behncke, B., Branca, S., Corsaro, R. A., De Beni, E., Miraglia, L., and Proietti, C. (2014). The 2011–2012 summit activity of Mount Etna: birth, growth and products of the new SE crater. *J. Volcanol. Geother. Res.* 270, 10–21. doi: 10.1016/j.jvolgeores.2013.11.012
- Bombrun, M., Jessop, D., Harris, A., and Barra, V. (2018). An algorithm for the detection and characterisation of volcanic plumes using thermal camera imagery. *J. Volcanol. Geother. Res.* 352, 26–37. doi: 10.1016/j.jvolgeores.2018.01.006
- Bonaccorso, A., and Calvari, S. (2013). Major effusive eruptions and recent lava fountains: balance between erupted and expected magma volumes at Etna volcano. *Geophys. Res. Lett.* 40, 6069–6073. doi: 10.1002/2013GL058291
- Bonaccorso, A., and Calvari, S. (2017). A new approach to investigate an eruptive paroxysmal sequence using camera and strainmeter networks: lessons from the 3–5 December 2015 activity at Etna volcano. *Earth Planet. Sci. Lett.* 475, 231–241. doi: 10.1016/j.epsl.2017.07.020
- Bonaccorso, A., Calvari, S., Currenti, G., Del Negro, C., Ganci, G., Linde, A., et al. (2013a). From source to surface: dynamics of Etna's lava fountains investigated by continuous strain, magnetic, ground and satellite thermal data. *Bull. Volcanol.* 75:690. doi: 10.1007/500445-013-0690
- Bonaccorso, A., Calvari, S., Linde, A., and Sacks, S. (2014). Eruptive processes leading to the most explosive lava fountain at Etna volcano: the 23 November 2013 episode. *Geophys. Res. Lett.* 41, 4912–4919. doi: 10.1002/2014GL060623
- Bonaccorso, A., Currenti, G., Linde, A., and Sacks, S. (2013b). New data from borehole strainmeters to infer lava fountain sources (Etna 2011–2012). *Geophys. Res. Lett.* 40, 3579–3584. doi: 10.1002/grl.50692
- Bonadonna, C., and Phillips, J. C. (2003). Sedimentation from strong volcanic plumes. *J. Geophys. Res.* 108:2340. doi: 10.1029/2002JB002034
- Bonadonna, C., Pistolesi, M., Cioni, R., Degruyter, W., Elisondo, M., and Baumann, V. (2015). Dynamics of wind-affected volcanic plumes: the example of the 2011 Cordón Caulle eruption, Chile. *J. Geophys. Res.* 120, 1–20. doi: 10.1002/2014JB011478
- Box, G. E. P., and Cox, D. R. (1964). An analysis of transformations. *J. R. Stat. Soc. Series B* 26, 211–252.
- Bruno, V., Ferlito, C., Mattia, M., Monaco, C., Rossi, M., and Scandura, D. (2016). Evidence of a shallow magma intrusion beneath the NE Rift system of Mt. Etna during 2013. *Terra Nova* 28, 356–363. doi: 10.1111/ter.12228

- Burnham, K. P., and Anderson, D. R. (2003). *Model Selection and Multimodel Inference: A Practical Information-Theoretic Approach*. New York, NY: Springer Science & Business Media.
- Bursik, M. (2001). Effect of wind on the rise height of volcanic plumes. *Geophys. Res. Lett.* 28, 3621–3624. doi: 10.1029/2001GL013393
- Calvari, S., Neri, M., Pompilio, M., and Scribano, V. (1994). Etna: eruptive activity. *Acta Vulcanologica* 6, 1–3.
- Calvari, S., Salerno, G. G., Spampinato, L., Gouhier, M., La Spina, A., Pecora, E., et al. (2011). An unloading foam model to constrain Etna's 11–13 January 2011 lava fountaining episode. *J. Geophys. Res.* 116:B11207. doi: 10.1029/2011JB008407
- Calvari, S., and the whole scientific staff of INGV-Sezione di Catania (2001). Multidisciplinary approach yields insight into Mt. Etna 2001 Eruption. *EOS Trans. Am. Geophys. Union* 82, 653–656. doi: 10.1029/01EO00376
- Cannata, A., Di Grazia, G., Giuffrida, M., Gresta, S., Palano, M., Sciotto, M., et al. (2018). Space-time evolution of magma storage and transfer at Mt. Etna Volcano (Italy): the 2015–2016 re-awakening of voragine crater. *Geochem. Geophys. Geosyst.* 19, 471–495. doi: 10.1002/2017GC007296
- Cannata, A., Spedalieri, G., Behncke, B., Cannavò F., Di Grazia, G., Gambino, G., et al. (2015). Pressurization and depressurization phases inside the plumbing system of Mount Etna volcano: evidence from a multiparametric approach. *J. Geophys. Res.* 120:1–18. doi: 10.1002/2015JB012227
- Cannavò, F. A., Cannata, C., Cassisi, G., Di Grazia, P., Montalto, M., Prestifilippo, E., et al. (2017). A multivariate probabilistic graphical model for real-time volcano monitoring on Mount Etna. *J. Geophys. Res.* 122, 3480–3496. doi: 10.1002/2016JB013512
- Carbone, D., Zuccarello, L., Messina, A., Scollo, S., and Rymer, H. (2015). Balancing bulk gas accumulation and gas output before and during lava fountaining episodes at Mt. Etna. *Sci. Rep.* 5:18049. doi: 10.1038/srep18049
- Carey, S. N., and Sparks, R. S. J. (1986). Quantitative models of the fallout and dispersal of tephra from volcanic eruption columns. *Bull. Volcanol.* 48, 109–125.
- Chhikara, R., and Folks, L. (1989). *The Inverse Gaussian Distribution: Theory, Methodology and Applications*. New York, NY: Marcel Dekker.
- Clarke, A. B., Voight, B., Neri, A., and Macedonio, G. (2002). Transient dynamics of vulcanian explosions and column collapse. *Nature* 415, 897–901. doi: 10.1038/415897a
- Cohen, J. (1988). *Statistical Power Analysis for the Behavioral Sciences*. New York, NY: Routledge.
- Coltelli, M., d'Aranno, P. J. V., de Bonis, R., Guerrero Tello, J. F., Marsella, M., Nardinocchi, C., et al. (2017). The use of surveillance cameras for the rapid mapping of lava flows: an application to Mount Etna Volcano. *Remote Sens.* 9:192. doi: 10.3390/rs9030192
- Corradini, S., Montopoli, M., Guerrieri, L., Ricci, M., Scollo, S., Merucci, L., et al. (2016). A multi-sensor approach for volcanic ash cloud retrieval and eruption characterization: the 23 November 2013 Etna Lava Fountain. *Remote Sens.* 8:58. doi: 10.3390/rs8010058
- Corsaro, R. A., Andronico, D., Behncke, B., Branca, S., Caltabiano, T., Ciancitto, F., et al. (2017). Monitoring the December 2015 summit eruptions of Mt. Etna (Italy): implications on eruptive dynamics. *J. Volcanol. Geother. Res.* 341, 53–69. doi: 10.1016/j.jvolgeores.2017.04.018
- De Beni, E., Behncke, B., Branca, S., Nicolosi, I., Carluccio, R., D'Ajello Caracciolo, F., et al. (2015). The continuing story of Etna's New Southeast Crater (2012–2014): evolution and volume calculations based on field surveys and aerophotogrammetry. *J. Volcanol. Geother. Res.* 303, 175–186. doi: 10.1016/j.jvolgeores.2015.07.021
- Del Negro, C., Currenti, G., Solaro, G., Greco, F., Pepe, A., Napoli, R., et al. (2013). Capturing the fingerprint of Etna volcano activity in gravity and satellite radar data. *Sci. Rep.* 3:3089. doi: 10.1038/srep03089
- Dellino, P., and Kyriakopoulos, K. (2003). Phreatomagmatic ash from the ongoing eruption of Etna reaching the Greek island of Cefalonia. *J. Volcanol. Geother. Res.* 126, 341–345. doi: 10.1016/S0377-0273(03)00154-9
- Donnadieu, F., Freville, P., Hervier, C., Coltelli, M., Scollo, S., Prestifilippo, M., et al. (2016). Near-source Doppler radar monitoring of tephra plumes at Etna. *J. Volcanol. Geother. Res.* 312, 26–39. doi: 10.1016/j.jvolgeores.2016.01.009
- Edwards, M. J., Pioli, L., Andronico, D., Scollo, S., Ferrari, F., and Cristaldi, A. (2018). Shallow factors controlling the explosivity of basaltic magmas: the 17–25 May 2016 eruption of Etna volcano (Italy). *J. Volcanol. Geother. Res.* 357, 425–436. doi: 10.1016/j.jvolgeores.2018.05.015
- Ganci, G., Harris, A. J. L., Del Negro, C., Guéhenneux, Y., Cappello, A., Labazuy, P., et al. (2012). A year of lava fountaining at Etna: volumes from SEVIRI. *Geophys. Res. Lett.* 39:L06305. doi: 10.1029/2012GL051026
- Giuffrida, M., Viccaro, M., and Ottolini, L. (2018). Ultrafast syn-eruptive degassing and ascent trigger high-energy basic eruptions. *Sci. Rep.* 8:147. doi: 10.1038/s41598-017-18580-8
- Gouhier, M., Harris, A. J. L., Calvari, S., Labazuy, P., Guéhenneux, Y., Donnadieu, F., et al. (2012). Lava discharge during Etna's January 2011 fire fountain tracked using MSG-SEVIRI. *Bull. Volcanol.* 74, 787–793. doi: 10.1007/s00445-011-0572-y
- Guerrieri, L., Merucci, L., Corradini, S., and Pugnaghi, S. (2015). Evolution of the 2011 Mt. Etna ash and SO₂ lava fountain episodes using SEVIRI data and VPR retrieval approach. *J. Volcanol. Geother. Res.* 291, 63–71. doi: 10.1016/j.jvolgeores.2014.12.016
- Harris, A. J. L., Dehn, J., and Calvari, S. (2007). – Lava effusion rate definition and measurement: a review. *Bull. Volcanol.* 70, 1–22. doi: 10.1007/s00445-007-0120-y
- Harris, A. J. L., Steffke, A., Calvari, S., and Spampinato, L. (2011). Thirty years of satellite-derived lava discharge rates at Etna: implications for steady volumetric output. *J. Geophys. Res.* 116:B08204. doi: 10.1029/2011JB008237
- Harris, A. J. L., Steffke, A., Calvari, S., and Spampinato, L. (2012). Correction to “Thirty years of satellite-derived lava discharge rates at Etna: implications for steady volumetric output”. *J. Geophys. Res.* 117:B08207. doi: 10.1029/2012JB009431
- Hazewinkel, M. (2001). *Correlation (in Statistics) in Encyclopedia of Mathematics*. Springer Netherlands.
- Head, J. W. III., and Wilson, L. (1987). Lava fountain heights at Pu'u 'O'o, Kilauea, Hawaii: indicators of amount and variations of exsolved magma volatiles. *J. Geophys. Res.* 92:B13. 13,715–13,719.
- Horwell, C. J., Sargent, P., Andronico, D., Lo Castro, M. D., Tomatis, M., Hillman, S. E., et al. (2017). The iron-catalysed surface reactivity and health-pertinent physical characteristics of explosive volcanic ash from Mt. Etna, Italy. *J. Appl. Volcanol.* 6:12. doi: 10.1186/s13617-017-0063-8
- Kendall, M. G., and Gibbons, J. D. (1990). *Rank Correlation Methods, 5th Edn*. London: Edward Arnold.
- Kowalski, C. J. (1972). On the effects of non-normality on the distribution of the sample product-moment correlation coefficient. *Appl. Stat.* 21, 1–12.
- Martin, R. S., Watt, S. F. L., Pyle, D. M., Mather, T. A., Matthews, N. E., Georg, R. B., et al. (2009). Environmental effects of ashfall in Argentina from the 2008 Chaitén volcanic eruption. *J. Volcanol. Geother. Res.* 184, 462–472. doi: 10.1016/j.jvolgeores.2009.04.010
- Métrich, N., Allard, P., Spilliaert, N., Andronico, D., and Burton, M. (2004). 2001 flank eruption of the alkali- and volatile-rich primitive melt responsible for Mount Etna's evolution in the last three decades. *Earth Planet. Sci. Lett.* 288, 1–17. doi: 10.1016/j.epsl.2004.09.036
- Montopoli, M. (2016). Velocity profiles inside volcanic clouds from three-dimensional scanning microwave dual-polarization Doppler radars. *J. Geophys. Res. Atm.* 121, 7881–7900. doi: 10.1002/2015JD023464
- Neri, M., De Maio, M., Crepaldi, S., Suozzi, E., Lavy, M., Marchionatti, F., et al. (2017). Topographic maps of Mount Etna summit Crater's Area, 14 December 2015. *J. Maps* 13, 674–683. doi: 10.1080/17445647.2017.1352041
- Newhall, C. G., and Self, S. (1982). The volcanic explosivity index (VEI): an estimate of explosive magnitude for historical volcanism. *J. Geophys. Res.* 87, 1231–1238. doi: 10.1029/JC087iC02p01231
- Parcheta, C. E., Houghton, B. F., and Swanson, D. A. (2012). Hawaiian fissure fountains 1: decoding deposits—episode 1 of the 1969–1974 Mauna Ulu eruption. *Bull. Volcanol.* 74, 1729–1743. doi: 10.1007/s00445-012-0621-1
- Patrick, M. R. (2007). Dynamics of Strombolian ash plumes from thermal video: motion, morphology, and air entrainment. *J. Geophys. Res.* 112:B06202. doi: 10.1029/2006JB004387
- Patrick, M. R., Harris, A. J. L., Ripepe, M., Dehn, J., Rothery, D. A., Calvari, S. (2007). – Strombolian explosive styles and source conditions: insights from thermal (FLIR) video. *Bull. Volcanol.* 69:769. doi: 10.1007/s00445-006-0107-0
- Patrick, M. R., Swanson, D., and Orr, T. (2016). Automated tracking of lava lake level using thermal images at Kilauea Volcano, Hawai'i. *J. Appl. Volcanol.* 5:6. doi: 10.1186/s13617-016-0047-0

- Pearson, K. (1895). Notes on regression and inheritance in the case of two parents. *Proc. R. Soc. Lond.* 58: 240–242.
- Pompilio, M., Bertagnini, A., Del Carlo, P., and Di Roberto, A. (2017). Magma dynamics within a basaltic conduit revealed by textural and compositional features of erupted ash: the December 2015 Mt. Etna paroxysms. *Sci. Rep.* 7:4805. doi: 10.1038/s41598-017-05065-x
- Rinne, H. (2011). “Location-scale distributions,” in *International Encyclopedia of Statistical Science*, ed M. Lovric (Berlin; Heidelberg: Springer), 752–754.
- Sahetapy-Engel, S. T., and Harris, A. J. L. (2009). Thermal-image-derived dynamics of vertical ash plumes at Santiaguito volcano, Guatemala. *Bull. Volcanol.* 71, 827–830. doi: 10.1007/s00445-009-0284-8
- Schmith, J., Hoskuldsson, A., Holm, P. M., and Larsen, G. (2018). Large explosive basaltic eruptions at Katla volcano, Iceland: fragmentation, grain size and eruption dynamics. *J. Volcanol. Geother. Res.* 354, 140–152. doi: 10.1016/j.jvolgeores.2018.01.024
- Scollo, S., Boselli, A., Coltelli, M., Leto, G., Pisani, G., Prestifilippo, M., et al. (2015). Volcanic ash concentration during the 12 August 2011 Etna eruption. *Geophys. Res. Lett.* 42, 2634–2641. doi: 10.1002/2015GL063027
- Scollo, S., Prestifilippo, M., Pecora, E., Corradini, S., Merucci, L., Spata, G., et al. (2014). Eruption column height estimation of the 2011–2013 Etna lava fountains. *Ann. Geophys.* 77:S0214. doi: 10.4401/ag-6396
- Shapiro, S. S., and Wilk, M. B. (1965). An analysis of variance test for normality (complete samples). *Biometrika* 52, 591–611.
- Slatcher, N., James, M. R., Calvari, S., Ganci, G., and Browning, J. (2015). Quantifying effusion rates at active volcanoes through integrated time-lapse laser scanning and photography. *Remote Sens.* 7, 14967–14987. doi: 10.3390/rs71114967
- Spampinato, L., Calvari, S., Oppenheimer, C., and Lodato, L. (2008). Shallow magma transport for the 2002–03 Mt. Etna eruption inferred from thermal infrared surveys. *J. Volcanol. Geother. Res.* 177, 301–312. doi: 10.1016/j.jvolgeores.2008.05.013
- Spampinato, L., Sciotto, M., Cannata, A., Cannavò, F., La Spina, A., Palano, M., et al. (2015). Multiparametric study of the February–April 2013 paroxysmal phase of Mt. Etna New South-East crater, *Geochem. Geophys. Geosyst.* 16, 1932–1949. doi: 10.1002/2015GC005795
- Sparks, R. S. J., Bursik, M. I., Carey, S. N., Gilbert, J. S., Glaze, L. S., Sigurdsson, H., et al. (1997). *Volcanic Plumes*. Chichester: John Wiley & Sons.
- Spearman, C. (1904). The proof and measurement of association between two things. *Am. J. Psychol.* 15, 72–101.
- Steinskog, D. J. (2007). A cautionary note on the use of the Kolmogorov-Smirnov test for normality. *Am. Meteor. Soc.* 135, 1151–1157. doi: 10.1175/MWR3326.1
- Taddeucci, J., Alatorre-Ibargüen, M. A., Moroni, M., Tornetta, L., Capponi, A., Scarlato, P., et al. (2012). Physical parameterization of Strombolian eruptions via experimentally-validated modeling of high-speed observations. *Geophys. Res. Lett.* 39:L16306. doi: 10.1029/2012GL052772
- Tournigand, P.-Y., Taddeucci, J., Gaudin, D., Peña Fernández, J. J., Del Bello, E., Scarlato, P., et al. (2017). The initial development of transient volcanic plumes as a function of source conditions. *J. Geophys. Res. Solid Earth* 122, 9784–9803. doi: 10.1002/2017JB014907
- Vulpiani, G., Ripepe, M., and Valade, S. (2016). Mass discharge rate retrieval combining weather radar and thermal camera observations. *J. Geophys. Res. Solid Earth* 121, 5679–5695. doi: 10.1002/2016JB013191
- Wadge, G., and Guest, J. E. (1981). Steady-state magma discharge at Etna 1971–81. *Nature* 294, 548–550.
- Walker, G. P. L. (1980). The Taupo pumice: product of the most powerful known (Ultraplinian) eruption? *J. Volcanol. Geother. Res.* 8, 69–94.
- Wilson, L., and Head, J. W. III. (1981). Ascent and eruption of basaltic magma on the Earth and Moon. *J. Geophys. Res.* 86, 2971–3001. doi: 10.1029/JB086iB04p02971
- Wilson, L., Parfitt, E. A., and Head, J. W. III. (1995). Explosive volcanic eruptions-VIII. The role of magma recycling in controlling the behaviour of Hawaiian-style lava fountains. *Geophys. J. Int.* 121, 215–225. doi: 10.1111/j.1365-246X.1995.tb03522.x
- Wolfe, E. W., Neal, C. A., Banks, N. G., and Duggan, T. J. (1988). Geologic observations and chronology of eruptive events. *USGS Prof. Paper* 1463, 1–98.
- Woodhouse, M. J., Hogg, A. J., Phillips, J. C., and Sparks, R. S. J. (2013). Interaction between volcanic plumes and wind during the 2010 Eyjafjallajökull eruption, Iceland. *J. Geophys. Res. Solid Earth* 118, 92–109. doi: 10.1029/2012JB009592

Conflict of Interest Statement: The authors declare that the research was conducted in the absence of any commercial or financial relationships that could be construed as a potential conflict of interest.

Copyright © 2018 Calvari, Cannavò, Bonaccorso, Spampinato and Pellegrino. This is an open-access article distributed under the terms of the Creative Commons Attribution License (CC BY). The use, distribution or reproduction in other forums is permitted, provided the original author(s) and the copyright owner(s) are credited and that the original publication in this journal is cited, in accordance with accepted academic practice. No use, distribution or reproduction is permitted which does not comply with these terms.

Advantages of publishing in Frontiers



OPEN ACCESS

Articles are free to read
for greatest visibility
and readership



FAST PUBLICATION

Around 90 days
from submission
to decision



HIGH QUALITY PEER-REVIEW

Rigorous, collaborative,
and constructive
peer-review



TRANSPARENT PEER-REVIEW

Editors and reviewers
acknowledged by name
on published articles

Frontiers

Avenue du Tribunal-Fédéral 34
1005 Lausanne | Switzerland

Visit us: www.frontiersin.org

Contact us: info@frontiersin.org | +41 21 510 17 00



REPRODUCIBILITY OF RESEARCH

Support open data
and methods to enhance
research reproducibility



DIGITAL PUBLISHING

Articles designed
for optimal readership
across devices



FOLLOW US

[@frontiersin](https://twitter.com/frontiersin)



IMPACT METRICS

Advanced article metrics
track visibility across
digital media



EXTENSIVE PROMOTION

Marketing
and promotion
of impactful research



LOOP RESEARCH NETWORK

Our network
increases your
article's readership